

1
AGARD-LS-42-VOL. 1

AD 747878
AGARD-LS-42-VOL. 1

AGARD

ADVISORY GROUP FOR AEROSPACE RESEARCH & DEVELOPMENT

7 RUE ANCELLE 92 NEUILLY SUR SEINE FRANCE

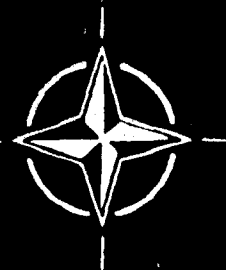
AGARD LECTURE SERIES No. 42

Volume 1

Aerodynamic Problems of Hypersonic Vehicles

8

NORTH ATLANTIC TREATY ORGANIZATION



DISTRIBUTION AND AVAILABILITY
ON BACK COVER

234

**Best
Available
Copy**

NORTH ATLANTIC TREATY ORGANIZATION
ADVISORY GROUP FOR AEROSPACE RESEARCH AND DEVELOPMENT
(ORGANISATION DU TRAITE DE L'ATLANTIQUE NORD)

AGARD Lecture Series No.42
AERODYNAMIC PROBLEMS OF HYPERSONIC VEHICLES

K.Enkenhus & J.F.Wendt
Lecture Series Directors

R.C.Pankhurst
Editor

Published in Two Volumes

VOLUME 1

Details of this series are
given in the AGARD Lecture Series
Programme.

THE MISSION OF AGARD

The mission of AGARD is to bring together the leading personalities of the NATO nations in the fields of science and technology relating to aerospace for the following purposes:

- Exchanging of scientific and technical information;
- Continuously stimulating advances in the aerospace sciences relevant to strengthening the common defence posture;
- Improving the co-operation among member nations in aerospace research and development;
- Providing scientific and technical advice and assistance to the North Atlantic Military Committee in the field of aerospace research and development;
- Rendering scientific and technical assistance, as requested, to other NATO bodies and to member nations in connection with research and development problems in the aerospace field.
- Providing assistance to member nations for the purpose of increasing their scientific and technical potential;
- Recommending effective ways for the member nations to use their research and development capabilities for the common benefit of the NATO community.

The highest authority within AGARD is the National Delegates Board consisting of officially appointed senior representatives from each Member Nation. The mission of AGARD is carried out through the Panels which are composed of experts appointed by the National Delegates, the Consultant and Exchange Program and the Aerospace Applications Studies Program. The results of AGARD work are reported to the Member Nations and the NATO Authorities through the AGARD series of publications of which this is one.

Participation in AGARD activities is by invitation only and is normally limited to citizens of the NATO nations.

Published July 1972

629.7.015.3
629.7.016.55
629.7 02



Printed by Technical Editing and Reproduction Ltd
Harford House, 7-9 Charlotte St, London. W1P 1HD

PREFACE

A Lecture Series, directed by Professor Kurt Enkenhus, was held in January, 1970 at the von Kármán Institute, Rhode-St-Genèse, near Brussels. In April, 1971 the Fluid Dynamics Panel of AGARD agreed to the publication of these lectures, to which have been added subsequently two further papers (on viscous and real-gas effects), which formed part of a VKI Lecture Series entitled High-altitude Aspects of Lifting Re-entry Vehicles, held in May, 1971, with Dr John Wendt as Lecture Series Director.

The resultant set of papers now appears in two volumes. The second of these is concerned entirely with propulsion, and has already been published as ONERA Note Technique No.169 ("Propulsion des véhicules hypersoniques", 1970); acknowledgement is due to ONERA, France, for permission to reproduce this paper in its original form.

Acknowledgement is also due to several of the lecturers for modifying their original manuscripts in order to make them more suitable for publication in printed form. The AGARD Fluid Dynamics Panel member responsible for review of the original material and for general editing of the publication was Dr R.C.Pankhurst (UK).

PREFACE

Un cycle de conférences a été organisé en Janvier 1970, à l'Institut von Kármán de Rhode-Saint-Cenèse, près de Bruxelles, sous la direction du Professeur Kurt Enkenhus. En Avril 1971, le Groupe de Travail de Dynamique des Fluides, de l'AGARD, approuva officiellement la publication de ces conférences, auxquelles furent ajoutées ultérieurement deux communications (sur les effets de la viscosité et des gaz réels), présentées dans le cadre d'un cycle de conférences de l'IVK sur "Les aspects, aux altitudes élevées, des véhicules de rentrée portants", qui eut lieu en mai 1971 sous la direction du Dr John Wendt.

Ces exposés font l'objet de deux volumes. Le second est entièrement consacré à la propulsion et a déjà été publié par l'ONERA en tant que Note Technique No. 169 ("Propulsion des véhicules supersoniques", 1970). Nous remercions l'ONERA (France) de nous avoir permis de reproduire cette publication sous sa forme originale.

Nous exprimons également nos remerciements aux conférenciers qui ont modifié le texte original de leurs exposés afin de les rendre plus adaptés à l'impression. Le membre du Groupe de Travail de Dynamique des Fluides de l'AGARD, responsable de la révision des textes originaux et de leur préparation à la publication, est le Dr R.C.Pankhurst (Royaume Uni).

GENERAL INTRODUCTION

The purpose of the Lecture Series on "Aerodynamic Problems of Hypersonic Vehicles" held in January 1970 was to review current progress on specific areas of hypersonic vehicle design. Some general conclusions from the course can be stated. The cost of developing hypersonic air-breathing propulsion systems is so high that the design of vehicles using hypersonic ramjets is continually being postponed. It was speculated that the next development we were likely to see would be the orbital ferry, a two-stage rocket-propelled vehicle with recoverable stages, a prediction that is presently being fulfilled by the NASA Space Shuttle. The aerodynamics and propulsion of air-breathing vehicles are so closely interrelated that no progress can be made without considering both problems simultaneously. Interesting lectures on vehicle optimisation were presented in which a generalised approach was used and the concept of the wave-rider was thoroughly discussed. Heating was highlighted as one of the most important problem areas in the aerodynamic design of hypersonic vehicles. Considerable emphasis was placed on the need to develop large hypersonic facilities in which complete configurations can be tested and on the desirability of conducting free-flight tests.

Two papers that fall within the general subject area of hypersonic aerodynamics were presented at another VKI course held in May 1971. They treated the subjects of viscous interaction and non-equilibrium real-gas heat transfer respectively, and thus contributed information on the high-altitude aspects of high-speed flight. Methods for treating two-dimensional viscous flows with the combined effects of incidence, displacement, and bluntness were reviewed as well as current efforts on such subjects as finite-chord and finite-span effects, corner flows, and delta wings at incidence. Although non-equilibrium effects have only a small influence on forces and moments for delta planforms, appreciable departures from the equilibrium predictions of heat transfer for areas removed from stagnation regions can be expected. The authors made clear the point that although high altitude effects will certainly not dominate the design philosophy of hypersonic vehicles, nevertheless, our understanding of flow phenomena around real bodies of interest in this regime is presently in a very rudimentary state.

Sincere thanks are expressed to the lecturers for their efforts and to their respective organizations for providing them with the encouragement and time required to carry out such a task, and to Dr R.C.Pankhurst who has been responsible for the overall editing of these volumes.

Kurt R.Enkenhus
Lecture Series Director
"Aerodynamic Problems
of Hypersonic Vehicles"

John F.Wendt
Lecture Series Director
"High Altitude Aspects of
Lifting Re-entry Vehicles"

March 1972

CONTENTS

	Page
PREFACE	iii
GENERAL INTRODUCTION	iv

VOLUME 1

	Reference
LECTURE 1 - AERODYNAMICS AT MODERATE HYPERSONIC MACH NUMBERS by P.L.Roe	1
LECTURE 2 - OPTIMUM SHAPES by P.L.Roe	2
LECTURE 3 - THEORY OF "WAVERIDERS" by P.L.Roe	3
LECTURE 4 - THIN SHOCK-LAYER THEORY by P.L.Roe	4
LECTURE 5 - MOMENTUM THEORY by P.L.Roe	5
LECTURE 6 - FLOWS WITH HEAT ADDITION by P.L.Roe	6
LECTURE 7 - SPECIAL TOPICS IN HYPERSONIC FLOW by R.D.Neumann	7
LECTURE 8 - SOME DESIGN ASPECTS OF HYPERSONIC VEHICLES by W.L.Hankey	8
LECTURE 9 - REAL GAS EFFECTS ON LIFTING RE-ENTRY AEROTHERMODYNAMICS by K.N.C.Bray	9
LECTURE 10 - VISCOUS INTERACTION EFFECTS ON RE-ENTRY AEROTHERMODYNAMICS: THEORY AND EXPERIMENTAL RESULTS by J.L.Stollery	10

VOLUME 2

	Page
PARTIE 1 - CHOIX DU MODE DE PROPULSION par R.Marguet	5
PARTIE 2 - PROPULSION PAR FUSÉE par Marcel Barrère	23
PARTIE 3 - STATORÉACTEURS par R.Marguet	61
PARTIE 4 - PROBLÈMES AÉRODYNAMIQUES par René Cérésuela	95

Lectures 1 to 6 are British Crown Copyright material and are reproduced by permission of Her Majesty's Stationery Office.

LECTURE 1

AERODYNAMICS AT MODERATE HYPERSONIC MACH NUMBERS*

P.L.Roe

Royal Aircraft Establishment, Bedford, England

In each of my subsequent lectures I shall be dealing with a research topic in the theory of inviscid hypersonic flow. In this introductory talk I want to do three things. I want to define what I mean by hypersonic, I want to justify the interest in inviscid flow, and I want to introduce briefly each of my future topics.

Almost everyone has their own definition of the term hypersonic. If we were to conduct something like a public opinion poll amongst those present, and asked everyone to name a Mach number above which the flow of a gas should properly be described as hypersonic there would probably be a majority of answers round about five or six, but it would be quite possible for someone to advocate, and defend, numbers as small as three, or as high as 12.

I shall, therefore, adopt a different sort of definition. A good working rule in science is to classify together phenomena which can be understood by means of the same explanation, and by "explanation" we usually mean "theory". Hypersonic flow, then, is flow which needs a particular sort of theory to describe it, and I must describe the sort of theory that I have in mind. Because I shall not be talking about rarefied gases, or dissociation effects, or strong viscous interactions, some people might deny that I was talking about hypersonics at all. But it does seem necessary both as a basis for these advanced topics, and as a subject in its own right, to have a hypersonic flow theory which treats air as a continuum substance, in thermodynamic equilibrium, and lacking in viscosity. This is the sort of theory I shall be talking about, and the reason why I describe it as "hypersonic" rather than merely "supersonic" is that I wish to concentrate on those aspects which cannot adequately be described by linear theory. I shall be concerned with flows where the perturbation velocities are not particularly small, and in which shock waves generate strongly rotational flow fields. I shall assume, however, that the effects of viscosity can be represented entirely by very thin boundary layers, and by shock discontinuities.

To justify anything more than an academic interest in these flows, I must show that there could exist at least one sort of aircraft to which such flows are relevant, and so I shall spend some time considering the feasibility of a hypersonic transport aircraft. I have in mind something not totally different from a contemporary airliner: something which operates from conventional airports and whose main purpose is to carry goods and people over the globe. Such a vehicle will offer a service to society and a profit to its makers only if it fulfils a need. The most convincing need that an increase of speed might satisfy is not simply the reduction of journey times on existing routes, but the opening up of entirely new travel prospects.

In all the history of travel it is possible to observe two constants which, because they concern human nature, may confidently be extrapolated into the future. One of these is the significance of personal contact between people, whether traders or politicians or the general populace. The other is the reluctance of most people to undertake frequently journeys which last for more than a few hours. Regardless of how any of us personally regards the prospect of a "global village" in which all men are members of a truly international society, it does seem very probable that this is the eventual destiny that a peaceful earth must tend toward, but it cannot come about until all major cities are brought within a few hours of each other.

Let us look briefly at some of the consequences which extending the range of convenient travel might have. Consider some particular centre of population. How many journeys will its inhabitants wish to make over distances lying between R and $R + dR$? The region that can be reached by such journeys is ring shaped, and we may suppose that the number of journeys people will wish to make to that region depends in some way on the number of attractions to be found in that region. For example, the number and size of trading centres, political capitals, and holiday resorts, or perhaps the mineral wealth of the region. If we suppose, to a very rough approximation, that the total "attractiveness" of the region is proportional simply to its area, then for a spherical earth we obtain the formula

$$J(R) = \sin\left(\frac{\pi R}{R_E}\right). \quad (1.1)$$

* Since the original lecture material was written, a number of new relevant papers have been published. Some of these are listed in the Appendix (page 6-10), with brief comments. Also included are a few older papers that have only recently come to the author's attention.

where

$J(R)$ is the requirement for journeys of length "roughly equal to R " i.e. between $R - \Delta R$ and $R + \Delta R$ where ΔR is an arbitrary constant

and

R_g is the "global range", equal to half the earth's circumference.

This formula is used to plot J versus R in Figure 1, from which we can deduce that the potentially most heavily used transport routes would be those which run about one quarter of the way around the globe (a distance of about 6,200 statute miles, or 5,380 nautical miles, or 10,000 kilometres).

An alternative approach would be to say that the potential travel between any two centres is proportional to the product of their respective populations. Therefore Naysmith has analysed data for all cities having current populations greater than three quarters of a million. For every pair of such cities he obtained the distance between them, and a number proportional to the potential travel between them. His results are given in histogram form in Figure 1. They depart from the idealised curve for two reasons. The first reason, which nothing can alter, is that the earth's land masses are rather irregularly distributed. The second reason is that at the present time, some of those land masses are much more highly developed than others. The "peak" at the left-hand side of the graph represents travel within the already developed areas, such as North America and Western Europe. We may expect that with time the graph will approach close to the ideal, but already the conclusion is striking enough; there is a very large potential market for travel over ranges of about one quarter of the earth's circumference.

The same results are plotted in cumulative form in Figure 2.

Now I remarked earlier that travel over a given route would increase greatly as soon as it met certain standards of convenience. To be included in these standards are things like surface travel and airport management, which are not within my province. Undoubtedly they raise severe problems, but these do not look insoluble. One very important criterion of course, is simply travel time, and we shall take it that the task of the aircraft designer is mainly to reduce this to an acceptable level. As a guess, we shall take two hours as a good target to aim at.

What sort of speed, then, do we need to cruise at, in order to cover about 5,500 n.m. in two hours? According to estimates given in Reference 2 the answer is that the cruise Mach number should be about 4.5. The aircraft would be required to carry about 30% of its take-off weight as fuel, and able to carry about 10% as payload.

This, then, is our starting point. The question to be asked is how we set about designing the aerodynamic shape of a cruise vehicle intended to operate somewhere in the Mach number range between three and seven (giving us a generous margin for error on either side of 4.5). The first thing to be noted about this speed range is that it is too fast for supersonic linear theory to be valid, and too slow for Newtonian theory. Therefore, either our designs must rely wholly on experiments, which will certainly be very wasteful and costly without theoretical guidance, or we must develop new theories.

Let us first, however, try to be more specific about the sort of aircraft shapes we are interested in. We have to remember that even if the aircraft cruises hypersonically, it must remain safe and economical at all slower speeds, down to the take-off and landing speeds. To minimise the problems associated with transonic and low speed operation it will be advisable to make the layout not too different from those already known to be satisfactory. There seem to be three main alternatives:-

1. Conventional take-off and landing, using more or less straight wings, achieved by variable geometry
2. Conventional take-off and landing, using a fixed delta wing, and
3. Unconventional take-off and landing, e.g. using direct-lift engines.

Of these three, the second appears simplest and safest, and also most economical, in that the alternatives involve severe weight penalties. We begin to think, then, in terms of something like a delta wing.

One feature that seems worth introducing into the design right from the beginning is an integration of those parts of the aircraft which provide volume and propulsion³. The basic idea behind this can be gathered from Figure 3. Here we imagine a "two-dimensional aircraft", flying at zero lift. We suppose that it has to be of a specified length, l , and to enclose a specified area, A . We ask how small the wave drag can be made, and use linear theory to compute the answer. It turns out to depend on the base thickness, h_b , and is a minimum when

$$h_b = \frac{3A}{2l} \quad (1.2)$$

the section profile being then a parabolic arc which is streamwise at the base. This profile has only one quarter the wave drag of the profile having $h_b = 0$.

In itself this is not a practical solution, because of the large "base drag" associated with the extensive wake behind such a body, but this disadvantage can be avoided as follows.

At speeds above about Mach two, the efficient internal design of jet propulsion units requires a duct whose cross-section is considerably greater at exit than at inlet. Basically, the highly compressed air needs a large expanding nozzle to receive the pressures which provide the main thrust forces. Squire³ quotes area ratios of 2 or 3 at Mach four. Now a duct of these proportions, accommodated in an externally carried nacelle, would have a large external drag (see upper parts of Figure 4). However, we can contrive a marriage of the bluff-based body with the expanding nacelle, such that we retain the advantages of both and the drawbacks of neither (lower part of Figure 4). By comparison with the layout at upper left, this merged configuration has lost 75% of the body wave-drag, and all of its external nacelle drag. The penalties paid for this are a small loss of useful volume, and the ingestion into the intake of some boundary-layer air, but the balance is overwhelmingly favourable.

Exactly how far these benefits are realised on three-dimensional lifting shapes is not clear, and depends on many factors. Squire³ estimated that at Mach four an integrated layout would achieve maximum lift-drag ratios about 1.5 higher than a non-integrated competitor, and all the subsequent evidence seems to suggest that this is about right.

So far our recipe for a hypersonic cruise vehicle reads – "a delta wing with integrated propulsion unit". Next we ask what sort of aspect ratio will be appropriate. The slender wing concept out of which Concorde developed was based on trying to restrict the aircraft well within its own Mach cone. By this means it is hoped to gain three advantages.

1. The disturbances caused in the air should be relatively small i.e. causing only small energy losses.
2. The air is able to flow round the leading edge, developing local suction forces which reduce the drag.
3. The leading edge flow subsequently rolls up into separated vortices, which induce strong lift forces by increasing the upper surface suction.

Now at high supersonic speeds, suction forces contribute relatively little to the overall picture, so it will not be worth much to try and achieve advantages two and three. Moreover, as Mach number rises, the Mach cone shrinks (Fig.5), leaving no room for anything but an extremely fine and pointed shape. Thus we are led to examine the possibility of shapes which are not aerodynamically slender, and which therefore cause strong disturbances to the air.

A further clarification of the design concept can be achieved at this stage by making the extreme assumption that these strong disturbances are so strong that Newtonian theory can be used. It is then a simple matter, as we shall see in Lecture 2, to find the wing which has the greatest possible lift-drag ratio. In deriving it, we make only one assumption, that all wings are subject to a friction drag proportional to their wetted area times a known constant (C_f). Thus, roughly,

$$C_{D\text{friction}} = 2C_f.$$

where C_f is of the order of 0.001.

The optimum wing turns out to have a perfectly flat undersurface. By making the upper surface streamwise we can provide volume with no loss of performance, and the resulting finite base area is available for integration into the propulsion system (see Figure 6). The optimum incidence for the lower surfaces depends on the assumed value of C_f and so therefore do the volume and base area of the configuration. The lift/drag ratio to be expected from these wings is shown in Figure 7, plotted as a function of C_f .

The conclusion to be drawn from this seems to be that not only should the part of the aircraft that provides volume be integrated with the propulsion system, but it should also be integrated with the lifting system. However, before we give our complete acceptance to this principle, we should try to find out what the penalties are for contravening it. To do this we devise non-integrated comparison shapes, which provide, at each value of C_f , the same lift and volume and planform area. All the lift is supposed to come from a thin flat wing, and all the volume from a non-lifting "¼-power" body of revolution. From Figure 7 it can be seen that the non-integrated configuration has about a 30% lower performance than the integrated optimum.

Figure 8 shows the sort of layout that we have arrived at. A good deal of relevant information and discussion about it has been given by Küchemann⁴ (also in Reference 2). Most of his conclusions have been unaltered by the passage of time, and much of what I have to say in the next few minutes will merely summarise these. The one conclusion that does require modification is that generalised design methods have extended the applicability of the "waverider" concept to lower Mach numbers than were indicated in References 2 and 4.

Let us then consider how we may set about obtaining more detailed design information for the sort of vehicle depicted in Figure 8. In the first place, for the sort of Mach numbers we are considering, inviscid, ideal gas calculations with separate treatment of the boundary layer will be quite adequate. However, it is also clear that calculations using the full non-linear equations of inviscid motion with arbitrary boundary conditions are still some way into the future. Therefore a sensible policy for the time being will be to try and extract as much information as we can from inviscid theories which are in various ways approximate.

It also seems legitimate to design on the assumption that the leading edges are perfectly sharp. Such an idealised edge would soon be eroded in flight, due to the high heating rate associated with large shear across the initially thin boundary layer, but the blunting needed to alleviate the effect is fairly small at these speeds, a radius of much less than an inch being adequate for a vehicle whose length is, say, two hundred feet. Therefore the effects of bluntness may be incorporated as small corrections at a late stage in the design procedure.

If the leading edges are almost sharp then for non-slender shapes the shock wave will be almost attached, and for most purposes the upper and lower surfaces of the shape will be aerodynamically independent. Accordingly they may be designed separately. Of the two the lower surface is by far the more important, contributing about 80% of the lift or even more, within the Mach number range of interest. In almost everything that follows we shall concentrate our attention on the lower surface. This should not however, be taken as implying that the upper surface design is irrelevant. Careful attention to its design, and the proportion of lift that it carries, will certainly lead to gains in performance which are worth having. The reason for not saying more about it is simply that so far not much work has been done in this area.

No attempt has yet been made to work out the full consequences of the integration of the lifting body with the propulsion unit. One reason for this is that the ideal proportions of the propulsion unit cannot be worked out without knowing something of the characteristics of the engine to be used, the speed and altitude for cruise flight and the wing loading. In the absence of any project study giving this sort of detail we can nevertheless proceed with refinements to the aerodynamic design, noting simply that finite base areas roughly 10% of the planform area can be accepted and replaced by exhaust nozzle area. Of course we should also try to ensure that this base area is of a convenient shape, i.e. concentrated in a fairly small region of the span.

This completes my definition of the sort of shape we are trying to design, and the assumptions and simplifications that it seems reasonable to make.

In my second lecture I shall describe some of the results of optimisation theory, as applied to various problems involving non-linear lifting aerodynamics. Such results are generally restricted to very simplified sub-problems that can be handled analytically. Because of their simplicity, however, they do have a good chance of increasing our physical insight into the more complex questions that we would really like to answer.

In my third lecture I shall treat the subject of "waveriders" or wings designed so as to support simple wave systems and so be amenable to exact (inviscid) calculation. I want to show how the geometry of the wave systems that we are able to calculate restricts the shapes of the resulting bodies, but also I shall indicate the means so far found to create "realistic" shapes within these restrictions. I shall give a typical example of a shape that combines a fair degree of realism with good calculated performance. Finally I shall discuss the problems that arise when we try to calculate the flow about these shapes in flight conditions for which they are not designed; this gives rise to rather puzzling questions about the behaviour of three-dimensional shock waves.

In my fourth lecture I want to discuss what seems to me one of the most promising approximate methods for calculating general flows in this speed range, thin shock layer theory. So far this theory has only been developed for conical flow. Despite some basic mathematical difficulties which arise when treating attached shock waves, the agreement with experiment is very good. I shall present a new approach to this theory, which allows several very simple properties of the flow pattern to be clearly seen.

In my fifth lecture, I shall discuss an offshoot of the waverider approach, which permits a discussion of the lift and drag forces in terms of momentum changes in the adjacent flow.

Lastly, in my sixth and final lecture, I shall deal with the changes brought about by direct heat addition to the flow about a lifting body.

All these subjects are at quite early stages of their development. What I have tried to do is to give some idea of the current research status in them. The loose ends will probably be very apparent; it will be very gratifying if other people feel able to take them up.

REFERENCES

1. Naysmith, A. *Population Distribution and Air Transport*. RAE TR 69227, 1969.
2. Küchemann, D.
Weber, J. *An analysis of some performance aspects of various types of aircraft designed to fly over different ranges at different speeds*. Progress in Aeronautical Sciences, Vol.9, Pergamon Press, 1968.
3. Squire, L.C. *The use of excess engine exit area over intake area to reduce zero-lift drag at high supersonic speeds*. Aero Quarterly, Vol.16, 3, 1965.
4. Küchemann, D. *Hypersonic aircraft and their aerodynamic problems*. Progress in Aeronautical Sciences, Vol.6, Pergamon Press, 1965.

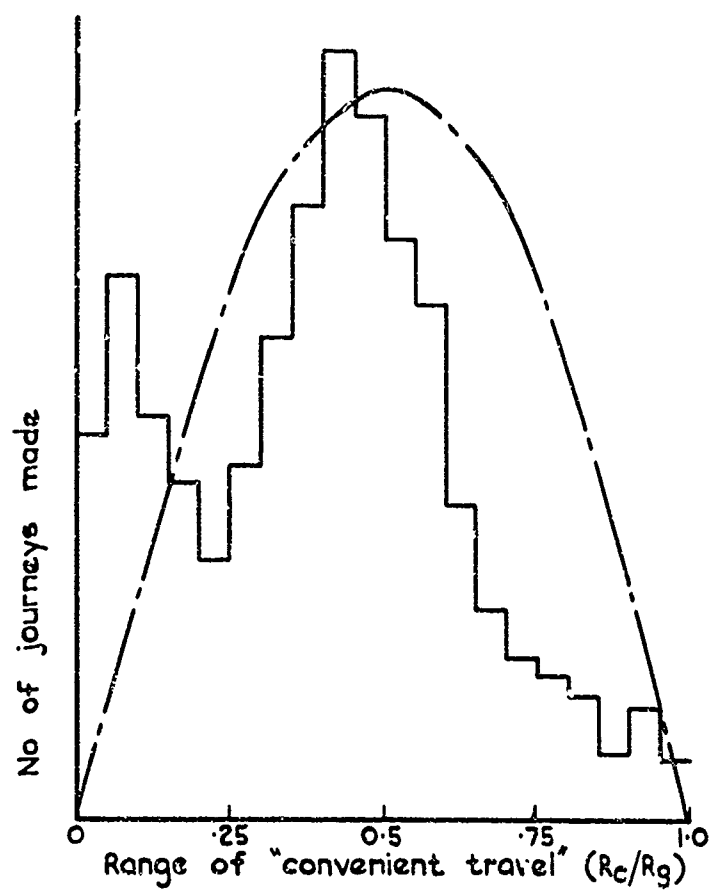


Fig.1 Potential market for long range transport

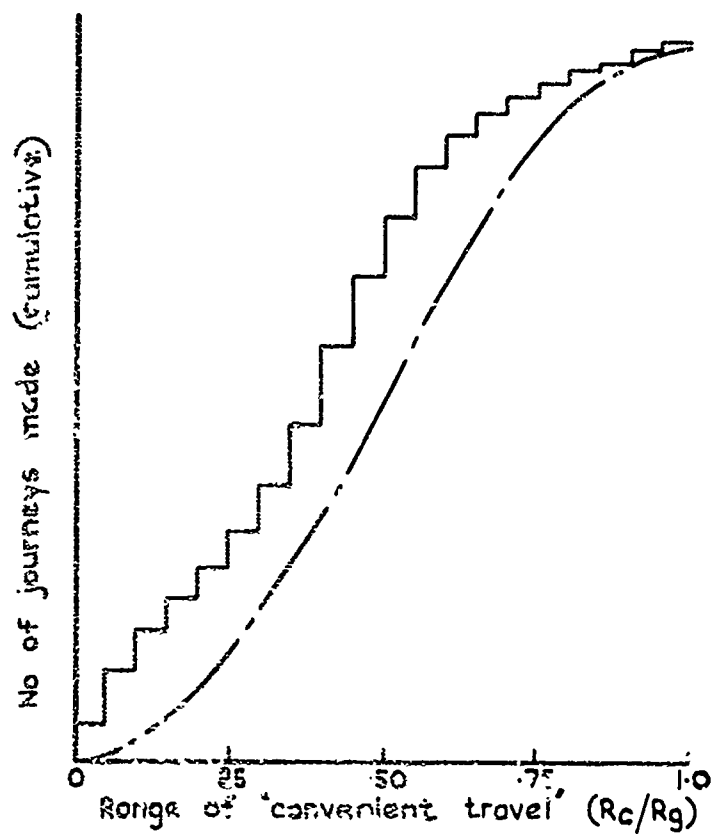


Fig.2 Cumulative plot

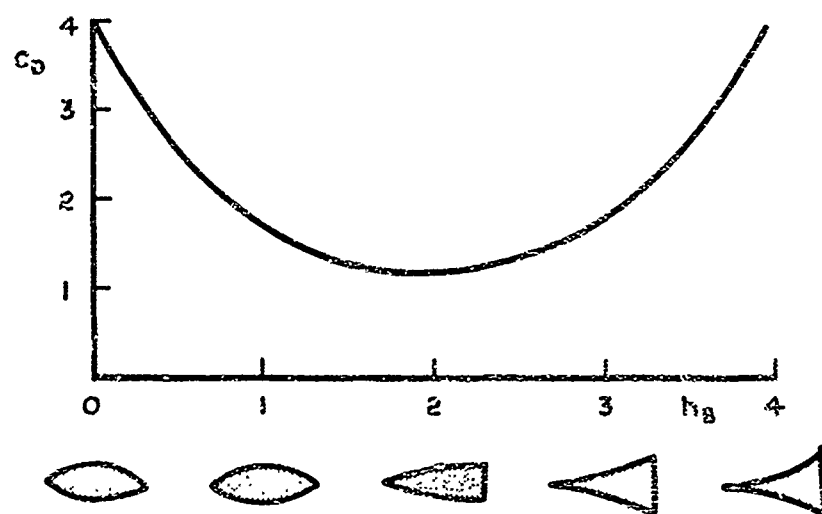


Fig.3 Drag of optimised two-dimensional wings having given length and area versus base height.

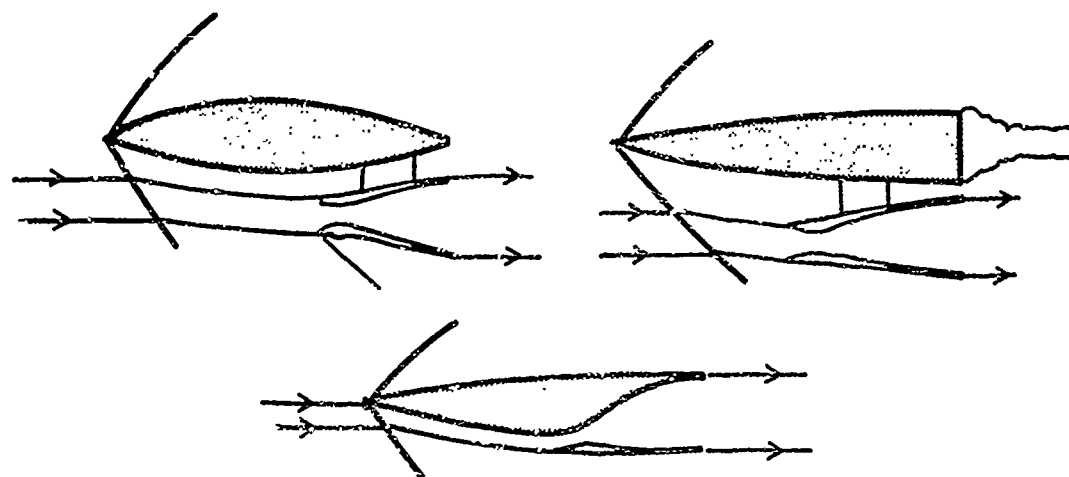


Fig.4 The principle of engine-airframe integration

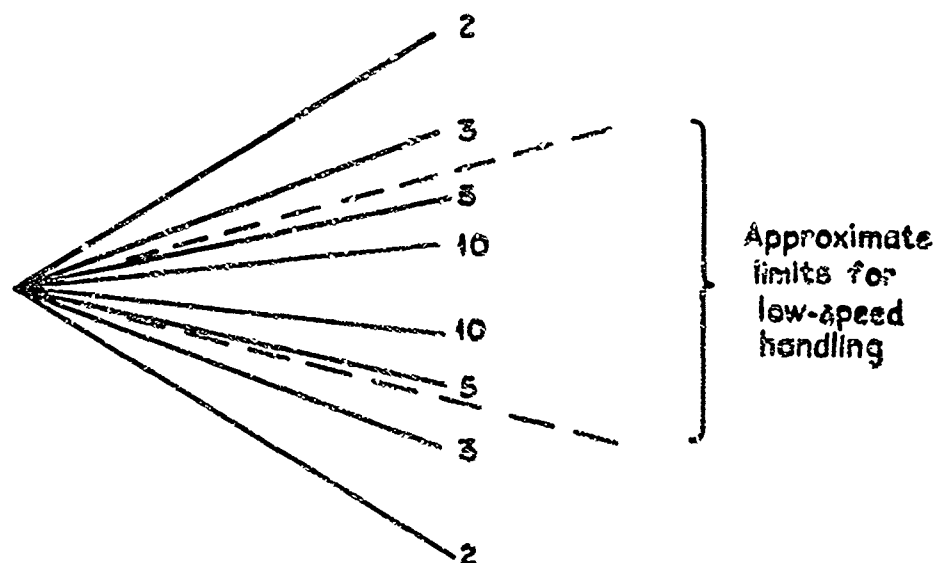


Fig.5 The shrinking Mach cone



Fig.6 Optimum wing (Best L/D) according to Newtonian theory

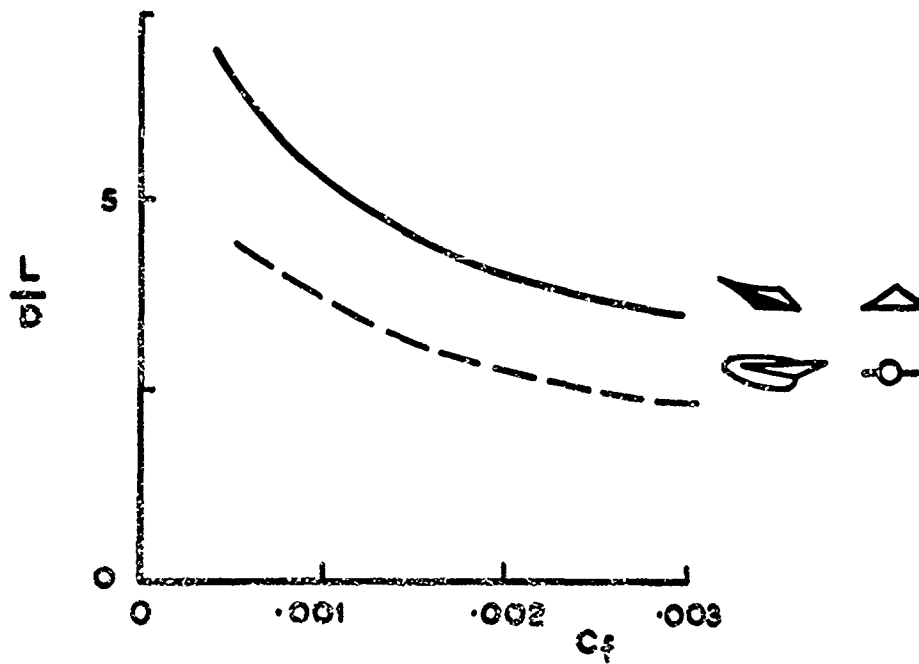


Fig.7 Comparison between integrated and non-integrated designs (Newtonian theory)

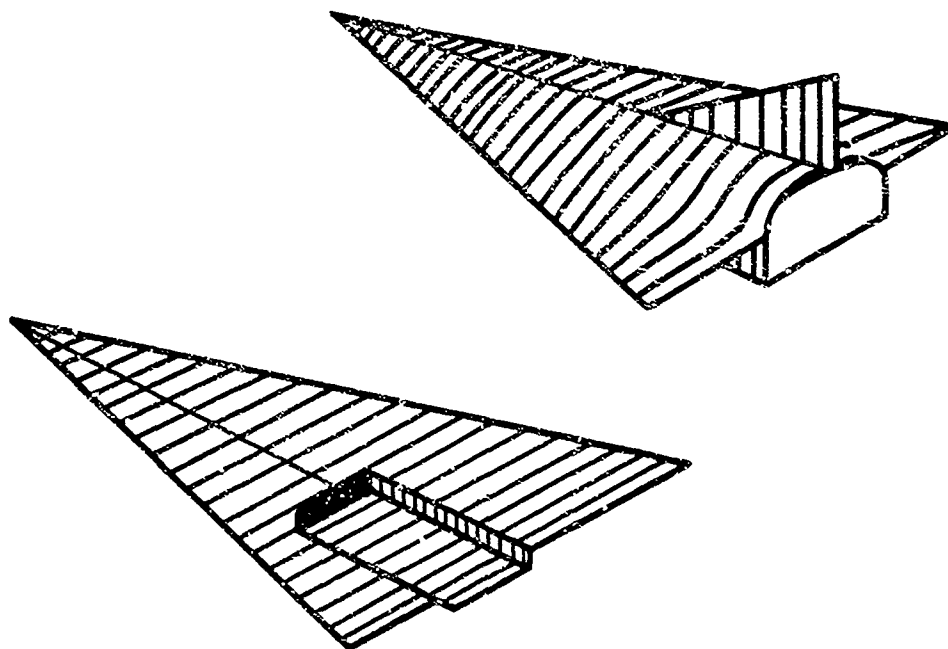


Fig.8 Plausible layout

LECTURE 2

OPTIMUM SHAPES

P.L.Roe

Royal Aircraft Establishment, Bedford, England

In this lecture I want to review the progress that has been made in the application of optimisation methods to hypersonic wing theory. The sort of wing I shall consider is that described in my first lecture, sharp-edged and non-slender. It will help to set the current achievement in perspective if we first consider the enormity of the work involved in a really general and soundly-based solution to the problem.

First of all we should need a computer programme capable of calculating the inviscid flow past a general three-dimensional wing-like shape. For this programme to inspire real confidence, it would have to be based on the complete Euler equations of inviscid motion, and its logical structure would have to be sophisticated enough to take account of shock waves in a priori unknown locations, possibly embedded in the flow field as well as attached to the leading edges.

Quite a lot of simplifications would follow if we could assume that the shock wave was attached everywhere, so that the upper and lower surfaces were independent, but even so, any such calculations seem at the moment a rather remote prospect. The most that has been achieved to date is a pair of solutions for the upper and lower surfaces of a plane delta wing¹⁻³. In both cases the solution is greatly aided by the conical self-similarity of the solution, and by knowledge that the solution near the leading edge is of rather elementary form, being identical with the solution for a yawed wedge. However, even in these cases, there are difficulties. The success of Babaev's solution (Fig.1) for the lower surface flow depends rather strongly on being able to make an intelligent first guess at the unknown shock shape near the centre¹, which would be less easy in a more general problem. In the case of the upper surface (Fig.2), there has been controversy^{4,5} over the nature of the embedded shock wave, and the numerical results in Reference 3 depend on an approximate, even if numerically accurate, treatment of the rotational region. Again, both the nature of the solution and its numerical treatment, would be more difficult to establish in a general case.

It is clear that we cannot hope for a general solution for some years to come, and that even if it does eventually arrive, the computer time necessary to compute one case is more likely to be measured in hours than minutes. But just one case would only be a very small part of an optimization procedure. It would be necessary to specify the unknown optimum shape by a large number of parameters, and to treat all these as independent unknowns in some sort of multi-dimensional search technique, the strategy of which would form a research subject in itself. And even then one would only have solved the inviscid problem.

Set against these considerations the achievements I am about to describe may appear rather puny and insignificant. However, we can take courage from two considerations. In the first place, even the sort of programme I have been describing, allied with a really good three-dimensional compressible boundary layer analysis would fall very far short of acknowledging the complexity of form of a practical aircraft. It is really not foreseeable that an "optimised" calculated shape could do anything more than give a guide to the designer. Secondly, it is only a guide that the designer actually wants from the aerodynamicist. He would really be a little embarrassed to be offered a perfect aerodynamic shape, which he would then have to carve holes in, add fairings to, and so on, in order to satisfy such mundane requirements as that the pilot should be able to see where he is going or that people have somewhere convenient to get in and out.

The real purpose of optimisation theory can only be to provide a catalogue of good shapes, together with the assumptions used to obtain them, and some sort of explanation of the way these assumptions are reflected in the geometry of the shapes. This catalogue is now beginning to take shape. A good review of optimum aerodynamic shapes, with a basic account of their derivation through the calculus of variations, was given in the book by Miele⁶. However, even since then, there have been several important contributions, some of them due to Miele himself and his associates.

A lot of these have made use of the very simplest aerodynamic theory that has any pretence to realism, simple Newtonian theory. It seems worthwhile, therefore, to undertake a short digression to examine this theory.

It is often derived by something very like the original method⁷. The fluid is supposed to be made up of completely inelastic particles, which therefore do not rebound on collision with a solid body, but follow on round its surface in a very thin layer. From the fact that the flow in every impinging streamtube would thereby have its momentum normal to the surface completely destroyed, it is an easy deduction that the pressure coefficient at all forward-facing points of the body is

$$C_p = 2 \sin^2 \theta, \quad (2.1)$$

where θ is the local inclination of the surface to the free stream. Sometimes a better agreement with experiment can be achieved by "adjusting" Equation (2.1) to read

$$C_p = k \sin^2 \theta, \quad (2.2)$$

where k , sometimes called the "impact coefficient" is chosen to secure agreement at, for example, the stagnation point.

For some purposes the accuracy obtained from Equation (2.2) is good enough to allow its use as a prediction method, but generally speaking it cannot be relied on. A fairly typical comparison with experiment is shown in Figure 3, taken from Reference 8. The figure shows values of a "local impact coefficient", defined as $k = C_p / \sin^2 \theta$, plotted against local inclination θ , for several points on a cone-segment body at various angles of attack in a supersonic flow of Mach number 4.3. For large values of θ , k is not far from its simple Newtonian value of 2.0, but obviously no constant value would represent these results satisfactorily.

The "unrealistic" derivation of the Newtonian pressure formula, and the unreliability of its predictions, sometimes leads people to suppose that there can be little value in its use for optimization exercises and little confidence in the resulting shapes. This distrust, however, is probably not wholly justified, for Newtonian theory can be related rather more convincingly to conventional gasdynamic analysis. To begin with, consider the expressions for flow deflection, density, and pressure coefficient behind an oblique shock of angle θ in an ideal gas, flowing with Mach number M_∞

$$\tan \delta = \frac{2 \cot \theta (M_\infty^2 \sin^2 \theta - 1)}{2 + M_\infty^2 (\gamma + 1 - 2 \sin^2 \theta)} \quad (2.3)$$

$$\frac{\rho}{\rho_\infty} = \frac{(\gamma + 1) M_\infty^2 \sin^2 \theta}{(\gamma - 1) M_\infty^2 \sin^2 \theta + 2} \quad (2.4)$$

$$C_p = \frac{4(M_\infty^2 \sin^2 \theta - 1)}{(\gamma + 1) M_\infty^2} \quad (2.5)$$

If the gas is such that the ratio of specific heats, γ , can be thought of as close to unity, these equations simplify, thus

$$\tan \delta = \frac{\cot \theta (M_\infty^2 \sin^2 \theta - 1)}{1 + M_\infty^2 \cos^2 \theta} \quad (2.6)$$

$$\frac{\rho}{\rho_\infty} = M_\infty^2 \sin^2 \theta \quad (2.7)$$

$$C_p = \frac{2(M_\infty^2 \sin^2 \theta - 1)}{M_\infty^2} \quad (2.8)$$

and from these we find that, as the Mach number becomes very large, $\tan \delta \rightarrow \tan \theta$, $\rho \rightarrow \infty$, and $C_p \rightarrow 2 \sin^2 \theta$. Thus, in the double limit $\gamma \rightarrow 1$ and $M_\infty \rightarrow \infty$, the flow behind an arbitrary three-dimensional shock wave becomes very dense and follows the shock wave direction.

Moreover, the pressure just behind the shock takes on the value predicted by simple Newtonian theory. It is very important, however, to observe that we have not justified its use to predict pressures on the body. In order that the fluid inside the shock layer may follow a curved path around the body it is necessary that a pressure difference should exist across the layer. Taking this into account gives the "centrifugal correction" due to Busemann⁹, written¹⁰ in terms of a streamfunction ψ .

$$C_p = 2 \sin^2 \theta - 2 \frac{d(\cos \theta)}{d\psi} \int_0^\psi \cos \theta \, d\psi. \quad (2.9)$$

which applies both to two-dimensional bodies for which $\psi = \rho_{\infty} U_{\infty} y$, and to axis-symmetric bodies for which $\psi = \frac{1}{2} \rho_{\infty} U_{\infty} r^2$. The nature of the correction is more complicated for more general bodies, because the paths followed by the streamlines are less simple. In general they will be geodesics of the body surface¹⁰.

The decision whether or not to incorporate the Busemann correction in an optimisation study is not particularly easy. Although it does ensure that more of the physics of the real flow is represented, so that the conclusions are more likely to be qualitatively correct, its inclusion does not usually seem to improve the numerical accuracy of pressure distributions^{11,12}. We shall see these two considerations clearly in one of the ensuing examples.

Before proceeding to an examination of shapes, we shall take a brief look at a non-lifting problem, that of the slender body of revolution causing least drag for given length and base area. For slender axis-symmetric bodies the Newton-Busemann pressure law can be simplified to

$$C_p = 2r'^2 + Ar'' \quad (2.10)$$

where $A = 1$ if the Busemann correction is to be incorporated, and zero if it is to be neglected. Suppose for the sake of simplicity, that we only consider power-law bodies, whose profile is given by

$$r = Cx^n \quad (2.11)$$

then the following expression is easily derived for the drag of the body

$$\frac{C_D}{C_{D \text{ cone}}} = \frac{n^2 + \frac{1}{2} A n^2 (n-1)}{2n-1} \quad (2.12)$$

where $C_{D \text{ cone}}$ is the drag of the cone ($n = 1$) which has the given length and base area. Equation (2.12) has its minimum value when $n = \frac{1}{2}$ if $A = 0$ and when $n = \frac{3}{2}$ if $A = 1$.

Now the reason for considering this particular problem is that it seems to be about the only example of an optimisation study using Newtonian theory for which comparative experimental data exist^{12,13}. These are shown in Figure 4. Although there is some scatter amongst the experimental results, it does seem clear (bearing in mind that all curves must pass through the point (1,1)) that a power law exponent of about 0.7 is best. This is an example of a phenomenon that recurs rather frequently. Quite simple aerodynamic theories predict optimum shapes that are closely confirmed by more accurate treatments. The confirmation by experiment is rarer because the experiments have often not been performed.

Note that we have only considered here the particular variational problem for which we have experimental data, namely, selecting the optimum member of the class of power-law bodies. The problem of finding the optimum body without restriction on its form is fully discussed in Reference 6, where it is shown, using calculus of variations, that the optimum slender body of revolution is in fact a $\frac{3}{2}$ power body according to simple Newtonian theory, but according to the Newton-Busemann theory it has a more complicated form consisting of a $\frac{3}{2}$ -power forebody for 60% of its length, followed by a "free layer" in which the centrifugal term exactly cancels the impact term to leave no pressure force on the body (Fig.5a). For such a body, $C_D/C_{D \text{ cone}} = 0.577$, compared with 0.667 for the best ($n = \frac{3}{2}$) "pure" power-law body.

The Newton-Busemann theory predicts^{6,10} an even greater drag reduction (down to $C_D/C_{D \text{ cone}} = 0.422$) for cowled bodies (Fig.5b). However I know of little that has been done to see how far these additional gains are truly realisable.

We now pass to consideration of a simple lifting problem, to find the wing which creates least drag while supporting given lift. In consequence of the remarks in my introductory lecture I shall consider only the wing lower surface by itself. The problem as stated has a trivial solution in inviscid flow. We have only to make the wing area (A) very large, and the angle of incidence (δ) very small, in such a way that the lift (proportional to $A\delta$) keeps its desired value, and the drag (proportional to $A\delta^2$) will become as small as we please. A meaningful problem can only be got by imposing some additional constraints. Thus we might suppose that there will be a skin friction drag directly proportional to A , or that the surface was required to meet certain geometrical conditions. A particularly simple mathematical treatment can be given if we take the following set of conditions, some of which we will subsequently see do not affect the character of the solution.

1. Both the lift (L) and the planform area (A_p) of the wing are assumed to be given.
2. The pressure is a function of the local surface inclination only.
3. There is no skin friction.

The second assumption is common to various theories. These include, for three-dimensional calculations, simple Newtonian theory, tangent-wedge theory or tangent-cone theory. For two-dimensional calculations, the list extends to include both linearized (Ackeret) and second-order (Busemann) theory. In all these cases it is assumed that

$$C_p = F(\alpha), \quad (2.13)$$

where F and its first derivative F' , are positive for $0 < \alpha < \pi/2$. I shall now show that for any such pressure law the wing which has least drag under the stated conditions is a flat plate. The simplest proof given here in rather sketchy form, is to consider such a wing, and show that any small departure from it which does not alter the lift cannot reduce the drag. Thus, we consider a wing for which α is given by

$$\alpha = \alpha_0 + \epsilon \alpha_1(x, y),$$

where α_0 is a constant, α an arbitrary function of order unity and ϵ a small parameter. The lift of such a wing is given by

$$\frac{L}{q_\infty} = \iint_{A_p} F(\alpha) dA_p,$$

which by Taylor's theorem can be written

$$\frac{L}{q_\infty} = \iint_{A_p} F(\alpha_0) dx dy + \epsilon F'(\alpha_0) \iint_{A_p} \alpha_1(x, y) dx dy + O(\epsilon^2)$$

and since we wish to consider only perturbations which do not change the lift, the integral of α_1 must be zero.

Now, if a small element of the wing surface has a vertical projection equal to dA_p , it must have a streamwise projection greater than or equal to $dA_p \tan \alpha$, and so we can write

$$\frac{D}{q_\infty} > \iint_{A_p} F(\alpha) \tan \alpha dA_p$$

which becomes, if we expand both terms of the product as Taylor series,

$$\frac{D}{q_\infty} > \iint_{A_p} (F(\alpha_0) + \epsilon F'(\alpha_0) \alpha_1(x, y)) (\tan \alpha_0 + \epsilon \sec^2 \alpha_0 \alpha_1(x, y)) dx dy + O(\epsilon^2).$$

However, we have just seen that the terms in ϵ do not contribute to the integral, and so

$$\frac{D}{q_\infty} > \iint_{A_p} F(\alpha_0) \tan \alpha_0 dx dy + O(\epsilon^2). \quad (2.14)$$

Therefore, the wing having least drag under the stated conditions is the one for which the equality sign holds in Equation (2.14), and this is only so for a flat plate.

We have derived this result by assuming that no skin friction was involved. If we make a crude allowance for skin friction according to the formula

$$\frac{D_f}{q_\infty} = A_p \times C_f$$

with C_f a constant, the friction drag has the same value for all wings with the same planform area. It therefore does not affect the optimisation process just considered. The proof given is sufficient to show that a flat wing is optimum in the sense of having the greatest lift-drag ratio when any combination of any of the three quantities, lift, planform area and friction coefficient are prescribed. In the case where the friction coefficient alone is given, for example, suppose that some other wing were better, and that it was associated with area A^* and lift L^* . It would follow that this was also the wing which had least drag when A was prescribed equal to A^* , and L equal to L^* , and this would contradict what we have just shown. Knowing that this particular optimum wing is flat, we can very easily find its other properties. Let its surface inclination be α^* . Then

$$L = q_\infty A_p F(\alpha^*)$$

$$D = q_\infty A_p (F(\alpha^*) \tan \alpha^* + C_f).$$

Maximising L/D leads to

$$L \frac{dD}{d\alpha} = D \frac{dL}{d\alpha}$$

or

$$F(\alpha^*) (F'(\alpha^*) \tan \alpha^* + F(\alpha^*) \sec^2 \alpha^*) = (F(\alpha^*) \tan \alpha^* + C_f) F'(\alpha^*) .$$

i.e.

$$C_f = \frac{F^2(\alpha^*) \sec^2 \alpha^*}{F'(\alpha^*)} , \quad (2.15)$$

which is an implicit formula for α^* .

It is instructive to examine the form taken by (2.15) for different pressure laws. In simple Newtonian theory $F(\alpha) = n \sin^2 \alpha$, and Equation (2.15) gives

$$C_f = \frac{1}{2} n \tan^3 \alpha .$$

For small values of α , one can translate this into a statement that the friction drag should be roughly one half the pressure drag, or alternatively, one third of the total drag. This agrees with the conclusion reached by Mi le¹⁵, in an investigation of thin lifting wings.

If, on the contrary, we were to suppose a linear pressure law

$$F(\alpha) = k\alpha ,$$

then Equation (2.15) gives

$$C_f = k\alpha^2 ,$$

which says that the friction drag should be equal to the pressure drag, or one half of the total drag. A tangent-wedge or tangent-cone treatment would usually yield a friction somewhere between one half and one third.

Let us now summarize the results of our examination of this problem. A simple flat plate turns out to be the best lifting surface under quite a variety of constraints according to several aerodynamic theories, although these differ rather substantially in the way they advise the drag to be distributed between pressure and friction forces.

We will treat the same lifting problem by theories which do not assume $C_p = F(\alpha)$. The simplest such theory is the Newton-Busemann theory, and we will begin with that, our approach being taken from Reference 10. The simplest way to derive expressions for the lift and drag is to consider a momentum balance using the control volume of Figure 6. Since the flow outside and inside the shock layer is hypersonic we can neglect all pressure terms with respect to momentum terms. Let the momentum carried by the shock layer at any point along its length be $U_\infty P(x)$ and let the momentum carried by the shock layer when it leaves the body (with inclination σ) be $U_\infty P_1$. Then the lift (per unit depth) can easily be found as

$$L = U_\infty P_1 \sin \sigma$$

and the pressure drag

$$D = \rho_\infty U_\infty^2 y_1 - U_\infty P_1 \cos \sigma .$$

Consider for the moment wings with fixed values of x_1 , y_1 and σ . Then because the quantity P_1 serves to increase the lift and reduce the drag we obviously want to make it as large as possible. For a body shape P can be found by considering the incremental momentum given to the layer by each entering streamtube

$$dP = \rho_\infty U_\infty \cos \theta dy ,$$

so that

$$P_1 = \rho_\infty U_\infty \int_0^{y_1} \cos \theta dy$$

and the problem is to maximise this integral. Because the length of the wing is fixed, there is a constraint,

$$\int_0^{y_1} \cot \theta dy_1 = x_1$$

and since both integrands involve only θ the solution must be $\theta = \text{constant} = \alpha$, where $\tan \alpha = y_1/x_1$. Therefore

$$P_1 = \rho_\infty U_\infty y_1 \cos \alpha,$$

so that

$$L = \rho_\infty U_\infty^2 y_1 \cos \alpha \sin \sigma,$$

and

$$D = \rho_\infty U_\infty^2 y_1 (1 - \cos \alpha \cos \sigma)$$

or, in terms of lift coefficient based on streamwise chord length

$$C_L = 2 \sin \alpha \sin \sigma \quad (2.16)$$

$$C_D = 2 \tan \alpha - 2 \sin \alpha \cos \sigma. \quad (2.17)$$

Now, in general, the minimum value of C_D for C_L fixed does not involve having $\sigma = \alpha$. In fact, it turns out that

$$\cos \sigma = \cos^3 \alpha \quad (2.18)$$

i.e., $\sigma > \alpha$, so that the optimum wing has a small corner at its trailing edge (Fig.7). We can imagine that in a more accurate physical picture of the flow this might appear as a highly loaded flap, narrow compared with the chord length, but wide compared with the shock layer. We shall return to this point later, but if we grant it temporary acceptance, we can find the properties of an optimum class of wings from Equations (2.16) - (2.18). For small values of α , we can obtain

$$\sigma \approx \sqrt{3} \alpha$$

and

$$C_D \approx 0.620 C_L^{3/2}.$$

For a wedge aerofoil, which we found to be optimum under simple Newtonian theory,

$$C_L \approx 2\alpha^2$$

$$C_D \approx 2\alpha^3$$

and so

$$C_D = \frac{1}{\sqrt{2}} C_L^{3/2} = 0.707 C_L^{3/2}.$$

Therefore, the Newton-Busemann theory promises to improve on the performance of simple wedges by about 12.3%. To see whether this promise is fulfilled, we continue examining the same problem with more realistic methods.

Pike¹⁵ has investigated the performance of shapes which are small perturbations of plane wedges (Fig.8). He considers that the perturbation has both a direct effect (as though it took place in a uniform infinite stream at $M = M_2$) and an indirect effect due to disturbances reflected back from the shock wave. These reflected disturbances are weakened by a factor 2 each time they encounter the shock wave, and under most circumstances it is numerically small¹⁶. Assuming that the shape perturbations are of order δ , Pike develops an expression for the pressure distribution in which the direct effects are represented by terms of order

$$\delta, \delta^2, \delta^3, \text{ etc.}$$

the effects of disturbances reflected once from the shock wave by terms of order

$$\lambda\delta, \lambda\delta^2, \lambda\delta^3, \text{ etc.}$$

the effects of doubly reflected disturbances by terms of order

$$\lambda^2\delta, \lambda^2\delta^2, \lambda^2\delta^3,$$

and so on. He then assumes that λ and δ are numerically of the same order, and truncates his double power series after the second order terms. Thus his expression for the perturbation pressure consists of terms in δ , δ^2 , and $\lambda\delta$. Applying the calculus of variation to this expression, he finds that the minimum drag surface having a prescribed lift coefficient is a double wedge (Fig.9), folded in such a way that disturbances originating at the fold just fail to regain the wing surface. This is an encouraging similar result to the one derived from the Newton-Busemann approximation. However, the numerical magnitude of the gains turns out to be very much less. Figure 10, taken from

Pike's report, shows the percentage over plane wedges, the calculations being carried out for $\gamma = 1.4$. The improvement in almost all cases shown is less than one percent, and we may ask why there should be this discrepancy with the Newton-Busemann result of over twelve percent. To settle this question it would be necessary to examine Pike's analysis in the double limit $M_\infty \rightarrow \infty$, $\gamma \rightarrow 1$.

A direct comparison is difficult, however, because the form of series solution used by Pike fails to converge as $M_\infty \rightarrow \infty$, even though it converges well at $M_\infty = 10$. He presents, therefore, an alternative analysis based on hypersonic small disturbance theory ($M_\infty \rightarrow \infty$, $M_\infty \delta \rightarrow \infty$, $\delta \ll 1$), and finds the percentage drag reduction as a function of γ . For $\gamma = 1.4$, this works out at 0.95%, which is still very small. As γ decreases towards unity, the possible improvements become greater, but again the convergence of the series breaks down for γ less than about 1.15. This seems principally due to the reflection coefficient λ , which was assumed small, becoming numerically larger. Indeed³, as $\gamma \rightarrow 1$, $\gamma \rightarrow -1$. A direct comparison is, therefore, not possible.

It is also worth mentioning a rather similar study by Cole and Arcesty¹⁷. They consider only the hypersonic small disturbance theory limit, and develop series expression for the lift and drag of slightly perturbed wedges in which only terms of the form $\lambda^n \delta$ are retained. They show that perturbation shapes exist for which the lift-drag ratio is improved whilst the lift coefficient remains unaltered but because they retain no quadrature terms in δ , the improvement appears to be a linearly increasing function of δ . Under the arbitrary geometric constraint that the surface shall be contained between the lines $\theta_0 + \epsilon \theta_0$ they find the optimum shape to be a corrugated "multi-wedge" as shown in Figure 11, although they also show that this is only fractionally better, by a factor $(1 + |\lambda|)/(1 - |\lambda|)$, than the double wedge advocated by Pike. It is not clear how their conclusions would be modified by the incorporation of terms involving δ^2 .

For practical purposes, at least, the conclusion is clear. The best two-dimensional lifting wing is very close to a flat plate over the whole range of supersonic Mach numbers. There is, however, considerable theoretical interest in the way the Newton-Busemann theory hints at the nature of the true optimum shape. We also note that it only became possible to improve on the plane wedge when we used an aerodynamic theory which allowed for the interference between different surface elements.

If we now turn to the corresponding problem in three dimensions, we may expect larger interference effects (because, roughly speaking, the pressure waves due to an element extend from it along oblique Mach lines rather than directly downstream of it) and therefore, probably, larger gains. This expectation is certainly fulfilled at low supersonic speeds. There is an extensive literature on drag minimisation using linear theory. Chapter 8 of Reference 6 is devoted to this subject and some other pertinent references are listed as 18 to 21. The amount of drag reduction that can be achieved depends on the wing planform, for delta wings with supersonic leading edges Germain¹⁸ has shown that the reduction is greatest (about 11%) when the edge is nearly sonic, and decreases to zero as the aspect ratio increases toward infinity. Cohen²⁰ has studied the shapes of such optimum wings, insofar as they can be approximated by double power series. Some indication of the accuracy of this representation is that when the leading edge is sonic, six terms of the series can represent a wing whose drag is 8.9% less than the flat plate, and ten terms are enough to reduce the drag by 9.6%. The shape of the optimum surface derived from a six-term representation of a wing whose sweep angle X is given by $\cot X = 1.2/\beta$ is shown in Figure 12.

This figure reveals the mechanism by which the drag reduction takes place. The incidence is highest along the centerline, and progressively "washed-out" toward the tips. High pressures are generated in the central region, but spread out to the tip region where the small surface inclinations allow them to contribute effectively to the lift without adding greatly to the drag. This is the typical mechanism of favourable interference, and one which we must expect to find at work in the higher speed ranges also.

Attempts to exploit the concept of favourable interference have led to the study of many configurations. Some of these are distinctly unorthodox, like the famous Busemann biplane²², or the half-ring wing^{23,24}, and our main theme. From a practical point of view, attempts to exploit the inter-action between a wing and a central fuselage are more attractive. The properties of interfering systems are most easily studied using linear theory (for example, see Reference 25). Reliable calculations of non-linear interference effects on realistic shapes are at present beyond us, but some indication of the way that interference effects change with flow Mach number can be got from studying certain artificial configurations, which accordingly I make no apology for considering next.

Consider (Fig.13a) a flat plate of unlimited extent, aligned parallel with a uniform supersonic stream. Let there be a wedge, with its apex pointing into the stream, projecting vertically from the plate. Initially, we suppose this wedge to be of infinite height. According to linear theory, the plate experiences a uniform pressure, due to the wedge, over a region bounded by two parallel lines swept at the Mach angle. Now, let the projecting wedge be cut off at a finite height, so that its leading edge terminates at the point A (Fig.13b). The Mach cone from A intersects the plate in a hyperbola, asymptotic to the leading rays of the interference pressure region. The area between this hyperbola and these rays is unaffected by removal of the outer part of the wedge, and continues to experience a uniform pressure. Moreover, it still does so if the whole of the rest of the plate is removed, and all the wedge beyond the Mach line AE. We are left with a configuration which is a sort of rudimentary wing-body combination. All of its drag derives from a uniform pressure acting on the wedge, and all of its lift from the same pressure acting on the "wing". Since the area of the wing is in principle unlimited, there are seemingly no theoretical bounds on the lift-drag ratios that can be obtained in this way.

Theoretical limits on the efficiency of such an arrangement can only be discovered by considering the non-linear features of the flow. Taking these into account, we observe that the front of the interference region would really be an oblique shock wave, and the rear boundary a Mach cone of the flow behind the shock wave. The two boundaries would always therefore intersect at a finite distance, and the lift-drag ratios are therefore restricted.

The performance of such a configuration is easily calculated from exact shock wave theory, and finding its optimum form can be reduced to a purely geometrical problem²⁶. One wishes, in fact, to draw trailing edges on the wedge and on the plate which terminate the configuration in such a way that the ratio of wing area to body area is maximised, and no pair of points on either trailing edge are joined by a line making less than the Mach angle with the local flow. This problem is solved in Reference 26, if the Mach cone from A intersects the wing leading edge at T, then the Mach plane through the straight line AT intersects the wing and the wedge along the optimum trailing edge. It is then shown that the results of exact calculations on configurations designed in this way collapse onto a single diagram (Fig. 14), where the vertical scale is the reciprocal of the "induced drag factor", and the horizontal scale a similarity variable deduced from a small disturbance analysis. The performances of optimised interference configurations cluster very closely about a single curve, and the performances of plane (two-dimensional) wedges lie within a narrow fan. Over the range of Mach numbers considered, the interference configuration turns out to be better provided

$$\frac{M_\infty^2 C_L}{M_\infty^2 - 1} < 1.$$

In Figure 15 this criterion is used to illustrate those combinations of Mach number and lift coefficient for which one or other method for generating lift is preferable. From this we may conclude that pure aerodynamic interference is most suited to flight conditions which create relatively weak disturbances.

In Reference 27, however, Pike has extended this analysis to show that for any combination of Mach number and lift coefficient, interference effects can always be incorporated to improve lift-drag ratios beyond the wedge value. His demonstration utilises a generalisation of the simple swept wing. In the usual way (Fig. 16) we draw a stream surface behind a plane shock wave retaining for simplicity the customary V-shaped leading edge. We may terminate the wing by any trailing edge that is not subsonic. Suppose that this edge is not now symmetrical about the ridge line, and consider the forces which will act on the wing. The pressure is constant over the surface, and so there will be a lift proportional to the vertical projected area, a drag proportional to the streamwise projected area, and a sideforce proportional to the net area in side view. The lift coefficient (based on planform area) and lift-drag ratio will be the same as those of the two-dimensional wedge from which the shape is derived.

Now let the configuration be rotated about the free stream vector. Nothing will happen to alter the forces, except as regards to the direction in which they act. The drag force is completely unaltered, but the forces which we previously described as "lift" and "sideforce" will rotate with the configuration, as will their resultant, which we will describe as the "transverse force". If we wish to obtain the maximum vertical force, we must rotate the configuration until the transverse force is vertical. In doing so, we do not alter the lift coefficient, because the surface is always acted on by the same constant pressure, neither do we alter the drag force, but we do increase the lift force, and hence the lift-drag ratio. As in the previous paper the maximisation of the effect involves only geometrical considerations. The ratio of the areas of the two wing facets must be as great as possible, subject to the constraint that the trailing edge is fully supersonic. Again the optimum trailing edge turns out to lie on a Mach plane.

Pike²⁷ has calculated the maximum percentage improvement for various Mach numbers and lift coefficients, and finds that it depends only on the similarity variable $M_\infty^2 C_L / \beta_\infty^2$ encountered previously (Fig. 17). The maximum improvements are striking, and the shapes can be made a little more realistic by combining them in pairs, as shown in Figure 15. Of course, they are still very far from being "aircraft shapes" but they do provide the only demonstration I know that the two-dimensional wedge is not an optimum lifting surface under any combination of lift coefficient and Mach number.

Both of these last two configurations feature highly swept trailing edges, and in both cases the trailing edge *must* be swept before any advantage in performance is achieved. It has been known for a long time that sweeping the trailing edge of a plane delta wing (converting it to an "arrow wing") is a simple way to improve its performance. Some calculations using linear theory taken from Reference 28 are shown in Figure 19. It remains unclear just how much the efficiency of Pike's wings is due to "favourable interference" and how much to "planform effect". The two effects are in any case inter-related. If we concentrate the volume of a configuration toward the middle in the hope that it will have a favourable effect on the outboard regions, it would seem necessary to make these outboard regions as extensive as possible.

However, these highly swept configurations do suffer from practical disadvantages over and above their evident structural defects. Amongst other things the low speed aerodynamics is complicated by undesirable behaviour of the separated upper-surface vortices as they pass over the swept trailing edge²⁹.

Experimental tests of shapes incorporating interference concepts have often been disappointing. Simple configurations consisting of half-cones placed underneath flat delta wings were first suggested by Eggers and Syvertson²⁹ (see Fig. 2) and have been the subject of extensive experimental study in the USA. A very simple criterion for determining

the effectiveness of the interference concept is to compare the set of performance achieved by this design with the performance obtained by turning it upside down. Such a comparison, due to Becker²⁰ and typical others, is shown in Figure 21. The fact that the configurations actually work better upside down at higher Mach numbers is surprising at first sight, but a number of reasons for it can be found. Becker attributes part of the decline in interference benefits to the increasing effects of viscous interaction, as Mach number rises, and also uses this to explain the discrepancies between results at identical Mach numbers. However, the downward trend of this graph with increasing Mach number could be explained without reference to viscosity. In the idealised studies we have seen that the benefits of interference fall off anyway with increasing Mach number, because of the smaller areas available for the induced overpressures to act on. Moreover, we can reasonably assume that at very high Mach numbers the predictions of Newtonian theory become more nearly correct, and the optimum surface becomes more closely a flat plate.

Therefore we may expect that the amount of interference lift that one should optimally include in a design will be a quite strong function of Mach number. It seems very likely that in the half-cone + delta design the amount of interference employed is appropriate at lower speeds, but somewhat overdone at very high speeds.

We have already noted that the favourable effect of cambering a delta wing can be regarded as a kind of interference, and we can well suppose that these benefits also decline with increasing Mach number. The maximum reduction in induced drag factor was, we saw, 11% according to linear theory, on a source-leading-edge delta, and less at higher aspect ratios. It seems safe to assume that the greatest reduction is associated with the lowest aspect ratio because a given high incidence region (say, at the apex) has then the chance to influence the greatest fraction of the total wing area. Thus, if the overall properties of an aircraft are fixed by, say, low speed handling criteria, the faster we try to fly it, the less change interference effects, including camber, have to enhance the performance.

However, we are not as yet in a position to answer the question, at what combination of Mach number and lift do the benefits to be derived from camber become negligible? The question can only be answered with real confidence after tackling optimisation problems almost having the full complexity of the one I began this lecture by describing, but useful, even if tentative, answers can be given by studying the "waveriders" to which I shall refer in a later lecture.

So far I have been dealing with the optimisation of designs where only the lift coefficient was given in advance. I want to go on now to discuss the problem where volume is also prescribed.

A very simple example illustrating some features of the problem can again be taken from the two-dimensional case (when we must consider wings of fixed profile area). For additional simplicity we can consider only wings with streamwise upper surfaces (Fig. 22) and we shall neglect base drag.

We will suppose that the pressure law has the form

$$C_p = C_1 \frac{dy}{dx} + C_2 \left(\frac{dy}{dx} \right)^2, \quad (2.19)$$

which includes as special cases:

(a) Linear theory

$$C_1 = 2/\beta, \quad C_2 = 0.$$

(b) Busemann's second-order theory

$$C_1 = 2/\beta, \quad C_2 = \frac{(M^2 - 2)^2 + \gamma M^4}{2\beta^4}.$$

(c) Newtonian theory for slender bodies

$$C_1 = 0, \quad C_2 = 2.$$

Then, for a wing having fixed (unit) chord, we can write

$$C_L = \int_0^1 C_1 y' + C_2 y'^2 dx$$

$$C_D = \int_0^1 C_1 y'^2 + C_2 y'^3 dx$$

and (see Figure 22)

$$A = \int_0^1 (1-x)y' dx.$$

To find the minimum value of C_D with C_L and A given, is equivalent ⁶ to minimizing the integral

$$\int_0^1 F dx,$$

where

$$F = C_1 y'^2 + C_2 y'^3 + \lambda_1 (C_1 y' + C_2 y'^2) + \lambda_2 (1 - x) y'$$

and λ_1, λ_2 are Lagrange multipliers. The Euler equation satisfied by the optimum contour is in this case

$$\frac{\partial F}{\partial y'} = \text{constant}$$

and the transversability condition, applied at $x = 1$, shows this constant to be zero. Therefore the contour is described by the differential equation

$$2C_1 y' + 3C_2 y'^2 + \lambda_1 (C_1 + 2C_2 y') + \lambda_2 (1 - x) = 0. \quad (2.20)$$

In the special case of linear theory ($C_2 = 0$) Equation (2.20) reduces to

$$C_1 y' + \lambda_1 C_1 + \lambda_2 (1 - x) = 0,$$

which integrates to give

$$y = -\lambda_1 x + \frac{\lambda_2}{2C_1} ((1-x)^2 - 1). \quad (2.21)$$

That is, the optimum contour is parabolic, with λ_1 and λ_2 determined by the required values of C_L and V .

To see how this works out in terms of actual shapes, we can note that

$$y(1) = \int_0^1 y' dx = \frac{C_L}{C_1},$$

i.e., all wings having a given C_L pass through the same point in the base plane. Of these, we already know that the one with the least drag of all is the wedge (see Figure 23). Let the area of that wedge = $\frac{1}{2} y(1) = A^*$. Suppose we actually need $A > A^*$. Then we can see that the best way of adding the extra area is by means of a corner parabolic curve. Suppose on the other hand that our requirements for A were not as great as A^* . The best policy then would be to use the wedge section, since this has less drag than any other, and also offers without penalty a bonus volume over and above our needs.

The same general conclusions hold when the case $C_2 \neq 0$ is considered, all that happens is that the detailed shape of the section is altered. The shapes can still be found analytically, because Equation (2.20) can be solved for y' to give something of the form

$$y' = a + (b - cx)^{1/2}$$

and thus

$$y = ax - \frac{2}{3} (b - cx)^{3/2}. \quad (2.22)$$

where a, b, c depend rather cumbrously on C_1, C_2 and the prescribed values of C_L and A . Generally, the effect of adding the non-linear term is to concentrate the volume farther aft.

To treat even the two-dimensional problem with any greater accuracy than this would be a formidable task. It is unlikely that any approximations can be used in the way that Pike treated the volume-free problem described earlier, because the optimum shape will generally not now be close to any simple shape like a wedge. Bartlett³¹ has computed the optimum proportions of double wedges (see Figure 24) and found them to be convex in all cases considered.

If we go on to consider lifting three-dimensional wings with a volume constraint we find, so far as I know, no published work based on anything except Newtonian theory, the most comprehensive treatment being that of Maikaper³². He considers three-dimensional wings (Fig.25) whose lower surfaces are defined by

$$z = z_1(x, y)$$

and whose upper surfaces are defined by

$$z = z_2(x, y).$$

The wing has a completely free planform area, and is subject to a given friction coefficient. The pressure is assumed to be given by

$$C_p = k \left(\frac{\partial z}{\partial x} \right)^2.$$

The wing is sought which has the greatest lift/drag ratio of any wing enclosing a given volume. Thus the lift coefficient cannot be fixed in advance, but emerges as part of the problem solution.

Maikapor finds that the best wings are symmetrical about an incidence plane, and that the upper surface is always streamwise at the trailing edge. The actual profile shapes are $3/2$ power law, of the same form as Equation (2.22). It is interesting to note that the same airfoil profile also turns up in the solution to the slender, three-dimensional *non-lifting* wing⁶. Maikapor²² also gives two extreme profile shapes, between which the optimum profiles always lie (Fig.26). He does not, however, consider the optimum shape of the planform. All his results are true for any chosen shape, but do not give rise to the same performance in each case.

I know of no work in which lifting three-dimensional wings are optimised within more complex constraints. Evidently many more constraints would be necessary to approximate all the considerations that an aircraft designer must take into account, but as I said earlier, it is questionable to what extent the full design process could ever come under the province of optimisation theory rather than empirical judgement. Of the constraints which I have not discussed, probably the most important is centre of pressure position. This must be made to coincide with the centre of gravity, if the aircraft is to be trimmed for level flight, and the centre of gravity is, within limits, fixed. An alternative attitude, however, is to optimize the aircraft design on other grounds, and then to ask whether, with the centre of pressure in the resulting position, the internal design of the aircraft can be juggled so as to make the centre of gravity match up.

In this lecture I have tried to give an outline of the ways in which, at the present moment, optimisation theory can help to define shapes for hypersonic transport vehicles. To date, it has only been possible to apply the theory using rather simple aerodynamics, such as linear or Newtonian theories, at any rate on the three-dimensional case. Nevertheless, a consistent picture begins to emerge of what a good integrated aircraft shape should look like.

REFERENCES

1. Babaev, D.A. *Numerical solution of the problem of supersonic flow past the lower surface of a delta wing*. Zhurnal Vychislitel'noi Matematiki i Matematicheskoi Fiziki, Vol.2, No.6, Nov 1962, English translation in AIAA J Vol.1, No.9, Sept. 1963.
2. Babaev, D.A. *Flow about a triangular wing for large values of M*. Zh. vych. mat. Vol.3, No.1, 1963.
3. Babaev, D.A. *Numerical solution for the problem of the flow of a supersonic stream past the upper surface of a triangular wing*. Zh. Vych. mat. Vol 2, No.2, 1962. English translation in FTD-TT 62-1582.
4. Reyin, J.W. *Differential-geometric considerations on the hodograph transformation for irrotational conical flow*. Arch for Rational Mech. and Analysis, Vol.6, p.299, 1960.
5. Bulakh, B.M. *Comments on a paper of J.W.Reyin*. Prikl. Mat. i Mekham, Vol.76, p.793, 1962.
6. Miele, A. *Theory of Optimum Aerodynamic Shapes*. Academic Press, 1965.
7. Newton, Sir Isaac *Mathematical Principles of Natural Philosophy*, translated from the Latin by A.Motte, revised by A.Cajori. University of California Press, 1934.
8. Akers, A. *Some studies of pressure distributions on windward surfaces of conical bodies at high supersonic speeds*. RAE Tech Note 2911, Sept. 1963.
9. Busemann, A. *Flussigkeits- und Gasbewegung Handwörterbuch der Naturwissenschaften*. Vol.4, 2nd Edition, Gustav Fischer, 1933.

10. Hayes, W.D.
Probstein, R.F. *Hypersonic Flow Theory*, Vol.1, Inviscid flow. Academic Press, 1966.
11. Eggers, A.J.
et al. Bodies of revolution having minimum drag at high supersonic airspeeds. NACA Report 1306, 1957.
12. Feckham, D.H. Measurements of pressure distribution and shock wave shape on power-law bodies at a Mach number of 6.85, RAC TR 65075, 1965.
13. Kubota, T. Investigation of flow around simple bodies of hypersonic flow. GALCIT Memo No.40, June 1957, P65132.
14. Miele, A. Maximum lift to drag ratio of a slender wing at hypersonic speeds. Z. für Flugwissenschaften Vol.15, 1967.
15. Pike, J. Minimum drag surfaces of given lift which support two-dimensional supersonic flow fields. Aero. Res. Coun. R and M. 3543, Sept. 1966.
16. Chernyi, G.G. *Introduction to hypersonic flow*. Academic Press, 1961.
17. Cole, J.D.
Aroesty, J. Optimum hypersonic surfaces close to flat plates. AIAA J Vol.3, No.8, August 1965.
18. Germain, P. Sur le minimum de traînée d'une aile de forme en plan donnée. Comptes Rendus Vol 244, No.9, 1957.
19. Jones, R.T. Minimum drag of thin wings in frictionless flow, J. Aero Sci, Vol.18, No.2, 1951.
20. Cohen, D. The winging of triangular wings for minimum drag at supersonic speeds. J. Aero Sci, Vol.24, No.1, 1957.
21. Heasloet, M.A.
Fuller, F.B. Drag minimization for wings in supersonic flow, with various constraints. NACA TN 4227, 1958.
22. Liepmann, H.W.
Roshko, A. *Elements of gas dynamics*. John Wiley, 1957.
23. Moore, K.C.
Jones, J.G. Some aspects of the design of half-ring wing body combinations with prescribed wing loadings. RAE TR 2860, 1962.
24. Boyd, J.A. Optimal utilisation of supersonic favourable interference to obtain high lift-drag ratios. AIAA Paper No.65-752, 1965.
25. Ferri, A.
Clarke, J.H. On the use of interfering flow fields for the reduction of drag at supersonic speeds. J. Aero. Sci.
26. Roe, P.L. Some exact calculations of the lift and drag produced by a wedge in supersonic flow, either directly or by interference. Aero. Res. Coun. R and M 3478, 1967.
27. Pike, J. Theoretical performance of lifting surfaces supporting plane shock waves. Aero. Res. Coun., 1969.
28. Jones, R.T.
Cohen, D. Aerodynamics of wings at high speeds, Section A of Vol.7 of *High Speed Aerodynamics and Jet Propulsion*. Princeton University Press, 1957.
29. Eggers, A.J.
Forsverson, C.A. Aircraft configurations developing high lift-drag ratios at high supersonic speeds. NACA RM A55L05 March, 1956.
30. Dean, J.V. Studies of high lift/drag ratio hypersonic configurations. AIAA Paper 64-551, 4th ICAS Congress, 1964.
31. Bartlett, R.S. High lift-drag ratio double wedges which support two-dimensional supersonic flow fields. RAE TR 66306, 1966.
32. Maikapor, G.J. A wing with the maximum lift-drag ratio at supersonic velocity P.M.M. Vol.30, No.1, 1966.



Fig. 1 Flow past lower surface of a delta wing
(after Babaev)



Fig. 2 Flow past upper surface of a delta wing
(after Babaev)

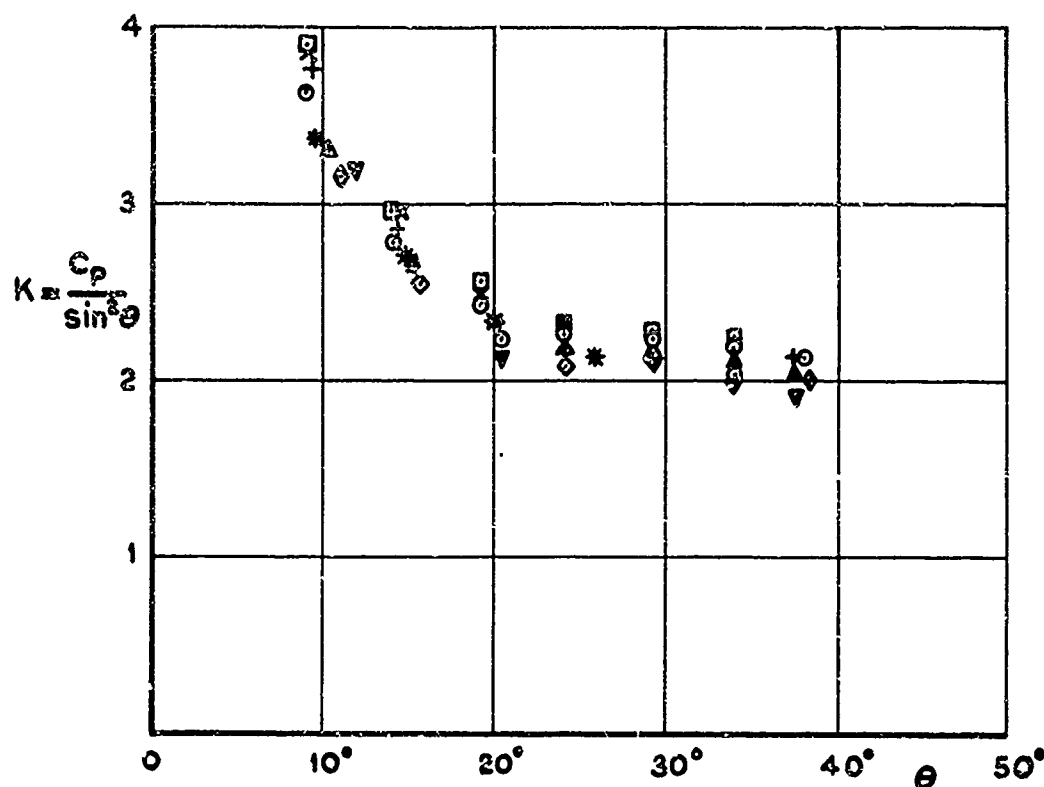


Fig. 3 Pressure correlation on 1/8 cone segment body at $M_\infty = 4.3$

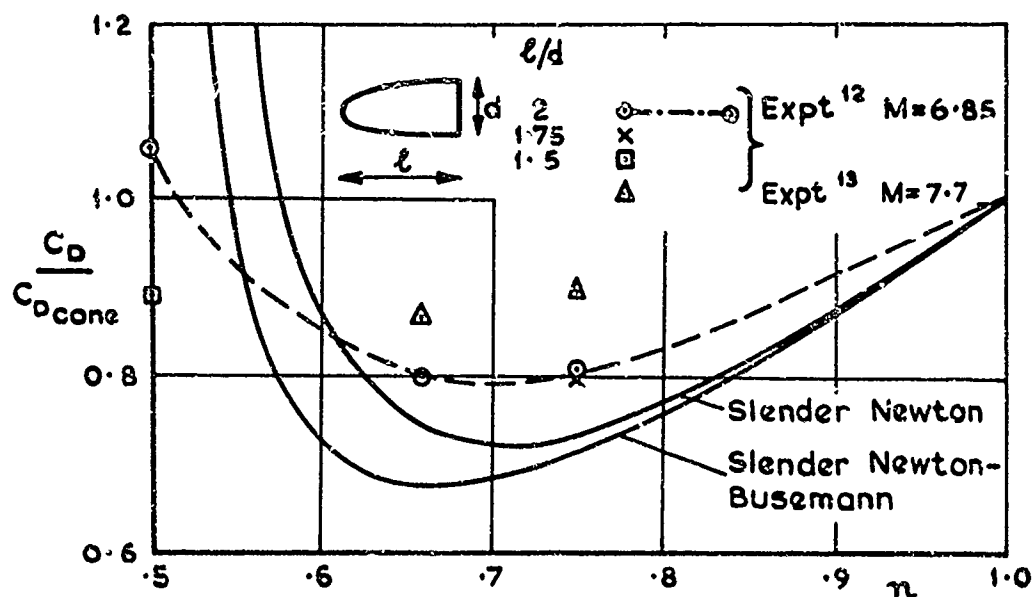


Fig. 4 Variation of C_D with power-law exponent (n)

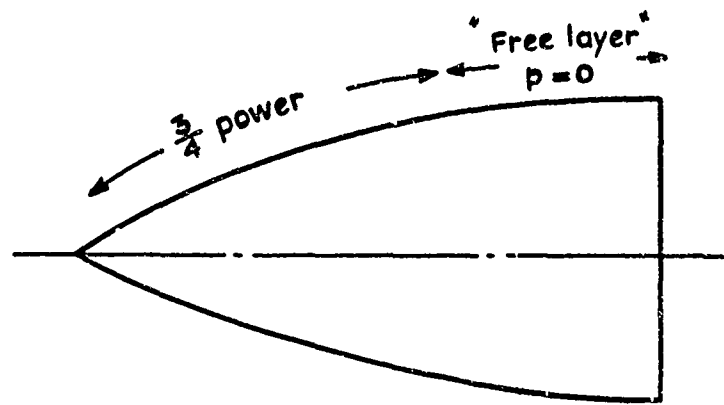


Fig.5a Optimum nose shape, according to Newton-Busemann theory (proper optimum)

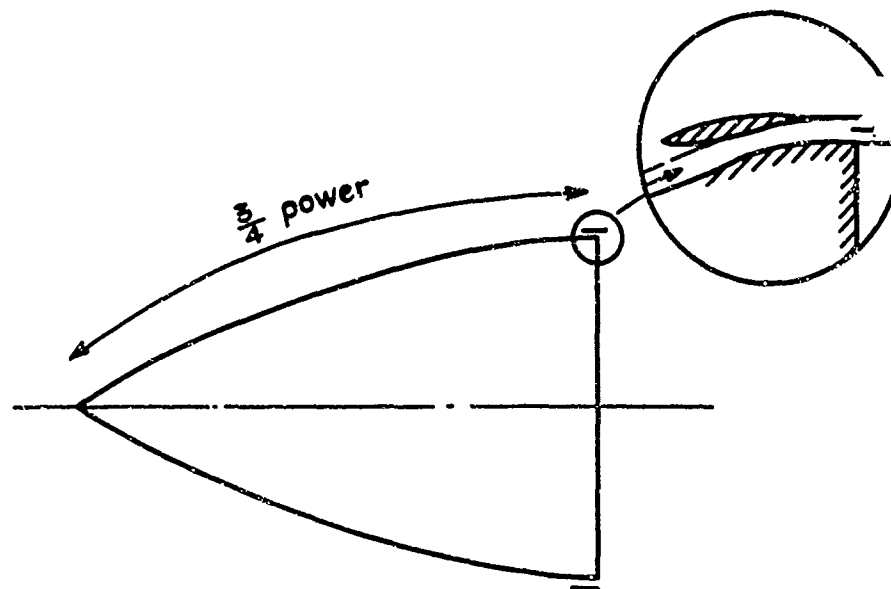


Fig.5b Optimum cowed nose shape, according to Newton-Busemann theory (absolute optimum)

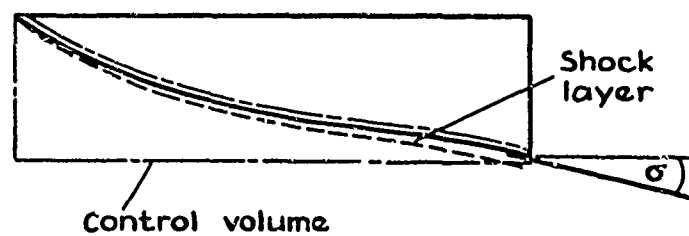


Fig.6 Control volume to calculate forces on two-dimensional wing using Newton-Busemann theory

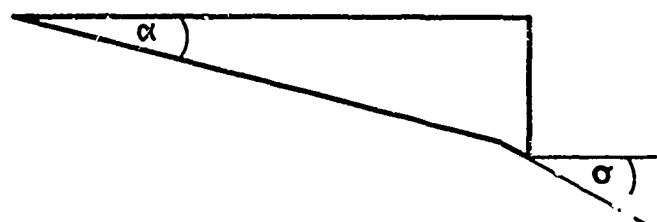


Fig.7 Optimum wing according to Newton-Busemann theory

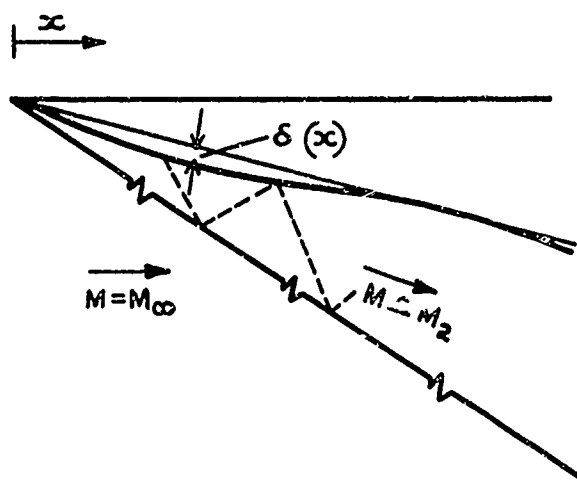


Fig.8 Flow past a two-dimensional quasi-wedge

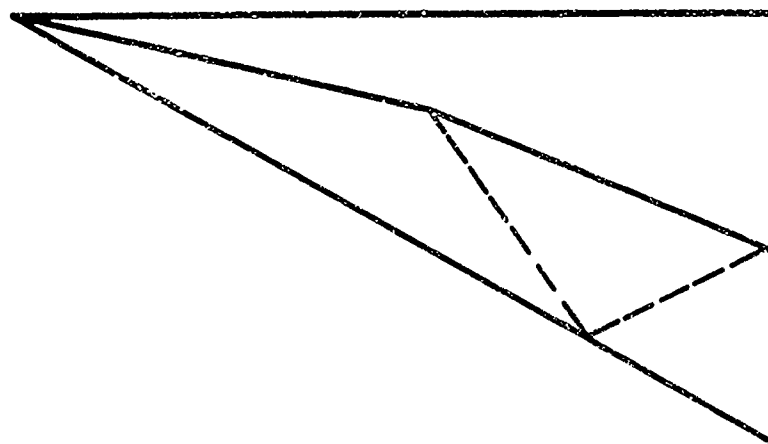
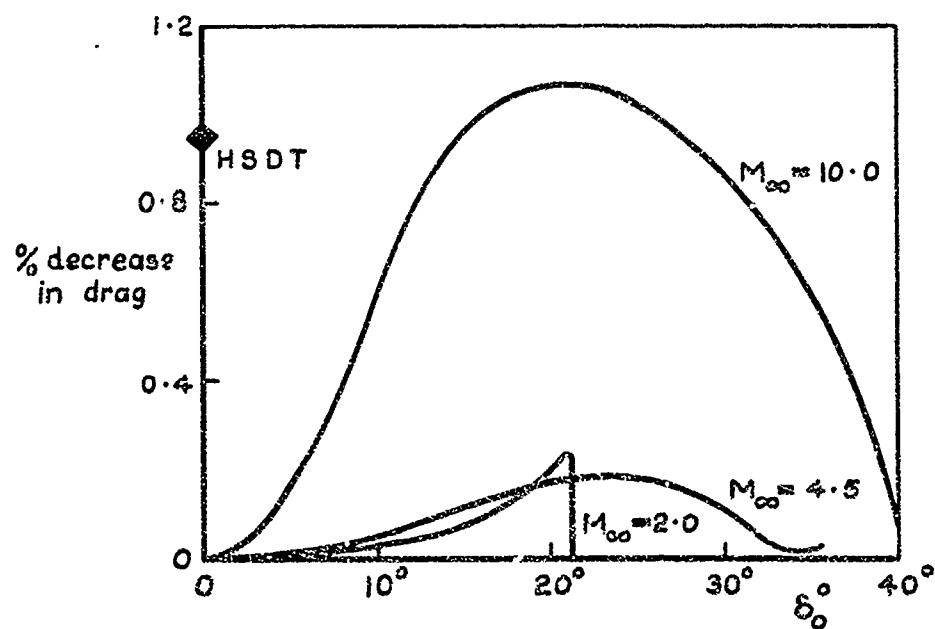


Fig.9 Optimum wing according to Pike's theory

Fig.10 Percentage reductions in drag for given lift, according to Pike (δ_0 = angle of unperturbed wedge)

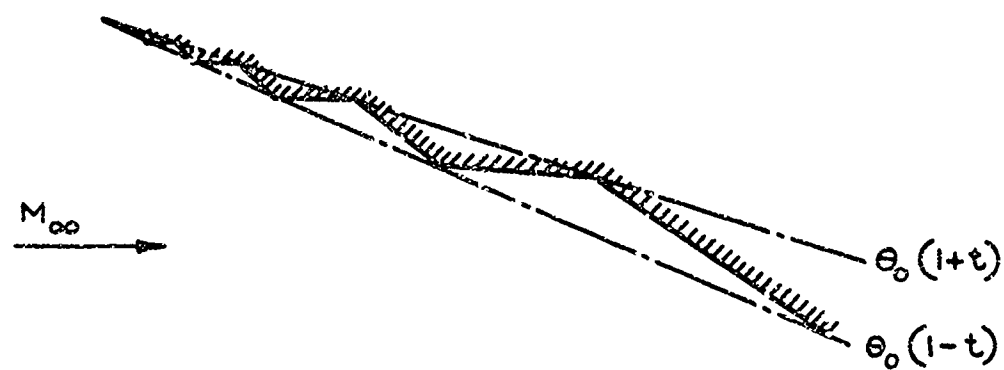


Fig.11 Optimum wing shape, according to Cole and Aroesty

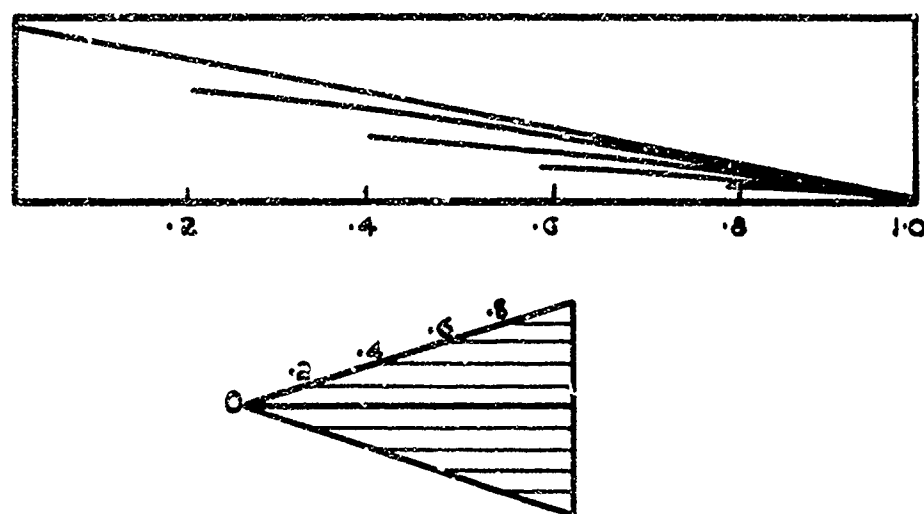


Fig.12 Chordwise sections of optimum delta wing, according to linearized theory

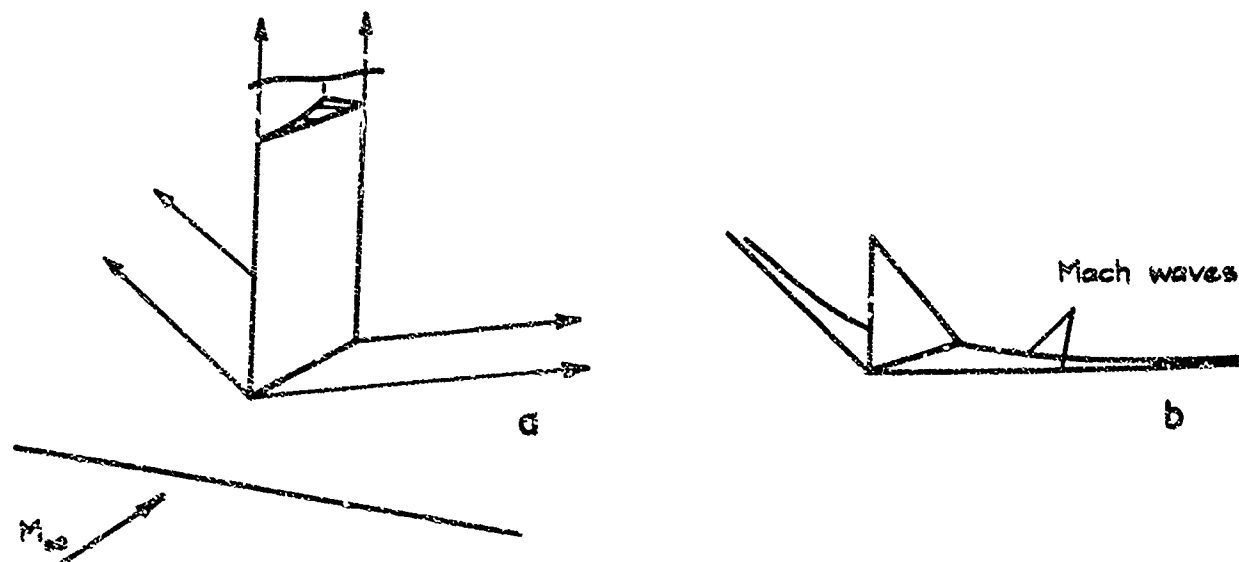


Fig.13 Wedge-interference concept, according to linear theory

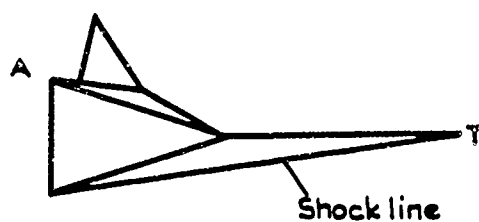


Fig.14a Wedge-interference concept (non-linear theory)

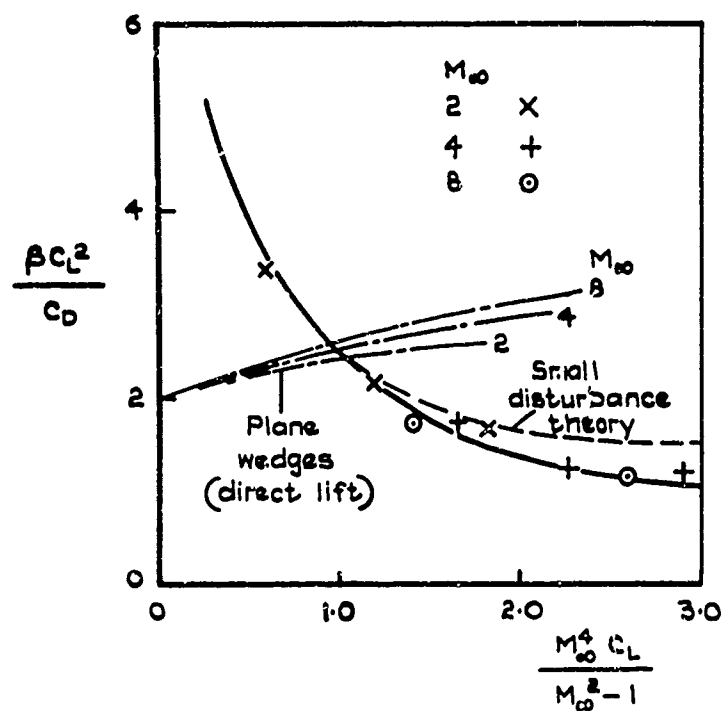


Fig.14b Comparison between direct and interference lift of plane wedges

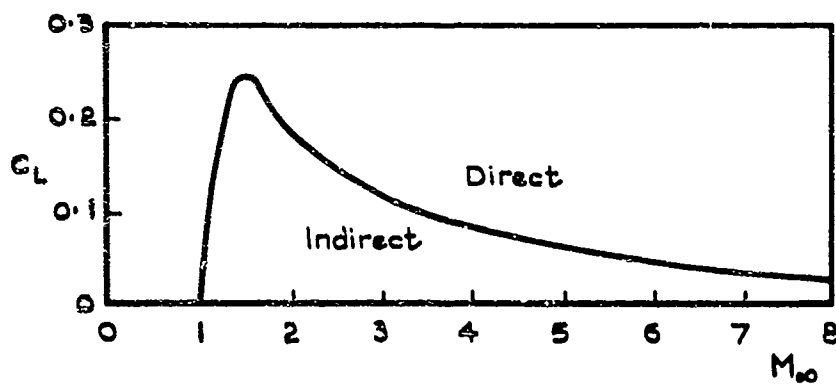
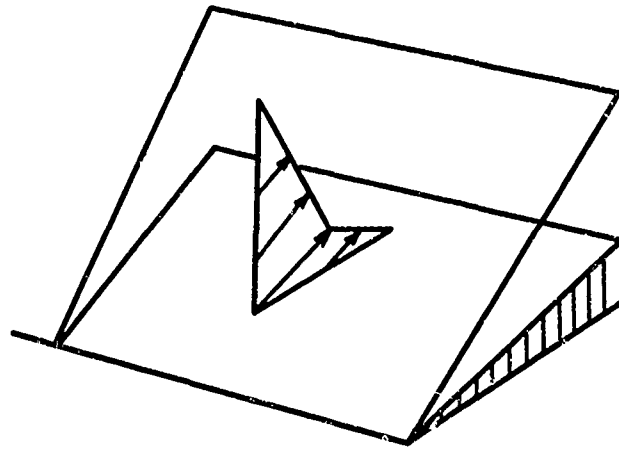
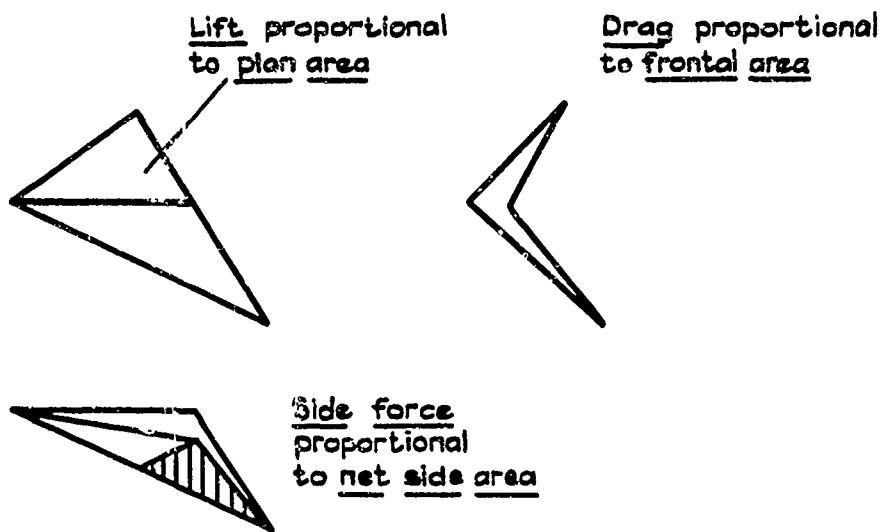


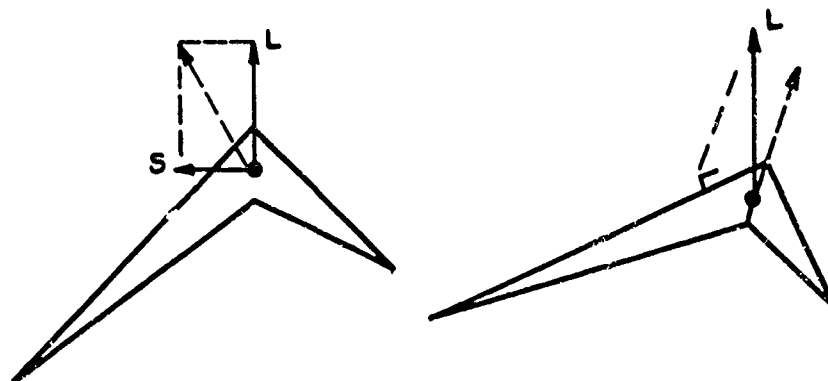
Fig.15 Regions of preference for direct and indirect lift



a



b



c

Fig.16 Properties of an asymmetric caret wing

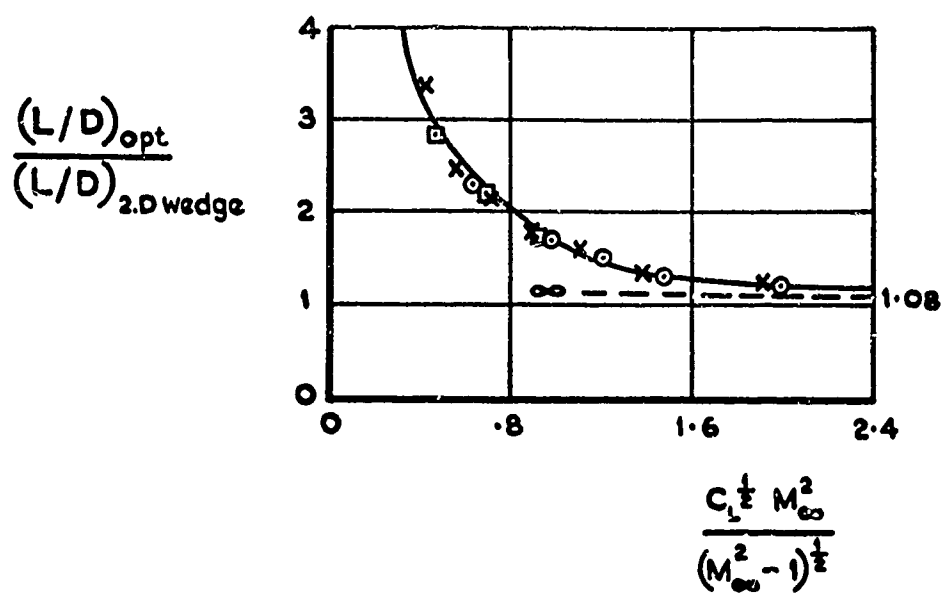


Fig.17 Optimum performance of asymmetric caret wings

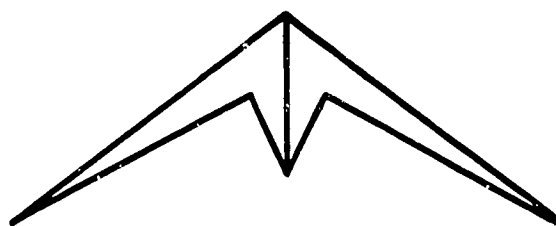


Fig.18 A pair of asymmetric wings

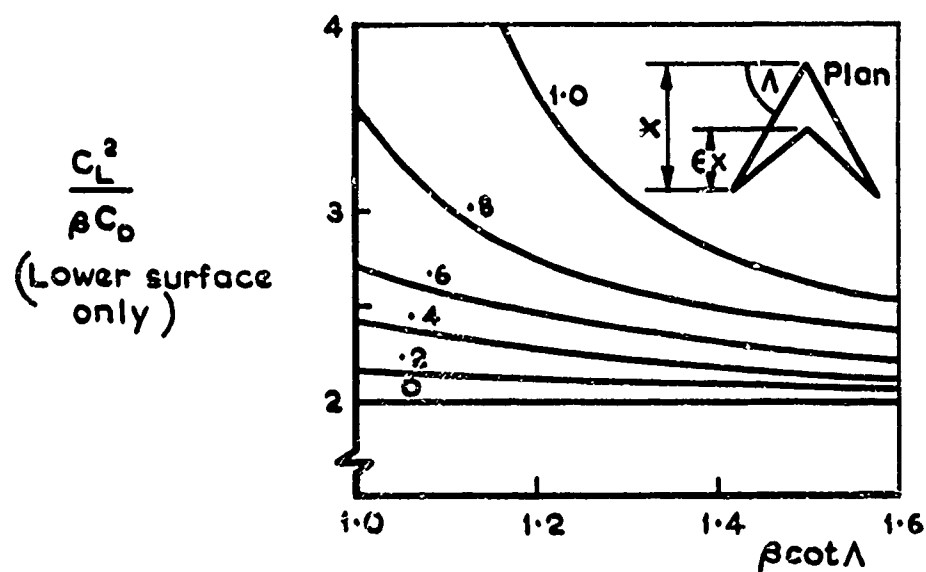


Fig.19 Performance of arrowhead wings, according to linear theory

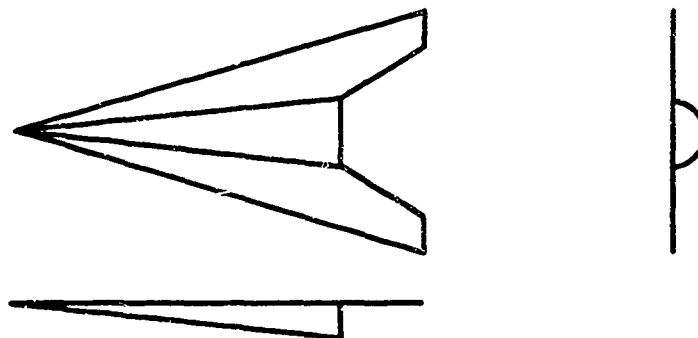


Fig. 20 Half-cone and wing

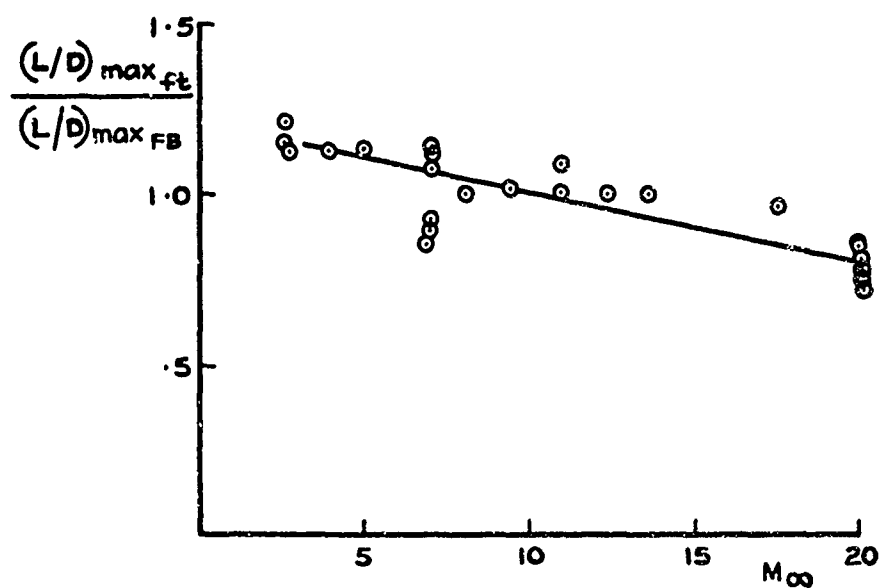
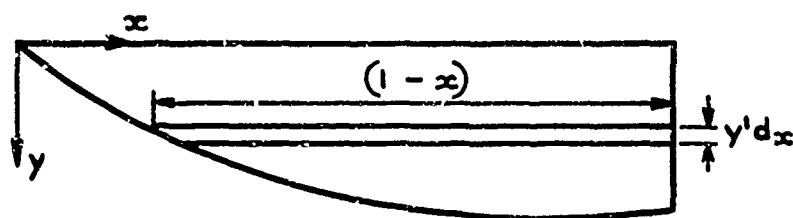
Fig. 21 Comparison of $(L/D)_{\max}$ for 5° half-angle cones+delta-wings in "design" and "inverted" configurations

Fig. 22 Two-dimensional wing

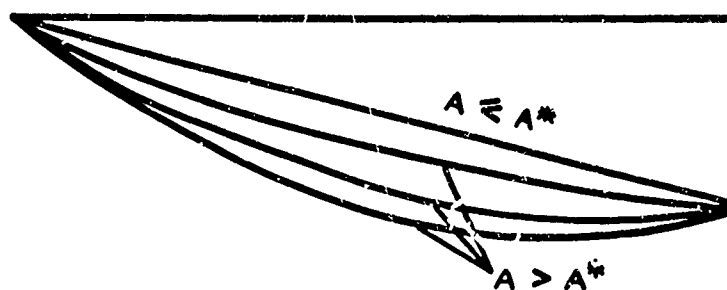


Fig.23 Family of optimum wings, according to linear theory

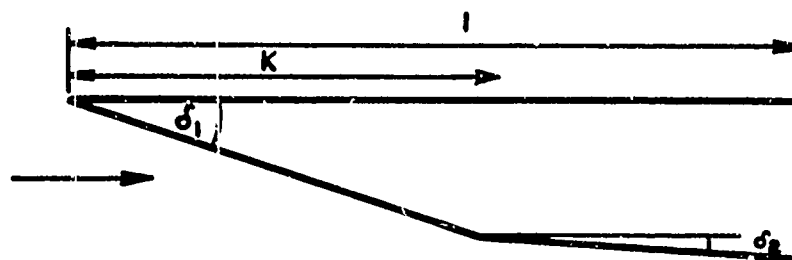


Fig.24 Bartlett's problem

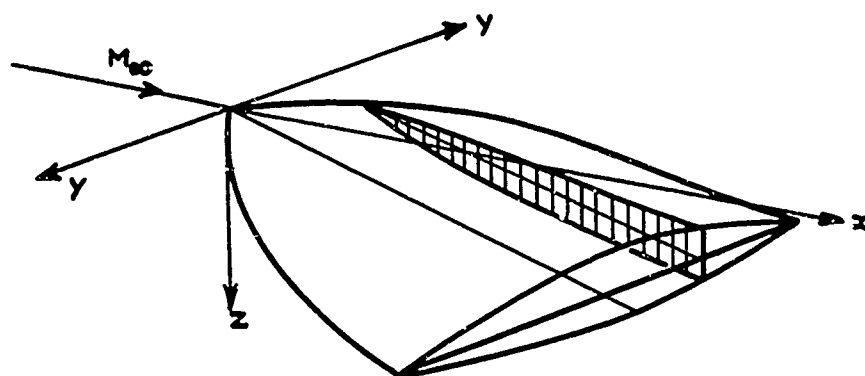


Fig.25 Maikapar's problem

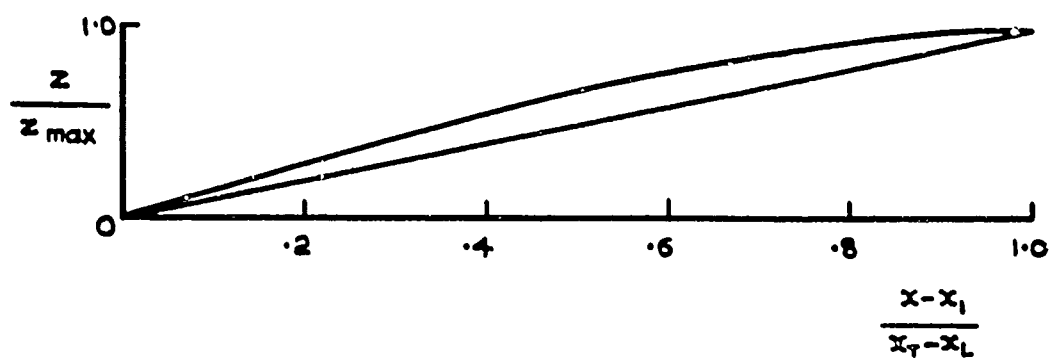


Fig.26 Limiting optimum profiles

LECTURE 3

THEORY OF "WAVERIDERS"

P.L.Roe

Royal Aircraft Establishment, Bedford, England

All the methods we have available at the present time for predicting directly the hypersonic behaviour of a given shape are approximate to an extent that precludes full confidence in the deductions we can make from them. It is useful therefore to have available for comparison more accurate solutions even if these are of the inverse kind, where wing shapes cannot be arbitrarily chosen in advance. Solutions whose accuracy is limited only by the need to assume a perfect gas can be obtained by tracing wing-like streamsurfaces in calculated flow patterns which have some simplifying feature, for example, they may be two-dimensional or axisymmetric. Because it is not the shape of the wing which in this process is chosen in advance, but rather the wave formation, they have come to be known as "waveriders" and it is in this sense that I shall use that term.

It is useful to list what we may hope to achieve by studying waveriders.

1. We can use them, instead of expensive experimental data, to check the accuracy of approximate prediction methods.
2. We can study systematic families of shapes and draw general conclusions as to the effects of aspect ratio, contained volume, distribution of volume, etc., on performance characteristics.
3. We can establish levels of performance which will serve as criteria by which to judge the excellence of designs achieved by other methods.
4. Although the flow about a waverider in its design condition has a deceptive simplicity, the flow in conditions just slightly "off-design" may provide a point of entry for the study of more general and more complex flows about wing-like shapes.

When using this approach to consider any of these four items, we must constantly keep in mind two reservations. First, that the shapes we consider, although varied, are still in some sense special, so that the conclusions we draw may only have a restricted validity. Second, that the value of the study will increase insofar as we are able to make the waverider shapes share the qualitative features of practical aircraft designs.

We shall begin, then, by considering some very simple waveriders, and the extent to which their shapes may or may not be manipulated. The simplest waverider is the caret wing^{1,2}. This is designed by starting with the flow past a two-dimensional wedge. The flow pattern associated with the wedge is, of course, a plane shockwave followed by uniform flow parallel to the wedge surface (Fig.1a). We shall perform a simple thought-experiment on this flow. In imagination, we draw a pair of intersecting straight lines lying in the plane of the shock, and visualise the stream-surface which stems from them. It consists of a pair of intersecting planes (Fig.1b). Suppose now that we construct a very thin sheet of stiff material, having exactly the shape of this surface, and suppose that we introduce it carefully into the flow field, from behind the shockwave, aligning it exactly with the flow direction. In a frictionless fluid we can do this without causing any flow disturbance, provided the sheet does not protrude through the shock surface. If the sheet is positioned so that its leading edge lies exactly in the shock surface, we can divide the flow into three regions (Fig.1b), region I being the undisturbed stream. Now it may be noted that there is no path by which an acoustic signal can pass from region II to region III. A strongly compressive signal might pass if it were strong enough to deform the shock wave outward from the leading edge of the sheet, but an expansion wave cannot make the journey in any circumstances. Suppose now that the wedge with which we began is slowly worn away and disappears. In the process, the part of the shock wave separating regions I and II will weaken and vanish, but no news of the event can reach region III, so that the original flow pattern persists there unaltered.

In the above argument I have tacitly assumed that the flow pattern extends to infinity downstream, but it can be made to apply equally well to finite systems if the sheet is supposed to terminate in a trailing edge that is everywhere supersonic with respect to the flow behind the shock wave. Then we define regions I, II, and III with similar

properties to the above except that now region III is bounded by (Fig.1(c))

- (a) the shock wave
- (b) the stream surface
- (c) the downstream Mach envelope from the trailing edge.

We must note that this extension is not valid if the shock wave is so strong as to cause subsonic flow to exist, for then there is no surface (c).

By such an argument we convince ourselves that a flow pattern consisting of a plane shock wave followed by a parallel flow can exist on the thin sheet, if it is placed in isolation in a uniform stream of the right Mach number (Fig.1d). The basic waverider *hypothesis* is that this flow pattern is the *unique solution* for this shape under design conditions of Mach number and incidence. This is a very reasonable hypothesis and well supported by all the experimental evidence, but it is not entirely beyond question, as we shall see later on.

For the moment, however, we put on one side the difficult question of uniqueness, and accept the thought-experiment as satisfactory. The surface which we have designed bears some resemblance to a rudimentary wing. Being infinitely thin it is not very practical, but we can remedy this by adding material on the upper surface, so long as we do not add so much that we detach the shock wave, and spoil the designed flow. If we wish to have a known flow everywhere, we can most easily achieve this by making the upper surface parallel to the free stream. The result is the simple "caret wing" which has been the subject of many experimental studies^{3-7, 17}. We shall now consider, in increasing order of complexity, some possible variants on the theme.

The simplest thing to vary is planform shape. Instead of drawing simply a pair of straight lines on the shock surface and taking these to represent the leading edge, we could choose a quite arbitrary curve, whose vertical projection would become the planform of the wing.

All wings so designed support the same constant pressure, and therefore have the same lift coefficient based on planform area. Moreover, they all have the same lift-drag ratio, which is the cotangent of the angle of the wedge, and the centre of pressure always coincides with the centre of area.

There seems no reason of principle why the shape of the curve should be restricted in any way. The thought-experiment described above seems equally valid however irregular the curve may be, whether it is topologically open or closed or even reentrant, but of course the wing designer is only interested in shapes which are, in some sense, "natural". However the fundamental condition that the leading edge shall lie in the plane of the shock wave is rather restrictive. The slope of this plane is fixed by the basic design requirements of Mach number and lift coefficient, according to the formula

$$\sin^2 \theta = \frac{1}{M_\infty^2} + \frac{2C_L}{(\gamma + 1)} \quad (3.1)$$

Any curve drawn in this plane has a similar appearance whether viewed from in front or on top (Fig.2) the two projections being affine transformations of each other. In aerodynamic parlance this means that if part of the leading edge is highly swept, it must also be very anhedral and if the wing has overall a low aspect ratio it must also have strong anhedral, and hence a large ratio of wetted area to planform area, and therefore, also a large friction drag. For simple wings of this type there is then of necessity a relationship between aspect ratio and friction drag. This puts them at a disadvantage compared with less special shapes if there is a design requirement for either

- (a) low cruise Mach number
- (b) high lift coefficient
- (c) or relatively low aspect ratio.

In particular, it appears that caret wings are much less efficient than slender wings over the Mach number range three to five where both might be considered. However, this disadvantage is typical of caret wings only, and not of waveriders as a class, as we shall see.

Summarising so far, we have seen that when designing waveriders using the flow past a two-dimensional wedge, we have an unlimited choice of planform area, but little opportunity to utilise this choice advantageously.

The next idea we might try is to alter the details of the flow field. Let us suppose that instead of a plane wedge we begin with some other two-dimensional shape. Again this can in principle be as general as we please but there is probably little point in studying shapes which are anything other than simple and smooth. For example, we can choose to start with the flow over a smooth convex wedge (Fig.3). Such flows can be calculated by the method of characteristics⁸, and generally the streamline curvature will be in the same sense as that of the body, so that any waverider shapes that we develop will also be convex (Fig.4).

This is a very useful degree of freedom. Disadvantages of the caret wing are that its lift and volume are both centred too far aft to be representative of practical designs, but this change remedies both defects simultaneously. Moreover, the lift/drag ratio of the shapes is no longer a function of design Mach number and lift coefficient alone, we can in principle easily investigate a family of shapes to find what sort of effects a redistribution of volume, say, has on performance. One way of doing this is to fix a planform shape and vary the shape of the two-dimensional body that generates the flow field.

Pike⁹ has done this for waveriders of delta planform and given lift coefficient. He employs a similar theory to that described in Lecture 2 for calculation of the flow field. That is, the generating body is supposed to be nearly a plane wedge, the departures from this wedge being of order δ . Disturbances reflected from the shock wave are supposed to be attenuated by a factor λ , and terms of order δ , $\lambda\delta$, and δ^2 are accounted for in the pressure distribution. He finds, as one might expect, that the optimum generating body is very close to a wedge, consisting of two nearly collinear straight sections joined by a curved mid-section. The optimum waverider derivable from two-dimensional flow fields is therefore very close to a caret wing.

If the shape is also required to enclose a given volume (assuming always the same upper surface shape) the problem is more complex, and not easy to treat by any realistic non-linear theory. In unpublished work, Pike has simplified the problem by considering linearized flow fields, and finds that, for wings of delta planform, the optimum generating body has a quadratic representation

$$y(x) = ax^2 + bx + c, \quad (3.2)$$

where the constants depend on the free stream conditions, the constrained values of lift and volume, and on the aspect ratio. Given reasonably "practical" values of these quantities, the shapes turn out to be convex. Fortunately therefore, we find all our requirements tending in the same direction.

Nevertheless, these waveriders based on two-dimensional flows do still suffer from the basic disadvantage that the leading edges must lie very close to the plane defined by Eqn (3.1). Under many circumstances they will be very anhedralled, and so be subject to large skin friction drags. If we are to pursue our ambition of finding configuration shapes that are both "good" and "realistic", we shall need to use more general flow fields.

The first step in this direction was taken by Jones¹⁰, who obtained more realistic shapes by starting from the flow past an unyawed cone (Fig.5). This at once produces a very useful change in the geometry. Suppose that we choose our waverider surface (Fig.6) by taking as our leading edge the intersection of the conical shock wave with a plane surface. The leading edge will then be a hyperbola lying in that plane, and the shock wave will curve well outside the plane, as it does, e.g., on a plane delta wing. Waveriders designed in this way are much flatter, and therefore have less friction drag, than those designed from two-dimensional flows. Three such shapes have been tested experimentally¹¹ to confirm this extension of the design method.

These uses of the simple cone-flow do, however, carry their own disadvantages. The streamlines of the flow are all concave with positive pressure gradients along them and so any waverider surface we choose will have, in even more exaggerated form, the rearward centres of volume and pressure that were part of our reasons for rejecting the caret wing. Therefore, we have to generalise yet again and this time we go to the flows about arbitrary bodies of revolution. Some details of this extension are given in Reference 12, here I shall partly summarise that work, and partly describe more recent developments.

To calculate the flow past bodies of revolution, we need a computer programme based on the method of characteristics or an equivalent. Such a programme can be greatly simplified if the body nose is initially a cone, because tabulated cone flow solutions can then be used to start the programme off. Otherwise, if the body is initially curved, the programme must take special measures to circumvent a singularity in the equations at the apex. The shapes shown in Reference 12 were computed using an existing flow-field programme which assumed a conical nose, but this turned out to be rather restrictive. We wish in fact to make the initial curvature of the innermost streamlines as strong as possible, so as to concentrate the volume of the resulting waveriders in a convenient and efficient way.

A fresh programme was therefore written, but so as not to be troubled by the singularity on the axis (which, after all, we do not need to include in the chosen part of the flow field) we have considered axisymmetric bodies with an annular hole (Figs.7-8). Such bodies normally present no special computational difficulties. This programme is part of a suite written by Moore and Pike at R.A.E. Bedford, which calculates axisymmetric flow fields, traces the stream surfaces within them, and evaluates their performance when considered as waveriders.

Typical results from these programmes are shown in Figure 9. A section of the flow field used is shown at the top, and then there follows a three-view drawing of a waverider taken from it. The planform was chosen to be a delta of semi-span to length ratio 0.35. In the side view the leading edge is represented by a solid curve, and the centre-line by a dotted curve. It will be observed that the wing lower surface is quite flat.

At its design Mach number of 4.0 the lift coefficient of the lower surface is 0.0571 and the drag coefficient is 0.00543 if skin friction is supposed zero. The lift/drag ratio is then about 10.5. If we assume that the drag coefficient is increased due to skin friction by an amount

$$\frac{(\text{lower surface wetted area}) \times c_f}{(\text{planform area})},$$

then the lift/drag ratio will be reduced as shown in Figure 9(c). This performance curve is very close indeed to what one gets from a two-dimensional wedge producing the same lift at the same Mach number, and subject to the same c_f . It is rather better than one could get from a caret wing, and that fact, combined with the more plausible shape and convenient camber of the shape in Figure 9, can be taken as justifying the additional work involved in computing these generalised waveriders.

So far no account has been taken of the possibility that the upper surface might be anything but streamwise. It will of course not often be the case that a streamwise upper surface is best. Broadly speaking, it will be advisable, whenever we require a large lift coefficient, to make the upper surface also contribute to the lift. On the other hand, if the need is for a large volume, we can get some of this by "building up" the upper side, so that it too becomes a compression surface.

In either case, it is possible to define the contours of the upper surface also by means of the streamline tracing technique, and so preserve everywhere the calculable nature of the flow. In what follows I shall give an account of the process to be followed if an expansion flow is desired.

Figure 10 shows the simplest possibility, as first suggested by Flower¹³. The flow field employed is a simple Prandtl-Meyer expansion, shown in perspective in Figure 10(a). Figures 10(b) and 10(c) show how a stream surface can be taken from the flow. In this case, if the surface of Figure 10(c) were to be placed in isolation in the "design" stream conditions, its leeward side would experience simply the Prandtl-Meyer flow pattern. The geometric shortcomings of this shape are, however, similar to those of compression surfaces based on wedge flow. The leading edge of the expansion surface must lie in a Mach plane, whose inclination is

$$\theta = \sin^{-1} \frac{1}{M_\infty} \quad (3.3)$$

If the edge is to be swept back, it must also be dihedralled (the edge of a wedge flow wing had to be anhedralled) and so again subject to high friction losses. Therefore, it seems again that we have to reject two-dimensional flows as a basis for design. It should be remembered, though, that waverider shapes based on two-dimensional flow might in some circumstances be fruitful subjects for study. As one example, they may provide simple cases for developing an understanding of shock wave behaviour, we return to this point later. As another, they may offer simple calculable environments in which to study the development of three-dimensional boundary layers¹⁴.

However, returning to our efforts to design a suitable shape for the upper surface, we try again to generalise our approach. More general two-dimensional flows will not solve the problem, we turn therefore once more to axisymmetric flow. Figure 11 shows the flow over the tapering end of a body of a revolution, whose forebody we can suppose to be semi-infinite and parallel. Stream surfaces from such a flow can be found which are relatively flat (Fig. 12) and can be used in conjunction with designed lower surfaces so as to form complete configurations^{12, 15}.

The most promising technique, however, employs an ingenious idea due to Pike¹⁶ (see Figure 13). Two axisymmetric expansion flows are supposed to be placed side by side in such a way that their Mach cones intersect. For the moment, we ignore the region of their mutual interaction. We draw a stream surface which starts upstream of the expansion regions and is initially parallel to the main flow. As soon as it enters either expansion region it curves inward. We overcome the interaction of the two fields by placing a vertical fin surface between them. If the overall geometry is correctly chosen^{12, 16}, it is possible to make the sides of the fin surface also conform to stream surfaces of the two flows.

The particular advantage of this method lies in the fact that volume is selectively removed from the mid semi-span positions, and left untouched near the centre (see Figure 13(b)). Thus the resulting base shape approximates quite closely to the shape shown as our design aim in Figure 8 of Lecture 1.

Now almost everything I have said up to this point has had to do with the geometrical process, with trying to achieve the most general and realistic configurations. The problem of maximising performance is partially treated in Lecture 5, in addition to the methods described there one may also try to apply the lessons learnt in Lecture 2 (convex streamlines, incidence washed out toward the tips). There remains the question of the behaviour of these shapes "off-design".

If a waverider shape operates at conditions far removed from its design point, then it loses all of its special properties, and becomes from the point of view of computation no different from any arbitrary sharp edged shape. But at conditions only just removed from the design point it may be possible to solve the flow by small perturbation techniques. One such technique has been worked out by Pike, and will be published shortly.

The other relationship between design and off-design conditions is that we must recover the design solution as a special case of a more general calculation procedure. Let us then tentatively outline such a procedure for the shock attached case and see whether it will meet that basic test. We will suppose that either some three-dimensional characteristics technique or other finite difference scheme is available to deal with the main part of the disturbed flow. On the wing surface there will be a boundary condition of tangential flow, and at the outer edge of the flow we shall have to satisfy the oblique shock relationships. On the line where these two surfaces meet (i.e., the leading edge), we must satisfy both conditions. The free stream flow must there be turned parallel to the surface by the attached shock wave.

So it would seem that we can already make a start on the solution by calculating the flow just at the leading edge and this should provide part of the boundary conditions for the remaining calculations. There are various ways of computing the flow at a swept edge, the simplest and best known being the following. We consider a region of the leading edge which is so small that we can think of it as straight, and of the local surface and shock wave as planar. The problem then is equivalent to finding the flow over a yawed wedge (Fig. 14). To do this, we construct a plane which is normal to the leading edge and resolve the incident flow into a component along the edge, and a component in the plane. This latter component we show as M_n . We can argue that in inviscid flow the other component has no effect, since the wedge could be translated parallel to itself without changing the flow. The problem reduces therefore to solving for a stream of Mach number M_n , deflected through an angle δ_n .

The angle θ_n , which determines the local position of the shock wave, then follows from the shock cubic

$$a \sin^6 \theta_n + b \sin^4 \theta_n + c \sin^2 \theta_n + d = 0, \quad (3.4)$$

where

$$a = M_n^6$$

$$b = M_n^4 \{ (\gamma+1) \sin^2 \delta - 1 \} - 2M_n^2$$

$$c = M_n^4 \{ (\gamma+1)^2 \sin^2 \delta \} + M_n^2 \{ (\gamma+1) \sin^2 \delta + 2 \} + 1$$

$$d = -1.$$

This is just the ordinary two-dimensional shock cubic with M_∞, θ, δ , replaced by M_n, θ_n, δ_n . In general we know that there will be either two, one or no thermodynamically permissible solutions.

If there are no solutions we must suppose that our hypothesis of an attached shock wave is contradicted, and that the shock is in fact detached.

If there is only one solution then we suppose the shock is about to detach.

If there are two solutions, we may, by analogy with the two-dimensional case, call them "weak" and "strong", or perhaps more precisely, to show how they are derived, the "weak normal" and the "strong normal" solutions. We define the "weak normal" solution as the one which lies closer to the surface, and we may observe that of the two it has the smaller pressure rise and causes the less energy degradation (entropy rise). It will be very natural to take this "weak normal" solution as our leading edge boundary condition.

Unfortunately, a very simple example is enough to show that there are difficulties. Figure 15 shows a family of caret wings all derived from the same wedge flow. They differ only in aspect ratio. Now as the aspect ratio gets very high, the corresponding wing is identical with the original wedge, and in that case the shock wave is evidently "weak normal". In the other limit, as the aspect ratio gets very low, each facet of the wing becomes only negligibly inclined to the incident stream. And yet we believe, from the thought-experiment described at the beginning, that the wing still supports the same finite pressure rise across the leading edge shock wave. A little reflection should convince the reader that the shock wave in this case is of the "strong normal" type.

If we now imagine the shock wave being steadily reduced from infinity to zero, there will be a changeover from "weak normal" to "strong normal" shock waves. For any particular case there is no difficulty in calculating numerically where this point is. All we need to note here is that there does exist a class of wing for which the computation scheme we outlined above breaks down, and that for wings of this class the flow, with its attendant "strong normal" shock waves, is found experimentally^{6, 17}.

The interesting question now is this. Are these cases that we have discovered "freaks" brought about by our particular waverider technique, or do they have a more general relevance? We shall begin our attack on this problem by considering the flow regimes which may occur on a given delta wing as its test conditions are varied.

In Figure 16 we present diagrammatically some of the things we think we know. The axes (M_∞ , α) represent particular test conditions with α being the incidence of the ridge line. (We do not here consider yaw effects.) Suppose that for all (M_∞ , α) we calculate the position of the weak normal shock wave, relative to the plane of the leading edges. For some values, the shock will lie below the plane, and for others above it. For a particular set of values (ST in Figure 16a) the shock lies in the plane. The curve ST is the same curve that one would calculate from two-dimensional theory and for high aspect ratio wings extends to $M_\infty = \infty$. It is the so-called "design curve" of the caret wing (see, e.g., Reference 2). The other significant curve on the figure is the one along which the weak and strong normal solutions coincide (PR) and above which no solution exists. For each region defined by these curves a small sketch is drawn, showing the typical positions of the two solutions. There seems no reason to suppose that the weak normal solution does not hold everywhere.

The picture becomes more complex as the aspect ratio is reduced. The curve defining conditions for which the weak normal shock lies across the leading edges shortens to the finite length SQ, and a new curve QT appears, defining conditions for which the strong normal shock replaces it as the design solution. The two curves run smoothly into each other. The "detachment curve" PR shifts round somewhat so as to touch the design curve at Q. In Figure 16b we have reason to believe that the "strong normal" solution holds along QT. Let us suppose that it continues to hold in some neighbourhood of QT.

If this is the case, we can imagine an experiment in which the wing, originally at a design point on QT, has the oncoming Mach number altered whilst the angle of incidence is kept constant. One can easily convince oneself that the resolved leading edge deflection angle (δ_n in Figure 14) is also held constant, whereas M_n varies in proportion to M_∞ . Then as the stream Mach number is reduced, say, M_n is reduced also. Therefore θ_n is reduced (we are considering strong solutions which do have this property) and the shock moves inward closer to the body. Conversely as the Mach number is increased, the shock wave moves outward. This is certainly contrary to one's expectations, it is also contrary to the results of preliminary attempts at a perturbation flow field analysis, and moreover contrary to experimental evidence¹⁷.

The paradox can be resolved in more than one way. I indicate in Figure 17 the one which seems simplest and most natural to me. It is known that the flow patterns corresponding to conditions inside SQT may contain powerful embedded shock waves⁶. A consistent picture can be formed which assumes that the strength of these shocks increases with increasing incidence, and that they simultaneously move outward, finally reaching the leading edge when the incidence crosses QT. At that stage they join up to occupy exactly the plane of the leading edges. With still further increase of incidence, the whole shock system detaches, so that the real detachment line is PQT.

I must emphasize however, that the whole of this last paragraph is so far purely conjectural, and not yet confirmed by really careful experimental measurements.

If these conjectures prove to be correct, we will have shown that although "strong normal" shock waves do exist on caret wings, they happen only for conditions that are very rare (mathematically speaking) and so it might seem that in our proposed calculation method we could safely neglect them after all. However, when we go on to non-circular shapes, the situation looks very unclear.

Consider a waverider surface with a strongly curved leading edge generated from a wedge flow as in Figure 18. We can easily arrange for part of the shock wave to be "weak normal" and for the other part to be "strong normal". If a wing were formed from such a surface and placed in a stream at its design condition, what would now happen? For every point on the leading edge δ_n will stay the same, and M_n will decrease. It may be appropriate to leave the consequences of this as "an exercise for the reader". The problem is certainly not trivial, and seems to have more than one possible solution.

It may be mentioned in passing that these "mixed" leading edge shock waves are the rule rather than the exception so far as "axisymmetric" waveriders are concerned (Fig. 19). Nevertheless, Pike¹¹ found no very remarkable off-design behaviour in his experimental tests of cone-flow waveriders. His tests were, however, conducted before the present approach was formulated, and no particular effort was made to look for the relevant phenomena.

The final topic I want to discuss in relation to the waverider programme is some special solutions that can be found for caret wings of rather extreme geometry in rather far off-design conditions¹⁸. One such solution, formed from a pattern of four intersecting shock waves separating regions of uniform flow is shown in Figure 20. The pressure distribution across the span of the wing is shaped like a top hat. The flow pattern occurs only if the angle between the facets is less than 90°. This flow pattern is mentioned not because of any practical application that it may have, but because of an interesting question of general principle that emerges from it. It turns out¹⁸,

that under certain very extreme geometrical conditions (the apex angle of the facets has to be greater than about 30° , and the angle between them less than about 5°) there can be non-uniqueness in the solution for the flow over a caret surface. Figure 21 shows two curves in an (M_∞, α) plot. On one curve the "wing" can support a plane shock wave, and on the other it can support the special flow shown in Figure 20. For the extreme geometries described above, the two curves cross¹⁸, and at that point either flow is possible.

A close examination reveals that at points on the design curve shown by the dotted line, the flow behind the single shock wave is subsonic. Therefore the "waverider thought experiment" is not valid, and we do not necessarily believe in the single-shock solution*. Nevertheless, both solutions do satisfy exactly the Euler equations and all the boundary conditions, and it would be a clever computer that could choose between them.

In a later lecture (Lecture 5), I shall take up the subject of waveriders again, and I shall deal there with the question of how to select a flow field likely to yield efficient waveriders. What I hope to have shown at this stage is that the waverider concept offers a considerable flexibility in the choice of shape, and that provided this flexibility is taken full advantage of, shapes can be obtained which have many features of realistic design sketches, and also offer high performance levels. I hope also to have shown that the study of such shapes arising from their design conditions plunges us at once into intriguing problems of basic fluid mechanics that may turn out to be of very general significance.

REFERENCES

1. Nonweiler, T.R.F. *Delta wings of shape amenable to exact shock wave theory.* J.R.Ae.S. Vol.67, nr 39, 1963.
2. Peckham, D.H. *On three-dimensional bodies of delta planform which can support plane attached shock waves.* ARC CP 640, 1962.
3. Squire, L.C. *Pressure distributions and flow patterns on some conical shapes with sharp leading edges at $M = 4.0$.*
4. Peckham, D.H. *Pressure distribution measurements on a series of slender body shapes at Mach numbers of 6.85 and 8.60.* ARC CP 791, 1962.
5. Picken, J.
Greenwood, G.H. *Free flight measurements of heat transfer and observations of transition on a caret wing at Mach numbers up to 3.6.* R.A.E. TR 65237, 1965.
6. Crabtree, L.F.
Treadgold, D.A. *Experiments on hypersonic lifting bodies.* 5th ICAS Congress, London, 1966, also R.A.E. TR 67004.
7. Kipke, K. *Experimental investigation of waveriders in the Mach number range from 8 to 15* DvFLR Report, Germany.
8. Ferri, A. *The method of characteristics.* In "High Speed Aerodynamics and Jet Propulsion". Vol.VI, Princeton University Press, 1954.
9. Pike, J. *Minimum drag surfaces of given lift which support two-dimensional supersonic flow fields.* R.A.E. TR 66305.
10. Jones, J.G. *A method for finding lifting configurations for high supersonic speeds using the flow fields of non-lifting cones.* R.A.E. R 2 , 1963.

* The experimental evidence in References 6 and 17 mentioned earlier as showing the existence of the design shock wave even when of "strong normal" type, does not involve subsonic flow. There are in fact no experiments which cover this case.

11. Pike, J. *Experiments on three cone-flow waveriders.* AGARD CP 30.
12. Jones, J.G.
et al. *A method for designing lifting configurations for high supersonic speeds, using axisymmetric flow fields.* Ingenieur-Archiv, 37, 1, 1968.
13. Flower, J.W. *Configurations for high supersonic speeds derived from simple shock waves and expansion.* J.R.Ae.S. 67, 287, 1963.
14. Cooke, J.C.
Jones, O.K. *The boundary layer on a Townend surface.* R.A.E. R Aero 2687, 1963.
15. Moore, K.C. *The application of known flow fields to the design of wings with lifting upper surfaces at high supersonic speeds.* R.A.E. TR 65034, 1965.
16. Pike, J. *A design method for aircraft basic shapes with fully attached shock waves using known axisymmetric flow fields.* R.A.E. TR 66069, 1966.
17. Keldysh, V.V. *An experimental investigation of the flow past wings formed by V-shaped stream surface behind plane compression jumps.* Zh.Zhid.i Gaza, 1967; to appear as RAE Library translation.
18. Roe, P.L. *A special off-design flow for caret wings.* R.A.E. Report in preparation.

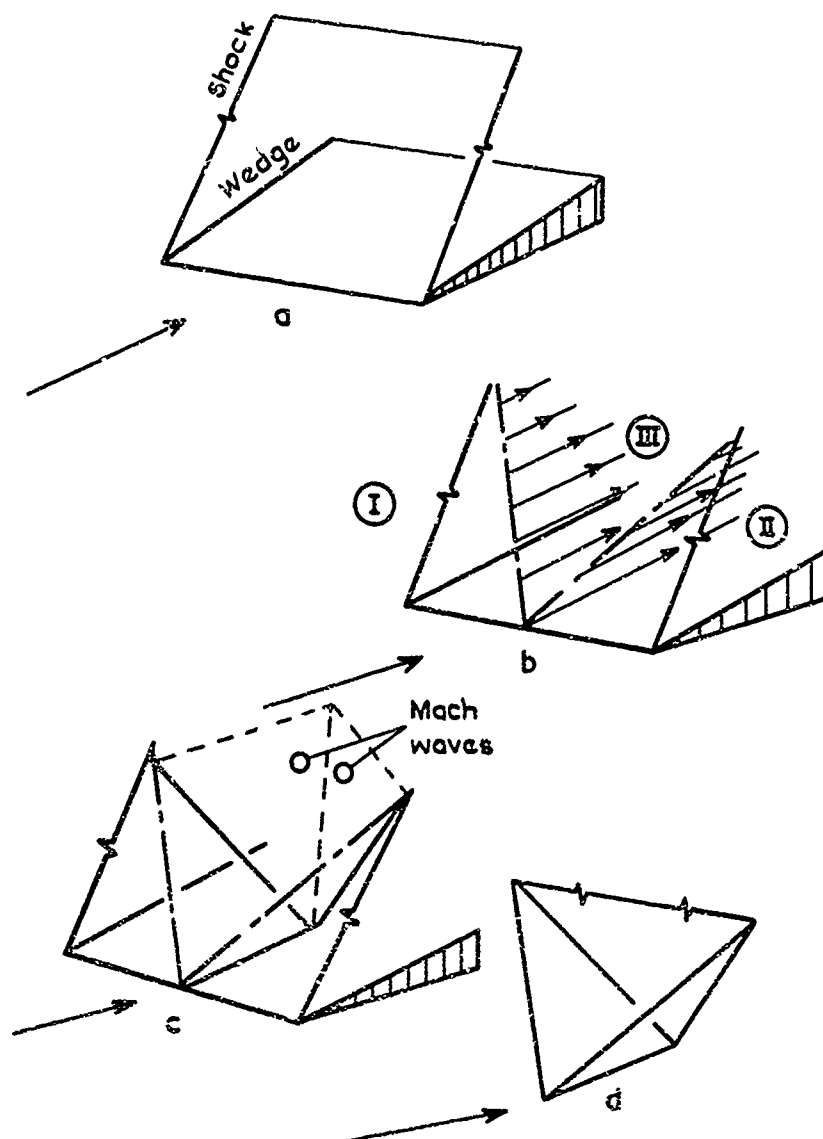


Fig.1 Construction of simple caret wings

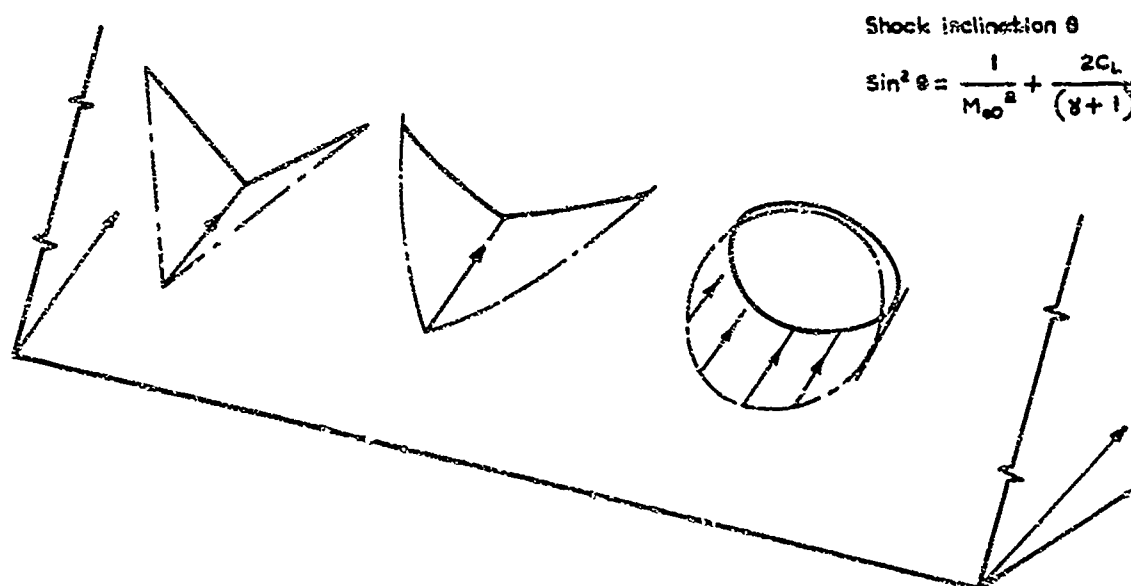


Fig.2 Family of "waveriders" derived from the same wedge flow

Shock inclination θ

$$\sin^2 \theta = \frac{1}{M_\infty^2} + \frac{2C_L}{(\gamma + 1)}$$

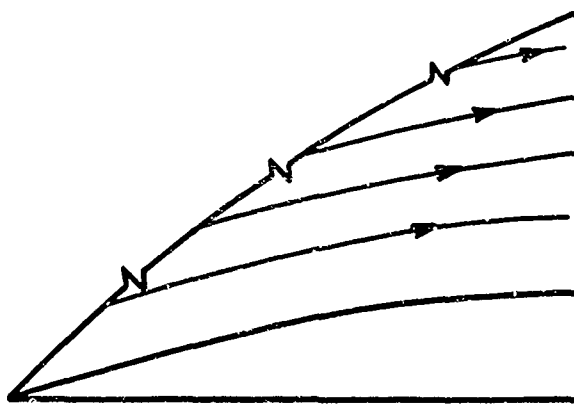


Fig.3 Two-dimensional flow past a curved wedge

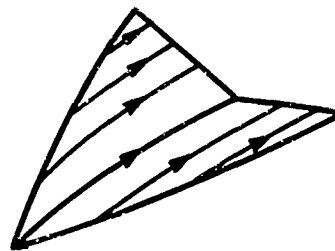


Fig.4 Waverider derived from the above flow field

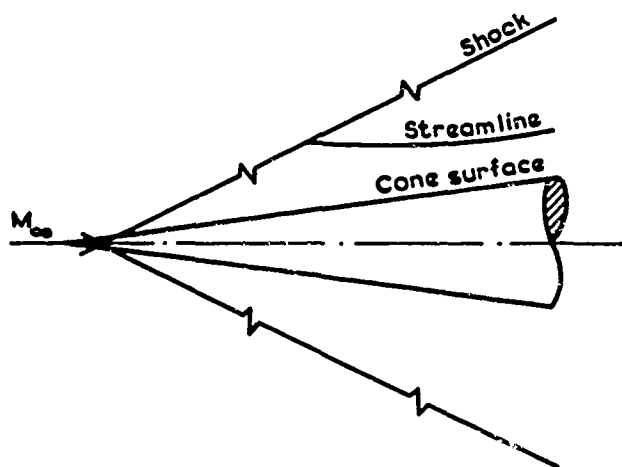


Fig.5 Flow past unyawed cone

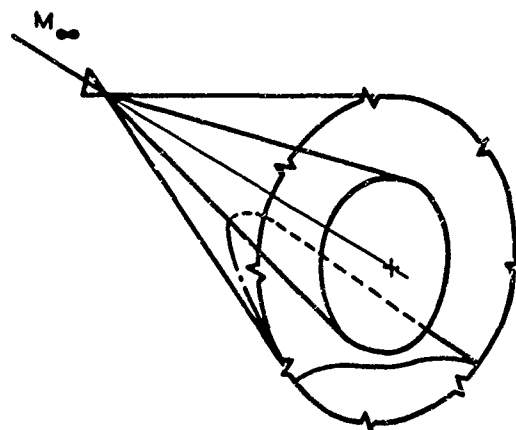


Fig.6 Streamsurface in above flow

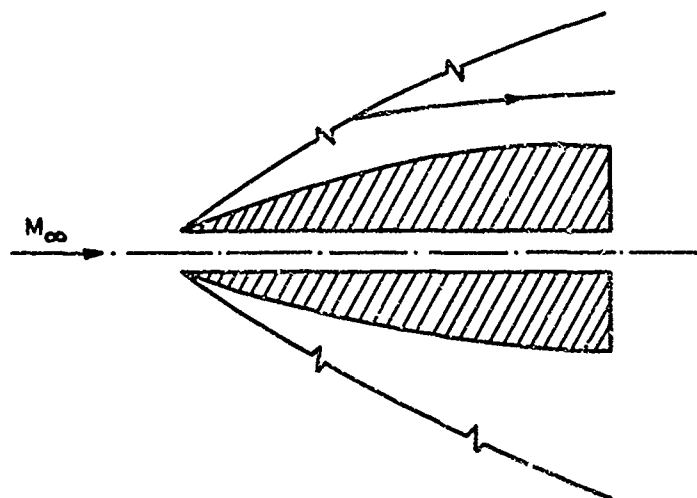


Fig.7 Flow past annular body of revolution

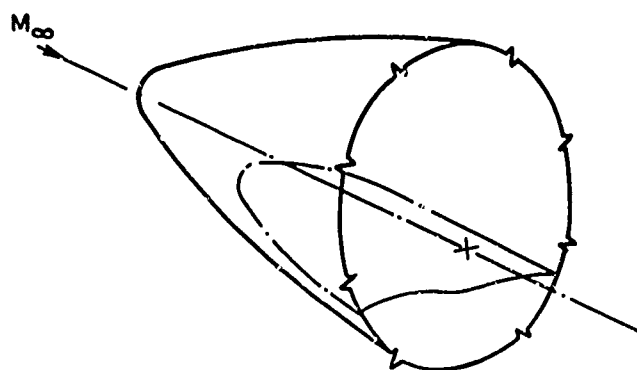
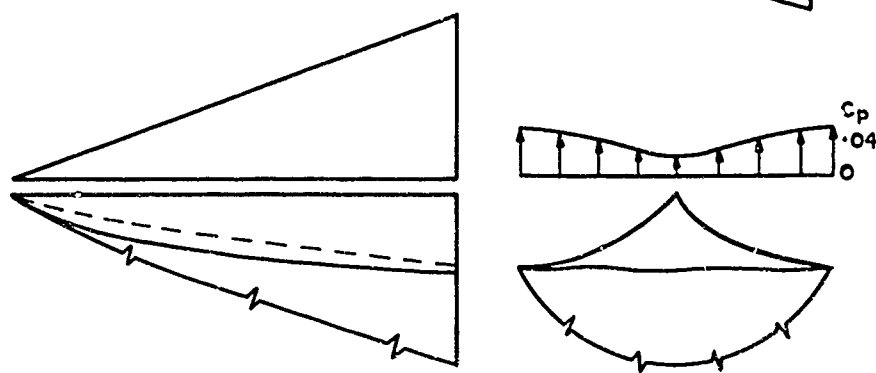
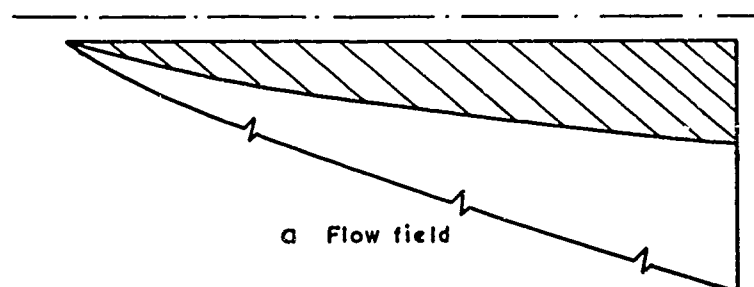


Fig.8 Streamsurface in the above flow



b Three-view drawing and trailing edge pressure distribution

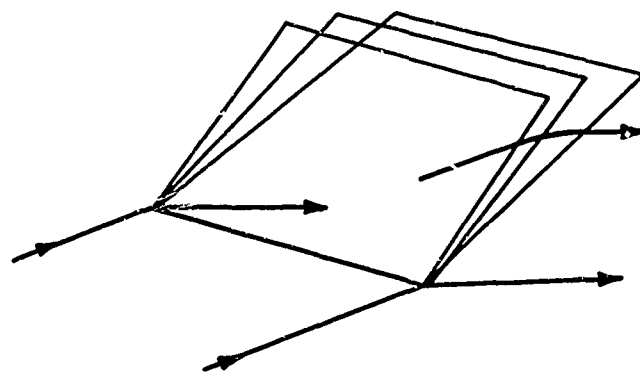
c L/D vs assumed C_f

$$M_{\text{design}} = 4.0$$

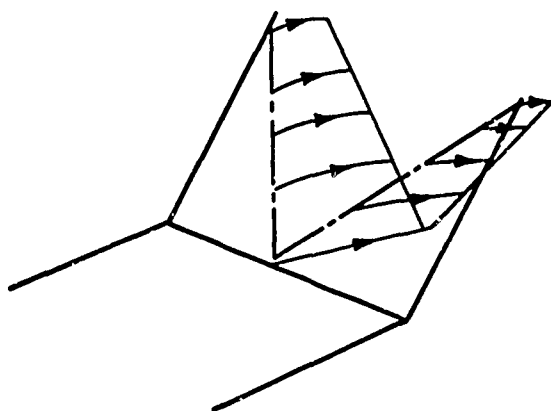
$$C_L = 0.0571$$

$$C_{D \text{ pressure}} = 0.00543$$

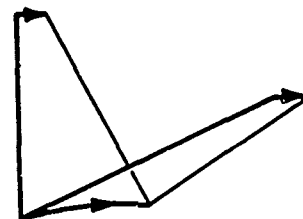
Fig.9 Axisymmetric flow and designed lower surface (after Pike)



(a) Expansion over two-dimensional corner



(b) Streamsurface in above flow



(c) Designed expansion surface

Fig.10 Using a two-dimensional flow to design an expansion surface

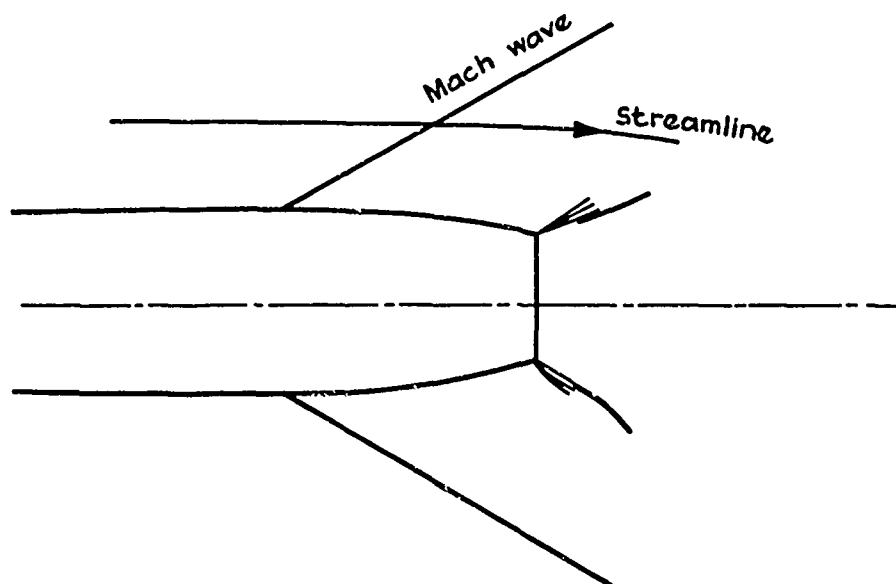


Fig.11 Axisymmetric expansion flow

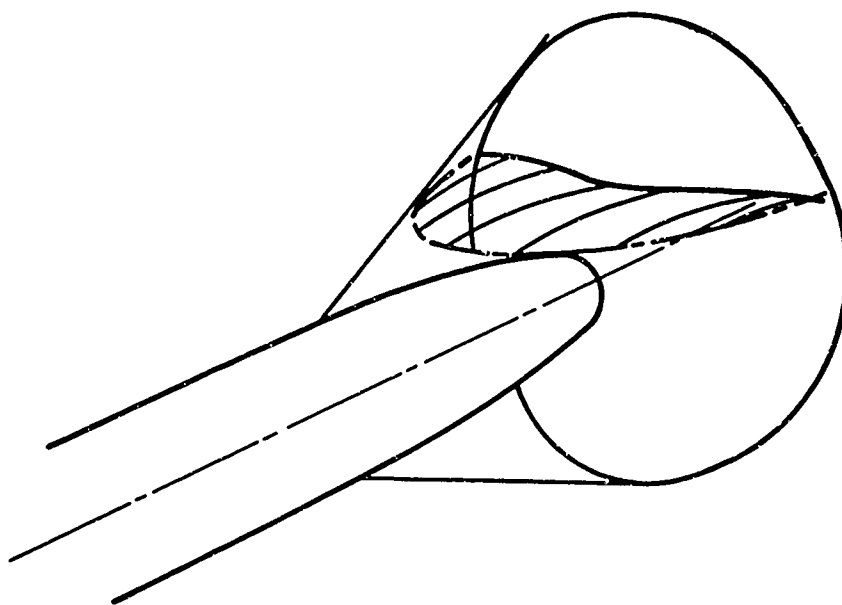
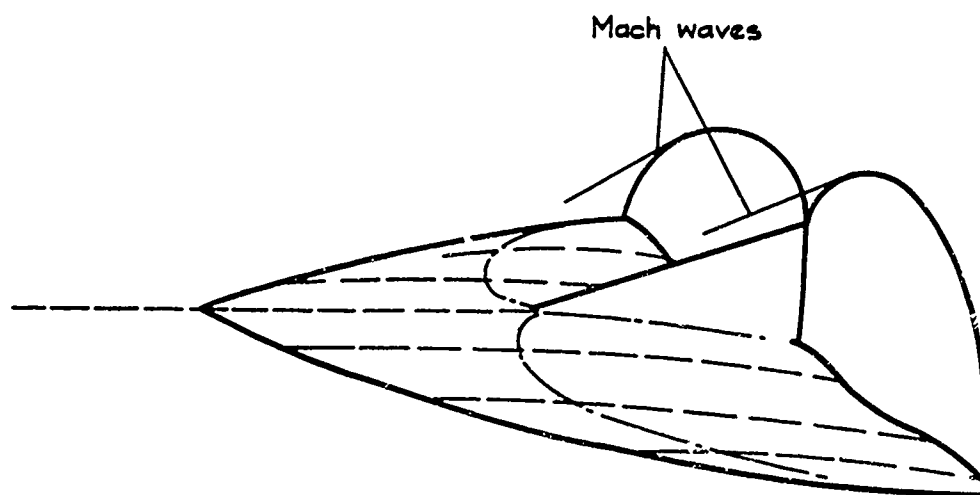
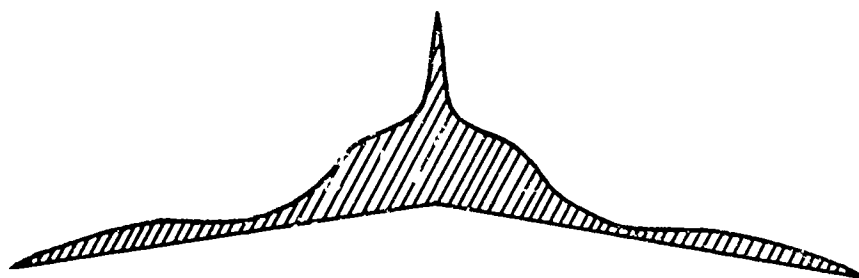


Fig.12 Streamsurface in above flow



(a)



(b) Base shape of Pike's design

Fig.13 Use of twin expansion flows

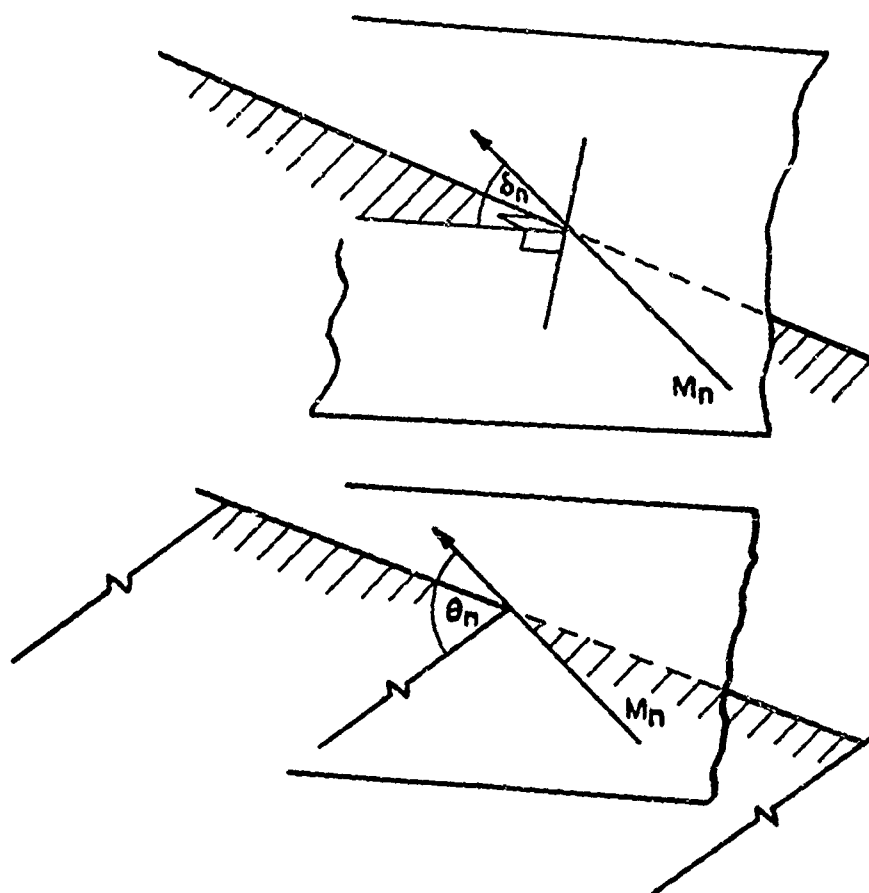


Fig.14 Construction of flow at a general leading edge

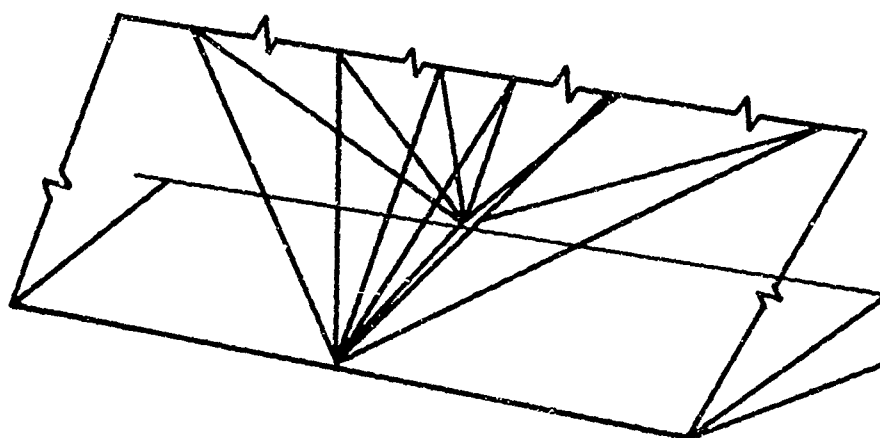
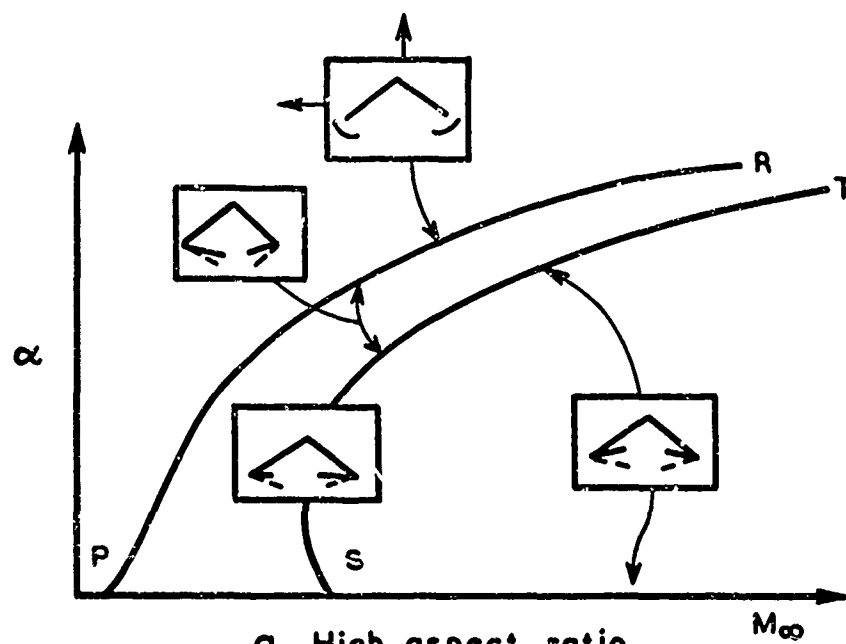
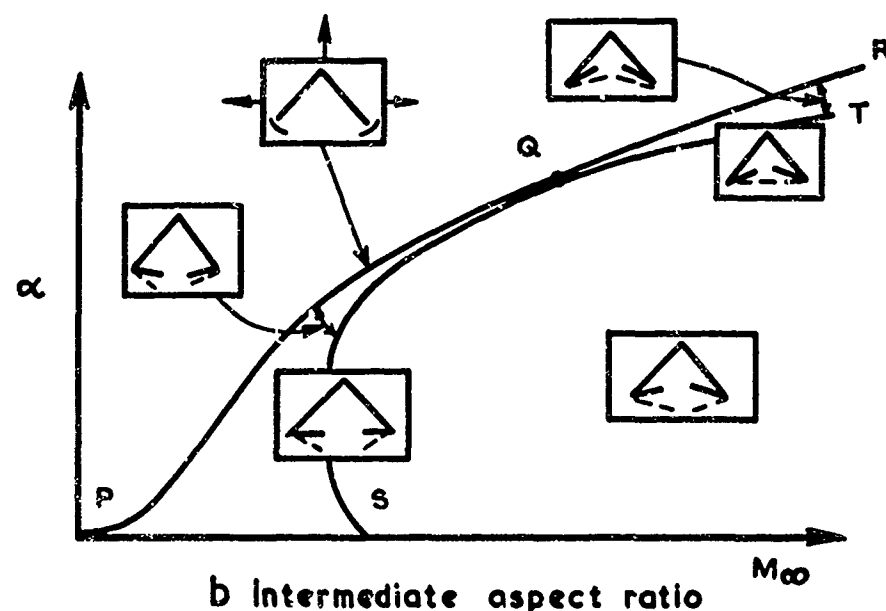


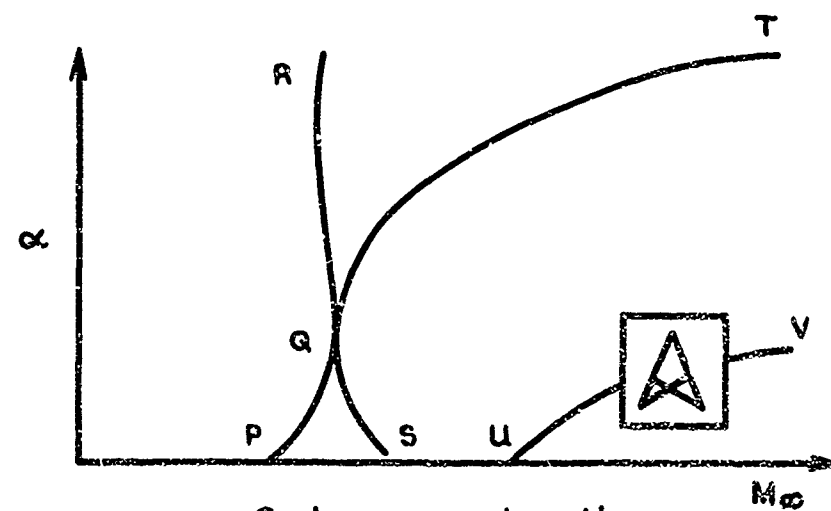
Fig.15 Family of caret wings with differing aspect ratios



a High aspect ratio



b Intermediate aspect ratio



c Low aspect ratio

Fig.16. Possible shock patterns

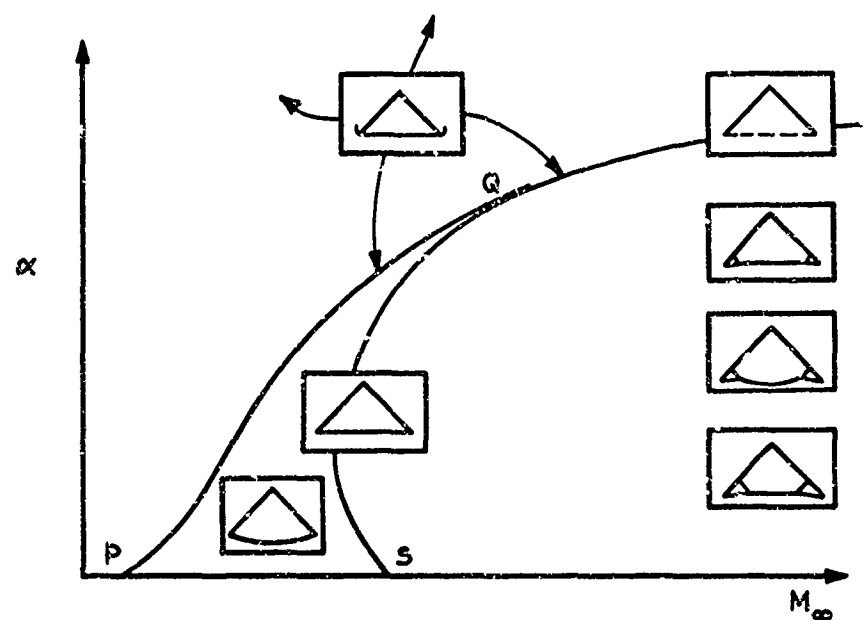


Fig.17 Tentative resolution of Fig.16

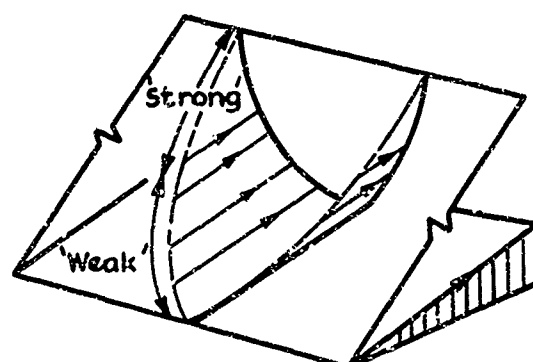


Fig.18 Waverider with "mixed" shockwave

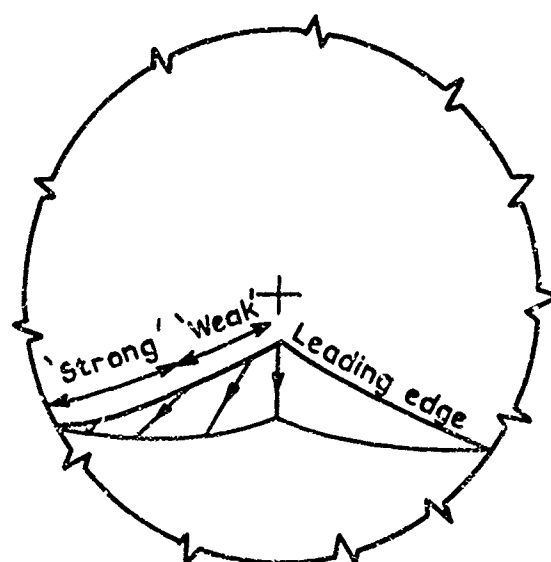


Fig.19 Front view of axisymmetric waverider

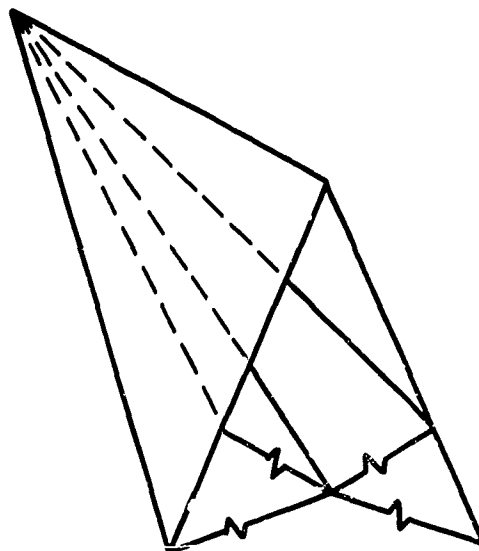


Fig.20 Caret wing with "crossed" shocks

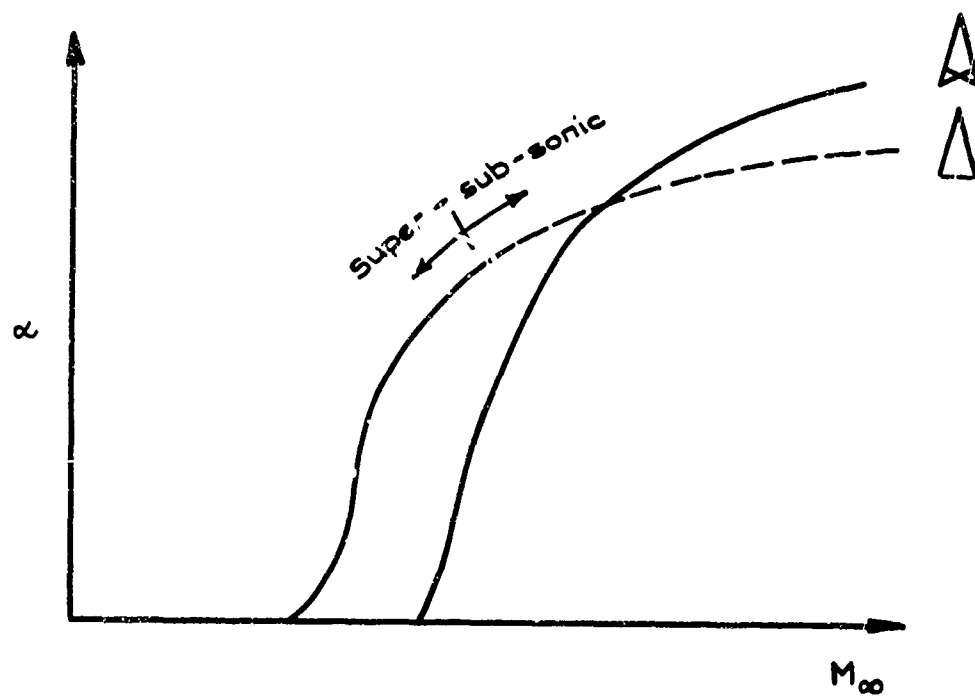


Fig.21 Occurrence of non-unique solutions

LECTURE 4

THIN SHOCK-LAYER THEORY

P.L.Roe

Royal Aircraft Establishment, Bedford, England

At the present moment the theory of thin shock-layers as applied to wing-like shapes seems to be in a state offering considerable interest both to the mathematician and to the aerodynamicist. Its interest to the aerodynamicist lies in the fact that in many circumstances it yields highly accurate answers to significant problems, and its interest to the mathematician in the fact that such accuracy seems highly unlikely at an a priori examination. In this lecture I shall outline the development of the subject and its present status, and I hope I shall be able to indicate some directions for future research.

The theory is essentially a first order correction to simple Newtonian theory, and it will be convenient to start by discussing that I have already said something about Newtonian flow in Lecture 2, but it is necessary now to expand those remarks a little. We noted there that in the double limit $M_\infty \rightarrow \infty$, $\gamma \rightarrow 1$, the flow behind a given shock wave became infinitely dense and the initial deflection of a streamline crossing the shock became identical to the local inclination of the shock itself. This leads us to consider a model of the flow in which the shock wave and the body surface almost coincide and all the captured air flows in a very thin layer between them.

Even in this limit, however, the flow in the layer exhibits features which are recognisable as degenerate cases of real gas flow patterns. The key observation is that a layer of infinitely dense fluid cannot be accelerated by merely finite pressure gradients. Since the streamlines follow the (generally curved) body surface, they do have curvature normal to the surface, and the necessary infinite pressure gradients are supplied, in Busemann's model, by finite pressure changes across the infinitesimal thickness of the layer. However, for smooth body shapes the pressure distribution is also smooth, so that pressure gradients in the surface are finite everywhere. We conclude that the streamlines have no curvature in the surface. In geometrical terms, this implies that they follow the surface geodesics, or paths of shortest distance. The tracing out of these paths, for a general body shape, is a non-trivial problem in differential geometry, but given the geodesics, the aerodynamics is simple. We observe that each streamline, when it strikes the body, takes an initial direction in the surface such that the actual turning angle is minimised ("path of steepest descent" or "fall line"). Thereafter it follows that geodesic which passes through the initial point in that direction.

For many body shapes this approach yields a consistent and satisfactory picture of the flow structure, but for certain body shapes anomalies appear. These do not necessarily detract from the usefulness of the approach; rather they may enhance it. Hayes and Probstein¹ have written "... the anomalies of Newtonian theory are not to be avoided, but rather sought out, in order to discover phenomena which may be important in hypersonic flow but which have no counterparts in flows at more moderate speeds. In addition, the methods developed in Newtonian theory suggest analogous methods in more realistic theories". It will very likely be profitable to take a similar attitude toward the thin-shock-layer approximation.

Applications of this theory to wing-like shapes have so far been restricted either to conical wings^{2,3}, or to wings at very high incidence⁴. The former application appears the more promising, and it is this one that we shall consider here.

Let us briefly consider the flow past a conical wing in the Newtonian approximation. Since the wing is conical, its surface is "developable", i.e., can be unrolled without stretching to yield a flat surface. The geodesics (streamlines) of a conical wing are therefore straight lines in the developed surface. If we look at a true view (Fig.1(a)) of this developed surface, we see that a streamline arriving at the surface takes some initial direction that depends on the local geometry, and subsequently follows this same direction, undeviatingly. The rays through the wing apex O can be divided into two classes lying to the right or to the left of the ray which is parallel to the given streamline. Only rays in the outboard class are crossed by the streamline. We mention this property because it is an unrealistic feature which persists into our higher approximation. Generally, we would expect a streamline to continue cutting across rays until it arrived at one where the pressure was at a minimum. For the case of a flat delta wing, this would be at the centreline (Fig.1(b)).

A more serious anomaly occurs if the initial deflection directs the streamline toward the centreline. This happens if the wing is anhedralled, and the simple theory then predicts that the streamline continues straight across onto the other half of the wing (Fig. 1(c)), which it cannot do without colliding with its "opposite number". The situation can be resolved within the Newtonian approximation by remembering that the Mach number inside the layer, as well as in the free stream, is infinite. Thus a consistent explanation is given by supposing that the left and right-hand flows collide on the centreline, and are turned parallel to it, to form a narrow streamtube within which the density is "infinitely squared". Such a streamtube is termed a Newtonian shock line¹. An analogous phenomenon occurs in the higher approximation and its resolution there is not yet clear.

Having seen that an intelligible and interesting theory can be constructed on the assumption that the shock layer is of infinitesimal thickness, it is natural to go on and see what results from assuming it to be merely very thin. This is the theory that we are about to study. As a numerical measure of how thick the shock layer is likely to be in a given problem, we may take the density ratio across some typical part of the shock wave, and denote this by $\epsilon = \rho_\infty / \rho_s$, where

$$\epsilon = \frac{\gamma - 1}{\gamma + 1} + \frac{2}{(\gamma + 1)M_\infty^2 \sin^2 \sigma} \quad (4.1)$$

for a perfect gas, with σ the local shock inclination angle. Since the shock layer is anyway supposed to be thin, we may take as a typical value of σ the actual incidence of the surface, α , so that our basic assumption for a perfect gas is going to be that

$$\epsilon = \frac{\gamma - 1}{\gamma + 1} + \frac{2}{(\gamma + 1)M_\infty^2 \sin^2 \alpha} \quad (4.2)$$

is a numerically small quantity. At first sight this is unpromising, because we can see that ϵ will never be less than $(\gamma - 1)/(\gamma + 1)$ and for air this quantity is one-sixth. Substantially smaller values of ϵ occur if the shock wave produces changes in the molecular structure of the gas, so that Equations (4.1) and (4.2) no longer apply, and we might expect the theory to be more applicable in such cases. However, numerical calculations reported in References 6 and 7 show very useful agreement with experiment at very moderate incidence and Mach numbers, even when the allegedly "small" parameter ϵ is of order unity (see Figure 2).

Before embarking on the mathematical analysis we must choose a coordinate system. This choice is discussed in Reference 1. For a general investigation it would be convenient to adopt flexible coordinates adapted to the geometry of the shape being studied. For example, if the problem were to calculate the flow past the conical body shown in Figure 3, the coordinate system drawn there might be convenient, compounded of normals to the body surface and curves orthogonal to them. Alternatively, if the problem were to compute the flow behind a given shock wave, a coordinate system based on that might be preferable. Such generated coordinates are employed in References 1, 4 and 5.

Here, however, so as to simplify the algebra as much as possible, we employ straightforward cartesian coordinates. We may note that these would in any case be appropriate provided that either the body or the shock does not deviate too far from a plane, and that for lifting wings this will probably be the case.

Following Messiter², we begin the analysis by defining right-handed cartesian coordinates (x, y, z) oriented with respect to some "mean plane" of the wing under consideration (Fig. 4(a)), and define corresponding velocity components to be $(\bar{u}, \bar{v}, \bar{w})$. If we agree to call the fluid density ρ and the static pressure P , then we have the following equations of motion:

Continuity

$$(\rho \bar{u})_{\bar{x}} + (\rho \bar{v})_{\bar{y}} + (\rho \bar{w})_{\bar{z}} = 0.$$

\bar{x} -momentum

$$\bar{u} \bar{u}_{\bar{x}} + \bar{v} \bar{u}_{\bar{y}} + \bar{w} \bar{u}_{\bar{z}} + \frac{1}{\rho} P_{\bar{x}} = 0.$$

\bar{y} -momentum

$$\bar{u} \bar{v}_{\bar{x}} + \bar{v} \bar{v}_{\bar{y}} + \bar{w} \bar{v}_{\bar{z}} + \frac{1}{\rho} P_{\bar{y}} = 0.$$

\bar{z} -momentum

$$\bar{u} \bar{w}_{\bar{x}} + \bar{v} \bar{w}_{\bar{y}} + \bar{w} \bar{w}_{\bar{z}} + \frac{1}{\rho} P_{\bar{z}} = 0.$$

Entropy

$$\bar{u} \left[P_{\bar{x}} - \left(\frac{\gamma P}{\rho} \right) \rho_{\bar{x}} \right] + \bar{v} \left[P_{\bar{y}} - \left(\frac{\gamma P}{\rho} \right) \rho_{\bar{y}} \right] + \bar{w} \left[P_{\bar{z}} - \left(\frac{\gamma P}{\rho} \right) \rho_{\bar{z}} \right] = 0;$$

(4.3)

and these shock relationships

$$1 - \frac{\rho_\infty}{\rho_s} = 1 + \frac{q_s \cdot \underline{n}}{c} = \frac{2}{\gamma + 1} \left(1 - \frac{u_\infty^2}{c^2} \right) = \frac{P_s - P_\infty}{\rho_\infty c^2} \quad (4.4)$$

$$0 = (-\bar{v}_s \bar{y}_{s\bar{z}} - \bar{v}_s - U \bar{y}_{s\bar{z}} \sin \alpha) \underline{i} + (\bar{u}_s \bar{y}_{s\bar{z}} - \bar{w}_s \bar{y}_{s\bar{z}} - U \bar{y}_{s\bar{z}} \cos \alpha) \underline{j} + (\bar{u}_s + \bar{v}_s \bar{y}_{s\bar{z}} - U \cos \alpha + U \bar{y}_{s\bar{z}} \sin \alpha) \underline{k} \quad (4.5)$$

In these equations:

1. Suffix ()_s denotes conditions just behind the shock,
2. Other suffices denote partial differentiation,
3. U is the free stream velocity,
4. α is the incidence of the reference plane,
5. \underline{i} , \underline{j} , \underline{k} are unit vectors in the $(\bar{x}, \bar{y}, \bar{z})$ directions,
6. $\bar{y} = \bar{y}_s(\bar{x}, \bar{z})$ is the equation of the shock wave,
7. \underline{n} is a unit vector normal to the shock wave, directed into the free stream,
8. $c = \underline{q}_\infty \cdot \underline{n}$ is the component of the free stream velocity normal to the shock wave.

Now we set out to simplify these equations on the assumption that the shock layer is thin. To begin with, we need a 'stretched' coordinate system that will be described by quantities of order unity. The choice for the x and y coordinates is fairly obvious (Fig.4(b)); we take our stretched (starred) variables to be

$$\left. \begin{aligned} x^* &= \bar{x} \\ y^* &= \frac{\bar{y}}{\epsilon \tan \alpha} \end{aligned} \right\} \quad (4.6)$$

The choice of a z -transformation is less obvious, but it is helpful to note that interesting problems of flow structure, such as shock detachment, occur on wings whose aspect ratio is of the same order as the Mach angle in the shock layer, and this angle can easily be shown to be $O(\epsilon^{1/2})$. Provisionally, then we set

$$z^* = \frac{\bar{z}}{\epsilon^{1/2} \tan \alpha} \quad (4.7)$$

where the factor $\tan \alpha$ is introduced to simplify the later algebra.

Next we need to estimate the orders of magnitude of the independent variables. This can be done by considering the known solution for attached flow at a swept leading edge, and assuming that all flow quantities have the same order of magnitude elsewhere that they have there. The details are given in Reference 2, here we will note only the resulting scalings:

$$\left. \begin{aligned} \frac{\bar{u}}{U} &= \cos \alpha + \epsilon (\sin^2 \alpha / \cos \alpha) u + \dots \\ \frac{\bar{v}}{U} &= \epsilon \sin \alpha v + \dots \\ \frac{\bar{w}}{U} &= \epsilon^{1/2} \sin \alpha w + \dots \\ \frac{P - P_\infty}{\rho_\infty U^2} &= \sin^2 \alpha + \epsilon \sin^2 \alpha p + \dots \\ \frac{\rho_\infty}{\rho} &= \epsilon - \frac{\gamma - 1}{2} \epsilon (2u + w^2) - \epsilon^2 (1 + p) + \dots \end{aligned} \right\} \quad (4.8)$$

The last of these equations is not independent, but is a consequence of the previous four and of the conservation of total enthalpy. The quantities u , v , w , and p which appear in Equations (4.8) are all of order unity and represent corrections to the Newtonian solution. The equations that they obey can be found by substituting (4.6), (4.7) and (4.8) into the equations of motion and the shock relationships. The result is

$$\left. \begin{aligned}
 &\text{Continuity} \\
 &\quad v_{y^*} + w_{z^*} = 0. \\
 &\text{x-momentum} \\
 &\quad u_{x^*} + v u_{y^*} + w u_{z^*} = 0. \\
 &\text{y-momentum} \\
 &\quad v_{x^*} + v v_{y^*} + w v_{z^*} = -p_{y^*}. \\
 &\text{z-momentum} \\
 &\quad w_{x^*} + v w_{y^*} + w w_{z^*} = 0.
 \end{aligned} \right\} \quad (4.9)$$

Shock relationships

$$\left. \begin{aligned}
 u_s &= -\partial y_s^* / \partial x^* \\
 v_s &= (\partial y_s^* / \partial x^*) - (\partial y_s^* / \partial z^*)^2 - 1 \\
 w_s &= -\partial y_s^* / \partial z^* \\
 p_s &= 2(\partial y_s^* / \partial x^*) - (\partial y_s^* / \partial z^*)^2 - 1.
 \end{aligned} \right\} \quad (4.10)$$

In all these equations the relative error is of order ϵ . We may note that the equations are now not only much shorter, but also quite drastically changed in form. We have lost one of the original five equations of motion by making use of the explicit solution for ρ , but even more importantly, we have lost much of the coupling between the remaining four. The equations of continuity and z-momentum contain only v and w as independent variables, and can therefore be solved without reference to the others. Then the x- and y-momentum equations can be solved for u and p respectively.

Moreover, these equations imply several very simple properties of the flow. In Equations (4.9) the x-momentum equation can be interpreted as a statement that u remains constant along streamlines, and the z-momentum equation implies that w also has this property. Turning back to Equations (4.8) we see from the last of these that if u and w are both preserved along streamlines, then so are the leading terms in the expression for density. Thus along any given streamtube, both density and x-wise velocity are constant to first order, and it follows from continuity that all sections of a streamtube, cut by planes $x = \text{constant}$, have the same area. This last result can also be established as a geometrical consequence of the simplified continuity equation.

For the remainder of this lecture, we shall consider only conical flows, that is, if we introduce conical coordinates

$$\left. \begin{aligned}
 y &= y^* / x^* \\
 z &= z^* / x^*
 \end{aligned} \right\} \quad (4.11)$$

we will consider flows in which u , v , w , and p depend only on y and z . If we recast the equations of motion so that y and z are the independent variables, we obtain

$$\left. \begin{aligned}
 v_y + w_z &= 0 \\
 (v-y)u_y + (w-z)u_z &= 0 \\
 (v-y)v_y + (w-z)v_z &= -p_y \\
 (v-y)w_y + (w-z)w_z &= 0.
 \end{aligned} \right\} \quad (4.12)$$

The shock wave is completely described by an equation of the form $y = y_s(z)$ and the shock relationships then become

$$\left. \begin{aligned} u_s &= -v_s + zy'_s \\ v_s &= y_s - zy'_s - y_s'^2 - 1 \\ w_s &= -y'_s \\ p_s &= 2v_s - 2zy'_s - y_s'^2 - 1 \end{aligned} \right\} \quad (4.13)$$

Equations (4.12) and (4.13) together constitute Messiter's very simple formulation of the conical thin shock layer problem, and since his original paper² have supplied the basis for work by Hida³, Squire^{6,7}, and Woods⁸. The discussion to be given here is based partly on these papers, and partly on my own work, so far not published.

First of all we look at the mathematical structure of these approximate equations of motion and compare it with the structure of the full Equations (4.3). The full equations can be thought of as four independent equations for three unknown velocity components and one unknown pressure, with density and entropy eliminated by means of the energy equations and the equation of state. In a conical coordinate system involving just two independent variables the characteristic directions of the set can be sought.

For a set of equations involving four unknowns there will be in general four characteristic directions through every point¹⁰. The equation which gives these directions for the case of rotational conical supersonic flow has generally either two or four real roots. Two of these roots are coincident, and correspond to the streamline direction. The other two are inclined to this direction at an angle corresponding to the Mach angle of the cross-flow¹¹, and disappear when this cross-flow becomes subsonic, i.e., when the velocity component normal to the ray through the apex becomes less than the local speed of sound. When this happens there are no longer enough characteristic equations to solve for all the unknown quantities, and the equations are essentially elliptic in character. These different regimes are illustrated in Figure 5.

Now let us look at the structure of the approximate Equations (4.12). As already remarked, the first and last of these equations can be solved independently of the others, and their behaviour determines that of the whole system. Effectively we are now dealing with two equations in two unknowns, and therefore there can be no more than two characteristic directions. In fact, there are always just two, which can easily be found to be

$$\left. \begin{aligned} \frac{dy}{dz} &= \frac{v - y}{w - z} \\ \text{and} \quad dz &= 0 \end{aligned} \right\} \quad (4.14)$$

The first of these (see Figure 6) is the streamline direction, and therefore corresponds to a feature of the full equations. The second is an unrealistic feature, which implies that disturbances can be transmitted instantaneously across the shock layer. Since both sets of characteristics exist everywhere, the flow has everywhere a hyperbolic character, which is another unrealistic feature. However, when we solve these equations we shall see that vestigial traces of the elliptic region do in fact remain. On reflection, this seems a fairly satisfactory state of affairs, for we clearly cannot expect the full structure of a system having four characteristic directions to be represented by an approximation which has only two.

In Reference 2 the following method is adopted to solve Equations (4.12) and (4.13). By taking account of the differential equations for v and w , the shock relationships and the boundary conditions on the body (which we have not yet mentioned) a rather complex integral relationship is set up between the shape of the shock $y_s(z)$ and the shape of the body $y_b(z)$. The equation is in fact

$$y'_b = y'_s + \frac{1}{y'_s + z} + \int_z^\infty \frac{ds}{[y'_s(s) + s]^2} \quad (4.15)$$

where ξ is the solution of the equation

$$-y'_s(\xi) = z.$$

In cases where $y_s(z)$ is known (inverse problems) Equation (4.15) yields the unknown body shape by straightforward quadrature. In cases where $y_b(z)$ is known, the solution of (4.15) to find $y_s(z)$ is not straightforward; it seems best to transform it into a differential equation^{2,6} which can be treated numerically. This process, or a similar one, has been the basis for the work in References 1-7. In Reference 8 a different, and a very much simpler approach was taken, but limited to a special class of solutions. The differential equations were considered by themselves, independently of the boundary conditions on shock wave or body, and solutions of "simple wave" type, that is, having constant properties along the "streamline" characteristics, were discovered. It was found that shock waves

compatible with these solutions were straight or parabolic, and that solutions satisfying the boundary conditions for a flat delta wing with an attached shock could be built up if the shock wave were supposed to consist of straight segments.

We follow here a process which may be thought of as a generalisation of this last scheme. We repeat here the two equations which have to be solved for v and w within the flow field:

$$\frac{\partial v}{\partial y} + \frac{\partial w}{\partial z} = 0 \quad (4.16)$$

$$(v - y) \frac{\partial w}{\partial y} + (w - z) \frac{\partial w}{\partial z} = 0 \quad (4.17)$$

We may note that once we have solved these equations to obtain v and w everywhere, we can draw in the streamlines by following the differential equation for their slope

$$\frac{dy}{dz} = \frac{v - y}{w - z} \quad (4.18)$$

Thus, (4.16) and (4.17) in effect give the streamlines of the flow. We may ask whether there are any properties of the streamlines which can be deduced from them directly. The following short piece of algebra provides an affirmative answer to this question.

Consider two streamlines lying very close to each other (Fig.7(a)). Each will be associated, as we have seen, with a particular, constant, value of w . Let these values be w and $w + dw$. Let the streamline shapes be $y = y(z)$ and $y = y(z) + \Delta(z)$, where $\Delta(z)$ is the small vertical distance between them. If we want to know how rapidly the lines are converging we can look at the quantity

$$\frac{1}{\Delta} \frac{d\Delta}{dz}$$

It is easy to show that this is equal to the vertical rate of change of streamline slope $\partial S / \partial y$, where $S = (v - y) / (w - z)$. Now we can find $\partial S / \partial y$ from Equation (4.18), and the result is

$$\frac{\partial S}{\partial y} = \frac{1}{\Delta} \frac{d\Delta}{dz} = \frac{(w - z)(\partial v / \partial y - 1) - (v - y) \partial w / \partial y}{(w - z)^2} \quad (4.19)$$

The right-hand side can be simplified by use of Equations (4.16) and (4.17) and we get

$$\frac{1}{\Delta} \frac{d\Delta}{dz} = - \frac{1}{(w - z)} \quad (4.20)$$

Now, since w is constant along streamlines we can regard (4.20) as an ordinary differential equation, valid along any streamline, so long as w is given the appropriate constant value. The integral of this equation is simply

$$\Delta = \text{const} \times (w - z) \quad (4.21)$$

Thus, any two narrowly separated streamlines approach each other linearly with z and intersect when z has the value w .

From this theorem many equally simple consequences follow. First, we may observe that in general any two streamlines must be separated from each other by a linearly varying vertical distance, because the sum of any number of linear functions is itself a linear function (Fig.7(b)). This holds only if all the intervening streamtubes are continuous, i.e., none of them comes to a stop in the region considered. That is to say, if any one streamtube can be expressed by

$$y = f(z) + Az + B \quad (4.22)$$

On differentiating this, we get

$$\frac{dy}{dz} = f'(z) + A, \quad (4.23)$$

so that any two streamlines differ in slope by a constant amount. A further differentiation produces

$$\frac{d^2y}{dz^2} = f''(z). \quad (4.24)$$

Therefore, all streamlines which cross a given z -section have the same second derivative. In particular, if one of them has an inflexion point, they all have.

The fundamental property (4.21) also allows us immediately to sketch in the various patterns which a set of streamlines can form. These patterns are shown in Figure 8. On the left are patterns formed by streamlines running toward the plane of symmetry ($w < z$), and on the right patterns formed by streamlines running away from the plane of symmetry ($w > z$). The top picture shows streamlines which each have the same value of w , and which therefore (Eqn (4.21)) all meet in the same point. Immediately below this we show the case (b) where w increases smoothly and monotonically from top to bottom of the bundle. Below this again we show the similar case (c) with w decreasing. In both cases the locus of intersection points forms a smooth envelope to the family of streamlines.

By combining patterns (b) and (c) we can form patterns in which w reaches either a maximum value (case (d)) or a minimum value (case (e)). In these cases the envelope curve may be either simple or cusped. Finally, in (f) and (g) we show cases where w is discontinuous. The essential feature of these patterns is that there is a dividing streamline which is intersected by its neighbour from above and its neighbour from below at widely different points.

It is not at all difficult to imagine more complicated patterns involving more complicated behaviour of w . One very interesting question is the extent to which these patterns correspond to features of more accurate solutions.

The other interesting point to emerge from these patterns is the question of the boundary condition to be applied on the body. Since the body is a solid surface it must, in a conical view, be either a streamline or an envelope of streamlines, or, as we shall see later, partly the one and partly the other. Where the body surface is a streamline, the boundary condition to be applied is $dw/dz = 0$; where it is an envelope curve, the boundary condition is $w = z$. This ambiguity is a source of difficulty, the correct boundary condition is not known a priori everywhere on a given body.

So far everything we have said follows from a consideration of the differential equations alone. The shock relationships enter into the solution in such a way as to determine both constants in the equation

$$\Delta = \text{const} \times (w - z).$$

Let the shock wave be given by the equation $y = y_s(z)$. Let a pair of closely adjacent streamlines intersect this curve at point $z = \xi$, $z = \xi + d\xi$ (Fig.9).

Then, from the third of the shock relationships (4.13) we see that the value of w on these streamlines is

$$w = -y'_s(\xi) \quad (4.25)$$

and thus that they intersect where

$$z = -y'_s(\xi), \quad (4.26)$$

which point may, of course, be either inboard or outboard of $z = \xi$.

The initial slope of the streamlines is given by the general expression for streamline slope (4.14) which just behind the shock takes on the value

$$S_s = \frac{v_s - y_s}{w_s - z_s}$$

which, on insertion of the shock relationships becomes

$$S_s = y'_s(\xi) + \frac{1}{y'_s(\xi) + \xi}. \quad (4.27)$$

From this, the initial spacing between the streamlines follows at once; it is equal to $d\xi$ times the difference between the slopes of the shock wave and the streamlines (Fig.9) and is therefore

$$\Delta_s = \frac{d\xi}{y'_s(\xi) + \xi} . \quad (4.28)$$

Using this result, one can calculate very simply the area enclosed between these two streamlines,

i.e.,
$$\int \Delta dz = dA .$$

Since Δ is a linear function of z , this area is just one half of the maximum value of Δ , which is Δ_s , times the horizontal extent of the area, which is $\xi - w(\xi)$, or $\xi + y'_s(\xi)$. From Equation (4.28) it follows that

$$dA = \frac{1}{2} d\xi . \quad (4.29)$$

So far in our study of the approximate equations we have made no use of the concepts of conically subsonic or conically supersonic flow. The structure of the solution has not involved such ideas, nor should we expect it to, as the approximate equations of motion involve no characteristic velocity. Nevertheless, conically sub- and supersonic regions of the flow can be identified, and turn out to be of importance. To find them, we need the speed of sound in the shock layer: it can easily be shown that this is

$$a = \epsilon^{1/2} U \sin \alpha + C(\epsilon^{3/2}) . \quad (4.30)$$

The flow will be conically sub- or supersonic according to whether this quantity is greater or less than the velocity component normal to the ray. This component is $\epsilon^{1/2} U \sin \alpha |w - z|$ and so the flow is conically supersonic if

$$|w - z| > 1$$

and conically subsonic if

$$|w - z| < 1 .$$

Although these conditions seem irrelevant to the differential equations, they turn up, rather surprisingly, in the shock wave relationships. To begin with, we repeat here the equations for streamline slope just behind the shock wave

$$S_\xi = y'_s(\xi) + \frac{1}{y'_s(\xi) + \xi} . \quad (4.27)$$

In this equation, suppose that we are given $S_\xi = C$ (say), when $\xi = \Omega$, in other words we are solving for y'_s at a given leading edge. Equation (4.27) then becomes a quadrature for y'_s , but it is more convenient to work with the value of $w(= -y'_s = w_0$ (say)) as the unknown, and even more so to work with $(\Omega - w_0)$. Accordingly we rewrite Equation (4.27) as

$$C + \Omega = (\Omega - w_0) + \frac{1}{(\Omega - w_0)} . \quad (4.31)$$

A little consideration of this equation shows that it has no solution unless $(C + \Omega) > 2$; if this is not the case we must assume the shock wave to be detached. If there is an attached shock, Equation (4.31) shows that there are two solutions for $(\Omega - w_0)$, one the reciprocal of the other. The one for which $(\Omega - w_0) > 1$ gives conically supersonic flow, and the one for which $(\Omega - w_0) < 1$ gives conically subsonic flow. There is, pleasingly, a close correspondence between these two solutions and the "weak" and "strong" solutions of exact shock wave theory.

The subsonic/supersonic distinction turns up again if we calculate the streamline "curvature" (more properly the second derivative d^2y/dz^2). It will be recalled that this is constant on lines of constant z . We may expect therefore, that it can be expressed solely in terms of shock wave properties at a given z -station. This is, in fact, the case and the calculation proceeds as under (see Figure 10).

The required curvature can be written as

$$\frac{d^2y}{dz^2} = \frac{S_2 - S_1}{d\xi} .$$

Now from Equations (4.19) and (4.20)

$$S_1 - S_3 = \frac{\Delta_s}{y'(\xi) + \xi},$$

and by differentiating Equation (4.27) along the shock wave we get

$$S_2 - S_1 = y_s''(\xi) - \frac{1 + y_s''(\xi)}{[\xi + y_s'(\xi)]^2}.$$

Putting all these together with Equation (4.28) yields the desired result

$$\frac{d^2 y}{dz^2} = y_s''(\xi) \left\{ 1 - \frac{1}{[\xi + y_s'(\xi)]^2} \right\}. \quad (4.32)$$

Now the factor in curly brackets is positive if the flow immediately behind the shock wave is conically supersonic, in that case the shock and the streamlines will have curvatures of the same sign (Fig. 11). If the flow behind the shock wave is conically subsonic, the factor in curly brackets is negative, and the streamlines curve in the opposite direction to the shock wave.

If the flow behind the shock is conically sonic, the factor is zero, and therefore *either* the streamline curvature is zero, *or* the shock wave curvature is infinite. This latter possibility has been suggested by Messiter as providing an appropriate boundary condition for the leading edge of a wing with a detached shock; the outflow is conically sonic (see Figure 12) and the shock curvature infinite. The analogy thereby suggested between flow round a leading edge, and choked flow in a nozzle may be worth following up.

One final simple property of the solution will be noted here. an expression that allows the pressure distribution to be found when the above results have been used to obtain the streamline pattern. The streamline curvature can be written in two alternative forms:

$$\frac{d^2 y}{dz^2} = \frac{\partial S}{\partial z} + S \frac{\partial S}{\partial y}. \quad (4.33)$$

If we expand the right-hand side using Equation (4.18) and then simplify according to the equations of motion (4.12), the result is

$$\frac{d^2 y}{dz^2} = - \frac{\partial p / \partial y}{(w - z)^2}. \quad (4.34)$$

This shows that the streamline curvature is related to the vertical pressure gradient alone.

We now apply some of the results given above. As I have already mentioned, the "inverse problem" of finding the flow field and body shape associated with a given shock wave is almost trivial. There are two possible ways, and it is not difficult to prove their equivalence. One of these is to use the quadrature formula given by Messiter²,

$$y(\xi, z) = y_s(z) - \int_{\xi}^z \frac{w(s) - z}{[w(s) - s]^2} ds, \quad (4.35)$$

where $y(\xi, z)$ is the ordinate of a streamline that has crossed the shock at a spanwise station ξ and subsequently travelled to a spanwise station z .

A much quicker, if slightly less accurate, alternative is a graphical method. The shock wave shape is drawn as in Figure 13, together with the beginning of one streamline, assumed straight (Fig. 13(a)). Then we move a little outboard, and draw in the next streamline, also straight until it comes under the first one. Then we draw in the rest of the second streamline, assuming that its separation from the first one is a linear function of z , zero when $z = \frac{1}{2}(w_1 + w_2)$, i.e., the average value of w for the two streamlines. Subsequent streamlines follow in the same way.

The inner region is difficult to draw in this way because the streamlines are almost vertical. It can either be treated analytically, or else the body shape, pressures, etc., can be faired in "by eye".

Figure 14 shows the flow behind the shock wave,

$$y_s = 1 - \frac{z^2}{8}, \quad (4.36)$$

drawn in this way. The "body" consists of an inner region HI which is an envelope of streamlines, and an outer one IJ which is identical with a particular streamline. The "source point" is marked on the shock wave. Note that, as predicted, all the streamlines inflect as they pass below this point. Also marked are the points at which the sonic condition is reached on each streamline, although as already observed this has no particular significance in the solution.

A "feel" for the way these thin-shock-layer solutions behave can be developed by drawing large numbers of inverse solutions. The possibilities are enormous, but the interested reader can easily draw up his own catalogue. Only a few examples will be given here.

If we modify the above shock shape by making it straight outboard of $z = 1.8$, we get the pattern shown in Figure 15. The streamlines flowing from the straight portion all have the same value of w and therefore form a centred fan, which causes the body shape to be kinked.

The total area occupied by the flow pattern originating between $z = \xi_1$ and $z = \xi_2$ is therefore just $\frac{1}{2}(\xi_1 - \xi_2)$. It follows that for flows with attached shock waves (see Figures 14-15) the average thickness of the shock layer across the span is one half.

Another possibility which turns out to be of importance is that the shock wave may have a discontinuity in slope (Fig. 16). These discontinuities are needed to satisfy certain problems, although their significance is not altogether clear. What is clear, however, is that the shock on both sides of the discontinuity should give rise to the same streamline slope. When this happens we shall provisionally use the term "permissible discontinuity". If the streamline slopes on either side of the discontinuity are $(y'_s)_1$ and $(y'_s)_2$, then the condition for a permissible discontinuity is (from Equation (4.27))

$$(y'_s)_1 + \frac{1}{(y'_s)_1 + \xi} = (y'_s)_2 + \frac{1}{(y'_s)_2 + \xi}.$$

If we discard the trivial solutions $(y'_s)_2 = (y'_s)_1$, this simplifies to

$$[(y'_s)_1 + \xi][(y'_s)_2 + \xi] = 1. \quad (4.37)$$

From this we see that there is a transition between supersonic and subsonic flow across the discontinuity. In Figure 16 an example is shown where subsonic flow outboard of the discontinuity changes to supersonic inboard. The body surface is ridged and it is possible to think of the discontinuity as representing a sudden expansion associated with this ridge. The streamline RS must be an approximate representation of a region of intense shear.

Two examples of flows with detached shock waves are shown in Figure 17.

We now have enough results to be able to tackle the direct problem (body given). We begin by discussing the case of a detached shock wave. Provided it can be assumed that the flow pattern is of one of the types shown in Figure 17, i.e., the body is everywhere an envelope of streamlines, the integral which connects the shock and body shapes (4.15) is the same everywhere, and can be transformed^{2,6} into a second order ordinary differential equation for the unknown shock shape, which has to meet just two boundary conditions. By symmetry we have

$$y'_s(0) = 0 \quad (4.38)$$

and at the wing tip, where $z = \Omega$,

$$y'_s(\Omega) = -(1 + \Omega) \quad (4.39)$$

(from the discussion following (4.29)).

At the wing tip we also have that $y''_s(\Omega)$ is singular like $(z - \Omega)^{-1/2}$, but this can be deduced from (4.29) and (4.36) and is therefore not an independent condition.

Some solutions for normal force on a flat delta wing were given by Messiter², who gave no details of his numerical method. Subsequently, Hida³ developed a method applicable to wings of more general cross-section, assuming that both the shock and body shapes could be expressed by simple power series in z . Squire⁶ compared

Hida's solutions with experimental pressure distributions, and found that although they compared well for flat wings, the agreement was not good for diamond cross-sections, and was not improved by taking more terms of the series. This is not very surprising, for no series representation could be expected to converge well near the leading edge where y_s'' is singular. Squire also found, however, that a full numerical solution of the differential equation did give results that agreed very well with experiment (see Figure 2). There seems to be no difficulty of principle about extending this solution to general smooth cross-section shapes, and this particular aspect of the problem can now probably be regarded as fully solved.

When we come to wings with attached shock waves we encounter a fundamental difficulty. If we assume for the moment that the problem again reduces to a second order ordinary differential equation, we find that the problem appears to be overconstrained, because we have to satisfy three boundary conditions, viz.

$$\text{At the centreline: } y_s'(0) = 0 . \quad (4.40)$$

$$\text{At the wing tip: } y_s(\Omega) = y_B(\Omega) . \quad (4.41)$$

$$\text{Also at the wing tip } y_s'(\Omega) = -\frac{1}{2} \{ (\Omega + C) \pm [(\Omega - C)^2 - 4]^{1/2} \} , \quad (4.42)$$

which is a consequence of (4.28), and quite independent of (4.41).

A mathematical purist would probably abandon the problem at this stage, claiming that our approximation is so crude as to preclude a solution. However, 'solutions' have been obtained, by using one of two artifices. Hayes and Probst¹ and Woods⁸ have proposed discontinuous solutions analogous to the one shown in Figure 6. The solutions that they each propose are, however, quite different. Squire⁷ has waived the body boundary condition over part of the span, and has thereby obtained flows over wings that are close to plane deltas. In what follows we shall reexamine the flow over a plane delta wing using the simple results derived earlier, and note how these three treatments differ.

At the wing tip, we have, setting $C = 0$ in Equation (4.42),

$$y_s'(\Omega) = -\frac{1}{2} \{ \Omega \pm (\Omega^2 - 4)^{1/2} \} . \quad (4.43)$$

It seems that the minus sign corresponding to the weak solution is to be taken in all practical cases. Note also that an attached shock wave is only possible if $\Omega \geq 2$. As an example we may take $\Omega = 2.5$, in which case

$$y_s'(2.5) = -\frac{1}{2} .$$

Then the streamline originating at this point is associated with a value of $w (= w_0$, say) given by $w_0 = \frac{1}{2}$ and extends inward as far as $z = \frac{1}{2}$. This streamline must represent the body surface over the range $\frac{1}{2} < z < 2\frac{1}{2}$, and must therefore be straight. But we have seen that all streamlines at a given z -station have the same curvature. Therefore, all streamlines in the flow are straight for $\frac{1}{2} < z < 2\frac{1}{2}$.

Now streamline curvature and shock curvature are related by Equation (4.32), and setting streamline curvature equal to zero in this equation gives

$$y_s''(\xi) \left[1 - \frac{1}{[\xi + y_s'(\xi)]^2} \right] = 0 , \quad (4.44)$$

which admits the alternative solutions

$$\left. \begin{aligned} y_s''(\xi) &= 0 , \\ \text{or } y_s'(\xi) + \xi &= \pm 1 . \end{aligned} \right\}$$

Thus the shock wave can be either straight, with arbitrary inclination, or else parabolic, of the form

$$y_s(\xi) = A - \frac{1}{2}(1 - \xi)^2 . \quad (4.45)$$

Now except for the special case $\Omega = 2$, Equation (4.43) cannot match the requirement on y_s' at $\xi = \Omega$; we conclude that the shock must be initially straight, with slope chosen to match the tip boundary condition. We can therefore start to draw in the flow pattern (Fig. 18(a)). It is easy to show that this straight section does not extend all the way in to $z = \frac{1}{2}$. (Even if the centre-section of the shock were horizontal, the average thickness of the layer would come out greater than its known value of one half.) Therefore, the shock wave must change shape somewhere within $\frac{1}{2} < z < 2\frac{1}{2}$ but it must still satisfy (4.44). It can change discontinuously to another

straight section, if the compatibility condition (4.37) is met. However, if we look at the "exact" solutions due to Babaev^{12,13} of the full equations, it seems preferable to make a smooth transition if possible. Therefore, we join the straight portion onto the parabolic solution (4.45), which can be done only at the single point $z = 1 + w_0$ ($= 1\frac{1}{2}$ in our example) that is to say at the sonic point. We can now draw in a second stage in the construction of the flow pattern (Fig.18(b)). The streamlines which cross the parabolic section can be drawn inboard of $z = \frac{1}{2}$ by using the condition that they envelope onto the wing surface. It will be found that to do this they must turn discontinuously at $z = \frac{1}{2}$.

Now the shock wave cannot follow the parabolic arc for long, since this arc curves downward inboard of $z = 1$. But the streamlines are straight for $z > 1$. Therefore yet another solution to (4.44) is required. It can only be another straight section, and if it joins the parabola at a "transition point" $z = z^*$, its slope must be $-(z^* - 1)$. We can now construct a third stage of the flow pattern (Fig.18(c)), which, in a continuous solution, must hold right in to the point $z = \frac{1}{2}$.

It is when we try to cross $z = \frac{1}{2}$ that we have to admit a discontinuity. We have noted that the streamline curvature is singular there, and according to Equation (4.32) the shock curvature will also be singular unless $[\frac{1}{2} + y'_s(\frac{1}{2})] = \pm 1$. That is to say $y'_s(\frac{1}{2})$ must be $+\frac{1}{2}$ (which is obviously wrong) or $-1\frac{1}{2}$. But we know that its slope is actually $(1 - z^*)$, and so z^* must equal $2\frac{1}{2}$ (which is also absurd). Therefore the shock wave, despite all efforts to keep it smooth, must be discontinuous here at least. If the discontinuity is accepted, the solution can be continued. We shall not give details here, but the process involves choosing z^* by trial and error so as to meet the boundary condition $y'_s(0) = 0$. An infinity of further discontinuities are encountered between $z = \frac{1}{2}$ and $z = 0$ (see Figure 18(d)). A similar solution is described qualitatively in Reference 1, but no numerical results seem to have been worked out.

An alternative procedure, much simpler computationally, and no more objectionable mathematically, is that adopted by Woods⁸. He has proposed a solution in which the shock wave is composed entirely of straight line segments. The first break occurs just inboard of the sonic point and the first step in the numerical solution is to make a guess at its position. The slope of the second section is found from Equation (4.37) and this section is assumed to continue to $z = w_0$ (Fig.19(b)). The streamlines entering through the second section are supposed to turn discontinuously at $z = w_0$, and since they are all associated with the same value of w they converge to a single known point on the wing (E).

Another straight section of shock wave DF is then determined by the condition that the streamline through D has slope DE. This pattern is supposed to repeat indefinitely. By numerical experiment Woods⁸ found that there was a unique choice of position for the first break that caused the pattern to "converge" to the centreline.

The third variant is due to Squire⁷, who requires the shock wave to be smooth, and to achieve this relaxes the boundary condition over part of the body. Near the wing tip (Fig.20(a)) Squire adopts the same solution as Hayes and Probstein, i.e., a straight section AY and a parabolic section YS. By the general theory of characteristics this determines the body shape from A into N. Near the centreline, he assumes that all streamlines through a smooth section RS of the shock wave envelope onto the body in a region PQ, and in effect solves the integral Equation (4.15) to obtain the shape of RS, given that PQ is flat. The solutions to this problem form a one parameter family and Squire selects the one which matches smoothly at some point with the outboard solution. With the entire shock wave now determined, the full flow field can be found by inverse means as discussed earlier. The shape of the body between Q and N has not been specified in the solution, and does not generally have the desired flat shape. However, the errors seem to be quite small.

Which of these solutions is "best" remains so far an unanswered question. As far as the predicted pressure distribution is concerned, there seems little difference between Squire's and Woods' solutions, despite their very different natures (Fig.21). As already mentioned, there appear to be no numerical examples of Hayes and Probstein's solution. In computational effort, Woods' solution requires rather less work than Squire's and both considerably less than Hayes and Probstein. However, if wing shapes, more general in cross-section than the flat delta, are to be considered, it is fairly clear how to extend the Hayes and Probstein treatment, but not clear how to extend the other two (although they will cope with wings of diamond and caret section^{7,8}).

These criteria are essentially practical in nature. A more fundamental criterion would be to ask, which solution forms the best basis for proceeding to higher approximations (in which we might hope that the anomalous features would disappear)? This question would probably be a good starting point for a future research project. Certainly, we shall not attempt to answer it here, but we shall briefly discuss one important "higher approximation".

This is simply the matter of giving "uniform validity" to the present approximation, a question which has been treated in References 1, 4, and 5. To see how the problem arises, we must go back to the spanwise momentum equation, which we write below in conical, dimensional coordinates,

$$(\bar{v} - \bar{u}\bar{y})\bar{w}_{\bar{y}} + (\bar{w} - \bar{u}\bar{z})\bar{w}_{\bar{z}} = -\frac{1}{\rho} \bar{P}_{\bar{z}} \quad (4.46)$$

This can also be written

$$(\bar{w} - \bar{u} \bar{z}) \frac{d\bar{w}}{dz} = -\frac{1}{\rho} P_z, \quad (4.47)$$

where the differentiation on the left-hand side is carried out along streamline projections. Now let us reintroduce the dimensionless quantities, defined by (4.8) and (4.11) which we have been using so far; then

$$[w - z + O(\epsilon)] \left[\frac{dw}{dz} + O(\epsilon) \right] = -\epsilon p_z + O(\epsilon^2). \quad (4.48)$$

Now hitherto we have neglected the right hand-side of this equation, on the grounds that it is "smaller" than the left-hand side. But this is not a consistent approximation, because at the terminal points of streamlines we have encountered the condition $w = z$, which would make the two sides of (4.48) of the same magnitude. We may consider, then, the alternative equation

$$(w - z) \frac{dw}{dz} = -\epsilon p_z. \quad (4.49)$$

Over most of the flow field the inclusion of the extra term has negligible effect, but near the terminal points it obviously produces greater realism. For example, Equation (4.49) states that a streamline can only terminate ($w = z$) provided the lateral pressure gradient is zero. For a more fundamental derivation, see Reference 1. Now Equation (4.49) proves surprisingly difficult to solve analytically (see References 1, 4, 5). The straightforward attempt to expand w as a series

$$w = w_0(z) + \epsilon w_1(z) + \epsilon^2 w_2(z) \quad \text{etc.}$$

fails to converge. To illustrate, suppose in a particular example we had $p_z = \text{const} = 1$, so that

$$(w - z) \frac{dw}{dz} = -\epsilon.$$

Substituting the above expansion we get

$$(w_0 - z + \epsilon w_1 + \epsilon^2 w_2 + \dots)(w'_0 + \epsilon w'_1 + \epsilon^2 w'_2) = -\epsilon.$$

Evidently, the first approximation is

$$\left. \begin{aligned} w_0 &= \text{constant} = W \quad (\text{say}) & (A) \\ \text{or} & & \\ w_0 &= z & (B) \end{aligned} \right\} \quad (4.50)$$

For the next approximation

$$w_1 w'_0 + w'_1 (w_0 - z) = -1$$

and the solution to this is

$$\left. \begin{aligned} \text{either} & & w'_1 (W - z) &= -1 \\ \text{i.e.} & & w_1 &= \text{const} + \log(W - z) & (A) \\ \text{or} & & w_1 &= -1 & (B) \end{aligned} \right\} \quad (4.51)$$

These two solutions are shown in Figure 22, together with the exact solution, which can be found in this simple case to be

$$w = \text{const} + \epsilon \log(w - z + \epsilon), \quad (4.52)$$

with the constants in (4.51A) and (4.52) both chosen to make the solution pass through $z = 2$, $w = 1$.

Evidently the approximation scheme breaks down near $z = W$ due to the discontinuous nature of the first approximation. Methods are available¹⁴ to deal with this sort of thing, and have been tried in the present case.

Specifically, the method of matched asymptotic expansions has been employed in Reference 4, and the Poincaré-Lighthill-Kuo technique of "coordinate straining" in References 4 and 5.

From these studies it emerges that the problem is essentially one involving three layers, one in which w is nearly constant along a streamline (the "outer layer", with which the earlier parts of this chapter were concerned), another in which w is very nearly equal to z , (the inner layer), and a transitional layer, across which orders of magnitude change abruptly. Mathematically, the inner and outer layers are distinguished by

$$\begin{aligned} (w - z) &= O(1), & \frac{dw}{dz} &= O(\epsilon) & \text{(outer layer)} \\ (w - z) &= O(\epsilon), & \frac{dw}{dz} &= O(1) & \text{(inner layer).} \end{aligned}$$

An illustration of these layers in relation to the streamline pattern is shown in Figure 23. To estimate how important each of these regions is in the overall solution we may work out the area which a given "streamtube" (pair of streamlines) takes up in each layer. I find myself unable to give a short proof but the answer is known^{1,4}. If the area of the streamtube in the outer layer is taken as reference, the area in the transitional layer is $O(\epsilon^2)$ times this, and the area in the inner layer is $O(\exp\{-1/\epsilon\})$ times it. Thus the inner layer would almost certainly be swamped by the boundary layer in a real flow, but the transitional layer could well be significant.

In an inverse problem it would be quite easy to work out solutions incorporating the inner and transitional layers. The outer layer solution is found as described earlier. For each streamtube the pressure is found as a function of z for $z > w$. It can be assumed that the streamtube continues into the minimum pressure point, as an infinitely thin layer ($\Delta = 0$) making infinitely slow progress ($w = z$). Then we have a first approximation to pressure, spanwise velocity, and streamtube height (Fig. 24). Now it will be a good approximation to assume that $p(z)$ is not much altered by taking the two inner layers into account, so we can use the first approximation for p to develop, via Equation (4.49) a second approximation for w . Having done this we can also use Equation (4.49) to write Equation (4.19) as a uniformly valid equation for Δ .

$$\frac{1}{\Delta} \frac{d\Delta}{dy} = - \frac{1 + dw/dz}{(w - z)} \quad (4.53)$$

With this carried out for all streamtubes in the flow, the streamline pattern can be redrawn, and new pressures worked out, e.g. from (4.38). The cycle can be repeated as often as may be worthwhile.

Now, it is very likely that the mathematical status of the outer solution for the direct problem can be restored by considering the inner layers in this way. This has already been shown to be the case in a very similar problem by Cole and Brainerd⁹. They applied the thin-shock-layer theory of Equations (4.9) and (4.10) to the two-dimensional flow past a blunt plate, and obtained the basic system

$$\begin{aligned} u_x + v_y &= 0 \\ uv_x + vu_y &= 0 \end{aligned}$$

with shock boundary conditions

$$\begin{aligned} v_s &= x_s' \\ u_s &= 1 + x_s'^2 \end{aligned}$$

This very simple system is not capable of meeting the boundary conditions on arbitrary bodies directly, but Cole and Brainerd showed that it would do so indirectly, if a single inner layer were interposed between the body and the outer solution (Fig. 26). Thanks to the very simple nature of their outer solution, they were able to carry out analytically processes which in the conical case probably have to be done numerically.

A useful theoretical answer to the question, which of the three available outer solutions is best, could very likely be, "the one which best lends itself to the above extensions".

Starting from the two basic assumptions of a thin shock layer and an aspect ratio of the same order as the Mach angle in the disturbed flow, we have seen that it is possible to develop a theory remarkably rich in simple results. I have tried to show that this simplicity is much enhanced by treating the streamline pattern as the main unknown. This simplicity makes it possible to see clearly the connections between existing treatments, and gives confidence that significant refinements can probably be made without overwhelming analytic complexity. Finally, I have indicated one form that these refinements might take.

REFERENCES

1. Hayes, W.D.
Probstein, R.F. *Hypersonic Flow Theory, Vol. I: Inviscid Flow.* Academic Press, 1966.
2. Messiter, A.F. *Lift of Slender Delta Wings According to Newtonian Theory.* AIAA Journal 1, 1963, pp.794-802.
3. Hida, K. *Thickness Effects on the Force of Slender Delta Wings in Hypersonic Flow.* AIAA Journal 3, 1965, pp.427-433.
4. Melnik, R.E.
Sheuing, R.A. *Shock Layer Structure and Entropy Layers in Hypersonic Conical Flows.* Hypersonic Flow Research, Academic Press, 1962, pp.379-420.
5. Melnik, R.E. *A Conical Thin-Shock-Layer Theory Uniformly Valid in the Entropy Layer.* Report No.FDL-TDR-64-82, 1965.
6. Squire, L.C. *Calculated Pressure Distributions and Shock Shapes on Thick Conical Wings at High Supersonic Speeds.* Aero. Quarterly, Vol.XVIII, 1967, pp.185-206.
7. Squire, L.C. *Calculated Pressure Distributions and Shock Shapes on Conical Wings with Attached Shock Waves.* Aero. Quarterly, Vol.XIX, 1968, pp.31-50.
8. Woods, B.A. *Hypersonic Flow over Delta Wings with Attached Shock Waves.* Aero. Quarterly, Vol.XXI, November 1970, pp.379-399.
9. Cole, J.D.
Brainerd, J.J. *Slender Wings at High Angles of Attack in Hypersonic Flows.* Hypersonic Flow Research, Academic Press, 1962, pp.321-344.
10. Courant, R.
Friedrichs, K.O. *Supersonic Flow and Shock Waves,* Interscience, 1948.
11. Maslen, S.H. *Supersonic Conical Flow.* NACA TN 2651, 1952.
12. Babaev, D.A. *Numerical Solution of the Problem of Supersonic Flow Past the Lower Surface of a Delta Wing.* AIAA Journal 1, No.9, September 1963.
13. Babaev, D.A. *Flow about a Triangular Wing for Large Values of M .* USSR Computational Mathematics and Mathematical Physics, Vol.3, No.2, 1963.
14. Kline, S.J. *Similitude and Approximation Theory,* McGraw-Hill, 1965.
15. Squire, L.C. *Pressure Distributions and Flow Patterns at $M = 4.0$ on some Delta Wings.* ARC R & M 3373, 1963.

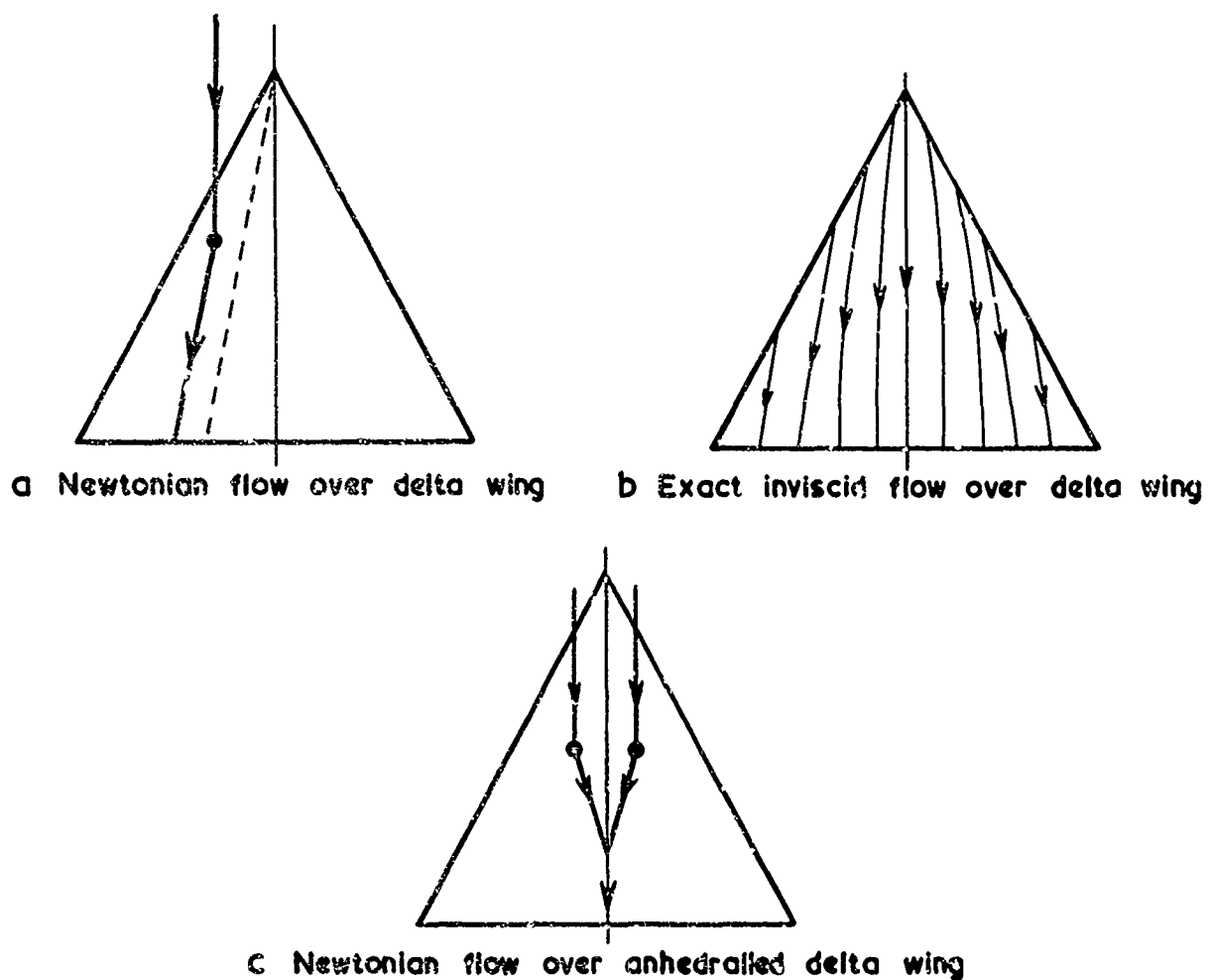


Fig.1 Surface flow patterns

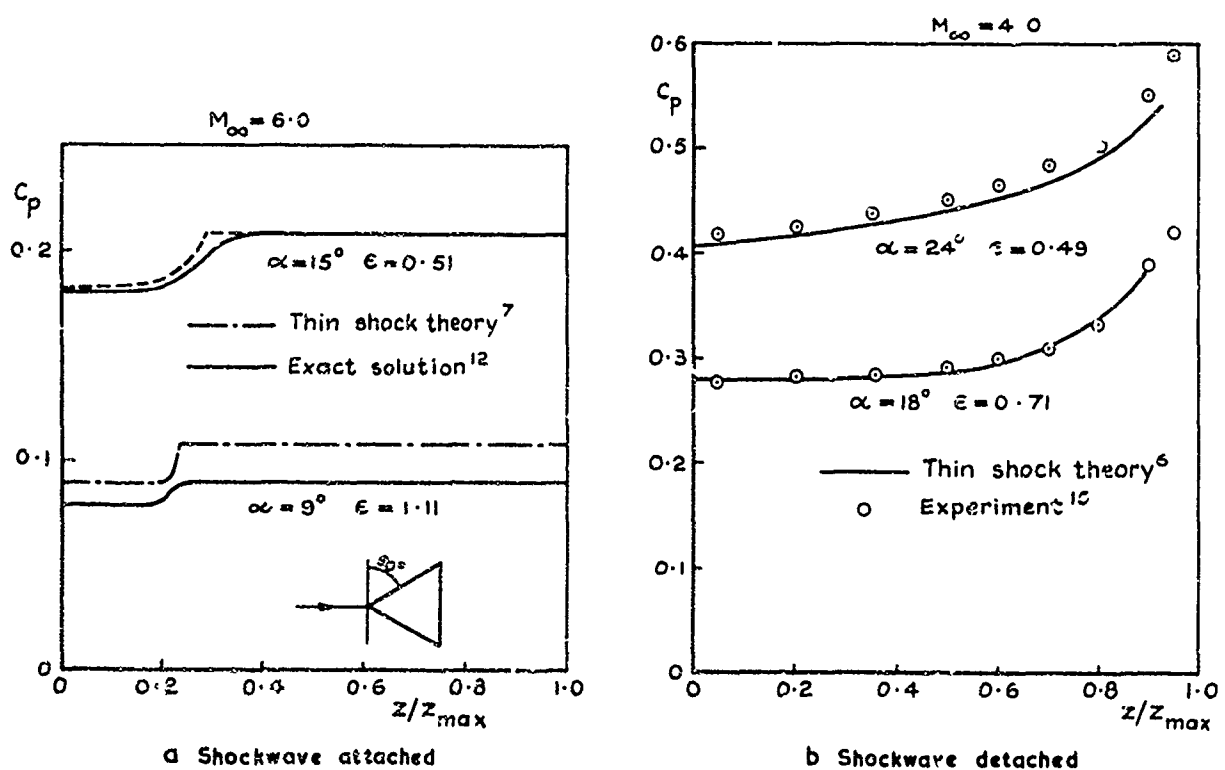


Fig.2 Pressure distributions predicted by thin-shock-layer theory

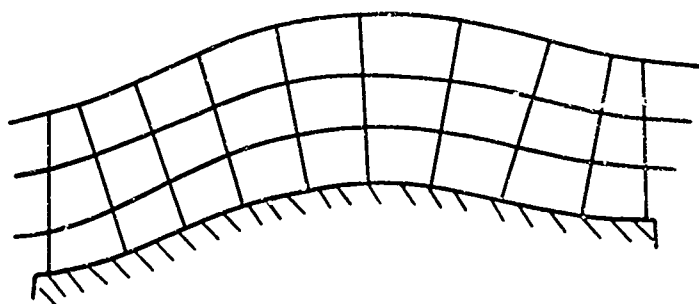


Fig.3 General conical coordinates

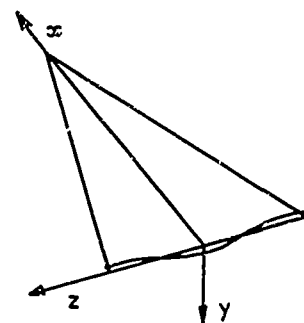


Fig.4(a) Cartesian coordinates

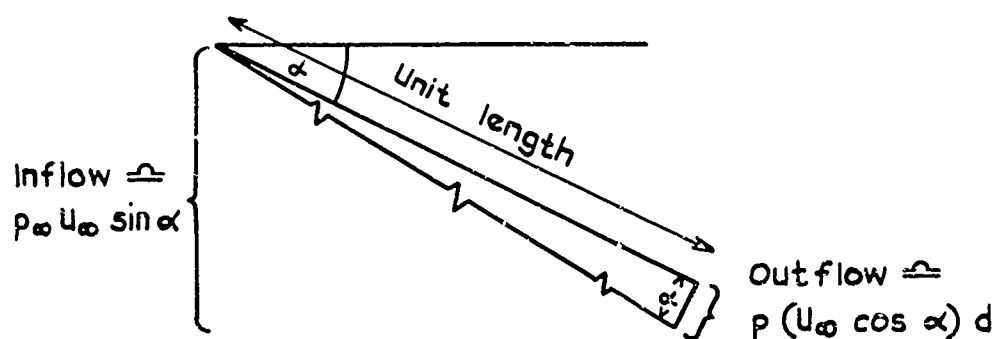


Fig.4(b) Sketch to determine coordinate stretching

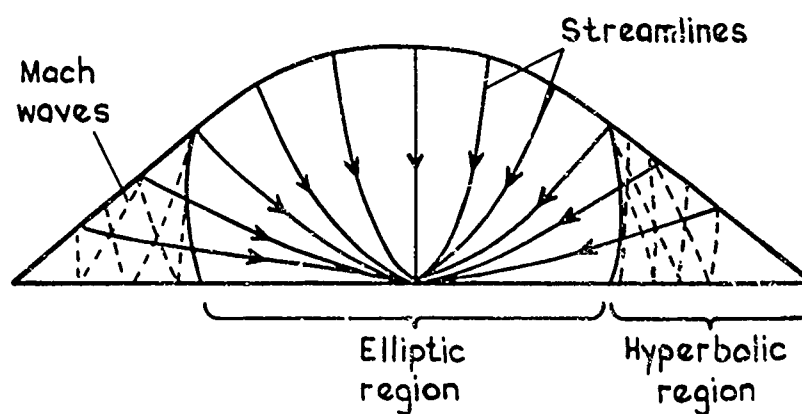


Fig.5 Characteristic pattern for full equations

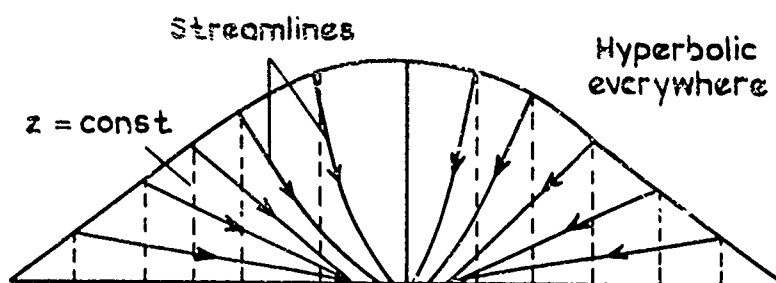
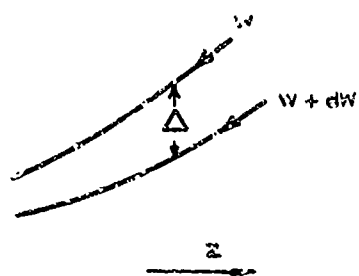


Fig.6 Characteristic pattern for Equations (4.12)



a A pair of streamlines



b / bundle of streamlines

Fig.7 Streamline geometry

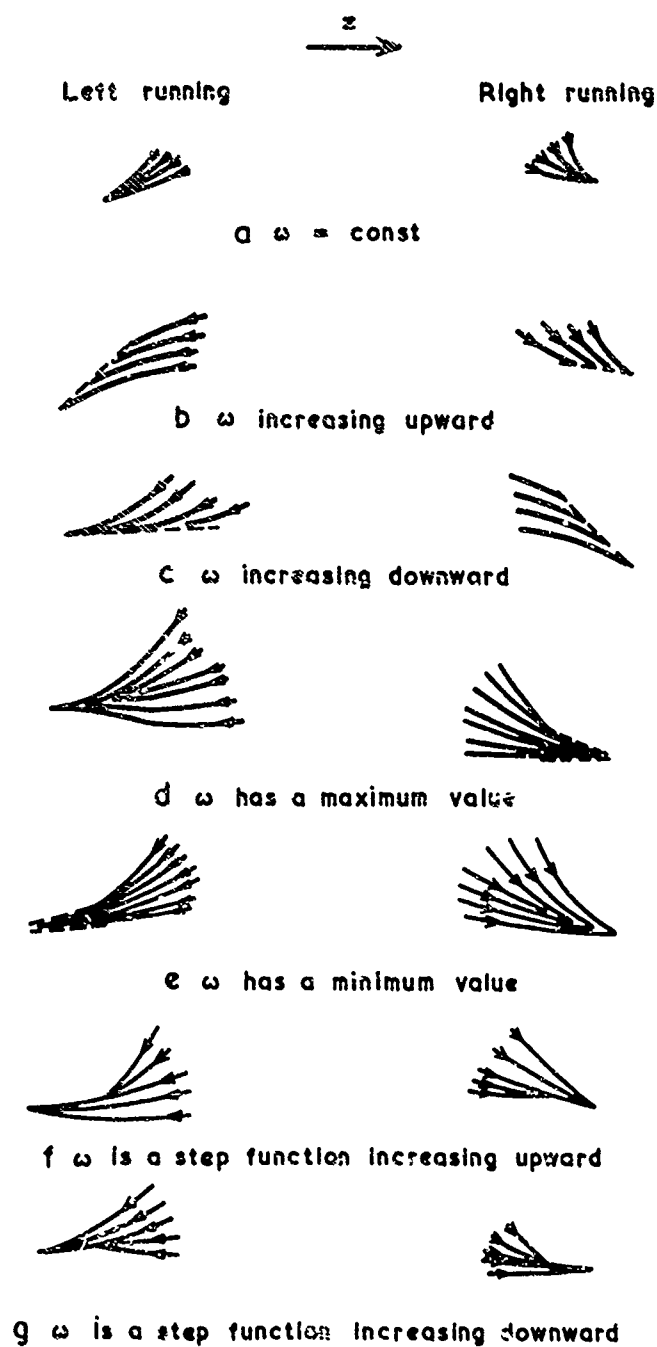


Fig.8 Possible streamline patterns

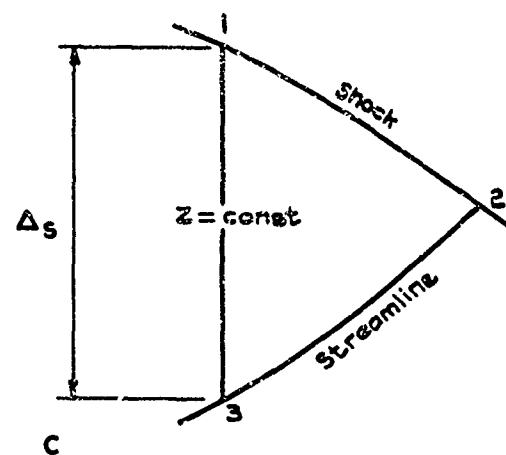
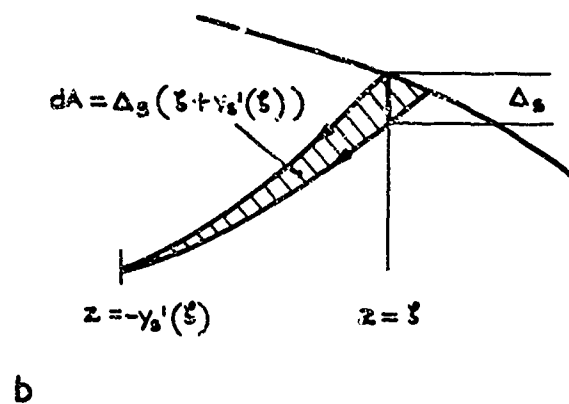
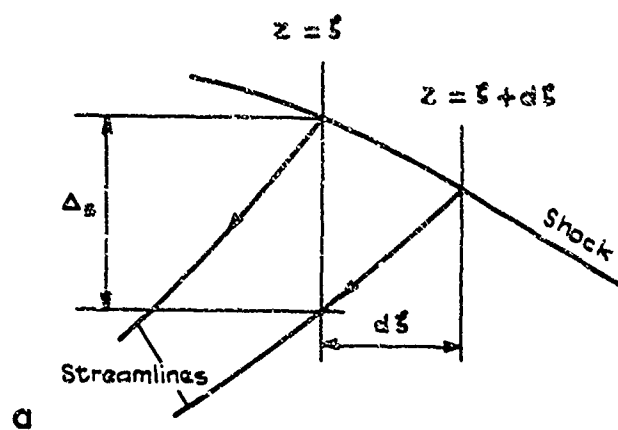


Fig.9 Determination of constants in streamline geometry

Fig.10 Notation for deriving Equation (4.31)

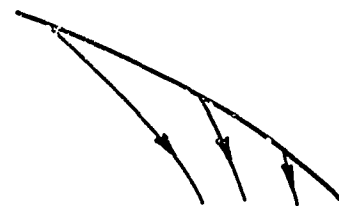
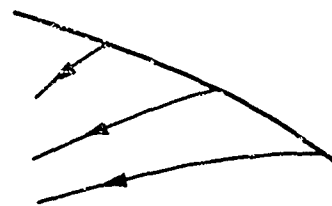


Fig.11(a) Conically supersonic flows

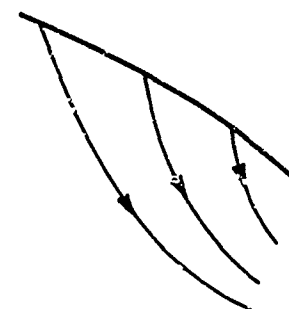
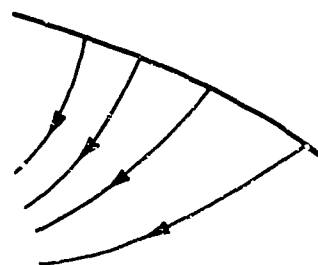


Fig.11(b) Conically subsonic flows

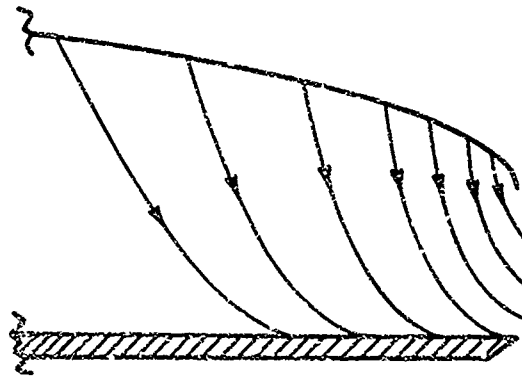


Fig.12 Flow at a wing tip

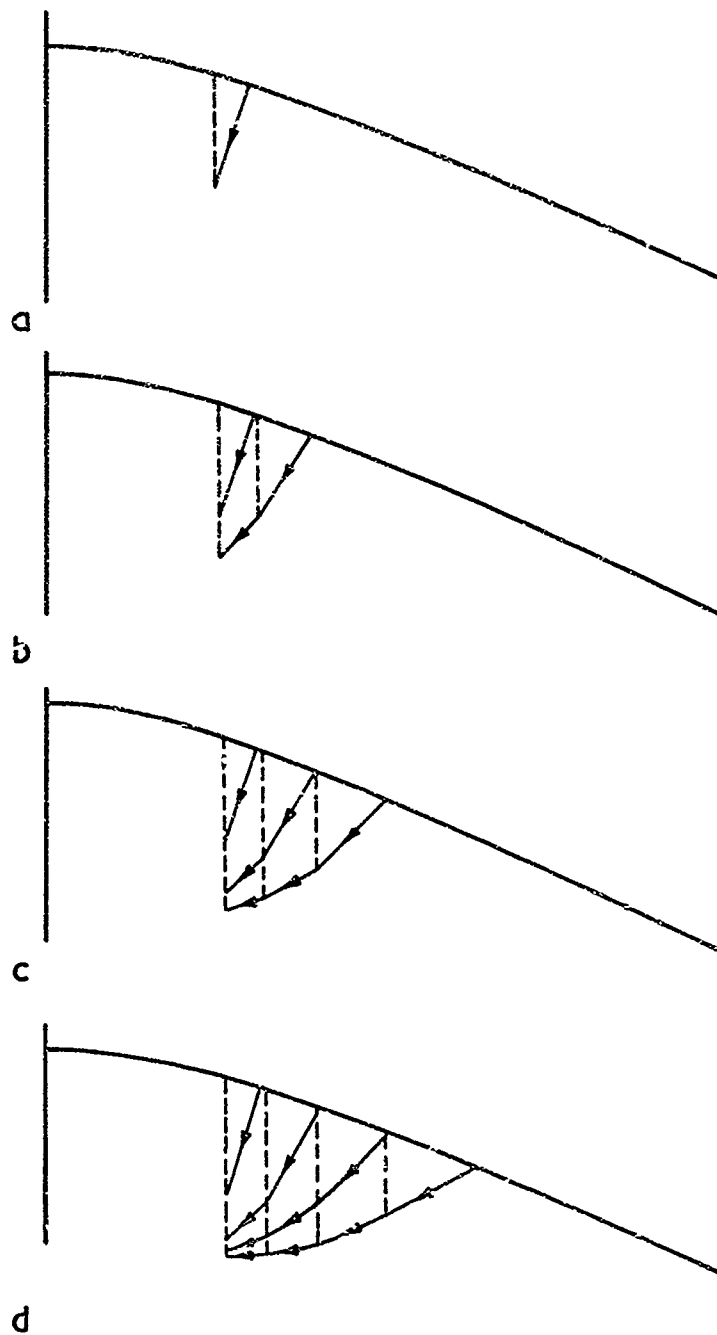


Fig.13 Graphical solution of inverse problem (shock wave given)

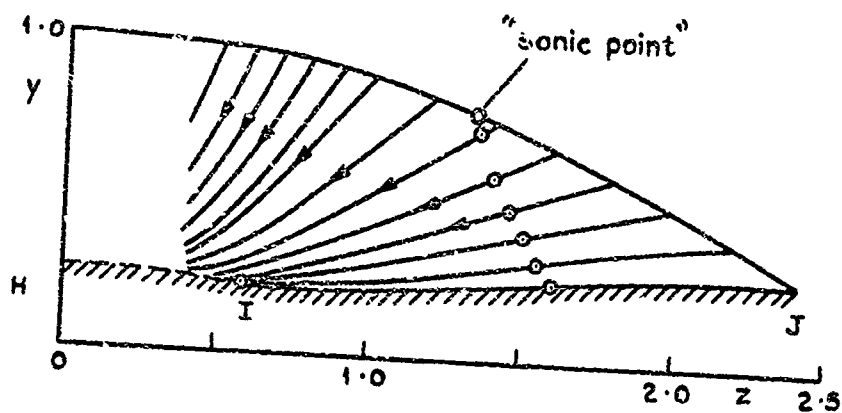


Fig.14 Flow behind shock wave $y_s = 1 - z^2/8$

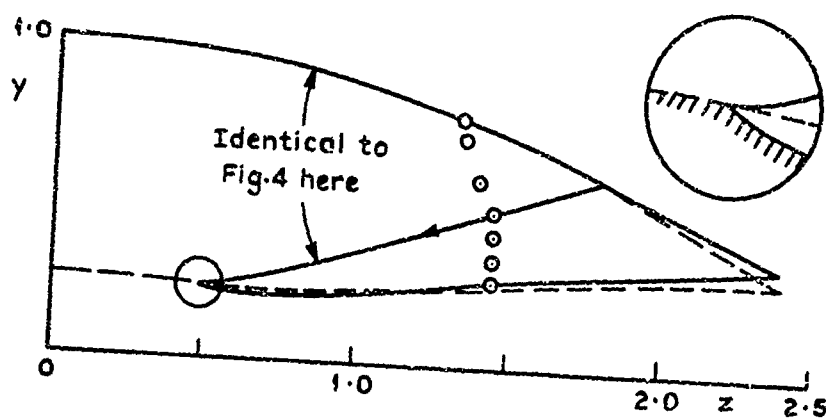


Fig.15 Flow behind a shock wave with a straight segment

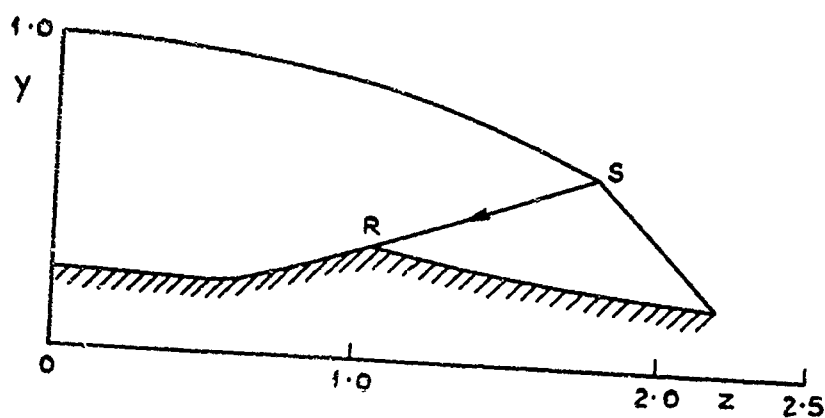


Fig.16 Flow behind a shock wave with a slope discontinuity

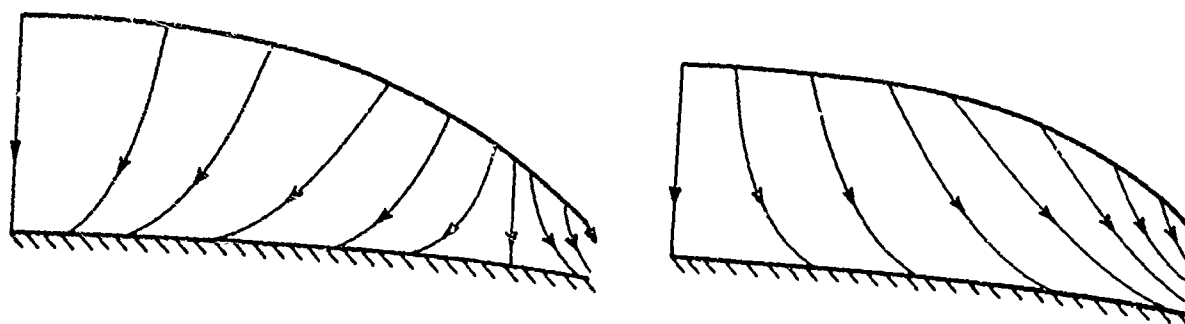


Fig.17 Flows with detached shock waves

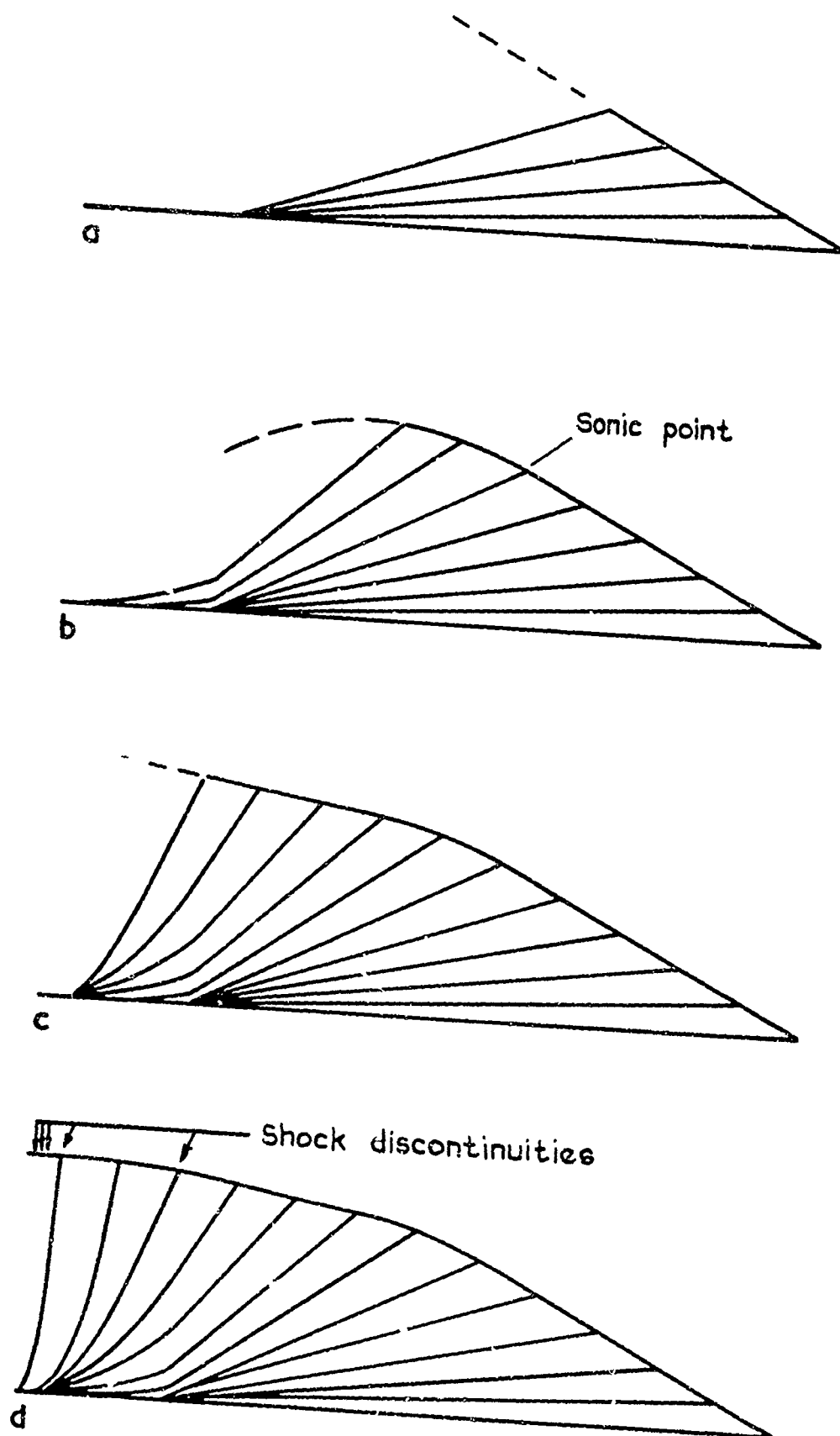


Fig.18 Hayes and Probstein's solution

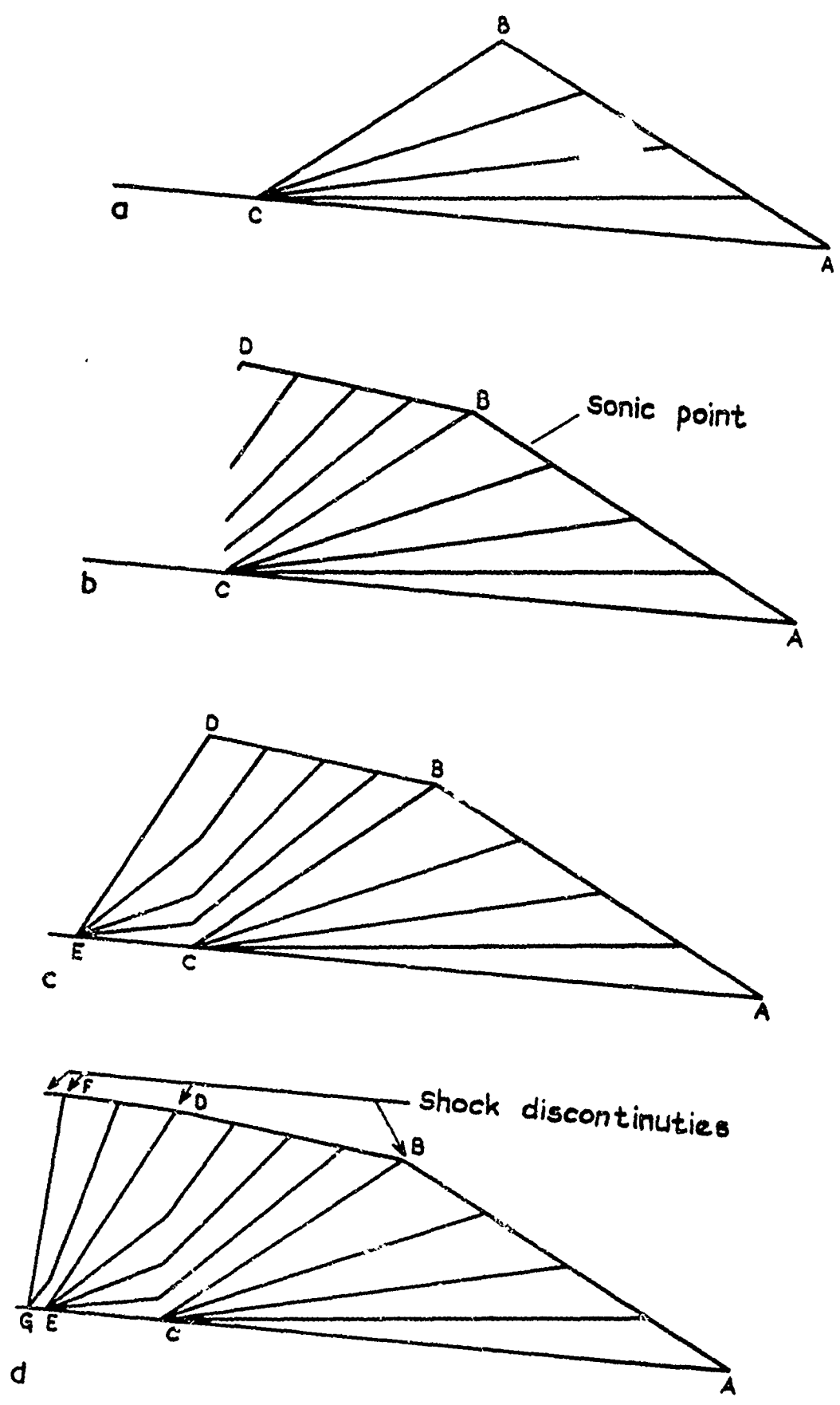


Fig. 19 Woods's solution

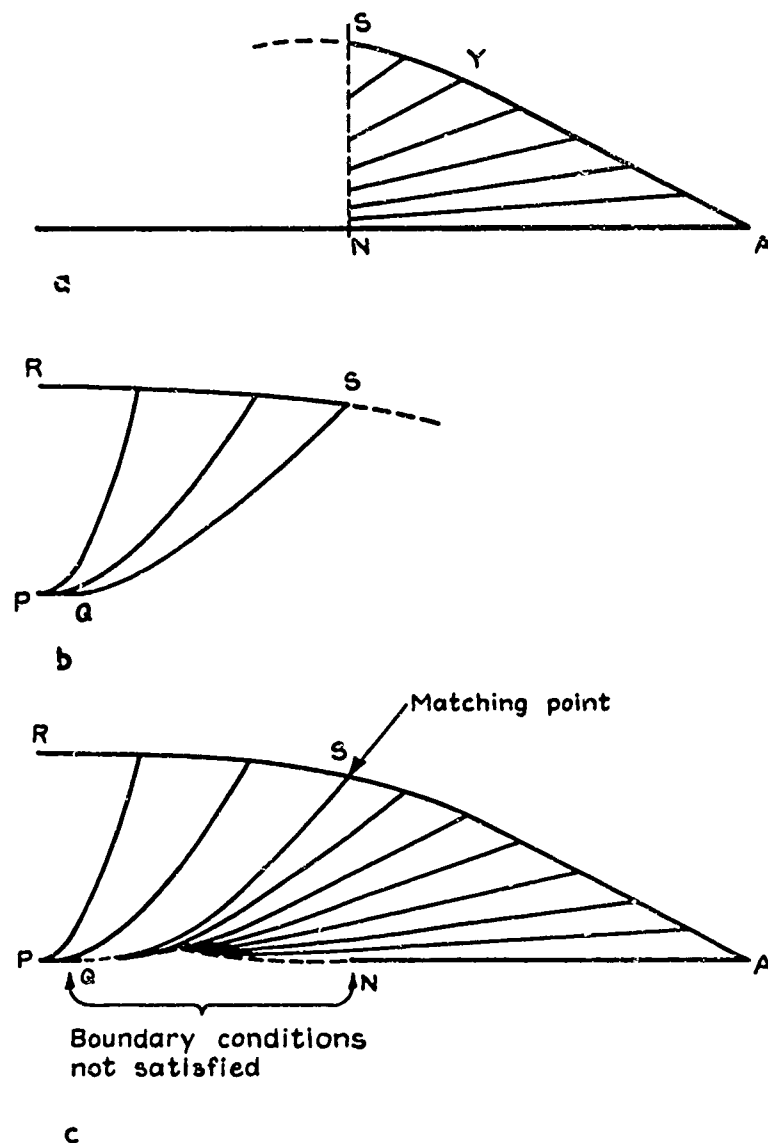


Fig.20 Squire's solution

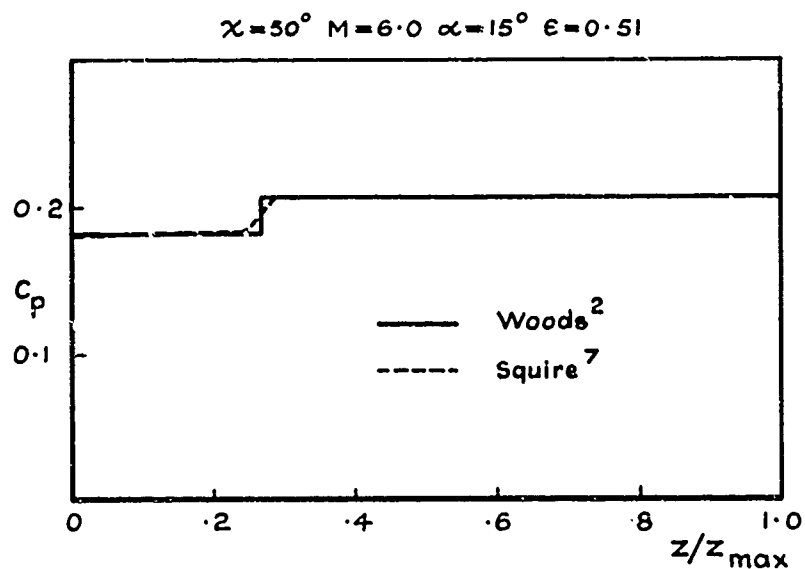
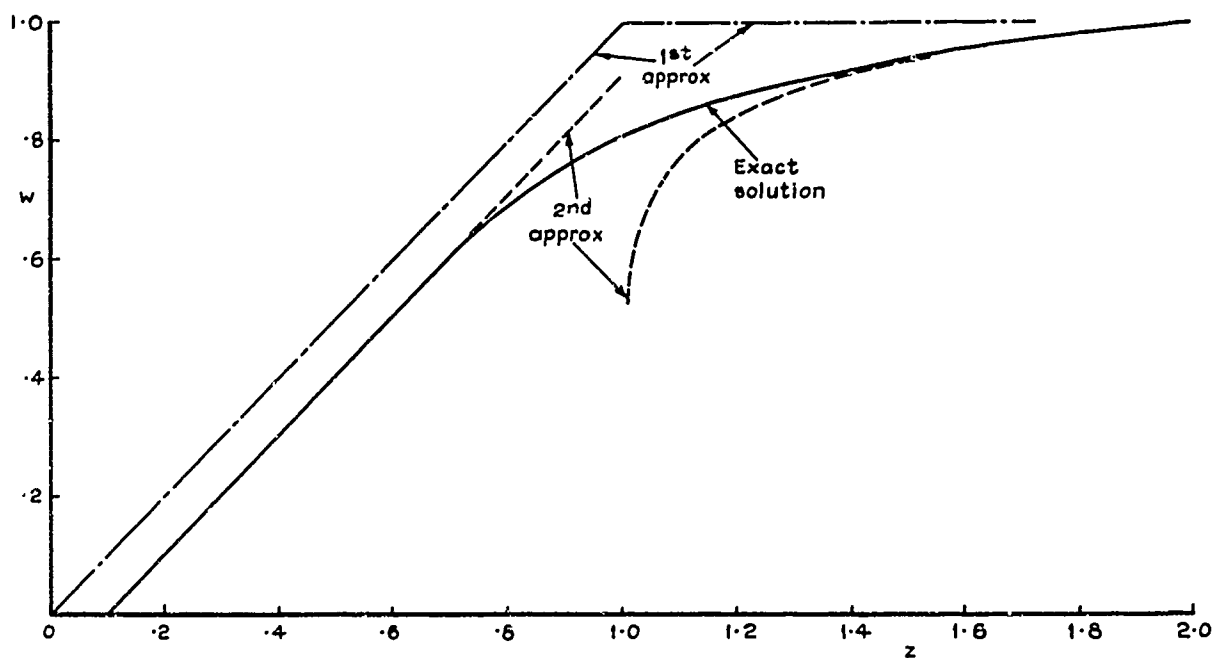


Fig.21 Two thin-shock-layer solutions for flow over a plane delta wing

Fig.22 Solution of $(w - z)dw/dz = -0.1$

————— Uncorrected streamlines
 - - - - - Corrected streamlines

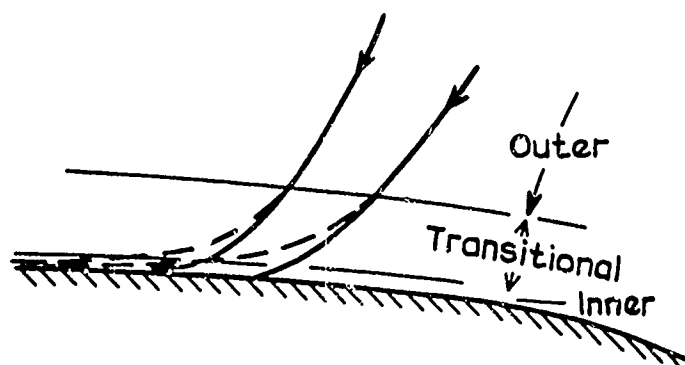


Fig.23 Streamlines in uniformly-valid solution

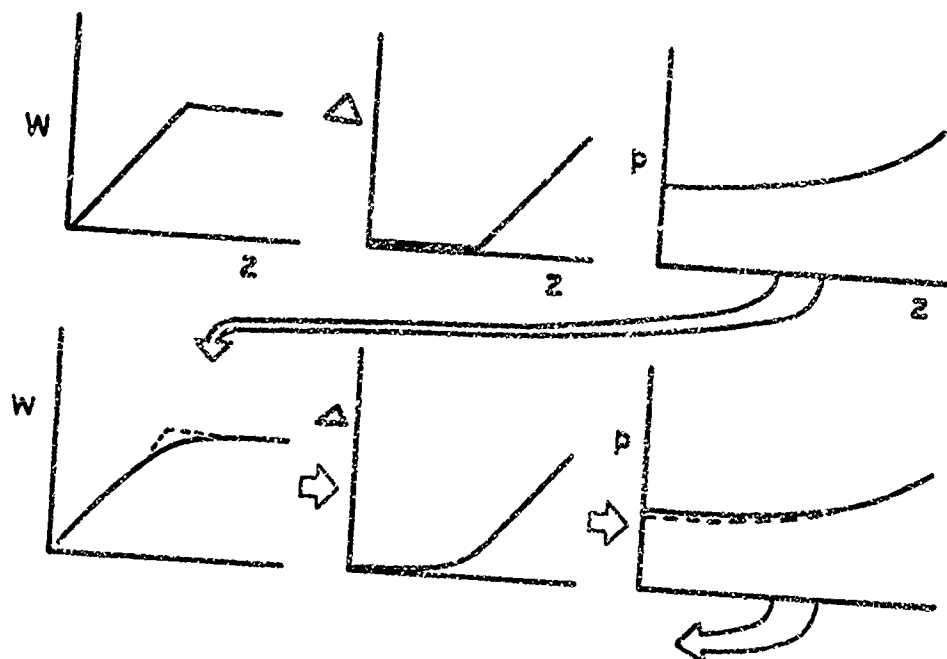


Fig.24 Successive approximation scheme

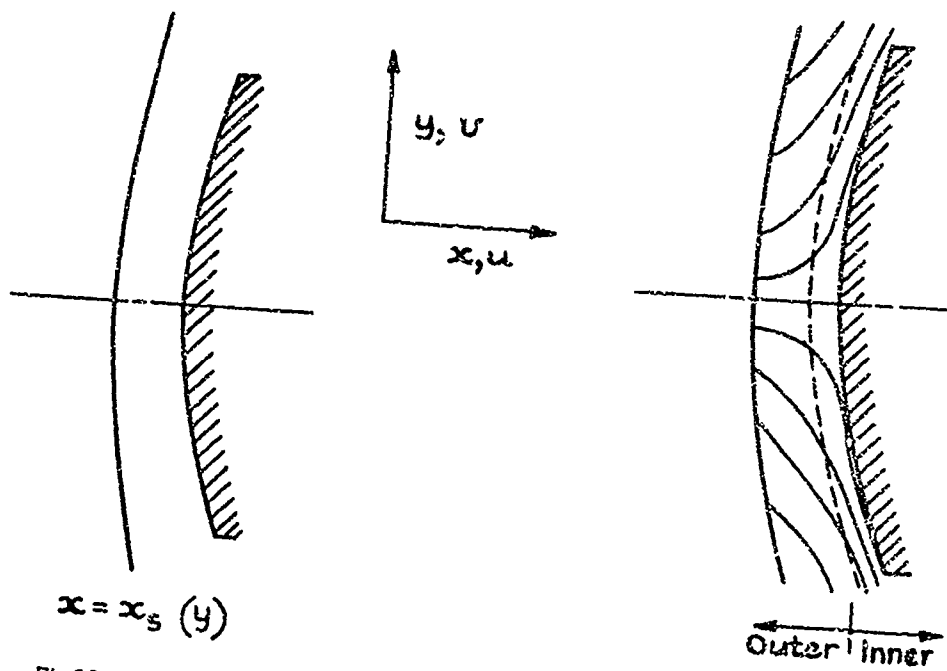
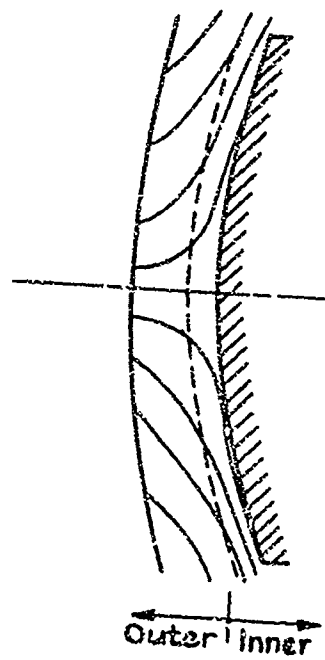
Fig.25 Cole and Brainerd's problem
(thin two-dimensional shock layer)

Fig.26 Structure of two-dimensional problem

LECTURE 5

MOMENTUM THEORY

P.L.Roe

Royal Aircraft Establishment, Bedford, England

The subject of this lecture can probably best be approached by regarding it as an offshoot of the "waverider" design technique. The distinguishing feature of that approach is that calculation of the wave system and flow pattern precedes the selection of the actual lifting shape. Therefore as soon as the shape is chosen, we already have in hand all the necessary information to find the aerodynamic forces acting on it by means of a momentum balance. By comparison with integration of the surface pressures, the momentum method offers some computational advantages. More importantly, however, it provides a fresh and stimulating way to study the efficient generation of aerodynamic lift.

In calculating a momentum balance, the first step is always to choose a suitable control volume. The one we employ here is shown in Figure 1. Separate, independent "boxes" are drawn to evaluate the force contributions made by the upper and lower surfaces. When we select the boundaries for these boxes certain surfaces suggest themselves very naturally. Fairly obviously one boundary ought to be the wing surface being considered, the pressure integral over this surface is the thing we want to know, and the momentum flux through it is zero. Another boundary that suggests itself is the upstream limit of the flow disturbances caused by the surface. This may be a shockwave or a Mach wave, in either case we draw the boundary just on the upstream side of it, where the flow conditions are those of the free stream.

The choice of the third boundary is less obvious. Evidently it must intersect the wing surface at the trailing edge. Two boundaries which meet this condition and which also have physical significance are the upstream and downstream characteristic surfaces through the trailing edge. At the present stage of the investigation, however, no advantage has been found in their use, and the third surface has been chosen purely on the grounds of computational simplicity. We chose the rear boundary to be composed entirely of vertical generators, so that no pressure terms appear in the calculation of the lift. If the trailing edge is unswept, as it is in Figure 1, and as it often will be in practice, the third surface becomes a plane normal to the free stream.

The chosen control volume is redrawn in Figure 2. This shows only the control volume for the lower surface. Indeed from this point on we shall consider only lower surface flows, although it will be obvious that upper surface flows can be analysed in the same way. Figure 2 also shows a particular streamtube passing through the control volume. It is identified, for a reason which will appear later, by the plan view area (dA_p) of the curve in which it intersects the upstream boundary (shockwave).

Now the forces acting on the surface* can be obtained, according to the momentum theorem, by integrating the appropriate components of pressure and momentum flux over the upstream and downstream boundaries, and taking the difference. Every streamtube that enters the control volume through the upstream boundary leaves it through the downstream boundary. It contributes therefore, to both integrals. The difference between these two contributions may be thought of as its contribution to the force on the surface.

Let the "contribution" as defined above, of a given streamtube to the lift force be

$$(q_\infty dA_p) \times f_L$$

where

$$q_\infty = \text{free stream dynamic pressure,}$$

$$dA_p = \text{small area defined by Figure 2,}$$

*The pressure force acting on a closed body can be written as $\mathbf{F} = \iint p \mathbf{n} dA$, where \mathbf{n} is the inward unit normal to the surface element dA . This can be put into the alternative form $\mathbf{F} = \iint (p - p_r) \mathbf{n} dA$, where p_r is any convenient constant reference pressure. This is because for any closed body $\iint \mathbf{n} dA = 0$. If we try to consider any part of the body in isolation, e.g. the wing lower surface, then $\iint \mathbf{n} dA \neq 0$ and the value chosen for p_r will make a difference. This should not affect the validity of the answers provided we subsequently choose the same p_r when studying the other surfaces. Here, however, we do intend only to study the lower surface, which is the most important lifting element, and must therefore choose a p_r which gives the most useful answers. We have taken $p_r = p_\infty$, so that $\mathbf{F} = \iint (p - p_\infty) \mathbf{n} dA$. This is then the force which would act on a body obtained by coupling the given lower surface with a streamwise upper surface, if base drag can be neglected.

and f_L is a nondimensional quantity associated with that streamtube which we shall call its "lift function".

Similarly we suppose the same streamtube contributes to the drag force by an amount

$$(q_\infty \times dA_p) \times f_D$$

and we shall call f_D the "drag function"

The quantities f_L and f_D will depend on the state of the flow at entry and at exit. The algebraic expressions for them have been found in Reference 1. For the special case where the trailing edge is unswept and the rear control boundary is normal to the stream these expressions are:

$$f_L = \frac{2l}{n} \frac{v_z}{v_\infty} \quad (5.1)$$

$$f_D = \frac{2l}{n} \left[1 - \frac{v_x}{v_\infty} - \frac{p - p_\infty}{\rho v_\infty v_x} \right] \quad (5.2)$$

In these expressions, we have made use of a coordinate system (x, y, z) as shown in Figure 2. The shockwave, at the point where it is penetrated by the streamtube, has direction cosines (l, m, n) in this system, so that the fraction l/n which appears in (5.1) and (5.2) defines the ratio of the streamtube cross-section area before it meets the shock to the reference area dA_p . Of the other quantities appearing in (5.1) and (5.2), v_x and v_z are velocity components in the x and z directions, p is the static pressure, and ρ the density, all evaluated at the point where the streamtube crosses the exit plane. Free stream pressure is denoted by p_∞ , and free stream velocity by v_∞ .

Now the total lift acting on the wing is found by summing the contributions from all the captured streamtubes. It is therefore

$$L = \iint_{A_p} q \, f_L \, dA_p \quad (5.3)$$

The lift coefficient, based on planform area, defined as

$$C_L = \frac{L}{q_\infty A_p}$$

becomes

$$C_L = \frac{1}{A_p} \iint_{A_p} f_L \, dA_p \quad (5.4)$$

and evidently we shall also have

$$C_D = \frac{1}{A_p} \iint_{A_p} f_D \, dA_p \quad (5.5)$$

It was in order to obtain the simple "mean value" property expressed by Eqns (5.4) and (5.5) that dA_p was chosen as reference area in defining the lift and drag functions.

We shall now try to devise some applications for these results.

The first application is illustrated in Figure 4. We suppose that we have (somehow) chosen a flow field which is to be the basis of a waverider design, and that we are now trying to select the most suitable streamsurface from it. In part this will be a geometric problem, and this aspect was discussed in my third lecture. Now, however, we are concerned only with the lifting efficiency. Suppose that we have arbitrarily chosen some particular stream surface, and are considering the possibility of slightly altering our choice. We show this streamsurface, intersecting the shockwave in some "leading edge" in Figure 4.

Let us consider the consequences of slightly extending the leading edge, in the manner shown by the dotted line. The planform area of the wing increases as shown in the upper figure, and we shall call the amount of the increase dA_p . The new wing also "captures" an additional small streamtube from the flow field. Let the lift function of this streamtube be f_L and its drag function f_D . Then the lift of the wing is increased by an amount $q_\infty f_L dA_p$.

We can also, however, because of Eqn (5.4) make the following useful qualitative statement. If the lift function of the proposed additional streamtube is greater than the lift coefficient of the original wing, then, and only then, will the lift coefficient be increased by the modification. Again it is evident that a similar statement holds true with regard to the drag coefficient.

With the aid of these results, it is possible to establish very rapidly the potentialities of any given flow field as a source of waverider surfaces.

The flow field shown in Figure 4 is drawn as axisymmetric; this is not of course a necessary condition for the validity of the above results, which hold for any flow field (even one not prescribed in advance). However, since axisymmetric flows are at the moment the most general flows conveniently available for this work, it is of interest to investigate their special properties from this "momentum" viewpoint.

The general expressions (5.1) and (5.2) for the lift and drag functions simplify somewhat. In an axisymmetric flow any streamline lies entirely in a plane $\phi = \text{const.}$ (Fig. 5), and the element of shockwave through which it enters is normal to that plane. Let that element of shockwave be inclined at an angle θ to the axis of symmetry. Then

$$\frac{l}{n} = \frac{\tan \theta}{\cos \phi} \quad (5.6)$$

Also let the velocity vector of that streamline in the exit plane have magnitude v and make an angle δ with the axis of symmetry, then

$$v_x = v \cos \delta \quad (5.7)$$

$$v_z = v \sin \delta \cos \phi \quad (5.8)$$

Substituting these in (5.1) and (5.2) we get

$$f_L = 2 \tan \theta \frac{v \sin \delta}{v_\infty} \quad (5.9)$$

and

$$f_D = \frac{2 \tan \theta}{\cos \phi} \left[1 - \frac{v \cos \delta}{v_\infty} - \frac{(p - p_\infty)}{\rho v v_\infty \cos \delta} \right] \quad (5.10)$$

Now suppose the flow field is described in a cylindrical coordinate system (x, r, ϕ) . Then we can see that for a given exit plane ($x = 1$, say) the quantities $p, \rho, v, \theta, \delta$, which appear in (5.9) and (5.10) depend only on one variable, for instance the x -coordinate at which the streamline crosses the shockwave $r = r_s(x)$. Thus we have, for a streamline crossing the shockwave at $(x, v_s(x), \phi)$,

$$f_L(x, \phi) = f_L^*(x) \quad (5.11)$$

$$f_D(x, \phi) = f_D^*(x)/\cos \phi \quad (5.12)$$

The very simple nature of the dependence on ϕ makes it possible to reduce the double integrals for lift and drag to single integrals. Consider the streamtube which on entering the shockwave is bounded by lines $x = x_1$, $x = x_1 + dx$, and $\phi = \phi_1$, $\phi = \phi_1 + d\phi$. For this streamtube

$$dA_p = r_s(x_1) \cos \phi d\phi dx \quad (5.13)$$

Now insert (5.11), (5.12) and (5.13) into (5.4) and (5.5). The result is

$$C_L = \frac{1}{A_p} \int_{x_N}^{x_T} \int_{-\phi_L}^{+\phi_L} f_L^*(x) r_s(x) \cos \phi d\phi dx \quad (5.14)$$

and

$$C_D = \frac{1}{A_p} \int_{x_N}^{x_T} \int_{-\phi_L}^{+\phi_L} f_D^*(x) r_s(x) d\phi dx \quad (5.15)$$

In these expressions

x_N is the x-coordinate of the wing apex ,

x_T is the x-coordinate of the trailing edge

and

$\phi_L(x)$ is the ϕ -coordinate of the leading edge.

The integration with respect to ϕ is immediate, and comes out as

$$C_L = \frac{2}{A_p} \int_{x_N}^{x_T} y(x) f_L^*(x) dx \quad (5.16)$$

$$C_D = \frac{2}{A_p} \int_{x_N}^{x_T} r_s(x) \sin^{-1} \left(\frac{y(x)}{r_s(x)} \right) f_D^*(x) dx , \quad (5.17)$$

where $y(x)$ is the local wing semi-span. Analogous formulae have been derived by Jones and Woods², and Cole and Zien³.

Both these reports treat special cases of axisymmetric flow fields. Jones and Woods² consider only flow fields around unyawed circular cones, and use the formulae purely for their computational convenience. Cole and Zien³ consider self-similar flows generated by power-law axisymmetric bodies according to hypersonic small-disturbance theory. They then try to exploit the simple form of the expressions to find a family of optimum shapes. Part of the problem which they consider can be shown using our notation. We use Eqns (5.16) and (5.17) to write the actual lift and drag forces on a surface as

$$\frac{L}{2q_\infty} = \int_{x_N}^{x_T} y(x) f_L^*(x) dx \quad (5.18)$$

$$\frac{D}{2q_\infty} = \int_{x_N}^{x_T} r_s(x) \sin^{-1} \left(\frac{y(x)}{r_s(x)} \right) f_D^*(x) dx . \quad (5.19)$$

For a given flow field and a given value of x_T in it, f_L^* , f_D^* , and r_s may be regarded as given functions of x . We may choose $y(x)$, the function which defines the planform shape, so as to optimise some criterion. The problem proposed by Cole and Zien is given L and x_T , minimise D . The equation for $y(x)$ follows at once from standard results in the calculus of variations; it is

$$\frac{y}{r_s} = \left(1 - \frac{\lambda^2 f_D^2}{f_L^2} \right)^{1/2} , \quad (5.20)$$

where λ is a Lagrange multiplier.

Eqn (5.20) only gives sensible results if (f_D/f_L) is a decreasing function of x , in the contrary case Cole and Zien³ show that the "optimum" wing is defined by $y/r_s = \text{constant}$.

Eqn (5.20) is undoubtedly a very simple result. However, it treats only a very small part of the optimisation problem. The required amount of lift could have been obtained from the same flow field terminated at a different x_T , or from a quite different flow field. Cole and Zien go on to consider some of these further choices, but restrict their considerations, as mentioned earlier, to the self-similar flow past power-law bodies. They consider bodies defined by $r_b = \tau x^n$ with a fixed exponent n , but variable τ . For each value of τ , one particular choice of λ in Eqn (5.20) gives rise to the desired value of L . From amongst the family of "optimised" wings so obtained, they choose the value of τ which minimises D . They express their results in terms of an efficiency parameter $D/L^{4/3} (\rho_\infty U_\infty^2)^{1/3}$. The efficiency parameter takes on this form because the flow fields which they use in fact restrict the angle of attack and aspect ratio of the wings to be of the same order of magnitude. It has the following numerical values:

n	$D/L^{4/3} (\rho_{\infty} U_{\infty}^2)^{1/3}$
0.50	1.16
0.65	1.25
0.75	1.29
1.0	1.38
1.5	1.65
3.0	2.37
6.0	3.60
10.0	5.26

It will be seen that the best value occurs when $n = 1/2$. The hypersonic small-disturbance theory is not considered valid for smaller value of n . It is interesting to note that for plane delta wings whose angle of attack is equal to their semi-apex angle this efficiency parameter is unity. If angle of attack is then held constant while aspect ratio varies, the parameter is proportional to (aspect ratio) $^{-1/3}$. In summary, it may be said that the Cole and Zien approach gives results of rather limited significance, but might well be capable of useful extension.

We turn now to a rather different application of the momentum approach. The basic idea is a familiar one in the context of propulsion aerodynamics. There the generation of thrust is often regarded from the viewpoint of momentum and pressure changes in the jet or slipstream. One works out the ideal flow process which the jet should undergo, and then considers the implications of this for, say, the shape of a nozzle. The generation of aerodynamic lift can be thought of in the same way. The lift and drag are associated with certain changes of velocity and direction in the nearby air, and it is equally valid to regard these as being caused by the presence of a lifting body, or to regard the lift and drag as caused by the changes in the flow.

If we take the latter view, we can ask what changes it would be desirable to bring about, and then determine how these are compatible with the design of a lifting shape. As a first step in this approach we shall consider the following problem. A streamtube forming part of the flow field of a waverider wing is to be associated with a given value of the lift function f_L . What flow process which provides this will minimise the drag function f_D ?

For simplicity we shall consider only the flow in a plane of symmetry ($y = 0$). Then we write the expressions for f_L and f_D

$$f_L = 2 \tan \theta \frac{v_z}{v_{\infty}} \quad (5.21)$$

$$f_D = 2 \tan \theta \left[1 - \frac{v_x}{v_{\infty}} - \frac{(p - p_{\infty})}{\rho v_{\infty} v_x} \right] \quad (5.22)$$

For the time being we consider the family of flow processes with a given value of the initial shock strength θ . We will suppose that the subsequent flow is isentropic, because it can be shown that in the contrary case the efficiency can only be lowered. Then the various quantities entering into the lift and drag functions are not all independent; we have in fact

$$p = p(v)$$

$$\rho = \rho(v)$$

and if we also write

$$v_x = v \cos \delta$$

$$v_z = v \sin \delta$$

we shall have

$$f_L(v, \delta) = 2 \tan \theta \frac{v \sin \delta}{v_{\infty}} \quad (5.23)$$

$$f_D(v, \delta) = 2 \tan \theta \left[1 - \frac{v \cos \delta}{v_{\infty}} - \frac{k(v)}{\cos \delta} \right] \quad (5.24)$$

where

$$k(v) = \frac{p - p_{\infty}}{\rho(v) v v_{\infty}} \quad (5.25)$$

Now by systematically varying the two quantities v and δ , we can generate the full range of possible pairs of values (f_L, f_D) . An example is shown in Figure 6 for the special case of flow from a free stream at Mach number 8.0 through a shockwave inclined at 25° . The general features of the diagram are similar for any other set of conditions (M_∞, θ) , in particular there always appears an envelope which bounds the curves from below. This envelope can be found analytically, for the condition to be satisfied on it is

$$\frac{\partial f_L}{\partial v} \frac{\partial f_D}{\partial \delta} - \frac{\partial f_L}{\partial \delta} \frac{\partial f_D}{\partial v} = 0$$

and this simplifies to

$$k(v) \tan^2 \delta = \frac{v}{v_\infty} + v \frac{dk}{dv} \quad (5.26)$$

It can be shown further¹ that this relationship is satisfied for all δ by a value v_0 of v such that $k(v_0) = 0$, i.e. $p = p_\infty$. The envelope curve is therefore given parametrically by

$$f_L = 2 \tan \theta \frac{v_0 \sin \delta}{v_\infty} \quad (5.27)$$

$$f_D = 2 \tan \theta \left[1 - \frac{v_0 \cos \delta}{v_\infty} \right] \quad (5.28)$$

The envelope can be seen to be a circle of radius $2 \tan \theta (v_0/v_\infty)$ with its centre at the point $(0, 2 \tan \theta)$.

Pausing to assess the results obtained so far we note that the ideal lifting process involves returning all the "captured" air to ambient pressure, which evidently cannot be accomplished by any orthodox lifting surface. (It is, interestingly, nearly accomplished by Basemann's biplane). The limit which we have placed on lifting efficiency is overoptimistic, because we have neglected a most important constraint on the values which v and δ can assume, namely that it must be possible to find them paired in a flow field which is physically possible, i.e. satisfies the equations of motion. To incorporate this constraint even within a restricted family of lifting surfaces, such as waveriders, would be a formidable task, considerably more difficult than anything so far achieved*, but perhaps not impossible. What our partial solution does demonstrate is the existence of a limit which cannot be passed, and from Figure 6 we observe that the closer we can bring v to its ideal value, v_0 , the closer the lifting efficiency will approach to this limit.

There is one further respect, however, in which the ideal flow process can be improved. So far we have studied the possible processes behind shockwaves of given strength. If now, at some constant free stream Mach number, we allow the shock strength to vary, we obtain a family of limit curves (Fig. 7(a)) which themselves have an envelope, which is worked out analytically in Reference 1. The interesting result is that points on this envelope at any non-zero value of f_L correspond to non-zero values of the initial shock strength.

This comes about because a wing of given planform area "captures" a greater mass flow if the shock system is steeper. This gives us reason to suppose that the finite shock system necessarily associated with non-slender lifting shapes is not wholly disadvantageous.

The actual lifting efficiencies achieved by the ideal processes are shown in Figure 7(b). The efficiency is measured by comparing the drag function of the ideal process with the drag function that arises when a similar lift function is obtained by means of simple deflection through a plane shockwave. In other words we are comparing the "lift-drag ratio" of the ideal process with the "lift-drag ratio" of a plane wedge. Symbolically

$$\begin{aligned} \eta &= \frac{(f_D)_{\text{plane shock}}}{(f_D)_{\text{ideal process}}} \quad (\text{at same } f_L) \\ &= \frac{(f_L/f_D)_{\text{i.p.}}}{(f_L/f_D)_{\text{p.s.}}} \\ &= \frac{(f_L/f_D)_{\text{i.p.}}}{(C_L/C_D)_{\text{wedge}}} \end{aligned}$$

*For an interesting discussion of an analogous, simple, but nevertheless taxing problem, the design of optimised supersonic nozzles, see the articles by Rao⁴ and Guderley and Armitage⁵. In that case, a "one-dimensional" treatment of the optimum flow process is remarkably successful, and leads to an accurate solution of the axisymmetric problem.

From Figure 7(b) we can see that this ratio is never greater than 2.0.

It has been demonstrated¹ that flow processes which come very close to achieving these limiting efficiencies are in fact found in certain circumstances. The example quoted there was the flow field generated at $M_\infty = 3.0$ by a particular ogival body of revolution, where at one point in the flow η was equal to 1.95 with $f_L = 0.020$.

In our subsequent work at RAE Bedford on waverider design we have tried to use these results to guide our choice of flow fields and surfaces. One thing that has emerged is the unwisdom of striving to achieve very high lifting efficiency over a relatively small part of the flow. It always seems to happen that the overall efficiency is thereby compromised. Thus, although there is a theoretical interest in knowing that the limits exist, their practical importance is that they give a general qualitative recipe for the efficient production of lift. They show that below the trailing edge of a lifting wing we should try to achieve a combination of small pressure coefficients with large vertical velocity components, and that we need not worry too much about creating shockwaves of finite strength, provided these are not excessively strong.

It is interesting to compare this recipe with what we know we want on the surface of the wing itself. There we would like to see large pressure coefficients, coupled with small surface inclinations, which imply small vertical velocity components, in fact precisely the opposite mixture. This illustrates the way in which the two approaches complement each other. At the present moment neither approach is capable of offering a complete design method, but an attempt to synthesize the two may well offer eventually the most complete understanding of supersonic wing design.

REFERENCES

1. Roe, P.L. *A momentum analysis of lifting surfaces in inviscid supersonic flow.* ARC R & M 3576. 1969.
2. Jones, J.G.
Woods, B.A. *The design of compression surfaces for high supersonic speeds using conical flow fields.* ARC R & M 3539. 1968.
3. Cole, J.D.
Zien, T.F. *A class of three-dimensional optimum hypersonic wings.* AIAA Journal Vol.7, No.2, p.264, February 1969.
4. Rao, G.V.R. *One-dimensional approach to optimum rocket nozzles.* In *Theory of Optimum Aerodynamic Shapes*. Edited by A. Miele. Academic Press. 1965.
5. Guderley, K.G.
Armitage, J.V. *General approach to optimum rocket nozzles.* In *Theory of Optimum Aerodynamic Shapes*. Edited by A. Miele. Academic Press. 1965.

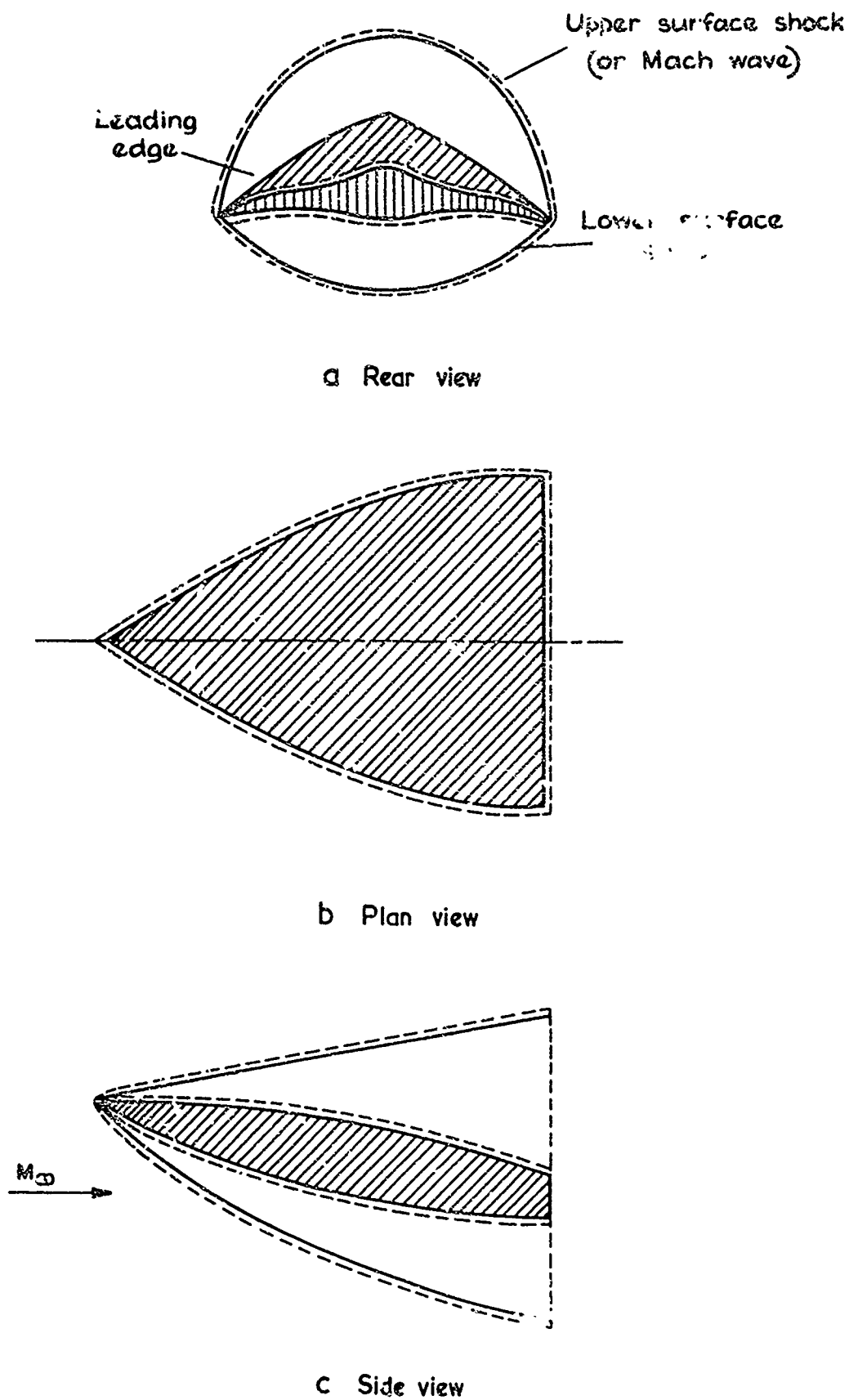


Fig. 1 Control volume for studying forces on a lifting shape

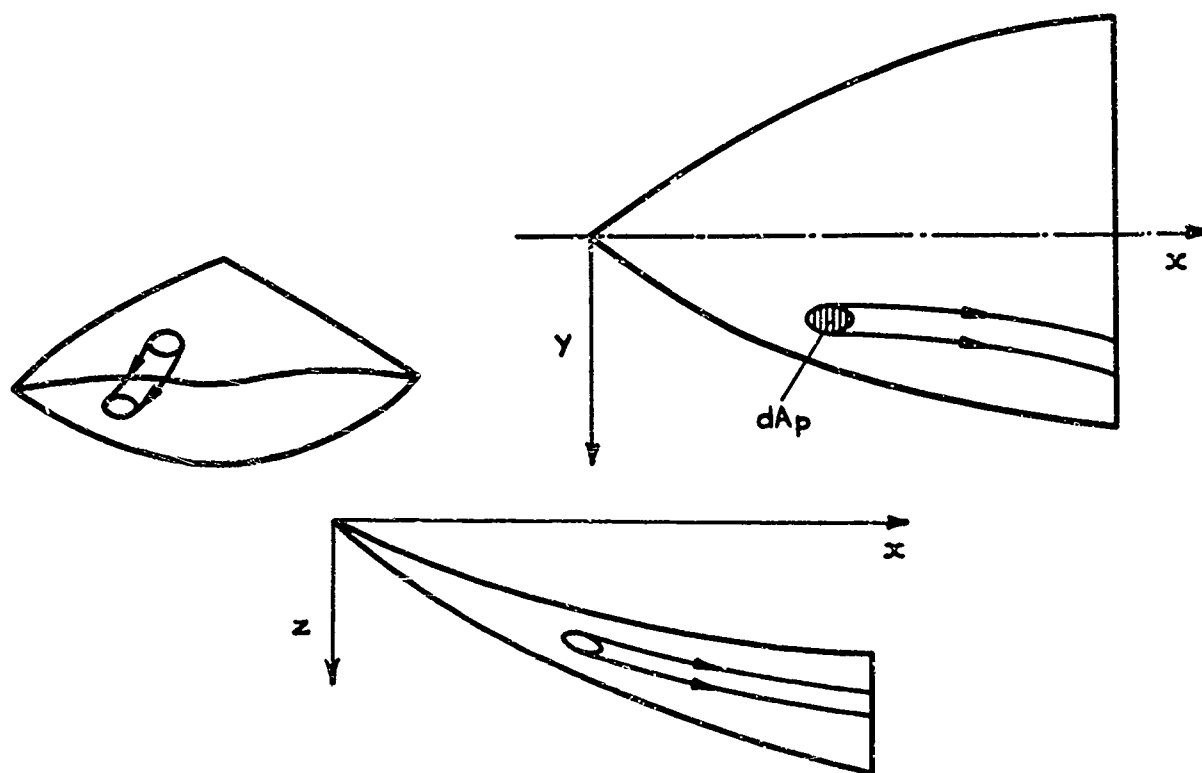


Fig.2 A streamtube passing through the lower surface control volume

$$C_L = \frac{1}{A_p} \iint f_L dA_p$$

$$C_D = \frac{1}{A_p} \iint f_D dA_p$$

where f_L, f_D are dimensionless lift and drag functions

$$f_L = \frac{2\ell}{n} \frac{v_z}{v_\infty}$$

$$f_D = \frac{2\ell}{n} \left[1 - \frac{v_x}{v_\infty} - \frac{p - p_\infty}{\rho v_x v_\infty} \right]$$

where $[\ell, m, n]$ are direction cosines of the shock surface at the entry point, p, ρ, v_x, v_z are flow properties at the exit point.

Fig.3 Definition of lift and drag functions

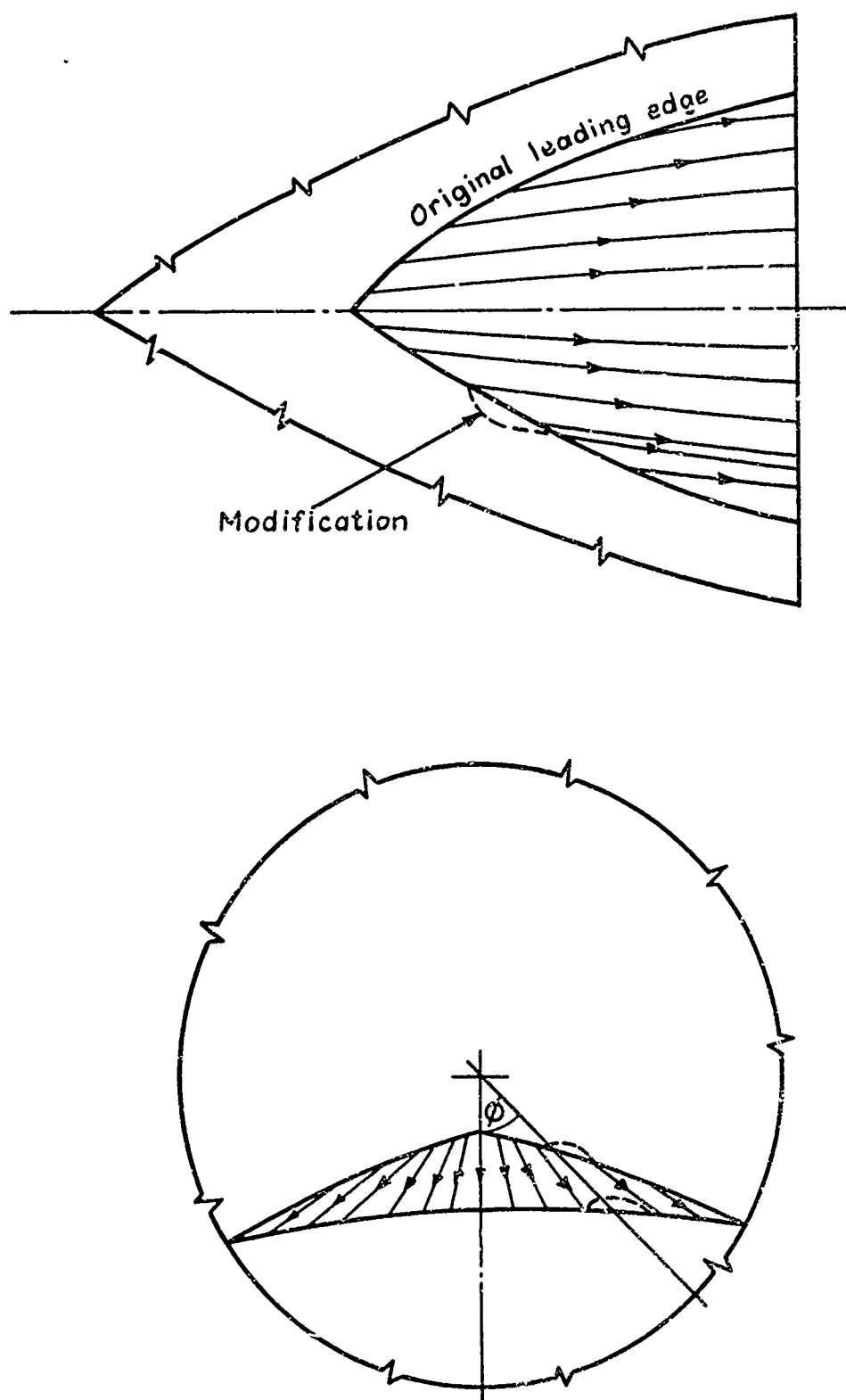


Fig.4 Choosing a streamsurface from an axisymmetric flow field

For an axisymmetric flow:-

$$f_L = 2 \tan \theta \frac{v_r}{v_\infty}$$

$$f_D = 2 \tan \theta \left[1 - \frac{v_x}{v_\infty} - \frac{p - p_\infty}{\rho v_x v_\infty} \right]$$

where θ is the shock inclination at the point of entry of the streamtube.

For flow without embedded shocks

$$p = p(\theta, v)$$

$$\rho = \rho(\theta, v)$$

If we write

$$\frac{v_r}{v_x} = \tan \delta$$

and

$$\frac{p - p_\infty}{\rho v v_\infty} = k(\theta, v)$$

then

$$f_L = 2 \tan \theta \frac{v \sin \delta}{v_\infty}$$

$$f_D = \frac{2 \tan \theta}{\cos \phi} \left[1 - \frac{v \cos \delta}{v_\infty} - \frac{k(v)}{\cos \delta} \right]$$

Now, in an axisymmetric flow v , δ and θ depend only on the x -coordinate of the entry point, and so

$$f_L(x, \phi) = f_L(x, 0) = f_L(x)$$

$$f_D(x, \phi) = \frac{f_D(x, 0)}{\cos \phi} = \frac{f_D^*(x)}{\cos \phi}$$

Inserting these in the formulae for C_L and C_D we can obtain

$$C_L = \frac{2}{A_p} \int_{LE}^{TE} y(x) f_L(x) dx$$

$$C_D = \frac{2}{A_p} \int_{LE}^{TE} r(x) \tan^{-1} \left(\frac{y(x)}{r(x)} \right) f_D^*(x) dx$$

Fig.5 Relationships in axisymmetric flow

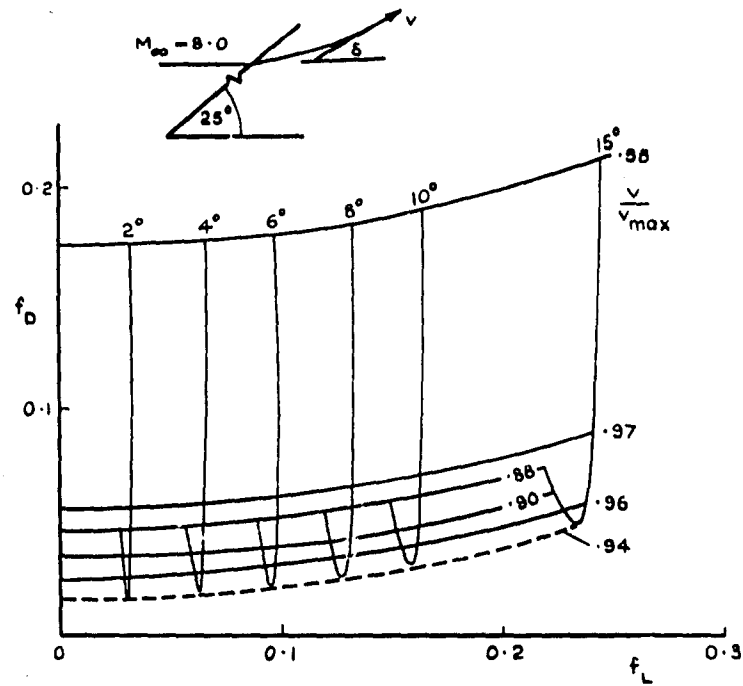


Fig.6 Lift and drag functions for arbitrary velocity and deflection behind a given shock wave

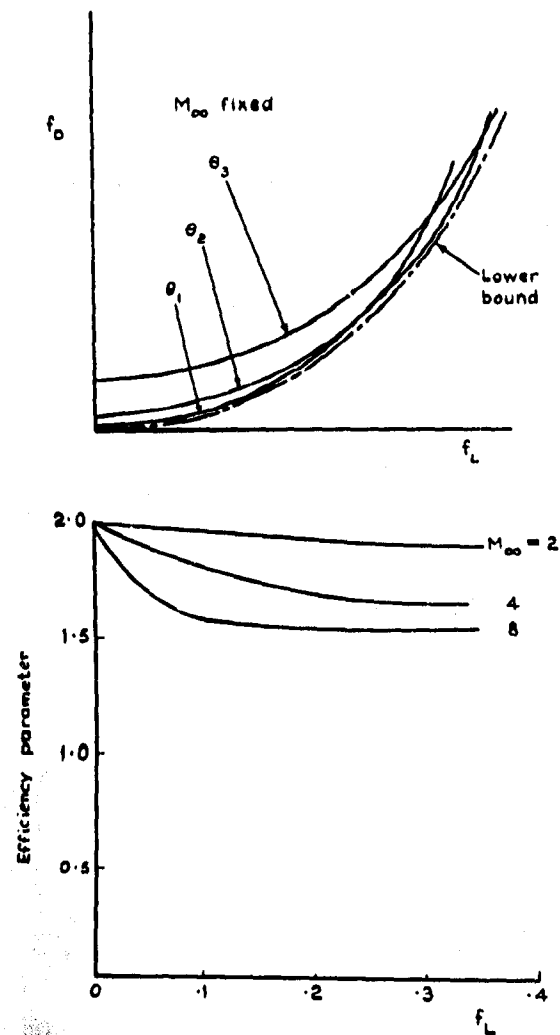


Fig.7 Lower bound to drag with given lift

LECTURE 6

FLOWS WITH HEAT ADDITION

P.L.Roe

Royal Aircraft Establishment, Bedford, England

It is always interesting to speculate about the simplest method of achieving some desired aim, the machine which accomplishes its end with the minimum of moving parts, for example. Sometimes we can see in principle how to arrange a very simple solution, but the practical difficulties defeat us, so that the idea has to be laid aside for a time, awaiting new techniques or new inspiration. The turbine-propelled motor car comes perhaps into this category.

It is with this philosophy in mind that I want now to examine the propulsion of hypersonic aircraft. We must begin by asking exactly what it is that we are trying to accomplish, and this in turn leads us to enquire into the fundamental nature of aerodynamic drag. An aircraft which is gliding without power loses energy at a rate equal to its drag times its velocity. This energy cannot disappear from the universe; it must be absorbed by the atmosphere, either as kinetic energy or as heat. Shock waves, wakes, and trailing vortices all contribute to the process.

Drag therefore involves the transfer of energy. Generally, it also involves the transfer of momentum. Suppose the aircraft to be gliding horizontally, and therefore decelerating. The horizontal momentum lost is transferred to the atmosphere. To convert this decelerating horizontal glide into sustained, steady, level flight, we must supply the atmosphere with a compensating source of momentum, usually the slipstream of a propeller, or the exhaust of a jet or rocket.

As far as the atmosphere is concerned, the rate at which it receives energy is probably increased by this new source of supply. Since the aircraft is in steady flight the atmosphere's energy is now being entirely supplied from the fuel, therefore the problem of efficient propulsion is basically that of supplying a given amount of momentum with the lowest expenditure of energy. If the propulsion unit provides some sort of jet or slipstream, it is easy to see that this means the jet should be as wide as possible.

Now to obtain a wide exhaust from a jet or rocket motor means a large nozzle, which would be heavy and subject to large friction losses. We look therefore for an unconventional solution, and in keeping with our ideas regarding simplicity, suppose that we can add heat directly to any part of the flow field we wish. To make our thinking a little more realistic, we can imagine that we do this by injecting fuel into the airflow upstream of the chosen point, and then somehow igniting it.

Very little is yet known about the feasibility of adding heat like this in a controlled manner. Before getting too involved in the practical difficulties, however, it seems sensible to answer the question, if we could do this, would it be worthwhile? Are the rather vague arguments in favour of the scheme really sound or are there limitations that we have not taken into account? I want to give an account of some of the theoretical difficulties to be overcome in a study of these problems.

Consider first a uniform stream of gas (Fig. 1) having velocity V_1 and static temperature T_1 . To this gas we add a quantity of heat q_{12} , in such a way that no external work is done, and as a result we suppose that the gas acquires velocity V_2 and static temperature T_2 . Conservation of energy states that

$$\frac{1}{2} (V_2^2 - V_1^2) + C_p (T_2 - T_1) = q_{12}, \quad (6.1)$$

which is to say that the heat may be received either as kinetic energy or as increased temperature. Conventionally, it is supposed that the kinetic energy is at least potentially useful, and that the temperature rise must be at least partially wasted, so that a thermal efficiency η_{th} is defined,

$$\eta_{th} = \frac{1}{2} (V_2^2 - V_1^2) / q_{12}. \quad (6.2)$$

If the process is one of producing a propulsive jet, so that $V_1 = V_\infty$, and $V_2 = V_j$, then this quantity measures the efficiency with which the heat supplied is converted into a usable jet. A second commonly used measure of efficiency compared the available propulsive work in the jet, $V_\infty(V_j - V_\infty)$, with the kinetic energy given up by the jet as it returns to free-stream conditions,

$$1/2 (V_j^2 - V_\infty^2)$$

Thus "jet efficiency", η_j , is given by

$$\eta_j = \frac{2}{1 + V_j/V} \quad (6.3)$$

The product of η_{th} and η_j is the propulsive efficiency (η_p), where

$$\eta_p = \frac{V_\infty (V_j - V_\infty)}{q} \quad (6.4)$$

In the assessment of conventional propulsion systems all these quantities are useful and significant. Their significance in the present context seems however, to be rather slight, and I shall show this by considering two extreme examples.

The first of these is shown in Figure 2, a flat-bottomed, two-dimensional "wing." Somewhere underneath this we suppose that heat is released across the station 1-2. This is the "burner disc" considered by Oswatitsch¹ and Küchemann². The effect of the disc is to produce a sudden large pressure rise. Behind it the heated air expands back towards the free-stream pressure, which we can suppose is more-or-less reached at station 3. After this, the jet will slowly return to free-stream temperature also, by a diffusive process. A schematic flow cycle for the process is shown in Figure 3.

The cycle seems to indicate that work is being done, and in a numerical example Küchemann² indicates that the thermodynamic efficiencies are quite high ($\eta_{th} = 0.37$ based on stations 1 and 3 and jet efficiency

$$\eta_j = \frac{V_1 (V_3 - V_1)}{\frac{1}{2} (V_3^2 - V_1^2)} = 0.92).$$

However, it is quite evident that no drag reduction is being achieved, because pressure changes are only being produced on streamwise surfaces. It is conceivable that small thrust forces are induced on the fuel injection system, but even these cannot occur if the fuel emerges, say, as a high speed jet which ignites as it breaks up.

Oswatitsch¹ resolves the paradox by noting that work is indeed being done, but only on the atmosphere. The work goes into the propagation of a wave system which is associated with the expansion of the heated jet (Fig. 2(b)).

A second example concerns the relief of base drag. A two-dimensional or axisymmetric blunt-based body in an unheated supersonic stream will usually experience flow like that shown in Figure 4(a), with a low velocity recirculating region behind it. The pressure in this region (p_b) is fairly uniform and quite small (often about equal to p_∞/M_∞) and the pressure difference ($p_\infty - p_b$), times the base area, is known as the base drag. Now experiments have shown³ that if fuel (hydrogen in the case of Reference 3) is injected into the boundary layer just upstream of the base, and ignited, a stable flow pattern can be produced which is of quite a different form. It does not in fact depart very far from the situation shown in Figure 4(b), with the pressure within the wake very nearly equal to p_∞ , and the external flow nearly parallel.

Since the flow is almost at constant pressure everywhere, a flow diagram on a pressure-volume chart would have almost no area, and it would appear that no useful work was available. Moreover, since the flow is almost at constant velocity, it appears η_p must be very small. However, it is quite clear that a useful result has been achieved; the base drag has been eliminated.

From these two examples, it is clear that the effectiveness of any external burning scheme can only be assessed by looking at the overall effect, and that it may be quite misleading to look at parts of the flow pattern in isolation.

I now want to consider some of the ways in which we might try to compute more general cases. Figures 5 and 6 show a pair of two-dimensional configurations that have been proposed by Küchemann² and Broadbent⁴. To evaluate such configurations it seems that a non-linear method is required because, to quote Oswatitsch¹ "Linearised formulae for this type of propulsion show that the field of application lies outside the linearisation region."

The configuration shown in Figure 5 consists of a wedge forebody, following which heat is added as a detonation wave⁵. The resulting high pressures are transmitted to a forward-facing afterbody surface, which provides the thrust. Some general remarks on this sort of configuration have been made by Oswatitsch⁶, Townend⁷ and Zierep⁸.

To determine just how effective such an arrangement might be it seems necessary at this stage to embark on the computation of some examples, aiming always to obtain insights into the principles involved and so improve the design. When this has been done, even if only for two-dimensional shapes, we should be better able to assess the promise of the concept.

Flows involving very sudden heat release can be computed using the properties of detonation waves⁵ plus standard methods (e.g. characteristics) for the unheated regions. I know of no generally available calculations on these lines, although work has been reported, by Townend⁹.

Flows with distributed heat release (which may be thought of as including the above case) have been investigated by Broadbent⁴, and since his method is rather novel it may be of interest to review it briefly here. We noted above that any useful investigation of flows with heat addition would have to employ the full, non-linear equations of motion. However, Broadbent has discovered a method of solving them which employs only linear algebra. This involves starting with an assumed pattern of streamlines, and asking what distribution of heat release would be compatible with them. For the purpose of building up a catalogue of solutions, and attempting to find their desirable properties, this approach is as valid as any other.

The streamlines, then, are assumed to be given, and distances along them are measured by a co-ordinate s . Distances along the orthogonals to the streamlines are measured by a co-ordinate n (see Figure 7). The width of a particular streamtube may be written as Δn , and generally will vary with s . The radius of curvature of a streamline is set equal to R . The state of the flow at any point is represented by pressure p , density ρ , velocity u , and enthalpy h . The heat addition per unit mass per unit time at any point is given by the quantity q .

Now the equations of motion in (s, n) co-ordinates are as follows:-

Continuity

$$\rho u \Delta n = C_1, \quad (6.5)$$

where C_1 is constant for any streamtube.

Momentum in flow direction

$$\rho u \frac{\partial u}{\partial s} = -\frac{\partial p}{\partial s}. \quad (6.6)$$

Momentum across flow direction

$$\frac{\rho u^2}{R} = -\frac{\partial p}{\partial n}. \quad (6.7)$$

Conservation of energy

$$u \frac{\partial}{\partial s} (h + \frac{1}{2}u^2) = q. \quad (6.8)$$

Now we can use (6.5) to substitute for (ρu) in eqns. (6.6) and (6.7), obtaining

$$\frac{\partial u}{\partial s} = \left(\frac{-\Delta n}{C_1} \right) \frac{\partial p}{\partial s} \quad (6.9)$$

$$u = \left(\frac{-R\Delta n}{C_1} \right) \frac{\partial p}{\partial n}. \quad (6.10)$$

If we assume that the streamline shapes are known, then the bracketed quantities are fixed, and Eqns (6.9) and (6.10) become a pair of linear differential equations for u and p . The system is hyperbolic with characteristics coinciding with the (s, n) co-ordinates, and can be solved easily if appropriate boundary conditions are given. Once u has been found, ρ can be got from Eqn. (6.2) and then finally q from Eqn (6.5). In this last step only it is necessary to assume some equation of state. The example shown later assumes a perfect gas with $\gamma = 1.4$.

Among the boundary value problems that can be solved is the one set out in Figure 8. Complete flow conditions are specified along one orthogonal, and the pressure alone is specified on one streamline. The solution then involves a straightforward marching process⁴. Broadbent has applied this to the solution of a class of lifting propulsive bodies, a typical member of which is shown in Figure 6. The body consists of a wedge-shaped nose AB, generating a plane shock AF. This shock wave is supposed to continue unweakened beyond F, implying the existence of a straight streamline FG, parallel to AB. This streamline is taken as one boundary of the "heating zone" BDGF. The curved portion of the body, BD, and the streamlines within BDGF are chosen to have simple analytic forms and the flow field then calculated as described above. A straight afterbody DE is drawn, along which the pressure decreases, and a straight upper surface AE. The point E is chosen to maximise the overall forward force, it is easy to see that the condition for this is that the pressure at E should be the same on both surfaces. (If the pressure is higher on the lower surface, the thrust can be increased by extending DE and accepting a more inclined upper surface).

A computed example is shown in Figure 9. Figure 9(a) shows the body shape and the temperature distribution in the heating zone. Figure 9(b) shows the "drag distribution" along the body. The abscissa for this figure is streamwise distance, x , and the ordinate is C_p times the tangent of the local surface inclination. The area between the curve and the x -axis is proportional to the streamwise force on the body. Results are shown for flows with and without heating. With heating the drag coefficient of the undersurface becomes very small, and the drag coefficient of the whole body (upper surface included) is 0.00204. This compares with a value of 0.00784 without heating.

The efficiency with which the added heat reduces the drag can be calculated from the formula

$$\eta = \frac{(D_u - D_h) \times U_\infty}{\dot{q}} \quad (6.11)$$

in which

D_u is the drag with unheated flow

D_h is the drag with heat flow

U_∞ is the flight speed

and

\dot{q} is the heat supply per unit time.

For the example shown η works out at 21.5%, which seems not too bad. However, the use of η as a criterion to assess the effectiveness of the scheme is open to some objections, and it is instructive to examine these

First, it would be preferable to compare the drag reduction to the fuel consumption rather than the heat release. In other words, to get a more realistic measure of the efficiency, we ought to multiply η as defined by the ratio (heat actually released)/(heat content of fuel released). However, this would require more knowledge of the likely combustion processes than we have at present.

Second, the heat release not only reduces the drag, but also greatly increases the lift acting on the body. This surely ought to appear on the credit side of any balance sheet, but it is not easy to see a simple "figure of merit" which accounts for it.

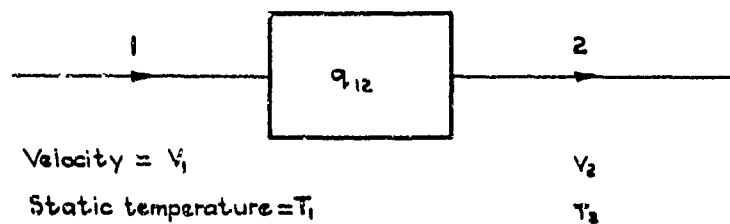
Third, although we note that the example given does not achieve complete drag cancellation (nor, indeed, do any of Broadbent's other numerical examples⁴) it is not clear whether this is really a disadvantage. We can imagine a hypersonic transport vehicle operating in something like a "boost-glide" trajectory, except that the glide phase might be power-assisted. That is, after an initial boost to high altitude and hypersonic velocity, there could be a flight phase involving incomplete drag cancellation, and therefore a gentle descent or deceleration. This could be not only acceptable, but might even be the most economical way of achieving a desired range. We may remark that the example in Figure 9 has, with heat on, a lift/drag ratio of just over 40.

This last paragraph brings out another aspect of the "integrated" nature of hypersonic aircraft. Not only is it impossible to consider the aerodynamic design of any component of the aircraft independently of the others, but at sufficiently high speeds it also becomes difficult to assess the economic efficiency of any part of the flight path by itself.

Having, I hope, said enough to convince you of the novelty and difficulty of some of the unsolved problems, I would not wish to end on too pessimistic a note. To put the problems of the innovator into some perspective, I would like to recommend to you Reference 10. In this, one of the pioneers of atomic energy imagines a situation in the remote future when the near-exhaustion of nuclear fuels prompts research into the long forgotten possibility of coal-fired power stations. Contemplation of the imaginary future researcher wrestling with what he supposes to be nearly insuperable difficulties may lead us to hope that many of the problems which are obscure today will appear laughably simple in times to come.

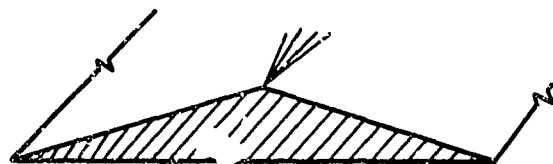
REFERENCES

1. Oswatitsch, K. *Autriebe mit Heizung bei Überschallgeschwindigkeit*. D.V.L.Bericht 90, 1959. Also in English, RAE Library Translation 811, 1959.
2. Küchemann, D. Hypersonic aircraft and their aerodynamic problems. *Progress in Aeronautical Sciences* Vol. 6, Pergamon Press, 1965.
3. Townend, L.H. *Some effects of stable combustion in wakes formed in a supersonic stream*. RAE T.N. Aero 2872, 1963.
4. Broadbent, E.G. Two-dimensional flows with heat addition, Pt. 1. Inviscid Flow. To be published in *Progress in Aeronautical Sciences*, Vol. 11.
5. Townend, L.H. *An analysis of normal and oblique detonation waves*. RAE TR 66081, 1966.
6. Oswatitsch, K. *Staub und Widerstand bei Warmezufuhr in Überschallströmung*. Acta Mechanica, Vol 3, 1966, p.1. Also in English, RAE Library Translation 811, 1967.
7. Townend, L.H. *Ramjet propulsion for hypersonic aircraft*. RAE TM Aero 917, 1966, presented to Euromech 3 at Aachen, February, 1966.
8. Zierep, J. *Über den Einfluss der Warmezufuhr bei Hyperschallströmung*. Acta Mechanica, Vol.2, 1966, p.2. Also in English, RAE Library Translation 1222, 1967.
9. Townend, L.H. *Detonation ramjets for hypersonic aircraft*. RAE TR 70218. 1970.
10. Frisch, O.R. On the feasibility of coal-driven power stations, in *The Expert Dreamers*, ed. Pohl, Victor Gollancz, 1962.

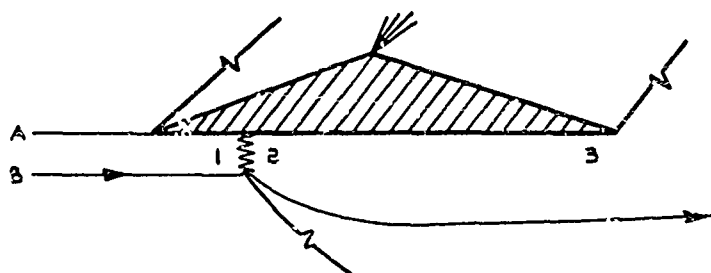


$$\frac{1}{2} (V_2^2 - V_1^2) + Cq_p (T_2 - T_1) = q_{12}$$

Fig.1 Effect of heat release



a No heat release



b Heat release

Fig.2 Simple wing with and without heat release

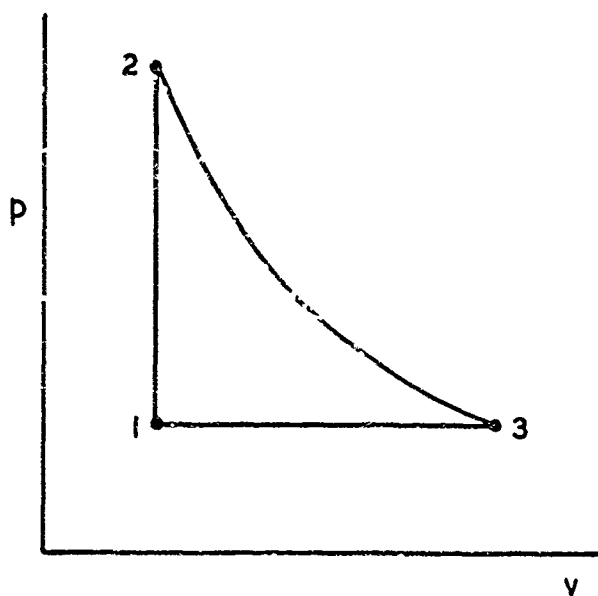
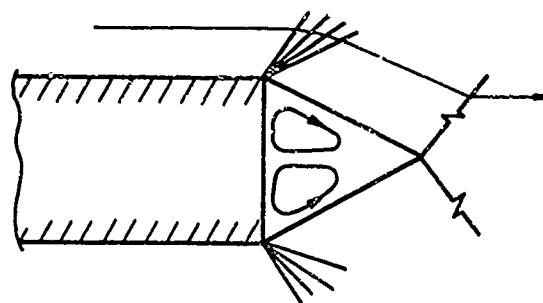


Fig.3 Schematic flow cycle for Fig. 2(b)



a No heat release

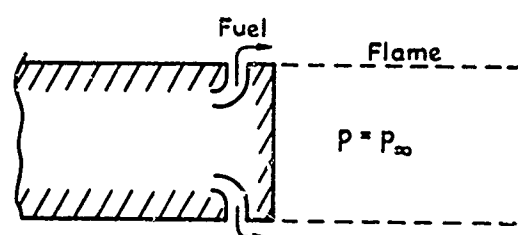


Fig.4 Base flow with and without heat release

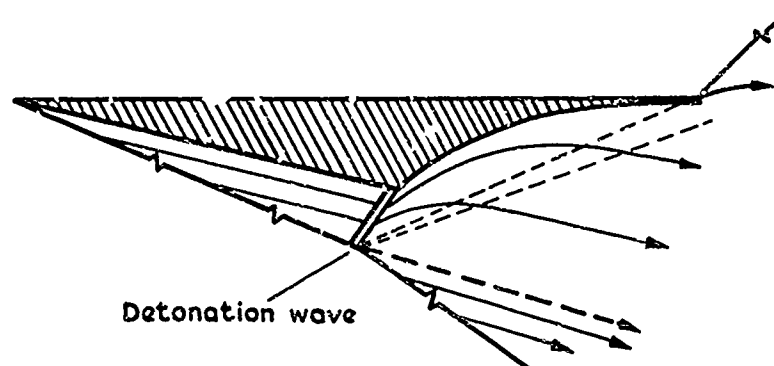


Fig.5 Lifting propulsive body (after Küchemann)

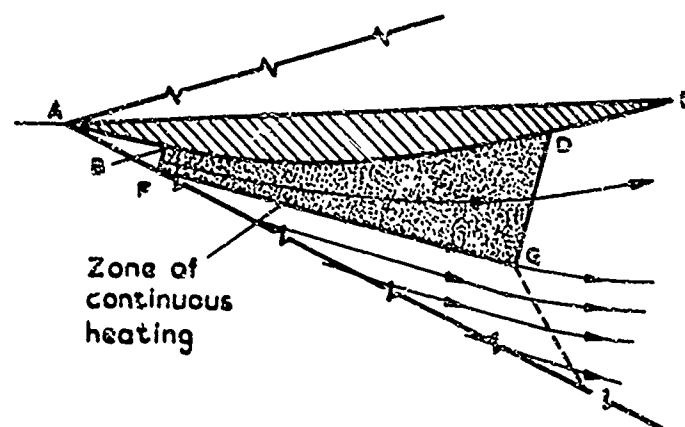
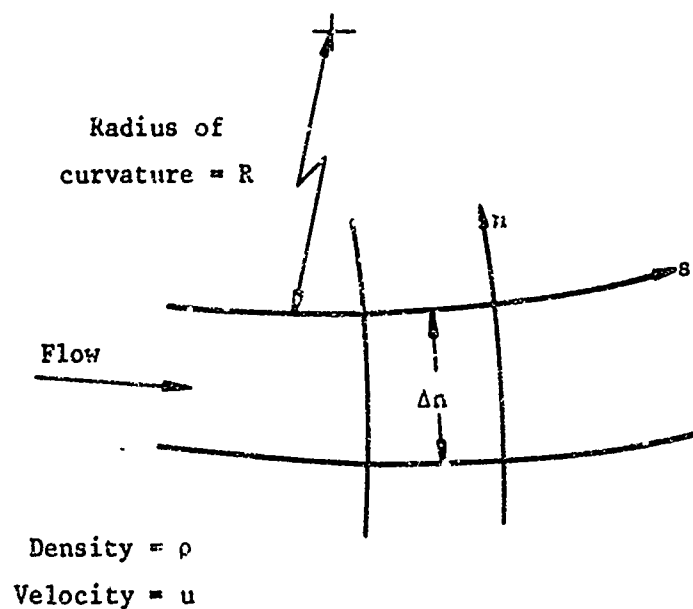


Fig.6 Lifting propulsive body (after Broadbent)



Continuity

$$\rho U \Delta n = \text{const.} = C_1 \text{ (say) } .$$

s-momentum

$$\rho u \frac{\partial u}{\partial s} = - \frac{\partial p}{\partial s} .$$

n-momentum

$$\frac{\rho u^2}{R} = - \frac{\partial p}{\partial n} .$$

Energy

$$u \frac{\partial}{\partial s} (h + \frac{1}{2} u^2) = q .$$

Fig.7 Equations of motion in natural coordinates

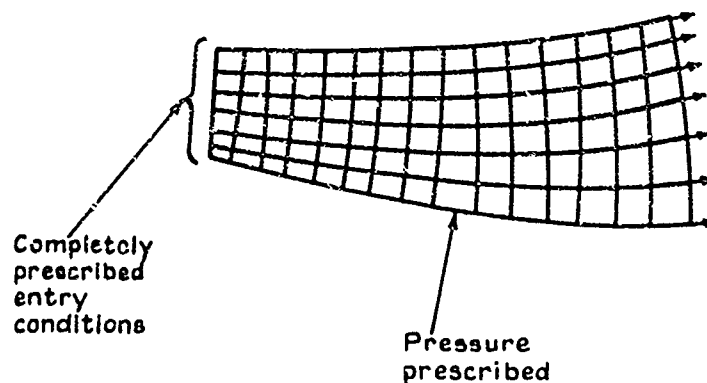
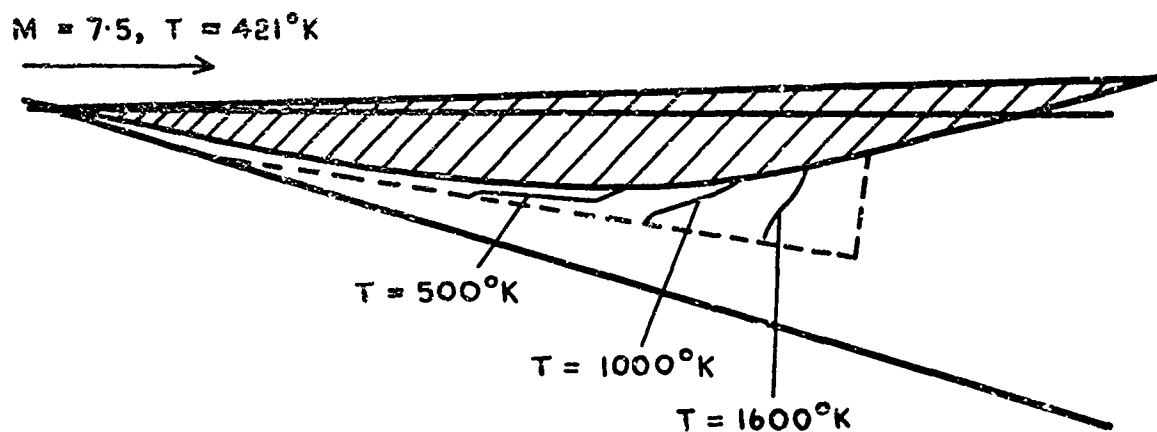
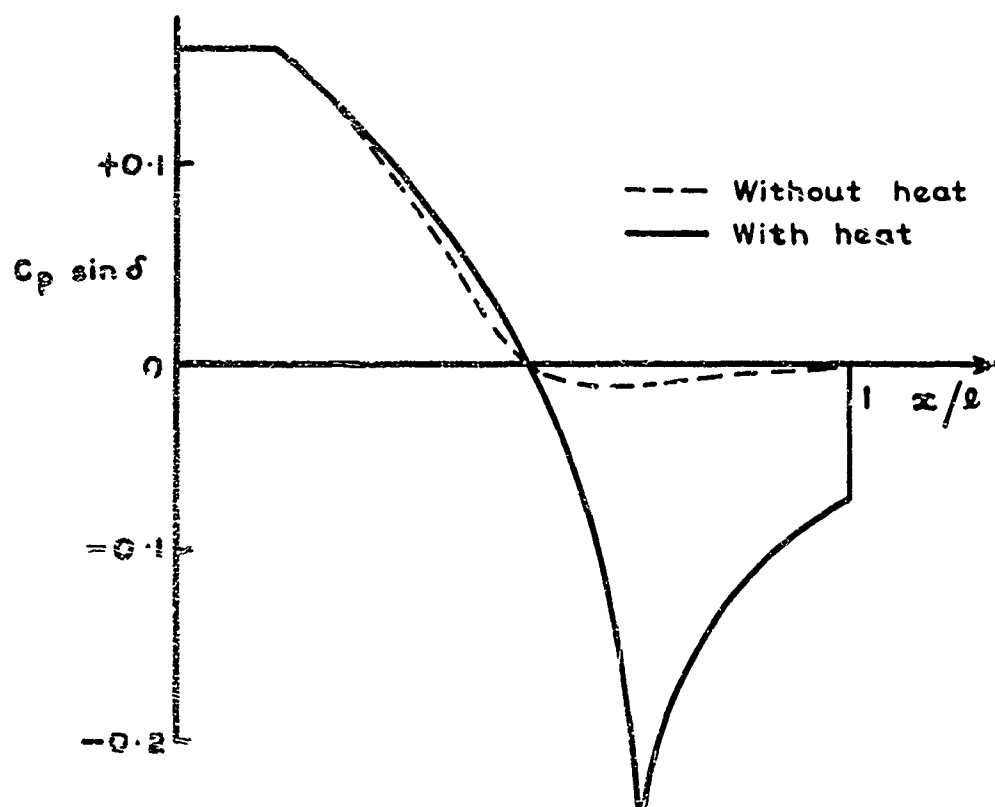


Fig.8 Example of sufficient boundary conditions



a Temperature distribution



b Drag distribution

Without heat $C_D = .00784$

With heat $C_D = .00204$

$$\eta_p = \frac{(\text{Drag reduction}) \times U_\infty}{\text{Heat supplied in unit time}}$$

$= 21.5\%$

Fig.9 Typical results

APPENDIX

Since the original lecture material was written, a number of new relevant papers have been published. Some of these are listed below, with brief comments. Also included are a few older papers that have only recently come to the author's attention.

LECTURE 2

Optimum Shapes

This chapter opened with a discussion of the general prediction problem for supersonic wings. A great deal of progress has taken place recently in this field, and the following papers describe methods based on the full equations of inviscid flow, the situation with regard to optimisation studies based on such methods is still, however, much as described.

- G.P.Voskresenkin *Numerical Solution of the Problem of a Supersonic Gas Flow Past an Arbitrary Surface of a Delta Wing.* Mekh. Zhid. i Gaza, Vol.4, 1968, p.134.
- J.South
E.B.Klunker *Methods for Calculating Non-Linear Supersonic Flows.* NASA SP 228, 1969.
- P.Kutler
H.Lomax *The Completion of Supersonic Flow Fields about Wing Body Combinations by "Shock-Capturing" Finite Difference Techniques.* To be published in Lect-Notes Physics.

At the end of the chapter an account was given of work by Maikapar based on Newtonian theory, a considerably extended account of this is available as

- G.I.Maikapar *Wing Shape Selection for Hypersonic Speeds* Mekh. Zhid. i Gaza, Vol.2, 1967, p.25, available in translation journal "Fluid Dynamics", Pergamon.

It was noted in the text that according to Newtonian theory the optimum wing under various constraints is a flat plate. However, under just those conditions where Newtonian theory is usually supposed to be most accurate, i.e. very high incidence and Mach number, this conclusion does not hold. Wings with concave undersurfaces, which cannot be adequately handled by Newtonian theory, generate more lift than flat wings. This result, which has important implications for re-entry flight, was first pointed out by

- L.H.Townend *Some Design Aspects of Space Shuttle Orbiters* RAE TR 71054, 1971.

A detailed theoretical and experimental investigation of this idea will be published in a paper L.Davies, et al to be given at the 10th AIAA Meeting, San Diego, February 1972.

LECTURE 3

An extension of the known flow fields design technique to generate a class of lifting wing body combinations has been described in

- J.Pike *Wing-Body Shapes from Known Flow Fields* RAE TR 20235, December 1970.

A method for calculating the off-design performance of caret wings in certain circumstances is given in

- J.Pike *The Flow Past Flat and Anhedral Delta Wings with Attached Shockwaves* RAE TR 71081, April 1971.

The latest developments in designing waveriders for high cruise efficiency are described in

- J.Pike *Lifting Configurations for High Supersonic Speeds from Axisymmetric Non-Homentropic Flow Field.* RAE TM Aero 1247, August 1970

LECTURE 4

Thin-Shock-Layer Theory

The streamline-pattern approach described in this chapter has been used to find a solution for flat delta wings.

F.L. Ree *A Simple Treatment of the Attached Shock Layer on a Plane Delta Wing.* RAE TR 70246, December 1970.

An application of the theory to designing optimum re-entry shapes is described in the paper by Davies, et al. mentioned in the notes to Lecture 3.

The extension of the theory to yawed wings is given in

R. Hillier *The Effects of Yaw on Conical Wings at High Supersonic Speeds.* Aero Quarterly, XXI, August 1970.

The study of non-conical wings has been commenced in Hilliers Ph-D thesis (Cambridge University Engineering Dept, 1970).

LECTURE 6

Flows with Heat Addition

Broadbent has continued his study by indirect means of desirable modes of heat addition to an external flow. His latest calculations, which show the effect of partial ducting, with a first attempt at designing suitable "intake" and "nozzle" processes are contained in

E.G. Broadbent *Flowfield Calculations for Some Supersonic Sections with Ducted Heat Addition.* RAE TR 71120, June 1971.

LECTURE 7

SPECIAL TOPICS IN HYPERSONIC FLOW

Richard D. Neumann

Technical Manager for Aerothermodynamics
 Gasdynamics Branch
 Flight Mechanics Division
 Air Force Flight Dynamics Laboratory

SECTION I - INTRODUCTION

This section sets out the basic relations relating to flight performance and aerodynamic heating of entry glide vehicles.

I-1 CONFIGURATION TRAJECTORY

The equations of motion for atmospheric flight are

$$D - W \sin \gamma = -\frac{W}{g} \frac{dV_\infty}{dt}$$

$$L + \left[\frac{W}{g} \frac{V_\infty^2}{R_e} - W \right] \cos \gamma = -\frac{W}{g} V_\infty \frac{d\gamma}{dt}$$

For gradual descent we assume:

$$\sin \gamma \ll 1 \quad \frac{d\gamma}{dt} = 0$$

$$\cos \gamma \cong 1 \quad \sin \gamma \ll \frac{1}{g} \frac{dV_\infty}{dt}$$

reducing the equations to the following

$$\frac{C_D A}{2W} \rho_\infty V_\infty^2 = -\frac{dV_\infty}{g dt}$$

$$\frac{C_L A}{2W} \rho_\infty V_\infty^2 = 1 - \frac{V_\infty^2}{V_c^2}$$

The equation for C_L is essentially that given by Sanger. This equation relates free-stream density to velocity, lift coefficient and wing loading. From this equation we can evaluate the equilibrium flight performance of entry glide vehicles.

I-2 VEHICLE CHARACTERISTICS

From Newtonian theory we can define the aerodynamics of an arbitrary lifting configuration.

$$C_L = C_{L0} \sin^2 \alpha \cos \alpha$$

$$C_D = C_{D0} + C_{DL} \sin^3 \alpha.$$

We will assume for the present discussion that $C_{L0} = C_{Pmax} = 1.83$ and $C_{DL} = C_{L0} = 1.83$.

Figure I-1 indicates the performance characteristics for a series of configurations having variable L/D capabilities.

Differentiation of the equation for C_L yields the max C_L given as

$$C_{Lmax} \cong 0.7 \quad \text{at} \quad \alpha \cong 55^\circ$$

and in general $L/D \cong \cot \alpha$ as shown in Figure I-1.

The maximum lift to drag ratio performance is primarily determined by C_{D0} - that is by the degree of bluntness and Reynolds number at which the vehicle operates

$$[L/D]_{max} = 0.65/C_{D0}^{0.33}.$$

Thus it can be seen that increasing the $(L/D)_{max}$ of a vehicle requires that one minimize C_{D0} which, in turn, is related to the configuration variables and operating attitude. The angle of attack for maximum L/D is given as

$$[\alpha]_{L/Dmax} \cong C_{D0}^{0.33}.$$

I-3 AERODYNAMIC HEATING

The configuration aerodynamic heating rates are also directly related to the trajectory flown, the configuration attitude, and geometric features.

As a first example, let us consider the stagnation point where for a laminar boundary layer, the convective heating rate may be written as:

$$q \propto \sqrt{\rho_\infty/D} V_\infty^3.$$

Employing the trajectory equation previously discussed this becomes

$$q \propto \frac{[1 - (V_\infty/V_c)^2]^{0.5}}{\sqrt{D} V_\infty} \left(\frac{2W}{C_L A} \right)^{0.5} V_\infty^3.$$

Thus it can be seen that the glide parameter (W/C_{LA}) which includes both wing loading and vehicle attitude through the lift coefficient, C_L , modifies stagnation point heating. Operation at C_{Lmax} clearly minimizes stagnation point heating. Further, the velocity term $[1 - (V_\infty/V_c)^2]^{0.5} V_\infty^2$ determines the velocity for peak stagnation point laminar heating.

This velocity, obtained through differentiation of velocity dependent terms is at $V_\infty = 21,000$ ft/sec for maximum stagnation point heating. This velocity is helpful as a representative point for design heating calculations employing radiation equilibrium structures where peak heating rates are important rather than the total integrated heat load and within the assumption of an equilibrium glide trajectory.

To the extent that other laminar heating points are related to the stagnation point, the stagnation point derived velocity for peak heating will be employed for all other laminar heating calculations.

Turbulent heating presents another velocity where peak heating will occur. In turbulent flow

$$q \propto \rho_\infty^{0.8} V_\infty^3$$

yielding a velocity of 17,700 ft/sec for peak turbulent heating (assuming transition has previously occurred).

I-4 THE FLIGHT ENVELOPE

Before we go further into heating prediction methods it would appear of some interest to discuss the generation of flight envelopes and maneuver corridors as outlined by Yoler in his review of Dyna Soar technology¹.

In Figure I-2 we see a typical flight envelope for a boosted lifting entry system. The accessible flight corridor is bounded below the trajectories by heating and load placards and above by recovery ceilings. The heating and load placards are important at different times during the entry and the practical design limit is an envelope of all such placards. Design margins between the placards and the design limit account for uncertainties in aerodynamic coefficients, heating rates, surface emittance, winds, materials allowables, etc...

The design limit line shown in Figure I-2 is not a unique function of velocity alone but for a given velocity is also a function of the vehicle angle of attack. Figure I-3 indicates the variation of temperature placards with angle of attack indicating the severity of the upper surface heating at low but positive angles of attack. Also noted in Figure I-3 is a positive maneuver margin throughout the angle of attack spectrum between the equilibrium trajectory and the configurational design limits. Such a margin is necessary in order to assure that the aircraft successfully recovers from nonequilibrium initial conditions which might arise during boost and/or re-entry.

SECTION I -- REFERENCE

1. Yoler, Y. *Dyna-Soar - A Review of Technology*. Aerospace Engineering, August 1961.

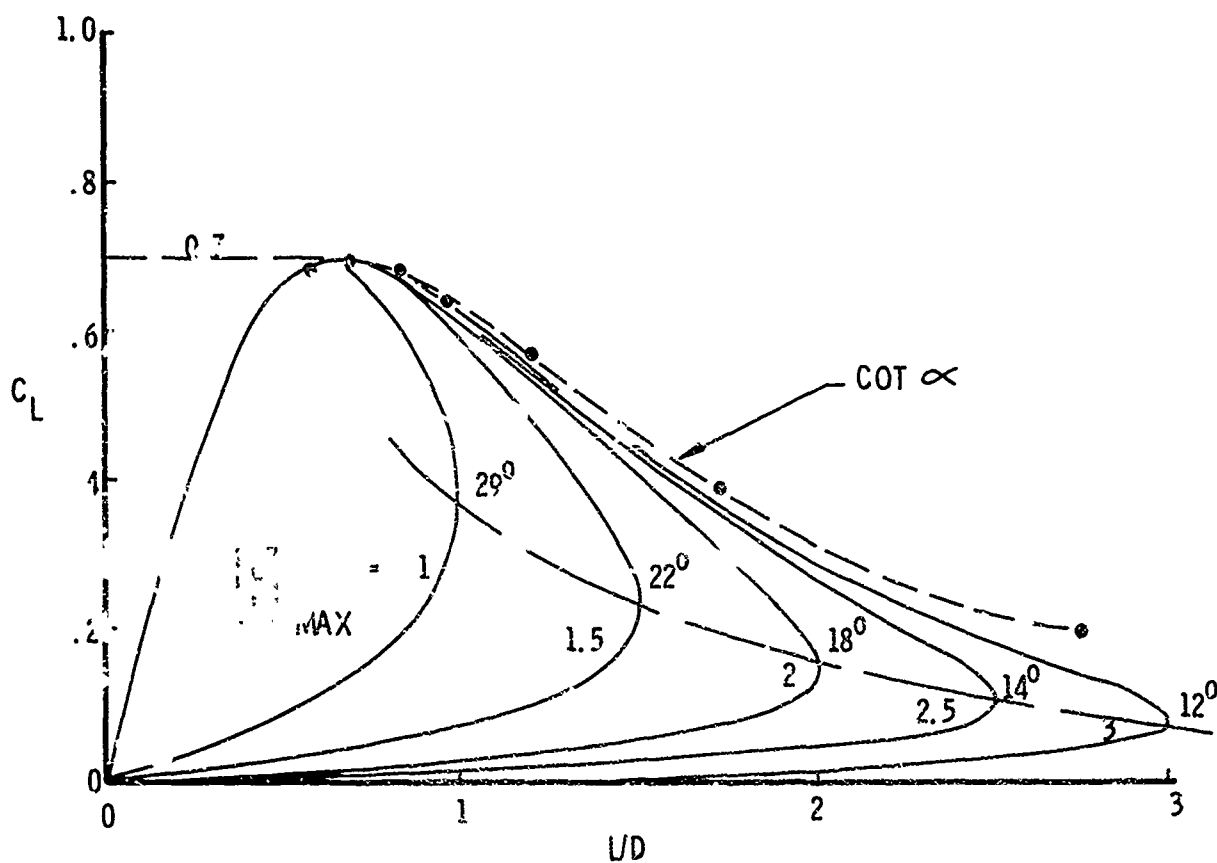


Fig.1-1 Map of aerodynamic performance for lifting entry gliders

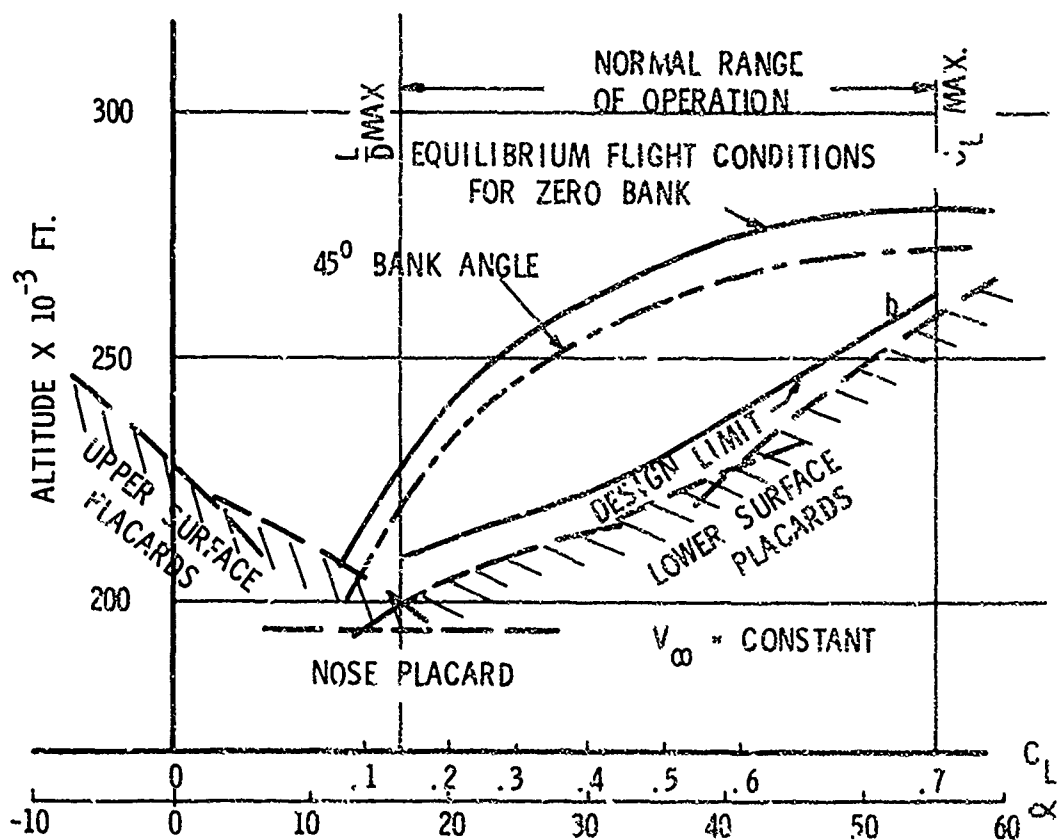


Fig.1-2 Typical maneuver corridor for lifting entry

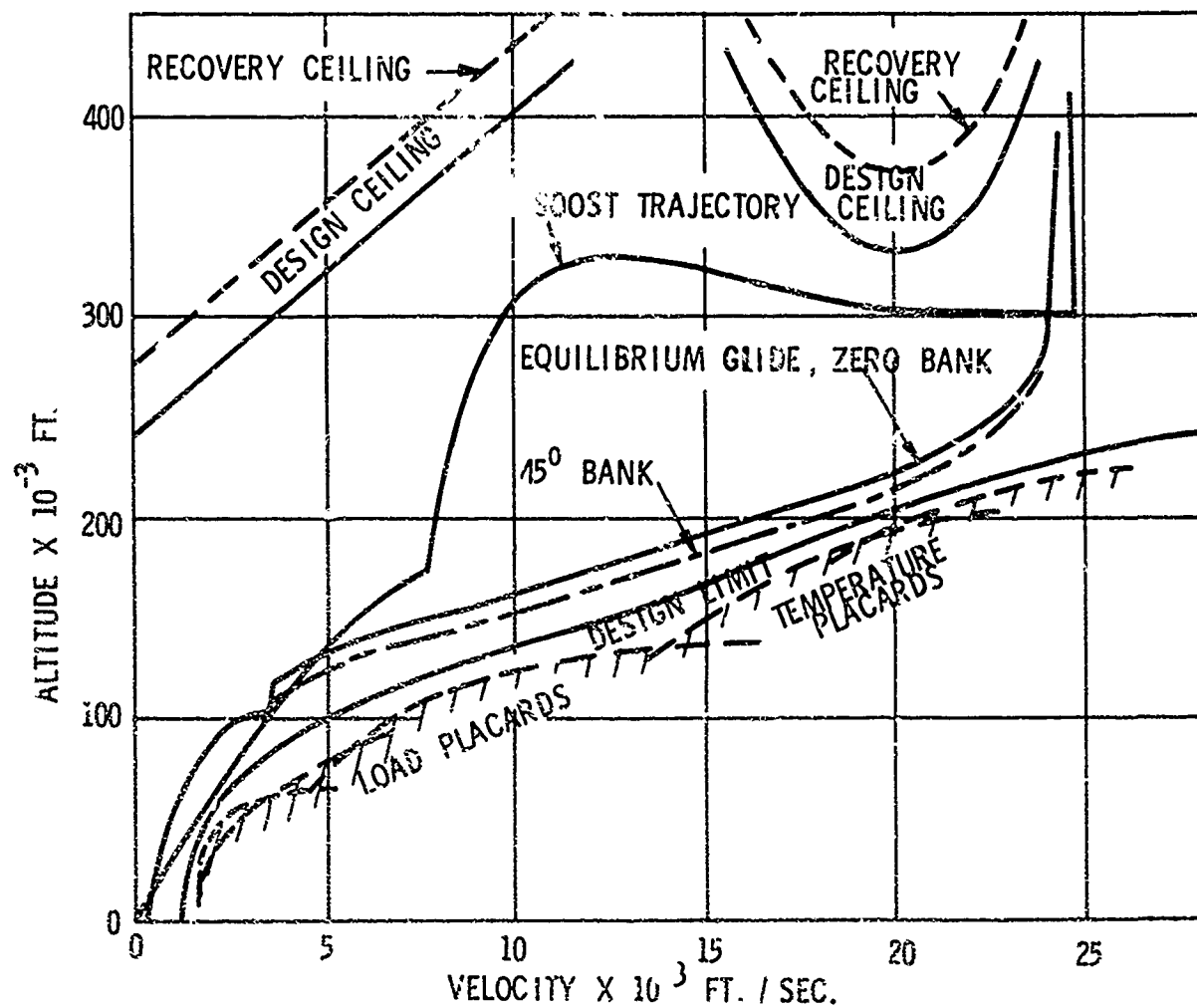


Fig.1-3 Typical flight envelope, for lifting entry

SECTION II - SURFACE PHENOMENA

Many of the aerodynamic heating problems encountered by practical re-entry vehicles are not representable by small scale wind tunnel models employing idealized and smooth loft line surface contours. It is important that due consideration be given to effects of surface condition and manufacturing irregularities early in the configuration formulation so that the research aerodynamicist and the manufacturer may resolve critical problems to the airframe. This section of the course will discuss several examples of such hardware oriented problems uncovered over the past decade of hypersonic design. The following examples will be discussed.

1. Aerodynamic bleed of the boundary-layer air through the configuration.
2. Surface distortion of the heat shield and its effect on aerodynamic heating, and
3. Surface boundary-layer distortion due to bleed flow.

II-1 BLEED FLOW AROUND CONTROL SURFACES

It is extremely difficult, if not impossible, to completely seal the gap between aerodynamic control surfaces and the configuration. The resultant bleed of high energy airflow between adjacent control surfaces may cause critical heat shield design problems not entirely because of the high heating rates but also because of the lack of radiation relief of the surfaces caused by very low radiation view factors between adjacent surfaces.

Design relief from such situations may require an adjustment in the aerodynamic contours to assure radiation relief and, as well, structural re-adjustment within the aerodynamic surfaces to allow the heat to radiate to cooler parts of the surface. Figure II-1 indicates such changes to a typical elevon gap region; the recommended changes did, in fact, significantly reduce the thermal placard altitude. It must be pointed out however that such changes to aerodynamic shape have important consequences both to the aerodynamic performance and structural design of the configuration. In the case of the elevon gap, allowing contour changes to assure aerothermodynamic integrity did significantly degrade the low speed performance of the configuration noted as a moment shift in Figure II-1.

Perhaps the most complete evaluation of bleed flow in gap regions about control surfaces was reported by Stern and Rowe¹. Stern's model shown in Figure II-2 allowed one to vary the gap from 0.05 to 0.35 in. 0.10 inch increments. He concluded that although some aerodynamic benefits did occur from bleed flow - e.g. retarding boundary-layer separation, and reducing the probability of boundary-layer transition - the aerodynamic heating problem was significant and self aggravating for ablating surfaces. Later work on gap effects in connection with deflected control surfaces has been conducted at NASA Langley and reported in References 2 and 3.

A dramatic example of the effects of aerodynamic bleed is to be found in an analysis of the recovered ASSET configuration. Figure II-3 indicates a gap region near the wing apex at the juncture of the leading edge, nose skirt and lower surface heat shield. This gap caused an internal bleed of high energy airflow through the interior of the aircraft along the bulkhead as shown in Figure II-4, expelling the flow on the upper surface shown in Figure II-5. The result fortunately caused no structural damage and was rectified by installing a heat barrier in subsequent flights.

Similar bleed phenomena were found during the X-15 flight program⁴ in which severe air leakage into the nose wheel compartment caused an aluminum tubing within the well to melt and other equipment to be damaged. In an earlier article⁵ leading-edge skin buckling was reported (see Figure II-6) to be caused by entrapped flow in the leading-edge expansion joints. The fix, also shown in Figure II-6, was a tab over the expansion joint to minimize the heat flow.

II-2 SURFACE DISTORTION

Surface distortion during re-entry is caused by any of a series of imposed phenomena. Manufacturing requirements, load deformations and thermal expansion effects are but a few causes. As a result of the Dyna Soar experience Jaeger⁶ presented data and theory on a series of basic configurations and covering a series of related surface irregularities. While the tests and results are not amenable to a generalized presentation, the following observations can be made.

1. Relatively small surface irregularities (with regard to the local boundary-layer thickness) can cause relatively large increases in heating. The heating increases are much greater than the corresponding pressure increases.
2. Roughness of the type evaluated (shallow waves) can in general be classed in relation to the local boundary-layer thickness. Those small in relation to the boundary-layer thickness are insensitive to external flow effects and the heating is caused by the protrusion of the wave into the higher energy portion of the boundary layer. Large scale roughness on the other hand should correlate with the measured pressure data.

3. Correlation of available data for shallow waves against the boundary-layer displacement thickness implies strongly that this parameter is of primary interest in design. Further, it indicates that regions near the configuration nose where the boundary layer is thin and the basic heating is highest are susceptible to the highest increments of roughness induced heating. It also implies that real gas effects on boundary-layer thickness are of importance as are three-dimensional effects.
4. For the rather specialized case of a shallow wave as bump above the mold line, correlation theory has been presented by Bertram et al.⁷ for both laminar and turbulent boundary-layer flow in terms of the ratio of roughness height, H , to smooth body displacement thickness, δ^* . Figure II-7 lists these correlation equations. Figure II-8 employs both the theory of Bertram and that of Jaeck⁴ (as presented for design purposes by Thomas) to indicate the relative height of a surface irregularity to cause a 20% increase in smooth body heating. Finally, Figure II-9 indicates the correlation of multiple wave data with the respective approaches.

II-3 LEAKAGE EFFECTS DOWNSTREAM OF A GAP

Downstream of a mold line gap the aerodynamic heating to the heat shield is augmented due to a thinning of the boundary layer. An empirical correlation of this heating increase was generated with the aid of a Nonsimilar Boundary-Layer Computer Program described in Appendix C of Reference 6. The resultant correlation curve for these computer generated data is shown in Figure II-10.

SECTION II - REFERENCES

1. Stern, Rowe, *Effects of Gap Size on Pressure and Heating Over a Flap of a Blunt Delta Wing in Hypersonic Flow* Journal of Spacecraft and Rockets (AIAA), January 1967, pp.109-114.
2. Hamilton, H. Dearing, J. *Effect of Hinge-Line Bleed on Heat Transfer and Pressure Distributions Over a Wedge-Flap Combination at Mach 10.4* NASA TN D 4686.
3. Dearing, J. Hamilton, H. *Heat Transfer and Pressure Distributions Inside the Hinge-Line Gap of a Wedge-Flap Combination at Mach 10.4* NASA TN D 4911.
4. Toll, T.A. Fischel, J. *The X-15 Project - Results and New Research* Astronautics and Aeronautics, March 1964, pp.29-28.
5. Row, P.V. Fischel, J. *The X-15 Flight Test Experience* Astronautics and Aeronautics, June 1963, pp.25-32.
6. Jaeck, C.L. *Analysis of Pressure and Heat Transfer Tests on Surface Roughness Elements with Laminar and Turbulent Boundary Layers* NASA CR 537, August 1966.
7. Bertram, M. et al *Effect of Two-Dimensional Multiple-Wave Distortions on the Heat Transfer to a Wall in Hypersonic Flow* AIAA Journal, October 1967.
8. Bertram, M. Wiggs, M. *Effect of Surface Distortions of Heat Transfer to a Wing at Hypersonic Speed* AIAA Journal, Vol.1, No.6, June 1963.

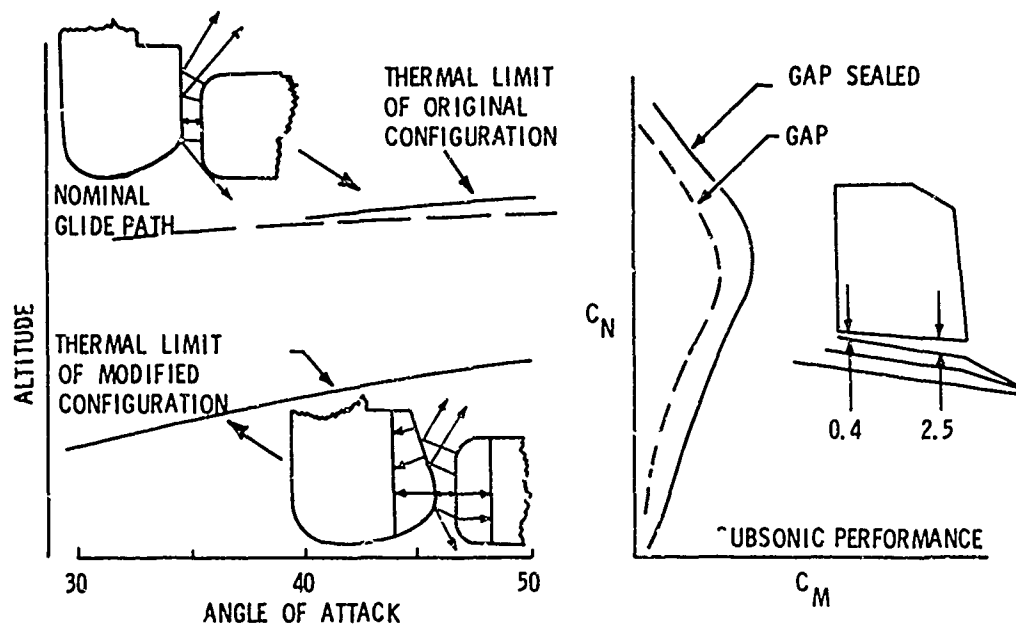


Fig.II-1 Relationship of aerothermodynamic and aerodynamic problems

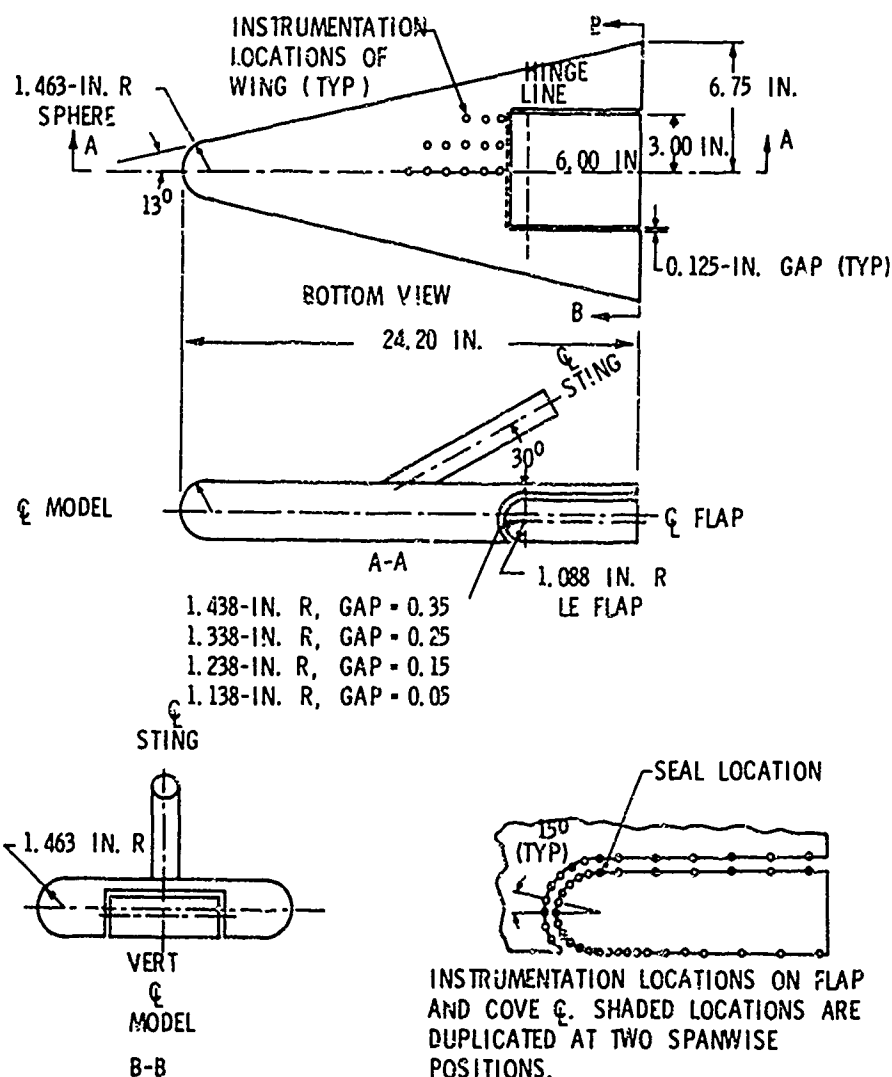


Fig.II-2 Model geometry for Stern's experiment

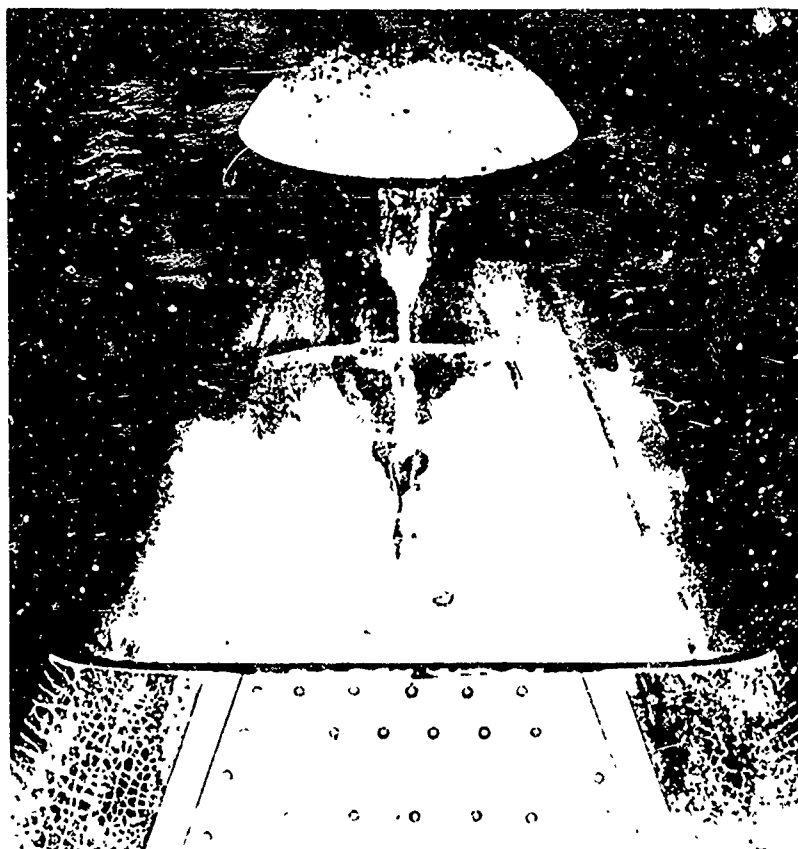


Fig. II-3 Recovered ASSI-T vehicle - gap near wing apex at juncture of leading edge nose skirt and lower surface heat shield

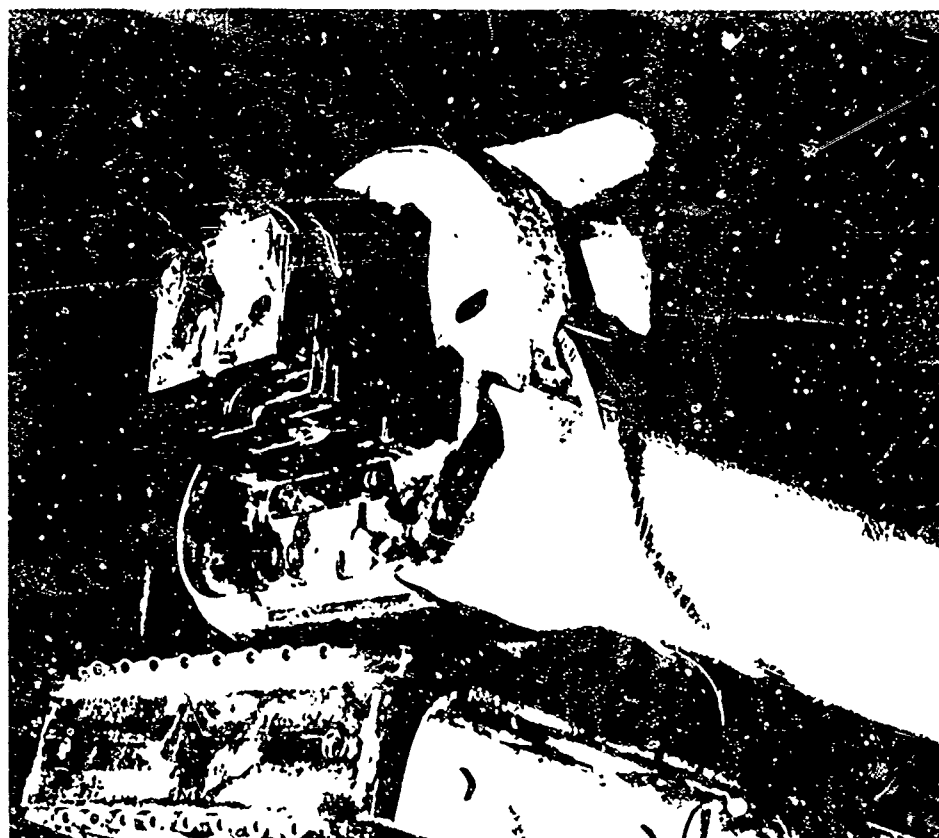


Fig II-4 Bulkhead of recovered ASSI-T vehicle

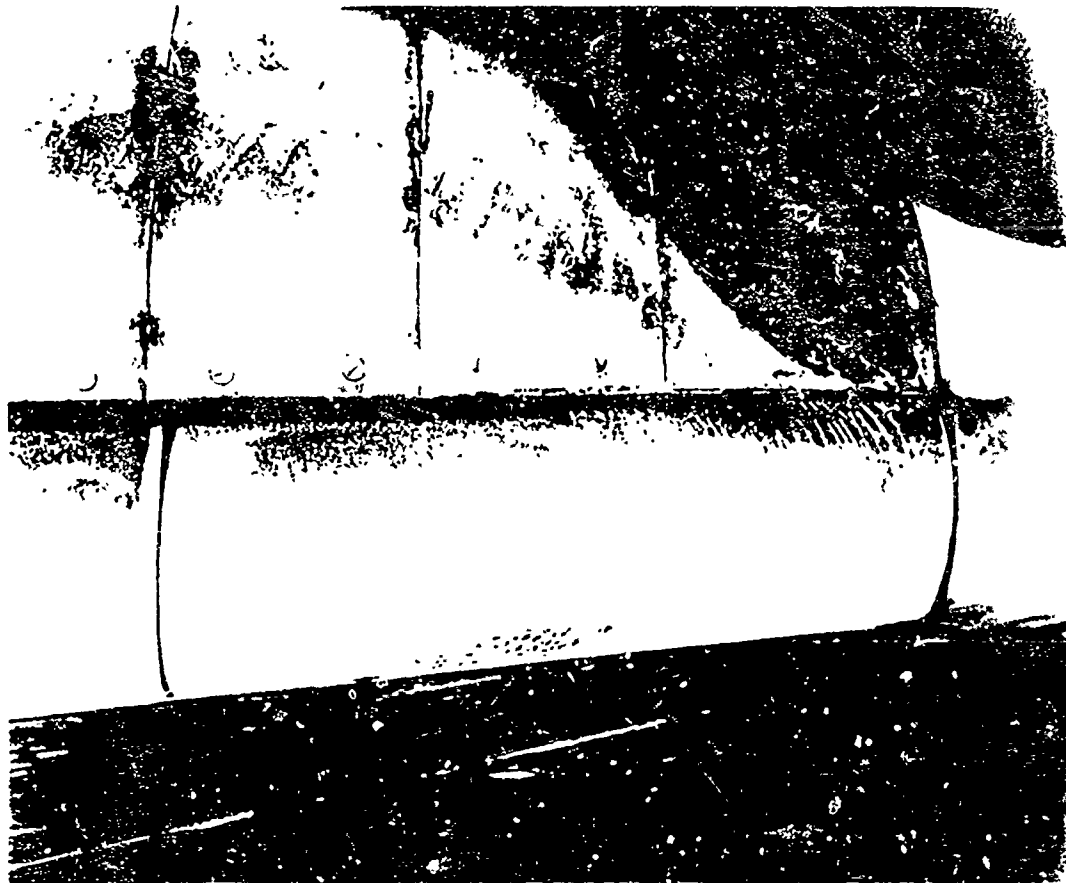


Fig II-5 Upper surface of recovered ASSI 1 vehicle

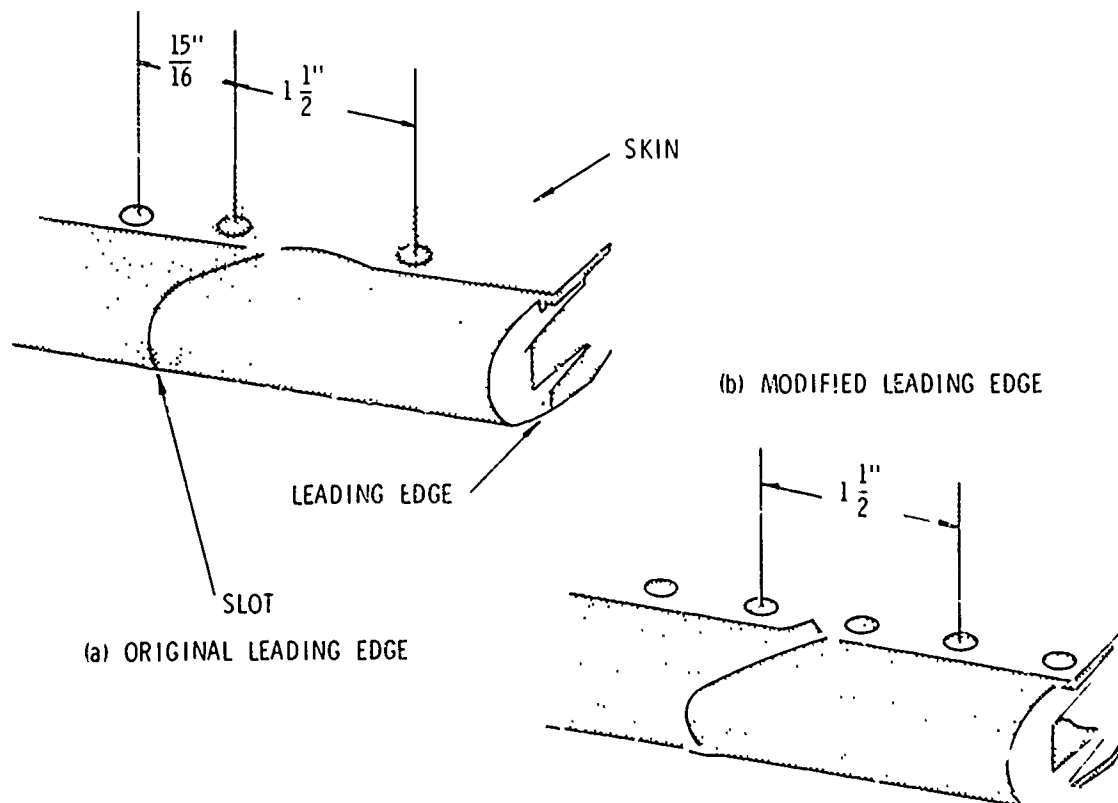


Fig II-6 X-15 leading edge buckling problem

$$\frac{H_{MAX}}{H_{FP}} = 1 + \frac{1}{36} \left(\frac{M_E}{\delta_L^* / H'} \right)^{1.9}$$

WHICH REDUCES TO

$$\frac{H_{MAX}}{H_{FP}} = 1 + \frac{1}{36} \left(\frac{H'}{X} \frac{\sqrt{R_E}}{GM_E \sqrt{C}} \right)^{1.9} \quad \text{LAMINAR}$$

$$\frac{\Delta \dot{Q}}{\dot{Q}_{FP}} = \frac{1}{2} \left\{ \frac{H'/W}{F} \left(1 - \frac{\delta_T^*}{H'} \right) - 2.5 + \sqrt{6.25 + \frac{5}{F} \frac{H'}{W} \left(1 + \frac{\delta_T^*}{H'} \right) + \left[\frac{H'/W}{F} \left(1 + \frac{\delta_T^*}{H'} \right) \right]^2} \right\}$$

TURBULENT

WHERE $F = \frac{\sqrt{M_E^2 - 1}}{8 \pi M_E^2}$

Fig.II-7 Surface roughness effects

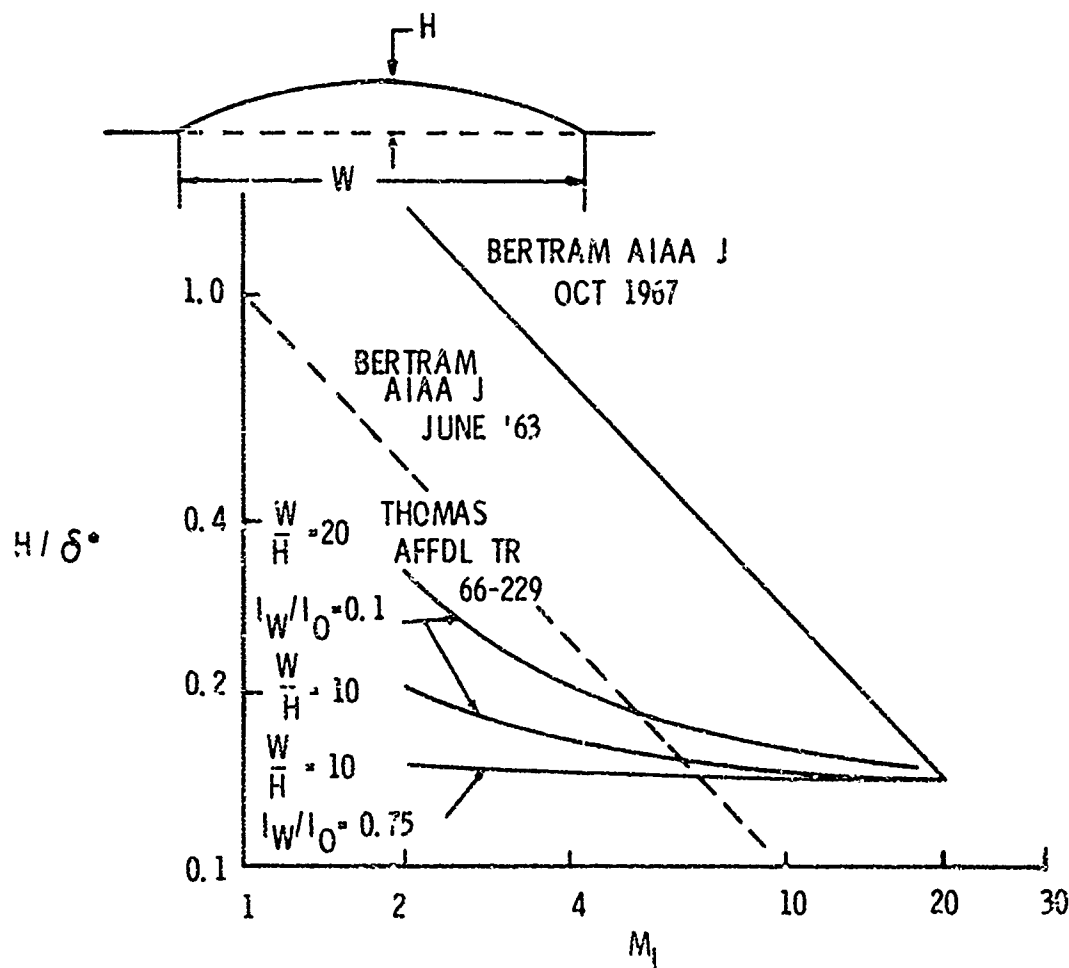


Fig.II-8 Percent of boundary-layer thickness required to increase smooth body heating by 20%

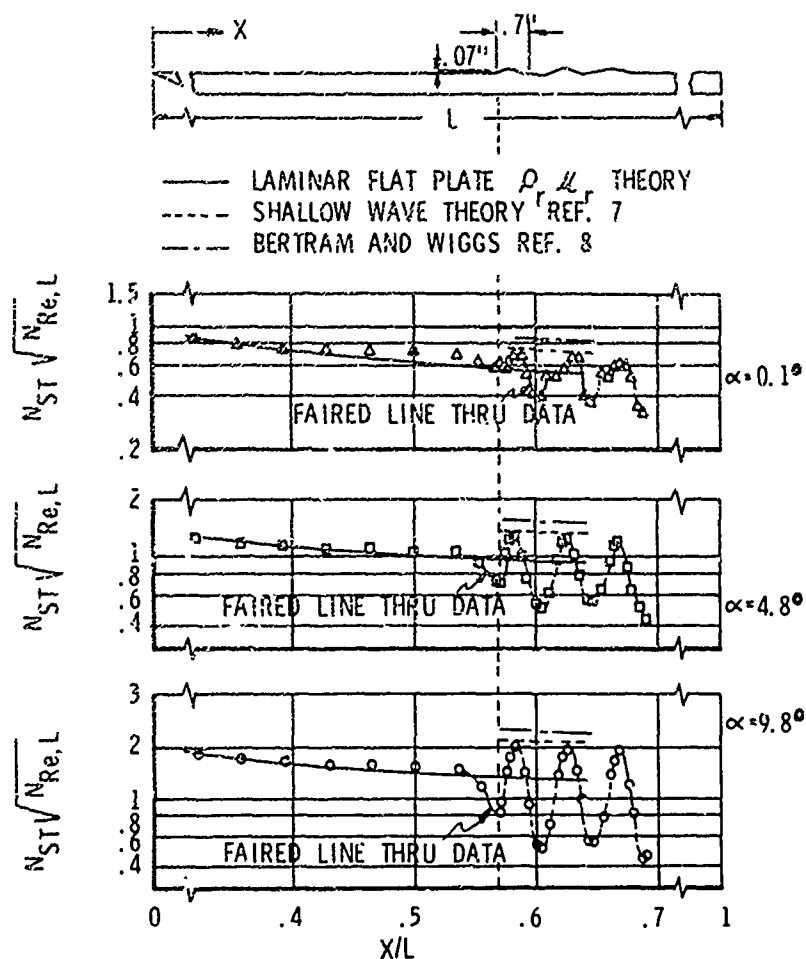


Fig.II-9 Laminar heat transfer distributions due to circular arc waves on a sharp flat plate, at $M_\infty = 10.1$

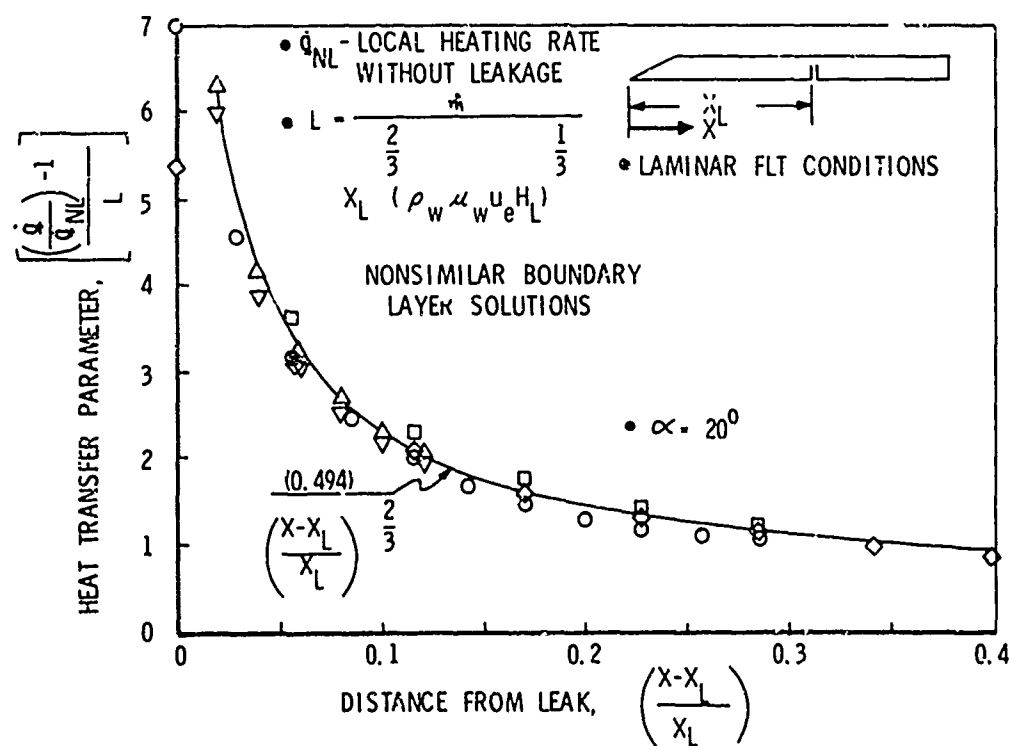


Fig.II-10 Effect of leakage on laminar heat transfer

SECTION III - INTERACTION HEATING

The interaction of one flow field with another is an inherent part of any flight configuration. As these phenomena are poorly understood at the present time, it is prudent in any design to attempt to minimize interactions. In spite of this, interaction problems were observed during the Dyna Soar development and continue to be important to both hypersonic aircraft and spacecraft designs. In this section I should like to discuss, (1) the interaction problems and their evaluation during the Dyna Soar development, (2) the current literature and trends in understanding both basic and configuration interactions, and (3) a detailed evaluation of particular interaction experiments which will illuminate some of the differences between two- and three-dimensional interactions.

III-1 THE DYNA SOAR EXPERIENCE

A fundamental design premise in the Dyna Soar configuration development was to minimize aerodynamic interactions. In spite of this, three areas of flow field interaction were noted on the Dyna Soar class of configurations, (1) the control surface interaction, (2) the wing/fin interaction problem, and (3) the canopy heating.

III-1.1 Wing/Fin Interaction

We have discussed and are generally more concerned with the flow field and aerodynamic heating generated on the compression surfaces of the highly swept leading edge. It is also important in a total design to evaluate the influence of the leading-edge shock on upper body heating. Such heating was discussed by Nagel¹ and is a characteristic of distinct wing/body entry vehicles. Figure III-1 indicates schematically the problem area and Figure III-2 outlines the "double shock method" postulated to handle such an interaction. In this method the fin leading edge was assumed to be a swept cylinder downstream of an arbitrary oblique shock. The angle of this oblique shock, θ_1 , was varied to maximize the heating on the fin leading edge. Figure III-3 indicates data generated at Mach 10 in comparison with the double shock method. It is interesting to note that the hot localized region on the fin leading edge was first observed during a temperature sensitive paint test of the configuration.

This problem of leading-edge interference was also noted during the development of the ASSET research configuration. Figure III-4 indicates data extracted from Reference 2 indicating a relatively hot localized region on the conical upper body caused by the wrapping around of the shock wave formed on the wing leading edge. This phenomena is noted to diminish in magnitude and occur higher on the conic upper body as the angle of attack is increased. The antenna area created yet another interference as it protruded from the configuration mold lines. High localized heating is also noted near the forward junction of the antenna with the body. Figure III-5 indicates a vapour screen flow visualization photograph of the flow over the upper surface of the ASSET in this region.

III-1.2 Canopy Heating

Pressure data on the canopy surface of a Dyna Soar research model are shown in Figure III-6 from Reference 1. In order to interpret the fluid mechanics associated with the experimental data, several rational fluid models were necessary, as shown, depending upon the configuration angle of attack. The shaded data band represents the locus of theoretical calculations corresponding to the analytical model. Similar results for the heat transfer data are shown in Figure III-7 for zero yaw and in Figure III-8 for moderate vehicle yaw angles. These examples of interaction heating were serious considerations at the lower vehicle angles of attack and formed a portion of the low angle of attack thermal placards discussed in the maneuver corridor figure of Section I.

III-2 X-15 EXPERIENCE

Severe interaction heating was also observed during the final flights of the X-15 due to the presence of the dummy ramjet pylon on the aft lower surface of the body. Figure III-9 indicates a post-flight picture of the interaction region.

III-3 INTERFERENCE HEATING TO HYPERSONIC AIRCRAFT

Hypersonic aircraft will encounter many interference heating situations not to be found in early re-entry configuration designs. These interactions arise due to the very characteristics of the vehicle, for example due to

1. The aircraft concept of operation and the capability for sustained and economical operation of the aircraft at all flight speeds
2. The aerodynamic effect of the propulsion system on the configuration - a major design consideration at higher flight Mach numbers.
3. The configuration length approaching 300 feet length.

As a point of departure from lifting entry configurations discussed earlier, the cruise configurations differ from these shapes due to

1. Configuration scale,
2. Configuration complexity,
3. The operating environment.

Configuration scale will be roughly twice the length of proposed space transportation systems and 5 to 10 times the length of earlier boosted glide vehicle designs. Such length increases mitigate the relative importance of transition and focus our attention on the difficulty of accommodating the existing turbulent boundary layer.

Configuration complexity will focus design attention on the inevitable heating increases caused by multiple flow field interactions. The principal characteristic of this class of configurations will be that of a flying interference region.

Finally, the hypersonic aircraft will operate at lower altitudes dictated by engine performance capabilities and the aircraft unit and total Reynolds number characteristics will surely challenge advanced aerodynamic facility designs in the developmental phase of the program. (This will be discussed in Section VI of these notes.)

Interaction heating of such configurations is today poorly understood and the subject of many unfounded speculations regarding aerodynamic heating levels. Today I should like to discuss several useful aerodynamic models for such interactions to reinforce what is already known about such interactions, to highlight fundamental differences between two- and three-dimensional interactions and to point out the problems involved with configurations having several simultaneous flow field processes occurring.

III-4 TWO-DIMENSIONAL INTERACTIONS

The classical problem of a remote generator impinging an incident shock on a known planar flow field has been evaluated by many authors. Configurations as shown in Figure III-10a have been evaluated experimentally over both hypersonic and supersonic Mach number ranges. The analytic expressions for heating generally relate interaction pressure rise to interaction heating rise, i.e.

$$\frac{h_{pk}}{h_{fp}} = \left[\frac{p_{pk}}{p_{fp}} \right]^n \quad \text{where } n = 0.5 \text{ for laminar flow} \\ n = 0.8 \text{ for turbulent flow.}$$

This relationship follows directly from flat-plate theory accounting for an additional pressure increment due to the impingement process. I have chosen to identify this correlation approach as pressure interaction theory. This approach assumes that the imposed heating does not disrupt the existing boundary layer but merely impresses an additional pressure increment upon it.

Employing this approach, turbulent data from several sources^{3,4} as well as data generated within the Air Force Flight Dynamics Laboratory were compared. For turbulent flow the correlation of data in Figure III-11 is noted to be excellent. As a point to note, the data from the Air Force Flight Dynamics Laboratory were taken under an induced turbulent boundary layer using a tripping device shown in Figure III-12. The reference flat-plate values were generated on the same plate without the remote generator and in these tests the flow was probed to assure that valid turbulent boundary-layer conditions did, in fact, exist.

Laminar boundary-layer data were also taken on the same model but at a more forward station and without the trip mechanism. These data are shown together with other "laminar" data^{5,6} in Figure III-13. A distinct lack of agreement is apparent in this figure which was assumed to be caused by boundary-layer transition.

Correlation of these initially laminar data under the aforementioned assumption was achieved by considering not only the relationship between peak heating and peak pressure in a turbulent boundary layer, which was validated in Figure III-12, i.e.

$$\left[\frac{h_{peak}}{h_{f.p.}} \right]_{turb} = \left[\frac{p_{peak}}{p_{f.p.}} \right]^{0.8}$$

but also the relationship between turbulent and laminar undisturbed flow from Eckert's formulation, i.e.

$$\left[\frac{h_{turb}}{h_{lam}} \right]_{no \text{ inter.}} = 0.08916 \left[\frac{Re_{\infty}}{in.} \right]^{0.3} \left[\frac{T_{\infty}}{T^*} \right]^{0.6} \frac{X_{lam}^{0.5}}{X_{turb}^{0.2}}$$

where the length dimension, X , has units of inches with the laminar distance measured from the plate leading edge to the interaction. The turbulent distance is measured either from onset of transitional flow ahead of the interaction or from the onset of nonlaminar flow when transition is not clearly discernible.

The results, which are shown in Figure III-14, indicate that turbulent flow was indeed the cause of the lack of data correlation. It also indicates the transitional nature of the Mach 10 data.

The correlation indicates that the pressure interaction theory is valid for two-dimensional flow. It is noted that such interaction tends to cause premature boundary-layer transition. The results point to the fact that the primary problem is in specifying the proper pressure level in the interaction using one of several available methods as for instance the recent paper by Rose, Murphy and Watson⁷.

III-5 THREE-DIMENSIONAL INTERACTION

Heating to three-dimensional interaction configurations such as the model shown in Figure III-10b presents a far different interaction problem for consideration. In order to understand such a flow field, let us first consider data generated by the Air Force Flight Dynamics Laboratory and then generalize the results to include the data of other authors.

Pressure data were generated in the interaction region for fins having varying deflection and sweep angles. These data, shown in Figure III 15, indicate that the pressure decay with sweep varies only as the 0.3 power of the cosine of the sweep angle and that all the data from the test could be correlated as shown in Figure III-16.

Initial correlations of the heat transfer data were made using the pressure interaction theory verified for the two-dimensional case and the previously correlated pressure data. The pressure interaction theory seriously under-predicted the heating data. Turbulent correlation of the laminar data as in the two-dimensional case improved the prediction somewhat, however, turbulent three-dimensional interaction data showed still higher and unaccounted for heating levels.

A new approach analogous to the control surface heating methods of Bushnell and Weinstein was adopted which postulated a new effective boundary layer caused by the interaction. This model has been identified for purposes of discussion as the effective boundary-layer model. This procedure is a modification of the two-dimensional approach to include a new boundary layer caused by the interaction process and initiating for convenience at present the fin shock wave. For simplicity, this new boundary layer is assumed to be planar in the direction of the free-stream velocity of the flow. A form of this approach was employed by Miller in 1963 (Ref.9). In Miller's correlation pressure interaction theory was modified to obtain the Mach 8 correlation by using plateau pressure in place of flat-plate pressure and basing Reynolds number on the distance from the start of reattachment.

The present approach is conceptually in agreement with Miller, however, the interference pressure increment was taken as that from undisturbed to peak pressure as it was not always true with our data that separation did occur. Further, and for the same reason, a more general flow boundary was selected to initiate the boundary layer, i.e. the interference shock. Finally, the Bertram-Feller term accounting for the presence of an adverse pressure gradient, K_3 , was acquired in our case by a correlation of the data using the assumed method, i.e.

$$K_3 = \frac{h_{\max}/h_{fp}}{\sqrt{P_{\max}/P_{fp}}}$$

The values so derived were both reasonable and in general agreement with the values derived by measuring the slope of pressure with distance. The latter method is open to some question as the origin of the distance, X , is not known and must be assumed.

Several checks of the data were made using both the Miller correlation and our approach. One example at Mach 8 for the laminar data indicated the following comparison:

X from LE = 16.5"		% Diff.
$h \times 10^4$ (Miller)	33.35	10.6%
$h \times 10^4$ (AFFDL)	38.9	4.3%
$h \times 10^4$ (DATA)	37.3	—

so that for laminar data the two methods tend to agree. The difference in methods applicability is that the AFFDL method can also be applied to cases where no separation occurs as for instance to turbulent boundary layers which are more resistant to separation.

Laminar correlation of the appropriate Mach 6 data employing both the effective boundary-layer model and the pressure interaction theory is shown in Figure III-17. Correlation of data with the effective boundary-layer model is excellent except at the highest angle of incidence, 20° , where transition onset is suspected. Corresponding data at Mach 8 are shown in Figure III-18.

Turbulent correlation of the higher Reynolds number Mach 6 data are shown in Figure III-19 again with the two methods outlined. The reverse trend of the data for long distances aft of the fin leading edge is considered to be indicative of local boundary-layer transition. Corresponding Mach 8 data are shown in Figure III-20.

Turning to data from other authors, Stainback⁸ of the NASA Langley Research Center presented a technical note outlining an experimental program at Langley in which fully developed interaction characteristics were not clearly present. Figure III-21 presents Stainback's data together with the effective boundary layer approach noting that the effective boundary-layer approach bounds and correlates the Stainback data far from the origin of the interaction.

Figure III-22 presents data generated by Miller⁹ of the Boeing Company as well as data from the present tests. The result indicates that relatively long distances are required to achieve a fully developed laminar interaction.

Figure III-23 indicates a composite of Miller's, Stainback's and the present data for sharp fin interactions. The effect of fin blunting is shown to reduce the heating at the same location within the interaction. This is due to the shape of the shock produced by a blunt fin interaction, the greater distance from the start of the new boundary layer to the location of peak heating and hence the lesser heating.

Figure III-24 presents a correlation of Mach 20 data taken by Watson and Weinstein¹⁵ in Helium flow. Both pressure and heat transfer rate data were given in Reference 15. A value of the Bertram and Feller parameter, K_3 , equal to 2 was selected based upon an extrapolation of 6, 8, and 10 data previously generated and presented. The value $\sqrt{0.215}$ accounts for the new effective boundary layer and is derived in Appendix III of Reference 16.

Three-dimensional experiments have shown a decidedly different character to the interaction which is caused by the additional dimension of the flow. The effective boundary-layer concept discussed is conceptual and requires refinement but it does indicate two related problem areas:

1. For large hypersonic aircraft designs, severe heating can occur far from the nose due to the formation of a new boundary layer.
2. In testing of such aircraft configurations, the experiment scale is important particularly in a turbulent boundary-layer environment which is the environment of practical interest.

III-6 REAL GAS PHENOMENA

To date all experimental data on the interaction heating problem have been generated in perfect gas wind tunnels. While these tests are important to develop the fluid mechanic relationship involved, there are indications from published papers by Nagel and Thomas¹¹ and Edney¹² that the increased density caused by real gas flows can significantly increase the interaction heating process. Such a conjecture is easily made through analysis but very difficult to prove experimentally. Real gas wind tunnels to generate a low γ test flow ($\gamma = 1.0$) must employ gases other than air since the high temperature air expansion process will freeze the airflow early in the expansion process and drive the ratio of specific heats, γ , toward the monatomic level $\gamma = 1.667$. Experiments in process at the Langley Research Center in a tetrafluoromethane (CF_4) Mach 6 facility¹³ should give us additional insight into the effect of real gas behavior on interference heating although, admittedly without the other factors present in a hypersonic free flight flow field.

SECTION III - REFERENCES

1. Nagel, A.L.
et al. *Analysis of Hypersonic Pressure and Heat Transfer Tests on Delta Wings with Laminar and Turbulent Boundary Layers.* NASA CR 535, August 1966.
2. Weinstein, I.
Howell, R.R. *Technique for Measuring High-Temperature Isotherm Patterns on Aerodynamically Heated Models with Experimental Results* NASA TN D-2769, May 1965.
3. Fabish, T.J.
Levin, V. *Thermal Effects of Shock Wave Turbulent Boundary-Layer Interaction at Mach Numbers 3 and 5.* North American Aviation, Inc., NA 62H-795, November 1962.
4. Sayano, S. *Heat Transfer in Shock Wave Turbulent Boundary-Layer Interaction Regions.* Douglas Report SM 42567, November 1962.
5. Kutschenreuter, P.H., Jr.
et al. *Investigation of Hypersonic Inlet Shock Wave Boundary-Layer Interaction Part II Continucus Flow Test and Analyses.* AFFDL TR 65-36, AD 636 981, Air Force Flight Dynamics Laboratory, Wright-Patterson Air Force Base, Ohio.
6. Holden, M. *Separated Flow Studies at Hypersonic Speeds Part II. Two-Dimensional Wedge Separated Flow Studies.* Cornell Aeronautical Laboratory, Inc., Report No. AF-1285-A-13(2), December 1964, AD 613 463.
7. Rose,
et al. *Interaction of an Oblique Shock Wave with a Turbulent Boundary Layer* AIAA Journal, Vol.VI, No.9, pp.1792-1795.
8. Stainback, P.C. *Aerodynamic Heating in the Vicinity of Corners at Hypersonic Speeds* NASA TN 4130, November 1967.
9. Miller, D.S.
Redeker, E. *Three-Dimensional Corner Flow Separation.* Presented at the 48th Meeting of the Bumblebee Panel, 10-11 September, 1963.
10. Bushnell, D.M. *Effects of Shock Impingement and Other Factors on Leading-Edge Heat Transfer.* NASA TN D-103, April 1968.
11. Nagel, A.L.
Thomas, A.C. *Analysis of the Correlation of Wind Tunnel and Ground Test Data to Flight Test Results* AIAA Paper 65-208.
12. Edney, B. *Anomalous Heating and Pressure Amplification on Blunt Bodies at Hypersonic Speeds in the Presence of an Impinging Shock.* Aeronautical Research Institute of Sweden, FFA Report 113, 1968.
13. Jones, R.A. *Use of Tetrafluoromethane to Simulate Real Gas Effects on the Hypersonic Aerodynamics of Blunt Vehicles* NASA TR R-312.
14. Myers, J.R.
Roberts, B.W. *An Investigation of Shock Impingement on Boundary Layers for Wing/Body Configurations at Mach 8* AEDC TDR 63-222.
15. Watson, R.
Weinstein, L. *A Study of Hypersonic Corner Flow Interactions.* AIAA Journal, July 1971, pp.1280-1286.
16. Neumann, R. *The Influence of Shock Wave Boundary-Layer Effects on the Design of Hypersonic Aircraft.* AFFDL TR 68-152.

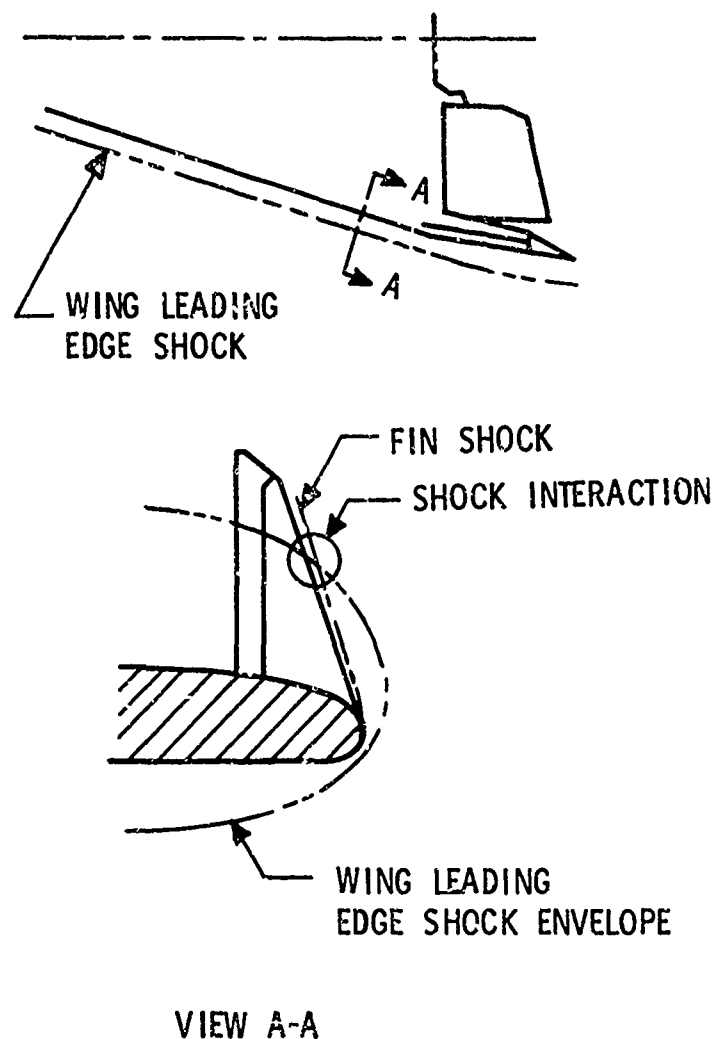


Fig. III-1 Schematic representation of wing/fin interaction

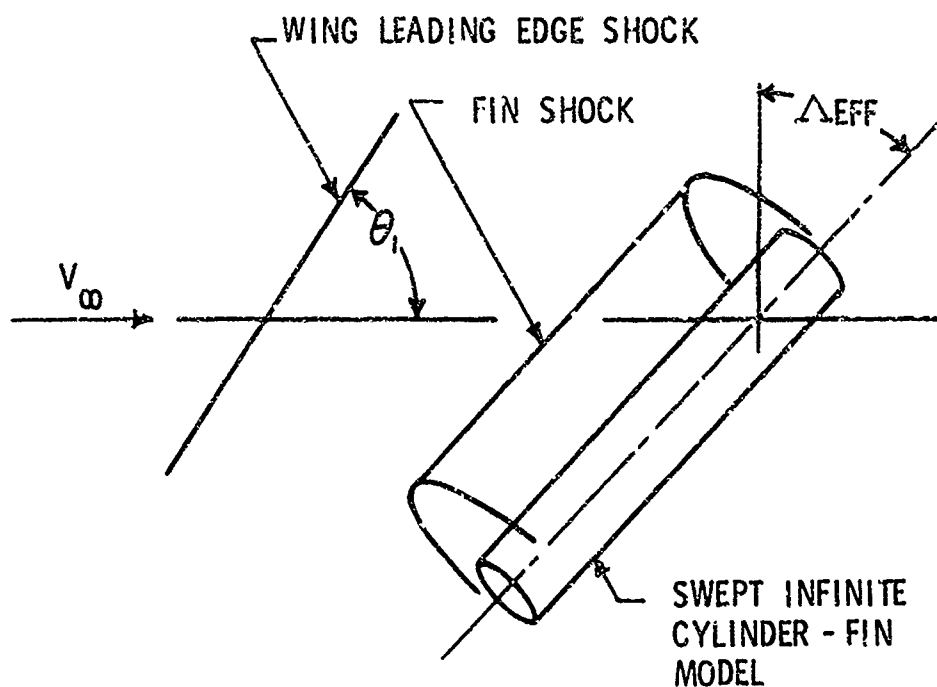
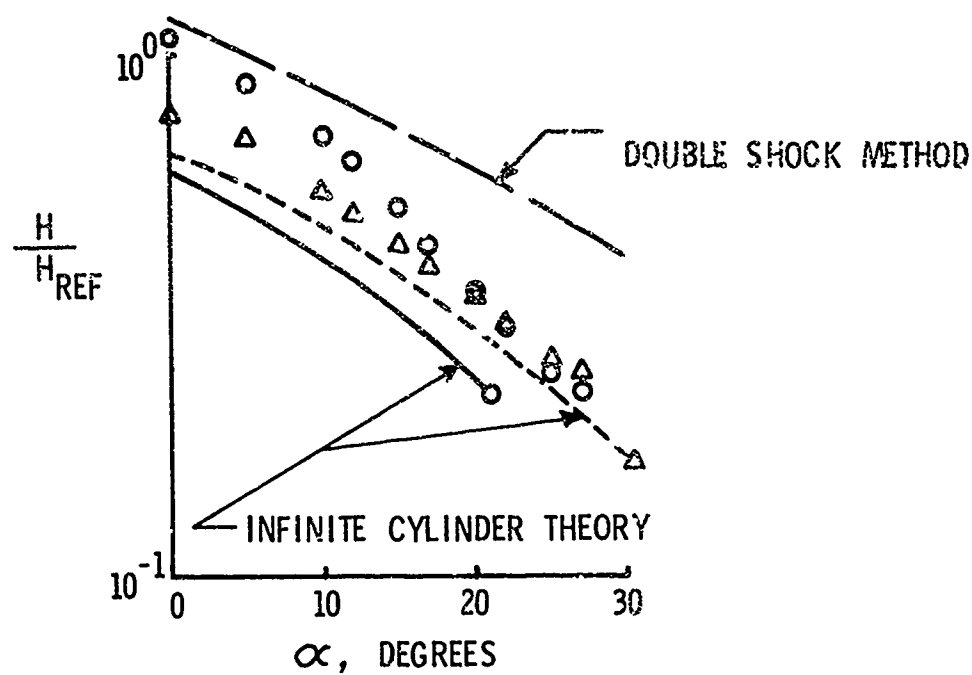
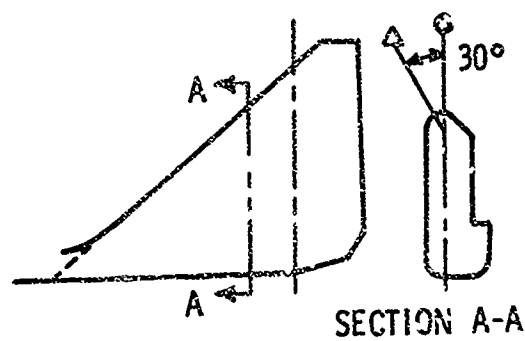
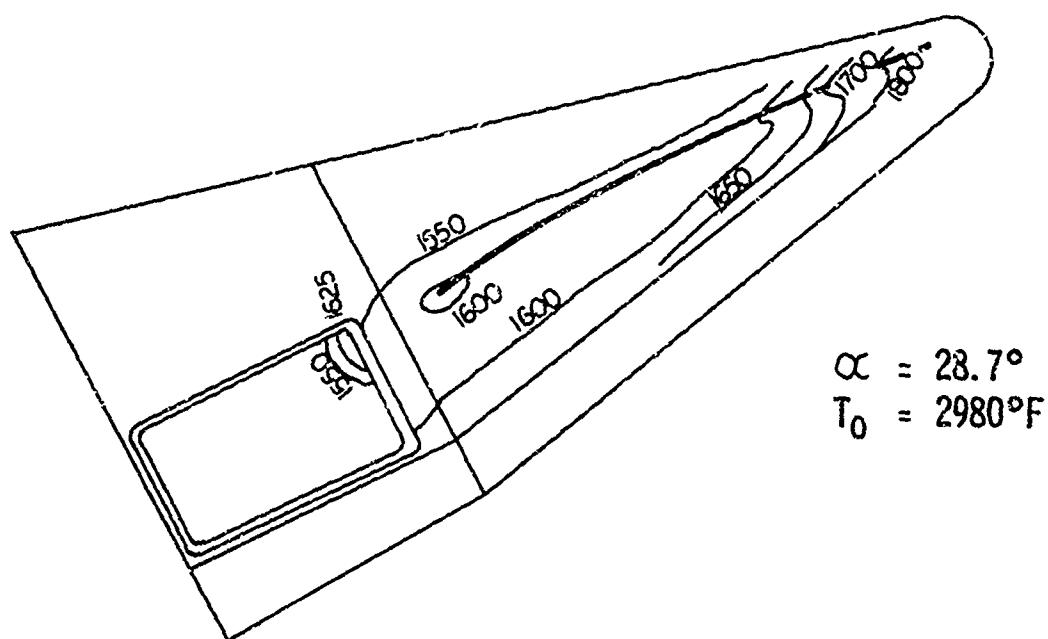
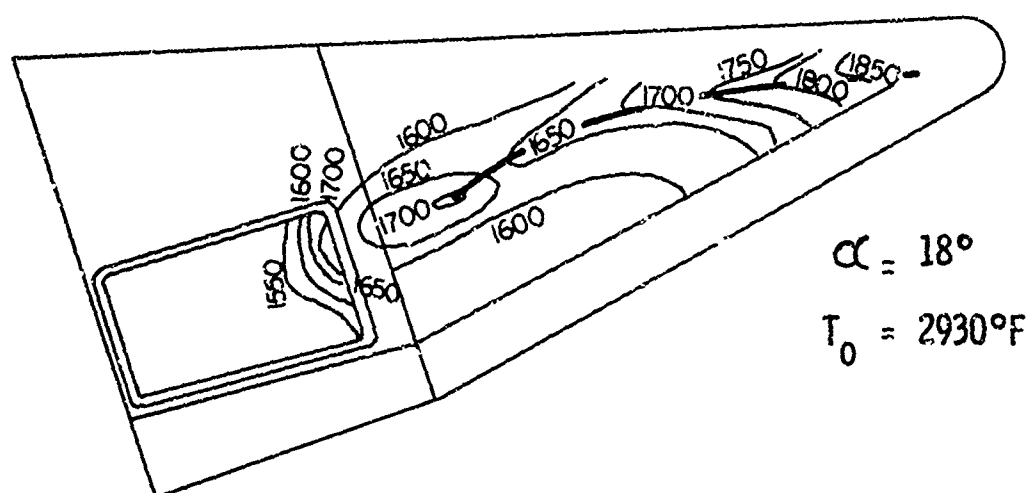
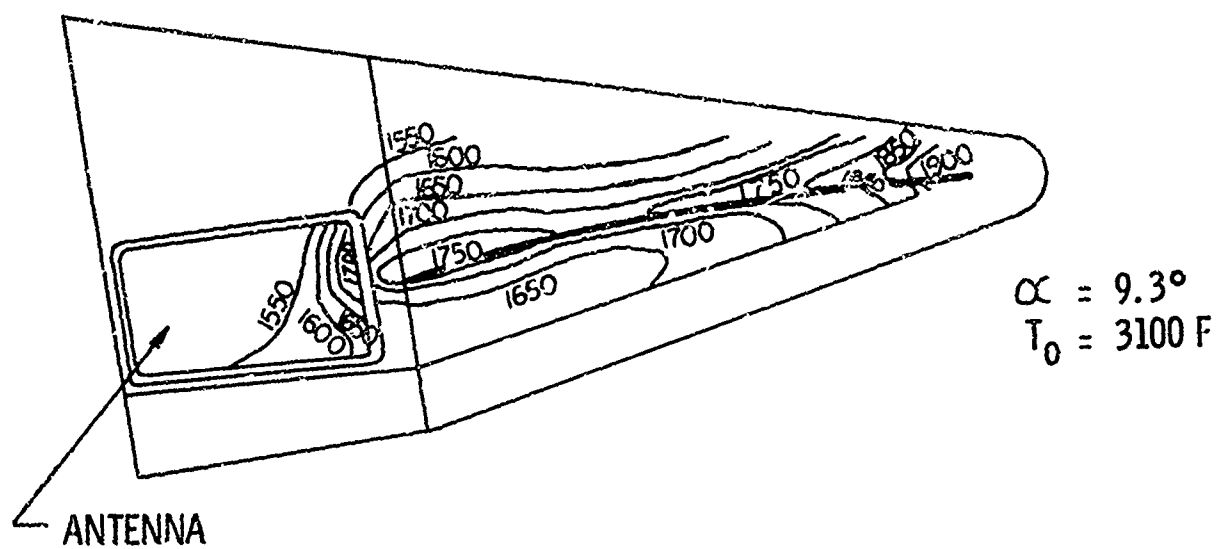


Fig. III-2 "Double shock method"



$$H_{REF} = .02911 \text{ BTU/FT}^2/\text{SEC DEGR}$$

Fig.III-3 Mach 10 data on fin interaction



MACH 7; RE/FT = 1.4×10^6

Fig.III-4 Interference data on "ASSET" configuration

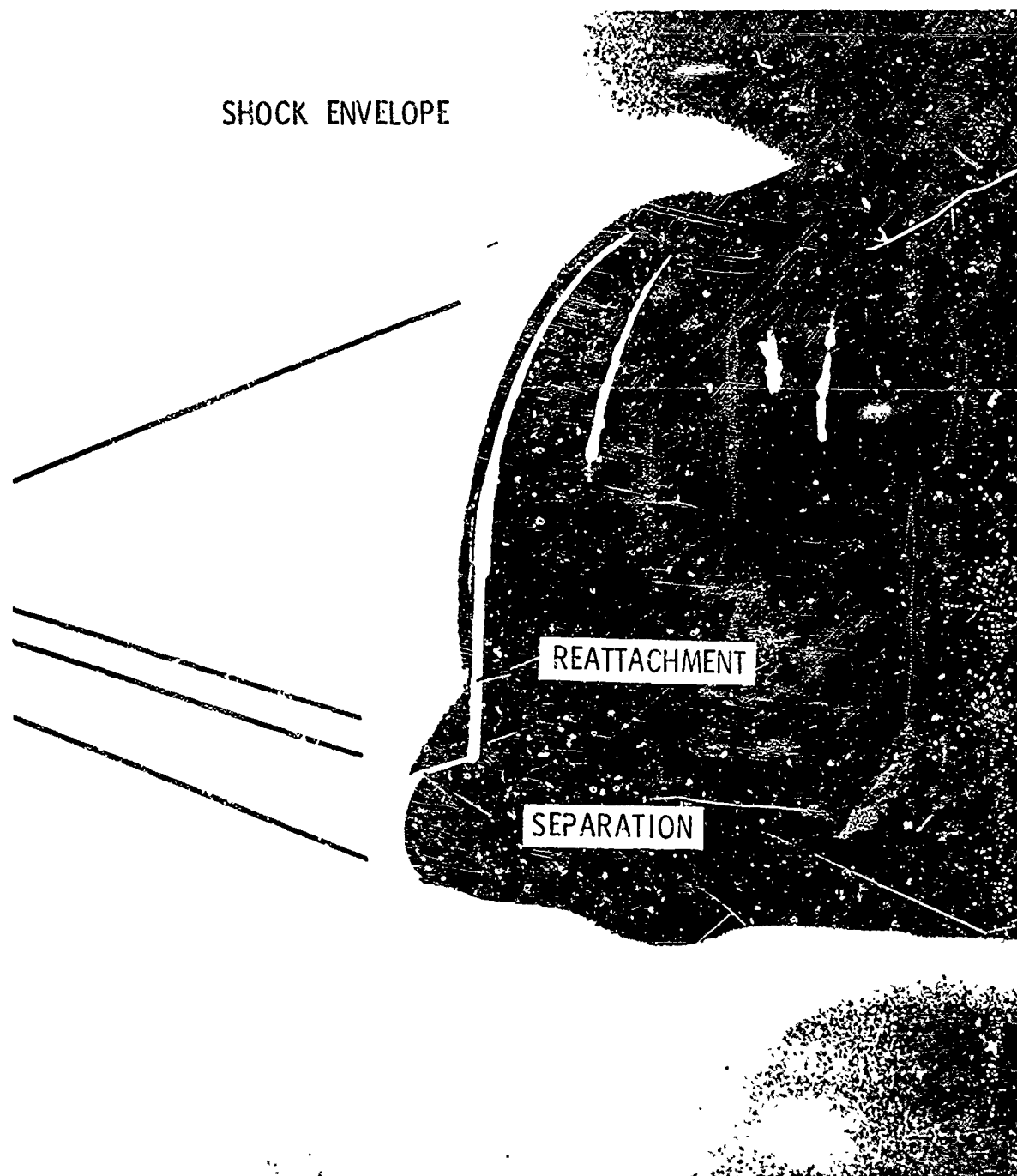


Fig III-5 Vapor screen photograph of ASME shock structure at flow rate of 1000 gpm

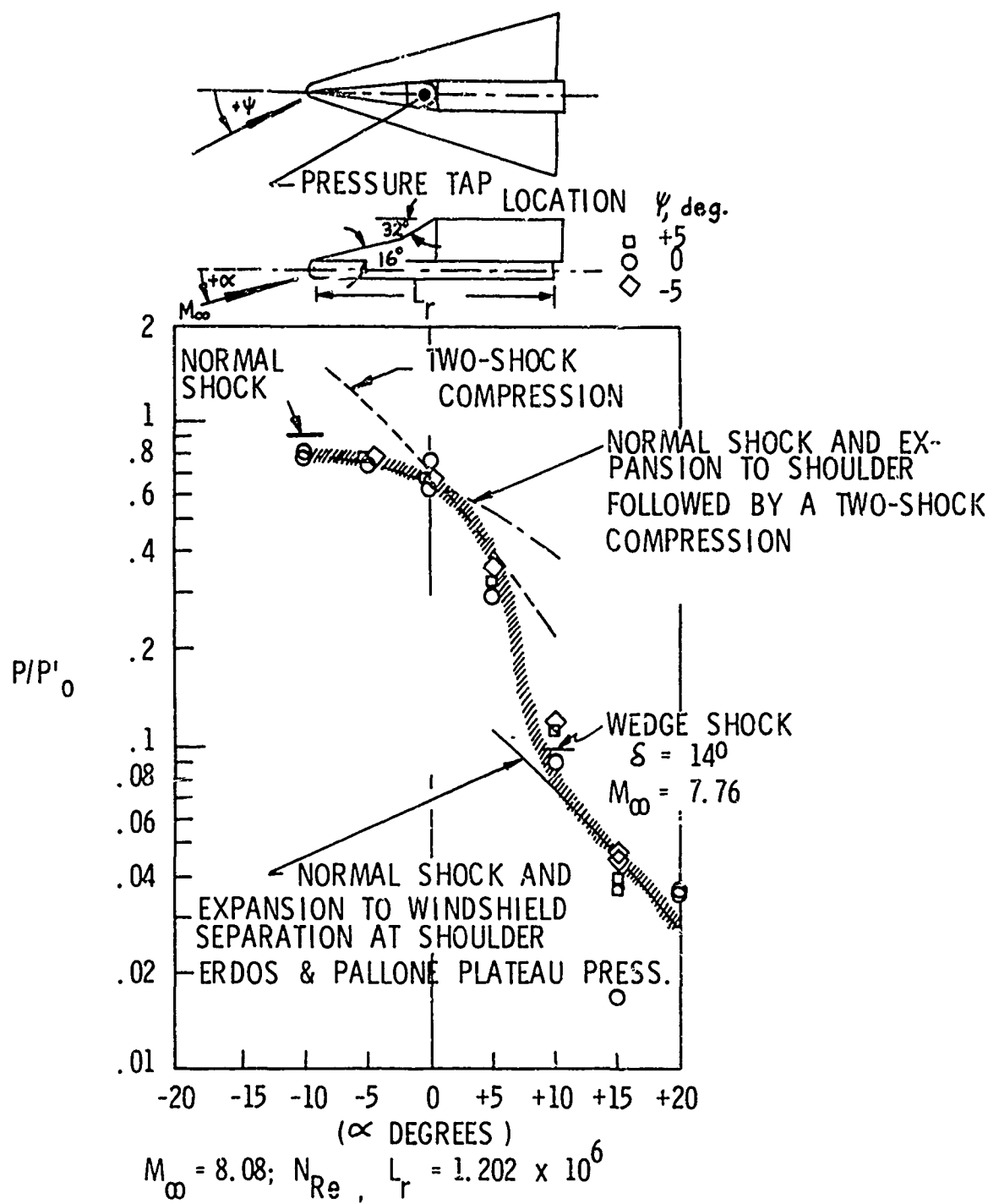


Fig.III-6 Pressure data on Dyna Soar canopy

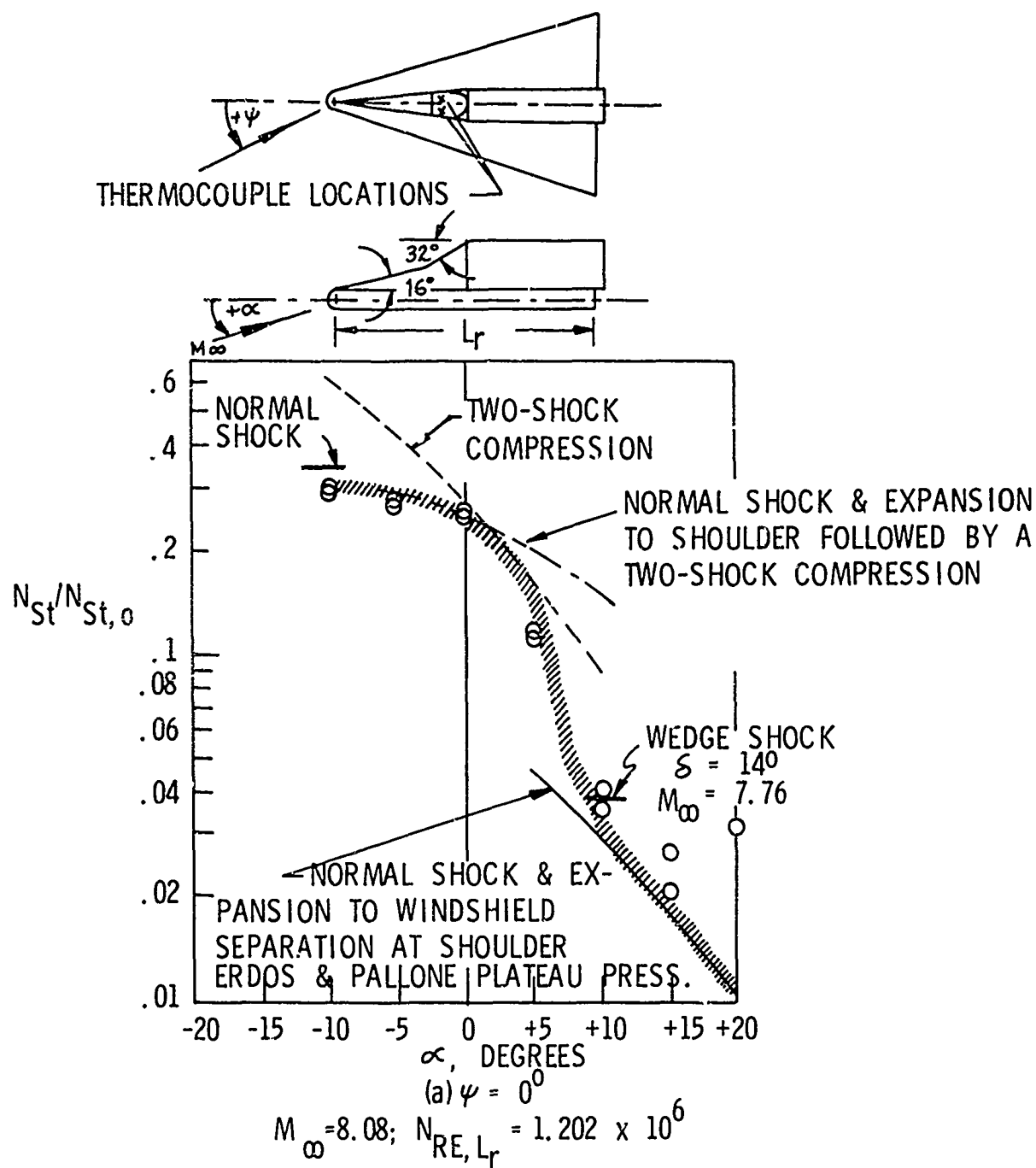


Fig.III-7 Heat transfer data on Dyna Soar canopy at zero yaw

OPEN SYMBOL, LEEWARD THERMOCOUPLE
 CLOSED SYMBOL, WINDWARD THERMOCOUPLE

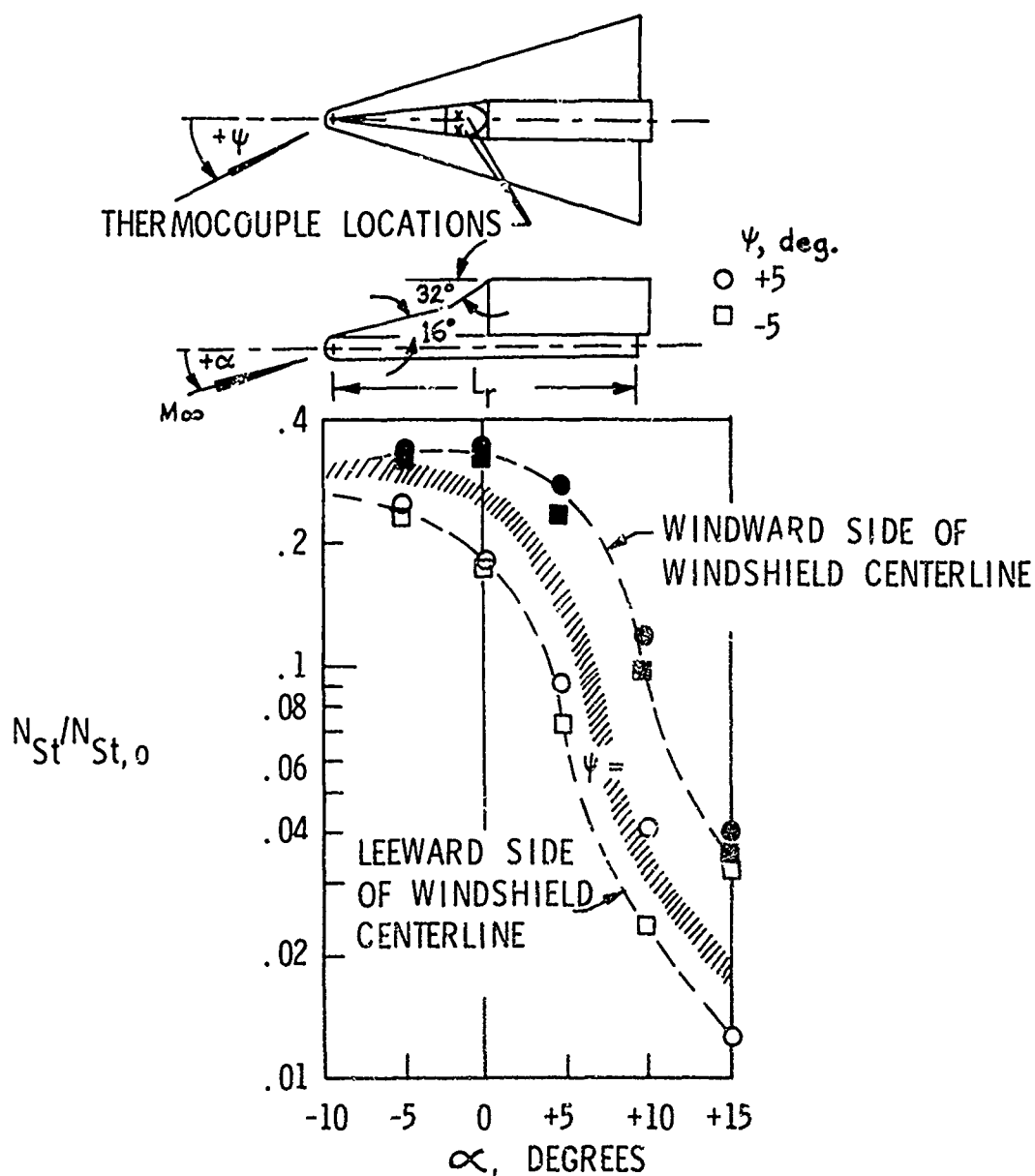


Fig.III-8 Heat transfer data on Dyna Soar canopy for small yaw angles

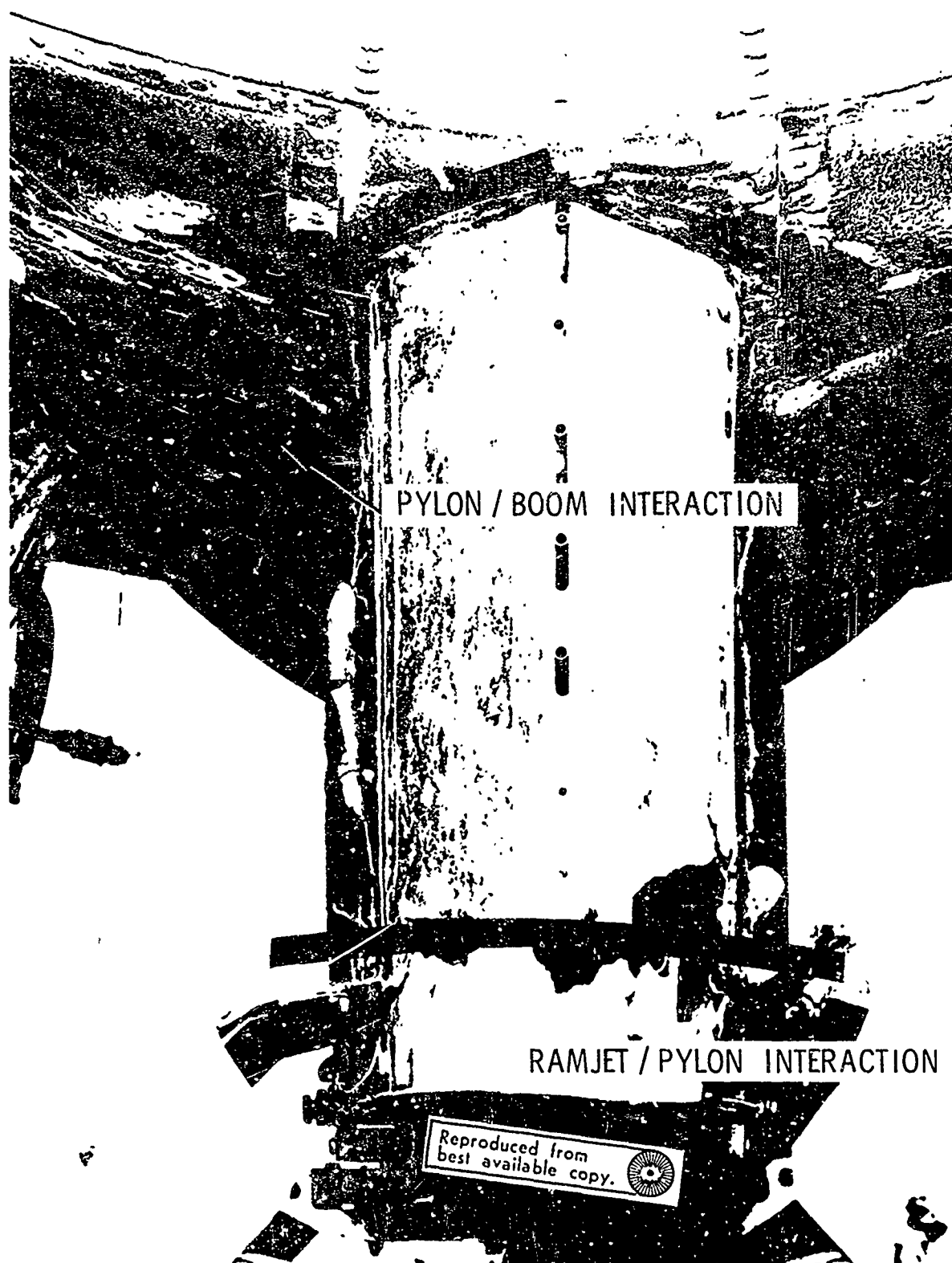


Fig III 9 Post-flight view of X-15 pylon interaction heating

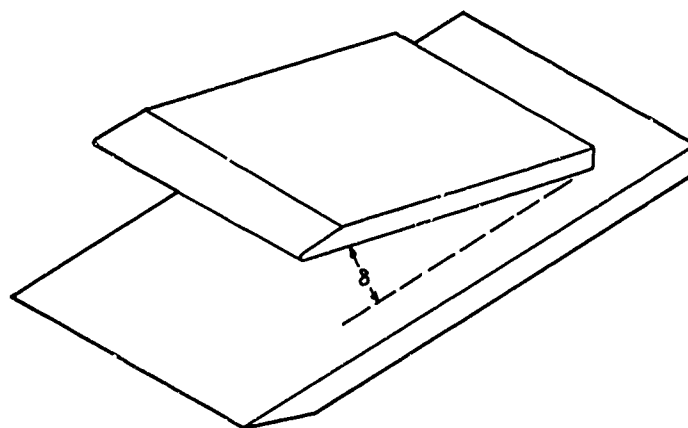


Fig.III-10a Two-dimensional interaction model

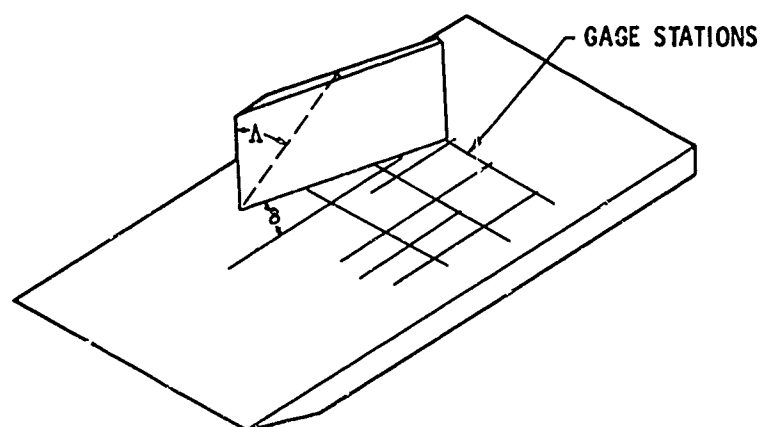


Fig.III-10b Three-dimensional interaction model

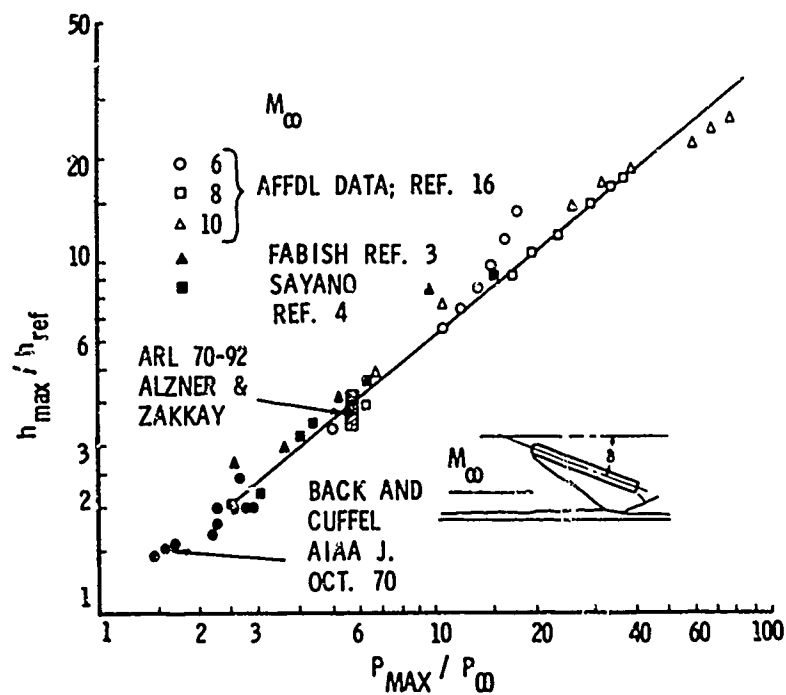


Fig.III-11 Turbulent interference heating caused by a remote shock generator

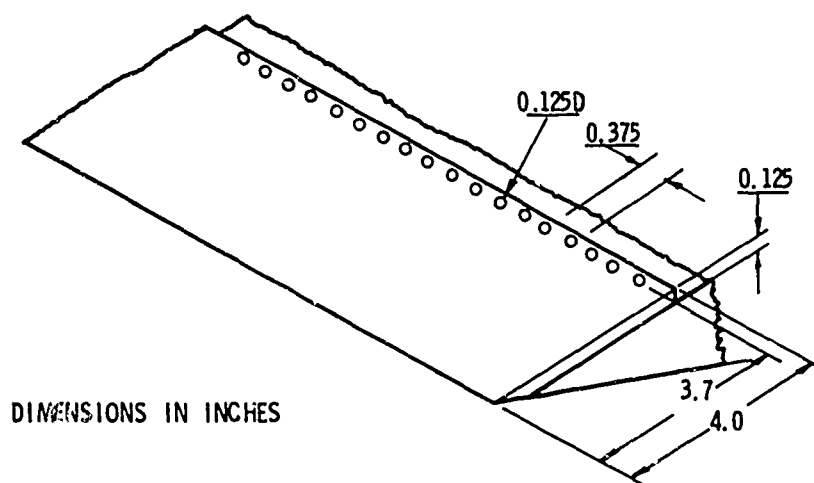


Fig.III-12 Trip device on flat plate model to achieve a turbulent boundary layer

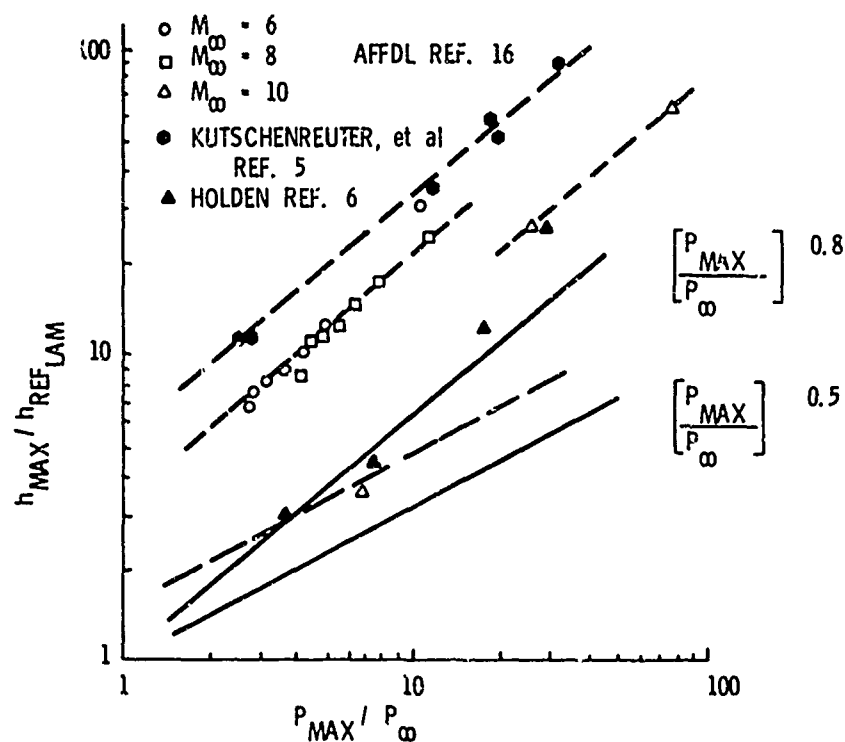


Fig III-13 Laminar two-dimensional interaction data

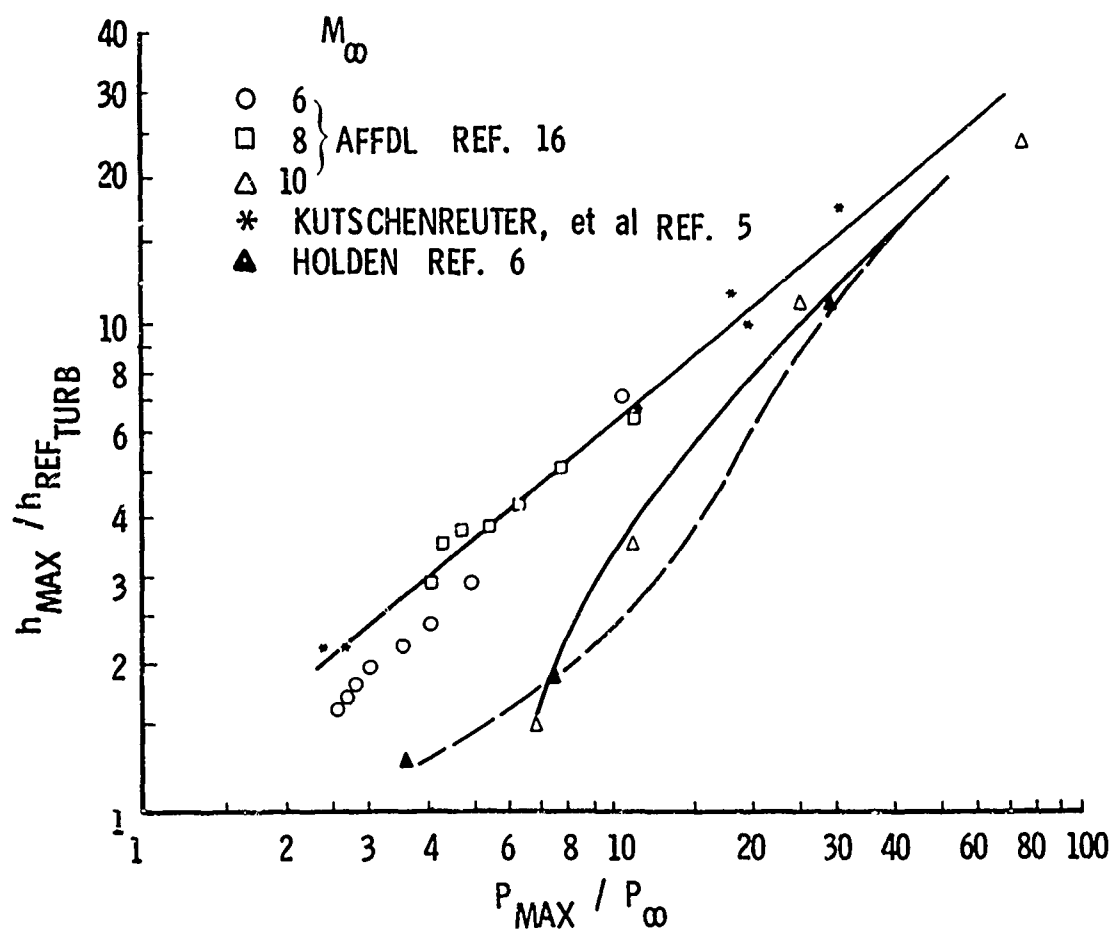


Fig. III-14 Initially laminar two-dimensional interaction data

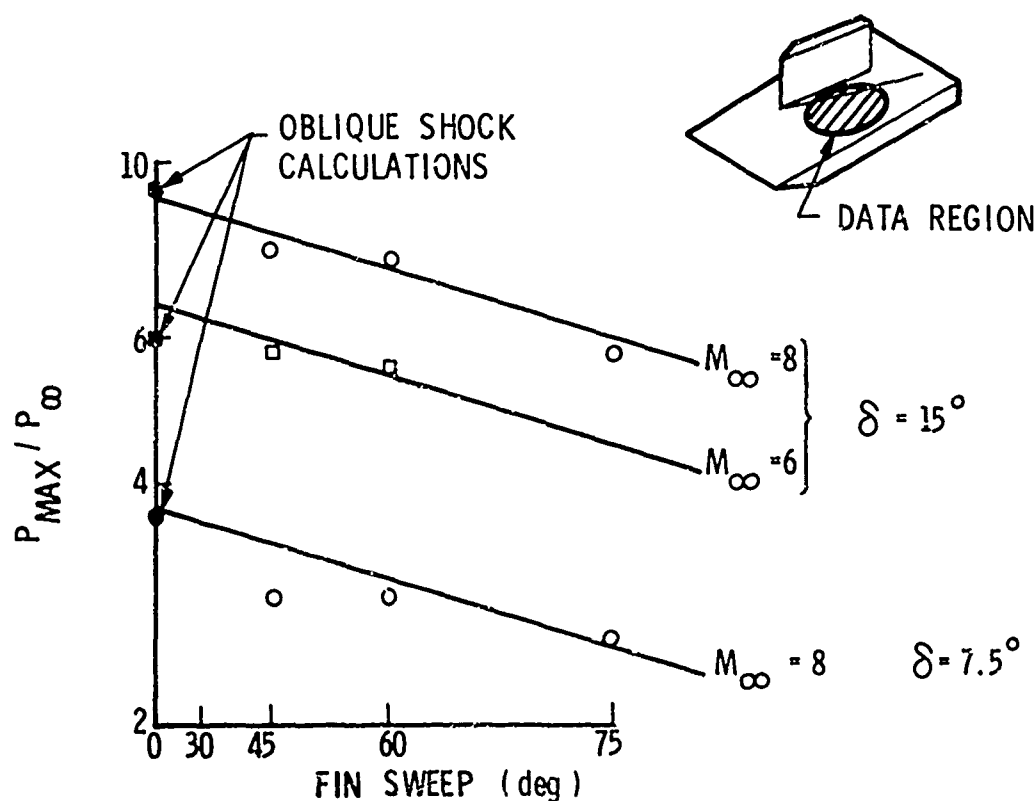


Fig. III-15 Effect of sweep on the maximum pressure in the fin interference region

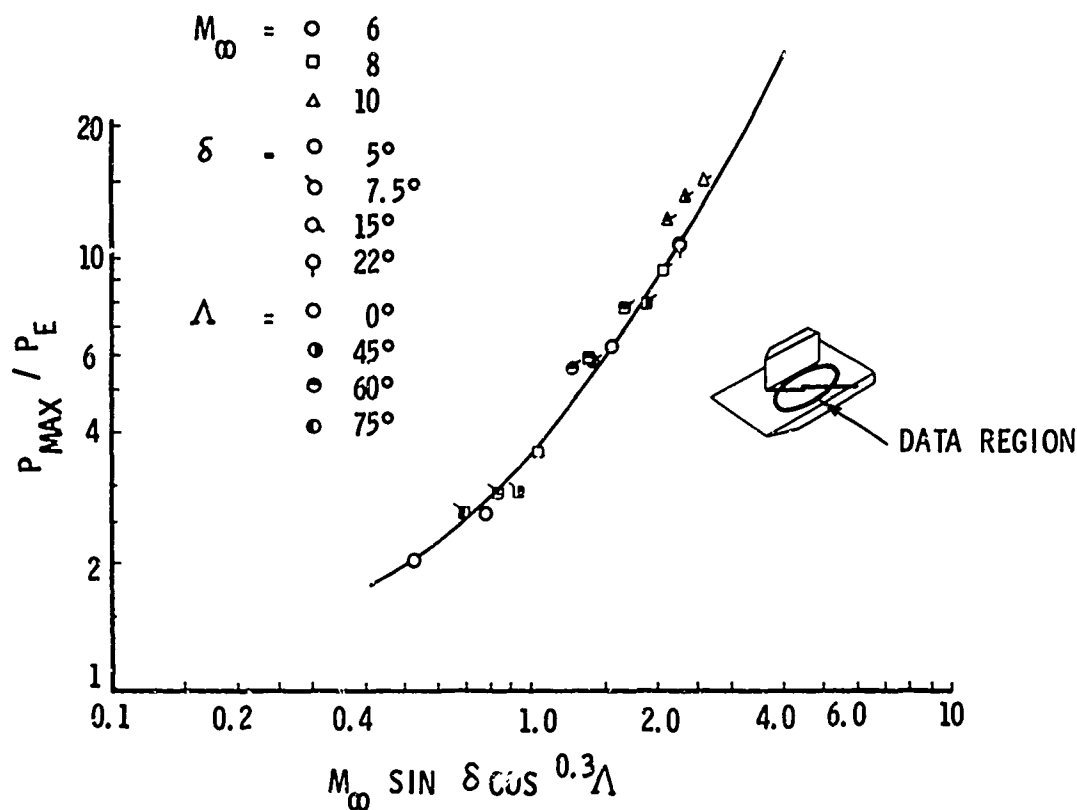


Fig.III-16 Correlation of peak pressure data measured in the fin interference region

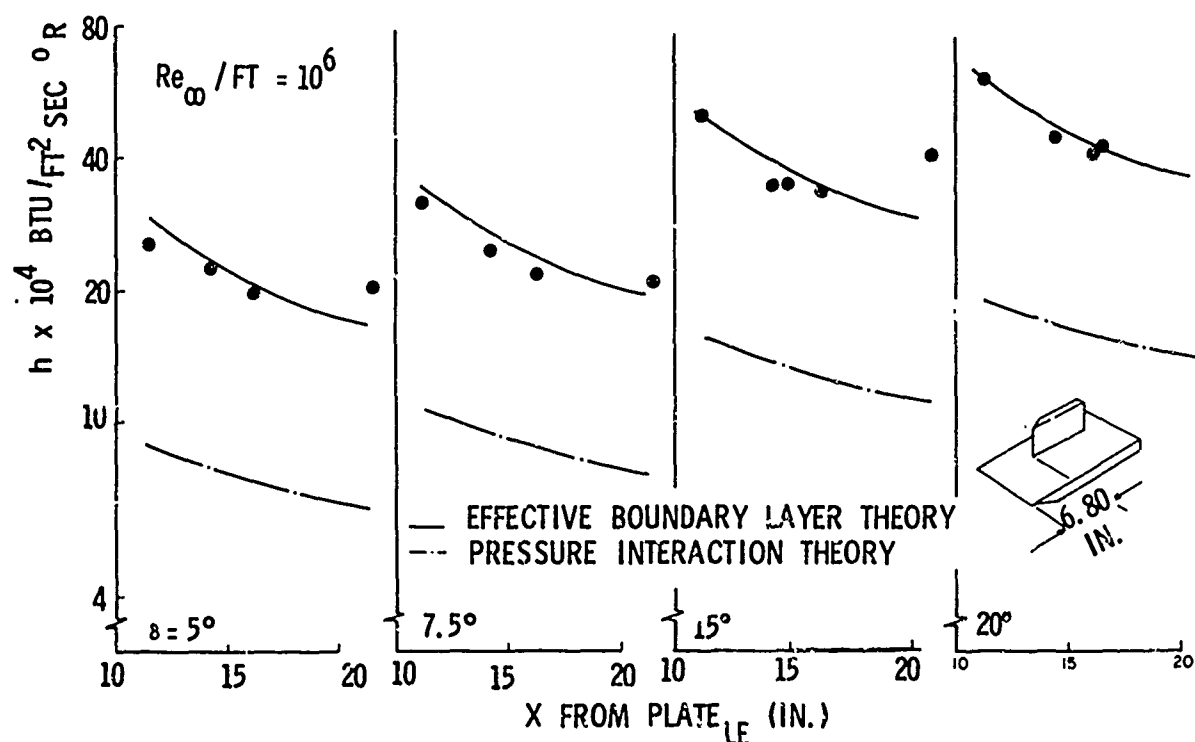


Fig.III-17 Correlation of the maximum heating in the fin interference region - Mach 6 laminar flow

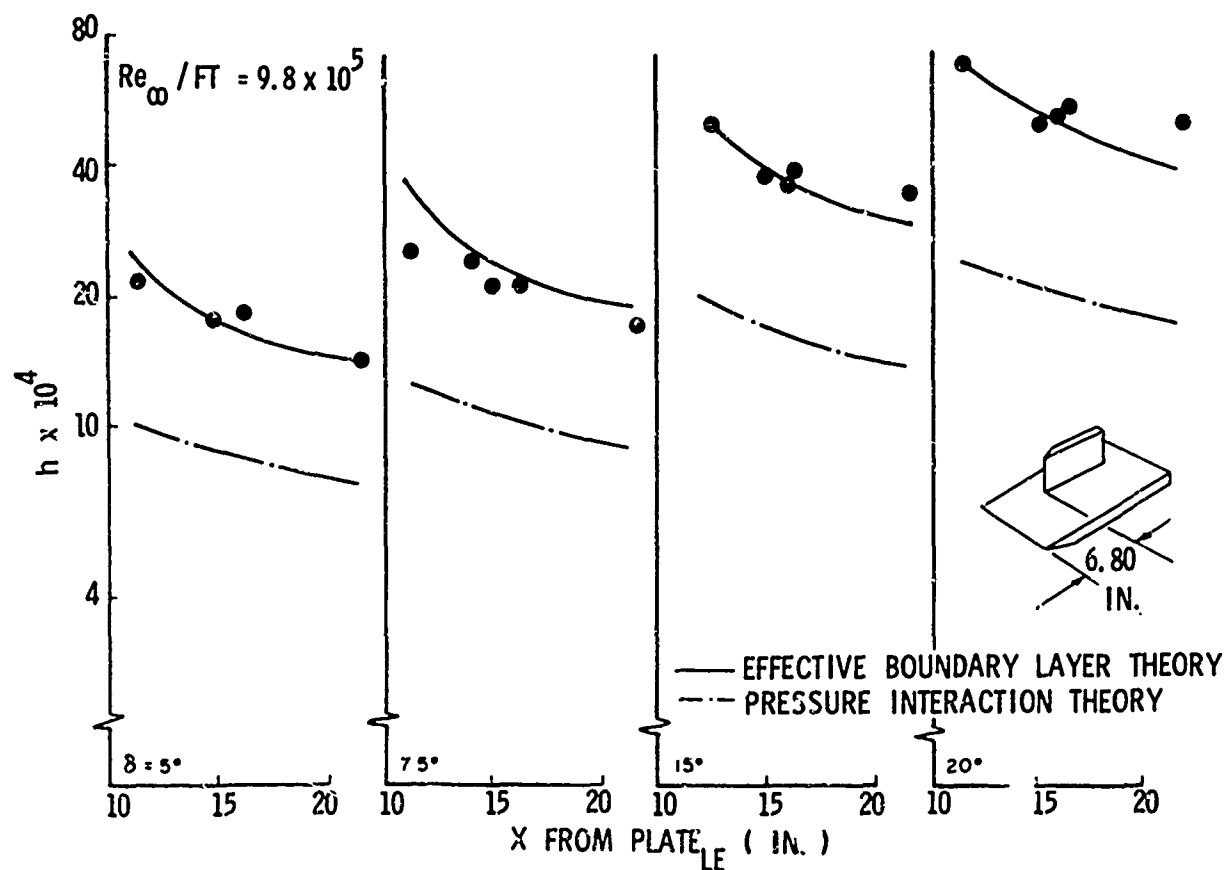


Fig.III-18 Correlation of the maximum heating in the fin interaction region - Mach 8 laminar flow

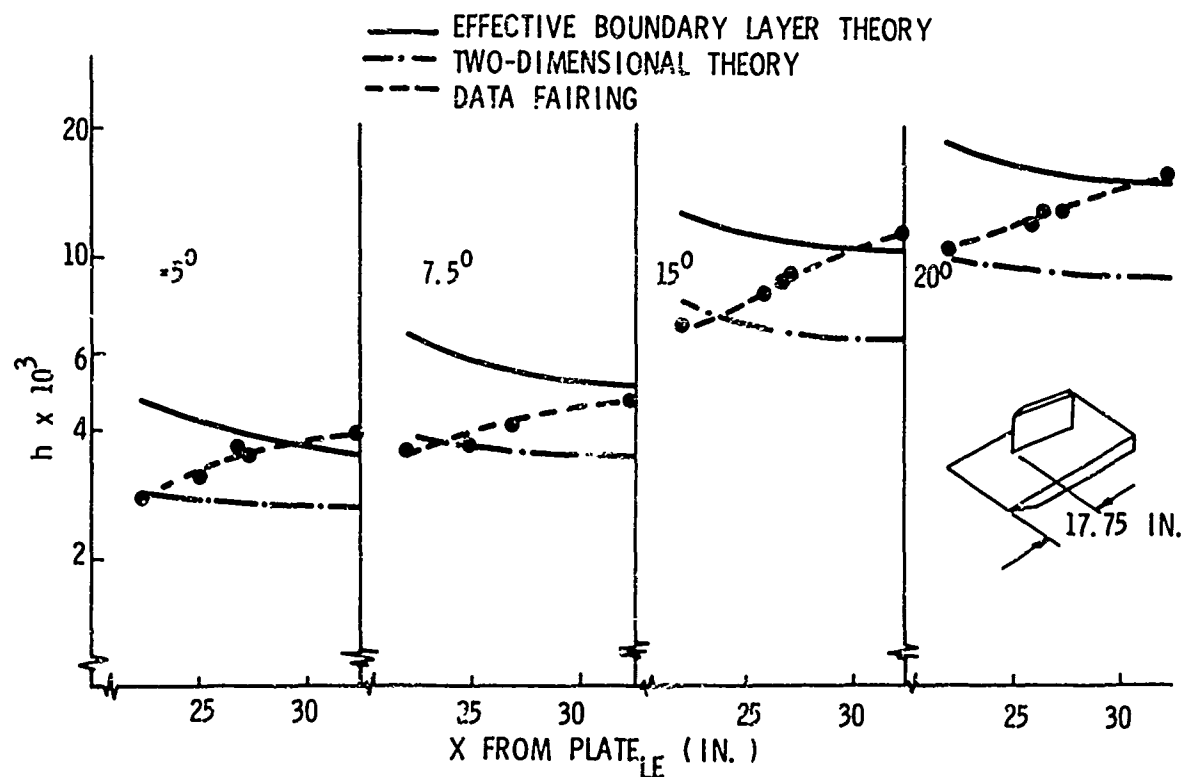


Fig.III-19 Correlation of the maximum heating in the fin interaction region - Mach 6 turbulent flow

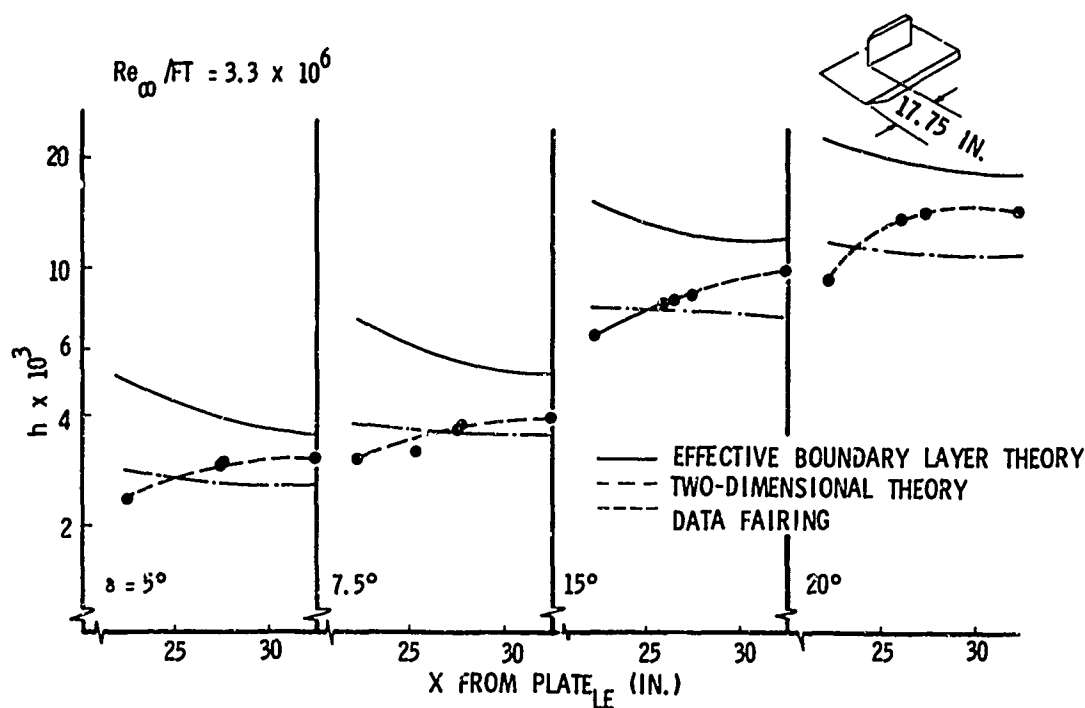
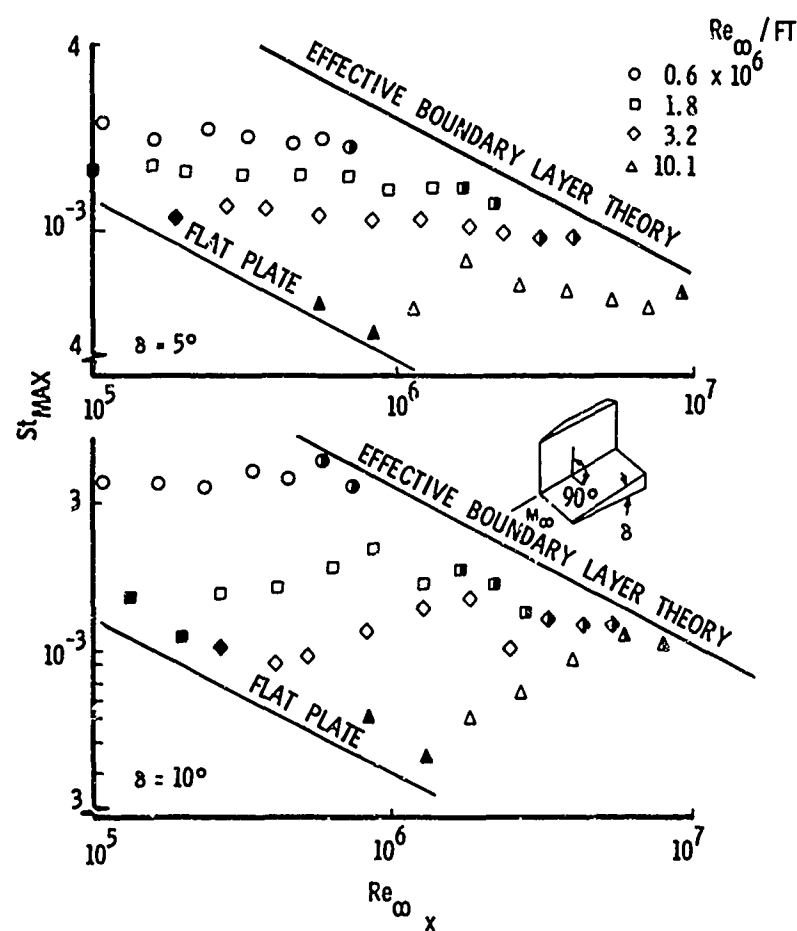


Fig.III-20 Correlation of the maximum heating in the fin interaction region Mach 8 turbulent flow



NOTE: SOLID SYMBOLS ARE AHEAD OF THE INTERACTION
HALF OPEN SYMBOLS ARE IN A FULLY DEVELOPED INTERACTION

Fig.III-21 Correlation of Stainback's Mach 8 fin interaction data

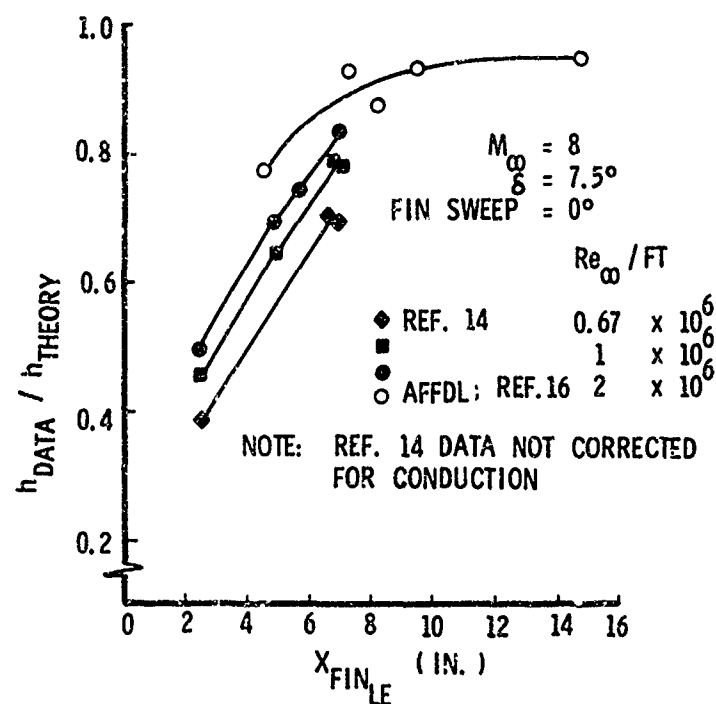


Fig.III-22 Comparison of fin interaction data taken

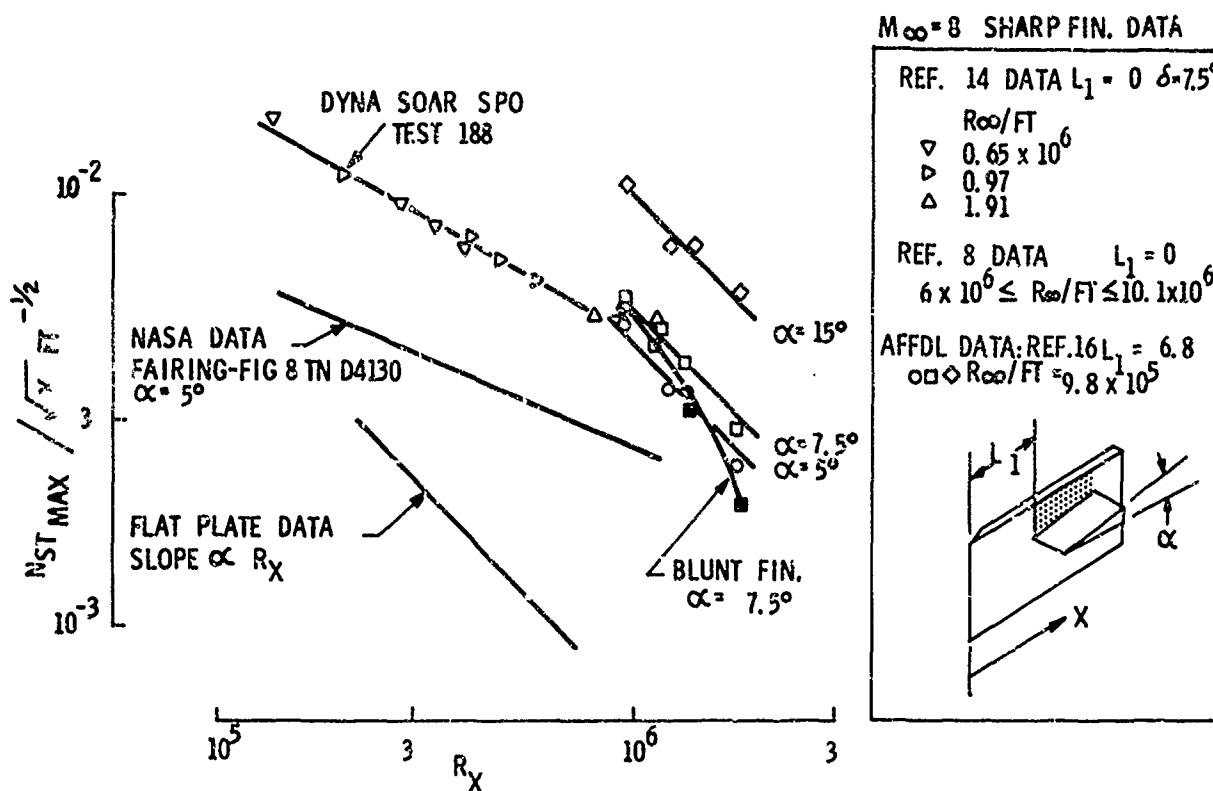


Fig.III-23 Comparison of data on three-dimensional interference heating

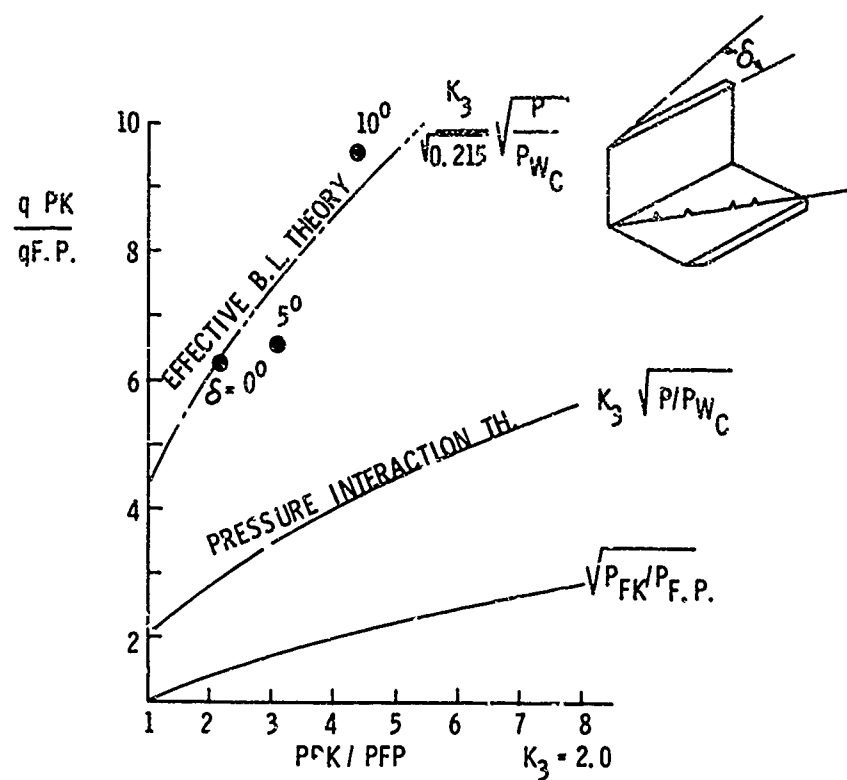


Fig.III-24 Correlation of data by Watson and Weinstein¹⁵ — at Mach 20 in helium

SECTION IV - NUMERICAL TECHNIQUES

IV-1 INTRODUCTION

The next decade or two will see a rather interesting competition in engineering to generate flow field data for conceptual configurations. The competition will be between high-speed digital computers generating so called "exact" numerical solutions to three-dimensional flow problems and the more traditional airflow measurement in wind-tunnel facilities. There are those who herald on the horizon the end of wind-tunnel facilities with the practical application of these exact methods and others, principally experimentalists, who foresee a cooperative inter-relationship between the two where experiments in either approach would be suggested by the success and/or lack of success in the other.

The area of numerical solution is relatively new. Two-dimensional solutions for perfect gas flows and for flows both in equilibrium and with finite reaction rates have been generated and these solutions and the programs which generate them have been openly reported. Three-dimensional solutions have been considered for the last 10 years with progress impeded by the size of, cost of and availability of computing equipment necessary to generate engineering solutions. The Air Force Flight Dynamics Laboratory has pursued a continuing program in the area of generating engineering solutions for fully three-dimensional flow fields over this time period sponsoring the work of Moretti of GASL, Powers et al. of Northrop and Strom of Cornell. Much progress has been made with respect to program formulation, accuracy and approach. However solutions have, in general, been limited to the more classical shapes of right circular cones at low angles of incidence. The generation of flow field data on more practical delta wing configurations is not yet to the engineering solution state and hence as yet there is no contest between the two approaches.

The challenge of the digital computer to generate competitive data to the classical wind tunnel is based to a large extent on the inability of the wind tunnel to support the design engineering efforts through a lack of diagnostic instrumentation compatible with three-dimensional shapes and, as well, a lack of rapid response to the design engineer early in the design evolution. In Section VI of this report ground test facilities will be discussed in greater depth with the emphasis toward generating data with which to prove a configurational concept. There are, however, various other goals for ground test facilities toward the understanding of three-dimensional shapes both in the more fundamental understanding of three-dimensional behavior and to guide in the design process and screen candidate concepts to focus on and eliminate undesirable configuration qualities early in the program. Facilities supporting this latter goal would generate representative hypersonic data but their range of operation and ultimate test capability would be subjugated to the limitations and capabilities of accurate instrumentation to evaluate three-dimensional flow fields. An excellent example of such a concept is the electron beam diagnostic work which allows one to visualize three-dimensional flow fields and evaluate shock-layer properties but which will only operate in facilities at pressure levels less than 1 mm Hg.

This section will indicate in some detail the present state of development and problem areas - both demonstrated and anticipated - in the generation of three-dimensional flow fields. It is not the intent of this section to develop mathematical detail but rather to give physical interpretation to the approaches and problems of three-dimensional flow.

IV-2 APPROACHES

The most direct approach to the solution of flow fields about generalized three-dimensional bodies, and probably the most meaningful approach physically, is to solve the complete Navier-Stokes equations. Unfortunately, even with modern high-speed computers, this approach is not presently practical. It is necessary, then, to simplify the equations into a more tractable form. The obvious way is to divide the flow into viscous and inviscid layers. The viscous layer must be further divided into laminar flow, turbulent flow, and separated flow. Only laminar attached flow solutions will be discussed here. For some methods it is necessary to divide the inviscid layer into subsonic and supersonic regions. Even with these simplifications the equations to be solved are nonlinear partial differential equations of the elliptic, hyperbolic or parabolic type, and do not lend themselves to analytic solutions. Numerical approaches must therefore be developed. These approaches can be broken down into two broad techniques, the method of integral relations, and the replacement of the partial differential equations by a system of difference equations.

The method of integral relations permits a direct numerical integration of the equations between two known boundaries (i.e. the shock wave and the body wall) and is of particular use in subsonic flow in front of a blunt body. The technique involves the reduction of the partial differential equation set to ordinary differential equations by approximation with a polynomial series. The resulting ordinary differential equations can be solved by numerical integration. The method was first suggested by Dorodnitsyn¹ and successfully demonstrated for axisymmetric flow by Belotserkovsky² and extended to problems in three-dimensional flow by Belotserkovsky and Chushkin³. Chushkin⁴ also reports the application of integral relations to three-dimensional supersonic flow about bodies at incidence by Katskova and Chushkin⁵.

These techniques are distinguished by their simplicity, however they do not supply data between the shock and body nor have they been demonstrated to function efficiently in purely three-dimensional supersonic flow. In addition, they may violate the zone of dependence which will be discussed later.

The method of finite elements which can also be used for solving a set of partial differential equations is related to the method of integral relations. The significant feature of this method is that the flow field must be divided into a set of finite elements or cells with the values of the dependent variables prescribed at specific points (nodes) or on the surfaces (faces) of the elements. The dependent variables must be continuous across the element and in general must be continuous at the interfaces between elements. Utilizing the functional relations between the independent and dependent variables and some appropriate method of solution (for example, the calculus of variations, the method of steepest descents, the residual finite element method), an expression for the dependent variables can be found subject to the boundary constraint. The form of this expression depends on the method of solution, but the expression can in general be evaluated by numerical methods.

The application of the boundary conditions is, in general, easy in the method of finite elements. However, the coordinates of the body must be transformed into some system to permit regular construction of the finite elements. This constraint is not as significant as it first appears in that the elements may be curvilinear, each boundary, however, must lie on the surface of a set of the elements. Because the functions must be continuous, discontinuities are not allowed in the flow field, although this constraint is also less restrictive than it might appear.

A paper by de Vries, Berard, and Norrie⁶ on the application of finite elements to two-dimensional steady, inviscid, irrotational, compressible flow has been reported by de Vries⁷. In principle, this technique is extendable to three-dimensional flow, but a practical program utilizing it has not yet been formulated.

The majority of three-dimensional programs developed to date have used difference equations. These approaches break down into two further groupings, steady and unsteady solutions. The steady state solutions can further be subdivided according to the direction and manner in which differences are taken. Only two possibilities will be considered here, differences along some physically defined surface and differences along some arbitrary coordinate system. The former are characteristic solutions and involve the most complex coding but boundary conditions are easy to apply and the solution follows the natural flow making interpretation easy. In general, the solutions will obey the stability criteria to be discussed later. The arbitrary coordinate system leads to a much simpler coding and in general much faster computer times. However, boundary conditions are not easy to apply and the stability criteria are difficult or impossible to impose.

The problem of stability is of utmost concern in any finite difference scheme. What is needed is a statement of the necessary and sufficient conditions for stability. Unfortunately, for nonlinear partial differential equations, necessary *and* sufficient conditions are not available.

The Courant-Friedrichs-Lewy (CFL) stability condition is well known. It states that the domain of dependence of the differential equations must be completely contained in the domain of dependence of the difference equation. The domain, or zone, of dependence can be seen in Figure IV-1, it is simply the locus of points on the initial value surface from which a disturbance signal can propagate through the new point P . The domain of influence is obviously the locus of a disturbance propagated forward from the initial value surface. The geometric meaning of the CFL stability condition is shown in Figure IV-2. For the differencing scheme to be stable, an irregular polygon connecting the points used in the difference equation must completely encompass the domain of dependence. Thus the lettered points must be used in the difference equation, the numbered points, if used, would result in an unstable solution.

The CFL is not a sufficient condition for stability, nor is it the only necessary condition. Another condition is the von Neumann stability condition which states that the absolute values of the eigenvalues of the amplification matrix must be sufficiently small for the differencing scheme to be stable. For linear equations this can be evaluated, in general for nonlinear equations it cannot. Bramerd⁸ reports that numerical experiments indicate that the maximum step size allowed by the von Neumann condition is, in many cases, more stringent than the CFL condition and may cut the maximum step size to one half that allowed under the CFL condition. More typical step sizes are 0.75 to 0.9 of the CFL value.

Both of the commonly used methods of solving the flow field problem rely on converting the boundary value problem into an initial value problem to permit numerical solutions. Thus each solution will be obtained by marching forward in steps from an initial value surface to a new data surface. At the completion of the new data surface, it will become the initial value surface for another step forward.

IV-3 STEADY-STATE SOLUTIONS

Spatial characteristics are, of course, applicable only to regions where the flow is supersonic. Several methods are available for providing an initial value surface in the supersonic flow region if the subsonic flow has rotational symmetry. For bodies without rotational symmetry in the subsonic region, only special cases can be handled. The existence of an initial value surface will be assumed for purposes of this discussion.

Many methods for locating the characteristic surfaces for three-dimensional characteristics have been suggested. Only three schemes will be described to illustrate the methods and problems.

One method is the tetrahedral characteristic line network shown in Figure IV-3. Suppose three points are chosen on the initial value surface and Mach cones are constructed from each point opening downstream in such a way that they have a common intersection. A surface tangent to a Mach conoid is a characteristic surface and the line of tangency is a bicharacteristic. Thus the three lines connecting the base points and the downstream point are by definition bicharacteristics.

A streamline can now be passed back through the intersection to the initial plane giving four equations to solve for four unknowns. This array has the very desirable feature of requiring only one interpolation in the initial plane (for the streamline intersection) with all other base point data known. Unfortunately this scheme violates the CFL criteria immediately. Referring to Figure IV-2, it can be seen that using the numbered points results in an unstable difference scheme.

Figure IV-4 shows a modification of this technique suggested by Thornhill⁹ and Ferri¹⁰ called the tetrahedral characteristic surface network, which makes use of three planes connecting the three known points on the initial plane and intersecting at the new point. While this does satisfy the CFL criteria, it does not necessarily satisfy the von Neumann condition. A program using this technique will be discussed later.

The best known characteristics programs in use today are based on characteristic surfaces and bicharacteristics as shown in Figure IV-5. A major problem faced in the development of any characteristic solution in three dimensions is the location of the new downstream point. It is immaterial whether Mach cones are extended forward and their intersection located, or a point chosen and a Mach cone extended back to the initial value surface, the location and data at this point will require iteration for nonlinear equations. Several schemes have been devised to reduce this problem. In one developed by Strom¹¹ a reference plane normal to the longitudinal axis of the coordinate system is constructed and a streamline from a known point or on the initial value surface passed forward to intersect this plane. Here, iteration is required to locate the intersection of the streamline and the plane, the path of the streamline being a function of density and velocity gradients along the streamline. A Mach cone is now passed back to intersect the initial value surface, the base points of the characteristics located and base point data obtained by surface fitting of the nine points surrounding the three base points. The principal advantage of this system lies in the following of the streamlines, allowing chemistry to be handled along the streamline without interpolation.

One difficulty encountered with this system is the "bunching" of streamlines and, consequently, the data becoming nonuniformly distributed on the new initial value surface. Experience with this program has shown stable step sizes to be very small, with the result of excessively long computer run times for useful bodies. Other difficulties with this method will be discussed later.

To simplify the locations of the new downstream point and maintain as uniform spacing of points as possible, Ferran¹² devised what has been called the method of near characteristics^{13,14} shown in Figure IV-6. This method has been adapted by Moretti¹⁵ and has also been modified by Rakich¹⁶. It is of at least historical interest that Ferran used this technique to hand calculate a three-dimensional flow field. In this technique two orthogonal sets of reference planes are established, one set being the initial data surface, the other meridional planes. In Moretti's method, two points on the initial value plane are chosen and Mach cones extended forward until they intersect. This constitutes a new point and the procedure is continued until all points on the new surface between the shock and the body have been located. These points do not, however, lie in a single plane and are therefore not suitable for use in a finite difference scheme to obtain cross derivatives (i.e. circumferential derivatives). To circumvent this, Moretti establishes a reference plane and locates the intersection of streamlines connecting the new points to the initial value surface. He then performs a linear interpolation along the streamline to obtain data for a new surface. When all the computations are complete, he has a new data surface (or reference plane) in which one dimension is constant and another dimension varies uniformly. Thus cross derivatives can be obtained by finite differencing techniques. This also leaves a new initial value surface for the next step forward.

In the modification of Ferran's near characteristics by Rakich, the reference plane is selected, based on the CFL criteria, prior to the beginning of a new plane of data. A streamline is passed forward to the new surface and a Mach cone extended back to the initial value surface. The bicharacteristics are then projected onto the meridional reference plane and the finite difference taken along these near characteristics. Note that in this system as opposed to Moretti's interpolation is done for the base points, not for the new initial value surface. Rakich also fits data on the meridional planes for cross derivatives using a Fourier Series. Thus a second degree interpolation is used in the meridional reference plane for base point data with the cross derivatives supplied by fitting circumferential derivatives with a Fourier Series.

The technique developed by Powers¹⁷ is similar to that of Strom¹¹, except the new initial value surface is a left-running characteristic. At each point on the initial value surface a streamline is passed forward until it intersects the next left-running characteristic surface. The spacing between characteristic surfaces is arbitrary. Therefore, the step size is set by a user controlled expression, which is a function of the meridional angle, allowing the step size to vary from the windward to the leeward. Once the intersection of the streamline and the left-running characteristic

is located, a Mach cone is constructed back toward the initial value surface and the base point data obtained by interpolation. These values are then used in the finite differencing to obtain data at the new stream point.

Without going into extensive detail on the various characteristic systems, there are some simple comparisons that can be made and significant differences that should be pointed out. First, in Moretti's method, cross flow must remain small or the equations are not valid. Rakich does not appear to be limited to small cross flow, but there is a question about the validity at low Mach numbers and highly three-dimensional flow. Rakich properly considers the CFL criteria (Moretti did not) but considers the von Neumann criteria only by implication. He observed stable solutions when the maximum step size was 80% of that allowed by the CFL criteria. This compares favorably with Brainard's⁸ estimate of the von Neumann limit. Rakich has used his technique to solve the flow about cones at angles of attack, and suggests the method can be applied to other shapes, for example slab delta wings. Moretti's program has been used for cones and angle of attack although it was developed for slab delta wing configurations.

Powers handles the surface fitting by transforming into a new coordinate system based on the streamline base point and the velocity vector at that point as shown in Figure IV-7. The coordinate system is described by defining a tangent to the initial value surface, choosing the Z axis as the cross product of the velocity vector. The base points of the Mach conoid opening upstream from the new point are now chosen to lie on (or near) the Y and Z coordinates. Thus interpolation is required only on one variable. Note, however, that this fitting is really a two-parameter fit, with one parameter assumed small in comparison to the other.

Strom also transforms to a local coordinate system, then literally surface fits data to obtain base point data. He chooses the 9 points on the initial value surface surrounding the streamline, and fits them with a polynomial containing 9 terms and including powers of $X^2 Z^2$.

The programs of Strom¹¹ and Powers¹⁷ were efforts to avoid any of the approximations used by Moretti and which may be present in Rakich's program. They result, however, in program logic far more complicated than either reference plane method, and more significantly, the requirement for two-parameter fits at the base points. At the present time this requirement appears to be the single most difficult problem in three-dimensional flow. As long as the flow remains reasonably uniform both work well, however, for many configurations, for example cones at angle of attack, slab delta wings, etc., the flow does not remain uniform, even over the small surface being fitted. This "warped" surface gives rise to bad base point data and results in eventual failures, generally due to pressure oscillation. In attempts to avoid this problem both programs make use of "averaging" techniques. Powers passes back four bicharacteristics, using the four resulting expressions in three sets of three to calculate the three unknowns. The resultant unknowns are then averaged, in some cases with certain combinations weighted, to obtain the final result. Strom actually passes back nine bicharacteristics and solves them as three groups of three for the unknowns, also averaging the results.

Both these techniques appear to be "smoothing" initial value plane data. When the initial value surface is not warped, they are adequate; they are not satisfactory when a warped surface occurs.

Because of the complexities of coding characteristic solutions and the difficulties encountered in numerical surface fitting, efforts have been made to develop a finite differencing scheme not tied to the physical flow. One of the most recent efforts is a program by Kutler and Lomax¹⁸ which is apparently very successful. By use of a differencing scheme suggested by MacCormack¹⁹ advancing through a fixed Eulerian mesh, the program has the property of shock capturing. Thus, given boundary conditions as the body boundary and the freestream, shock and expansion waves are allowed to form and decay automatically. Kutler has run the program on a digital computer employing interactive graphics allowing man-machine interaction to control any numerical instabilities that evolve. The program does have drawbacks, the grid used is closely related to the body shape as in Figure IV-8, requiring that the program be, in effect, rewritten for each different shape to be examined. The results differ slightly depending on the direction the shock is moving in the grid and whether forward or backward differences are being taken. Finally, it cannot supply a precise location or intensities of shocks.

IV-4 UNSTEADY SOLUTIONS

One of the problems encountered in any steady flow solution is the variable nature of the equations that must be solved. Thus several different techniques have to be used in various portions of the body to handle the subsonic, transonic and supersonic flow. In addition, if spatial characteristics are being used and the flow becomes subsonic in the afterbody or supersonic region, or encounters a shock, the hyperbolic equations cease to be valid, resulting in failure in the numerical program. To circumvent this problem, steady solutions can be obtained by utilizing unsteady techniques and allowing the time to become large so the flow has effectively reached a steady-state condition. Obviously, such techniques are applicable to unsteady problems which may have to be solved also.

The addition of time to the basic system of equations to be solved results in a system that is everywhere hyperbolic in time. Two choices are again available for solving the resulting set, making use of the characteristic property of the equations in the time plane and some finite difference scheme based on the coordinate grid.

A characteristic method for equations in four independent variables has been described by Roesner²⁰. The description of this technique in geometric form is obviously difficult, however the matrix equations used are straightforward. The tetrahedral characteristic surface network is the basis of this scheme. Each new point is located by the intersection of three planes extended in the "time-like" direction from lines connecting the three points on the "space-like" surface. Bicharacteristics are the lines of tangency between these planes and the characteristic conoid from the new point. Two choices are available, keeping the initial value points constant and allowing the new points to fall at various times or forcing all new points to lie on a constant time plane and interpolating in the initial value surface for base point data. Roesner chooses the former course with the argument that in this manner only one interpolation need be made and that made at the conclusion of the process when time is large (i.e., properties are relatively unchanging at a point). This technique is reported to have been used in the three-dimensional flow field. A major advantage of the system is the use of fixed base points, thus eliminating the requirement for much interpolation. The system is constrained to regions not having imbedded discontinuities thus violating one of the basic reasons for going to unsteady solutions.

Roesner states that by its very nature the technique cannot violate the CFL stability criteria. Because it is in four-space, it is difficult geometrically to show that this is indeed the case. He does point out that in each problem one must balance the requirement for accuracy with the storage capacity of the computing machine and the step size in the time plane (and consequently the running time of the problem).

There have probably been more unsteady solutions suggested utilizing a curvilinear coordinate system based on the body and shock (similar to the steady finite difference system) with the finite differencing done in the time plane. While the coordinate transform is not straightforward in all cases, in most practical cases it can be accomplished with a minimum of effort and the resulting set of equations does lend itself to straightforward machine work. For the most part such programs utilize Lax-Wendroff²¹ differences or a variation thereof. The best known published example of this type is the work of Moretti and Abbett²² although there are numerous internal publications describing schemes of this type.

The primary advantage of this system is the extreme ease of preparing the machine program for the calculation and the speed with which the individual calculations can be completed on the computing machine. The choice of utilizing a shock capturing approach or the sharp shock technique is available, the choice of implicit or explicit differencing is also available, although almost all choose an implicit differencing scheme. It is a very promising technique.

It does, however, have drawbacks. First, all of the points in the flow field for which calculations are to be done must be specified at the start of the calculation with all the initial data given. These points are all allowed to relax simultaneously to a steady-state solution. Because these points must all move forward in time together, the steepest gradient in the flow field controls the step size for the entire flow field. This effectively means that for practical three-dimensional problems, the number of flow field points required can tax the capacity of the largest computers and the time required to make the tremendous number of calculations necessary to reach a steady state is large even on the fastest computers. This is a particularly vexing problem when the body is large and suspected steep gradients are forcing closely spaced flow field points to supply the necessary detail.

There is one final problem common to all unsteady solutions that should be considered. The basic assumption is that the variable, or variables, used to identify the steady-state condition is approaching that condition along a steep gradient so that when the change in the value of the variable is less than some predetermined value during a time step, it can be said that the solution is reached. Unfortunately, this is not known in general at the beginning of the problem. It is entirely possible that the gradient is sufficiently shallow that the numerical accuracy limit imposed by the computing machine cannot detect the slope.

IV-5 BOUNDARY-LAYER ANALYSIS

Because of the complexity of three-dimensional boundary-layer theory, the most popular approach until recently was a quasi-two-dimensional calculation obtained by assuming small cross flow. There are two major drawbacks to this approach. First, for many shapes of practical interest, the cross flow is not small, moreover, even when cross flow is small, the cross flow derivatives, which are neglected in small cross flow theory, are not small. It has also been suggested that the term containing the cross flow derivative is a dominating term affecting three-dimensional boundary-layer separations.

In the second place, small cross flow calculations, in general, violate the influence principle suggested by Raetz and Der. A zone of influence is formed because a disturbance is convected at flow velocity along the streamlines. In general the streamline is curved and the centrifugal force is balanced by the cross flow pressure gradient. Because the pressure is constant across the boundary layer while the velocity varies, the flow angle must be varied to maintain the same centrifugal force. This results in an upstream wedge which forms the zone of dependence and a downstream wedge which is the zone of influence, as shown in Figure IV-10.

Several recent investigators have, however, developed three-dimensional boundary-layer techniques^{17, 23, 25}. All of these techniques are finite difference method, Der's¹⁷ being an explicit finite difference while Hall, Dwyer and Wang²³⁻²⁵ have used implicit schemes of the Crank-Nicholson type.

The method suggested by Raetz and Der and the method of Wang will be discussed briefly to show problems encountered.

Figure IV-9 shows the five boundaries required by Der's boundary-layer scheme, body surface, the inviscid-viscid interface, two side boundaries and an initial value boundary. The viscid-inviscid boundary conditions are supplied by an inviscid calculation and include pressure and/or temperature distribution plus the velocity vectors. These can be approximated by Newtonian theory for the initial try in the Der program.

The body conditions are normally defined as, for example the body geometry, wall temperature and boundary layer suction or injection. Side conditions are normally specified by choosing a plane of symmetry, for example, the top and bottom centerline. The initial value surface is in general unknown. This surface can be found by approximating the surface, then iterating until the inviscid and wall boundary conditions are satisfied.

Raetz and Der define an arbitrary, orthogonal grid composed of cells $\Delta\xi \times \Delta\zeta \times \Delta\eta$ where ξ is the down-stream coordinate, ζ is the lateral coordinate and η the normal to the body surface as shown in Figure IV-11. Normally $\Delta\zeta$ and $\Delta\eta$ are chosen so as to be equal. However, in order to obtain stability, Der¹⁷ found that $\Delta\xi$ must be much less than $\Delta\zeta$. Der cites an approximation in the finite differencing equation as the reason for this. The error introduced by the approximation is

$$\left(\frac{\Delta\xi}{\Delta\zeta}\right)^2 \frac{\partial^2}{\partial\xi^2}.$$

While this is no doubt true, a more physical, if not better, argument can be found. Remembering the zone of dependence and the CFL criteria, we see that, for large cross flow the distance between planes must be small to ensure the difference equations do indeed meet the CFL criteria. There can be no assurance of stability if the condition is not met. It should also be noted here that, as pointed out by Wang²⁵, the constraint $\Delta\xi$ very much less than $\Delta\zeta$ does not guarantee the CFL criteria will be met at each plane.

One unsolved problem in three-dimensional flow is the location of separated regions. Der numerically defines the approximate line separation as the line dividing regions of positive and negative longitudinal wall shear. Thus, when the longitudinal wall shear becomes zero or negative, the flow is assumed to have separated and no further calculations are made along that longitudinal coordinate.

Der has published results for boundary layers on a 15° spherecone at angle of attack²⁶, a delta wing with elliptical cross section and a 3.4.8 ellipsoid¹⁷. It must be noted that the solutions obtained are not completely satisfactory and solutions have not been obtained for all cases attempted. However, it may be due to poor inviscid-viscid interface conditions (specifically, the Newtonian pressure distribution).

Wang²⁵ attempts to avoid many of the problems encountered by Der by choosing a streamline coordinate system as shown in Figure IV-12 and an implicit finite differencing technique. The selection of a streamline coordinate system adds a major complication to the numerical computation, but it does allow the CFL criteria to be met at every step, regardless of cross flow. Wang also reports that his technique correctly handles streamwise vortices embedded in the boundary layer. By using a two-step finite differencing scheme, he requires boundary conditions at a body surface, the inviscid-viscid interface and two successive equipotential lines. Note that a symmetry plane is no longer required. Techniques are available to obtain the initial value lines.

Because of the stability of the Crank-Nicholson finite differencing, the step sizes reported by Wang are relatively large, particularly in comparison with Der's explicit method which requires a very small step size.

How successful Wang's method will be over a general body, for example a slab delta, remains to be seen. He is still faced with two of the difficulties encountered by Der and others. As yet there is no inviscid solution available to supply inviscid edge conditions for the boundary layer. There is also no good method to locate separation. Studies such as those of Wang may indeed improve the numerical understanding of separation, but the inviscid edge conditions must await the development of better inviscid calculations.

In summary, significant improvements in three-dimensional boundary layers must await improvements in the inviscid calculations so accurate edge conditions can be established.

SECTION IV - REFERENCES

1. Dorodnitsyn, A.A. *On a Method of Numerical Solution of Certain Nonlinear Problems in Aero-Hydrodynamics.* Proc. 3rd All-Union Math. Congr., 1956, Vol.3, Akad. Nauk SSSR, Moscow, 1958, pp.447-453.
2. Belotserkovsky, O.M. *On the Calculation of Flow Past Axisymmetric Bodies with Detached Shock Waves Using an Electronic Computing Machine.* J. Appl. Math. Mech. 24, 1960, pp.795-855.
3. Belotserkovsky, O.M.
Chushkin, P.I. *Numerical Method of Integral Relations.* Zh. Vych. Mat. i Mat. Fiz. 2, 1962, pp.731-759.
4. Chushkin, P.I. *Numerical Method of Characteristics for Three-Dimensional Supersonic Flows.* Prog in Aero. Sci., Vol.9, Pergamon Press Ltd, 1968, pp.41-122.
5. Katskova, O.N.
Chushkin, P.I. *Three-Dimensional Supersonic Flow about Bodies.* Paper presented to the VIIth Symposium on Advanced Problems and Methods in Fluid Dynamics, Juarata, Poland, 1965.
6. de Vries, G.
et al. *Application of the Finite Element Technique to Compressible Flow Problems* Mech. Eng. Rep. 18, Dept. of Mechanical Engineering, University of Calgary.
7. de Vries, G.
Norrie, D.H. *Application of Finite Element Methods in Fluid Dynamics.* Von Kármán Institute for Fluid Dynamics Lecture Series 34, Numerical Methods in Fluid Dynamics, 1971 (Unpublished notes.)
8. Brainerd, J.J. *Numerical Analysis of a Method for Calculating Three-Dimensional Supersonic Flow Fields.* UARI Research Report No.44, 1967.
9. Thornhill, C.K. *The Numerical Method of Characteristics for Hyperbolic Problems in Three Independent Variables.* Armament Research Establishment, Report N 29/48.
10. Ferri, A. *The Method of Characteristics.* Section G of "General Theory of High Speed Aerodynamics", Vol.VI, Princeton University Press, 1954.
11. Strom, C.R. *The Method of Characteristics for Three-Dimensional Real-Gas Flow.* AFFDL TR 67-47, July 1967.
12. Ferrari, C. *Determinazione della Pressione Sopra Solidi di Rivoluzione a Prora Accuminata Dispositi in Deriva in Corrente di Fluido Compressibile a Velocità Ipersonora* Atti Reale Accad. Sci., Torino 72, 1936.
13. Sauer, R. *Differenzenverfahren für hyperbolische Anfangswertprobleme bei mehr als zwei unabhängigen Veränderlichen mit Hilfe von Nebencharakteristiken.* Numer. Math., Vol.5, 1963. p.55.
14. Holt, M. *The Method of Near Characteristics for Unsteady Flow Problems in Two Space Variables.* University of California (Berkeley), inst. of Engr. Res. Rept. AS-63-2, Contract No. NONR-22(79), 1963.
15. Moretti, G.
et al. *Supersonic Flow About General Three-Dimensional Blunt Bodies.* ASD TR 61-727, 1962.
16. Rakich, J.V. *A Method of Characteristics for Steady Three-Dimensional Supersonic Flow with Application to Inclined Bodies of Revolution.* NASA TND-5341, 1969.
17. Powers, S.A.
et al. *A Numerical Procedure for Determining the Combined Viscid-Inviscid Flow Fields over Generalized Three-Dimensional Bodies.* AFFDL TR 67-124, December 1967.
18. Kutler, P.
Lomax, H. *A Systematic Development of the Supersonic Flow Fields over and Behind Wings and Wing-Body Configurations Using a Shock-Capturing Finite-Difference Approach.* (To be published, 1971), Ames Research Center, NASA Moffett Field, California.
19. MacCormack, R.W. *The Effect of Viscosity in Hypervelocity Impact Cratering.* AIAA 66-354, 1969, pp.1-7.

20. Roesner, K.G. *Numerical Treatment of Time-Dependent Three-Dimensional Flows.* Von Kármán Institute for Fluid Dynamics Lecture Series 34, Numerical Methods in Fluid Dynamics, 1971. (Unpublished notes.)
21. Lax, P.D.
Wendroff, B. *Systems of Conservation Laws.* Commun. on Pure and Applied Math., Vol.13, 1960, pp.217-237.
22. Moretti, G.
Abbett, M. *A Fast Direct, and Accurate Technique for the Blunt Body Problem.* GASL TR No.583, January 1966.
23. Hall, M.G. *A Numerical Method for Calculating Steady Three-Dimensional Laminar Boundary Layers.* RAE TR 6714, July 1967.
24. Dwyer, H.A. *Solution of a Three-Dimensional Boundary-Layer Flow with Separation.* AIAA, July 1968.
25. Wang, K.C. *Three-Dimensional Laminar Boundary Layer Over a Body of Revolution at Incidence.* KIAS TR 69-13, September 1969.
26. Der, J., Jr
Raetz, G.S. *Solution of General Three-Dimensional Laminar Boundary-Layer Problems by an Exact Numerical Method.* Institute of Aerospace Science, Paper No.62-70, January 1962.

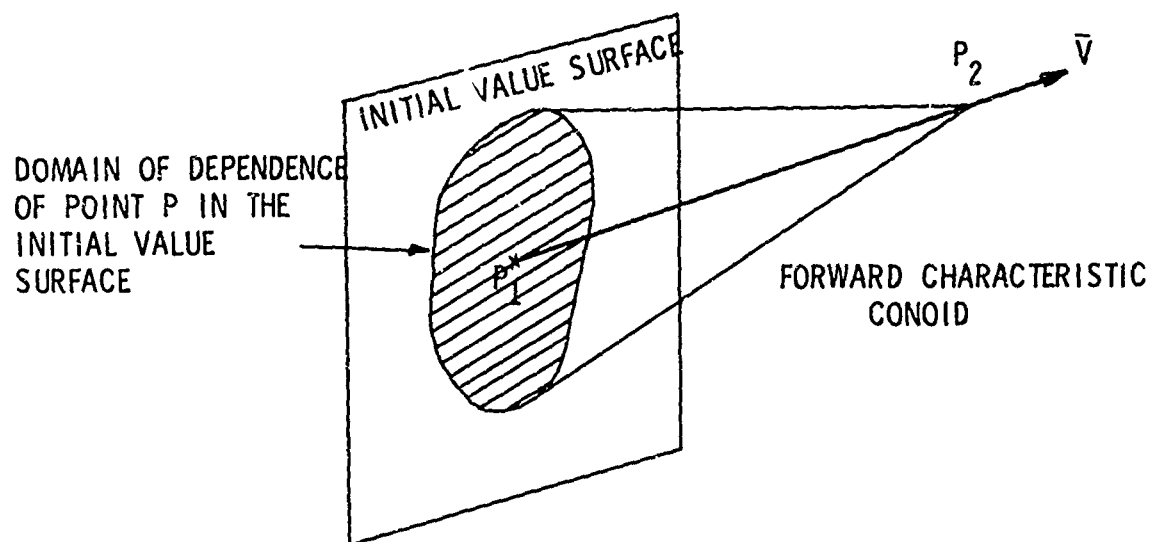
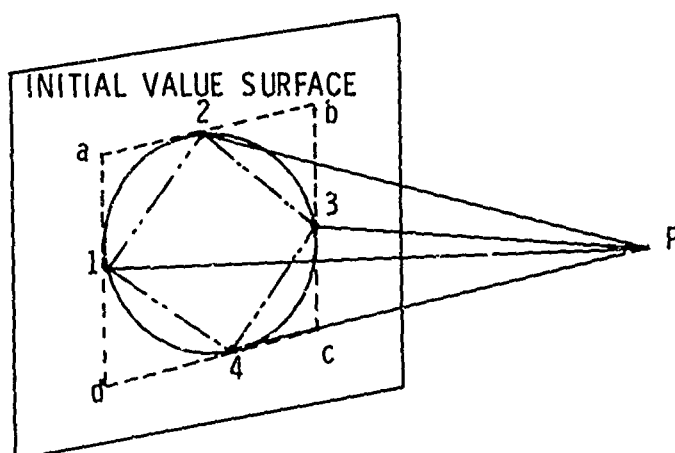


Fig.IV-1 Domain of dependence



BASE POINTS (a,b,c,d) SATISFY CFL CRITERIA
 BASE POINTS (1,2,3,4) DO NOT SATISFY CRITERIA

Fig.IV-2 Courant, Friedrichs, Lewy (CFL) condition for stability

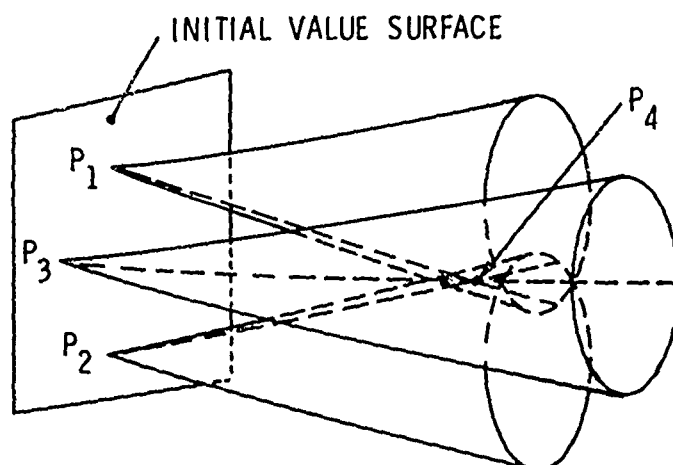


Fig.IV-3 Tetrahedral characteristic line network

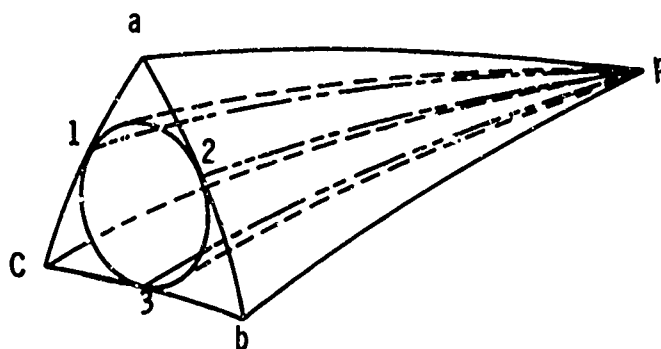


Fig.IV-4 Tetrahedral characteristic surface network

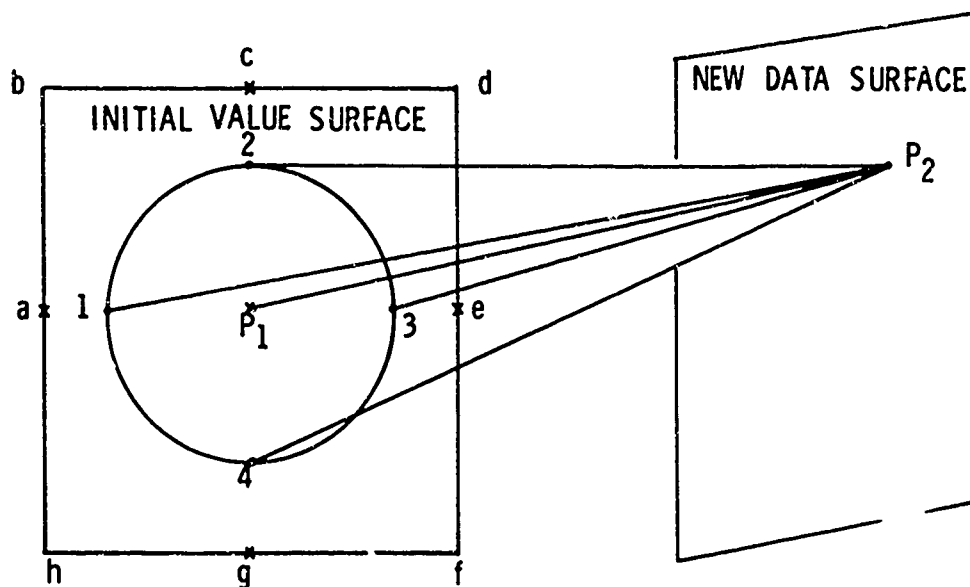


Fig.IV-5 Location of points in Strom's reference plane method

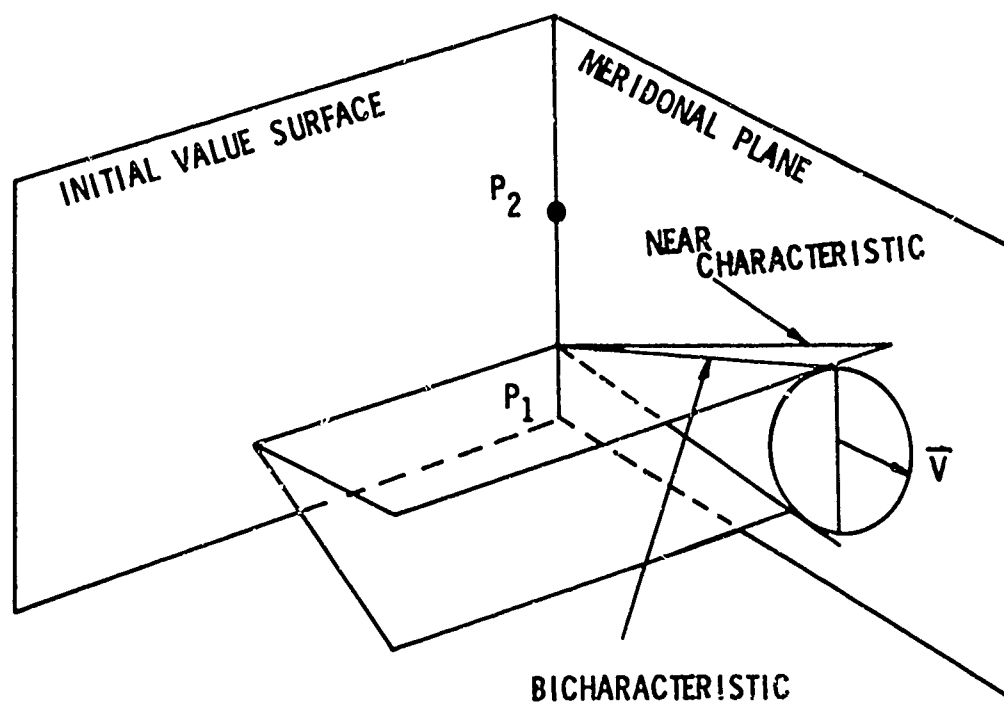


Fig.IV-6 Location of near characteristic

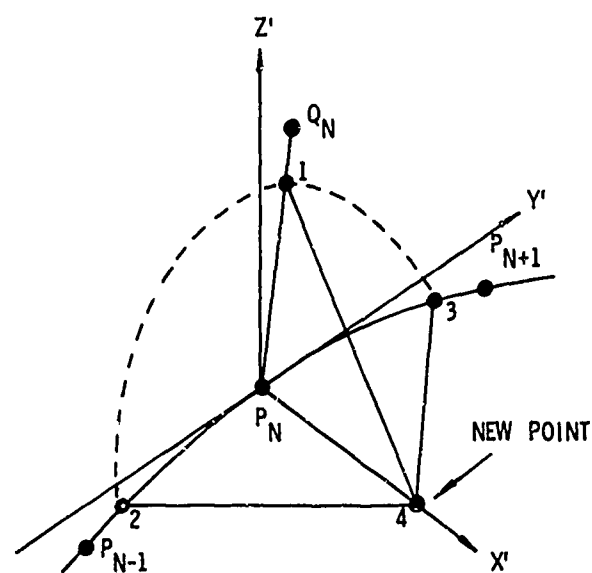


Fig. IV-7 Local coordinate system

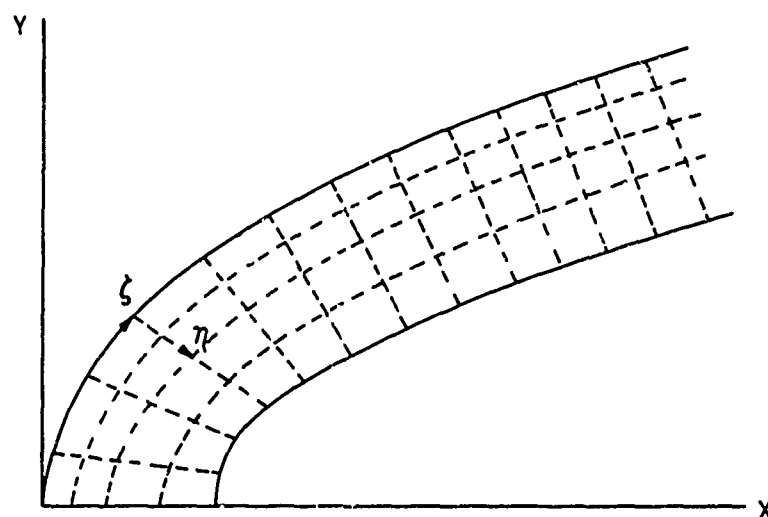


Fig. IV-8 Coordinate system for finite difference technique

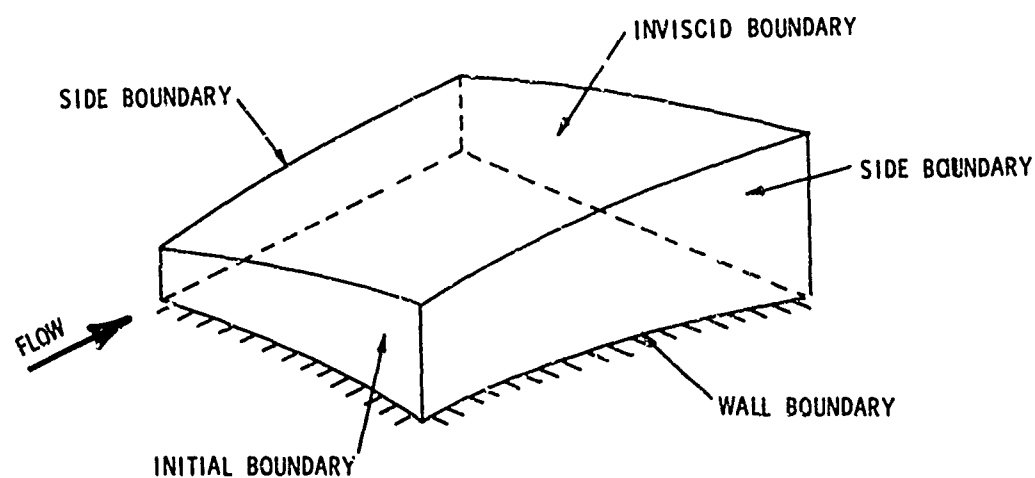


Fig. IV-9 Boundaries for three-dimensional boundary-layer integration

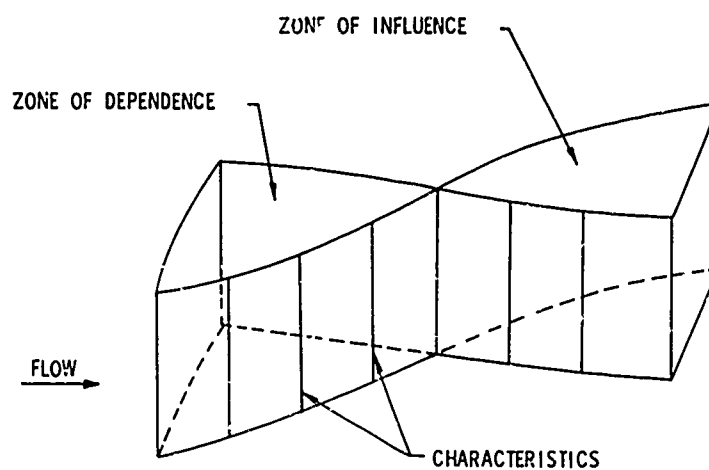


Fig.IV-10 Zones of influence and dependence

$$\Delta \xi \ll \Delta \zeta$$

$$\sim \left(\frac{\Delta \xi}{\Delta \zeta} \right)^2 \frac{\partial^2 \psi}{\partial \xi^2}$$

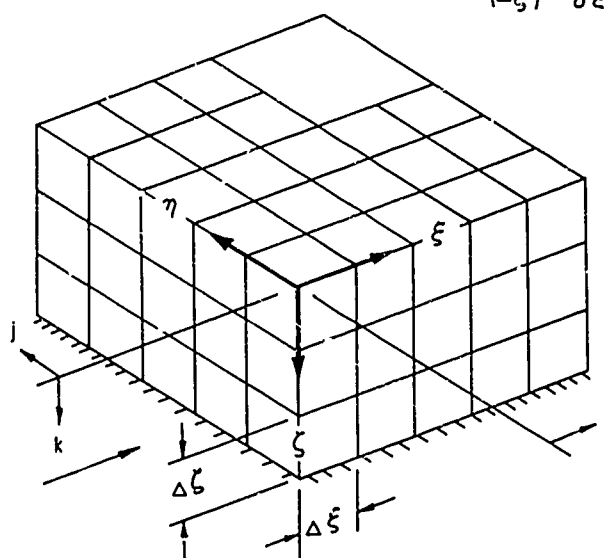


Fig.IV-11 Boundary-layer coordinate system

$\psi \sim$ STREAMLINES
 $\phi \sim$ EQUIPOTENTIAL LINES

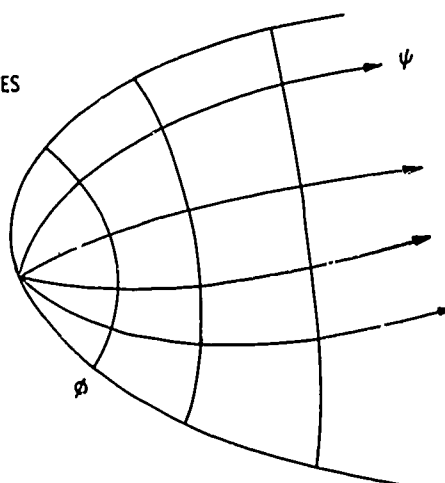


Fig.IV-12 Streamline coordinates

SECTION V - THE ASSET PROGRAM: PROBLEMS OF FLIGHT DATA REDUCTION

Early in the space program the Air Force Flight Dynamics Laboratory was evolving programs to employ aerodynamic lift during the entry process. Such studies were initiated in 1958 through both analytic and experimental studies of generalized delta wing configurations. These studies were not confined to the area of aerodynamics alone but involved all disciplines necessary to configure and design lifting spacecraft. These programs, while obviously influenced by early Dyna Soar research problems, were distinct in their goals and concepts.

In this same time period a research oriented booster program was initiated under NASA auspices and entitled SCOUT. The success of SCOUT as a NASA booster and the adaptation of SCOUT by the Air Force to research programs gave our Laboratory an available tool to employ in atmospheric experiments with subscale aerodynamic configurations. The availability of the SCOUT booster system coupled with the importance which was placed on duplicating the true environment through atmospheric experiments to all disciplines was the key to the initiation of the ACSET program.

Research studies on the preliminary design and operational feasibility of such a configuration were conducted both internally within the Air Force Flight Dynamics Laboratory and under contracts. Such studies were undisciplined in nature stressing either aeromechanics or structures but all studies were constrained by the practical limitations of the BLUE SCOUT* system as follows:

A maximum weight spacecraft of roughly 700 lb.

A maximum surface area of 10 ft².

Figures V-1 and V-2 indicate proposed configurations at this stage of development. Of particular note is the lower surface keel angle - a feature of early hypersonic delta-wing design to assure directional stability

Late in 1960 the individual program goals typifying earlier studies were merged into a single program which would evaluate aerodynamics, structures, and aerothermoelasticity of lifting spacecraft through flight test. This combined approach integrated the experimental objectives of all earlier programs into a single interrelated system and predated the contract with McDonnell Aircraft Corp. to perform the program known as ASSET. The contract with McDonnell was initiated in 1961 and was successfully concluded in 1966.

The name ASSET is derived from Aerothermodynamic/Elastic Structural Systems Environmental Tests which was the program goal. In the present lecture the problems involved and methods of data acquisition and evaluation will be outlined prefaced by this short introduction to the project. Program results are unfortunately classified and cannot be discussed.

Figure V-3 indicates the final ASSET configuration differing from previous designs in that a flat lower surface was employed and a larger equipment bay was incorporated. The configuration was statically stable at trim angle of attack and employed reaction controls to maintain stability about that point. Aerodynamic control surfaces were not employed.

The configuration heat shield was constructed of refractory metal panels insulated from the load-bearing structure. Leading edges were constructed of graphite and the nose cap of zirconia rod.

One immediate result of the fixed planform area constraint for the final flight vehicle, 14 ft², and the physical temperature limits of the nose cap, 4000°F, was that the design flight attitude of the configuration was somewhat higher than desirable and this was aggravated by inevitable increases in vehicle weight which further increased the flight angle of attack.

From Section I recall that functionally the stagnation point heat flux is given as

$$\dot{q} \propto f(V_\infty) \left[\frac{W}{C_L A} \right]^{1/2} R_0^{-1/2}$$

For the ASSET design at its design velocity (VMAX)

$$\dot{q} \propto (W/C_L A R_0)^{1/2}$$

As the planform area was fixed and as the available materials limit the nose heating, i.e. $\dot{q}/R_0 = \text{Const}$ and $A = \text{Const}$, a change in weight, W , must be balanced by an increase in lift coefficient

$$(q/R_0)A = \text{const} \propto W/C_L A$$

* The SCOUT booster was later replaced by Thor boosters allowing additional payload weight and planform area

which increases the vehicle angle of attack

$$C_L = K \sin^2 \alpha \cos \alpha$$

In such a design process the aerodynamic contours are firmed up much faster than the vehicle weight and for such a research mission, the vehicle total weight is highly variable due to the experimental nature of the configuration and payload so that large weight growth is not uncommon.

Increasing the configuration angle of attack reduces the stagnation flux but increases the heating to other body locations. The severity of such heating must be viewed not in absolute terms but in relation to the thermal potential of selected or available heat shield materials.

As a result, most heat shield panels as well as the nose were thermally stressed to their design limits by the configuration, which was flown at wing loadings up to 88 lb/ft².

Data were generated from flights through onboard recording and both real time and delayed playback telemetry. 95 channels of test data were recorded during the flight which included 35 channels of surface pressure and 42 channels of surface temperature data. Figures V-4 and V-5 indicate gage placement and gage type employed on the ASSET configurations.

While the pressure data were easily generated with no particular acquisition or evaluation problems, the thermal data posed several interesting problems both in acquisition and in interpretation which may be of interest to others contemplating such flight programs.

Due to the multiplicity of technical purposes for the ASSET flight test program, techniques for instrumentation employed for rocket propelled free flight models by the Langley Research Center¹ were not appropriate. As opposed to the short flight durations of the NASA probes, of the order of seconds, the ASSET flight duration was of the order of 1000 seconds. In place of a highly transient flight environment where copper or inconel (steel) skin material was employed together with spot-welded thin gage chromel/alumel thermocouples, material tests on high temperature re-radiative refractory metal panels were conducted and temperature levels approached radiation equilibrium which required tungsten thermocouples heavily sheathed against oxidation. Finally, in place of thin and idealized aerodynamic skins, actual spacecraft structures were employed. Figure V-6 indicates a cross section of such a structural arrangement including the refractory metal heat shield panels and subsurface insulation blankets.

Data reduction in such an environment was both complex and expensive. The major steps in such reduction were as follows.

1. Data smoothing to minimize transmitted noise and assure data quality of the transmitted temperatures. In this step, data tapes from several sources covering various phases of the flight were assembled into a single and unified record.
2. Generate a thermal model* for each thermocouple location representing all possible heat paths through the structure and modes of heat transfer.
3. To evaluate heat transfer rates from temperature data through the timewise satisfaction of the thermal models and boundary conditions.
4. To nondimensionalize the resulting iterated heating rate data for data correlations.

Obviously item 3 was the most complex part of the reduction and required large amounts of computer time to complete.

Looking in greater detail at this facet of the data reduction the following problem areas were found important

1. All temperature histories were measured below the mold line.
2. In most instances the heat sink caused by the mass of the thermocouple and its sheath was significant.
3. Thermal resistance between the thermocouple and structure due to mechanical attachments of thermocouples, particularly during large temperature transients, was significant†.
4. Surface emittance and material properties of various heat shield panels varied with temperature and required specific evaluation†.
5. The structure was non-homogeneous and was complex.
6. Thermal radiation was significant both externally and in many cases within the structure.

* The thermal model is a mathematical description of the physical configuration describing the various modes of heat transfer and temperature response of elemental volumes of material.

† Surface emittance data was primarily important throughout the gliding flight, however, material properties and contact resistance data were most important during rapid transients. Particular emphasis was placed on assuring good contact due to the mechanical attachment of thermocouples to the airframe.

Using the transmitted timewise temperature data, surface heat flux was generated by assuming a heat flux and comparing the calculated temperature response of a subsurface point or points with temperature measured at that point. The assumed surface heat flux was then corrected by successive iterations until agreement was reached.

The resultant aerodynamic heating data was of a generally acceptable quality during the glide portion of flight, however, the boost phase of the flight generated poor data due to low gage output at low surface temperature, thermal lags in the system and rapid aerodynamic flight transients. Of particular interest was the millivolt output of various thermocouples. Relative to that of a chromel/alumel thermocouple at 1500°F, the output of the tungsten-5% rhenium/tungsten-26% rhenium thermocouple was only 43% and that of platinum/platinum-10% rhodium thermocouple was only 22%. Of course chromel/alumel thermocouples are not usable at these higher temperatures where glide data were acquired but even at these temperatures the output of the tungsten thermocouple was only 88% of the chromel thermocouple at 1500°F and the platinum thermocouple was only 54%. Clearly then, although high temperature measurements can be made, the relative error is high due to the low gage output (mV/deg) and high temperature data are generated at the expense of low temperature boost data.

The outlined procedures employed in the ASSET flight were complex, difficult and yielded data with some potential errors. It is of some interest to note that little advance has been made in sensor design in the intervening years since ASSET. Flights today of vehicles like ASSET would still rely on high temperature thermocouples to measure submold line temperatures and infer heat flux. While improvements have been made in the thermal mass of the thermocouple system and in the telemetering process, we must still go through the formalism of constructing a complex thermal model for each gage. Error build-up from the transmission of temperature and the relationship that heating rate is proportional to the fourth power of the temperature is still the fundamental problem. Clearly there is a need for new forms of heat flux sensors to transmit heating rate directly and circumvent these problems.

SECTION V - REFERENCE

1. Rumsey, C.B. *Techniques and Instrumentation Associated with Rocket Model Heat-Transfer Investigations*. AGARD Specialists' Meeting on Use of Rocket Vehicles in Flight Research, AGARD Report 375, 1961.

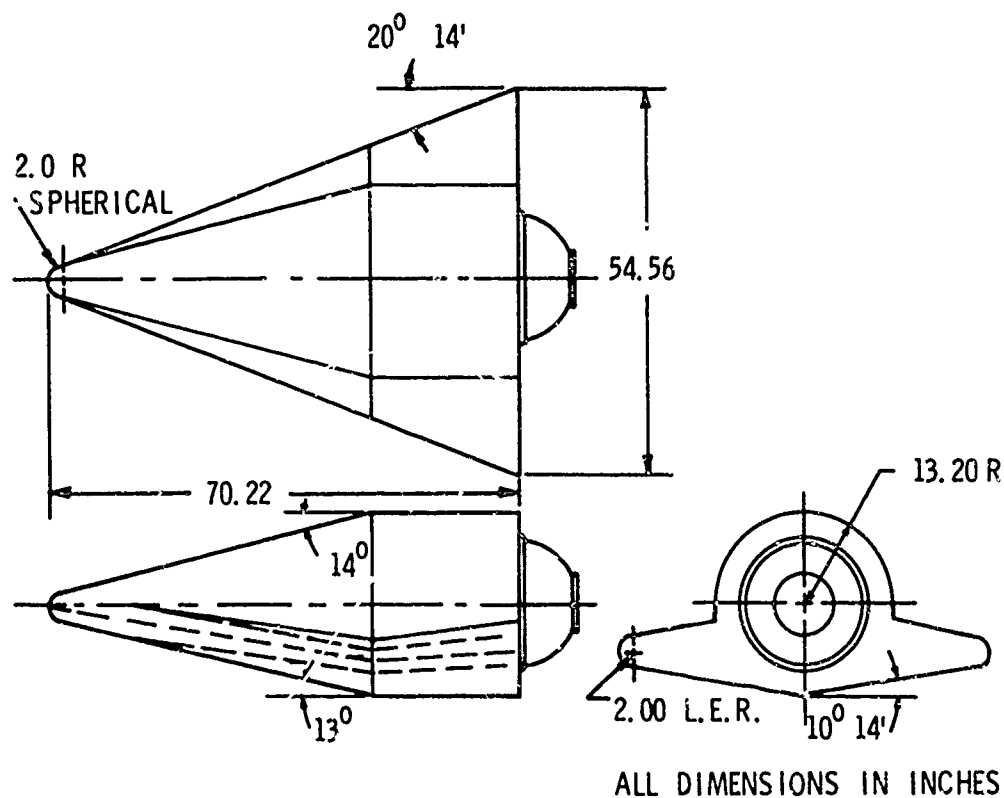


Fig.V-1 Proposed ASSET configuration - 1960

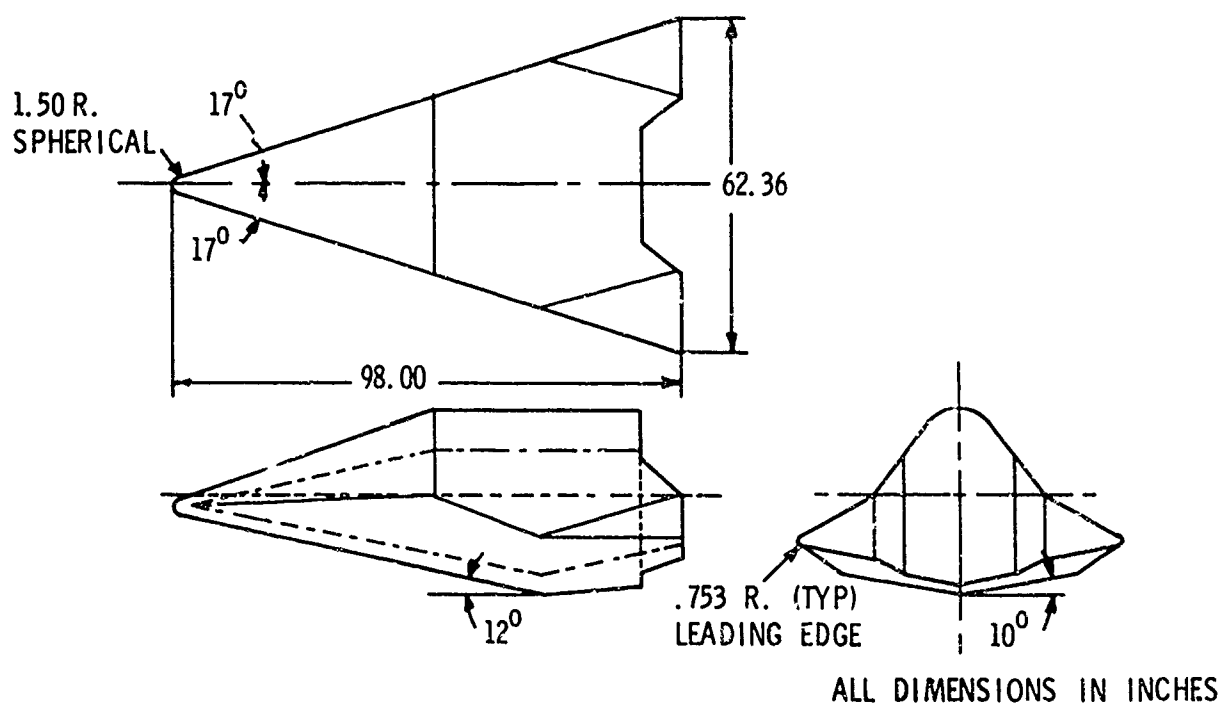


Fig.V-2 Proposed ASSET configuration - 1960

LENGTH	68.82 INCHES
SPAN	54.88 INCHES
HEIGHT	32.79 INCHES
WING SWEEP	70 DEGREES (TRUE)
WING AREA	14 SQUARE FEET
NOSE TIP RADIUS	3 INCHES
LEADING EDGE RADIUS	2 INCHES
AVERAGE WEIGHT	
AEROTHERMODYNAMIC	
STRUCTURE VEHICLE	1130 POUNDS
AEROTHERMOELASTIC	
VEHICLE	1225 POUNDS

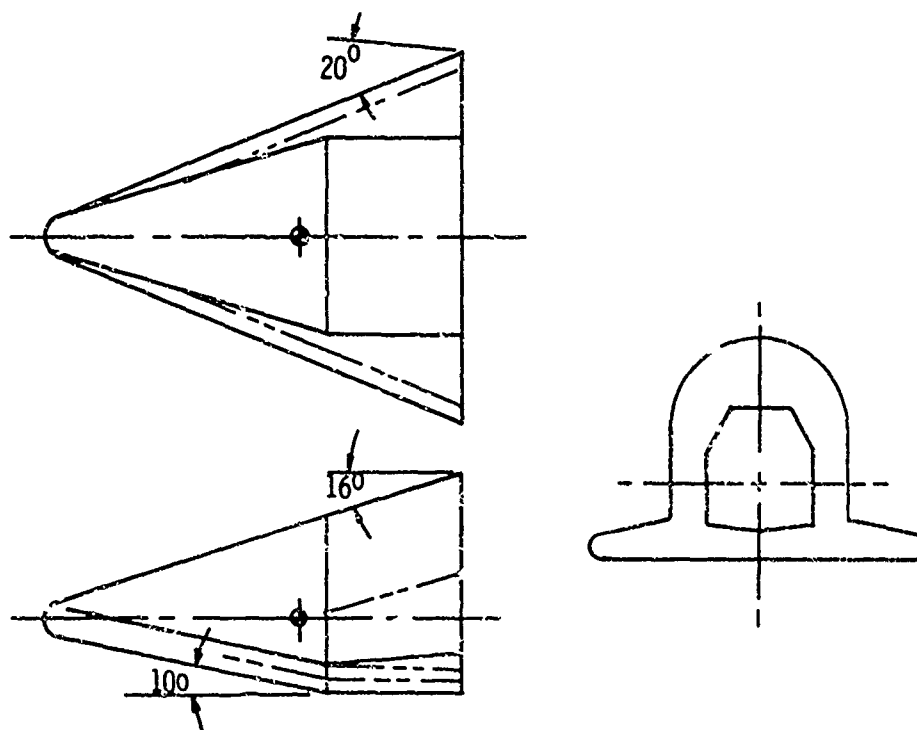


Fig.V-3 Final ASSET vehicle configuration

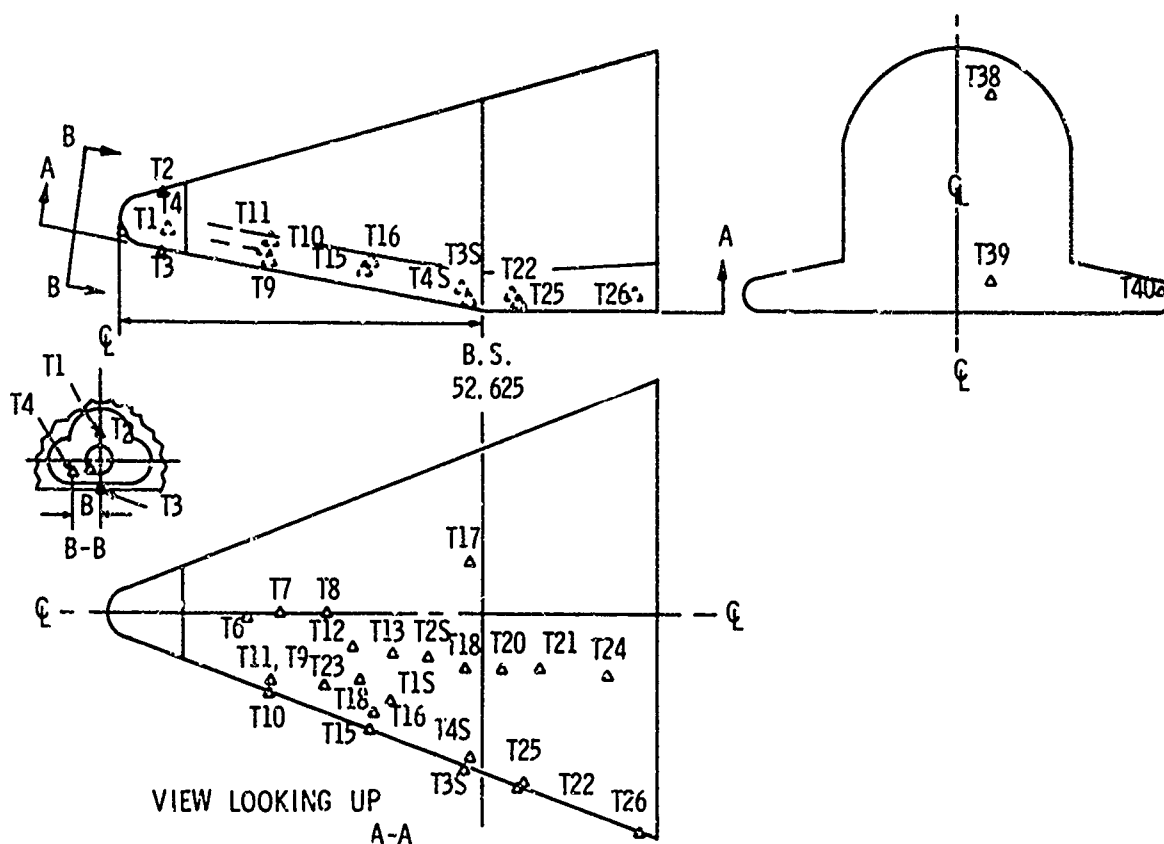


Fig.V-4 Location of lower body temperature sensors

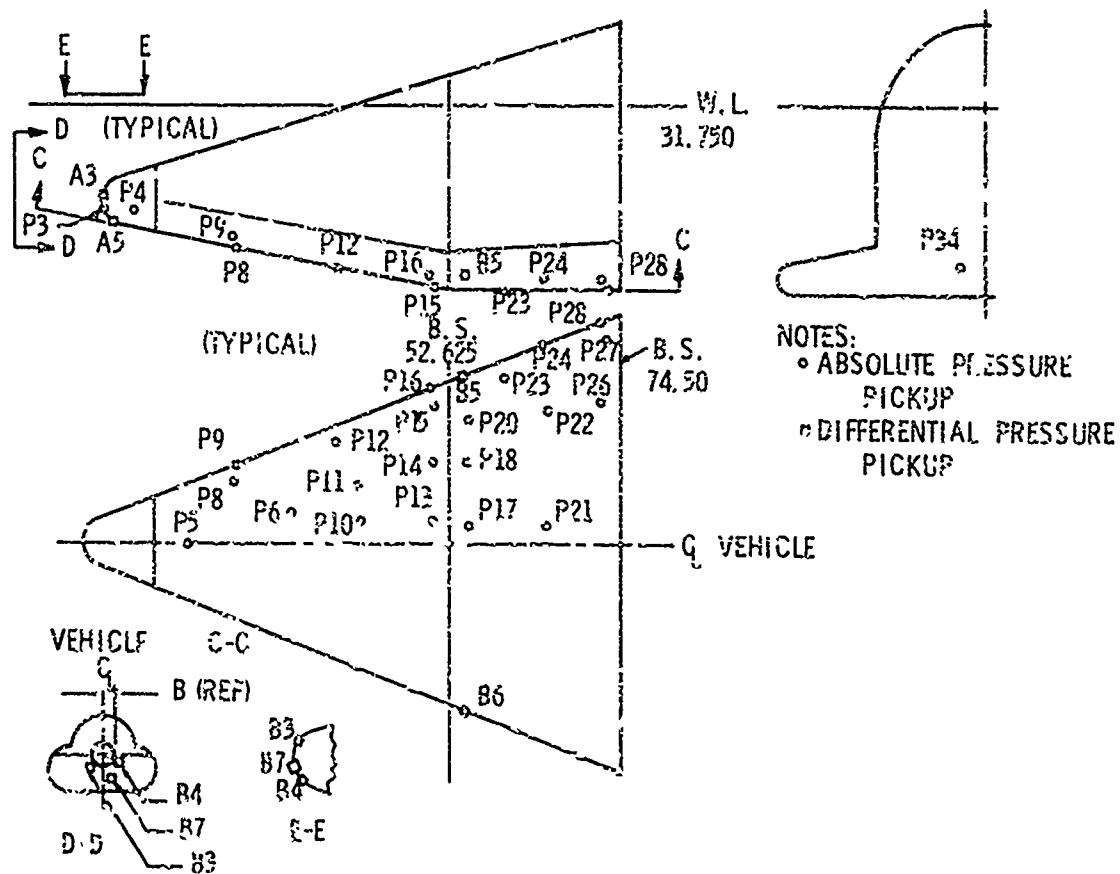


Fig.V-5 Location of lower body pressure sensors

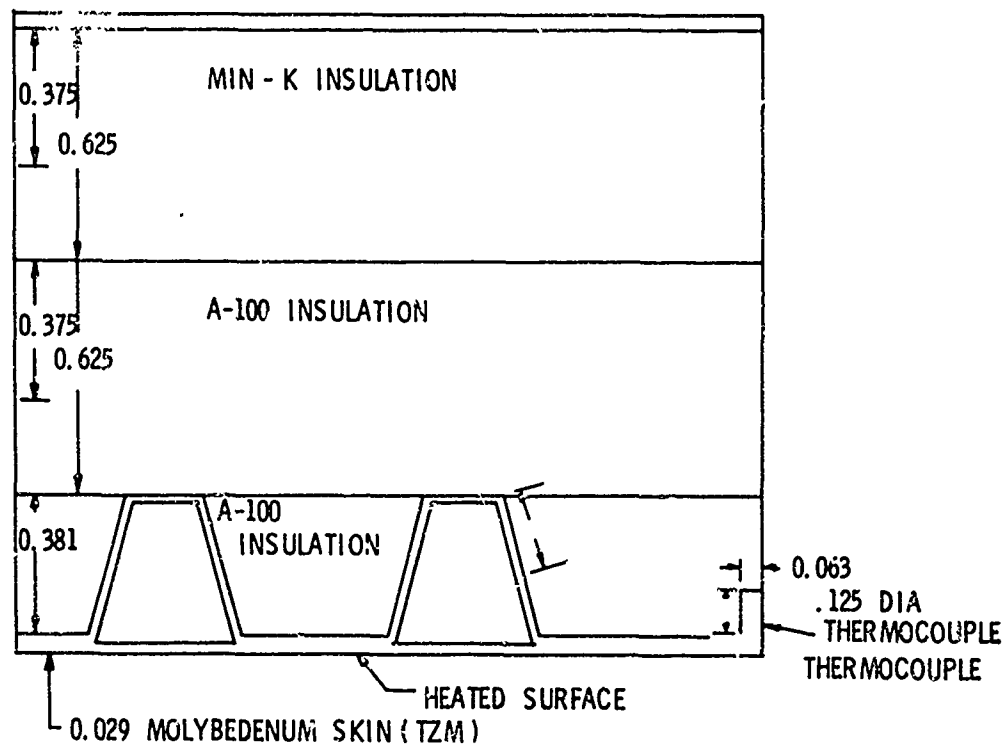


Fig.V-6 Typical thermocouple thermal model

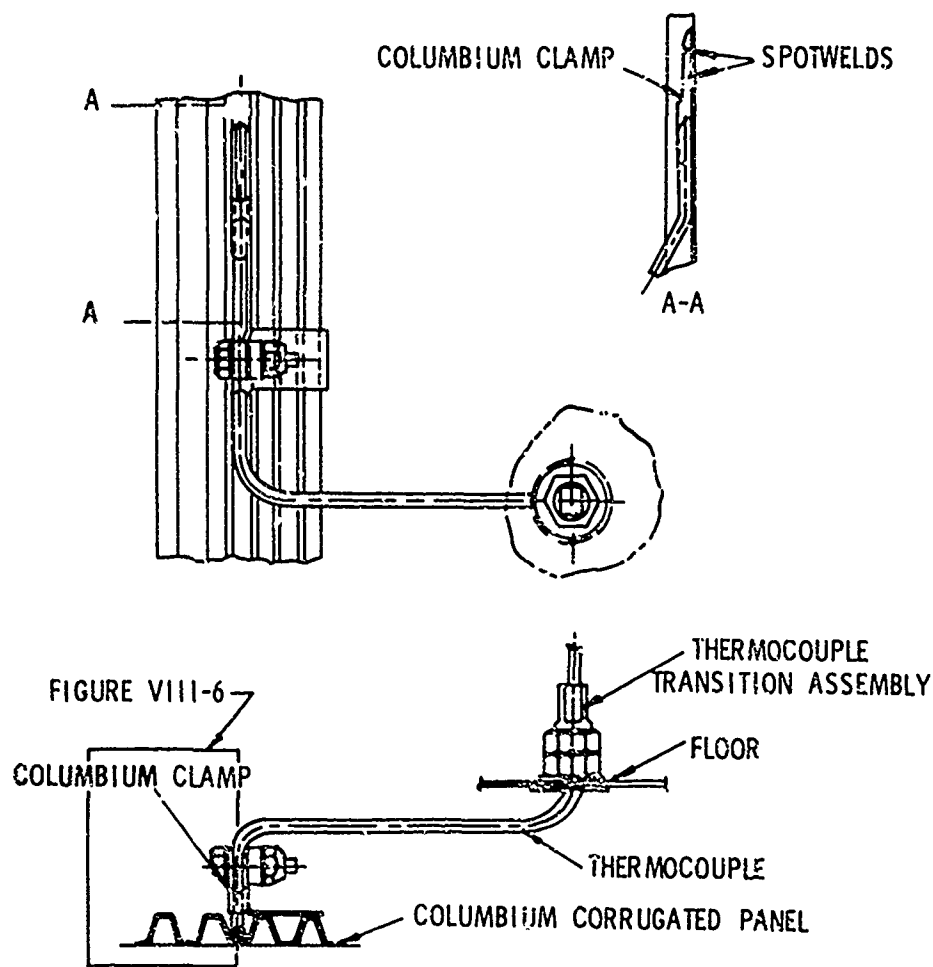


Fig.V-7 Typical thermocouple installation on columbium panel

SECTION VI - GROUND TEST FACILITIES

VI-1 INTRODUCTION

Hypersonic wind-tunnel facilities are indispensable tools in any configuration development program. From a design standpoint the configurations are too complex to be amenable to complete evaluation through present analytical approaches, which are mainly analogies to the actual flow situation based upon an understanding of the primary flow feature. More complete analytic approaches are in an embryonic stage of development with practical applicability still several years off.

As wind tunnels serve many functions in engineering, it is essential at the start to delineate those elements of ground test facilities which will be stressed in the present discussion. Specifically, the discussion will center on the application of ground test facilities to aerodynamic and aerodynamic-heating problems and will not consider such areas as materials response and structural duplication testing. Secondly, I will confine my remarks to the application of wind tunnels to configuration evaluation as opposed to more basic investigations of flow phenomena.

A general discussion of ground facilities and their problems and applications must also consider the classes and functions of proposed vehicles to be evaluated. In general there are two classes of interrelated configurations. (1) the hypersonic aircraft as an evolutionary development of classical aircraft design, and (2) the lifting entry vehicle. The hypersonic aircraft clearly will be a large and complex configuration of the order of 300 ft long which will possess many flow-field interactions and require detailed localized investigation. The lifting entry vehicle will also tend to be large as in the case of recently discussed space shuttle designs¹ and in general this class of configurations will be of the order of 150 ft long. The resultant unit Reynolds numbers of such configurations are shown in Figures VI-1 and VI-2 as a function of flight parameters.

Based upon the assumed nature of these configurations, the question arises how can such configurations be adequately tested? And perhaps more basic yet is what constitutes an adequate test?

In that context, we have three primary variables to evaluate with respect to flight simulation

1. Mach number,
2. Reynolds number, and
3. Flow enthalpy.

In addition to these there is one interesting and yet only implied variable that will permeate this entire discussion model scale.

It is obvious that independently each of these variables can be evaluated to a certain extent but together the total duplication of flight is not only difficult but of questionable merit.

Let us start by evaluating our ability to generate high Reynolds number flows at high Mach numbers. Figure VI-3 indicates the corresponding state of the art for operational hypersonic facilities in the United States both at the present time and during the Dyna Soar development program (shown under the cross-hatched curve). Also shown in this figure is the current Rocket Sled capability at SANDIA² and the various tunnel test section diameters available. Rocket sleds, of which the SANDIA sled is typical, will not be further considered as test tools within the context of aerodynamic testing of configurations due to the following practical limitations:

1. Sled model dynamics are very important, i.e. the model lift forces in combination with the sled must be balanced over the entire speed region to avoid gouging of the rails by the sled.
2. Model weights are restricted through propulsion requirements. The highest model weight discussed was 300 lb.
3. Instrumentation is severely limited. SANDIA has "flown" an 8-channel telemetry system to date.
4. Model recovery at Mach numbers greater than 6 is questionable.
5. Full-scale heating to partial scale models even for short durations would cause a serious and expensive model construction problem.

Thus while I have shown the data acquisition point for comparison, the potential at present for such devices appears to be in the development testing of new hardware rather than in research testing of new configurations. Through a review of facilities in generating this figure, it was noted that in general high Reynolds number simulation has been achieved through the use of relatively small scale nozzles and high pressure driver sections. Also, the facilities are impulse in duration. Finally, the peak Reynolds number has been achieved at a condition of minimum flow energy necessary to avoid liquefaction. This is due to the relationship between Reynolds number and supply conditions as follows:

$$\frac{Re}{ft} \equiv \frac{\rho_{\infty} U_{\infty}}{\mu_{\infty}} = \frac{P_{\infty}}{RT_{\infty}} \frac{M_{\infty} \sqrt{\gamma RT_{\infty}}}{\mu_{\infty}} = \frac{P_0}{C_{\mu} T_0^{3/2}} f(M_{\infty}) \sqrt{\frac{\gamma}{R}}$$

The conflict in simultaneously achieving both high Reynolds numbers and high-flow energy is thus clearly apparent.

High Reynolds numbers are important from two points of view, (1) the extrapolation of aerodynamic data to flight conditions, and (2) the investigation of boundary-layer transition and the resultant turbulent boundary-layer characteristics.

Due to the increase in the transition Reynolds number with Mach number, transitional and turbulent boundary-layer investigations of such configurations are at present limited to the lower Mach number regime ($M_{\infty} \cong 10$) and for some configurations possessing unusual aerodynamic contours or localized interference regions to much lower Mach numbers. This limitation may be relaxed somewhat by artificial boundary-layer tripping, however, tripping techniques have not proven to be successful at the higher Mach numbers [$M = (0)10$] and in general the roughness height caused by the tripping mechanism necessary at these Mach numbers must be many times the characteristic boundary-layer thickness¹. Such a large trip height itself will influence the aerodynamics to a considerable extent. NASA studies indicate that about 35% of the total drag of a delta wing was due to drag on the tripping device alone.

Higher Reynolds numbers may be generated either by increasing the supply pressure of the tunnel or by increasing tunnel scale. Supply pressures of the order of 30,000 lb/in² are employed today in both shock tunnels and hotshot facilities although the longshot concept at VKI increases this substantially. Unfortunately, such an increase in total pressure would go directly into raising the unit Reynolds number of the facility which in turn would increase the dynamic pressure of the flow and limit tests of slender lifting configurations through increasing the sting to model diameter past the point where one would interact on the other. Figure VI-4 indicates the practical limit for high unit Reynolds number testing near 3×10^7 per foot for an arbitrary ratio of sting diameter to model length based upon current materials at a typical design test point of Mach 10 and a length Reynolds number of 200×10^6 . The cross-hatched area indicates a feasible test area extending from full duplication of flight Reynolds number (top line) to turbulent flow occurring over the aft two thirds of the model. Extending this test limit, a sizable portion of our present test capability is currently unavailable for configuration testing, as shown in Figure VI-5, due to the potential interaction of the sting with the model. In addition, this technique would drive the unit Reynolds number still further from flight conditions, yielding further uncertainties in such areas as the effect of unit Reynolds number on transition.

The remaining direction available, which admittedly requires the largest hardware expenditure, is the more direct method of increasing tunnel scale and operating at moderate unit Reynolds numbers. Such a facility concept would allow us to understand details of the flow about large hypersonic craft with models of the order of 10 ft in length while operating at unit Reynolds numbers of the order of 10^7 per foot.

The discussion to this point has concentrated on minimal energy facilities to maximize Reynolds number. Let us now discuss the situation as flow energy is increased to free flight values. As we increase flow energy we must consider its effects on, (1) our ability to generate high pressure air, (2) fundamental limitation of throat heating, (3) run durations, and (4) model survivability.

From the previous discussion recall the relation

$$\frac{Re}{ft} \equiv \frac{P_0 f(M_{\infty})}{T_0^{3/2}}$$

so that the supply pressure, P_0 , increases as $T_0^{1/2}$ or as $f(M_{\infty})^{1/2}$ to maintain a required unit Reynolds number. As facilities are near the practical state of the art in driver pressures it must be concluded that new technology would be required to generate the substantially higher pressures perhaps 200,000 lb/in² necessary to generate high enthalpy high Reynolds number data. Figure VI-6 indicates the influence of increasing the flow enthalpy from near liquefaction to flight duplication on tunnel supply conditions and model heating rates for a moderate test point of Mach 10 and a unit Reynolds number of 10^7 per foot.

VI-2 THROAT HEATING

In any facility technique which adds energy to low velocity air flow prior to expanding the flow through a sonic throat, a limitation will occur when heat transfer to the nozzle throat is sufficiently high to cause throat melting. Studies by Vassallo and Nowlan² indicate the existence of definite limits on the enthalpy and pressure of a high performance reservoir. The governing equation for the heating of the throat of an impulse facility is

$$\frac{4}{n} \dot{q}^2 t_m = [T_m - T_i]^2 [\rho C k]_s$$

where

$$\dot{q} = 0.0265 \frac{k}{D^*} Re^{0.8} Pr^{0.33} [T_{aw} - T_{wi}]$$

Employing a tungsten throat, which was shown to be the most desirable, a representative throat heating limit line as a function of enthalpy and pressure in the reservoir can be shown in Figure VI-7. The limit line of course becomes more restrictive as the test duration increases and to a lesser extent as the throat diameter varies.

VI-3 NOZZLE NONEQUILIBRIUM

The lack of an equilibrium airflow expansion is detrimental to any operational facility as it is difficult to understand the tunnel test section conditions, as each run must be made with a test section flow calibration or rely on analytic estimates of the expansion process and as the instrumentation required to measure static density and temperature is complex and not conducive to production testing. Finally, if one can evaluate test section properties, the nonequilibrium flow field over a complex three-dimensional shape must also be evaluated and contrasted with the flight case which, in general, will be much different. As a result it appears reasonable to circumvent such problems and thus operate in equilibrium airflow test section. Studies have shown that significant enthalpy remains frozen for flow entropy levels (S/R) greater than 31. The resulting limit line as a function of reservoir enthalpy and pressure is shown in Figure VI-7.

VI-4 RUN DURATION

The useful run duration from shock tunnel facilities operating over a wide range of shock Mach numbers which also relates total flow temperature is shown in Figure VI-8. Gun tunnel and hotshot facilities can, of course, generate much longer test durations but at substantially low flow energy levels. Shock tubes generate comparable flow test times at shock Mach numbers greater than 10.

VI-5 MODEL SURVIVABILITY

Increasing the total pressure and total enthalpy in an attempt to more closely duplicate free-flight conditions raises many questions of model survivability. Heating rates on wind-tunnel models in today's high Reynolds number tunnels are already many times higher than in flight, and it is only the very short tunnel durations which allow us to employ easily formed materials. In spite of this, there is unavoidable long-term damage due to scouring of the model by foreign materials and significant gage loss through thermal effects. A significant increase in flow enthalpy could easily introduce new problems in model design, fabrication costs, and test feasibility.

From the foregoing discussion it is apparent that it will be difficult enough to evaluate transitional and turbulent heating on hypersonic aircraft without the added complexity of enthalpy simulation. Whereas high Reynolds number testing will require new hardware but existing technology enthalpy simulation in addition to Reynolds number simulation will require major state of the art advances in several areas of facility with questionable near-term success.

VI-6 INSTRUMENTATION

Facilities are only as good as the instrumentation available to extract information from them. It is therefore important to spend some time evaluating what can be accomplished in the facilities we have discussed. Recall that such facilities are impulse in duration or at best operate for the order of 1 second. Data will generally be required to validate over all forces and moments to the configuration as well as localized pressure and heat transfer. Our discussion will center about the following points: (1) how do instrumentation requirements affect the facility with regard to run duration and model scale? (2) what non-classical instrumentation techniques are required to supplement evolutionary and available instrumentation?

VI-6.1 Force Data

Force and moment data in impulse facilities must be measured by an acceleration compensated balance. The complexity of this balance and the need for balance compactness has increased with the evaluation of higher fineness ratio configurations and with the increased load ranges for high Reynolds number testing. To date, acceleration compensated balances have been designed on the premise that the test model being evaluated vibrates as a rigid body. Slender bodies and/or large models tend to generate vibrations within the model, yielding imperfect inertia compensation. For shock tunnels, a minimum frequency of roughly 1000 Hz can be tolerated and this limits the model scale

to something of the order of 18 in. for model slenderness ratio, $L/D = 10$. Increasing the test duration by an order of magnitude, however, allows one to select a minimum frequency of the order of 200 and 300 Hz and leads to model lengths of 60 in. with an $L/D = 10$. Clearly, the short duration shock tunnel flow severely limits model scale. Figure VI-9 indicates the largest configuration model evaluated in the Cornell Aeronautical Laboratory shock tunnel. This 24-in. model, a hypersonic transport configuration, was tested at Mach 8 to determine high Reynolds number-turbulent flow effects on vehicle aerodynamics. The full scale version of this model would be about 300 ft long.

VI-6.2 Pressure Tests

The generation of pressure data in any impulse facility requires the location of sensing transducers within the model and a minimization of tubulation length to the measurement point. Maximizing the number of measurements to assure data coverage and adequate measurements in the relatively thin regions caused by aerodynamic surfaces again requires large model scale.

VI-6.3 Heat Transfer Tests

Unlike the generation of pressure data, the thermal sensor employed for point measurements of aerodynamic heating is capable of some minimization. Figure VI-10 indicates the relative size of sensors as a function of the test flow duration. As the sensor must contain the imposed thermal pulse, its size will increase somewhat as the test duration increases. The Cornell-developed thin film gage is obviously quite compact and has been proven successful to very high heating rates. Therefore from the standpoint of gage size, the application of shock tunnels to heat transfer testing appears desirable. This, however, may be deceptive as the time to stabilize the flow over the model may be longer than the available test duration. Figure VI-11 indicates data on gage response in a shock tunnel on a two-foot model having a compressively deflected flap and flow separation ahead of the flap. The data at gage 2 near the nose stabilized in the order of 1 msec, however, data further back on the model, gage 25, required almost 3 msec to stabilize and when flow separation was present, over 3 msec were necessary to stabilize the flow. Nagel and Thomas⁵ indicate through a simplified analysis that flow stabilization time increases for both larger models and higher Reynolds number flows. Finally, a recent article by Davies and Bernstein⁶ indicates that in a turbulent boundary-layer flow, the model boundary layer should not be considered steady until the starting shock is at least one chord downstream of the model trailing edge. These studies tend to caution one to consider the use of longer duration facilities for the generation of data on large models particularly at turbulent flow conditions.

VI-6.4 Flow Survey Testing

For both the generation of pressure and more importantly heat transfer data, the researcher will also be faced with the fact that understanding of complex interaction regions will require an instrumentation density far in excess of that available in such facilities or economically feasible. It is for this reason that a new form of heat-transfer testing will be necessary as an integral part of the experimental program to evaluate these large complex configurations. The technique has many versions but it is generally classed as heat transfer survey testing. Figure VI-12 indicates the many forms and approximate test durations required of flow survey test techniques which are employed today. The potential features of such techniques are as follows:

1. Low cost model fabrication.
2. Capability of on-site configurational modification.
3. Comprehension of overall heating patterns.
4. Accuracy of technique comparable with that required for preliminary design.

There is a tendency to forget that at various stages of configuration development fundamentally different data are required. It is not correct to assume that highly accurate data are always required. Early in a design program our need is for trend data to screen approaches and select promising directions for future work. These data need not be highly accurate but must allow economical evaluation of many configurations. This trend data must give way to more precise data as the design progresses and selective approaches are progressively narrowed. Flow survey testing serves this earlier screening function magnificently. Further, let me stress overall flow comprehension. At the AEDC facility complex we can currently generate 8000 to 10,000 heat-transfer measurements per day¹. While sensor saturation of an important area on the vehicle may be valuable and needed and can certainly be done, the process of reconstructing the flow patterns requires far more time than the screening of a film of paint removal or evaluation of iso-density lines on a still photograph.

A review of Figure VI-12 indicates a survey testing technology capable of generating data in both impulse as well as continuous flow facilities. Of particular interest in the present context is the thermographic phosphor technique which has been successfully demonstrated in hotshot facilities⁷. The thermographic phosphor technique employs a thin coating of phosphors on a nonconductive model. The tunnel flow generates a characteristic heating pattern which is observed through a quenching of the phosphorescence with temperature rise. Rapid quenching rates (termed thermographic), high luminosity of the phosphor and high resolution, very fast film are required to

generate accurate data. In principle, data could be taken in shock tunnel flows [(0) 5 msec] and some progress has been made in this area by the Cornell Aeronautical Laboratory. The data generated on film are read as lines of constant intensity on an isodensitometer and reduced to heating rate data through a semi-infinite slab model of the aerodynamic configuration. Figure VI-13 indicates data generated on the tail fin of a lifting body design by the McDonnell Douglas Corporation and Figure VI-14 indicates data on a Gemini model.

For continuous flow facilities [(0, 10 sec duration)] the Tempilaq technique has proven quite successful in generating both qualitative and quantitative data and many heat transfer investigations are presently being conducted employing the Tempilaq coating technique exclusively. A major and general drawback to the application of temperature coatings in continuous tunnels is the development of more suitable and higher temperature materials. The highest temperature machinable material (Teflon) employed to date has a 1500°F potential but most castable materials are limited to 500 to 700°F. Further, castables have the general problem of nonrepeatable thermal properties which are necessary to evaluate data output and they are generally brittle and fail easily during repetitive testing.

Irrespective of the heat transfer survey test technique applied in a particular tunnel situation, such testing is and will be more necessary in the design evaluation and evolution of hypersonic aircraft and spacecraft. Not only will it serve to define the aerodynamic heating but it will serve as a necessary adjunct to aerodynamic force and moment tests in which the boundary layer will be composed of laminar, transitional and turbulent areas, where instantaneous transition of the boundary layer cannot be assured even with tripping devices and where a knowledge of transition will be necessary in the evaluation and extrapolation of data to free flight conditions.

VI-7 CONCLUSION

The review of facilities with regard to test durations necessary to allow meaningful measurements on models of large hypersonic aircraft and spacecraft indicates to me the necessity to consider facilities having test durations substantially larger than presently available or currently foreseen for shock tunnels. While these facilities have been of great value in the past decade and while they may remain useful for small scale testing, the next decades will see greater use made of the long duration gun tunnel approach or a refinement of the hotshot concept. Further, ground facilities will require entirely new test techniques of which the heat transfer survey testing is but a suggestion. Finally, I feel that these facilities will operate over a considerable Mach number range at high Reynolds numbers but at moderate enthalpy levels necessary to avoid the limits of liquefaction and real gas phenomena. Excursions into real-gas investigations will be made in supplemental and highly specialized facilities such as shock tubes and foreign gas flow channels.

SECTION VI - REFERENCES

1. Mueuler, G.E. *The New Future for Manned Spacecraft Developments.* Astronautics and Aeronautics, March 1969, Vol.7, No.3, pp.24-32.
2. Rigali, D.J.
Feltz, L.V. *The Application of High-Speed Monorail Rocket Stands to Aerodynamic Testing at High Reynolds Numbers.* AIAA Paper 68-365.
3. Sterrett, J.R.
et al. *Transition Fixing for Hypersonic Flow.* NASA TN 4129, October 1967.
4. Vassallo
Nowlan *High Temperature Nozzle-Throat Heat Transfer and Thermal Protection for the Hypersonic Shock Tunnels.* CAL Report HM-1510-Y-10, February 1964.
5. Nagel, A.L.
Thomas, A.C. *Analysis of the Correlation of Wind Tunnel and Ground Test Data to Flight Test Results.* AIAA Paper 65-208.
6. Davies, W.R.
Bernstein, L. *Heat Transfer and Transition to Turbulent Flow in Shock-Induced Boundary Layers on a Semi-Infinite Flat Plate.* J. Fluid Mechanics, Vol.36, Part 1, pp.87-112.
7. Czysz, P.
Dixon *Thermographic Heat Transfer Measurements* Instrumentation and Control Systems, October 1968.

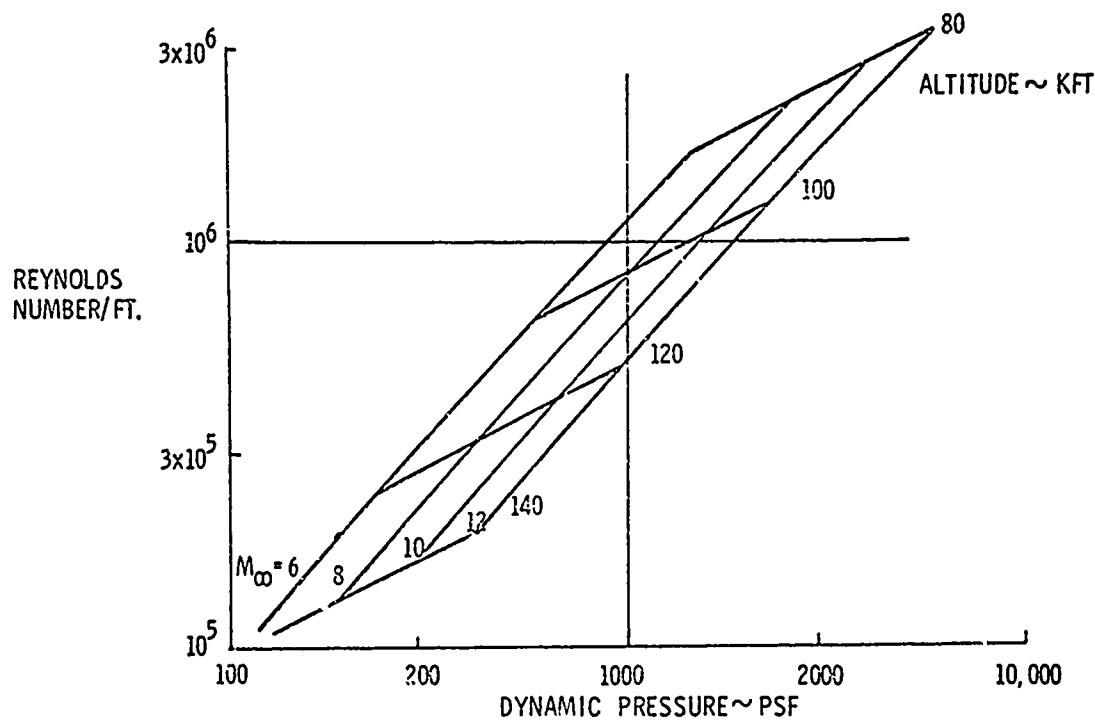


Fig. VI-1 Operating regime for hypersonic cruise configurations

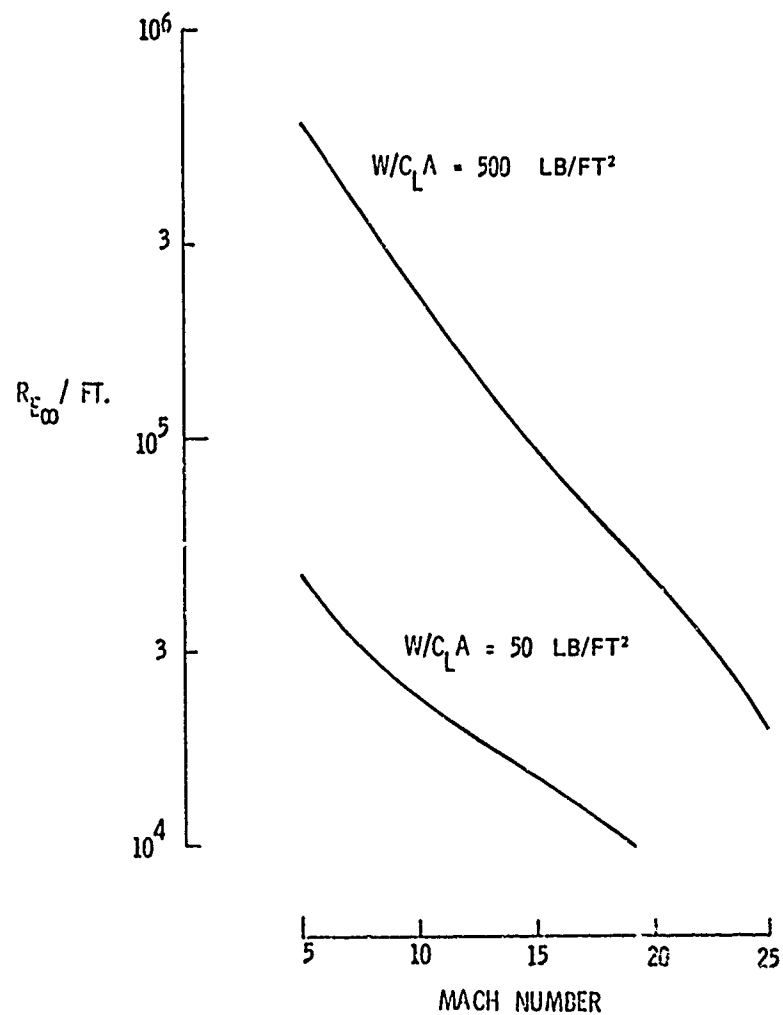


Fig. VI-2 Reynolds numbers and Mach numbers for hypersonic cruise configurations

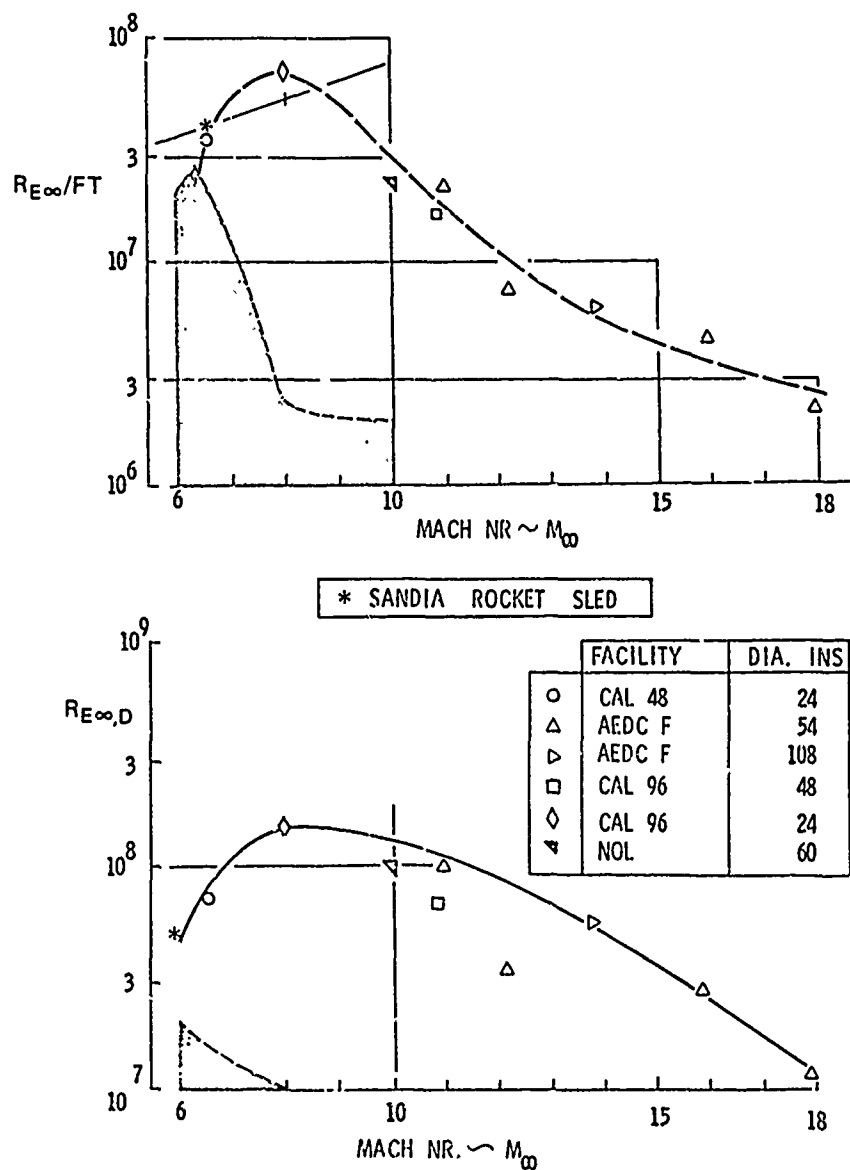


Fig.VI-3 Reynolds number and Mach number capabilities of operational hypersonic facilities in the United States

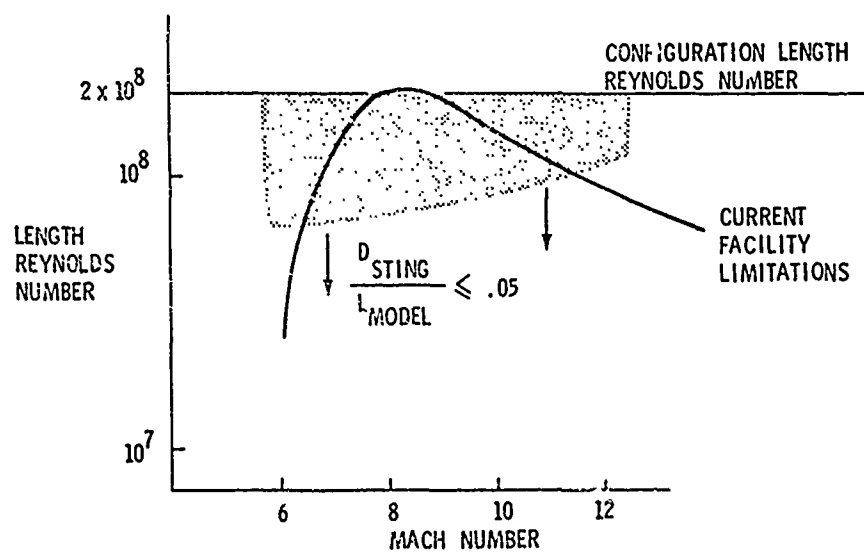


Fig.VI-4 Comparison of available and usable facility Reynolds numbers

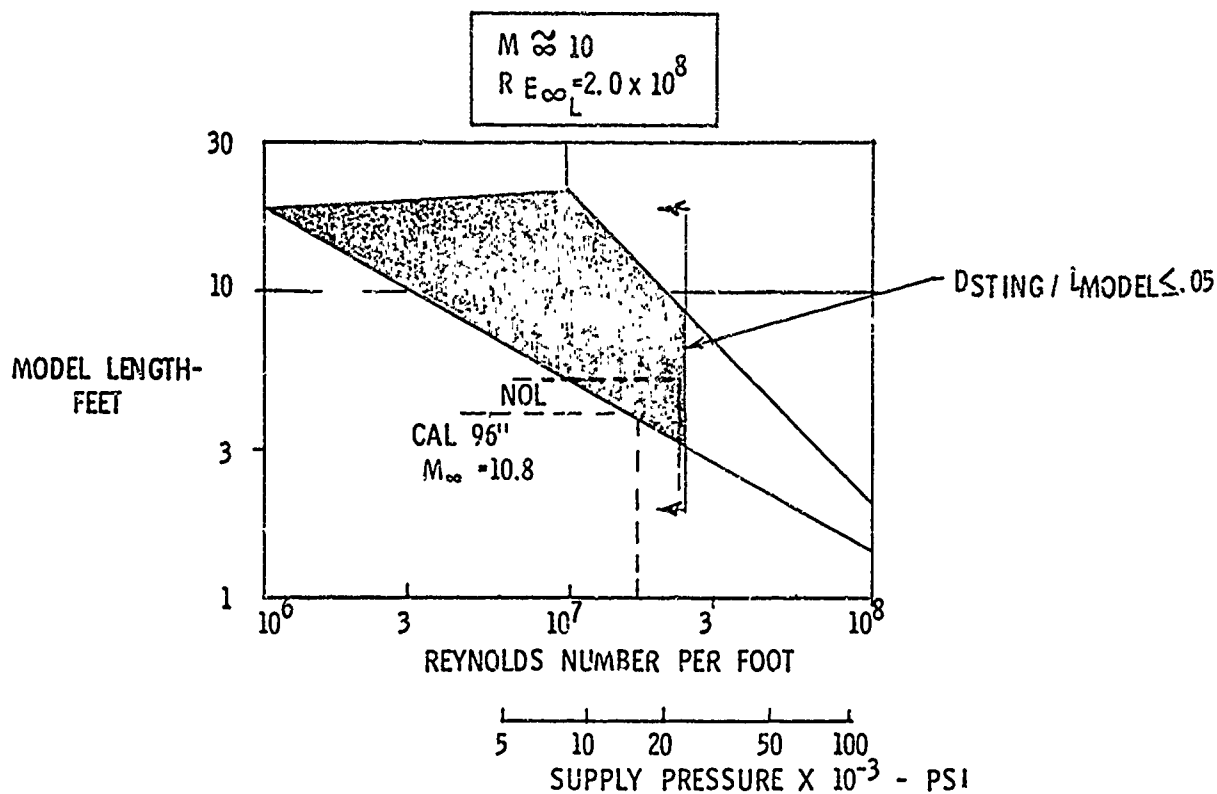


Fig. VI-5 Required Reynolds number/model length characteristics

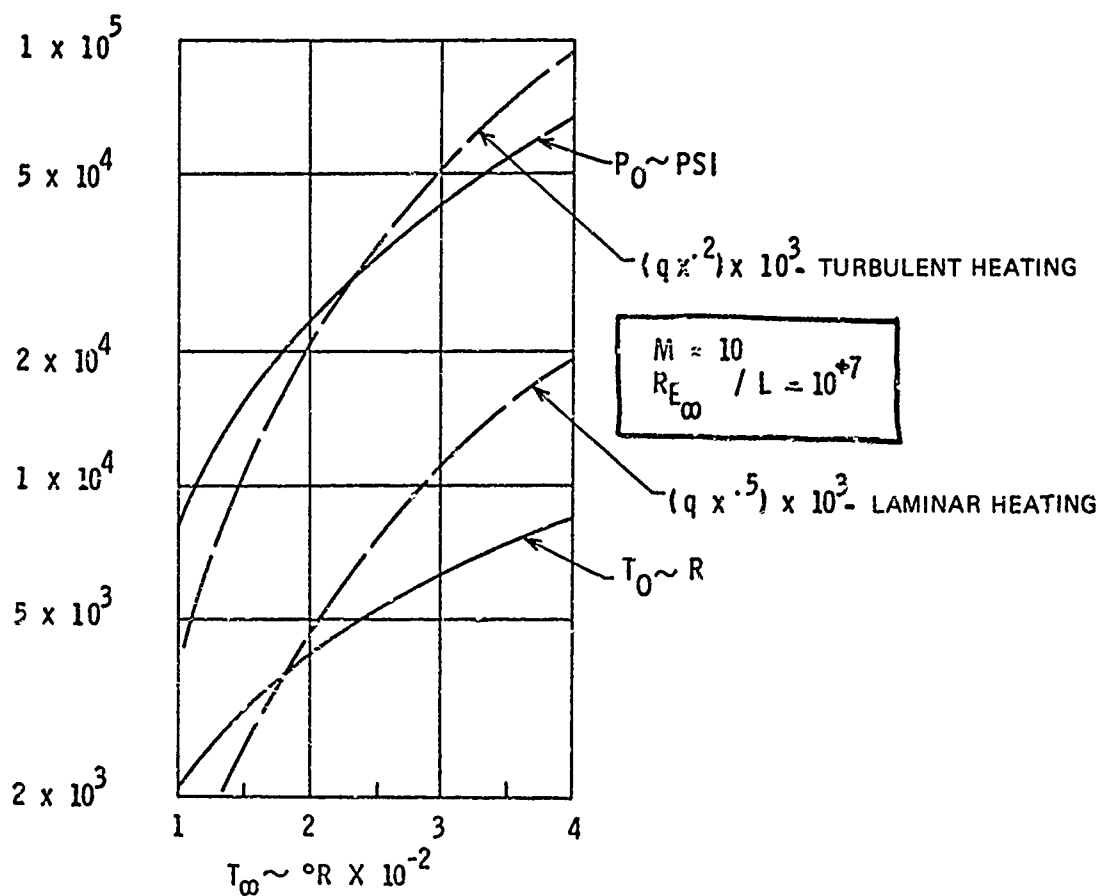


Fig. VI-6 Effect of varying total temperature on facility characteristics

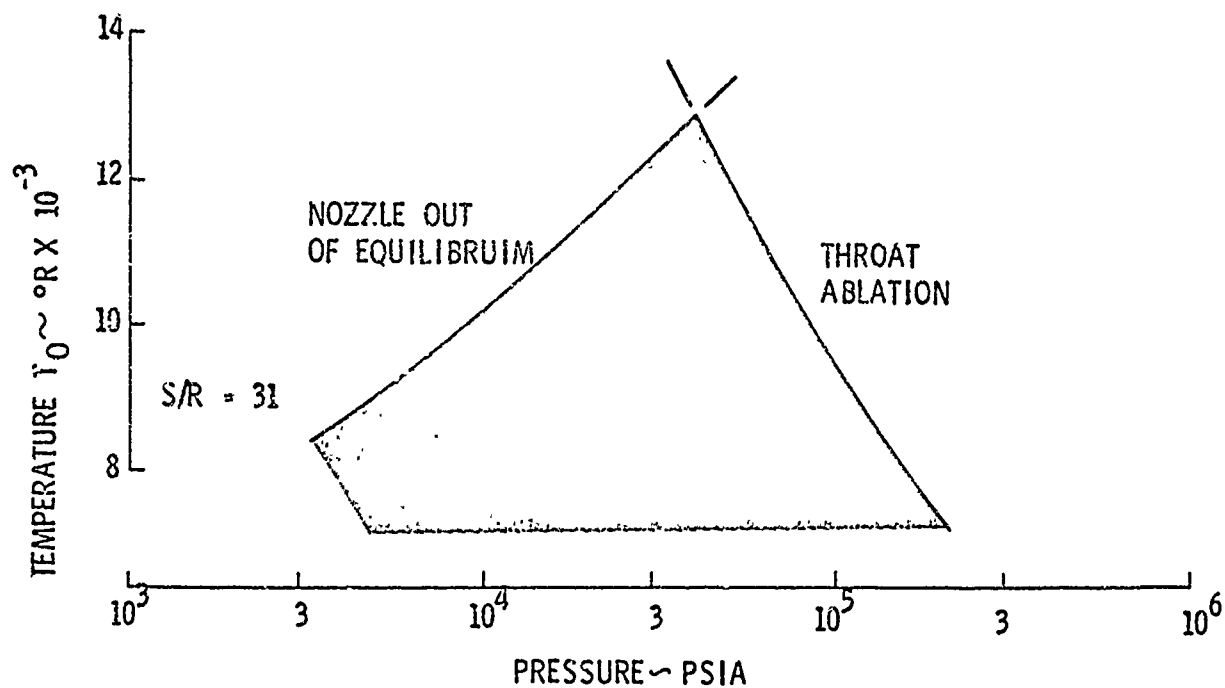


Fig.VI-7 Heating limits for tungsten throat

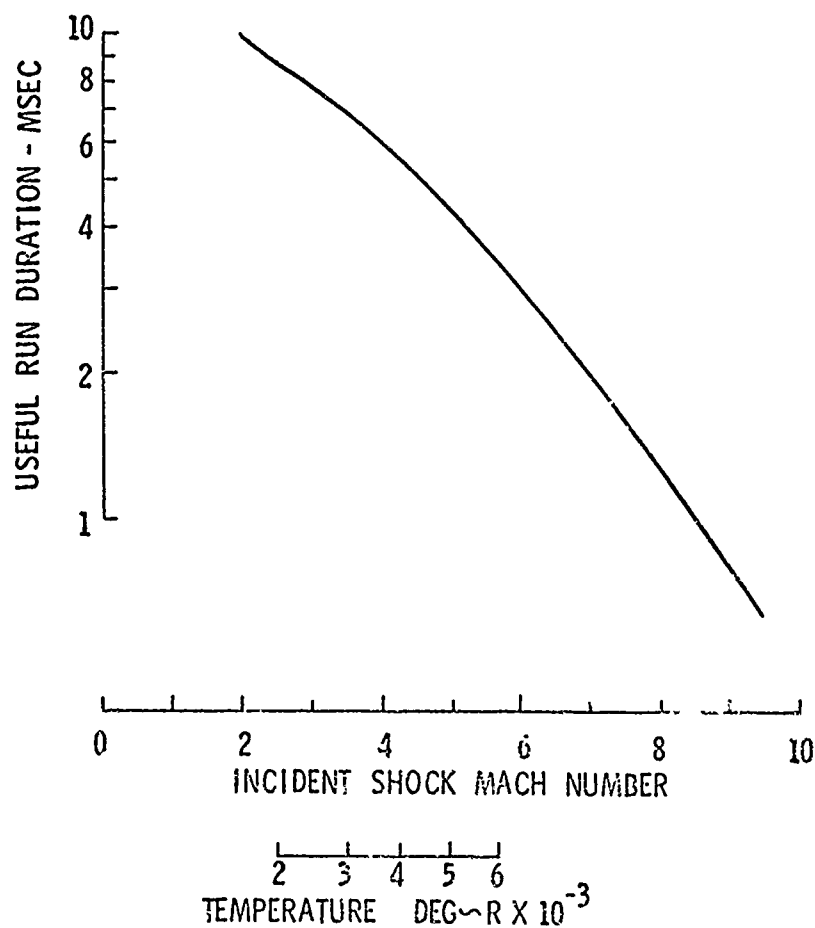


Fig.VI-8 Shock tunnel performance (typical)

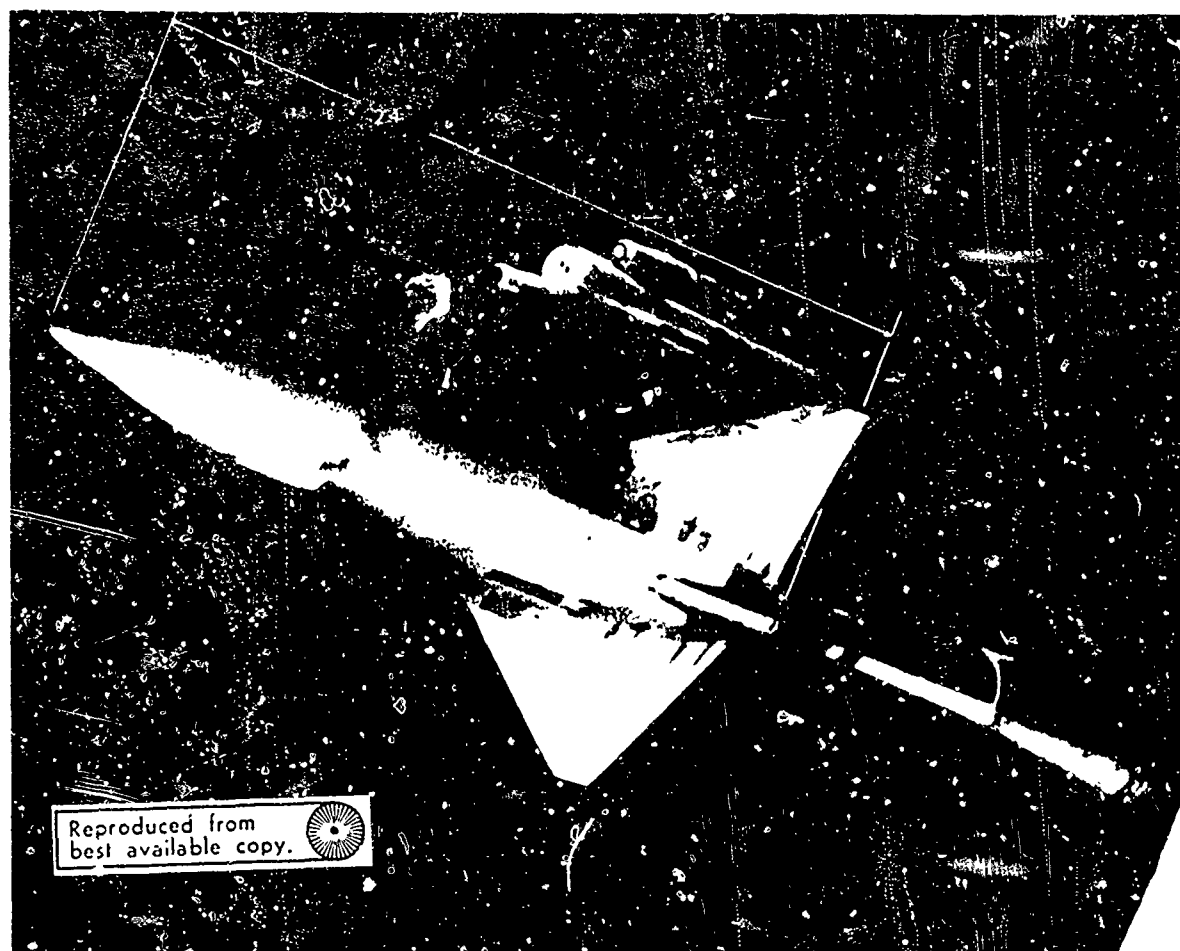


Fig VI 9. Largest configuration model exit of the Cornelia Aeronautical Engineering Co.

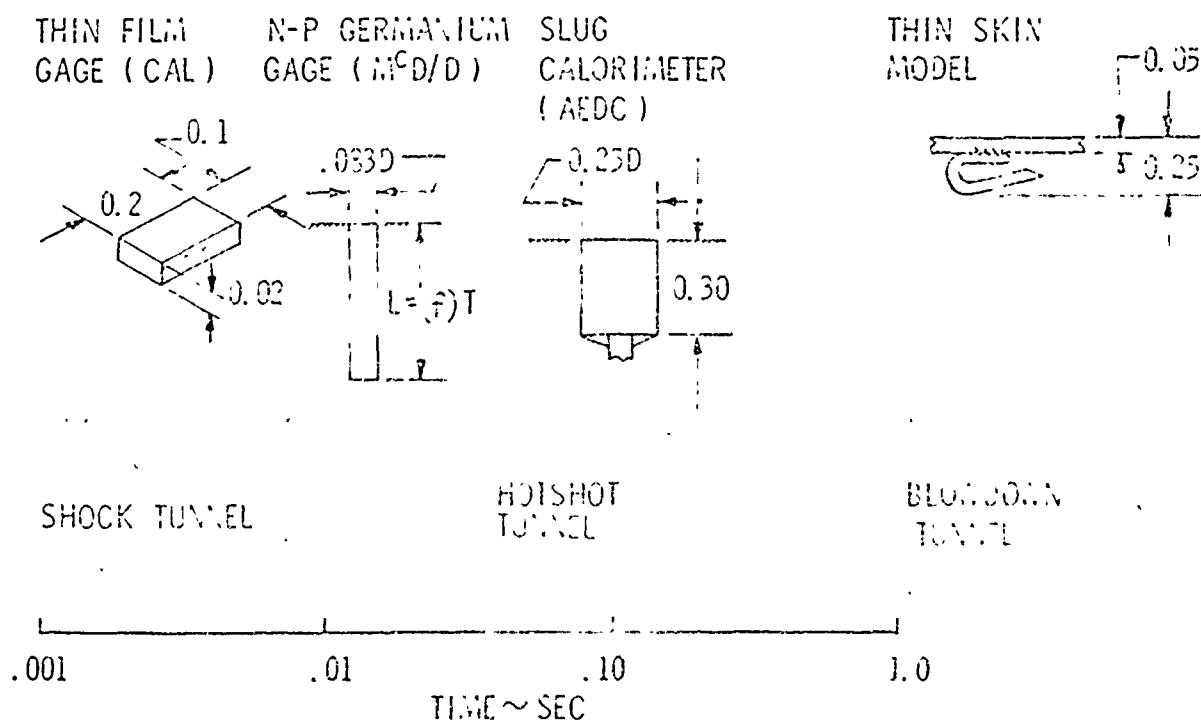


Fig VI 10. Hot gage calibration values for

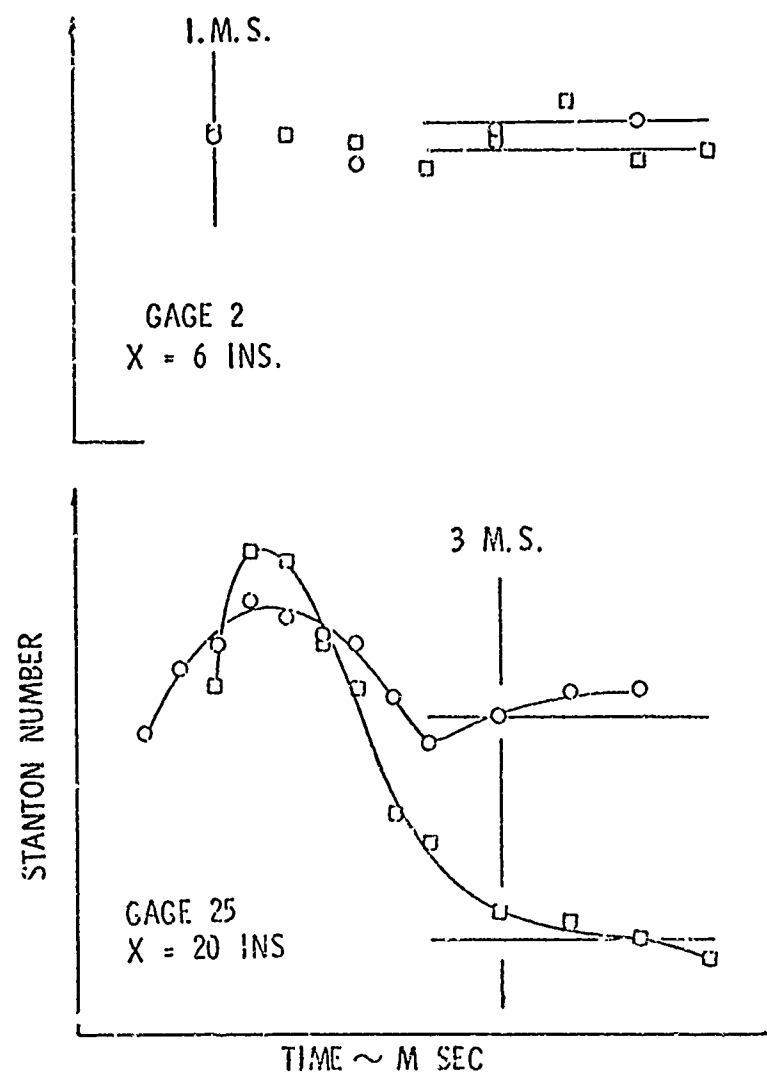


Fig.VI-11 Gage response data

TECHNIQUE	TEST DURATION
TEMPERATURE INDICATING PAINTS:	
DETECTOTEMP.	0 (10) SEC.
TEMPILAQ	0 (10) SEC.
REVERSIBLE COATINGS:	
LIQUID CRYSTALS	0 (10 ⁻¹) SEC.
THERMOGRAPHIC PHOSPHORS.	0 (10 ⁻²) SEC.
RADIATION SENSORS:	
PHOTOGRAPHIC PYROMETER	0 (10) SEC.
INFRARED CAMERA	0 (1) SEC.

Fig.VI-12 Heat transfer survey testing techniques

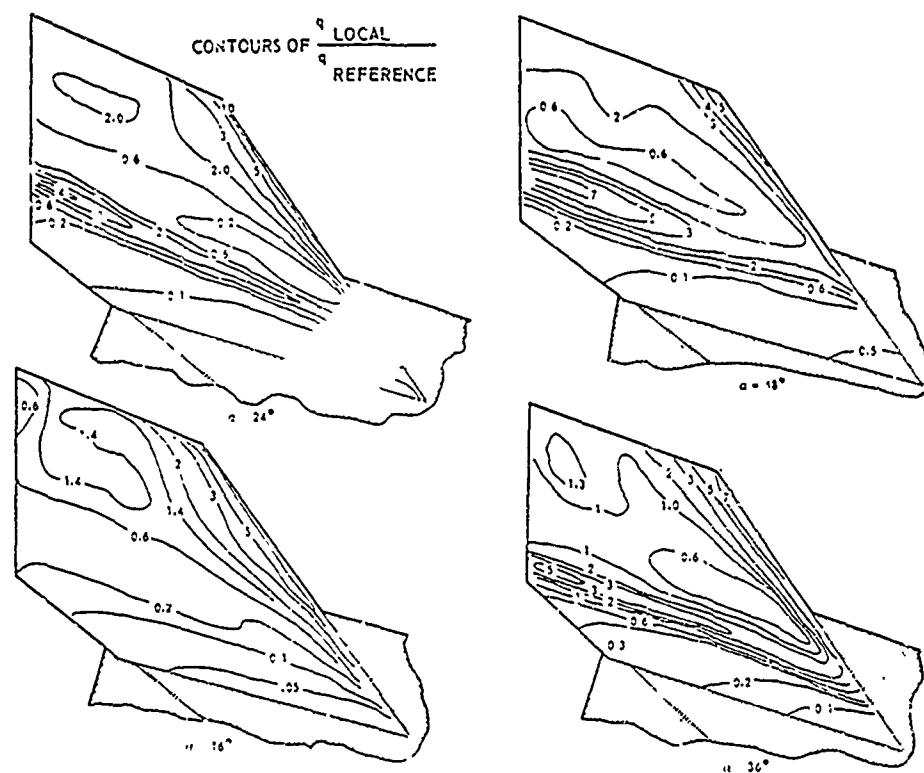


Fig.VI-13 Evaluated isodensitracer map of lifting body tail fin, angle of attack 16° to 48°

Rep.
b.c.
"from
le copy."



CONTOURS OF OPTICAL DENSITY.

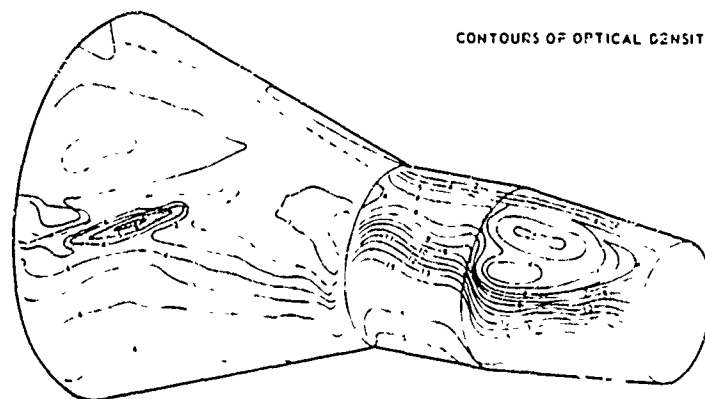


Fig.VI-14 Phosphor picture and evaluated isodensitracer map for Gemini model, angle of attack 20°

LECTURE 8

SOME DESIGN ASPECTS OF HYPERSONIC VEHICLES

W.L.Hankey

Hypersonic Research Laboratory, ARL
Wright-Patterson AFB, Ohio 45433, USA

NOTATION

<i>Symbol</i>	<i>Description</i>	<i>Units</i>
c_i	species concentration	—
C_A	axial force coefficient	—
C_Y	side force coefficient	—
C_N	normal force coefficient	—
C_l	rolling moment coefficient	—
C_m	pitch moment coefficient	—
C_n	yawing moment coefficient	—
C_f	friction coefficient	—
C_l	lift coefficient	—
C_D	drag coefficient	—
C_p	pressure coefficient or specific heat at constant pressure	— Btu/lb
D	drag or binary diffusion coefficient	lb —
g	acceleration of gravity	ft/sec ²
h	static enthalpy	ft ² /sec ²
h_s	total enthalpy	ft ² /sec ²
\underline{i}	unit vector in x direction	—
\underline{j}	unit vector in y direction	—
\underline{k}	unit vector in z direction	—
k	Newtonian modifier	—
L	lift	lb
Le	Lewis number	—
M	Mach number	—
\underline{n}	surface outward normal	—
p	pressure	lb/ft ²
q	dynamic pressure	lb/ft ²
\dot{q}	heating rate	Btu/ft ² sec
Re	Reynolds number	—

<i>Symbol</i>	<i>Description</i>	<i>Units</i>
R_E	earth radius	ft
S	reference planform area	ft ²
T	thrust or temperature	lb °R
t	time	sec
u	x-component of velocity	ft/sec
v	y-component of velocity	ft/sec
V	flight velocity or volume	ft/sec ft ³
W	weight	lb
x, y, z	orthogonal coordinate system in body axes	—
α	angle of attack	radians
β	angle of sideslip	radians
γ	flight path angle	radians
δ	body angle	radians
ξ	damping ratio	—
η	volumetric efficiency	—
θ	shock angle	radians
λ	mean free path	ft
μ	dynamic viscosity	lb sec/ft ²
ρ	density	slug/ft ³
τ	shear stress	lb/ft ²

1. FLIGHT MECHANICS

In analyzing hypersonic lifting vehicles one must first examine the trajectory and flight environment. In so doing, the influence of various design parameters may be placed in the proper perspective. The equations of motion for planar flight are listed as follows¹:

$$m\dot{V} = -D - mg \sin \gamma + T$$

$$mV\dot{\gamma} = L + \frac{mV^2}{R_E} \cos \gamma - mg \cos \gamma.$$

Lifting bodies permit gradual descent, hence, the following assumption for path angle of γ and $\dot{\gamma}$ equal zero may be used. Thus the last equation produces a simple algebraic relationship

$$\frac{L}{W} = 1 - \frac{V^2}{V_c^2}$$

where $V_c^2 = gR_E$.

Since $L = \frac{1}{2}\rho V^2 C_L S$, a relationship between velocity and density which is a function only of altitude results,

$$\rho(h) = \frac{2W}{SC_L} \left(\frac{1}{V^2} - \frac{1}{V_c^2} \right).$$

For a constant value of W/SC_L the flight corridor results. A typical value of 100 lb/ft² for W/SC_L permits a comfortable reentry between the "too high" and "too hot" regimes (Fig.1).

The time of reentry may be ascertained from the first equation.

$$\frac{\dot{V}}{g} = -\frac{D}{W}.$$

This equation may be integrated for constant L/D as follows:

$$\begin{aligned}\frac{\dot{V}}{g} &= -\frac{D}{L} \left(1 - \frac{V^2}{V_c^2}\right) \\ \int \frac{dV}{\left(1 - \frac{V^2}{V_c^2}\right)} &= -g \frac{D}{L} \int dt.\end{aligned}$$

Carrying out the integration for $V = 0$ at $t = 0$ produces

$$\frac{V}{V_c} = \tanh\left(\frac{-gt}{V_c L/D}\right).$$

Figure 1 shows reentry times which are independent of altitude indicating that long durations (measured in hours) are to be expected. Thermal protection systems for these lifting vehicles, therefore, must possess long duration capability.

Having a relationship between altitude and velocity for the flight corridor permits us to examine the régimes of fluid mechanics encountered. Air may be treated as a continuum provided the mean free path (λ) of the molecules (which is the average distance traveled between collisions) is small compared with some characteristic dimension of the vehicle. For standard conditions, λ is 2×10^{-7} ft at sea level but varies inversely with density and is one foot at 535,000 ft altitude. Since orbital speeds are attained by this altitude and since the vehicle dimensions we shall consider generally are larger than one foot, then continuum mechanics may be employed to predict the aerodynamic characteristics.

Next the condition of the boundary layer (i.e. laminar or turbulent) shall be examined. Figure 2 shows the free stream Reynolds number based on a characteristic length of 100 feet. There is a wide variation in observed transition Reynolds number among experimenters. However, selecting a transition Reynolds number of 3×10^6 indicates laminar flow above 200,000 ft and turbulent conditions at lower altitudes. Therefore, both hypersonic laminar and turbulent boundary layers must be considered.

Analysis of the aerodynamic characteristics requires a knowledge of the air properties at the energy levels associated with hypersonic flight. Air is composed of nitrogen and oxygen diatomic molecules which dissociate into atomic species at sufficiently high energy levels. Figure 3 shows, for conditions throughout the flight corridor, the constituent species in equilibrium air after undergoing a normal shock. Notice the small region in which ideal gas conditions prevail. One could conclude from this that ideal gas computations are worthless at hypersonic speeds. But let us examine the magnitude of the discrepancy between ideal gas and real gas calculations for surface pressure, shear stress, and heat transfer required in vehicle design. Figure 4 shows the normal shock pressure coefficient along the flight corridor for equilibrium air² and ideal air ($\gamma = 1.4$). At a Mach number of 20 the difference in pressure coefficient is only 7% for the stagnation point. Hence, we conclude that even though real gas effects begin to occur at Mach 3, only small pressure corrections result.

Examination of the Navier-Stokes equations is required in order to study shear and heat transfer effects.

$$\text{Continuity: } \frac{\partial \rho}{\partial t} + \nabla \cdot \rho \underline{V} = 0$$

$$\text{Momentum: } \rho \frac{D\underline{V}}{Dt} = \nabla \cdot \underline{P}$$

$$\text{Energy: } \rho \frac{D}{Dt} \left(h_s - \frac{p}{\rho} \right) = \nabla \cdot (\underline{P} \cdot \underline{V}) + \nabla \cdot \underline{q}$$

$$\begin{aligned}\text{Equation of} \\ \text{State: } \rho &= \rho(h, p),\end{aligned}$$

where

$$\underline{p} = \text{stress tensor (dyadic)} = \begin{vmatrix} \sigma_x & \tau_{xy} & \tau_{xz} \\ \tau_{xy} & \sigma_y & \tau_{yz} \\ \tau_{xz} & \tau_{yz} & \sigma_z \end{vmatrix} \sim \begin{vmatrix} -p\mu & \frac{\partial u}{\partial y} \\ \mu \frac{\partial u}{\partial y} & -p \end{vmatrix}$$

$$h_s = h + \frac{V^2}{2}.$$

For a two-dimensional boundary layer³

$$\frac{\partial}{\partial x}(\rho u) + \frac{\partial}{\partial y}(\rho v) = 0$$

$$\rho \left(u \frac{\partial u}{\partial x} + v \frac{\partial u}{\partial y} \right) = -\frac{dp}{dx} + \frac{\partial \tau}{\partial y}$$

$$\rho \left(u \frac{\partial h_s}{\partial x} + v \frac{\partial h_s}{\partial y} \right) = \frac{\partial}{\partial y}(u\tau) + \nabla \cdot \underline{\dot{q}},$$

where

$$\nabla \cdot \underline{\dot{q}} = \underbrace{\frac{\partial}{\partial y} \left[k \frac{\partial T}{\partial y} \right]}_{\text{conduction}} + \underbrace{\rho D \sum h_i \frac{\partial c_i}{\partial y}}_{\text{diffusion of energy}}$$

and

$$h = \sum h_i c_i$$

$$h_i = \int_0^T C_{pi} dT + h_i^0.$$

Therefore

$$\frac{\partial h}{\partial y} = \sum h_i \frac{\partial c_i}{\partial y} + \sum c_i \frac{\partial h_i}{\partial y}$$

$$\frac{\partial h_i}{\partial y} = \frac{\partial h_i}{\partial T} \frac{\partial T}{\partial y} = C_{pi} \frac{\partial T}{\partial y}.$$

But

$$\sum C_{pi} c_i = C_p \text{ of mixture.}$$

Hence

$$\nabla \cdot \underline{\dot{q}} = \frac{\partial}{\partial y} \left[k(1 - Le) \frac{\partial T}{\partial y} + Le \frac{k}{C_p} \frac{\partial h}{\partial y} \right]$$

where

$$Le = \rho \frac{DC_p}{k}.$$

Now if $Le = 1$ and $h = C_p T$ then $\nabla \cdot \underline{\dot{q}} = \partial T / \partial y$ which is the ideal gas result implying that the energy transferred is the same whether it is transferred by diffusion or conduction. Hence, if Lewis number is near unity (actually it is about 1.4), then the governing equations for real gas boundary layers are identical to the ideal equations. Thus we conclude that since Lewis number is near unity ideal gas calculations may be used to predict approximate numerical results even though the physical phenomenon represented is not appropriate. This is an extremely useful result enabling us to use many of the convenient tables and theories previously employed in the supersonic régime.

2. HYPERSONIC AERODYNAMIC CHARACTERISTICS

To obtain the aerodynamic characteristics, one seeks an engineering solution of the Navier-Stokes partial differential equations derived in the previous section for boundary conditions pertinent to the geometry of the vehicle of interest. The only part of the solution required, however, is the pressure and shear stress on the vehicle surface. Integration of these stresses over the body produces the aerodynamic forces.

First let us examine how to do the problem right. "Exact" numerical solutions of the Navier-Stokes partial differential equations are possible by employing finite differences. Several investigators have accomplished this feat. One of the most successful methods was developed by Dr John G. Trulio of *Applied Theory, Inc.*⁴. He computed the flow over a cylinder for a supersonic Mach number at a low Reynolds number. The resulting map of velocity vectors depicts the shock wave, boundary layer, separated wake and recirculation region. With the present generation of computers, meaningful solutions are possible only for two dimensions at Reynolds numbers less than about 100, which makes exact Navier-Stokes solutions of little practical importance in the design of aircraft. This is caused by the fact that the Reynolds number based on step size must be of order one in order to insure accurate, stable solutions in representing shock waves and boundary layers. Therefore since

$$Re_{\Delta x} \sim 1$$

$$\frac{L}{\Delta x} = N = \text{number of steps}$$

$$Re_L \sim N.$$

The capacity of the computer is proportional to N^2 and a grid work of about 100×100 utilizes the full capacity of today's machines.

With the rapid strides occurring in computer technology and the improvements taking place in programming, we are not too far away from practical solutions. In the meantime, however, we must resort to some approximate methods.

Flow fields may be broken up into an outer region in which viscous effects are insignificant and into an inner region in which the boundary layer assumptions apply. Even with these assumptions general three-dimensional solutions are not yet available. However accurate two-dimensional solutions are possible in both inner and outer regions (Fig. 5). Rotational characteristic programs with imbedded shocks have been devised⁵ and two-dimensional boundary layer solutions for compressible, laminar flows have been obtained⁶. For flows involving separation and reattachment, boundary layer solutions cannot be superimposed upon the inviscid pressure distribution due to the interaction between the inner and outer regions. These two flows must be again coupled and simultaneously solved. Two-dimensional solutions for these interacting flows have been obtained by Lees and Reeves⁷, Nielsen⁸, Reyhner and Flugge-Lotz⁹ and Holden¹⁰. Progress in this area is encouraging but until general three-dimensional solutions are obtained the designer must resort to simpler and even more approximate schemes.

2.1 Simplified Design Procedures

Recalling that only the pressure and shear stress on the surface are required and not detailed properties for the entire flow field then maybe something simpler is possible. If the shock shape is known, pressure may be precisely determined using the extremely accurate Rankine-Hugoniot shock relationships. For oblique shock waves the relationship between shock angle and body angle is as follows:

$$\sin^2(\theta - \delta) = \frac{M_1^2 \sin^2 \theta + 5}{M_1^2 (7M_1^2 \sin^2 \theta - 1)}$$

For modest angles and high Mach numbers

$$\theta - \delta \sim 0$$

and

$$C_p = \frac{M_1^2 \sin^2 \theta - 1}{0.6 M_1^2} \sim k \sin^2 \theta \sim k \sin^2 \delta.$$

Therefore, at hypersonic speeds pressure may be estimated by assuming the shock wave is tangent to the body surface (Fig. 6). The pressure coefficient is a function of body shape alone.

$$C_p = k(n \cdot i)^2.$$

Skin friction coefficients (C_f) have been obtained by Schmidt^{11,12} based on reference enthalpy techniques for flat plates at angle of attack at various flight altitudes and velocities.

$$C_f = C_f(Re_\infty, \delta).$$

Using these simple relationships the aerodynamic problem becomes elementary. The lift and drag equations for a general shape are as follows:

$$\frac{L}{q} = \oint [C_p(\underline{k} \cdot \underline{n}) - C_f(\underline{k} \cdot \underline{t})] dA$$

$$\frac{D}{q} = \oint [C_p(\underline{i} \cdot \underline{n}) - C_f(\underline{i} \cdot \underline{t})] dA$$

The problem becomes only one of geometry. The normal and tangential vectors must be determined and the two integrals evaluated over the body. This is quite often a tedious and laborious problem, however. Two schemes have been employed. In one scheme the surface is broken up in a grid, the pressure and shear coefficients determined, and numerical integrations performed to ascertain the forces. In the other method the configuration is approximated by segments of analytical surfaces, closed form integrations performed, and a set of algebraic relationships established for the force coefficients. The following set of equations is an example of a typical configuration (Fig. 7) which was successfully analyzed in this manner¹³:

Nose Equations

$$C_N = \frac{\pi R_N^2 k_N}{4S} \sin \alpha (1 + \cos \alpha)$$

$$C_A = \frac{\pi R_N^2 k_N}{4S} \frac{(1 + \cos \alpha)^2}{2}$$

$$C_m = C_N \frac{x_N}{\bar{c}} - C_A \frac{z_N}{\bar{c}}$$

$$C_{Y\beta} = -\frac{C_A}{\cos \alpha}$$

$$C_{l\beta} = \frac{C_A}{\cos \alpha} \frac{z_N}{b}$$

$$C_{n\beta} = -\frac{C_A}{\cos \alpha} \frac{x}{b}$$

All derivatives and all angles are in radians.

Leading Edge Equations

These equations are for a pair of leading edge elements.

$$C_N = \left(\frac{4R_{LE} l_{LE}}{3S} \right) k_{LE} \sin \alpha (\cos \Lambda_e + \cos \Lambda \cos \alpha)$$

$$C_A = \left(\frac{4R_{LE} l_{LE}}{3S} \right) \frac{k_{LE}}{2} \cos \Lambda (\cos \Lambda_e + \cos \Lambda \cos \alpha)^2$$

$$C_m = C_N \frac{x_{LE}}{\bar{c}} - C_A \frac{z_{LE}}{\bar{c}}$$

$$C_{Y\beta} = -\left(\frac{4R_{LE} l_{LE}}{3S} \right) k_{LE} \sin^2 \Lambda \cos \Lambda_e (1 + \cos \alpha_e)^2$$

$$C_{l\beta} = \frac{4R_{LE} l_{LE}}{3S} k_{LE} \sin \Lambda (1 + \cos \alpha_e) \left[\frac{z_{LE}}{b} \sin \Lambda \cos \Lambda_e (1 + \cos \alpha_e) - \frac{y_{LE}}{b} \sin \alpha \right]$$

$$C_{n\beta} = \left(\frac{4R_{LE} l_{LE}}{3S} \right) k_{LE} \sin \Lambda \cos \Lambda_e (1 + \cos \alpha_e)^2 \left(\frac{-x_{LE}}{b} \sin \Lambda + \frac{y_{LE}}{b} \cos \Lambda \right)$$

$$(\sin \Lambda_e)_L = \sin \Lambda \cos \alpha \cos \beta + \cos \Lambda \sin \beta$$

$$(\cot \alpha_e)_L = \cos \Lambda \cot \alpha \pm \frac{\sin \Lambda}{\sin \alpha} \tan \beta$$

l_{LE} for one leading edge.

Lower Surface Equations

$$C_N = k_\alpha \left(\frac{S_L}{S} \right) \sin^2 \alpha$$

$$C_A = G \left(\frac{S_w}{S} \right) \frac{0.45 \cos \alpha + 4.65 \frac{V_\infty}{10,000} \sin \alpha \cos^{2.2} \alpha}{\left(\frac{V_\infty c}{\nu_\infty} \right)^{0.5}} \quad (\text{laminar})$$

$$C_A = G \left(\frac{S_w}{S} \right) \frac{0.048 \sin (4.5\alpha) + 0.70 \frac{V_\infty}{10,000} \cos^{2.25} \alpha \sin^{1.5} \alpha}{\left(\frac{V_\infty c}{\nu_\infty} \right)^{0.2}} \quad (\text{turbulent})$$

$$C_m = C_N \frac{x_L}{c} - C_A \frac{z_L}{c}$$

$$C_{Y\beta} = - \frac{C_A}{\cos \alpha}$$

$$C_{l\beta} = \frac{C_A}{\cos \alpha} \frac{z_L}{b} - k_i \sin^2 \alpha \left(\frac{S_L}{S} \right) \frac{2y_{LE}}{9b}; \quad k_i = 3.8$$

$$C_{n\beta} = - \frac{C_A}{\cos \alpha} \frac{x_L}{b},$$

where

$$G = \frac{2}{n(1+n)} \left[\frac{1-m^{1+n}}{1-m^2} \right];$$

$$n = \begin{cases} 0.5 & \text{laminar} \\ 0.8 & \text{turbulent} \end{cases}$$

m = planform taper ratio.

Vertical Fin Equations*

$$C_N = - \frac{8R_F l_F k_{LE}}{3S} \cos^2 (\Lambda_F + \alpha) \sin \Lambda_F$$

$$C_A = 2k_F \frac{S_F}{S} (\lambda^3 \cos^2 \alpha) + \frac{8R_F l_F k_{LE}}{3S} \cos^2 (\Lambda_F + \alpha) \cos \Lambda_F$$

$$C_m = -2k_F \frac{S_F}{S} (\lambda^3 \cos^2 \alpha) \left(\frac{z_F}{c} \right) - \frac{8R_F l_F k_{LE}}{3S} \cos^2 (\Lambda_F + \alpha) \left[\frac{x_{FLE}}{c} \sin \Lambda_F + \frac{z_{FLE}}{c} \cos \Lambda_F \right]$$

$$C_{Y\beta} = -4k_F \frac{S_F}{S} (\lambda \cos \alpha)$$

$$C_{l\beta} = -4k_F \frac{S_F}{S} (\lambda \cos \alpha) \left(- \frac{z_F}{b} \right)$$

$$C_{r,\beta} = 4k_F \frac{S_F}{S} (\lambda \cos \alpha) \left(- \frac{x_F}{b} + \lambda \frac{y_F}{b} \right)$$

S_F = for one fin

l_F for one fin.

* The equations are for a pair of fins.

2.2 Ultra-Simplified Method

Considerable understanding and insight into the hypersonic aerodynamic characteristics of lifting vehicles can be achieved by examining the simple Newtonian approach.

Let

$$C_L = (k \sin^2 \alpha) \cos \alpha$$

and

$$C_D = (k \sin^2 \alpha) \sin \alpha + C_{D0}.$$

Therefore

$$\frac{L}{D} = \frac{\sin^2 \alpha \cos \alpha}{\sin^3 \alpha + C_{D0}/k}$$

and

$$\frac{L}{D} = \frac{L}{D}(\alpha, C_{D0}/k).$$

The maximum L/D for constant C_{D0}/k can be obtained by differentiation with respect to α . Optimum angle of attack and maximum values of L/D are shown in Figures 8 and 9 for the above equations. Two aspects should be noted: higher values of $(L/D)_{\max}$ are achieved at the lower angles of attack and (L/D) values much in excess of 4 are not possible due to skin friction alone.

3. STABILITY ANALYSIS

The dynamics of a vehicle must be such that the handling qualities are within the servo response capabilities of the pilot. The short period modes are the most critical, namely the longitudinal short period mode (pitching) and the lateral oscillation short period mode (Dutch roll). The equations of motion for these oscillations are as follows:

$$\ddot{\alpha} + \omega_\alpha^2(\alpha - \alpha_0) = 0$$

$$\ddot{\beta} + \omega_\beta^2 \beta = 0,$$

where

$$\omega_\alpha^2 = -\frac{qSc}{I_y} C_{m\alpha}$$

$$\omega_\beta^2 = qSb \left[\frac{C_{n\beta}}{I_z} \cos \alpha_0 - \frac{C_{l\beta}}{I_x} \sin \alpha_0 \right].$$

Aerodynamic damping at hypersonic speeds is generally small because the reduced frequency ($\omega c/V$, which is a measure of the dynamic angle of attack) is low due to V appearing in the denominator.

Pilot rated simulator studies have indicated the most desirable operating conditions are when the short period mode has the following characteristics:

$$f = \text{frequency} = 0.7 \text{ c/s} \pm 0.3$$

$$\zeta = \text{damping ratio compared to critical} = 0.7 \pm 0.3.$$

Oscillations of this type are within his servo response characteristics, yet the vehicle possesses satisfactory maneuverability (neither too sluggish nor too sensitive). Present day aircraft attain these handling qualities either by aerodynamic means or artificially by "adaptive control" features. Since negligible aerodynamic damping exists ($\zeta \rightarrow 0$) the handling quality criteria cannot be achieved for emergency situations in which artificial augmentation is inoperative. Zero damping implies periodic motion of constant amplitude for which the pilot must reduce any disturbance by "out-of-phase" control modulation. Long periods ($P > 10$ seconds) are required to effectively accomplish this feat. Therefore a hypersonic vehicle should be designed with a low dynamical frequency which implies neutral stability. This condition is not comfortable to fly, but is considered acceptable through flight simulator training as long as augmentation on all channels is not simultaneously inoperative. Thus

$$C_{m\alpha} = C_{n\beta} = C_{l\beta} = 0$$

is a design goal.

4. LANDING ANALYSIS

The low-speed flying requirements impose several constraints on a hypersonic lifting vehicle. First, the vehicle must be able to execute a satisfactory horizontal landing and, secondly, it must possess acceptable stability. Low-speed performance requirements are not considered as important since most of the maneuverability is accomplished at hypersonic speeds, although some low-speed maneuverability is a fall-out from the landing constraint. The point is that the vehicle will probably not be designed for good low-speed performance but must accept the amount available.

The method presently deemed most desirable for landing hypersonic aircraft is the "aiming point" technique used in the X-15. In this method the pilot dives the vehicle at a point on the earth's surface several thousand feet before the runway, then executes a flare at some predetermined altitude to a shallow glide angle, and decelerates by increasing the angle of attack until touchdown at some preselected speed. By the use of this "Dynamic Approach" technique, vehicles of low subsonic L/D may be safely landed. In this maneuver the highest lift coefficient is required at touchdown. For $\dot{\gamma} = 0$,

$$(C_L)_{\max} = \frac{W/S}{q_{TD}}.$$

The lift coefficient for low aspect ratio (AR) airfoils may be estimated by the theory of Jones

$$C_L = \frac{\pi}{2} AR \alpha.$$

When the last two equations are combined,

$$\frac{W}{S AR} = \frac{\pi}{2} q_{TD} \alpha.$$

For touchdown velocities less than about 200 knots and for angles of attack less than 15° ,

$$\frac{W}{S AR} \leq 50 \text{ lb/ft}^2.$$

Hence the preceding relationship between wing loading and aspect ratio becomes the simplest minimum landing constraint.

5. OPTIMIZATION SEARCHING ROUTINE

After the aerodynamic equations have been formulated, the best combination of the design parameters must be found. Hence an automated search routine is required.

One class of multivariable optimization problem is concerned with the maximization of a function θ (Ref.14). This function is commonly referred to as a payoff, criterion, cost, or performance function and is of the form

$$\theta = f(X_1, \dots, X_j),$$

which may be subject to constraints of the form

$$\Psi_i = f(X_1, \dots, X_n), \quad i = 1, 2, \dots, k < j,$$

where the X_i 's are variables which describe the system. In the case of aeronautical design the system may be a wing, where the performance function θ is the lift-drag ratio, and the constraints Ψ_i are wing volume, area, etc. The number of independent design variables of the system n is the number of description variables j minus the number of constraint relations k ,

$$n = j - k.$$

The optimization problem represented here is called an "ordinary" maximum-minimum problem to distinguish it from the variational calculus problem¹⁵.

There are, in general, two broad methods of optimizing ordinary functions. The first is the classical indirect method which involves finding the necessary conditions for a maximum or minimum. The second method is the so called direct method which involves, as the name implies, direct numerical evaluation of the criterion function θ and the constraint functions Ψ_i .

The method used for the optimization of a particular function depends upon the nature of the function and the form in which information is available. The indirect method is most conveniently applied to problems in which the algebraic form and continuity properties of the function to be optimized are known. The direct method of optimization, on the other hand, can be applied to a class of problems in which the structure and the nature of the function to be optimized are unknown. This class of problems has arisen more frequently with the advent of the high-speed digital computer in which a computerized mathematical model is used to synthesize the actual system.

Several direct search algorithms (Table I) have been combined into a single computer program called the Automated Engineering and Scientific Optimization Programs (AESOP) (Ref. 16). The program AESOP is independent of the problem being solved. In a vehicle synthesis problem, the computer program containing the algorithm for the evaluation of the vehicle performance can be linked to AESOP to determine the optimum configuration.

TABLE I

Basic Search Algorithms Contained in Program AESOP

1. *Sectioning* - Succession on one-dimensional optimization calculations parallel to coordinate axes. Variables may be perturbed in random or natural order.
2. *Pattern* - A Ray Search in the gross direction defined by a previous search or search combination.
3. *Magnification* - Straightforward magnification or diminution about the origin.
4. *Steepest-Descent* - Search along the weighted gradient-direction. Several weighting options available.
5. *Adaptive Creeping* - Search in small incremental steps parallel to the coordinate axes. Step-size adjusted automatically in the algorithm. Variables may be perturbed in random or natural order.
6. *Quadratic* - Second-order multivariable curve fit to the function being optimized, followed by search in direction of second-order surface optimum.
7. *Davidon's Method* - An attempt to achieve the advantages of second-order search from an ordered succession of first-order (steepest-descent) searches.
8. *Random Point* - Function to be optimized is evaluated at a set of uniformly distributed random points in a specified region.
9. *Random Ray Search* - Function is optimized by search along a sequence of random rays having a uniformly distributed angular orientation in the multivariable parameter space.

Three of these search options which have been most successful in vehicle synthesis will be discussed below.

The *random point method* randomly selects a series of design points from points which have uniform distribution throughout the design space. These design points are evaluated one by one and the design point with the highest value of the criterion function is retained. This method has an advantage in that its effectiveness is independent of the shape of the response surface. The method works as well on multimodal as on unimodal response surfaces. One disadvantage due to the vastness of the design space is that many points must be evaluated before attaining a high probability that the best point selected is actually at or near the optimum. The random method is useful during the early exploration of the design space when the response of the criterion function is unknown.

Another method which is useful in the early phases of the optimum configuration search is *sectioning*.

Search by sectioning is a series of one-dimensional searches along the entire ray in design space parallel to each of the coordinate axes. The one-dimensional ray in design space is formed by fixing all the search variables except the one on which the search is to be performed. The length of the ray is determined by the upper and lower bound of the design variables. The value of the variable giving the maximum performance is retained and the process is repeated for each of the remaining design variables.

The *adaptive creeper* method is a form of sectioning described above. However, instead of searching along the entire length of the ray parallel to the coordinate axis as in the global search, only small perturbations are made in one of the independent variables. Perturbations in the independent variable are continued until no further improvement in performance is possible. When the process has been repeated for each independent variable in turn,

a creeper search cycle is completed. In the case where there is no interaction between the independent variables, one search cycle is sufficient to locate a peak in the response surface. Usually, however, the shape of the response surface is such that more than one search cycle is required to locate a peak.

6. OPTIMIZATION OF HYPERSONIC LIFTING BODIES

The view taken herein is that the primary objective of a lifting body is to enclose a prescribed payload (volume requirement) with the minimum structural weight (wetted area limitation) and produce the highest possible hypersonic lift-to-drag ratio¹⁷. The geometric quantity that best represents payload-to-structural weight ratio is volumetric efficiency η , a dimensionless volume-area ratio referenced to that of a sphere.

$$\eta = \frac{6\pi^{1/2}V}{A_w^{3/2}}$$

Thus $\eta \leq 1$ always, being unity only for the sphere.

Besides meeting L/D and volumetric efficiency requirements, the vehicle must be capable of being trimmed, possess adequate stability, include the effects of skin friction, withstand aerodynamic heating, and provide safe terminal landing. To better understand the importance of certain of these constraints, three were singled out to be examined sequentially: namely, volumetric efficiency, nose heating, and skin friction. These constraints were imposed and the configuration determined which maximized hypersonic L/D .

The procedure utilized was to express a general closed geometric shape by a finite number of degrees of freedom, program the aerodynamic characteristic equations as a function of the geometric relationships, and employ a numerical searching routine to find the optimum. The details of this operation are presented in the following paragraphs.

The generalized shape (Fig. 10) was established with nine degrees of geometric freedom. This configuration is composed of four conical and four prismatic sections plus nose and base sections. (Lateral-directional stability requirements dictate symmetry about the $x-z$ plane). A Newtonian pressure distribution is assumed and laminar skin friction is considered. Integration of the pressure and shear forces produced relationships for L/D and η as shown in functional form.

$$\begin{aligned}\frac{L}{D} &= \frac{L}{D} \left(\frac{c}{h_1}, \frac{b_2}{b_1}, \frac{R_1}{R}, \alpha, \frac{h_1}{R}, \frac{b_2}{R}, \frac{h_2}{c}, C_{fc} \right) \\ \eta &= \eta \left(\frac{c}{h_1}, \frac{b_2}{b_1}, \frac{R_1}{R}, \alpha, \frac{h_1}{R}, \frac{b_2}{R}, \frac{h_2}{c}, \frac{\Delta c}{R} \right) = \text{prescribed} \\ \frac{h_2}{c} &= \epsilon = \text{prescribed} \\ C_{fc} &= \text{prescribed}\end{aligned}$$

These relationships contain eight geometric ratios which must be determined through the optimization procedure by maximizing L/D subject to the three constraint equations. The "adaptive creeper" searching routine was employed to ascertain the optimum geometric values.

6.1 Results

Case 1: Prescribed Volumetric Efficiency

The constraints are $\eta = \text{fixed}$, $\epsilon = \text{free}$ and $C_{fc} = 0$. One of the optimized configurations is shown in Figure 11 for an L/D of four. The resulting values of L/D are shown in Figure 12 as a function of volumetric efficiency. (Also shown for comparison are the X-20, ASSET and Gemini configurations). It is also interesting to note that simple wave-rider configurations produce about 1/2 the L/D value for the same η as the optimized shapes. These "classically" optimized configurations achieve the ultimate in hypersonic L/D in the absence of heating, skin friction, or other constraints.

For these optimum configurations, primarily only an increase in fineness ratio (c/h_1) is needed to increase L/D . In fact, for infinite fineness ratio (needle shaped) an infinite L/D results. Over most of the region of interest L/D is proportional to fineness ratio as follows:

$$\frac{L}{D} \approx 1.11 \left(\frac{c}{h_1} \right)$$

and also more fundamentally

$$\frac{L}{D} \sim 0.9 \left(\frac{2}{\eta^2} - 1 \right).$$

Case 2: Prescribed Volumetric Efficiency and Heating Constraints

The constraint equations are $\eta = \text{fixed}$, $\epsilon = \text{fixed}$ and $C_{fc} = 0$. The searching procedure was again employed for three different values of nose bluntness (ϵ). The optimized configurations tended to become blunted cones and approached a finite L/D limit even for a zero value of η (Fig.13).

$$\frac{L}{D} \approx \frac{0.45}{\epsilon^{0.55}} \quad \text{for zero } \eta.$$

Case 3: Prescribed Volumetric Efficiency and Skin Friction Constraints

The constraint equations are $\eta = \text{fixed}$, $\epsilon = 0$ and $C_{fc} = \text{fixed}$. Four values of skin friction were computed and again a finite limit on L/D occurs for zero η (Fig.14).

$$\frac{L}{D} = \frac{1}{1.5 (4C_f)^{1/3}} = \frac{0.42}{C_f^{1/3}} \quad \text{for zero } \eta.$$

This result is identical to that for a rectangular flat plate at angle of attack. The resulting optimum configurations approach a simple wedge in the limit of small η .

Case 4: Prescribed Volumetric Efficiency and Combined Heating and Skin Friction Constraints

The three constraint equations are $\eta = \text{fixed}$, $\epsilon = \text{fixed}$ and $C_{fc} = \text{fixed}$. For combined heating and skin friction constraints two relative maxima appeared. One configuration resembled a blunted cone which possessed superior L/D for $\epsilon/C_{fc} > 1$. The other configuration was more wedge-like and was superior for $\epsilon/C_{fc} < 1$. The resulting performance is shown in Figure 15.

The reason for the superior performance may be ascertained by examining the ratio of leading edge drag to skin friction drag.

$$\frac{D_{LE}}{D_f} \sim \frac{C_D h_2 b}{C_{fc} c b} \sim \frac{\epsilon}{C_{fc}}$$

The choice of the superior configuration is clear when this ratio is vastly different from unity; however, anticipated values of skin friction and nose bluntness for future systems indicate ϵ/C_{fc} near one. The designer then may choose between two drastically different geometries with nearly identical values of L/D . For example, Figure 16 shows two optimized configurations at an η of 0.4, $C_{fc} = 0.001$ and $\epsilon = 0.0015$. The cone-like geometry is superior since $\epsilon/C_{fc} = 1.5 > 1$ and possesses an L/D of 3.63 compared to 3.61. The resulting configurations are shown at similar scales to produce identical volumes and wetted areas. With large differences in geometry and only a subtle difference in L/D the designer would select one design over the other for practical constraints not considered here. Many hypersonic systems studies have been conducted on the cone-like configurations while the wedge-like configurations have received little attention.

6.2 Experimental Verification

To confirm the use of the simplified mathematical flow model of Newtonian pressure and elementary laminar skin friction, an experimental force test was conducted at $M \approx 14$ in the Aerospace Research Laboratories 20 inch hypersonic wind tunnel at WPAFB, Ohio. The model was 19 inches long and shaped as shown in Figure 11. The experimental results are presented in Figure 17 along with the theoretical prediction. The excellent agreement gives confidence in the applicability of the assumed flow model in predicting the integrated L/D value.

7. OPTIMIZATION OF A HYPERSONIC CRUISE VEHICLE

Examining the Breguet range equation shows an increased potential as velocity increases.

$$R = \frac{L}{D} I_{sp} \log_e \frac{W_1}{W_2} \left(\frac{V}{1 - \frac{V^2}{V_c^2}} \right).$$

where

$$L = W \left(1 - \frac{V^2}{V_c^2} \right)$$

$$T = \frac{dW}{dt} I_{sp} = L$$

$$R = \int V dt.$$

The velocity term approaches infinity at satellite speed. However, L/D , I_{sp} , and the weight fraction generally decrease with velocity. Answering the question of what happens to the product of these four terms at high velocities will tell us if a hypersonic transport is feasible.

An air traffic survey¹⁸ shows that an attractive market is in 4,000 to 6,000 nautical mile range (Fig.18). Since most of the land mass and population is contained within the northern hemisphere, global range (10,000 n.mi) would be rarely needed. Shorter ranges can be achieved adequately with the subsonic or supersonic transport, hence 5,500 n.mi range would be appropriate for a hypersonic transport. Figure 19 shows the time required to accomplish this range for different speeds. Time ceases to be an important factor after about $M = 8$.

Fuel selection for hypersonic propulsion systems may be determined by examining the following table of candidate fuel characteristics.

Property	Heat of Combustion Btu/lb	Heat Sink Btu/lb	Density lb/ft ³	M_{max}
Liquid H ₂	51,600	5100	4.4	16
Methane	21,500	1100	26.4	7
JP-4	18,600	165	50.0	3

Liquid hydrogen possesses better than twice as much chemical energy as either hydrocarbon. The main factor in fuel determination, however, is the cooling required for sustained cruise at hypersonic flight. Active cooling is essential in the combustion chamber of hypersonic vehicles. A qualitative estimate of the limiting velocity a vehicle can attain may be obtained by equating the heat sink of the fuel to the total enthalpy of the air flow. The last column indicates the maximum cruise Mach number for this condition. For sustained flight at Mach numbers above 7, only one fuel, LH₂, can be considered. Note the low density of LH₂ which necessitates much larger fuel volumes than required in conventional hydrocarbon fueled aircraft.

With fuel selected, the next feature to consider is the combustion process, i.e., subsonic or supersonic burning in a ramjet cycle. Previous studies have shown that subsonic combustion is more efficient below about $M = 8$ while supersonic combustion is more efficient for higher speeds. Therefore, in this study¹⁹ a supersonic combustion ramjet, hydrogen fueled, cruise vehicle will be considered for flight above $M = 8$.

A generalized configuration with 26 degrees of freedom was programmed and the aerodynamic characteristics determined in the following manner.

Inlet. A two-dimensional multiple-shock inlet with shock on cowl lip was employed. Forces were obtained using oblique shock relationships and turbulent skin friction superimposed. A minimum combustor entrance temperature of 2000°R corresponding to the auto-ignition value of the fuel-air mixture was imposed.

Combustor. A constant area ideal one-dimensional combustion cycle was employed utilizing real gas equilibrium conditions. Turbulent skin friction was superimposed.

Nozzle. A two-dimensional characteristic program was utilized with turbulent skin friction to obtain the nozzle forces.

Fuselage and Wing. Oblique-shock, Prandtl-Meyer and superimposed turbulent skin friction relationships were used to obtain the remaining body forces.

7.1 Constraints

In addition to the required geometric interrelationships, the following constraints were imposed:

1. Equilibrium Flight: $L = W \left(1 - \frac{V^2}{V_c^2} \right)$
 $T = D$.
2. Trimmed Conditions: $M_{c.g.} = 0$.
3. Vehicle Weight: Total weight, equipment and payload weight, structural panel density and fuel density were fixed.
4. Cooling: Aerodynamic heating requirements must not exceed the available fuel cooling capacity.

7.2 Results

The random search and adaptive creeper methods were employed to locate the maximum range condition for the optimal value of the configuration variables. Figure 20 shows that cruise range increases with velocity as anticipated from the Breguet range equation for the case without skin friction. However, for the realistic case with skin friction, little change in range was observed with speed. The Mach 10 optimized configuration is shown in Figure 21. The following qualitative conclusions can be deduced from this investigation.

1. Adequate cooling was available in the Mach range (8-12) considered.
2. The optimum configuration flies at about zero angle of attack so that the inlet develops no lift. A large pitchup moment is produced, however.
3. The optimum inlet geometry produces nearly maximum pressure recovery.
4. Minimum combustor entrance temperature is desirable (limited by the auto-ignition temperature).
5. Minimum combustor length was preferred limited by the combustion reaction time.
6. The optimum nozzle expansion angle was about 15° .
7. The combustor-nozzle cowl extension was minimum.
8. The upper fuselage angle was zero.
9. The maximum possible take-off weight was superior ("cube-square" law prefers largest scale possible, i.e. C5-A, 747).
10. The fuselage height nearly equaling the width is optimum.

REFERENCES

1. Hankey, W.L. et al. *Design Procedures for Computing Aerodynamic Heating at Hypersonic Speeds* (1960). WADC TR 59-610.
2. Feldman, S. *Hypersonic Gas Dynamic Charts for Equilibrium Air*. AVCO Research Report No.40, January 1957.
3. Dorrance, W.H. *Viscous Hypersonic Flow*. McGraw-Hill, New York, 1962.
4. Trulio, J.G. *Numerical Calculations of Separated Flows*. Proceedings of Symposium on Viscous Interaction Phenomena in Supersonic and Hypersonic Flow, Aerospace Research Laboratory Report, May 1969.
5. Johnson, J. *Investigation of the Low Speed Fixed Geometry Scramjet Inlet Design Practice Manual*. AFAPL-TR-68-7, February 1968.
6. Fitzhugh, H.A. *Numerical Studies of the Laminar Boundary Layer for Mach Numbers up to 15*. Journal of Fluid Mechanics, 1969, Vol.36, Part II, pp.347-366.

7. Lees, L.
Reeves, B.L. *Supersonic Separated and Reattaching Laminar Flows: 1, General Theory and Application to Adiabatic Boundary Layer/Shock Wave Interactions.* AIAA Journal, Vol. 2, 1964, pp.1907-1920.
8. Nielsen, J.N.
et al. *Theory of Laminar Separated Flows on Flared Surfaces including Supersonic Flow with Heating and Cooling.* AGARD Conference Proceedings No.4, Vol.1, May 1966.
9. Reyhner, T.A.
Flugge-Lotz, I. *The Interaction of a Shock Wave with a Laminar Boundary Layer* Int. J. No. 1 near Mechanics, Vol.3, Pergamon Press 1968, pp.173-199.
10. Holden, M.S. *Theoretical and Experimental Studies of Laminar Flow Separation on Flat Plate-Wedge Compression Surfaces in the Hypersonic Strong Interaction Regime* ARL 67-0112, May 1967.
11. Schmidt, J.F. *Laminar Skin Friction and Heat Transfer Parameters for a Flat Plate at Hypersonic Speeds in Terms of Free-Stream Flow Properties.* NASA TND-9, September 1959.
12. Schmidt, J.F. *Turbulent Skin Friction and Heat Transfer Coefficient for an Inclined Flat Plate at High Hypersonic Speeds in Terms of Free-Stream Flow Properties.* NASA TND-869, May 1961.
13. Hankey, W.L. *Optimization of Lifting Re-Entry Vehicles (1963).* ASD TDR 62-1102.
14. Wilde, D.J. *Optimum Seeking Methods.* Prentice-Hall, Inc., New Jersey, 1964.
15. Miele, A. *Theory of Optimum Aerodynamic Shapes.* Academic Press, New York, 1965.
16. Hague, D.S.
Glatt, C.R. *An Introduction to Multivariable Search Techniques for Parameter Optimization.* National Aeronautics and Space Administration, Ames Research Center, Moffett Field, California, April, 1968, Report No. NASA CR-73200.
17. Hankey, W.L.
Elliott, G.A. *Hypersonic Lifting Body Optimization.* Journal of Spacecraft and Rockets, Vol.5, No.12, December 1968, pp.1463-1467.
18. Jarlett, F.E. *The Hydrogen Fueled Hypersonic Transport.* Proceedings of Annual Aviation and Space Conference, June 1968
19. Walker, R.C. *Configuration Optimization of a Class of Hypersonic Cruise Vehicles for Maximum Range.* To be published as ARL-TR.

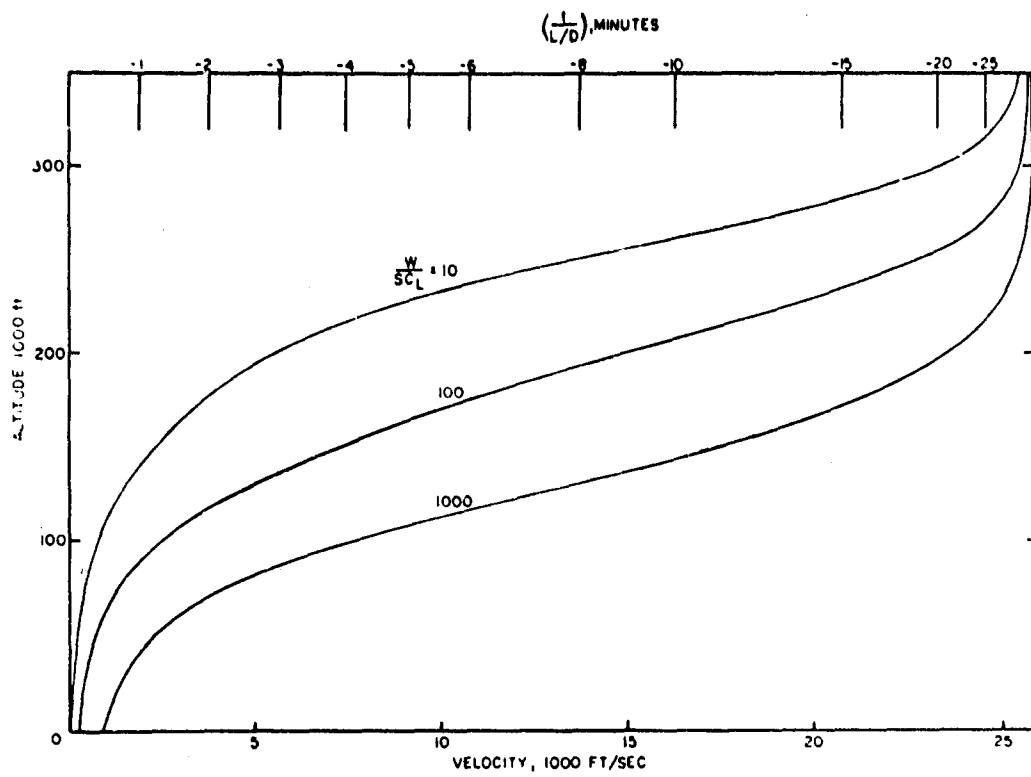


Fig. 1 Flight corridor

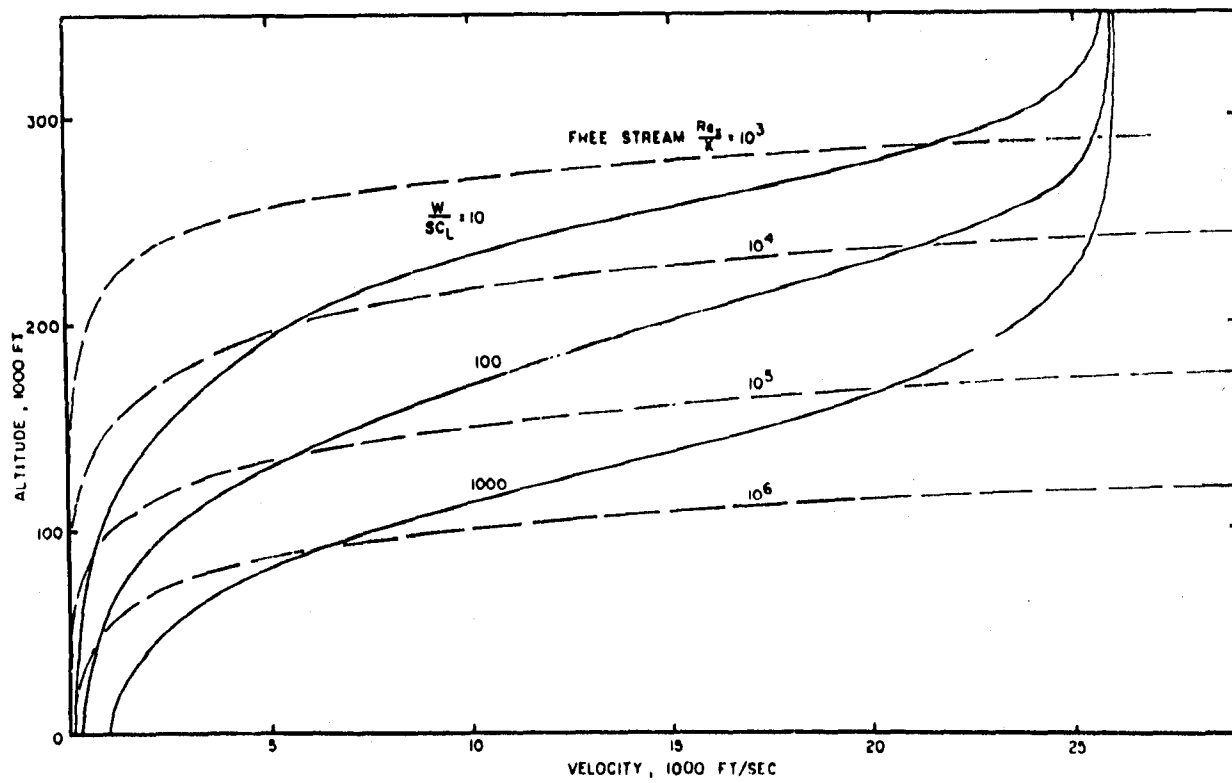


Fig. 2 Free stream flight Reynolds numbers

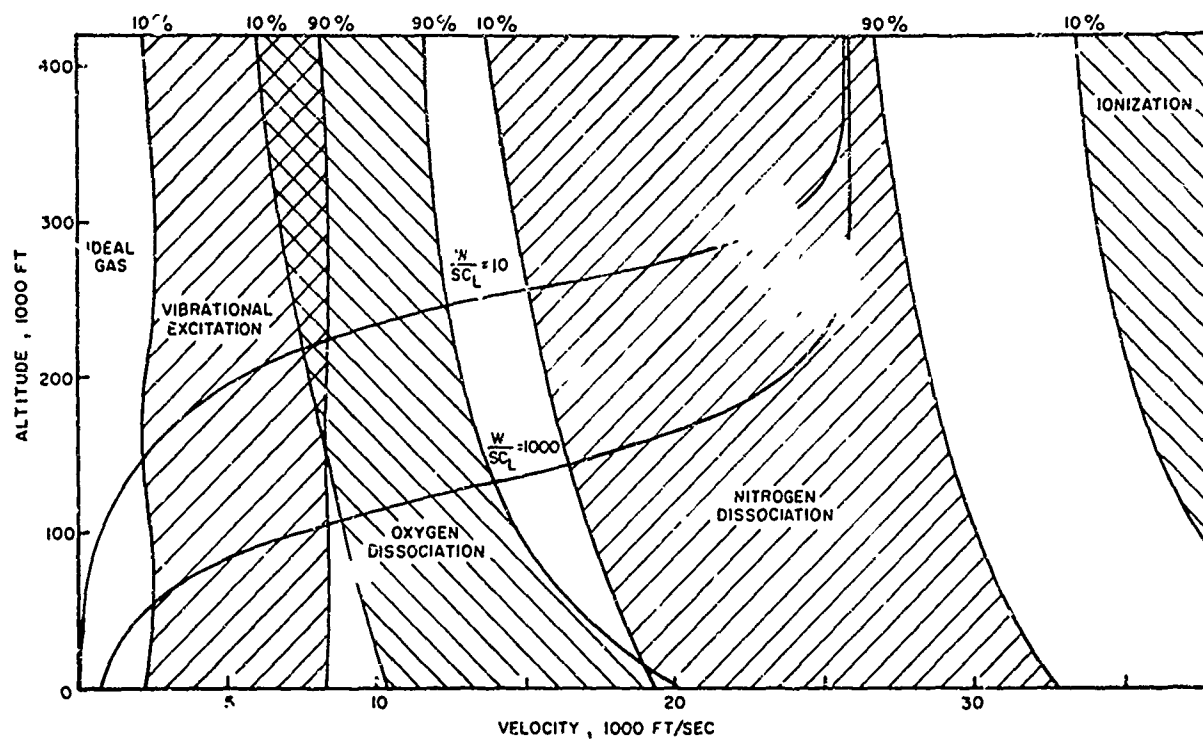


Fig.3 Energy excitation zones for the stagnation point

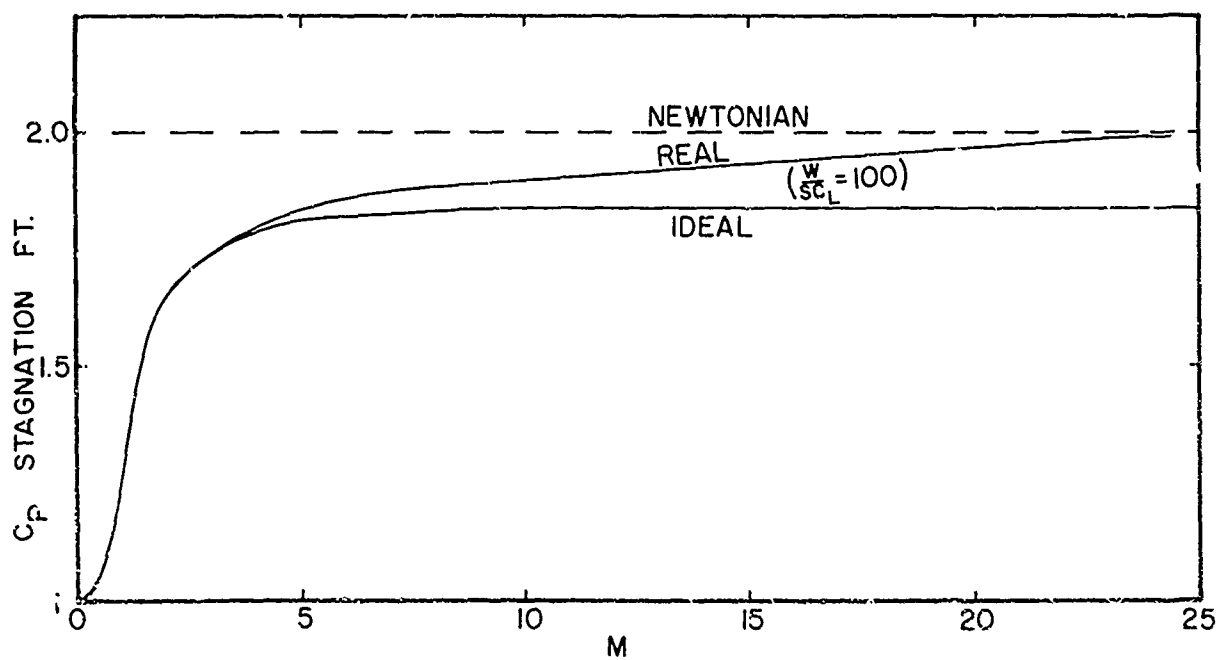


Fig.4 Stagnation point pressure coefficient

STATUS OF THEORY IN FLUID MECHANICS

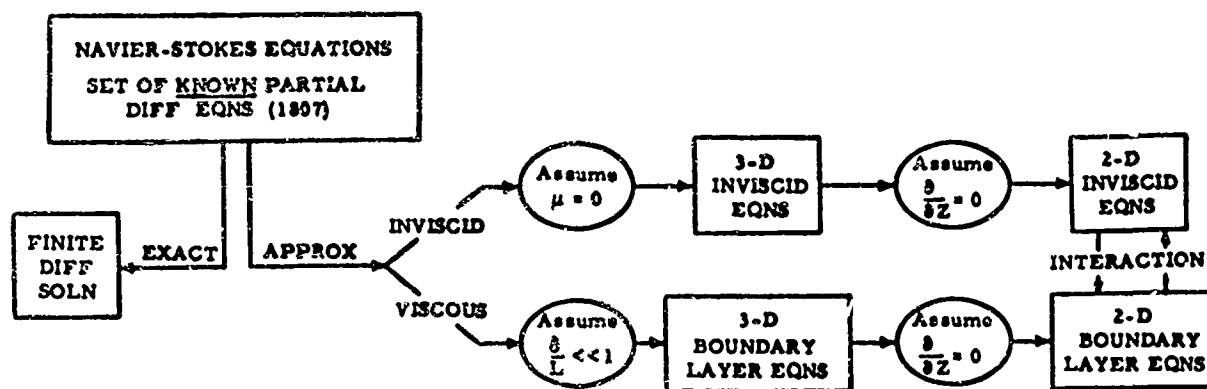


Fig.5 Status of theory in fluid mechanics

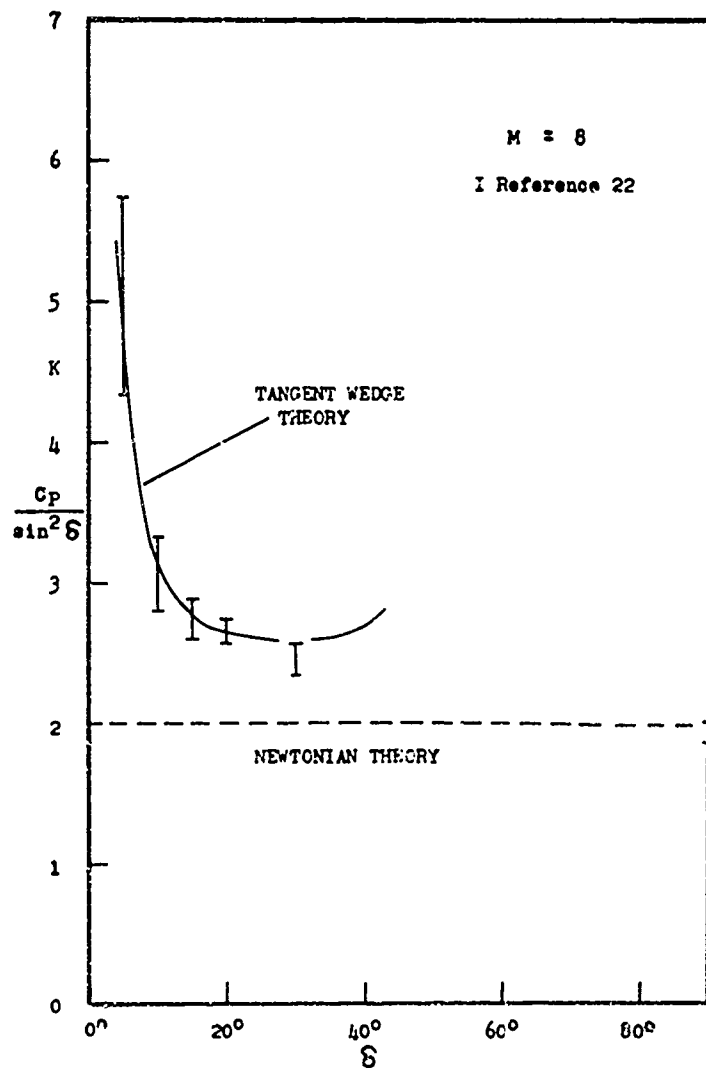


Fig.6 Lower surface pressure coefficients for a delta wing

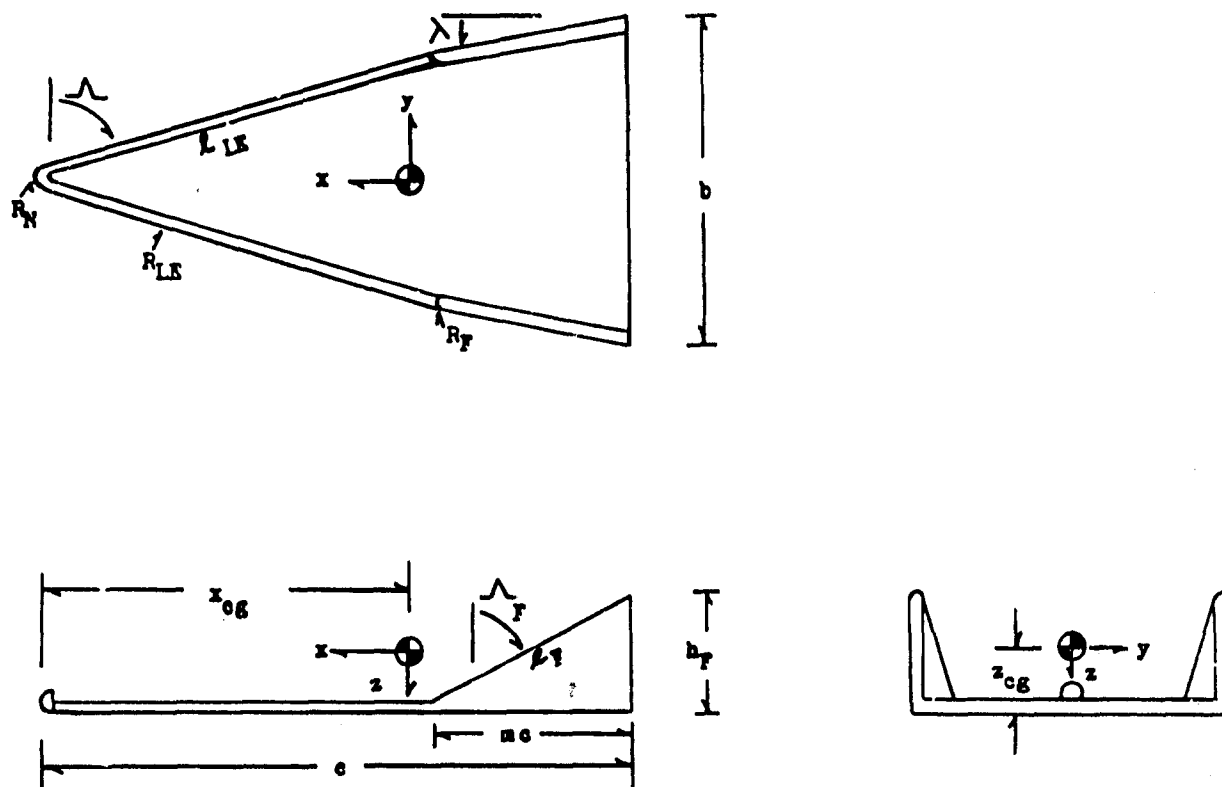


Fig.7 The generalized configuration geometry

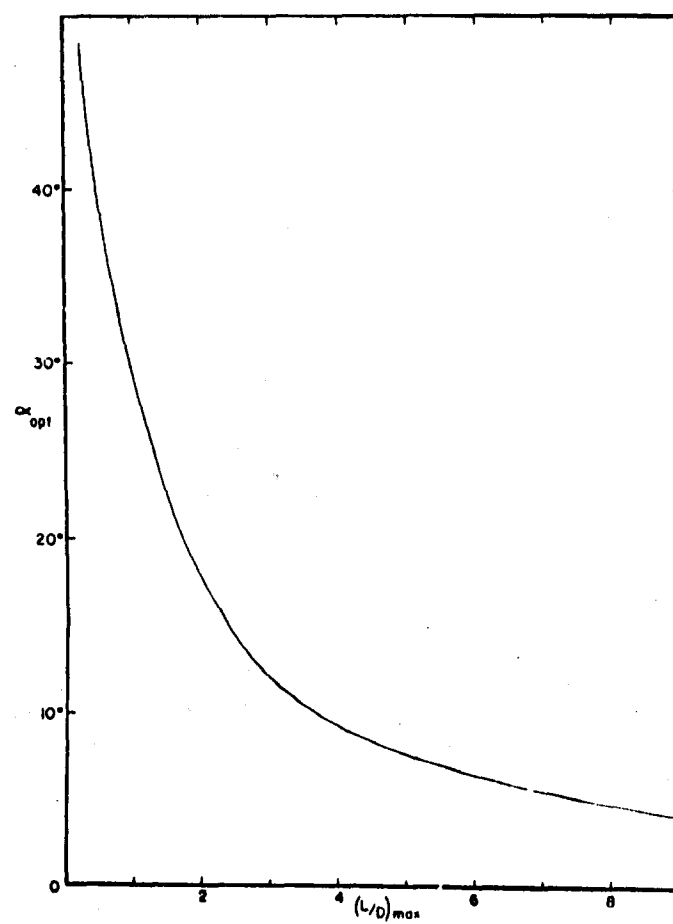


Fig.8 Optimum values of angle of attack

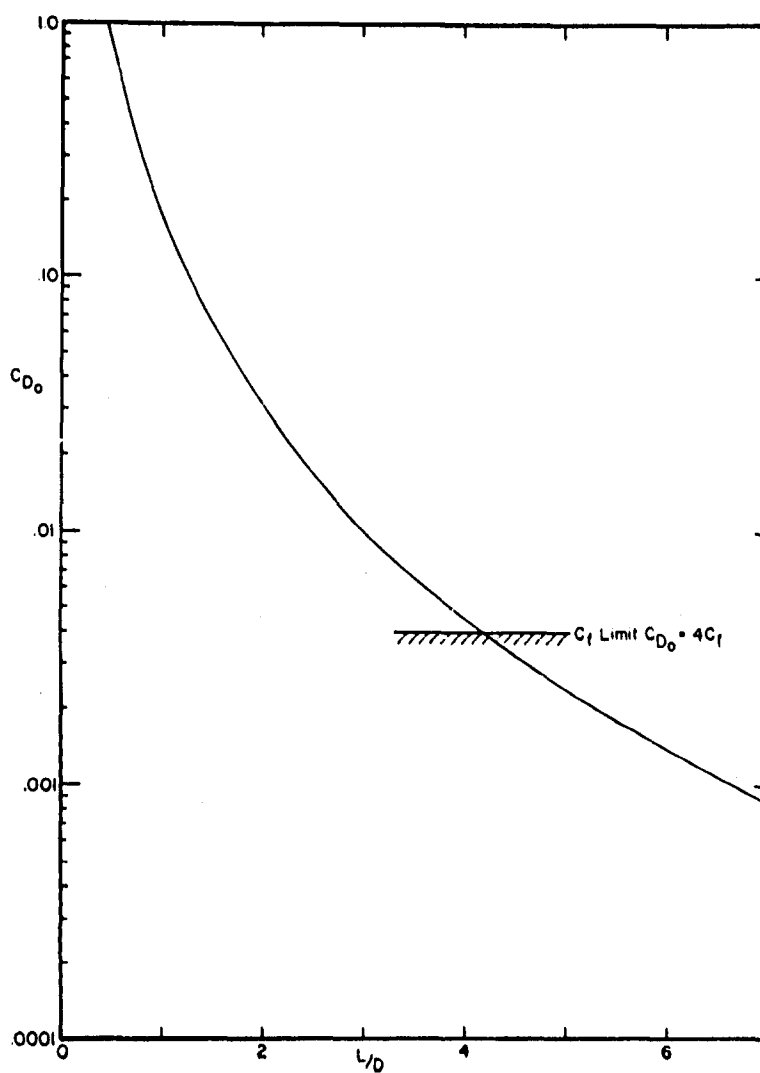
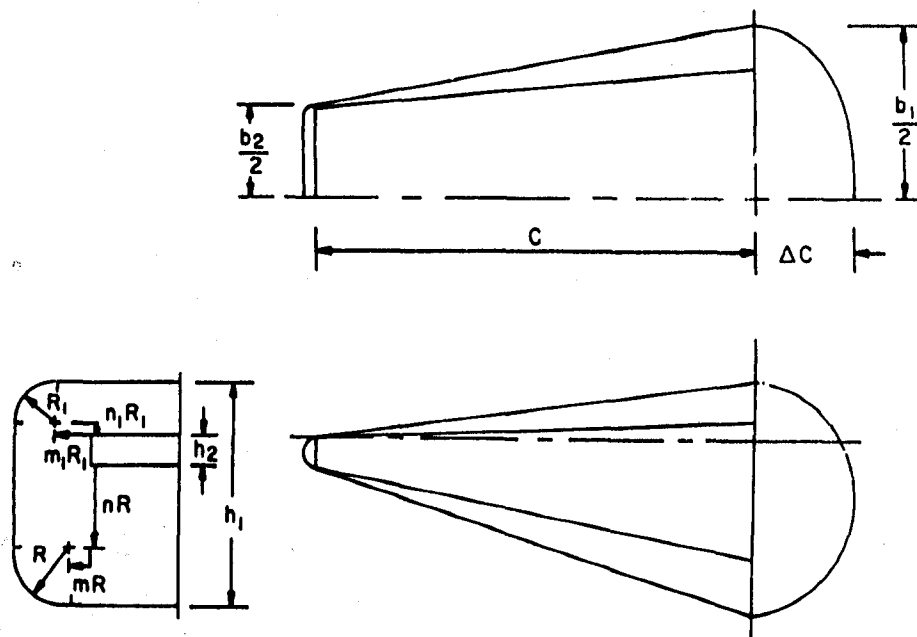
Fig. 9 $(L/D)_{\max}$ variation with C_{D0} 

Fig. 10 Generalized lifting body geometry

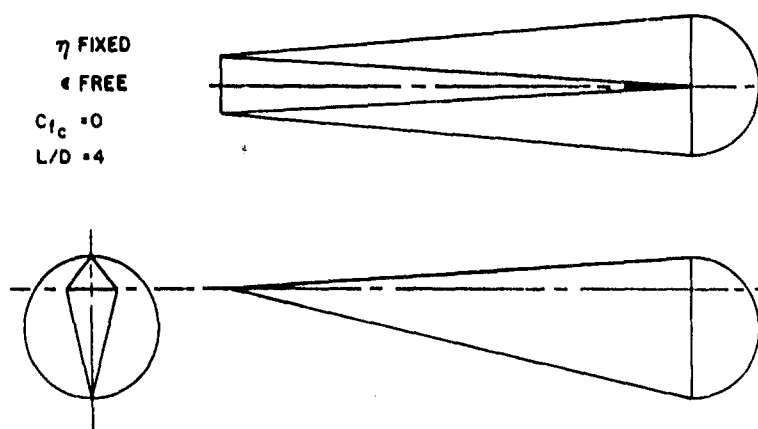
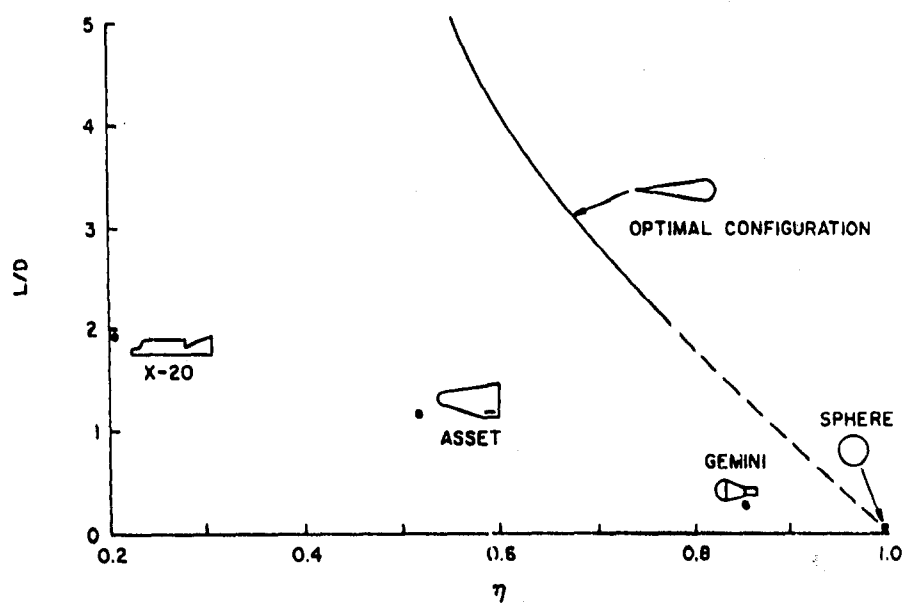
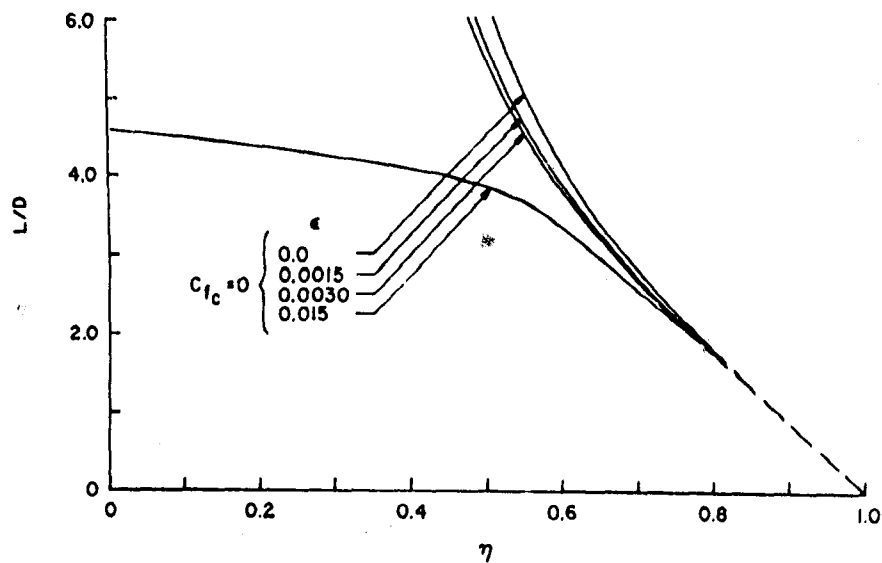
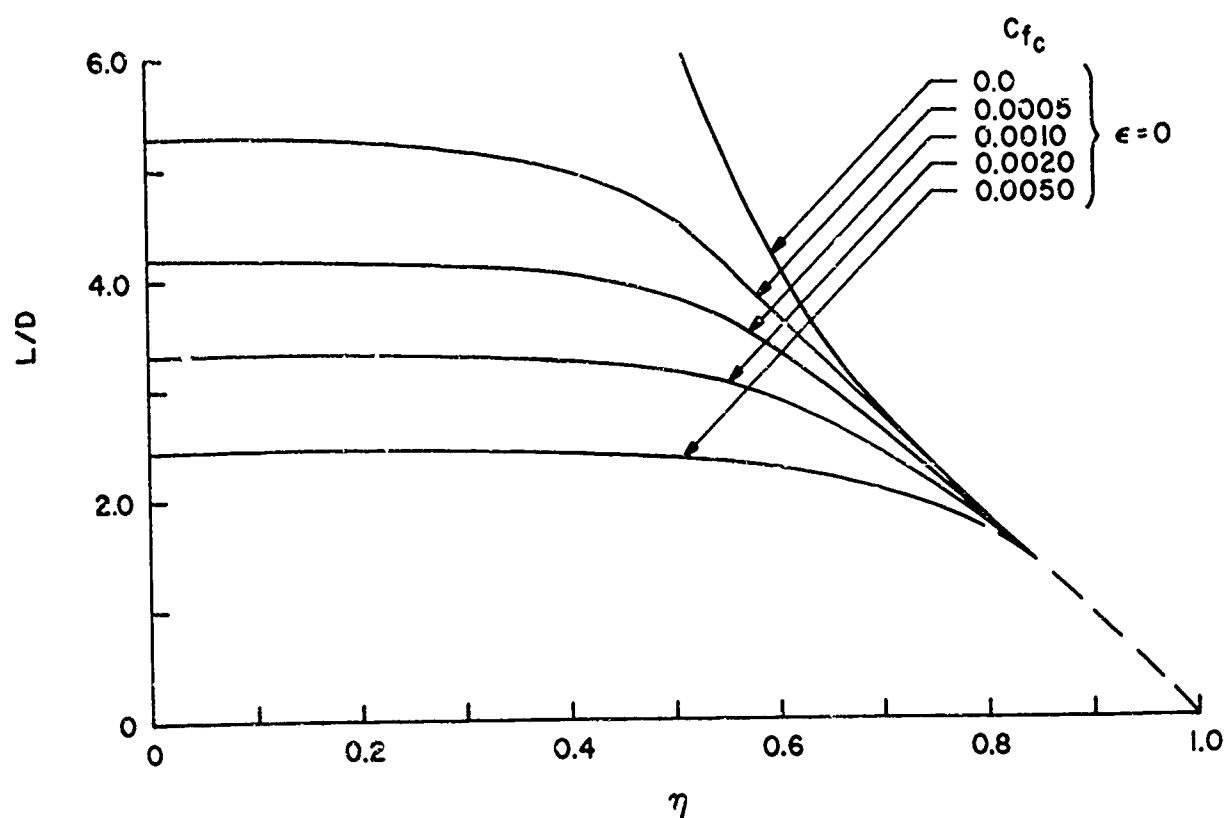
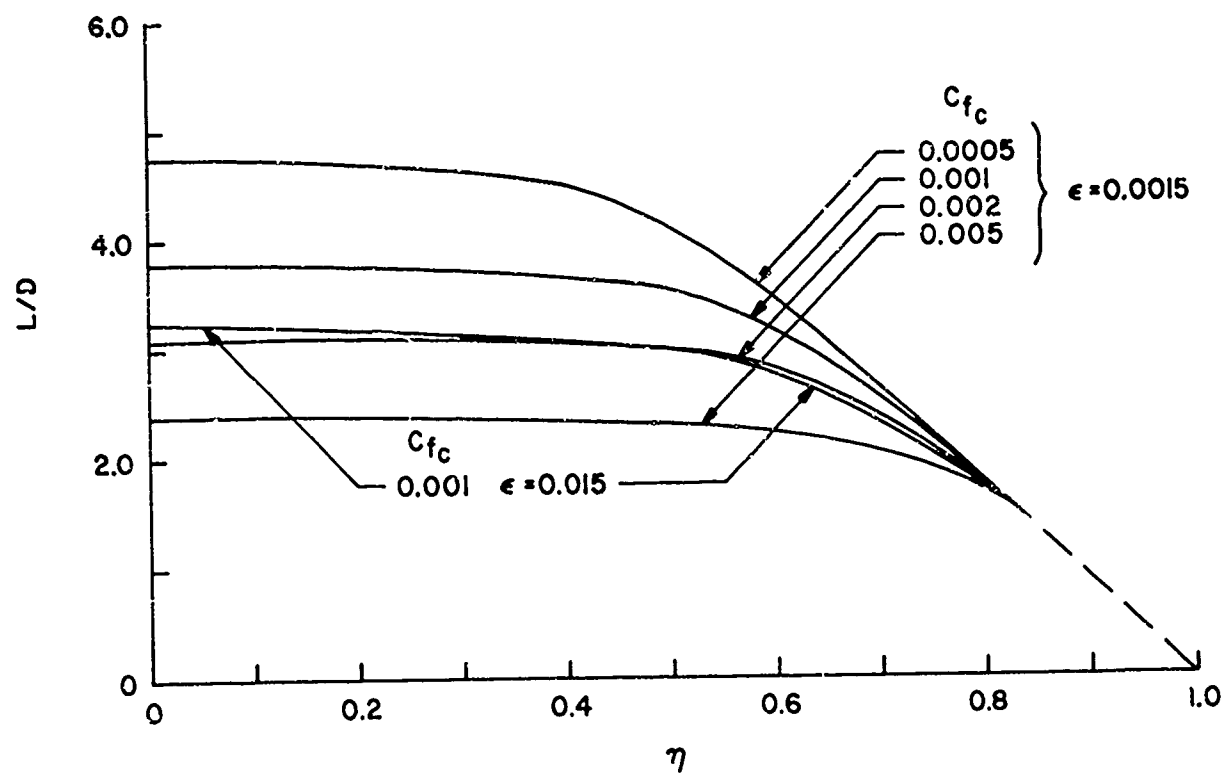


Fig.11 Typical optimized lifting body

Fig.12 L/D versus volumetric efficiency for no heating or skin friction constraintFig.13 L/D versus volumetric efficiency with heating constraint

Fig.14 L/D versus volumetric efficiency with skin friction constraintFig.15 L/D versus volumetric efficiency for both heating and skin friction constraint

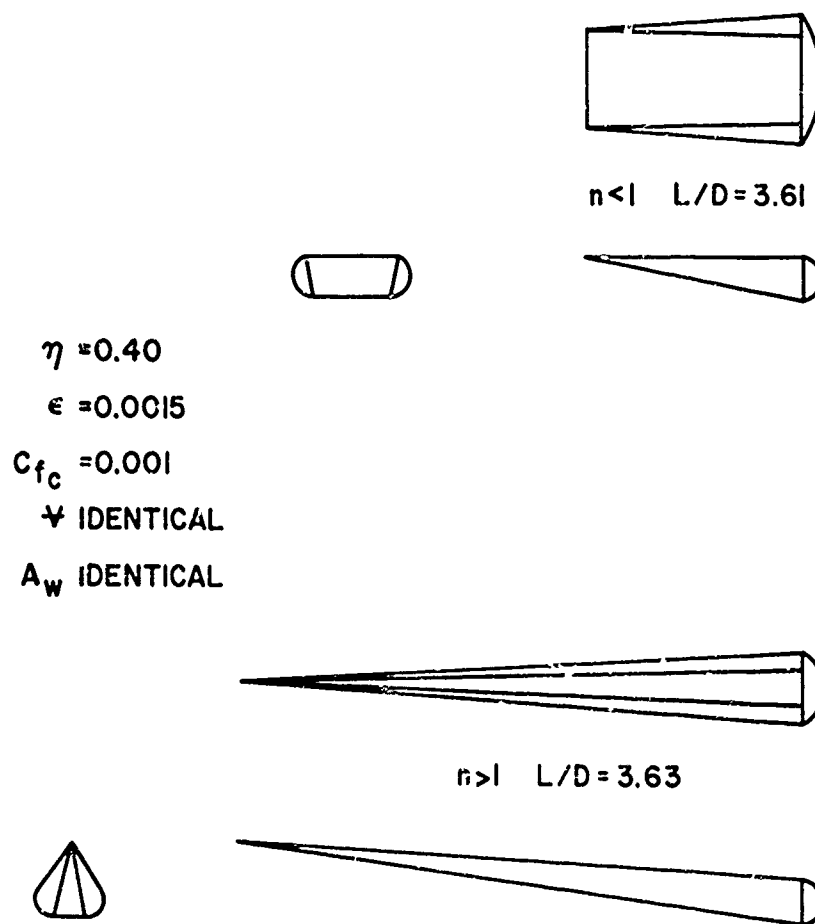
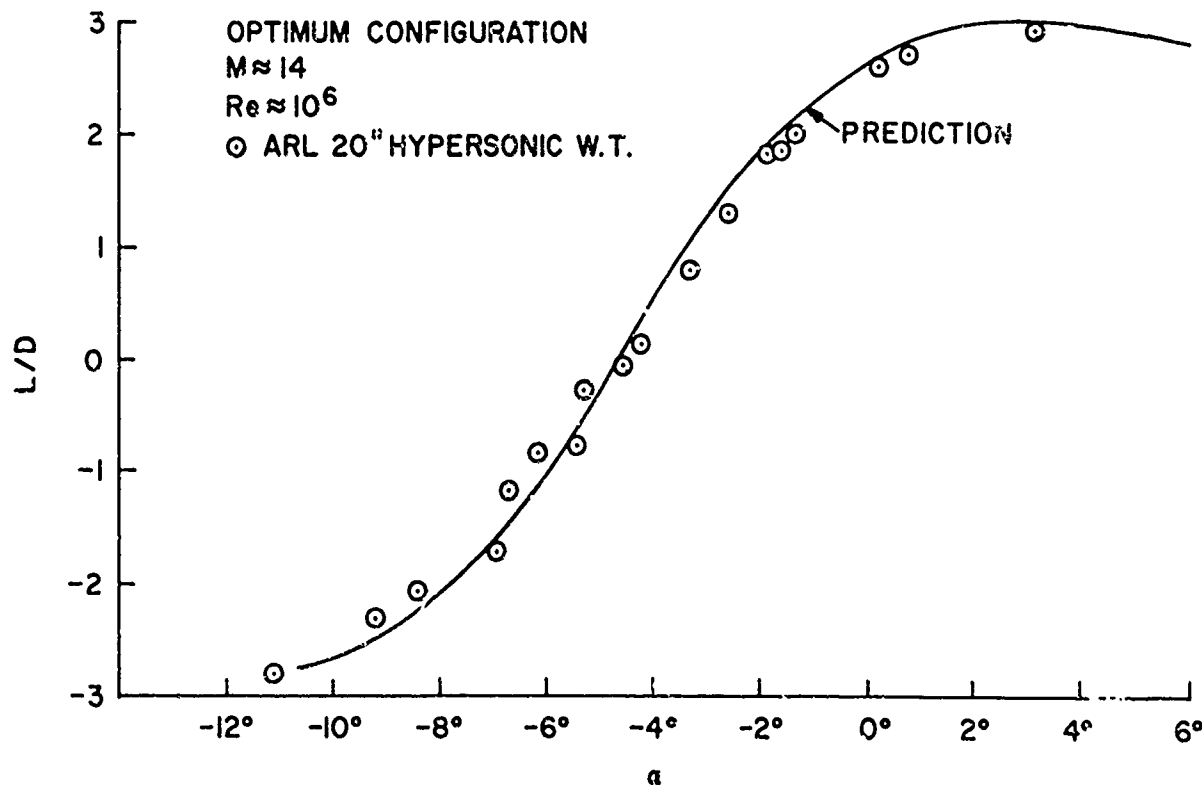


Fig.16 Comparison of optimized cone-like and wedge-like configurations

Fig.17 L/D comparison of theory and experiment

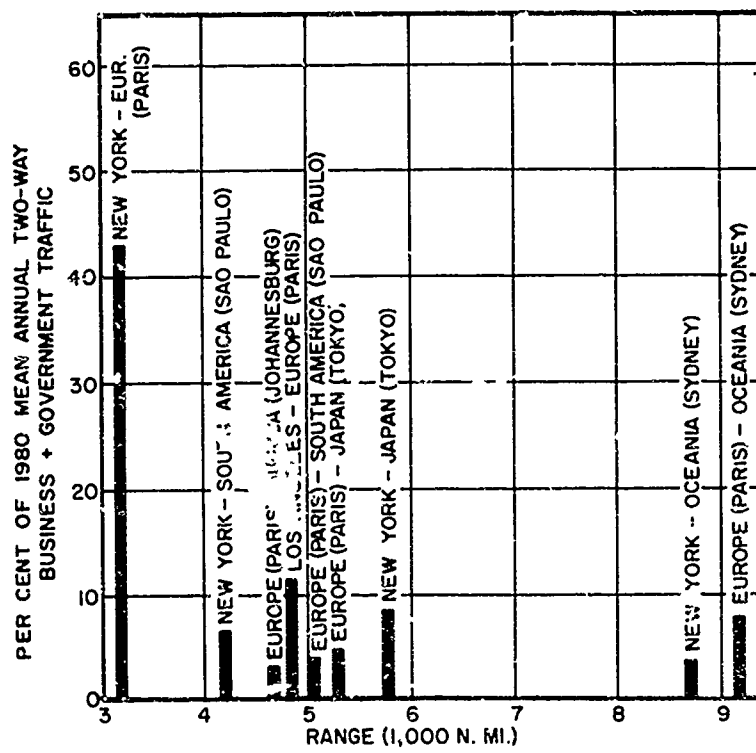


Fig.18 International business passenger traffic versus range

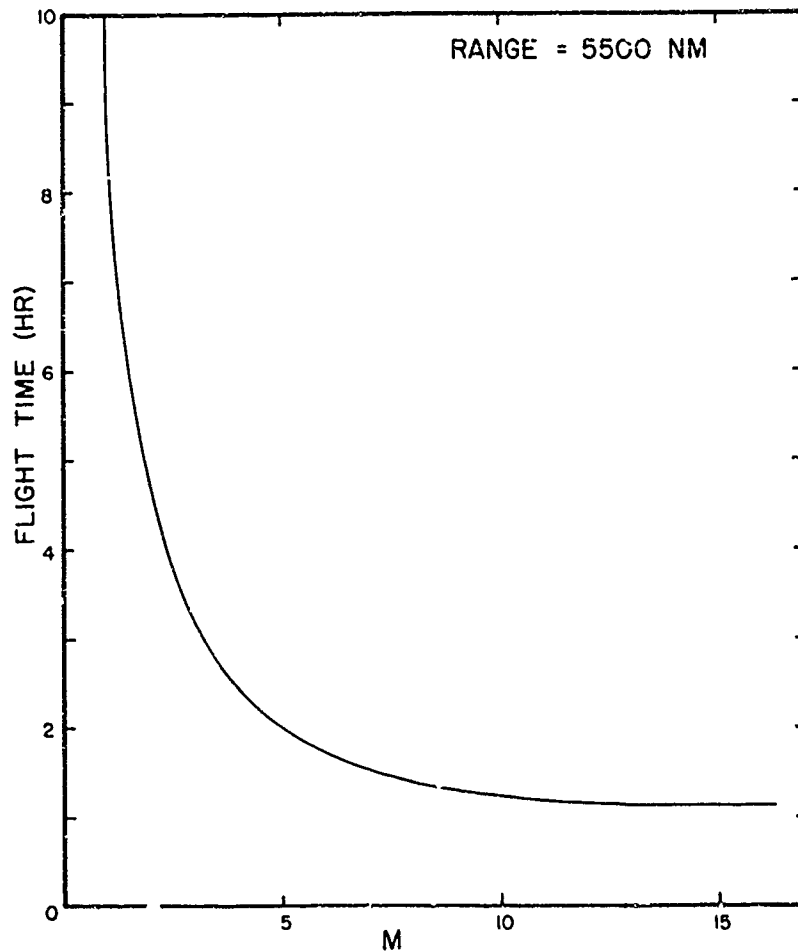


Fig.19 Flight time required to travel 5500 nautical miles

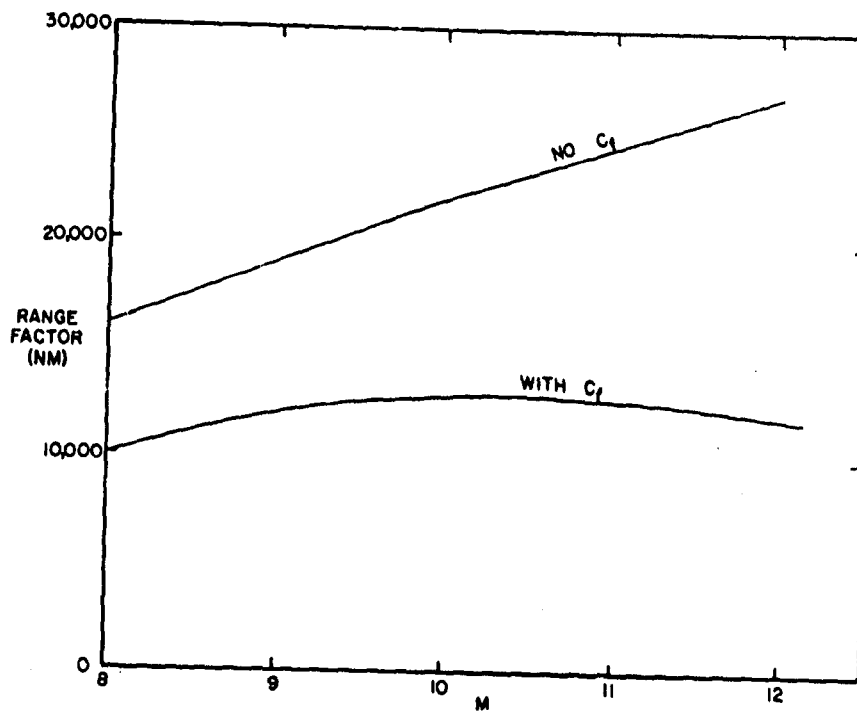


Fig.20 Variation of range factor with Mach number

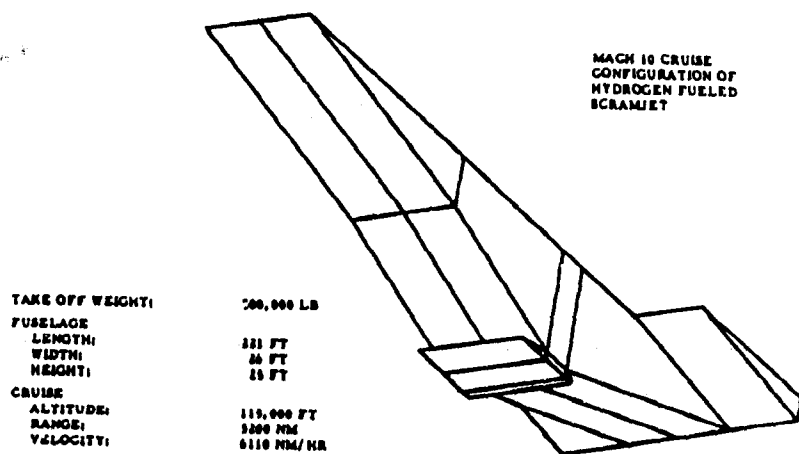


Fig.21 Optimized supersonic combustion ramjet vehicle

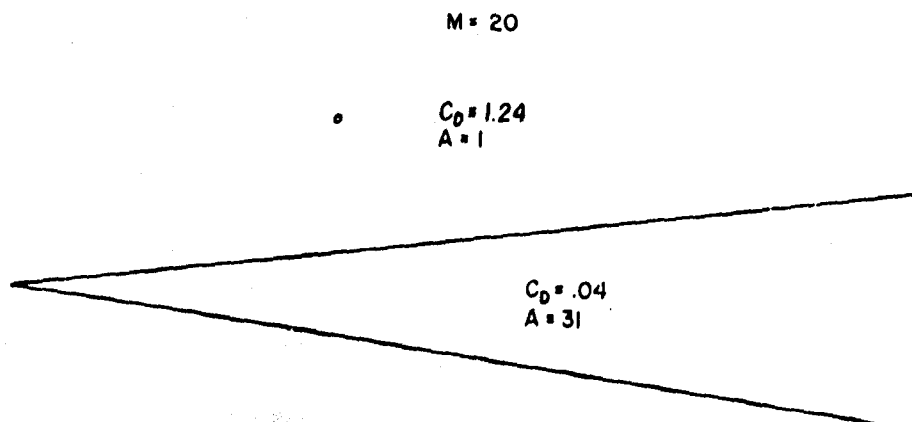


Fig.22 Identical drag configurations

LECTURE 9

REAL GAS EFFECTS ON LIFTING RE-ENTRY AEROTHERMODYNAMICS

K.N.C. Bray

University of Southampton, England

1. INTRODUCTION

In aerodynamics, the term real gas effect is applied to deviations in the thermodynamic properties of real air from an ideal gas with constant specific heats. These deviations result from various physical processes in air at high temperatures, namely, molecular vibrational excitation, chemical reactions and ionisation. Such processes occur at finite rates, which can be characterised by relaxation times, or by relaxation lengths in a flow of given velocity. If all relevant relaxation lengths are very much shorter than the smallest flowfield dimension of interest, the flow may be regarded as being in thermochemical equilibrium. The equilibrium thermodynamic properties of real air are well known¹, and may be incorporated without undue difficulty into flowfield calculations, so equilibrium real gas effects present no fundamental problems. The real gas flow may nevertheless be very different from that predicted on the assumption of a perfect gas with constant specific heats.

If relaxation lengths and flowfield dimensions are comparable, departures from thermochemical equilibrium will occur. The resulting nonequilibrium flow real gas effects may greatly influence aerodynamic properties. Prediction of nonequilibrium air flows requires detailed information on the mechanisms and rates of high temperature processes, and almost always involves very extensive numerical computations. Some fundamental nonequilibrium flow problems remain unsolved.

If all relevant relaxation lengths are very much greater than the largest flowfield dimension of interest, the flow may be regarded as being frozen, so that its vibrational energy, chemical composition and degree of ionisation remain constant. In this situation air may again be treated as a perfect gas with constant specific heats.

Entry into the earth's atmosphere starting from orbital velocity generates air temperatures in excess of 6000°K and, under such conditions, equilibrium air behaves very differently from a perfect gas with constant specific heats. Relaxation lengths range from many miles at orbital altitudes down to small fractions of an inch at sea level pressure. Similarly, flowfield dimensions of interest in the aerodynamics of a space shuttle vehicle may range from 100 ft or more (vehicle length) to a small fraction of a foot (stand-off distance in front of the leading edge of a wing or tail). It is inescapable that, for parts of the re-entry trajectory of the vehicle, relaxation lengths and flowfield dimensions will be comparable. Nonequilibrium flow must occur during re-entry.

The objectives of this review of nonequilibrium flow effects on space shuttle vehicle aerodynamics are as follows:

1. to estimate flight conditions under which nonequilibrium flow will occur;
2. to assess whether consequences of nonequilibrium flow may be important to vehicle design,
3. to discuss the adequacy of available methods of prediction for solving nonequilibrium flow problems likely to arise during design of a space shuttle.
4. to describe difficulties which will arise in attempting wind tunnel simulation of nonequilibrium flow past space shuttle shapes under re-entry conditions.

The theory of nonequilibrium flows is set out in References 2 to 6.

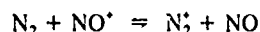
2. NONEQUILIBRIUM FLOW REGIMES IN FLIGHT

Chemical reaction mechanisms and rates in high temperature air have been studied in great detail during the past decade, and the information available is generally sufficiently accurate for the requirements of re-entry flowfield calculations. A possible exception is the influence of products of ablation on the kinetics of air

For conditions generated in flight at less than about 20,000 ft/sec (Ref.7), the following reaction scheme is adequate to describe chemical changes in the high temperature region behind a bow shock wave in pure air:



where M represents any of the neutral species present. Reaction rate data may be found for example in Reference 8. At velocities in excess of 20,000 ft/sec, charge transfer reactions such as



become progressively more important and generate significant concentrations of N_2^* , O_2^* , N^* and O^* . According to Reference 7, the 54 elementary reactions shown in Table 1 are then required for an adequate description of chemistry and ionisation history of the flow. It should be noted that for some of these reactions the rate coefficients and their variations with temperature are not yet known at all accurately. A further complication is that, at the very high temperatures existing just behind the bow shock wave, vibrational excitation of the molecules N_2 , O_2 and NO is not complete before dissociation begins. The various species also exchange vibrational energy. Under these conditions, with many competing processes occurring simultaneously, it is not possible to make a rigorous characterisation of the approach to equilibrium in terms of a single relaxation time. Many widely different time (and length) scales may be discerned. However, Figure 1 illustrates the definition⁹ of an empirical relaxation time for dissociation, based on the approach to equilibrium of the temperature T in the nonequilibrium flow behind a normal shock wave in air. If this dissociation time is multiplied by a velocity typical of the flow behind the normal shock wave, a characteristic length for dissociation, d, is obtained, as shown in Figure 1. The length d will be used to illustrate the existence of regions of nonequilibrium flow during re-entry. This will be done in terms of typical re-entry trajectories, and displayed on altitude - velocity plots.

Figure 2 shows typical¹⁰ re-entry trajectories for lifting and non-lifting vehicles. These trajectories do not represent the extremes of possible variations of velocity with altitude and in particular it appears feasible to design for re-entry with even higher altitudes at given velocity. For comparison, Figure 3 shows how freestream Reynolds number per unit length and the parameter W/SC_L vary with velocity and altitude. The lifting trajectory of Figure 3 has a W/SC_L which varies between 10 and 100 lbm/ft².

Current ideas of space shuttle re-entry vehicle configurations involve blunt noses which will support nearly normal shock waves during re-entry. Figure 4 shows the equilibrium stagnation temperature, T, compressibility, Z, and dissociation length, d, behind a normal shock wave in air, in the vicinity of the re-entry corridor. Since Z represents the number of particles for each molecule in the unshocked air, Z close to unity indicates conditions where dissociation effects are small, while dissociation becomes complete as Z approaches 2. A stand-off distance of the order of 1 ft may be expected at the nose of the vehicle. It may be seen from Figures 2 and 3 that d is comparable with the stand-off distance in regions of the trajectory where Z is considerably greater than unity, and so nonequilibrium effects are expected in the nose region.

Large angles of incidence (up to about 60°) are contemplated during re-entry and therefore large parts of the vehicle away from the nose region will meet air which has been processed by a strong oblique shock wave. Figures 5 and 6 show T, Z and the dissociation length, d, in air behind plane oblique shock waves making an angle of 60° and 30° to the flow. Because the flow behind an oblique shock wave has a velocity component parallel to the wave, the dissociation length d increases rapidly as the wave becomes more oblique. At the same time T and Z decrease. Figures 5 and 6 show values of d comparable with major dimensions of a vehicle, again indicating that chemical nonequilibrium will occur, over significant areas of the vehicle. For the 30° shock wave, Figure 6, conditions exist which may lead to important vibrational nonequilibrium as illustrated* by the vibrational relaxation length L for air under the conditions existing behind the shock wave.

Figure 7 shows the fraction of the stagnation enthalpy of the flow behind normal and oblique shock waves which becomes absorbed in chemical reaction when equilibrium has been achieved. It may be seen that this fraction increases with flight velocity, altitude and wedge angle, and that well over one half of the stagnation enthalpy is stored in this manner under conditions of interest.

* For given conditions, d should be greater than or equal to L. This is not so in Figure 6 because d and L have different arbitrary definitions, representing the length within which the flow approached within a different fraction of the equilibrium limit for a different variable.

Figure 8 and 9, obtained from Figures 4 and 5, show the variation of T , Z and d along the lifting trajectory of Figure 2, for normal and 60° shock waves. An example from these figures illustrates the region of the re-entry trajectory for which dissociation nonequilibrium is to be expected. The following typical flowfield dimensions are chosen:

stand-off distance at nose: 1.0 ft

stand-off distance at leading edge of wing or tail: 0.1 ft

wing chord with 60° incidence: 20 ft.

It is arbitrarily assumed that dissociation is nearly frozen when these dimensions are smaller than $0.1d$, that dissociation is close to equilibrium when these dimensions are greater than $10d$, and that dissociation involves negligible enthalpy when Z is less than 1.1. The resulting nonequilibrium region of the lifting trajectory is set out in Table 2.

It may be seen from Table 2 that the nonequilibrium region for dissociation extends from above 300,000 ft altitude to below 200,000 ft. Above about 300,000 ft, dissociation is almost frozen in the high-temperature nose, leading edge and under wing flows, and is slower in other cooler parts, so the whole flowfield is nearly frozen. Below about 200,000 ft, dissociation is still not fast enough to approach equilibrium, for this trajectory, but the flight velocity is sufficiently low so that dissociation is not dominant.

The corresponding information for re-entry along the zero-lift trajectory of Figure 2 is shown in Table 3. It may be seen that the boundary above which the flow will be nearly frozen is just above 300,000 ft, as in the lifting re-entry case. However, in contrast to the lifting case, the flow past the zero-lift vehicle achieves dissociation equilibrium at altitudes between 237,000 ft and 168,000 ft, with Z still much greater than unity (highly dissociated air). Nonequilibrium flow will in fact extend down to lower altitudes, in the present example, because this highly dissociated air will fail to maintain recombination equilibrium as it expands away from nose regions.

The difference between these two examples is that the zero-lift vehicle descends out of the nonequilibrium flight regime, maintaining high velocity, whereas the lifting vehicle decelerates out of the nonequilibrium regime, maintaining high altitude. In principle, it would be possible to design a lifting re-entry vehicle which slowed down at such a great altitude (say above about 300,000 ft) that it passed from the near-frozen flow regime straight into the low velocity, negligible dissociation regime (say below about 9,000 ft/sec). The regime of significant finite-rate chemical reaction could be avoided. However, published data suggests that current space shuttle designs decelerate at lower altitudes, and therefore do encounter this regime of significant finite-rate reaction.

3. OTHER EFFECTS OVERLAPPING THE NONEQUILIBRIUM FLOW REGIME

Having identified the altitude and velocity range of interest for nonequilibrium flow effects during lifting re-entry, we can enquire what other complicating effects will occur in the same flight regime. Since the equilibrium degree of ionisation is less than 1 percent except in the top right-hand corner of Figure 4, at higher velocities and altitudes than those considered here, it is clear that ionisation will not be thermally significant. Radiative heat transfer from the hot gas cap to the body¹³ becomes important only in the bottom right-hand corner of Figure 4, far from the trajectories of interest.

Viscous and low density effects near blunt leading edges may be assessed in the manner shown in Figure 10 (Probstein¹⁴). We consider the lifting vehicle. In the range of altitudes and velocities for which nonequilibrium flow occurs, as set out in Table 2, the nose and leading edge regions of the flow pass through the following two viscous flow regimes:

viscous layer (thin shock wave followed by viscous shock layer);

boundary layer (thin shock wave followed by inviscid shock layer followed by thin boundary layer).

Probstein's merged layer regimes, in which the thickness of the shock wave itself becomes significant, occur at greater altitudes where chemistry is almost frozen.

For a wing of 20 ft chord, the Reynolds number based on conditions behind a 60° shock wave increases from 1.8×10^3 to 4.2×10^5 in the nonequilibrium range of altitudes and velocities from Table 2. Boundary layers will be laminar under these conditions. However, Reynolds numbers based upon fuselage length become large enough for turbulent flow to be expected.

The viscous interaction parameter $M^3/R_E^{1/2}$, based on a 20 ft chord and conditions behind a 60° shock wave, has values of 0.5 and less in the nonequilibrium regime from Table 2. It is concluded that, in this particular example, the boundary layer on the lower surface of the wing will be predominantly in the weak interaction regime [$M^3/R_E^{1/2} < 4$ (Ref.15)]. On the other hand $M^3/R_E^{1/2}$, based on a 20 ft chord and free stream flow properties, can be as large as 270 in the same flight regime, showing that upper surfaces of wings and also lower surfaces at small

angles of attack will meet flows with strong viscous interaction effects. Without a more detailed specification of geometry and trajectory information, it is not clear whether important viscous interaction and nonequilibrium flow effects will occur simultaneously in flow past wings.

4. INFLUENCE OF NONEQUILIBRIUM FLOW ON VEHICLE DESIGN

4.1 Aerodynamic Forces and Moments

A two-dimensional wedge provides a simple starting point for a discussion of nonequilibrium flow effects in lifting re-entry aerodynamics. Below the shock wave detachment angle, equilibrium flow and frozen flow each consists of a plane oblique shock wave followed by uniform flow at constant pressure (Fig 11). The density rise across the shock wave is larger in the equilibrium flow, and therefore the shock layer is thinner, the shock wave more oblique, and the pressure on the wedge is lower. A real, nonequilibrium wedge flow¹⁶ involves a transition from frozen flow to equilibrium. The flow is frozen at the wedge vertex, so the wave angle and surface pressure appropriate to frozen flow apply there. The shock wave is convex in shape, its angle decreasing towards the equilibrium angle at large distances downstream of the vertex. Similarly the surface pressure falls from the frozen value towards the equilibrium value. The flow between the shock and the wedge is no longer uniform, and solutions must be obtained from the method of characteristics for nonequilibrium flow¹⁷. Reference 18 includes results of extensive oblique shock wave calculations for frozen and equilibrium air.

Figure 12 (Ref.19) shows the lift coefficient C_L of two-dimensional wedge-section wings, plotted against the angle α presented by the wedge to the flow. Curves for perfect gas (frozen flow) and real gas (equilibrium flow) are shown, for flight at $M = 15$ at an altitude of 200,000 ft. Because both of these flows produce constant pressure on the wedge surface, the percentage difference in C_L between perfect gas and real gas flow at given α is the same as the percentage drop in surface pressure as the actual nonequilibrium flow approaches equilibrium. For example, under the conditions of Figure 12, the fall in pressure along the surface of a wedge in nonequilibrium flow with $\alpha = 40^\circ$ is 10% of the pressure at the vertex. This percentage increases rapidly with α . It also increases²⁰ with velocity and altitude and values in excess of 20% are possible. A similar phenomenon occurs due to vibrational relaxation, involving a fall in pressure of up to about 5%.

The hypersonic flow past a wing of rectangular planform will be very similar to that past a wedge. The lift will be influenced by nonequilibrium flow as illustrated in Figure 12, and the pressure will fall with increasing distance from the leading edge, as described above. This fall in pressure will also cause a nose-up pitching moment whose magnitude depends on chemical reaction rates.

A caret wing has an undersurface shape which supports a plane oblique shock wave and a uniform flow past its lower surface, for flight under design conditions. Nonequilibrium flow will produce a curved shock wave and a non-uniform flow, for which solutions are not at present available. However, the caret wing close to the design condition has a flow very similar to a wedge flow, and it may be expected that nonequilibrium effects will be of similar magnitude in the two flows under comparable conditions.

Frozen flow past slender wings at large angles of attack has been studied by Messiter²¹ using an extended Newtonian, thin-shock-layer theory. The analysis has been extended by Squire¹⁹ and applied to a variety of wing shapes in both perfect gas (frozen) and real gas (equilibrium) flow. Some results are shown in Figure 12. It may be seen that under the conditions stated for a flat delta wing of aspect ratio 0.8, the lift in equilibrium flow is only very slightly less than in frozen flow. For example the reduction is 1.6% at $\alpha = 40^\circ$ (c.f. 10% for the wedge). The reason why the slender delta is influenced so little by real gas effects is that, because of the spanwise component of velocity, the shock wave for the delta lies much closer to the surface than for the wedge. Therefore the flow past the delta approaches more closely to the true Newtonian limit which is independent of gas properties. Although the caret wing is more susceptible to real gas losses of lift it remains superior to the flat delta in terms of C_{Lmax} and also L/D .

It is concluded that nonequilibrium flow effects on pressure distribution and aerodynamic forces are likely to be negligible for wings of slender delta planform at large angles of attack, but may not be negligible for wings producing nearly two-dimensional flows. Available methods of analysis for nonequilibrium flow^{16, 17, 22-25} do not appear to be entirely suitable for this situation, particularly if viscous interaction and wing/body interference effects must also be taken into account.

4.2 Heat Transfer

As noted from Figure 7, a large fraction of the stagnation enthalpy of the air passing through a strong shock wave becomes invested in dissociation and other reactions, at velocities and altitudes of present interest. An immediate consequence is that the rate of heat transfer from real air is several times greater than would occur from an ideal gas at the same temperature, Reynolds number, etc.

Finite rate gas-phase chemical reactions occur in the flow both outside and inside the boundary layer. Surface reactions also occur, involving catalytic recombination of atoms or possibly degradation of the surface. Departures from chemical equilibrium can either decrease or increase the real gas heat transfer rate. The influence of finite rate chemistry arises partly from its effects on the distributions of temperature and density around the vehicle, and partly from its influence on the number of atoms diffusing to the wall and recombining there.

Some of the possible effects may be illustrated by considering the case of heat transfer to the stagnation point of a blunt-nosed body. If chemical reactions are frozen within the boundary layer but finite rate catalytic recombination occurs at the wall, the rate of heat transfer is²⁶

$$q_w = 0.763(\beta\rho_e\mu_e)^{1/2}P_R^{-0.6}\Delta h \left\{ 1 + (L_E^{0.6} - 1) \frac{h_{chem}}{\Delta h} \frac{C}{1+C} \right\} \quad (4.1)$$

where β = inviscid velocity gradient at stagnation point

ρ_e = density at edge of boundary layer

μ_e = viscosity coefficient at edge of boundary layer

P_R = Prandtl number

Δh = enthalpy difference, $h_e - h_w$

h_e = enthalpy at edge of boundary layer

h_w = enthalpy at wall

h_{chem} = chemical contribution to h_e

L_E = Lewis number

C = surface reaction rate divided by convective diffusion rate.

it may be seen that, if $L_E = 1$ or if $C = 0$ (no reaction at wall) the heat transfer rate is simple proportional to the enthalpy difference Δh . However, if $L_E > 1$ and $C > 0$ (a more realistic situation), the chemical enthalpy h_{chem} increases the heat transfer rate through the curly bracket term in Equation (4.1), in addition to its direct effect in the term Δh . This occurs because, with $L_E > 1$, the diffusion of atoms transports energy through the boundary layer more efficiently than thermal conduction. With $C > 0$ some of this energy is given up to the wall.

The analogous equation when gas-phase reactions in the boundary layer are fast enough to maintain equilibrium is²⁶:

$$q_w = 0.763(\beta\rho_e\mu_e)^{1/2}P_R^{-0.6}\Delta h \left\{ 1 + (L_E - 1) \frac{h_{chem}}{\Delta h} \right\}^{0.6} \quad (4.2)$$

for a cold wall. It will be noted that this equation is very similar to Equation (4.1). The two equations are identical if $L_E = 1$ or if $h_{chem} = 0$. Even when L_E is not equal to unity, the two equations give very similar results, so long as C is much greater than unity. Thus the stagnation point heat transfer rate is not significantly influenced by the gas-phase reaction rate in the boundary layer, so long as the wall reaction rate is fast. On the other hand if the wall reaction rate is small ($C \rightarrow 0$) the frozen flow Equation (4.1) gives a much smaller heat transfer rate than the equilibrium flow Equation (4.2). Nonequilibrium flow outside the boundary layer influences q_w through its effect on β , ρ_e , μ_e and h_{chem} . The effects on the first three tend to cancel, for stagnation point flow, and it is not until departures from equilibrium reduce h_{chem} that a significant effect on heat transfer is to be expected for a catalytic wall.

It may be noted⁴ that metal surfaces tend to be efficient catalysts for recombination of oxygen and nitrogen atoms. Oxide surfaces may be much less catalytic, and some materials such as pyrex glasses are almost non-catalytic.

The situation becomes more complicated when we move away from the region adjacent to the stagnation point. Nonequilibrium flow boundary-layer theory²⁷ is not yet complete for the general case. However, the following trends are expected:

- (i) at altitudes so great that dissociation does not have time to occur, the heat transfer rate will be less than would be expected on the basis of equilibrium real gas calculations;
- (ii) at lower altitudes where some dissociation does occur but gas-phase reactions in the boundary layer remain frozen, a large reduction in heat transfer may be achieved by the use of a non-catalytic wall;

- (iii) it seems likely that heat transfer will be influenced by the large changes in velocity, density and temperature at the boundary-layer edge caused by nonequilibrium flow outside the boundary layer, these effects cannot be predicted with confidence at present.

It is concluded that, while the heat transfer rate in the vicinity of a stagnation point is well understood and can be predicted accurately, the situation is much less satisfactory for other parts of the vehicle. Of course the heat transfer rates are much lower than at the stagnation point, but predictions must still be made. The following aspects of the problem await solution:

- (i) three-dimensional, inviscid, nonequilibrium flow past realistic vehicle shapes, to provide flow properties at the boundary-layer edge;
- (ii) three-dimensional nonequilibrium laminar (and possibly turbulent) boundary-layer analysis, for realistic shapes, including surfaces of finite catalytic efficiency;
- (iii) nonequilibrium flow viscous interaction effects for realistic shapes, including self-induced pressure gradients, and the rate of ingesting of dissociated air from the bow shock region into a thick boundary layer.

4.3 Radio Communication Blackout During Re-Entry

The desire to communicate with earth during re-entry requires the placing of an aerial at a suitable forward-facing position in the vehicle. Electromagnetic waves are strongly attenuated by the plasma sheath surrounding the vehicle, so it is necessary to locate the aerial in a position where this effect may be minimised. For this purpose it is necessary to know the electron number density and collision frequency throughout the relevant parts of the plasma sheath. Nonequilibrium flow has a very large effect on these properties. Calculations^{2,25} must take account of the very large number of reactions which occur among the charged species in high temperature air (Table 1). Boundary-layer effects may be important⁷. Available methods of analysis are perhaps adequate in the vicinity of blunt-nosed stagnation points, but difficulties might be expected if it proved necessary to extend the calculations far downstream for complex shapes.

5. WIND TUNNEL TESTS

It has been suggested above that available methods of analysis are not adequate for predicting some aspects of vehicle aerodynamics in the nonequilibrium flow regime. Wind tunnel testing will therefore be desirable. Figure 13 shows the reservoir pressure p_0 and reservoir temperature T_0 required in a wind tunnel to duplicate flight conditions, assuming that full equilibrium is maintained in the wind tunnel nozzle. It may be seen that enormous values of p_0 and T_0 are required in order to duplicate conditions corresponding to high velocity flight.

A second difficulty arises, because departure from chemical equilibrium occurs²⁸ during expansion of the test air in the wind-tunnel nozzle. The composition freezes with excess O and N atoms, and sometimes excess NO molecules, and the test medium then does not properly represent the chemical properties of atmospheric air. For example, dissociation equilibrium will be achieved more rapidly behind a shock wave in a frozen wind tunnel flow than behind the equivalent shock wave in flight. A convenient measure of the importance of chemical freezing in a wind-tunnel nozzle is the ratio h_f/h_0 , where h_f is the chemical enthalpy of nonequilibrium species in the test section, and h_0 is the reservoir enthalpy. Figure 14 shows h_f/h_0 plotted as a function of altitude and flight velocity. The data was taken from Reference 29 for large wind-tunnel nozzles*, but a tenfold decrease in nozzle size increases the frozen enthalpy by only about 30%. It may be seen from Figure 14 that the fraction of reservoir enthalpy frozen in chemical energy increases rapidly with altitude to be simulated.

Figure 15 shows the reservoir requirements for a wind tunnel to duplicate flight conditions along the lifting vehicle trajectory of Figure 2. Also shown is the ratio h_f/h_0 from Figure 14. It may be recalled from Table 2 that, for this trajectory, the nonequilibrium flight regime extends approximately from 25,000 ft/sec down to 9,000 ft/sec. Figure 15 shows that at the peak reservoir condition of about 12,000°K and 10⁶ atmos, only about 3% of the reservoir enthalpy is frozen. However, these conditions cannot be generated in present-day wind tunnels. At higher and lower velocities p_0 and T_0 fall to more accessible values but at the same time h_f/h_0 rises rapidly to 10% or more. Vibrational freezing also becomes important at the lower end of the velocity range, because the relevant range of reservoir temperatures occurs along with very low reservoir pressures, for which vibration is almost completely frozen. At around 10,000 ft/sec the fraction h_v/h_0 rises to around 12%, see Figure 15, where h_v is the enthalpy locked up in vibrational freezing of nitrogen. It is concluded that difficulties arise in the duplication of conditions throughout the nonequilibrium flight regime, due either to the need for high reservoir temperatures and pressures or to freezing in the wind-tunnel nozzle.

In the absence of complete duplication of flight conditions, is it possible to simulate the most important conditions in wind tunnel tests? Simulation can be successfully achieved for nonequilibrium flow in the vicinity of the stagnation point of a blunt-nosed body, through the application of "binary scaling". According to this scaling, the

* Characteristic flow time at freezing point: $\tau = 10^{-5}$ sec, see Reference 29.

ratio of the dissociation length scale to a flowfield dimension will be correctly simulated in the wind tunnel if the product (density) \times (body dimension) is the same in flight as in the tunnel test. Thus small models may be tested in high density nonequilibrium flow. This scaling law, together with the Mach number independence principle of hypersonic flow¹⁵, has permitted the simulation of stagnation point heat transfer in shock tubes and electric arc flows. Binary scaling, which allows the simultaneous scaling of dissociation and Reynolds number effects, assumes that chemical reactions result from binary collisions only. This is correct so long as only dissociation is occurring. However, as soon as recombination starts to be important three body reactions come into play, and binary scaling fails. This occurs as soon as the gas expands round the shoulder of the blunt nose, and applies to the remainder of the flow field. With both binary and three-body reactions taking place, no density-length scaling is possible, and the only valid simulation is full scale. Also, chemical equilibrium occurs at too low a degree of dissociation, due to the higher density, in a binary-scaled model test.

In the absence of either flight duplication or correct flow simulation, wind tunnel tests must resort to one or more of the following expedients:

- (i) correct simulation of only a part of the nonequilibrium flow field (e.g. flow in the vicinity of a stagnation point);
- (ii) partial simulation (see for example Reference 30) in which not all of the similarity parameters of the flight situation are properly matched, but attempts are made to choose conditions which minimise the resulting errors;
- (iii) nonsimulation, in which tests are made under conditions known to be unrepresentative of flight (e.g. partly-dissociated free stream or incorrect velocity): results are used to validate nonequilibrium flow computer programmes, which may then be applied also to the real flight conditions.

6. CONCLUSIONS

1. A regime of nonequilibrium flow will occur during re-entry of a lifting vehicle.
2. Departure from equilibrium will influence forces, moments and heat transfer rates to a significant extent, order-of-magnitude effects are generally not expected, but the results of departure from equilibrium are large enough to require consideration.
3. Nonequilibrium flow determines the plasma sheath properties which control radio blackout.
4. Knowledge of the chemical kinetics of high temperature air is adequate for these purposes, at least in the absence of effects from products of ablation.
5. Further theoretical study is required of both inviscid and viscous nonequilibrium flows past complex three-dimensional shapes.
6. Correct wind-tunnel simulation of the complete nonequilibrium flow field past lifting re-entry vehicle shapes under conditions of interest appears to be impossible at the present time. Techniques involving incomplete simulation must be employed.

ACKNOWLEDGEMENT

This work was supported in part by the Procurement Executive, Ministry of Defence, UK.

The author gratefully acknowledges the permission granted by the respective publishers where illustrations have been reproduced from previous publications.

REFERENCES

1. Brahinsky, H.S.
et al. *Tables of Equilibrium Thermodynamic Properties of Air. Volume I, Constant Temperature; Volume II, Constant Pressure; Volume III, Constant Entropy; Volume IV, Constant Temperature with Specific Heat and Speed of Sound Data.* Arnold Eng. Dev. Center, AEDC-TR-69-89, 1969.
2. Vincenti, W.G.
Kruger, C.H. *Introduction to Physical Gas Dynamics.* Wiley, 1965.
3. Clarke, J.F.
McChesney, M. *The Dynamics of Real Gases.* Butterworths, 1964.
4. Dorrance, W.H. *Viscous Hypersonic Flow* McGraw-Hill, 1962.
5. Wegener, P.P. (Ed.) *Nonequilibrium Flows, (2 Parts).* Dekker, 1970.
6. Zel'dovich, Ya.B.
Raizer, Yu.P. *Physics of Shock Waves and High-Temperature Hydrodynamic Phenomena (2 Vols., Ed. W.D.Hayes and R.F.Probstein),* Academic Press, 1966.
7. Evans, J.S.
et al. *Computation of Ionisation in Re-Entry Flowfields.* AIAA Journal, Vol.8, 1970, p.1082.
8. Wray, K.L. *Chemical Kinetics of High Temperature Air, in Hypersonic Flow Research (Volume 7 of Progress in Astronautics and Rocketry).* (Ed. F.R.Riddell), Academic Press, 1962, p.181.
9. Feldman, S. *Trails of Axis-Symmetric Hypersonic Blunt Bodies Flying Through the Atmosphere.* Avco-Everett Research Rep.82, 1959.
10. Crabtree, L.F.
Peckham, D.H. Royal Aircraft Establishment, Farnborough, UK, private communication.
11. Hankey, W.L. This volume.
12. Vaglio-Laurin, R.
Bloom, M.H. *Chemical Effects in External Hypersonic Flow, in Hypersonic Flow Research. (Volume 7 of Progress in Astronautics and Rocketry).* (Ed. F.R.Riddell), Academic Press, 1962, p.241.
13. Kivel, B. *Radiation from Hot Air and Stagnation Heating.* Avco-Everett Research Rep.79, 1959.
14. Probstein, R.F. *Shock Wave and Flow Field Development in Hypersonic Re-Entry.* ARS Journal, February 1961.
15. Hayes, W.D.
Probstein, R.F. *Hypersonic Flow Theory.* Academic Press, 1959.
16. Spurk, J.H.
et al. *Characteristic Calculation of Flowfields with Chemical Reactions.* AIAA Journal, Vol.4, 1966, p.30.
17. Sedney, R. *The Method of Characteristics, in Reference 5, Part 2.*
18. Popinski, Z.
Ehrlich, C.F. *Development Design Methods for Predicting Hypersonic Aerodynamic Control Characteristics.* AFFDL-TR-66-85, 1966.
19. Squire, L.C. *A Comparison of the Lift of Flat Delta Wings and Waveriders at High Angles of Incidence and High Mach Number.* Aero. Res. Council (UK), ARC 32555, 1970.
20. Trimpi, R.L.
Jones, R.A. *A Method of Solution with Tabulated Results for the Attached Oblique Shock Wave System for Surfaces at Various Angles of Attack, Sweep, and Dihedral in an Equilibrium Real Gas Including the Atmosphere.* NASA TR R-63, 1960.
21. Messiter, A.F. *Lift of Slender Delta Wings According to Newtonian Theory.* AIAA Journal, Vol.1, 1963, p.794.
22. Vaglio-Laurin, R.
Bloom, M.H. *Chemical Effects in External Hypersonic Flow, in Hypersonic Flow Research. Volume 7 of Progress in Astronautics and Rocketry).* (Ed. F.R.Riddell), Academic Press, 1962, pp.205-254.

23. Kang, S.W. *Nonequilibrium Ionised Hypersonic Flow over a Blunt Body at Low Reynolds Number.* AIAA Journal. Vol.8, 1970, p.1263.
24. Hall, J.G.
et al. *Inviscid Hypersonic Airflows with Coupled Nonequilibrium Processes.* IAS Paper No.62-67, 1962.
25. Hall, J.G.
Russo, A.L. *Recent Studies of Nonequilibrium Flows at the Cornell Aeronautical Laboratory, in Recent Advances in Aerothermochemistry.* (Ed. I.Glassman), AGARD Conference Proceedings No.12, NATO, 1967, p.443.
26. Rosner, D.E. *Convective Heat Transfer with Chemical Reaction.* Aero. Res. Lab. (O.A.R., USAF), ARL 99, Part 1, 1961.
27. Chung, P.M. *Chemically Reacting Nonequilibrium Boundary Layers, Advances in Heat Transfer.* (Ed. J.P.Hartnett, T.F.Irvine), Vol.2, Academic Press, 1965, p.110.
28. Bray, K.N.C. *Chemical and Vibrational Nonequilibrium in Nozzle Flows,* in Reference 5, Part 2.
29. Ring, L.E.
Johnson, P.W. *Correlation and Prediction of Air Nonequilibrium in Nozzles.* AIAA Paper No.68-378, 1968.
30. Wittliff, C.E.
Sundaram, T.R. *A Study of Hypervelocity Slender-Body Flows and Similitudes Including the Effects of Nonequilibrium and Nose Bluntness.* AIAA Paper No.68-14, 1968.

TABLE I
Constants for Use in Reaction Rate Formulas

i	Reaction	μ_i	D_i	$\sigma_i(\text{cm}^2)$	i	Reaction	μ_i	D_i	$\sigma_i(\text{cm}^2)$
1	$\text{O}_2 + \text{O}_2 \rightleftharpoons \text{O} + \text{O} + \text{O}_2$	16.000	217.34	14.60×10^{-16}	28	$\text{O} + \text{NO} \rightleftharpoons \text{NO}^* + \text{O}^-$	10.435	330.70	1.00×10^{-16}
2	$\text{O}_2 + \text{N}_2 \rightleftharpoons \text{O} + \text{O} + \text{N}_2$	14.934	217.34	7.75	29	$\text{N} + (\text{O or N}) \rightleftharpoons \text{N}^* + \text{e}^- + (\text{O or N})$	7.000	617.80	1.00
3	$\text{O}_2 + \text{O} \rightleftharpoons \text{O} + \text{O} + \text{O}$	10.667	217.34	60.00	30	$\text{O} + (\text{O or N}) \rightleftharpoons \text{O}^* + \text{e}^- + (\text{O or N})$	8.600	578.40	1.00
4	$\text{O}_2 + \text{N} \rightleftharpoons \text{O} + \text{O} + \text{N}$	9.739	217.34	6.72	31	$\text{N}_2 + \text{NO}^* \rightleftharpoons \text{N}_2^* + \text{NO}$	14.50	268.90	20.00
5	$\text{O}_2 + \text{NO} \rightleftharpoons \text{O} + \text{O} + \text{NO}$	15.484	217.34	5.80	32	$\text{N} + \text{NO}^* \rightleftharpoons \text{N}^* + \text{NO}$	9.55	224.80	20.00
6	$\text{N}_2 + \text{O}_2 \rightleftharpoons \text{N} + \text{N} + \text{O}_2$	14.934	414.50	10.30	33	$\text{O} + \text{NO}^* \rightleftharpoons \text{O}^* + \text{NO}$	10.40	185.2	20.00
7	$\text{N}_2 + \text{N}_2 \rightleftharpoons \text{N} + \text{N} + \text{N}_2$	14.000	414.50	16.50	34	$\text{O}_2 + \text{NO}^* \rightleftharpoons \text{O}_2^* + \text{NO}$	15.50	120.20	20.00
8	$\text{N}_2 + \text{O} \rightleftharpoons \text{N} + \text{N} + \text{O}$	10.182	414.50	6.45	35	$\text{N}_2 + \text{O}_2 \rightleftharpoons \text{N}_2^* + \text{O}_2$	14.90	148.70	20.00
9	$\text{N}_2 + \text{N} \rightleftharpoons \text{N} + \text{N} + \text{N}$	9.334	414.50	72.00	36	$\text{N} + \text{O}_2^* \rightleftharpoons \text{N}^* + \text{O}_2$	9.74	104.50	20.00
10	$\text{N}_2 + \text{NO} \rightleftharpoons \text{N} + \text{N} + \text{NO}$	14.483	414.50	7.00	37	$\text{O} + \text{O}_2^* \rightleftharpoons \text{O}^* + \text{O}_2$	10.70	65.00	20.00
11	$\text{NO} + \text{O}_2 \rightleftharpoons \text{N} + \text{O} + \text{O}_2$	15.484	275.74	2.94	38	$\text{N}_2 + \text{O}^* \rightleftharpoons \text{N}_2^* + \text{O}$	10.20	83.70	20.00
12	$\text{NO} + \text{N}_2 \rightleftharpoons \text{N} + \text{O} + \text{N}_2$	14.483	275.74	3.12	39	$\text{N} + \text{O}^* \rightleftharpoons \text{N}^* + \text{O}$	7.47	39.51	20.00
13	$\text{NO} + \text{O} \rightleftharpoons \text{N} + \text{O} + \text{O}$	10.435	275.74	6.06	40	$\text{N}_2 + \text{N}^* \rightleftharpoons \text{N}_2^* + \text{N}$	9.34	44.19	20.00
14	$\text{NO} + \text{N} \rightleftharpoons \text{N} + \text{O} + \text{N}$	9.545	275.74	11.30	41	$\text{O}^* + \text{M} \rightleftharpoons \text{O} + \text{e}^- + \text{M}$	10.00	62.48	10.00
15	$\text{NO} + \text{NO} \rightleftharpoons \text{N} + \text{O} + \text{NO}$	15.000	275.74	14.80	42	$\text{O}_2^* + \text{M} \rightleftharpoons \text{O}_2 + \text{e}^- + \text{M}$	15.00	19.55	10.00
16	$\text{O} + \text{N}_2 \rightleftharpoons \text{NO} + \text{N}$	10.182	138.93	2.69	43	$\text{O}_2 + \text{e}^- \rightleftharpoons \text{O}^- + \text{O}$	5.4858×10^{-4}	155.14	0.10
17	$\text{O} + \text{NO} \rightleftharpoons \text{O}_2 + \text{N}$	10.435	71.24	1.10	44	$\text{O} + \text{NO}^* \rightleftharpoons \text{N}^* + \text{O}_2$	10.44	282.90	20.00
18	$\text{O} + \text{O} \rightleftharpoons \text{O}_2^* + \text{e}^-$	8.000	294.85	0.025	45	$\text{NO} + \text{NO}^* \rightleftharpoons \text{N}_2^* + \text{O}_2$	15.00	188.60	20.00
19	$\text{N} + \text{N} \rightleftharpoons \text{N}_2^* + \text{e}^-$	7.000	247.27	0.066	46	$\text{O} + \text{NO}^* \rightleftharpoons \text{O}_2^* + \text{N}$	10.40	178.40	20.00
20	$\text{N} + \text{O} \rightleftharpoons \text{NO}^* + \text{e}^-$	7.467	117.69	0.076	47	$\text{N} + \text{NO}^* \rightleftharpoons \text{N}_2^* + \text{O}$	9.55	130.00	20.00
21	$\text{N}_2 + \text{e}^- \rightleftharpoons \text{N}_2^* + \text{e}^- + \text{e}^-$	5.4858×10^{-4}	661.90	1.00	48	$\text{N} + \text{NO}^* \rightleftharpoons \text{O}^* + \text{N}_2$	9.55	46.31	20.00
22	$\text{N} + \text{e}^- \rightleftharpoons \text{N}^* + \text{e}^- + \text{e}^-$	5.4858×10^{-4}	617.80	1.00	49	$\text{NO} + \text{NO}^* \rightleftharpoons \text{O}_2^* + \text{N}_2$	15.00	39.93	20.00
23	$\text{O} + \text{e}^- \rightleftharpoons \text{O}^* + \text{e}^- + \text{e}^-$	5.4858×10^{-4}	578.40	1.00	50	$\text{N}_2 + \text{O}^* \rightleftharpoons \text{N}^* + \text{NO}$	10.18	178.40	20.00
24	$\text{O}_2 + \text{e}^- \rightleftharpoons \text{O}_2^* + \text{e}^- + \text{e}^-$	5.4858×10^{-4}	513.00	1.00	51	$\text{NO} + \text{O}^* \rightleftharpoons \text{N}^* + \text{O}_2$	10.44	97.71	20.00
25	$\text{NO} + \text{e}^- \rightleftharpoons \text{NO}^* + \text{e}^- + \text{e}^-$	5.4858×10^{-4}	593.00	1.00	52	$\text{N} + \text{O}_2^* \rightleftharpoons \text{O} + \text{NO}$	9.74	6.80	20.00
26	$\text{O} + \text{O} \rightleftharpoons \text{O}^* + \text{O}^-$	8.000	516.00	1.00	53	$\text{O} + \text{N}_2^* \rightleftharpoons \text{N}^* + \text{NO}$	10.18	94.74	20.00
27	$\text{O} + \text{N} \rightleftharpoons \text{N}^* + \text{O}^-$	7.467	555.50	1.00	54	$\text{O}_2 + \text{O}^- \rightleftharpoons \text{O}_2^* + \text{O}$	10.67	42.93	20.00

Reaction mechanism and rates for high temperature air⁷. For reactions 1 - 15:

$$k_{f,i} = N_A \sqrt{\frac{8RT}{\pi \mu_i}} \frac{4}{3\pi^{1/2}} \left\{ \frac{D_i T_i}{T} + \frac{1}{2} \right\}^{3/2} \sigma_i \exp \left[- \left\{ \frac{D_i T_i}{T} + 1 \right\} \right]$$

$$\text{For reactions 16 - 54: } k_{f,i} = N_A \sqrt{\frac{8RT}{\pi \mu_i}} \sigma_i \exp \left[- \frac{D_i T_i}{T} \right]$$

in gm. mole, cm. sec units, where N_A is Avogadro's constant, and $T_i = 273.16^\circ \text{K}$.

TABLE 2

Approximate Extent of Nonequilibrium Region of Re-Entry Flight
for Lifting Trajectory Shown in Figure 2

<i>Part of Vehicle</i>	<i>Type of Flow</i>	<i>Altitude k. ft</i>	<i>Velocity k. ft/sec</i>	<i>Z</i>
Nose	Near Frozen	302	25.0	1.73
	Small Dissociation	192	9.0	1.10
Leading Edge	Near Frozen	266	23.6	1.65
	Small Dissociation	192	9.0	1.10
Wing Chord	Near Frozen	316	25.1	1.58
	Small Dissociation	197	10.7	1.10

TABLE 3

Approximate Extent of Nonequilibrium Region of Re-Entry Flight
for Zero-Lifting Trajectory Shown in Figure 2

<i>Part of Vehicle</i>	<i>Type of Flow</i>	<i>Altitude k. ft</i>	<i>Velocity k. ft/sec</i>	<i>Z</i>
Nose	Near Frozen	302	25.4	1.77
	Near Equilibrium	223	24.6	1.70
Leading Edge	Near Frozen	266	25.4	1.75
	Near Equilibrium	168	20.0	1.44
Wing Chord	Near Frozen	316	25.4	1.59
	Near Equilibrium	237	25.0	1.55

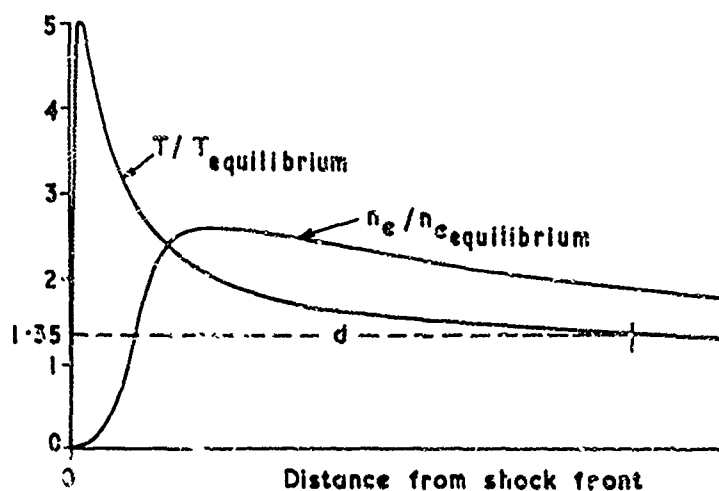


Fig.1 Definition⁹ of dissociation time and dissociation length d for flow behind a normal shock wave

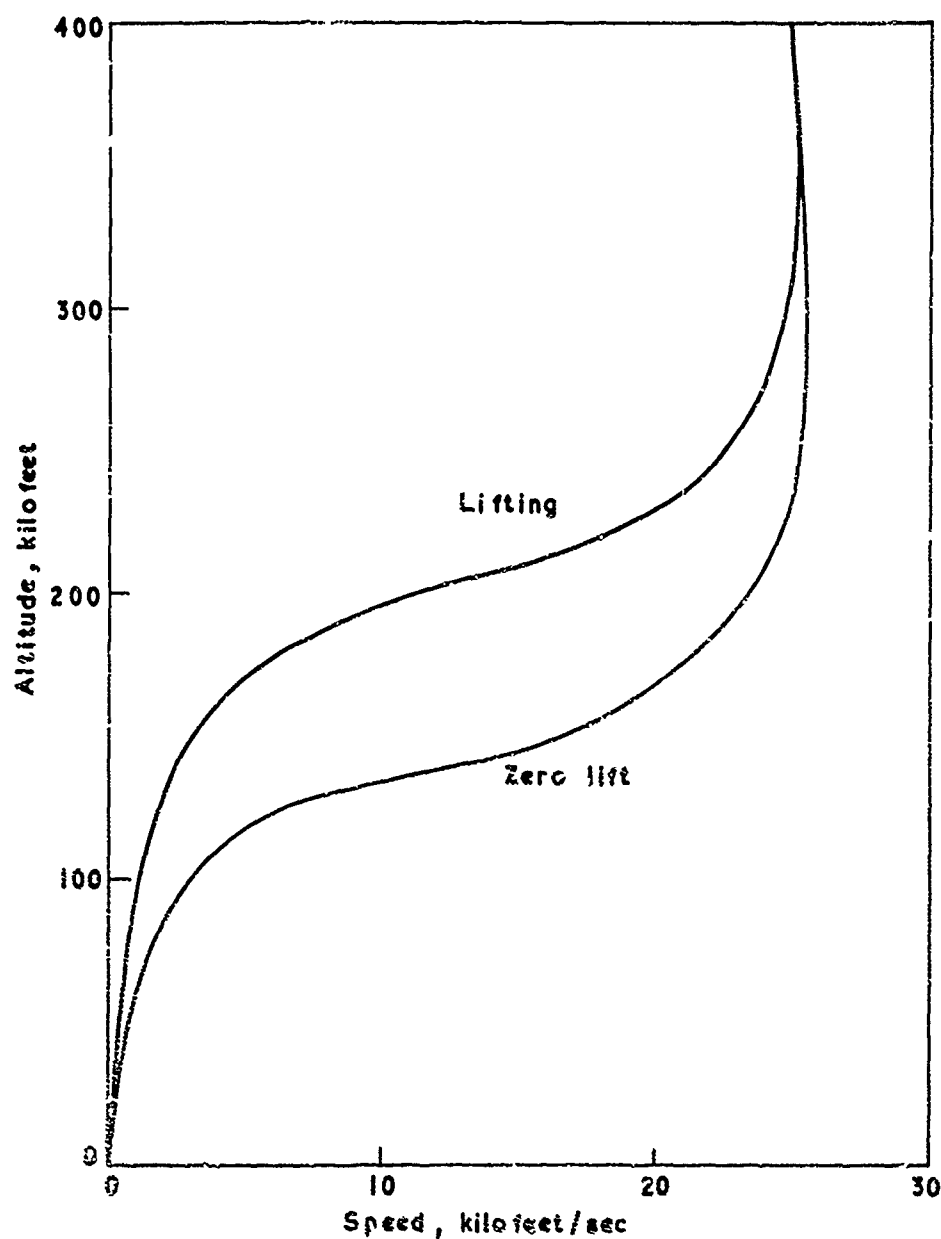


Fig.2 Lifting and non-lifting re-entry trajectories¹⁰

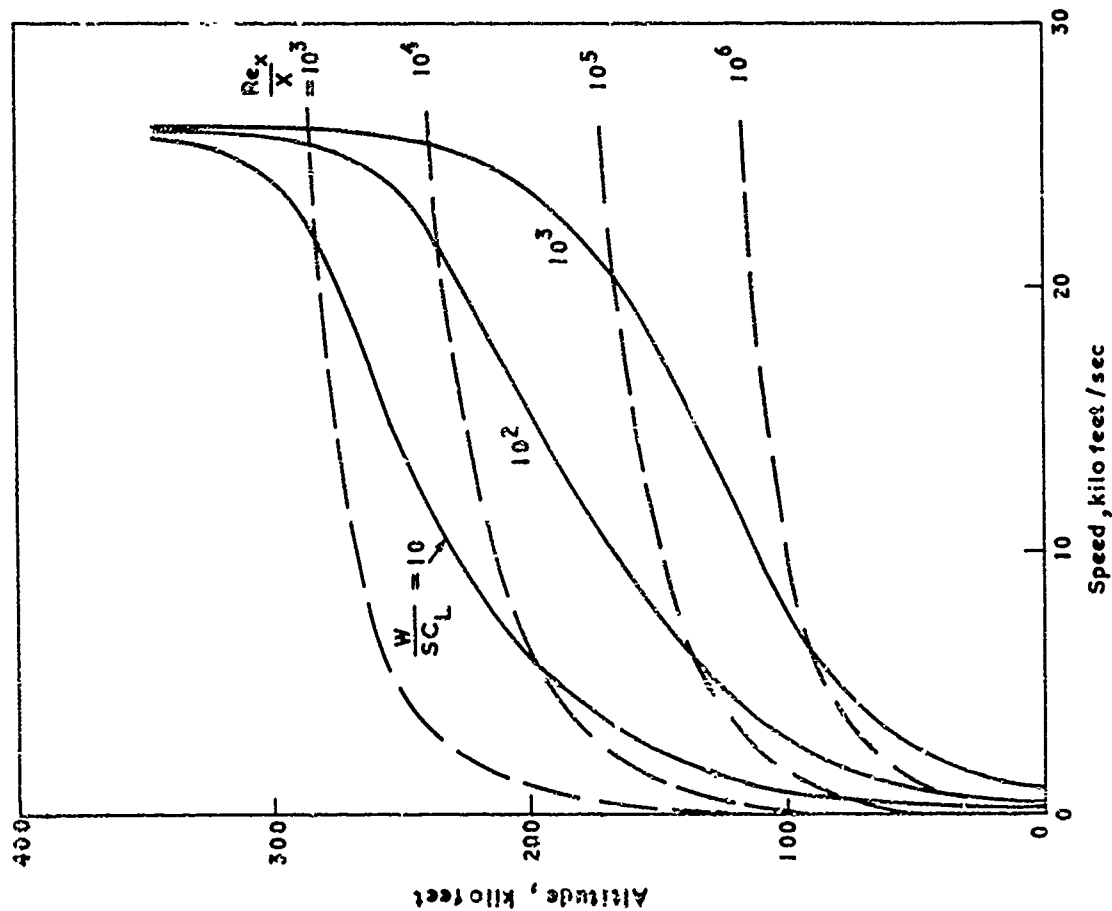


Fig.3 Freestream Reynolds number per foot and the parameter W/SC_L in lbm/ft^2 for lifting re-entry trajectories. Redrawn from Reference 11

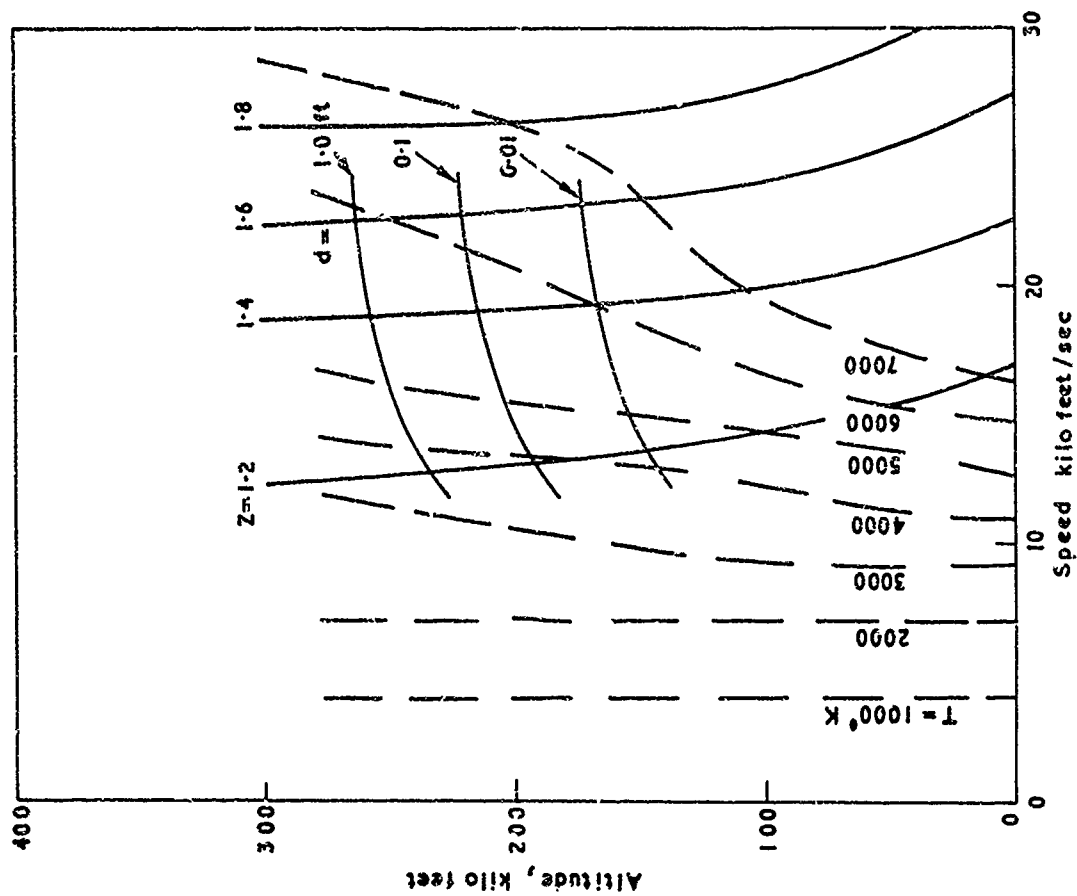


Fig.4 Equilibrium temperature and compressibility, also dissociation length d , behind normal shock wave

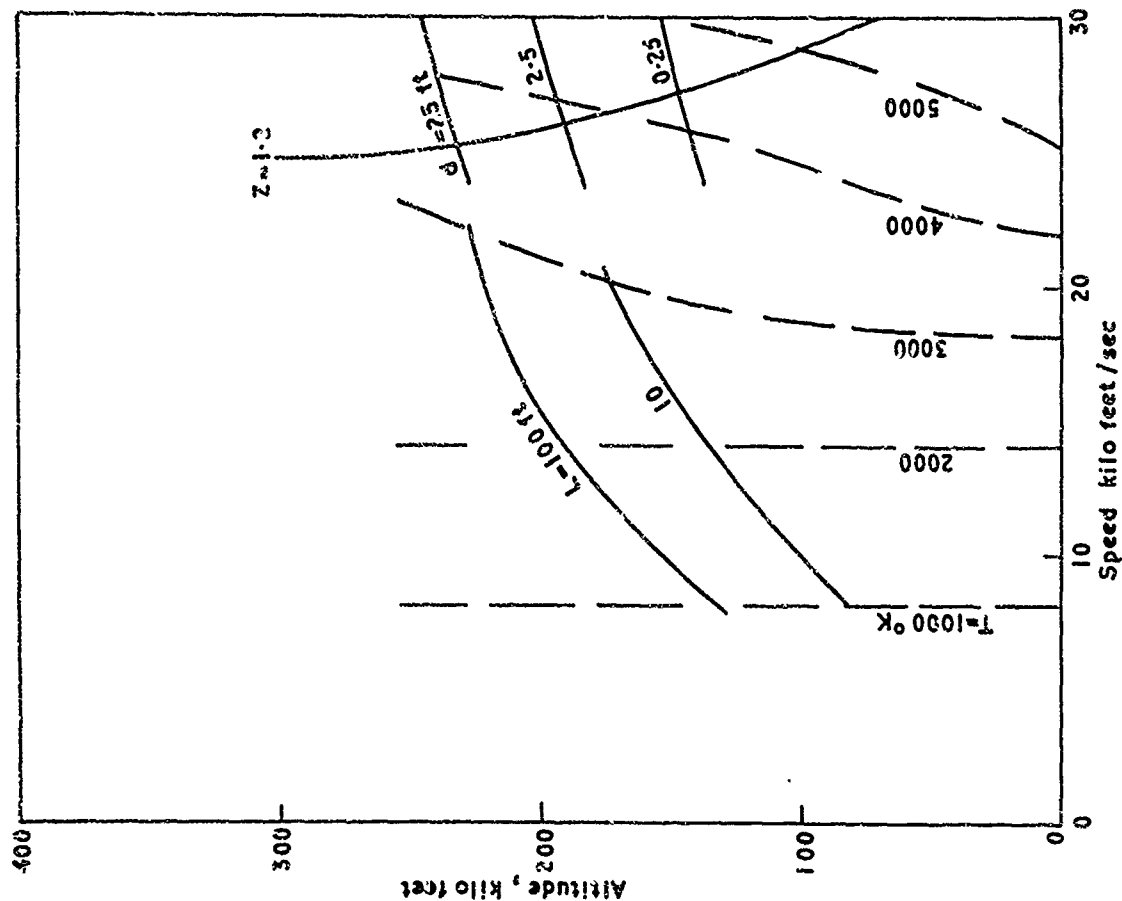


Fig.6 Equilibrium temperature and compressibility, dissociation length d and vibrational relaxation length, L , behind an oblique shock wave, wave angle 30°

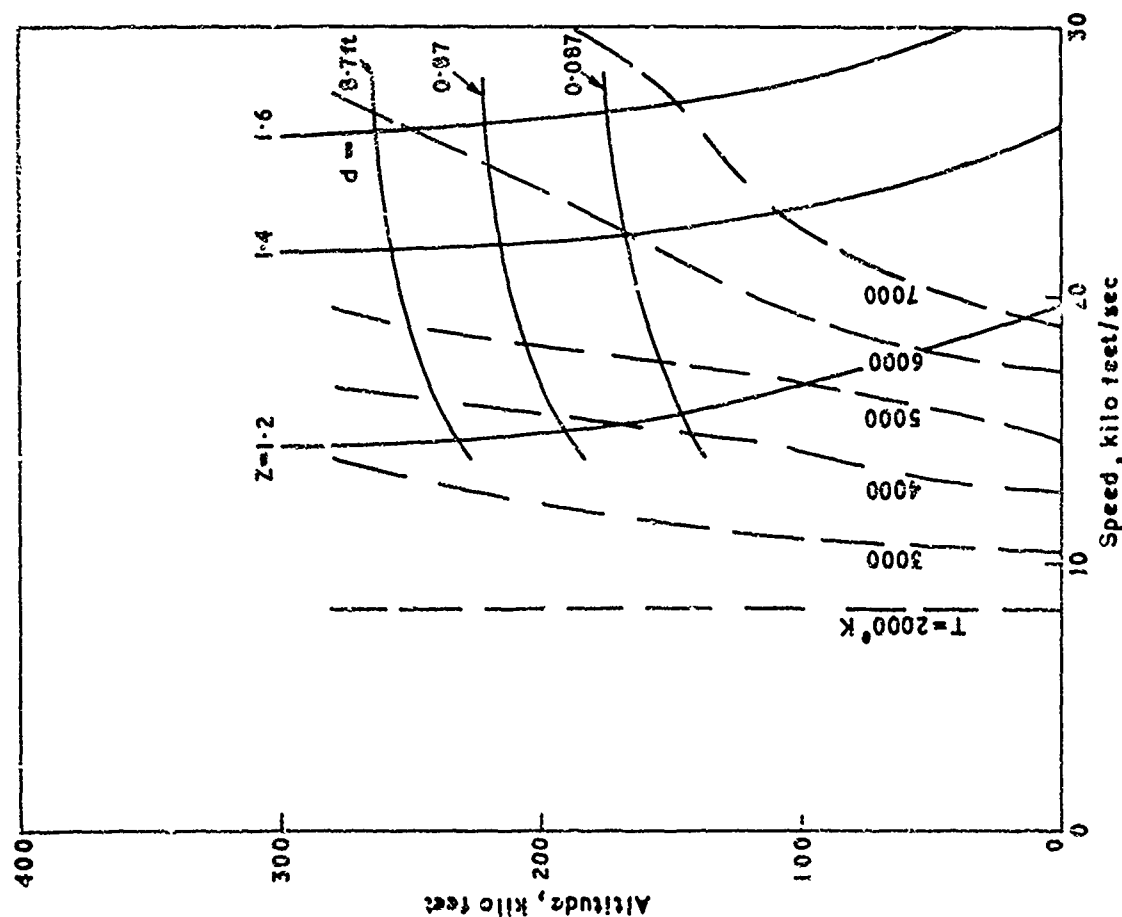


Fig.5 Equilibrium temperature and compressibility, also dissociation length d , behind an oblique shock wave, wave angle 60°

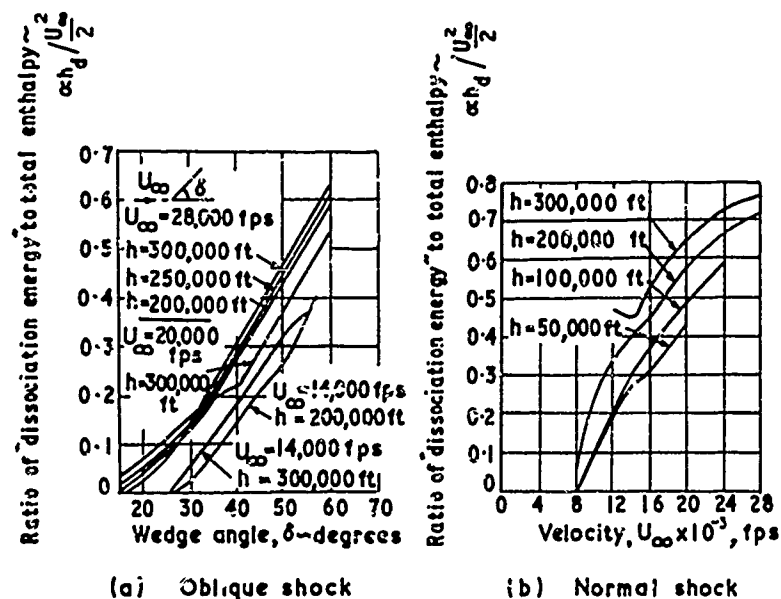


Fig.7 Ratio of dissociation energy to freestream kinetic energy for equilibrium conditions behind a shock¹²

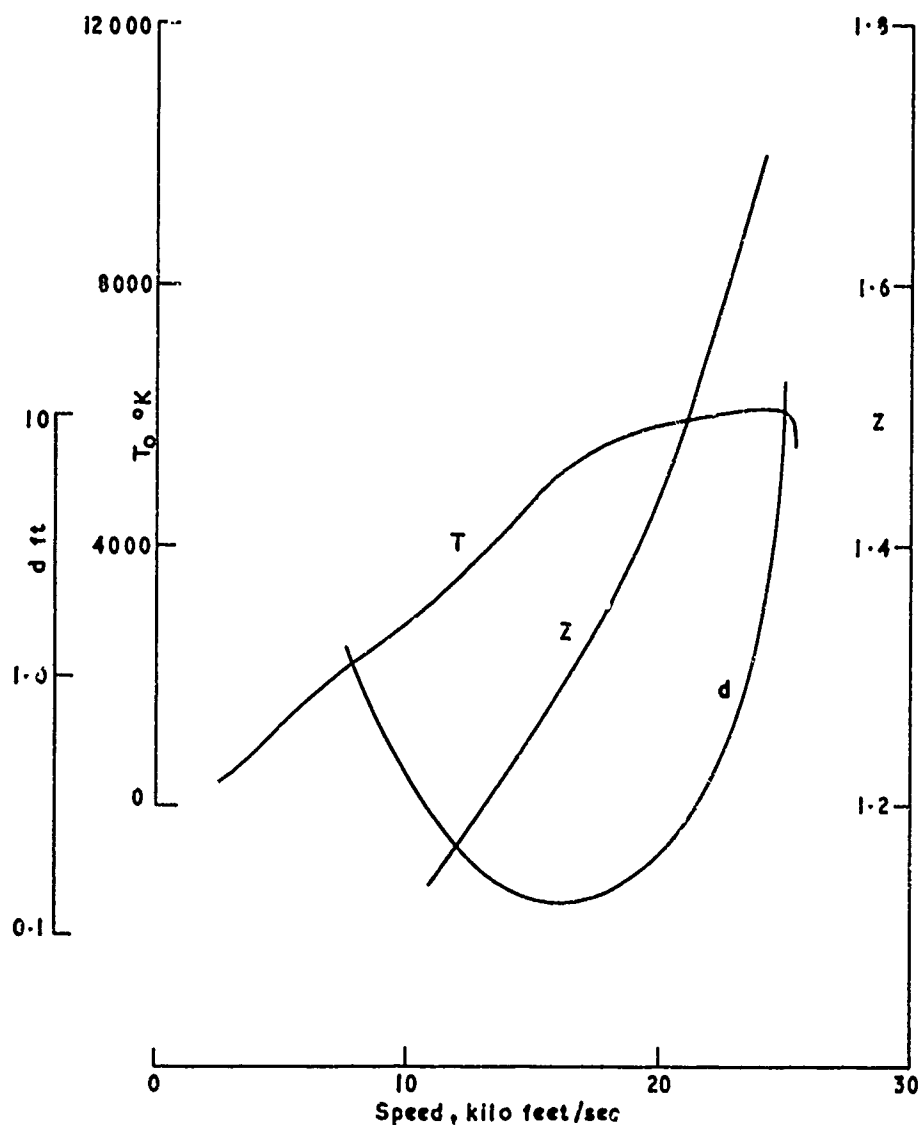


Fig.8 Conditions along lifting trajectory of Figure 2, for normal shock wave

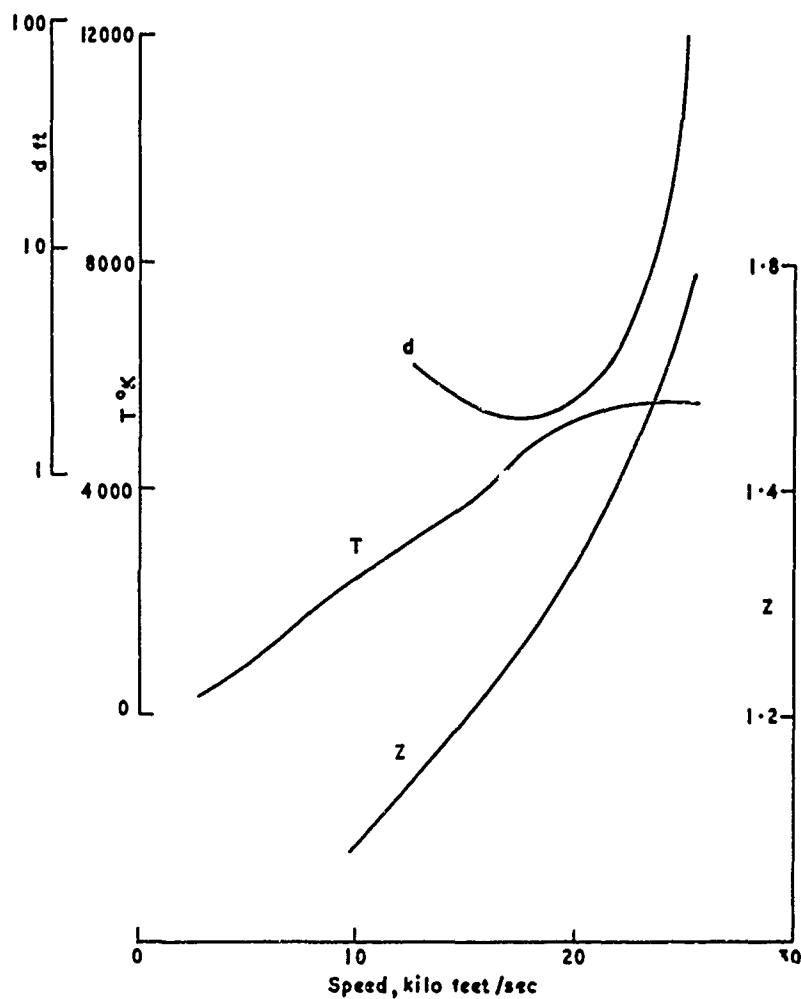
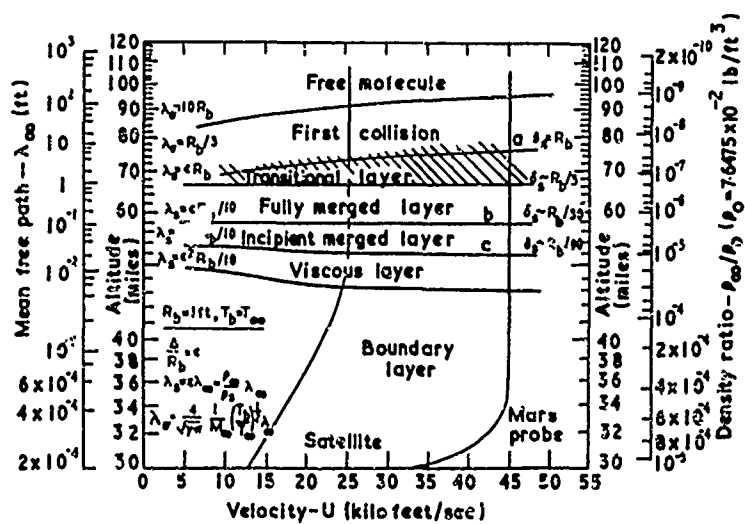
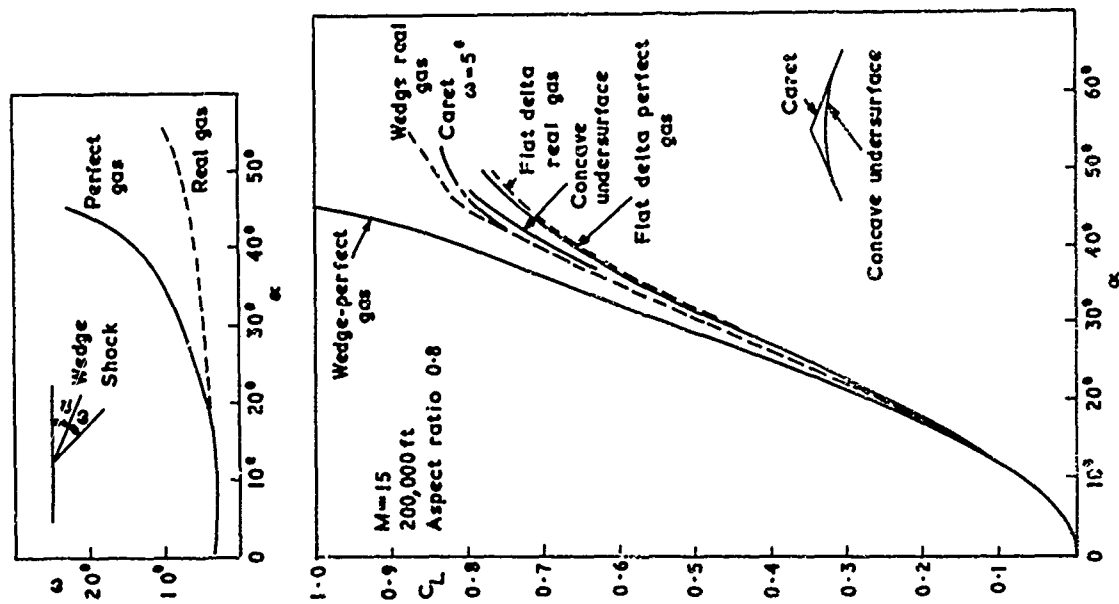


Fig.9 Conditions along lifting trajectory of Figure 2, for oblique shock wave, wave angle 60°



- a Shock forms
- b Shock thickens appreciably
- c Shock no longer discontinuity

Fig.10 Rarefied gas flow regimes for stagnation region of a highly cooled blunt body flying at hypersonic speed (Probstein¹⁴)



9-17

Fig.12 Shock wave angle and lift coefficient for wedge and other wing shapes, in perfect gas (frozen) and real gas (equilibrium) flow¹⁹

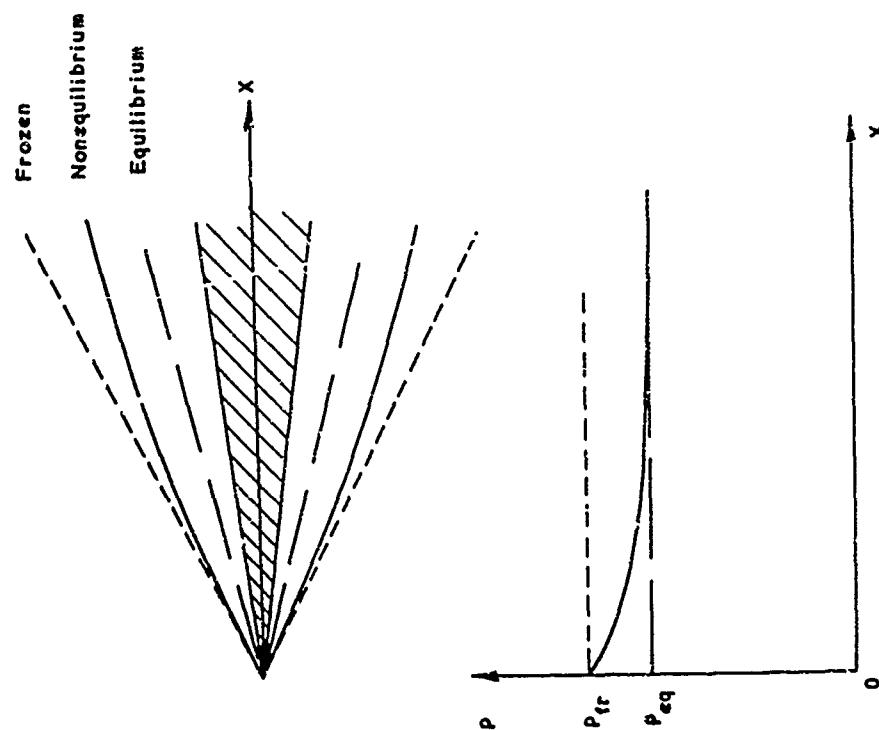


Fig.11 Shock wave shape and pressure distribution for frozen, equilibrium and non-equilibrium flow past a wedge. The changes in shock wave angle have been greatly exaggerated

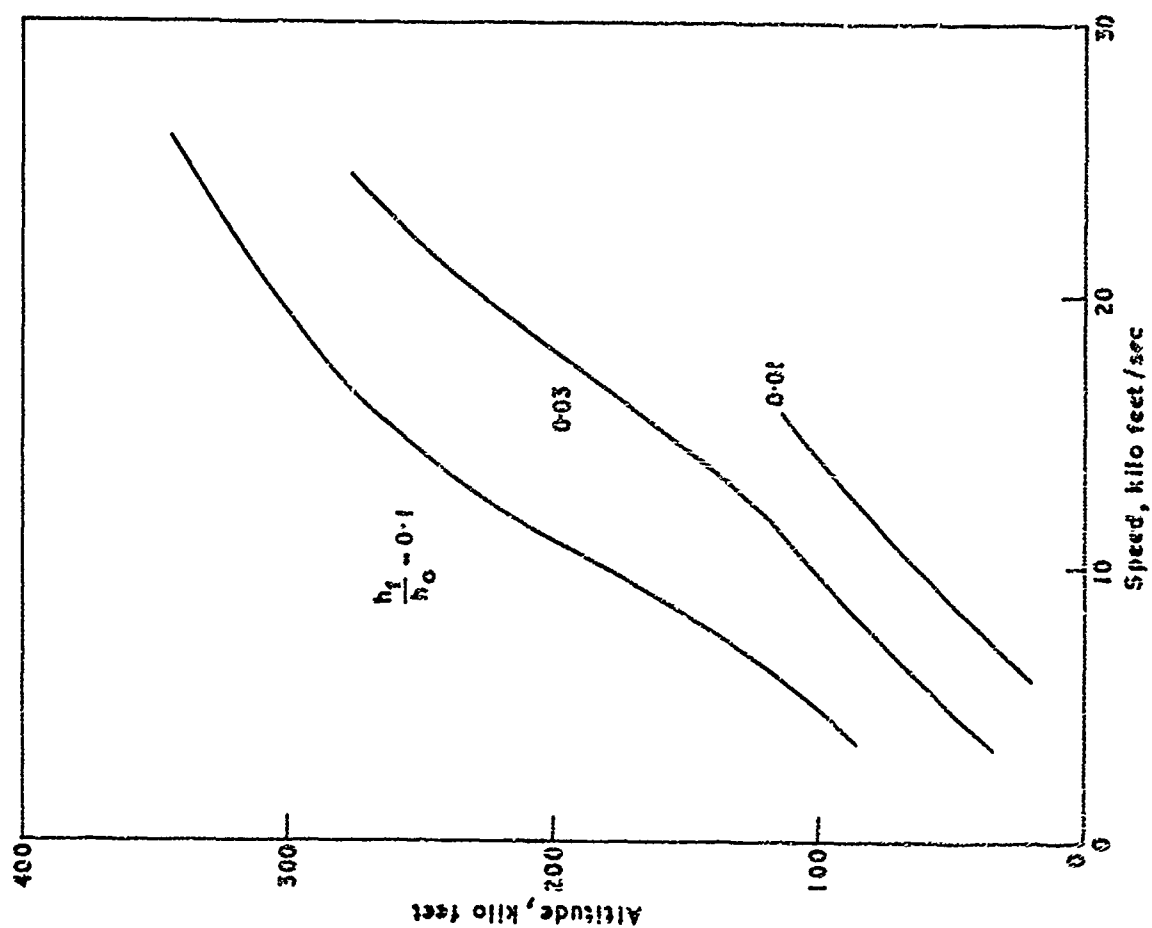


Fig.14 Fraction of reservoir enthalpy frozen in chemical energy

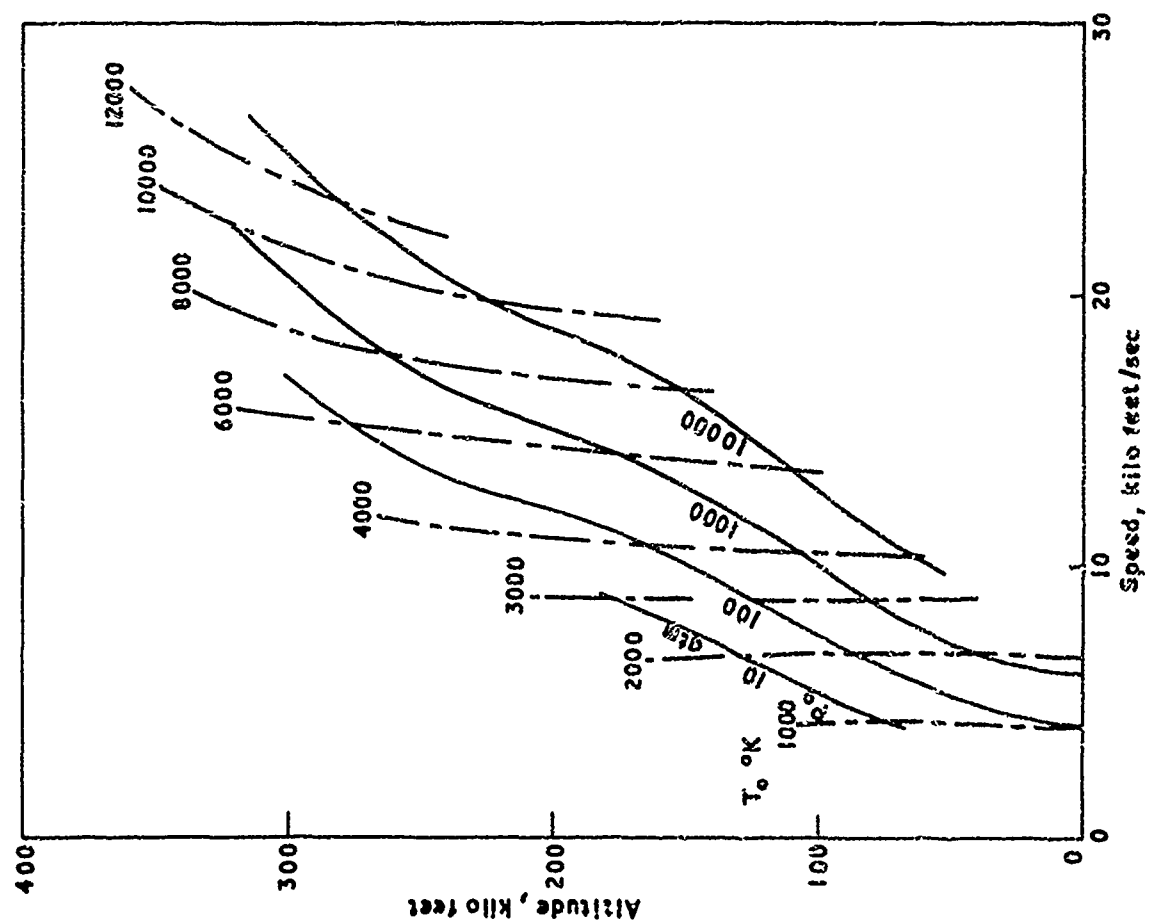


Fig.13 Wind tunnel reservoir conditions for flight duplication

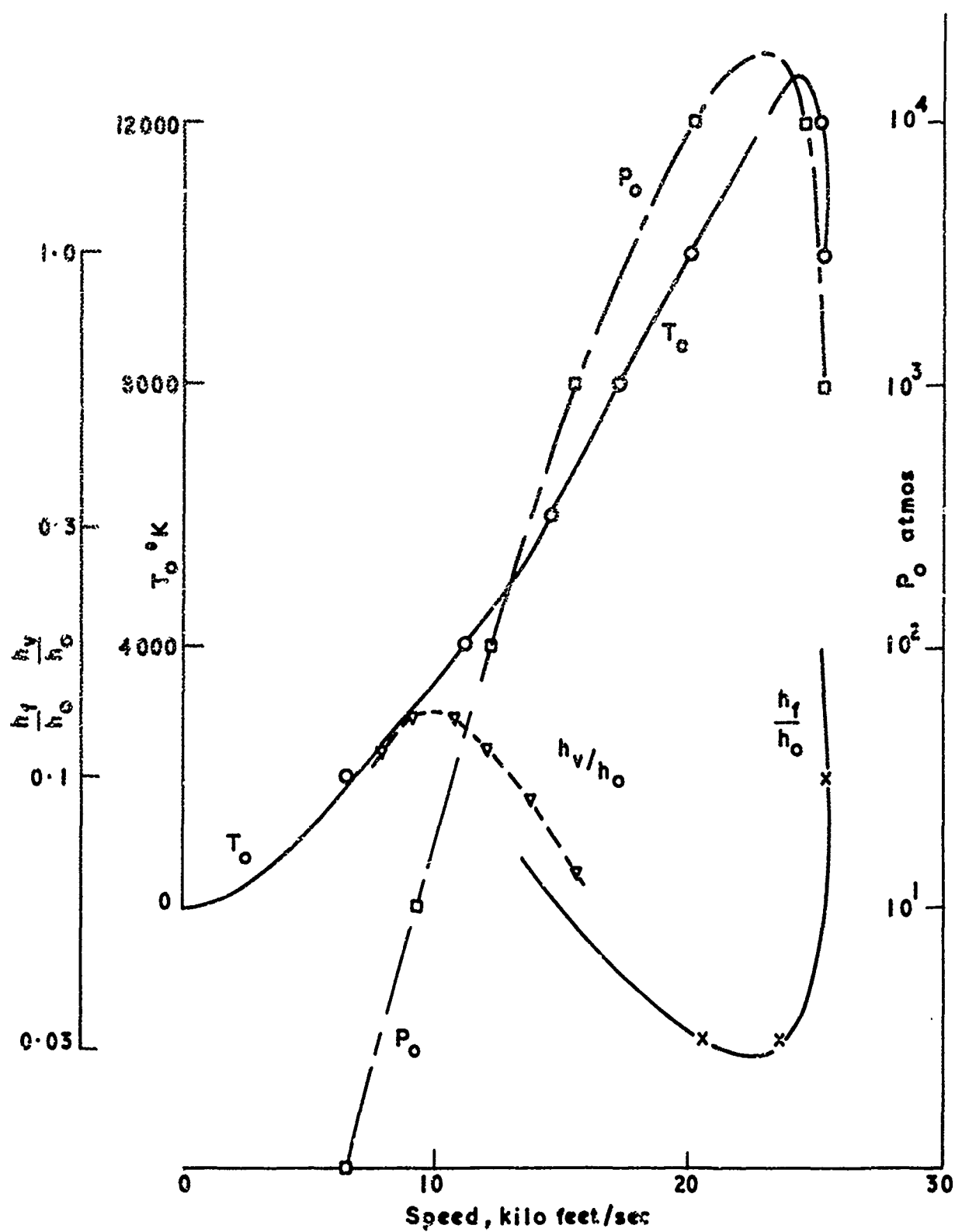


Fig.15 Wind tunnel conditions for lifting re-entry trajectory of Figure 2

LECTURE 10

VISCOUS INTERACTION EFFECTS ON RE-ENTRY AEROTHERMODYNAMICS:
THEORY AND EXPERIMENTAL RESULTS

J.L.Stollery

Imperial College of Science and Technology, London

NOTATION

a	speed of sound
$a_{1,2} \dots$	constants
A	$\frac{1}{2}(\gamma - 1) 0.664 (1 + 2.6 T_w/T_0)$, see Equation (2.4) et. seq.
$b_{1,2} \dots$	constants
c	$(\nu U/x)^{1/2}$, velocity characterising the spread of vorticity
C	constant of proportionality in the linear viscosity-temperature relation, see Equation (1.7)
C_f	skin friction coefficient
C_p	pressure coefficient
d	thickness of shock wave
k	a constant, or the nose drag coefficient, see Equation (2.27)
K	$M_\infty(dy_e/dx)$
K_e	$\frac{\gamma - 1}{2} M_\infty^3 \frac{kt}{x}$, a parameter controlling the bluntness effect
l	a characteristic length, defined in the text
l_i	extent of upstream influence
L	distance from leading edge to compression corner, see Section 6.
m	constant
M	Mach number
n	constant
p	pressure
P	pressure ratio p/p_∞
Pr	Prandtl number
r	nose radius
Re	Reynolds number
St	Stanton number

t	time or thickness of leading edge
T	temperature
u	velocity in the x direction
U, U_∞	free stream velocity
v	velocity in the y direction
V	rarefaction parameter $M_\infty/(Re_x)^{1/2}$ or $M_\infty C^{1/2}/Re_x^{1/2}$
x, y	rectangular coordinates along and normal to the free stream direction
z, ξ	variables related to y_e and x as defined in the text
α	local surface slope dy_w/dx
α_i	incipient separation angle
γ	ratio of the specific heats
Γ	$K_e \cdot M\alpha/2(A\bar{\chi})^2$ a parameter governing the interaction between the effects of bluntness, displacement and shape (incidence)
δ, δ^*	boundary layer and displacement thicknesses respectively
δ_1	thickness of subsonic part of the boundary layer
Δ	shock stand-off distance
ξ	see under z
λ	mean free path
Λ	sweep back angle
μ	viscosity
ν	kinematic viscosity
ξ	dummy x variable
ρ	density
$\bar{\chi}$	hypersonic viscous interaction parameter

Subscripts

b	edge of boundary layer
e	equivalent body (but note K_e above)
s	shock
t	thickness or bluntness
w	wall
0	total (but note St_0 defined in Equation (2.15))
∞	free stream

1. INTRODUCTION

A Definition

Viscous interaction may be defined as the mutual interaction between the external flow field and the boundary layer growth around a body of given shape. Two important examples are hypersonic viscous interaction near a sharp leading edge and shock-boundary layer interaction at both supersonic and hypersonic speeds.

Though viscous interaction is present to some degree in all flight situations, we need to highlight the conditions under which these effects are large.

1.1 The significance of ∇

Rayleigh's problem of an infinite flat plate jerked into motion in its own plane demonstrates very well how the spread of vorticity can be characterised by a velocity $c = \sqrt{\nu/t}$. Similarly the spreading velocity of a laminar boundary layer is given by

$$c = \frac{\delta}{t} = \frac{U\delta}{x} = \sqrt{\frac{U\nu}{x}} \quad (1.1)$$

Thus $\nabla = \frac{M}{\sqrt{Re}}$ may be written as

$$\nabla = \frac{U}{a} \sqrt{\frac{\nu}{Ux}} = \frac{\sqrt{\nu U/x}}{a} = \frac{c}{a} \quad (1.2)$$

$$= \frac{\text{spread of the vorticity field}}{\text{spread of the pressure field}}$$

or
$$\frac{\text{viscous diffusivity}}{\text{pressure diffusivity}}$$

This type of argument is perhaps more familiar in comparing the spread of heat and vorticity. The appropriate non-dimensional parameter is then the Prandtl number,

$$Pr = \frac{\nu}{K} = \frac{\text{viscous diffusivity}}{\text{thermal diffusivity}} \quad (1.3)$$

when $Pr = O[1]$ we anticipate the thermal and velocity boundary layers to be of similar size.

Similarly when $\nabla = O[1]$ we expect the boundary layer and shock layer to be "merged". At somewhat lower values of ∇ the boundary layer will be separately distinguishable within the shock layer but will occupy a significant fraction of it and viscous interaction will be important.

In subsonic and most supersonic flows $Re \gg M^2$ and the effect of boundary layer growth in changing the effective shape may be ignored. Under hypersonic high altitude conditions this is no longer true and viscous interaction effects become increasingly important.

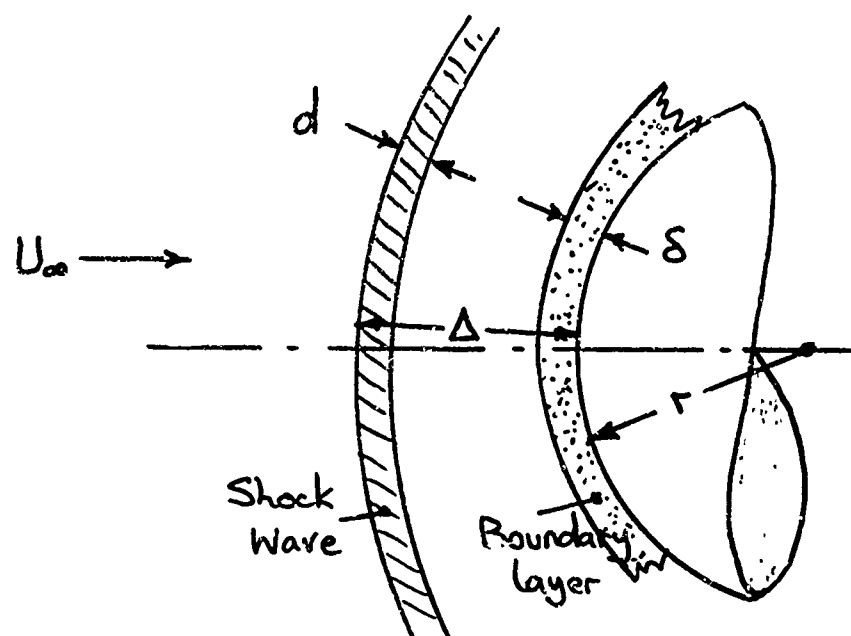
The importance of ∇ can also be demonstrated for hypersonic blunt body flows, see for example Van Dyke (1961).

Defining Re_∞ as $\frac{U_\infty r}{\nu_\infty}$ then with reference to the figure on the next page it can be shown that

$$\frac{\delta}{\Delta} \sim \frac{M_\infty}{\sqrt{Re_\infty}} \quad \text{and} \quad \frac{d}{r} \sim \frac{M_\infty^2}{Re_\infty}$$

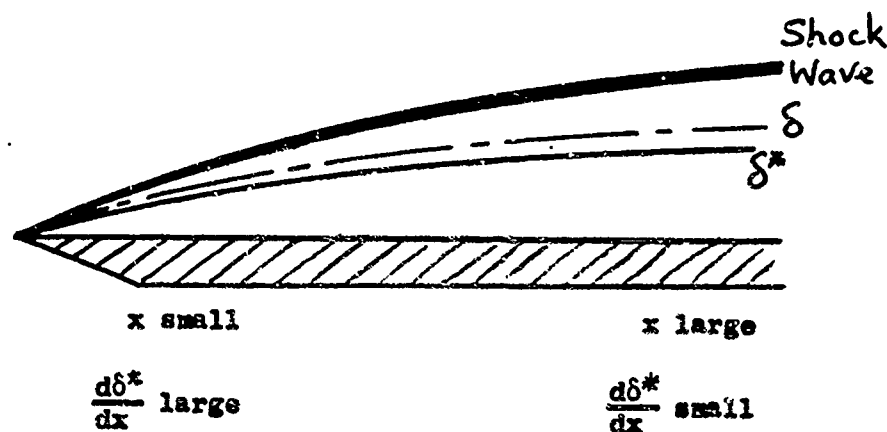
assuming $\mu \propto T$.

Again δ is a measure of the spread of the viscous field and Δ a measure of the pressure field. If ∇ is $O[1]$ then the two fields will be of similar size and hence to some extent "merged" making separate regions hard to distinguish.



1.2 The weak and strong viscous interaction parameters – an intuitive approach

1.2.1 Laminar flow



x small

x large

$\frac{d\delta^*}{dx}$ large

$\frac{d\delta^*}{dx}$ small

Now

$$\delta^* \sim \frac{x}{\sqrt{Re_x}} \sim \sqrt{\frac{x \bar{\mu}}{\bar{\rho} U_\infty}} \sim \sqrt{\frac{x \mu_\infty}{\rho_\infty U_\infty}} \cdot \sqrt{\frac{\rho_\infty}{\bar{\rho}} \cdot \frac{\bar{\mu}}{\mu_\infty}} \quad (1.4)$$

where barred values are average quantities in the boundary layer,

$$\text{but} \quad \frac{\rho_\infty}{\bar{\rho}} = \frac{\bar{T}}{T_\infty} \cdot \frac{P_\infty}{\bar{p}} \quad \text{equation of state} \quad (1.5)$$

$$\text{and} \quad \frac{\bar{T}}{T_\infty} \sim M_\infty^2 \dagger \quad (1.6)$$

$$\text{so assuming that} \quad \frac{\bar{\mu}}{\mu_\infty} = C \frac{\bar{T}}{T_\infty} \quad (1.7)$$

$$\text{then (4) becomes} \quad \delta^* \sim \sqrt{\frac{C}{Re_x}} \cdot \frac{M^2}{(p/p_\infty)^{1/2}} \quad (1.8)$$

† See boundary layer equations with $Pr = 1$ and $dp/dx = 0$, then $T_0 = Au + B$ is a solution where A and B are constants.

To relate p to the effective body shape ($y_b = y_w + \delta^*$) we use the tangent-wedge approximation

$$\frac{p}{p_\infty} = 1 + \frac{\gamma(\gamma+1)}{4} K^2 + \gamma K^2 \sqrt{\left(\frac{\gamma+1}{4}\right)^2 + \frac{1}{K^2}} \quad (1.9)$$

$$\text{where } K = M_\infty \left(\frac{dy_e}{dx} \right) = M_\infty \frac{d\delta^*}{dx} \text{ here, since } \frac{dy_w}{dx} = 0. \quad (1.10)$$

Strong viscous interaction $K > 1$, $K^2 \gg 1$.

For $K^2 \gg 1$ Equation (9) yields

$$\frac{p}{p_\infty} \approx \frac{\gamma(\gamma+1)}{2} K^2 = \frac{\gamma(\gamma+1)}{2} M_\infty^2 \left(\frac{d\delta^*}{dx} \right)^2. \quad (1.11)$$

Substitution in (1.8) and integrating gives

$$\frac{\delta^*}{x} \sim \left(\sqrt{\frac{C}{Re_x}} M_\infty \right)^{1/2} \sim \nabla^{1/2} \quad (1.12)$$

$$\text{so note that} \quad \delta^* \sim x^{3/4} \quad (1.13)$$

$$d\delta^*/dx \sim x^{-1/4} \quad (1.14)$$

$$\text{and} \quad p/p_\infty \sim x^{-1/2}. \quad (1.15)$$

$K^2 \equiv M_\infty^2 (d\delta^*/dx)^2$ may now be re-written from (1.12) as

$$K^2 \sim \sqrt{\frac{C}{Re_x}} \cdot M_\infty^3 \equiv \bar{\chi} \quad (1.16)$$

where $\bar{\chi}$ is termed the hypersonic viscous interaction parameter. Returning to (1.9) expanded by the binomial theorem we get

$$\frac{p}{p_\infty} = a_1 \bar{\chi} + a_2 + \frac{a_3}{\bar{\chi}} + \dots \quad (1.17)$$

Note for $\bar{\chi} \gg 1$ $p/p_\infty \approx a_1 \bar{\chi}$ so we could write this alternatively as

$$C_p = \frac{p - p_\infty}{\frac{1}{2} \gamma p_\infty M_\infty^2} = \frac{2a_1}{\gamma} \cdot \nabla. \quad (1.18)$$

Weak viscous interaction $K < 1$, $K^2 \ll 1$.

The tangent-wedge rule is re-written as

$$\begin{aligned} \frac{p}{p_\infty} &= 1 + \frac{\gamma(\gamma+1)}{4} K^2 + \gamma K \sqrt{1 + \frac{\gamma+1}{4} K^2} \\ &= 1 + \gamma K + \frac{\gamma(\gamma+1)}{4} K^2 + \dots \end{aligned} \quad (1.19)$$

So $p/p_\infty \approx 1$ and thus immediately from (1.8)

$$\frac{\delta^*}{x} \sim M_\infty^2 \sqrt{\frac{C}{Re_x}} \text{ or } \delta^* \sim x^{1/2} \quad (1.20)$$

and

$$K = M_\infty \frac{d\delta^*}{dx} \sim M_\infty^3 \sqrt{\frac{C}{Re_x}} \equiv \bar{\chi}.$$

Once again $\bar{\chi}$ is the relevant parameter and

$$\frac{p}{p_\infty} = 1 + b_1 \bar{\chi} + b_2 \bar{\chi}^2 + \dots \quad (1.21)$$

1.2.2 Turbulent flow

A similar analysis for turbulent flow putting

$$\frac{\delta}{x} \sim (\text{Re}_x)^{-1/5} \quad (1.22)$$

gives the following results:

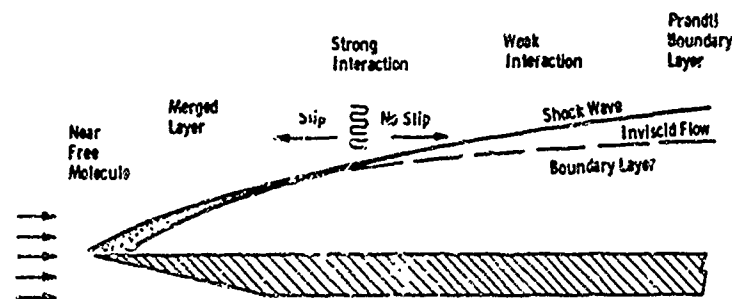
$$\text{Strong interaction} \quad \bar{\chi} = \left(\frac{M^2 C}{\text{Re}_x} \right)^{2/7} \quad (1.23)$$

$$\text{Weak interaction} \quad \bar{\chi} = \left(\frac{M^2 C}{\text{Re}_x} \right)^{1/5} \quad (1.24)$$

Transition Reynolds numbers are so high at hypersonic Mach numbers that strong turbulent viscous interaction is unlikely to occur.

1.3 The various flow regimes

The character of the flow field near the leading edge of a sharp flat plate in rarefied hypersonic flow is sketched below.



These particular notes concentrate on the continuum regime and in particular on strong and weak viscous interaction. Experiment shows that strong interaction is valid for $\bar{V} \leq 0.15$ and that above this value (i.e. closer to the leading edge) the pressure and heat transfer rate drop away as shown in Figure 1. The various flow regimes are plotted in Figure 2. The $\bar{V} = 0.15$ boundary shows that at low Mach number ($M < 6$ say) there is no strong interaction zone, the flow moving through the rarefied region straight into weak viscous interaction.

The significance of \bar{V} in continuum flow has already been described. Its utility in rarefied flow (\bar{V} is often called the rarefaction parameter) has been demonstrated experimentally but there is as yet no widely accepted theoretical reason for its significance though one "explanation" is given below.

1.4 Knudsen number (Kn) and the rarefaction parameter \bar{V}

In a rarefied gas flow which cannot be regarded as a continuum the dominant variable is Kn.

$$\text{Kn} = \frac{\lambda}{l} = \frac{\text{mean free path}}{\text{some characteristic length in the flow field}}$$

but $\nu \sim \lambda a$ where a is the speed of sound

$$\text{so that} \quad \text{Kn} = \frac{\lambda}{l} \sim \frac{M}{\text{Re}_l}$$

If the gas is only slightly rarefied then the typical linear dimension is better taken to be the boundary layer thickness (δ). Since $\delta \sim l/\sqrt{Re_l}$ we have

$$\frac{\lambda}{\delta} \sim \frac{M}{\sqrt{Re_l}} \equiv \nabla. \quad (1.25)$$

1.5 The effects of bluntness

So far the discussion has centred on bodies with a sharp leading edge whereas all real shapes are to some extent blunt. In order to compare the relative importance of bluntness and strong viscous interaction we will compare the pressure distributions induced by both near the leading edge.

For viscous flow on a sharp flat plate

$$\frac{p}{p_\infty} \sim \bar{x}, \quad \text{see Equation (1.17).}$$

For inviscid flow past a blunt flat plate blast wave theory predicts that

$$\frac{p}{p_\infty} \sim \left(\frac{M_\infty^3}{x/t} \right)^{2/3}. \quad (1.26)$$

Using suffices (t) for bluntness effect and (v) for viscous effect and replacing x/t by Re_x/Re_l then

$$\frac{p_t}{p_v} \sim \left\{ \frac{\bar{x}^{1/2} Re_l}{M_\infty^3} \right\}^{2/3}. \quad (1.27)$$

If the plate is to be effectively sharp (i.e. the $p_t \ll p_v$) then

$$M_\infty^3 \gg (\bar{x})^{1/2} Re_l,$$

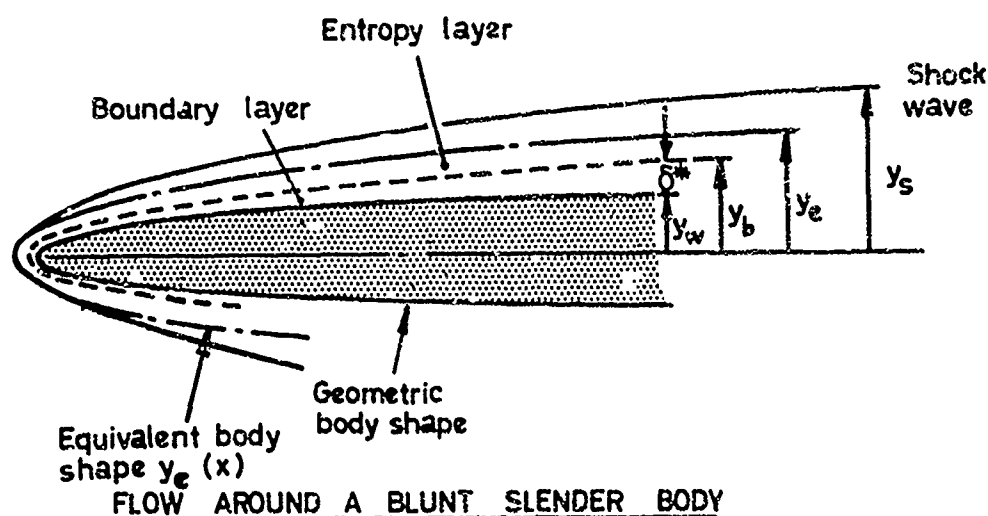
$$\text{i.e.} \quad Re_l \ll M_\infty^3 / \sqrt{\bar{x}}. \quad (1.28)$$

Taking $M_\infty = 10$ and noting that \bar{x} for strong viscous interaction is $O[10]^\infty$ then this criterion implies

$$Re_l \leq 100 \text{ say.}$$

The line $M_\infty^3 / \sqrt{\bar{x}} = 500$ is marked on Figure 2. Below this line it will be difficult to satisfy the relation (1.28) and hence bluntness effects may be important.

2. THE GENERAL PROBLEM OF VISCOUS INTERACTION IN 2D FLOW



In the most general case it is necessary to consider the combined effect of:

- (i) incidence (body shape)
- (ii) displacement (boundary layer growth)
- (iii) bluntness (entropy layer).

We shall follow the classic work of Cheng (1961) with subsequent modifications and extensions by Sullivan (1968) and Stollery (1970).

2.1 Plate with a sharp leading edge ($y_e = 0$)

We need $y_e = f_1(\delta^*)$ (2.1)

$$\delta^* = f_2(p_e) \quad (2.2)$$

$$p_e = f_3(y_e) \quad (2.3)$$

Many choices for these three basic equations are possible; we shall adopt rather simple relations for all three. For Equation (2.1) we assume

$$y_e = y_w + \delta^* \quad (2.1a)$$

so that $\frac{dy_e}{dx} = \frac{dy_w}{dx} + \frac{d\delta^*}{dx}$

Since δ^* is not a streamline this simple expression is only approximate. The correct coupling equation is

$$\frac{dy_e}{dx} = \frac{dy_w}{dx} + \frac{d\delta^*}{dx} - (\delta - \delta^*) \frac{d}{dx} (1/\rho_e u_e)$$

as shown for example by Lees and Reeves (1964). The last term is small and $\delta^* \rightarrow \delta$ as $M_\infty \rightarrow \infty$.

For Equation (2.2) the local flat plate similarity solution for hypersonic boundary layers is adopted. First derived by Lees (1956) for blunt body flows under cold wall conditions it was later used by Cheng and critically re-examined by Moore (1961). Readers are referred to these papers for a full discussion of the derivation. For unit Prandtl number the results are:

$$\frac{M_\infty \delta^*}{x} = \frac{A\bar{X}}{P} \left[\int_0^x P \frac{d\xi}{x} \right]^{1/2} \quad (2.4)$$

$$M_\infty^2 St = 0.332\bar{X} P \left[\int_0^x P \frac{d\xi}{x} \right]^{1/2} \quad (2.5)$$

$$C_f = 2 St \quad (2.6)$$

where

$$A = \frac{1}{2}(\gamma - 1) 0.664 \left(1 + 2.6 \frac{T_w}{T_0} \right) \quad (2.7)$$

and

$$P = p/p_\infty$$

For Equation (2.3) Cheng used the Newton-Busemann law

$$P = \gamma M_\infty^2 (y_e'^2 + y_e y_e'') = \gamma M_\infty^2 (y_e y_e')' \quad (2.8)$$

which, though mathematically a reasonable approximation, does not allow $P \rightarrow 1$ as $y_e' \rightarrow 0$ and leads to physically unrealistic oscillatory solutions in some cases. Thus Equation (2.8) is only suitable for strong viscous interaction.

Using (2.1a), (2.4) and (2.8) gives the fundamental equation for y_e given any shape of wall $y_w(x)$.

$$(y_e - y_w) \left\{ (y_e y_e')^{1/2} \right\}' = \left(\frac{A^2 \bar{X}^2 x}{4\gamma M_\infty^4} \right) \quad (2.9)$$

A number of examples can now be considered.

2.1.1 Flat plate at zero incidence

With $y_w = 0$ and writing

$$z = y_c/l \quad \text{and} \quad \xi = x/l \quad (2.10)$$

converts Equation (2.9) to

$$z \left[(zz')^{1/2} \right]' = 1 \quad (2.11)$$

provided that

$$l = \frac{A^2 \bar{x}^2 x}{4\gamma M_\infty^4} \quad (2.12)$$

This scaling immediately emphasises that, to the degree of approximation implicit in the analysis, the important parameter is $A\bar{x}/M_\infty^2 \equiv A\bar{V}$.

Substitution of $z = k\xi^m$ in Equation (2.11) shows that the familiar strong interaction solution is given by $m = 3/4$ and $k = 2^{5/2}/3^{1/4}$ so that

$$M_\infty \frac{\delta^*}{x} = \frac{2}{(3\gamma)^{1/4}} (A\bar{x})^{1/2} \quad \text{or} \quad \frac{\delta^*}{x} = \frac{2}{(3\gamma)^{1/4}} (A\bar{V})^{1/2} \quad (2.13)$$

$$\frac{P}{P_\infty} = P = \left(\frac{3}{4}\gamma\right)^{1/2} A\bar{x} \quad \text{or} \quad C_p = \left(\frac{3}{\gamma}\right)^{1/2} \bar{V} \quad (2.14)$$

$$\frac{St}{St_0} = \frac{1}{2} (3\gamma)^{1/4} (A\bar{x})^{1/2} \quad \text{or} \quad St = \frac{0.332}{2} (3\gamma)^{1/4} (A\bar{V})^{1/2} \quad (2.15)$$

where $St_0 = 0.332 (C/Re_x)^{1/2}$.

The weak viscous interaction solution where $P \rightarrow 1$ as $y_c' \rightarrow 0$ does not satisfy the Newton-Busemann relation and hence is not a solution of (2.11).

2.1.2 Surfaces described by $y_w = kx^n$

The family of shapes

$$\frac{y_w}{\alpha l} = \pm \left(\frac{x}{l}\right)^n \quad \text{or} \quad z = \pm \xi^n$$

is of some interest and includes the flat plate at both positive and negative incidence, ($n = \pm 1$). The governing Equation (2.11) may now be written as

$$(z \pm \xi^n) \left[(zz')^{1/2} \right]' = 1 \quad (2.16)$$

provided that

$$l = \frac{A^2 \bar{x}^2 x}{4\gamma M_\infty^4 \alpha^2} \quad (2.17)$$

In terms of the new variables the required physical quantities are

$$\frac{\delta^*}{\alpha l} = (z \mp \xi^n) \quad (2.18)$$

$$\frac{P}{\gamma M_\infty^2 \alpha^2} = (zz')' \quad (2.19)$$

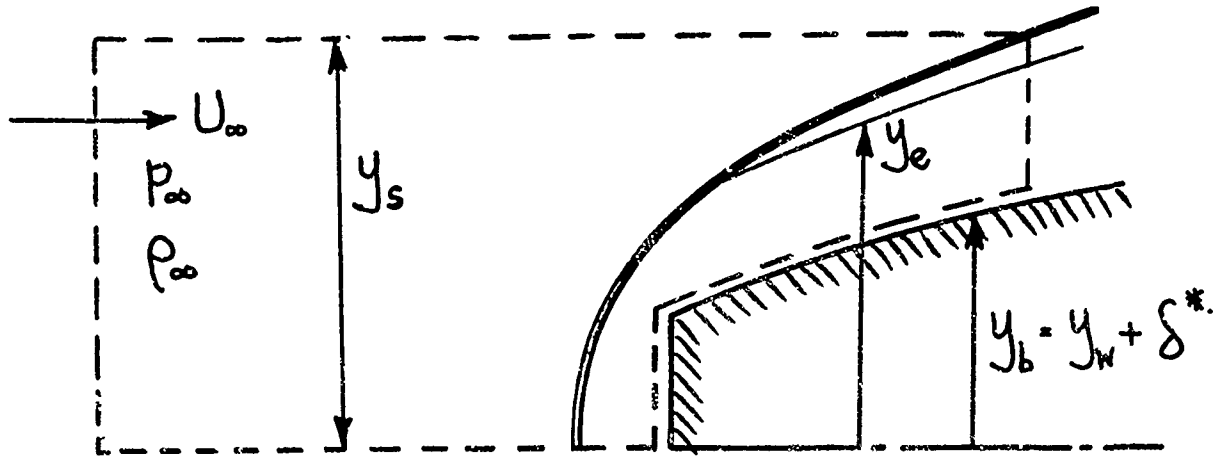
$$\frac{\Lambda St}{0.332 \alpha^2 4\gamma} = \frac{1}{(z \mp \xi^n)} = \left(\frac{\delta^*}{\alpha l}\right)^{-1} \quad (2.20)$$

The most significant point about the analysis is that it immediately highlights the important parameter when both strong interaction and incidence (shape) effects are present, namely,

$$A\bar{X}/M_\infty^2 \alpha^2 \quad \text{or} \quad \nabla/\alpha^2 . \quad (2.21)$$

2.2 Plate with a blunt leading edge $y_e \neq y_b$

A further relation is now required to relate the equivalent body shape (y_e) to the displacement body shape ($y_b \equiv y_w + \delta^*$) in terms of the body bluntness.* This is done most simply by applying the momentum equation to the control volume sketched below.



$$-\left(\frac{DN}{2} + \int_0^x p_b y'_b dx\right) + p_\infty y_s - \int_{y_b}^{y_s} p dy = \int_{y_b}^{y_s} \rho u^2 dy - \rho_\infty U_\infty^2 y_s . \quad (2.22)$$

The continuity equation is

$$\rho_\infty U_\infty y_s = \int_{y_b}^{y_s} \rho u dy . \quad (2.23)$$

Using the continuity equation and recognising that sufficiently far from the nose $u \approx U_\infty$ then the RHS of (2.22) becomes negligible and

$$\frac{DN}{2} + \int_0^x p_b y'_b dx = p_\infty y_s - \int_{y_b}^{y_s} p dy . \quad (2.24)$$

The energy equation with $u \approx U_\infty$ becomes

$$\frac{\gamma}{\gamma-1} \left(\frac{p_\infty}{\rho_\infty} - \frac{p}{\rho} \right) = \frac{v^2}{2} \quad \text{or} \quad \frac{\gamma}{\gamma-1} \left(p_\infty \cdot \frac{\rho}{\rho_\infty} - p \right) = \frac{\rho v^2}{2} . \quad (2.25)$$

Integrating with the use of continuity gives finally that

$$\int_{y_b}^{y_s} p dy = \frac{\gamma}{\gamma-1} p_\infty y_s - \frac{1}{\gamma-1} \int_{y_b}^{y_s} p dy - \int_{y_b}^{y_s} \frac{\rho v^2}{2} dy$$

so that

$$\frac{DN}{2} + \int_0^x p_b y'_b dx = \int_{y_b}^{y_s} \frac{p}{\gamma-1} dy + \int_{y_b}^{y_s} \frac{\rho v^2}{2} dy - \frac{p_\infty y_s}{\gamma-1} .$$

* It may be noted here that the effects of bluntness and displacement are similar in so far as they envelope the geometric body in layers of high-temperature, low-density fluid across which the pressure is approximately constant.

In this equation the major contribution to the LHS is the nose drag and on the RHS the first term is dominant. Hence to a first approximation, putting $y_s \approx y_e$,

$$\frac{D_N}{2} = \int_{y_b}^{y_e} \frac{p}{\gamma - 1} dy. \quad (2.26)$$

Cheng showed by an order of magnitude analysis that pressure changes across the entropy layer are negligibly small so it is possible to use the simplification that p is constant across the layer, hence $p_e = p_b = p_w = f(x)$ only.

The important bluntness equation is then

$$(y_e - y_b) \frac{p_e}{p_\infty} \cdot \frac{1}{\gamma M_\infty^2} = \frac{\gamma - 1}{4} kt \quad (2.27)$$

where

$$k = \frac{D_N}{\frac{1}{2} \rho_\infty U_\infty^2 t}$$

and t is the nose thickness.

The relevant equations are now

$$\left. \begin{aligned} (y_e - y_b) \frac{P}{\gamma M_\infty^2} &= \frac{\gamma - 1}{4} kt \\ P &= \gamma M_\infty^2 (y_e y_e')' \\ y_b &= y_w + \delta^* \\ \text{and } \frac{M_\infty \delta^*}{x} &= \frac{A \bar{X}}{P} \left[\int_0^x P \frac{d\xi}{x} \right]^{1/2} \end{aligned} \right\} \quad (2.28)$$

2.3 The flat plate with bluntness and displacement

Equation (2.28) reduces to

$$z(zz')' - \sqrt{zz'} = 1 \quad (2.29)$$

provided that

$$z = 8M_\infty (A \bar{X}/K_e)^2 (y_e/K_e x) \text{ and } \xi = 16(A \bar{X}/K_e^{2/3})^6.$$

Once again the analysis emphasises the important parameter, i.e. $\frac{A \bar{X}}{K_e^{2/3}}$

where

$$K_e = M_\infty^3 \frac{\gamma - 1}{2} \cdot \frac{kt}{x}$$

and

$$A = \frac{\gamma - 1}{2} 0.664 \left(1 + 2.6 \frac{T_w}{T_o} \right)$$

so

$$\frac{A \bar{X}}{K_e^{2/3}} \quad \text{or} \quad \frac{A \nabla}{kt/x} \text{ is the relevant ratio.} \quad (2.30)$$

For small values of $A \bar{X}/K_e^{2/3}$, i.e. bluntness dominant, the solution of (2.29) gives

$$\frac{M \delta^*}{x} = \left(\frac{9}{4} K_e \right)^{1/3}$$

and

$$P = \gamma \left(\frac{1}{18} \right)^{1/3} K_e^{2/3},$$

which are the blast wave solutions for two-dimensional flow.

2.4 The flat plate with bluntness and incidence

Equation (2.28) now becomes

$$(z \pm \xi)(zz')' = 1 \quad (2.31)$$

with $z = 4\alpha^2 y_e / (\gamma - 1)kt$ and $\xi = 4|\alpha|^2 x / (\gamma - 1)kt$.

The important parameter is then $\frac{x}{kt} \cdot \alpha^3$ perhaps better written as

$$\frac{M_\infty^2 \alpha^2}{K_e^{2/3}} \quad (2.32)$$

2.5 The flat plate with bluntness, incidence and displacement

The governing equation becomes

$$(z - \Gamma\xi)(zz')' - \sqrt{zz'} = 1 \quad (2.33)$$

where

$$z = 8M(A^2 \bar{\chi}^2 / K_e)^2 (\xi_e / K_e x), \quad \xi = 16 \left(\frac{A \bar{\chi}}{K_e^{2/3}} \right)^6 \quad (2.34)$$

and

$$\Gamma = \frac{K_e M \alpha}{2A^2 \bar{\chi}^2}, \text{ independent of } x. \quad (2.35)$$

One of the major accomplishments of this analysis is to point out the significance of the three parameters

$$M_\infty^2 \alpha^2, \quad A \bar{\chi} \quad \text{and} \quad M_\infty^2 \left(\frac{kt}{x} \right)^{2/3} \quad (2.36)$$

It is perhaps not surprising that they turn out to be those associated with (i) inviscid hypersonic flow over a sharp edged slender body (hypersonic small disturbance theory), (ii) viscous flow on a flat plate (viscous interaction theory), (iii) flow around blunt nosed slender bodies (blast wave theory). Cheng himself noted that often the empirical linear-combination laws gave results reasonably close to the more exact analysis described above.

2.6 Alternative expressions for the pressure law $P(y_e)$

The Newton-Busemann rule for pressure suffers two great disadvantages, it does not asymptote to the correct downstream limit ($P \rightarrow 1$ as $y_e' \rightarrow 0$) and it often over-corrects for centrifugal effects giving rise to unrealistic highly-oscillatory solutions. The scope of the theoretical analysis already described can therefore be greatly enhanced by using a pressure law which is capable of embracing both the strong and weak viscous interaction regimes and which ignores centrifugal effects. For example a simple Newtonian law could be used, i.e.

$$P = 1 + \gamma M_\infty^2 y_e'^2 \quad (2.37)$$

One of the most successful approximations at hypersonic speeds is the tangent-wedge rule

$$P = 1 + \gamma M_\infty^2 y_e'^2 \left[\left(\frac{\gamma + 1}{4} \right) + \left\{ \left(\frac{\gamma + 1}{4} \right)^2 + \frac{1}{M_\infty^2 y_e'^2} \right\}^{1/2} \right] \quad (2.38)$$

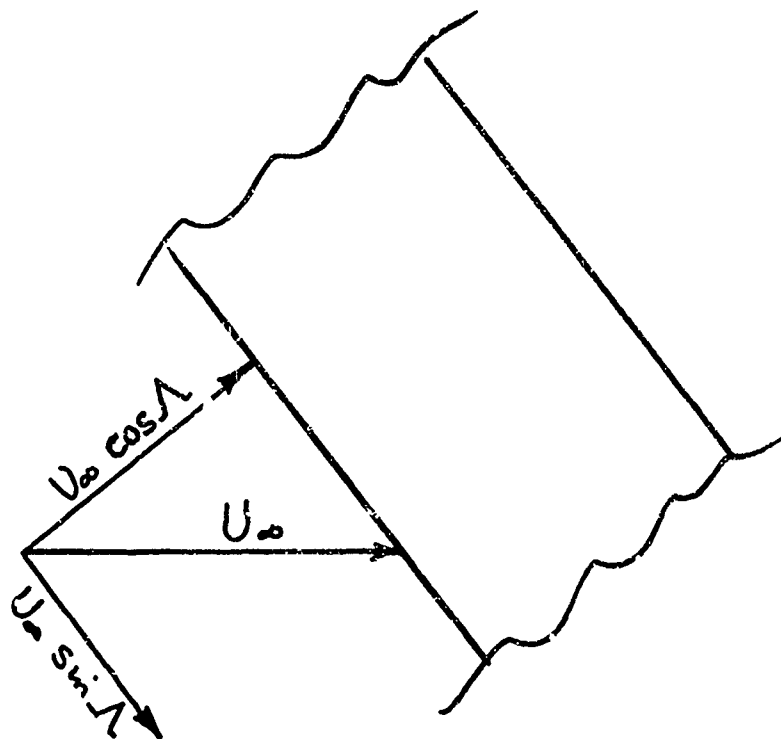
and both Sullivan and Stollery have used this to examine a number of different flows. Though the use of either of the above pressure relationships decreases the mathematical elegance there is a great gain in practical utility and the subsequent analysis is straightforward. Readers are referred to the paper by Stollery (1970) for details.

3. COMPARISONS WITH EXPERIMENTAL DATA

Comparisons are made between some experimental data and various theoretical predictions in Figures 3 to 9. As a sweeping generalisation it is true to say that comparisons employing log-log correlation look very good whereas

individual predictions compared with raw experimental data often look very bad. There is no doubt that use of the tangent-wedge rule improves the comparison and removes the oscillatory nature of the solutions for the flow over concave surfaces.

4. THE EFFECTS OF SWEEP



Boger and Aiello (1970) showed that Cheng's theory could be successfully developed to treat the yawed case for a two-dimensional wedge with leading edge bluntness and viscous interaction. The additional assumption then made was that there should be no variation in the flow along the span.

For the combined effects of bluntness, incidence and viscous interaction the governing equation is identical to (2.33) namely

$$(z - \Gamma \zeta)(zz')' - \sqrt{zz'} = 1 \quad (4.1)$$

but now

$$\Gamma = \frac{K_e(M_\infty \cos \Lambda) \alpha}{2\Lambda^2 \bar{\chi}^2}, \quad z = \frac{8(M_\infty \cos \Lambda)(A\bar{\chi})^4 y_e}{K_e^3 x}$$

where

$$K_e = (M_\infty \cos \Lambda)^3 \frac{\gamma - 1}{2} \cdot \frac{kt}{x}, \quad \zeta = 16(A\bar{\chi} \cdot K_e^{-2/3})^6,$$

$$\bar{\chi} = (M_\infty \cos \Lambda)^3 (C/Re_x)^{1/2},$$

and

$$Re_x = \rho_\infty (U_\infty \cos \Lambda) / \mu_\infty.$$

Equation (4.1) can be solved and expressed in series form. Boger and Aiello quote the pressure as

$$\frac{p_w}{p_\infty} = 0.382 \gamma K^{2/3} \left\{ 1 + i.04 \zeta^{1/6} + (0.505 + 0.162)\zeta^{1/3} \right\}. \quad (4.2)$$

Because of the sweep the effective values of $\bar{\chi}$ and K are decreased significantly so that p_w and the form drag are greatly reduced. Under these conditions skin friction may be more significant.

Tests were made on a blunt wedge and a blunt flat plate, see Figure 10, at sweep angles of 60° and 70° . A selection of results is shown in Figure 11.

Provided that the normal component of Mach number ($M_\infty \cos \Lambda$) is hypersonic, agreement between theory and experiment appears to be good.

5. EFFECT OF FINITE CHORD AND FINITE SPAN

5.1 Finite chord

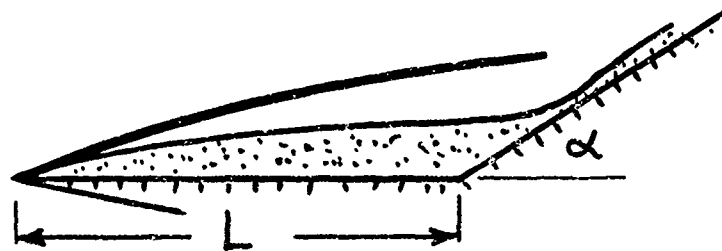
Whatever the freestream Mach number there will always be a subsonic region in which signals may propagate upstream. A recent analysis of compression corner flows showed that the upstream influence (before separation) was constrained to a distance (l_i) and that (l_i/δ) decreased with Mach number. A similar study by Bogdonoff (1969) on trailing-edge effects indicated the same trend. The dimensional distance (l_i) is often still significant because $\delta \sim M^2$. In both the studies mentioned an attempt was made to correlate l_i/δ_1 where δ_1 is the thickness to the sonic line. So far the scatter precludes worthwhile comment. What is expected and what is found experimentally is shown in Figure 12, the pressure changing ahead of the trailing edge so as to reduce the pressure difference between top and bottom surfaces.

5.2 Finite span

Nardo and Cresci (1970) have reported some machine calculations of merged layer flow over a finite width plate. Some of their results are shown in Figure 13. Although a region of constant (spanwise) pressure exists in the middle of the plate it can be considerably less than the two-dimensional value and is therefore no guarantee of 2D flow. Their report serves as a sober warning but results are too limited to give any overall picture of finite span effects.

6. CORNER FLOWS

6.1 Compression corners



For the simplest corner flow sketched above the adverse pressure gradient will depend on $(M_\infty \alpha)^2$ whilst the boundary layer growth along the plate will be governed by $\bar{\chi}$. Hence there is some reason to correlate incipient separation data by plotting $M_\infty \alpha_1$ vs $\bar{\chi}_L$ and indeed the experimental data currently available support a relation

$$M_\infty \alpha_1 = k \cdot \bar{\chi}_L^{1/2} . \quad (6.1)$$

The effect of wall temperature is harder to gauge but wind tunnel tests show that cooling the wall inhibits separation. Reasonable predictions can be made using

$$M_\infty \alpha_1 = 1.4 (1 - T_w/2T_0) \bar{\chi}_L^{1/2} , \quad (6.2)$$

see Nædham (1967).

6.2 Axial corners

Here the situation is much more complex and the reader is referred to the survey by Korkegi (1970). Charwat and Redekopp made detailed experiments in a corner constructed from intersecting wedges. Their measurements at $2.5 < M < 4$ laid the foundation for the inviscid flow model shown in Figure 14. Subsequent investigations with intersecting wedges in hypersonic flow have revealed the same basic flow features.

Currently (and probably quite rightly) the emphasis is on careful experiment though a theoretical merged layer analysis by Bloom et al (1969) shows promise for low density flows. For the higher density flows however there exists no adequate method of predicting even the inviscid flow structure.

7. APPLICATIONS OF VISCOUS INTERACTION THEORY TO SPECIFIC SHAPES

7.1 Straight wing designs

Reasonable estimates of the pressure, heat transfer, force and moment coefficients can be made by using the modification to Cheng's theory (employing the tangent-wedge rule for $P(y_e)$) already described.

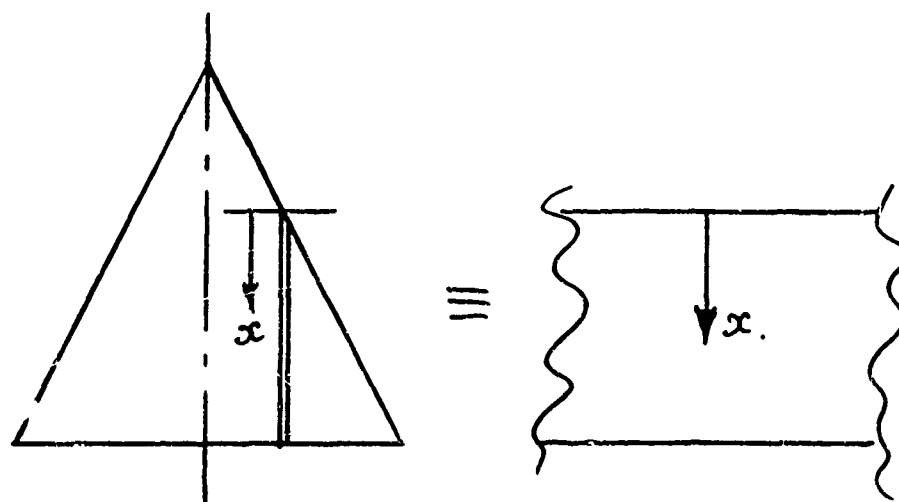
The effect of viscous interaction is to increase the lift-curve slope above the inviscid value but the pressure drag is also increased as is the skin friction. The usual result is a loss of maximum lift/drag ratio.

7.2 Caret wing designs

When "on design" the flow field is essentially two-dimensional and the remarks made above apply to strips parallel to the root chord. For convenience it may be useful to adopt the method due to Davies (1970) described under the section on delta wings.

7.3 Delta wing designs

Conventional strip theory, as applied to an infinite yawed wing or to a swept edge, considers the normal components of velocity and Mach number ($U_n = U_\infty \cos\Lambda$ and $M_n = M_\infty \cos\Lambda$) as the effective quantities for a subsequently two-dimensional approach. This approach fails in the neighbourhood of the root chord which is of course unswept. For highly swept delta wings in hypersonic flow the root area is dominant and it is more appropriate to apply 2D theory to strips parallel to the root chord. Thus the flow is assumed to lie in strips parallel to the centre-line with each strip independent of the other strips as shown in the sketch below.



This assumption is admittedly somewhat precarious in view of the observed delta wing flow patterns which indicate important three-dimensional effects particularly at incidence.

7.3.1 Sharp leading edge delta wings

At moderate incidence (up to say 20°) simple strip theory gives reasonable estimates on the windward or compression surface as far as heat transfer rate and skin friction is concerned. The prediction of pressure seems less accurate as shown for example in the study by Wallace and Burke (1963).

On the lee side of a delta wing 3D effects appear significant even at low incidence. Whitehead (1970) reported heating rates on the leeward meridian of a 75° swept delta wing at 5° incidence in $M = 6$ flow which were approximately three times the two-dimensional value.

If 2D strip theory is used for estimates on a delta wing then a convenient way of applying it has been described by Davies (1970) and is shown in figure 15. By taking strips parallel to the leading edge the value of ∇ , \bar{x} , etc. is constant along the strip though its numerical value is of course estimated using properties and distances measured in the freestream direction. He has estimated viscous interaction effects in this way and shows that there can be significant increases in the normal force coefficient of the lower surface and a forward movement of the C.P.

7.3.2 Blunt leading edge delta wings

Again strip theory can be applied but the question arises of how to modify the nose drag coefficient for sweep. One solution is to treat the leading edge as part of a yawed cylinder and put

$$C_{D_{N\Lambda}} = C_{D_{N\Lambda=0}} \times \cos^2 \Lambda .$$

However the data of Wallace and Burke show better agreement with estimates made using

$$C_{D_{N\Lambda}} = C_{D_{N\Lambda=0}}$$

i.e. making no sweep correction whatsoever.

7.4 Viscous interaction on high L/D vehicles ($L/D_{\max} > 2$)

The effect of viscous interaction on any but the simplest complete configuration is extremely difficult to estimate. As for example Koppenwallner (1970) has shown, the lift coefficient is usually slightly improved but the drag coefficient substantially increased. The net result is a significant reduction in lift/drag ratio as \bar{V} or \bar{X} is increased. The necessity for accurate knowledge of high altitude aerodynamics depends on the vehicle mission but as Hidalgo and Vaglio-Laurin (1967) point out, the influence of low Reynolds number effects can reduce the lateral range of a high performance space-shuttle by up to 45% and cause even greater reductions in longitudinal range.

7.5 Viscous interaction on low L/D vehicles

Boylan and Potter (1967) tested a number of different shapes shown in Figure 16. In all these cases not only did C_D rise but the C_L fell with increasing \bar{V} so that the lift/drag ratio was again reduced. More recent tests by Kusoy et al (1970) on the Faget SSV (Figure 17) at re-entry incidence ($\alpha \approx 50-60^\circ$) show a 40% reduction of L/D between altitudes of 200,000 and 340,000 ft. In this case the decrease is primarily due to the increased skin friction drag significantly reducing C_L .

A similar effect has been noted on the Gemini and Apollo re-entry capsules. Since these vehicles fly at an angle of attack the stagnation point is off centre, the flow around the blunt face is asymmetric so that pressure and shear forces do not balance out about the vehicle centre line. As shown in Figure 18 the surface shear on the front face produces a major component in the lift direction (tending to decrease the overall lift) and a smaller component which increases the drag. At high Re these shear effects are small but under high altitude low Re conditions they are very significant. Their neglect was the probable explanation as to why the three earliest manned Gemini flights all fell consistently short of the predicted splash points. Goldberg (1966) investigated these effects theoretically and his findings have recently been confirmed by Boylan and Griffith (1969) during extensive tests on the Apollo Command Module.

Figure 19 attempts to summarise the influence of high altitude effects on $(L/D)_{\max}$ for various types of vehicle. Though individual estimates are difficult the trend is both obvious and significant.

ACKNOWLEDGEMENTS

The author would like to thank Mr S.Metcalf and Dr L.Davies, RAE Teddington, for their helpful discussion of some of the material presented here.

REFERENCES

- Allegre, J., et al., (1967), *Comptes Rendus, Series A: Sciences Mathématiques*, Vol.264, 10, p.466.
- Bloom, M.H., et al., (1969), *Viscous Interaction Phenomena in Supersonic and Hypersonic Flow*, University of Dayton Press, p.493.
- Bogdonoff, S.M., (1969), *Viscous Interaction Phenomena in Supersonic and Hypersonic Flow*, University of Dayton Press, p.83.
- Boger, R.C., and Aiello, G.F., (1970), AIAA Paper No.70-783.
- Boylan, D.E., and Griffith, B.J., (1969), *J. Space and Rockets*, Vol.6, 3, p.334.
- Boylan, D.E., and Potter, J.L., (1967), *AIAA J.*, Vol.5, 2, p.226.
- Burke, A.F., et al., (1962), CAL-AA-1596-Y-1, Cornell Aeronautical Laboratory.
- Cheng, H.K., et al., (1961), *J. Aero Sci.*, Vol.28, 5, p.353.
- Creager, M.O., (1959), NASA MEM 12-26-58A.
- Davies, L., (1970), *British ARC* 32, 117.
- Feldhune, R.H., (1965), Internal Memo 8, Princeton University.
- Goldberg, L., (1966), AIAA Paper No.66-464.
- Hidalgo, H., and Vaglio-Laurin, R., (1967), *Proc. 18th Int. Astro. Congress*, Belgrade.
- Holden, M.S., (1971), *AIAA J.*, Vol.9, 1, p.84.
- Kemp, J.H., (1969), *AIAA J.*, Vol.7, 7, p.1280.
- Koppenwallner, G., (1970), ICAS Paper No.70-03.
- Korkegi, R.H., (1970), AIAA Paper No.70-781.
- Kusjoy, M.I., et al., (1970), *J. Space and Rockets*, Vol 7, 10, p.1267.
- Lees, L., (1956), *Jet Propulsion*, Vol.26, p.259.
- Lees, L., and Reeves, B.L., (1964), *AIAA J.*, Vol.2, 11, p.1907.
- Moore, F.K., (1961), *J. Aero. Sci.*, Vol.28, 10, p.753.
- Nardo, C.T., and Cresci, R.J., (1970), AIAA Paper No.70-784.
- Needham, D.A., (1967), *AIAA J.*, Vol.5, 12, p.2284.
- Rudman, S., and Rubin, S.G., (1968), *AIAA J.*, Vol.6, 10, p.1883.
- Stollery, J.L., (1970), *JFM*, Vol.43, 3, p.497.
- Sullivan, P.A., (1969), AIAA Paper No.69-137.
- Van Dyke, M., (1961), *Hypersonic Flow Research*, Academic Press, p.37.
- Vidal, R.J., et al., (1963), AIAA Paper No.63-435.
- Wallace, J.E., and Burke, A.F., (1963), USAF Report ASD-TDR-63-772.
- Whitehead, A.H., (1970), *AIAA J.*, Vol.8, 3, p.599.

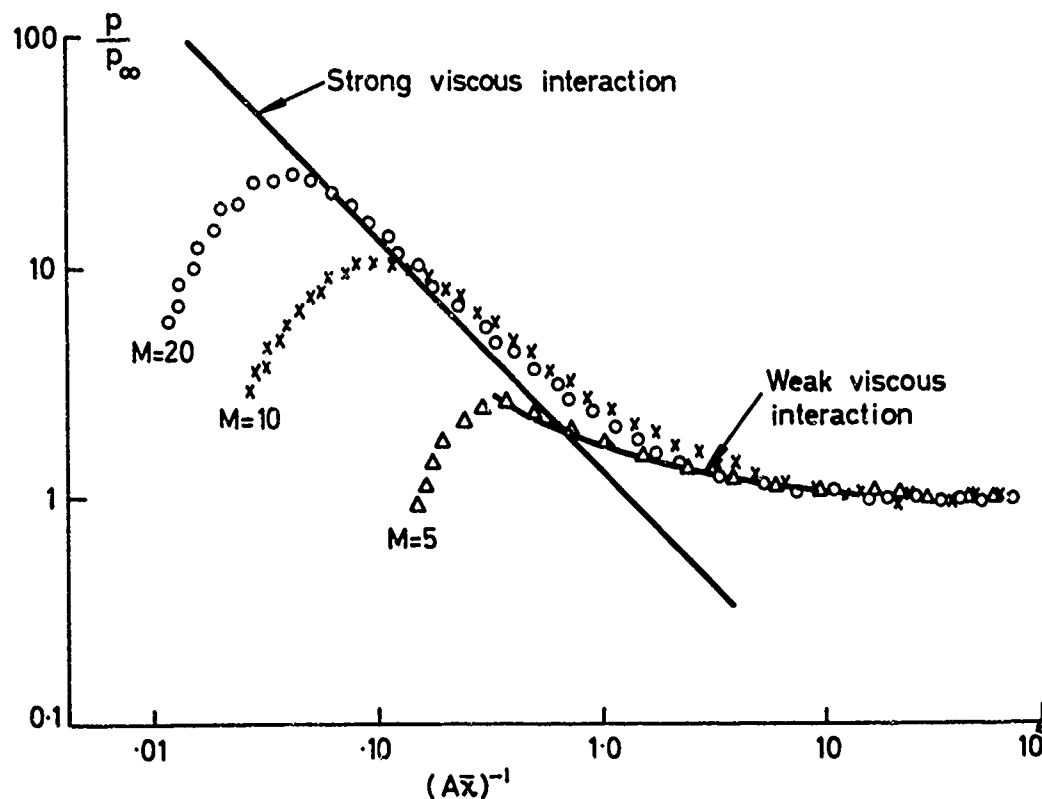


Fig. 1a The pressure distribution induced on a sharp flat plate at zero incidence

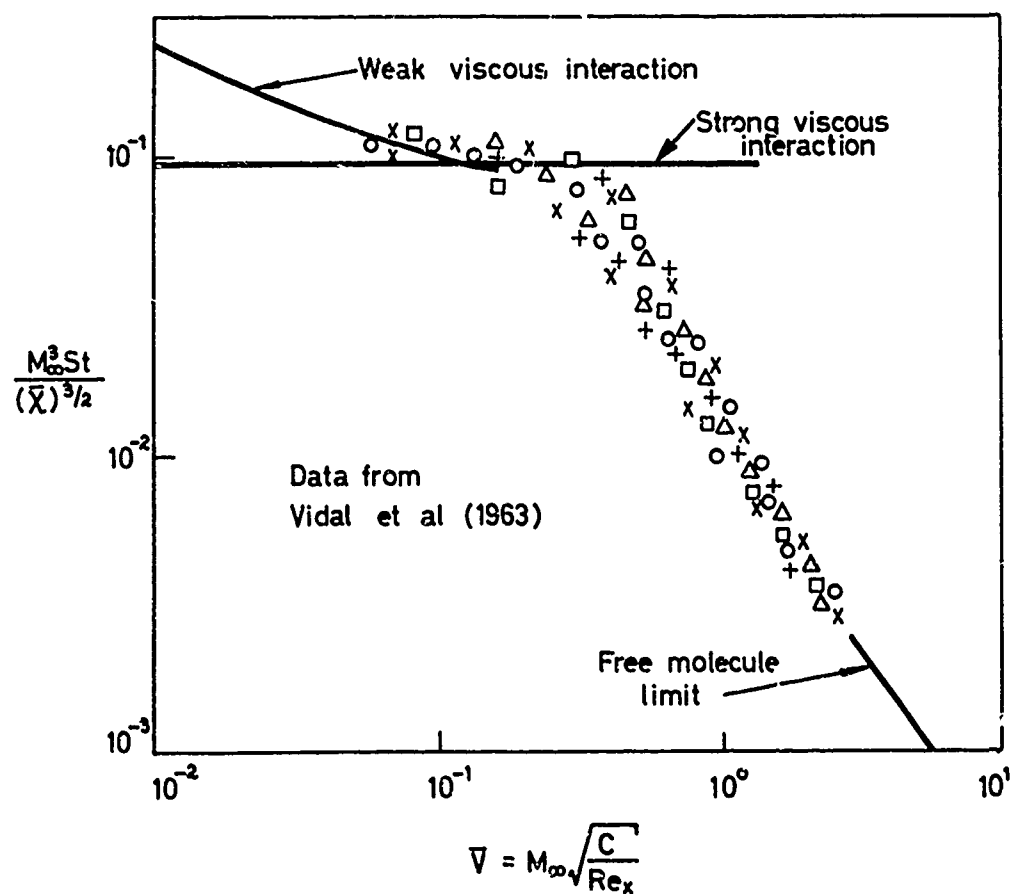


Fig. 1b Heat transfer rate to a sharp flat plate at zero incidence

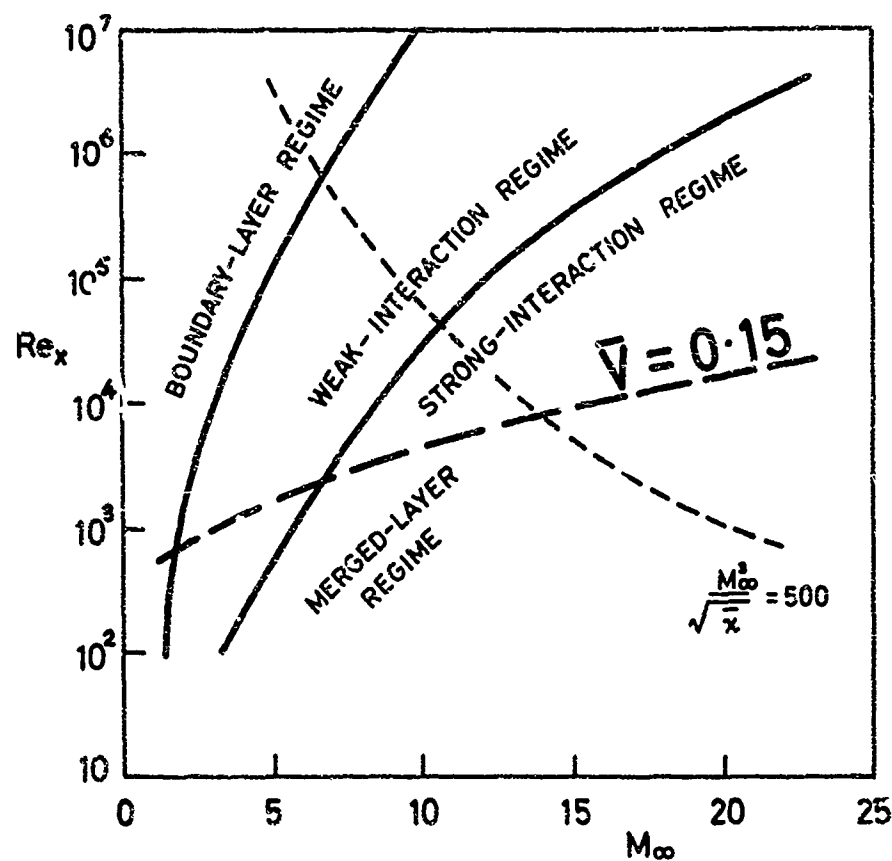


Fig.2 The various flow regimes

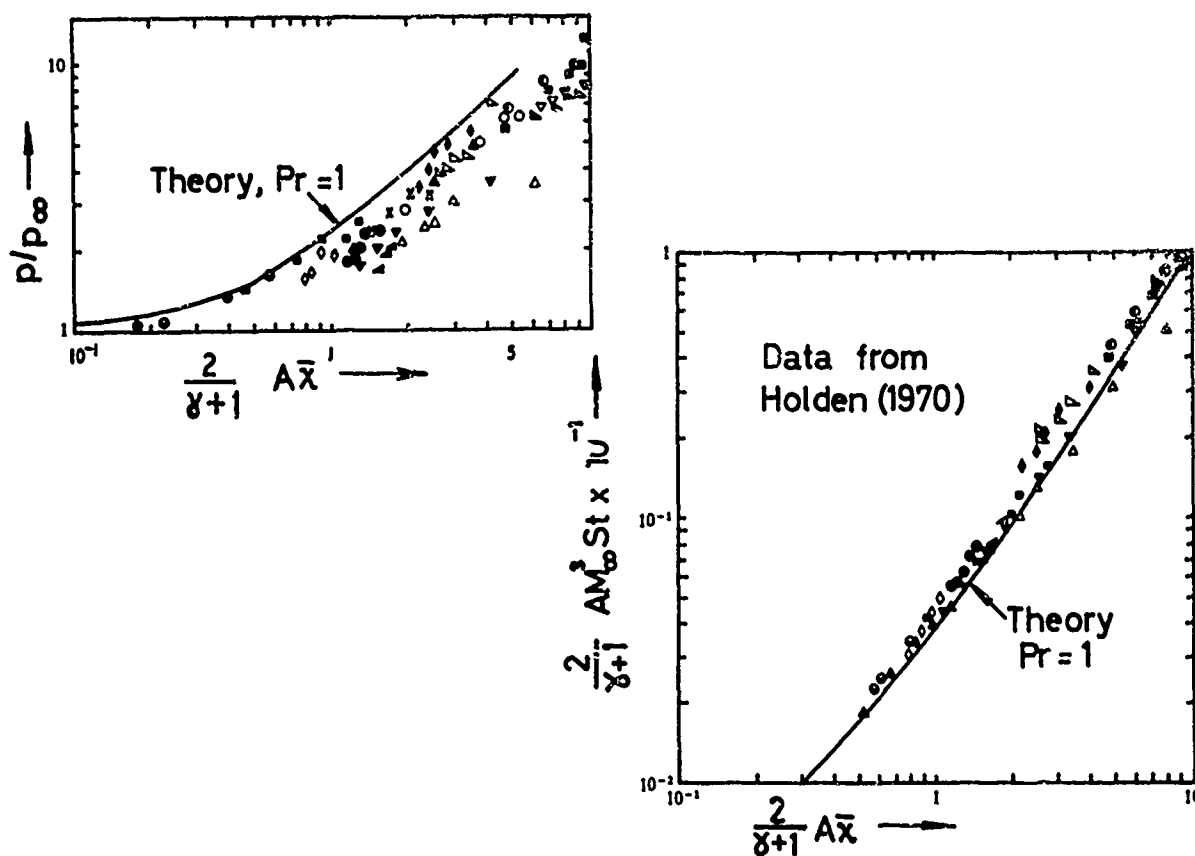


Fig.3 Viscous interaction on a sharp flat plate at zero incidence

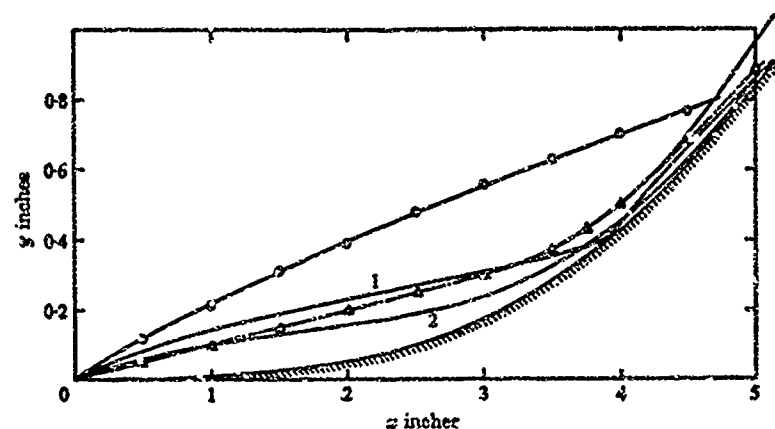


Fig.4 Boundary-layer growth over a cubic concave body, ($y_w = x^3/150$, where x and y_w are in inches).
 —1, δ^* Newton-Rusmann pressure law; —2, δ^* tangent-wedge rule; —○—, shock position from photograph; —△—, "edge" of boundary layer as measured from schlieren photograph

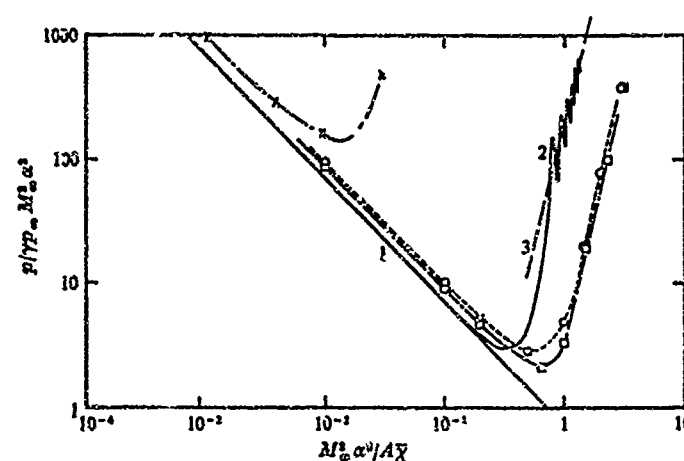


Fig.5a The pressure distribution on a concave surface of the form $y_w = kx^2$. —1, strong interaction, flat plate at $\alpha = 0$; —2, Cheng's theory; ---3, $96\gamma^2(M_\infty^2\alpha^2/A^*)^{1/2}$. Tangent wedge, $M_\infty\alpha$: x, 0.1; O, 1.0. $p_e/p_\infty = 1 + \gamma M_\infty^2 y_e'^2$, $M_\infty\alpha$: □, 1.0.

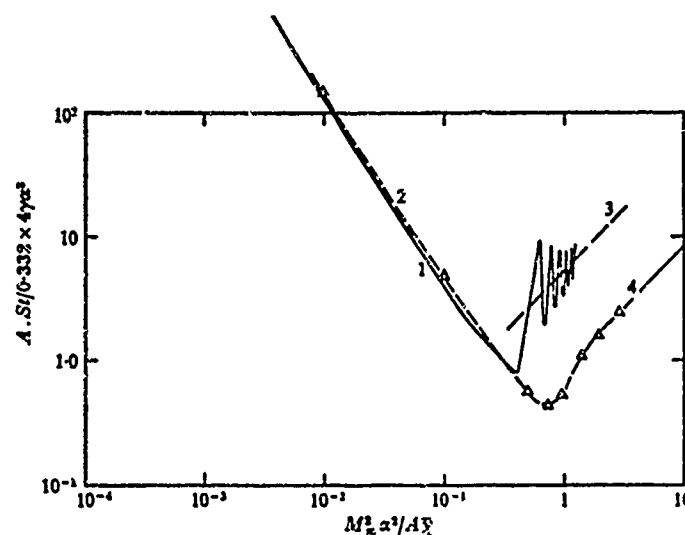


Fig.5b The heat transfer to a concave surface of the form $y_w = kx^2$. —1, Cheng's theory; ---2, solution using tangent-wedge rule, $M_\infty\alpha = 1$; ---3, $6(\frac{1}{2}\gamma)^{1/2}M_\infty^2\alpha^2/A^*$; - -4, asymptotic value, $y_e = y_w$.

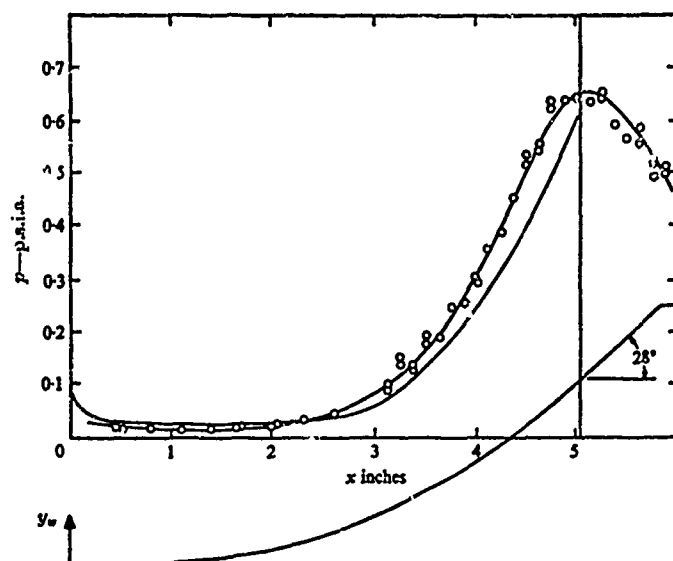


Fig.6 Pressure distribution on a concave cubic body. $y_w = x^3/150$ where x and y_w are in inches and $0 < x \leq 5.1$. —, theory; —○—, measurements, $M_\infty = 12.25$, $Re = 0.86 \times 10^5$ per inch

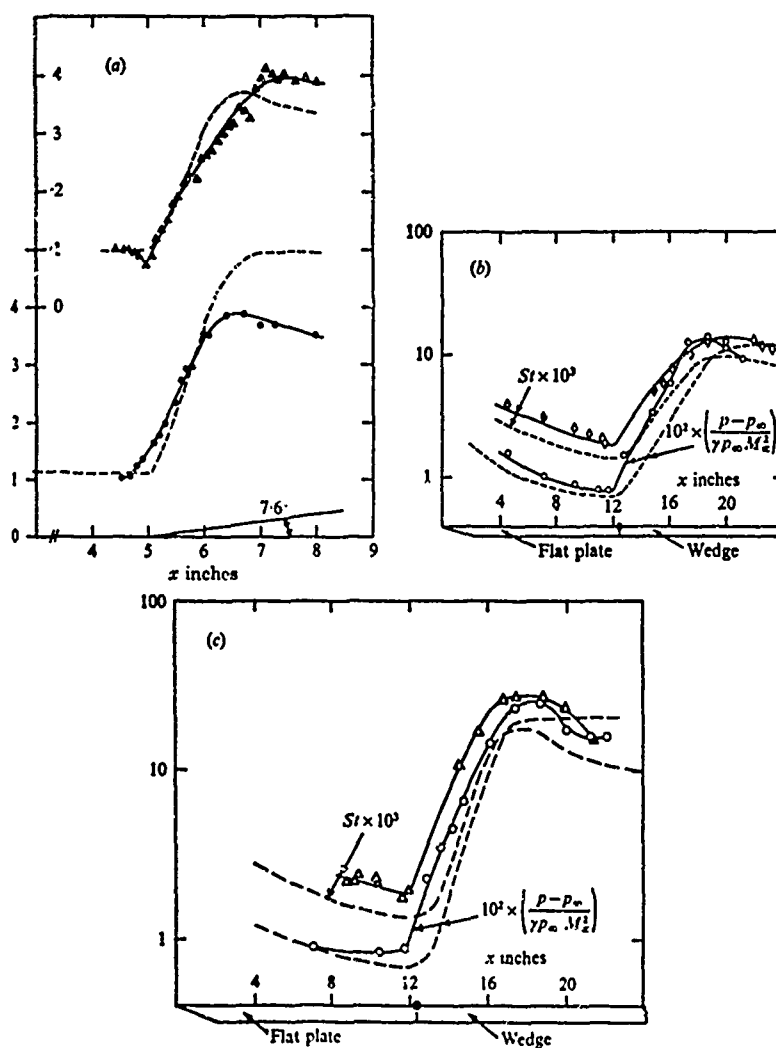


Fig.7 Comparisons between the theoretical and experimental distributions of pressure and heat transfer rate on a compression corner model. ---, theory; —○—, —△—, —◇—, measurements.

- (a) $M_\infty = 9.7$, $\alpha_{\text{wedge}} = 7.7^\circ$, $\bar{x} = 0.87$ at the hinge line.
 (b) $M_\infty = 20$, $\alpha_{\text{wedge}} = 16^\circ$, $\bar{x} = 19.8$ at the hinge line.
 (c) $M_\infty = 20$, $\alpha_w = 21^\circ$, $\bar{x} = 19.8$ at the hinge line.

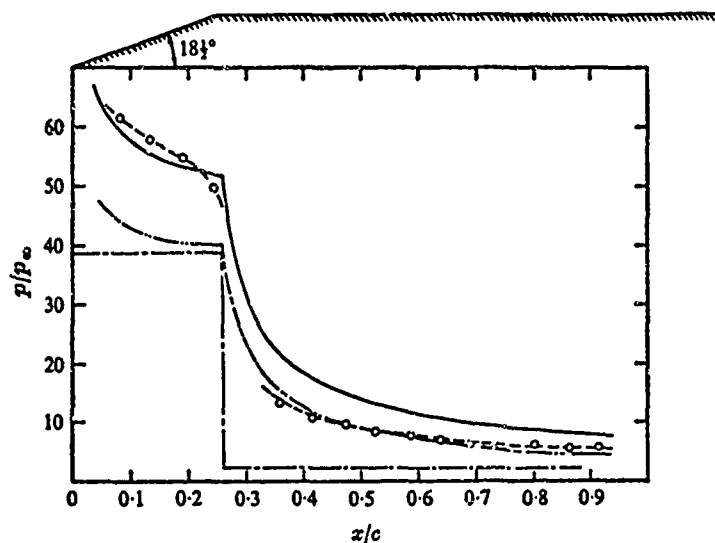


Fig. 8a Pressure distribution over an expansion corner model at zero incidence - a comparison between theory and experiment. --○--, measurements, $M_\infty = 14.8$, $\bar{\chi} = 18.9$ at the corner. Theory: —, Sullivan; ---, Cheng; -.-, inviscid.

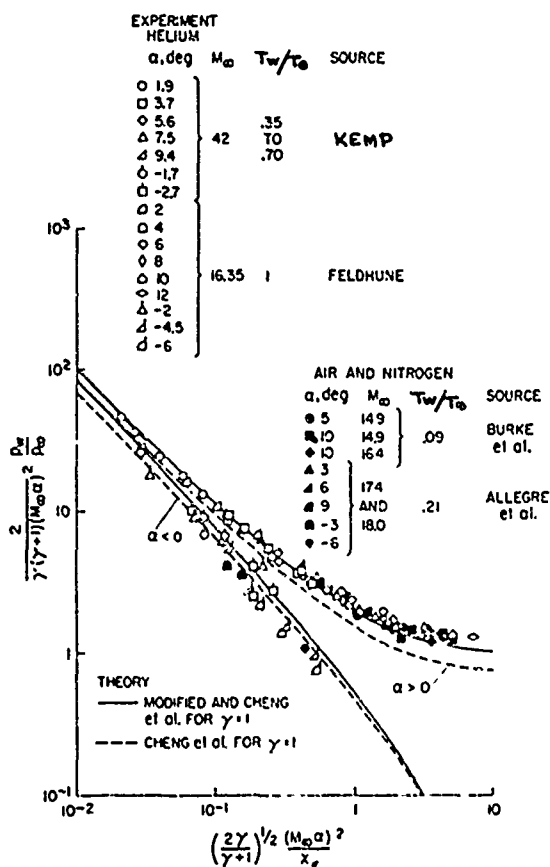


Fig. 8b Pressure on a sharp flat plate

N.B. $\chi_\epsilon = A\bar{\chi} \left(\frac{2}{\gamma+1} \right)$

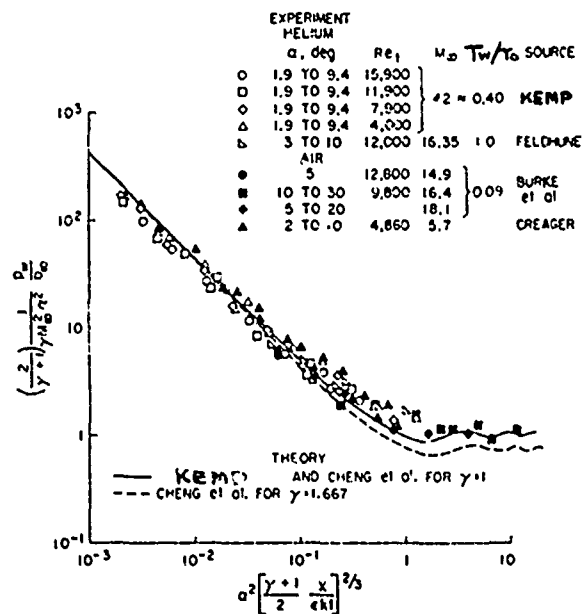


Fig. 8c Pressure on a very blunt flat plate

N.B. $\epsilon = \frac{\gamma-1}{\gamma+1}$

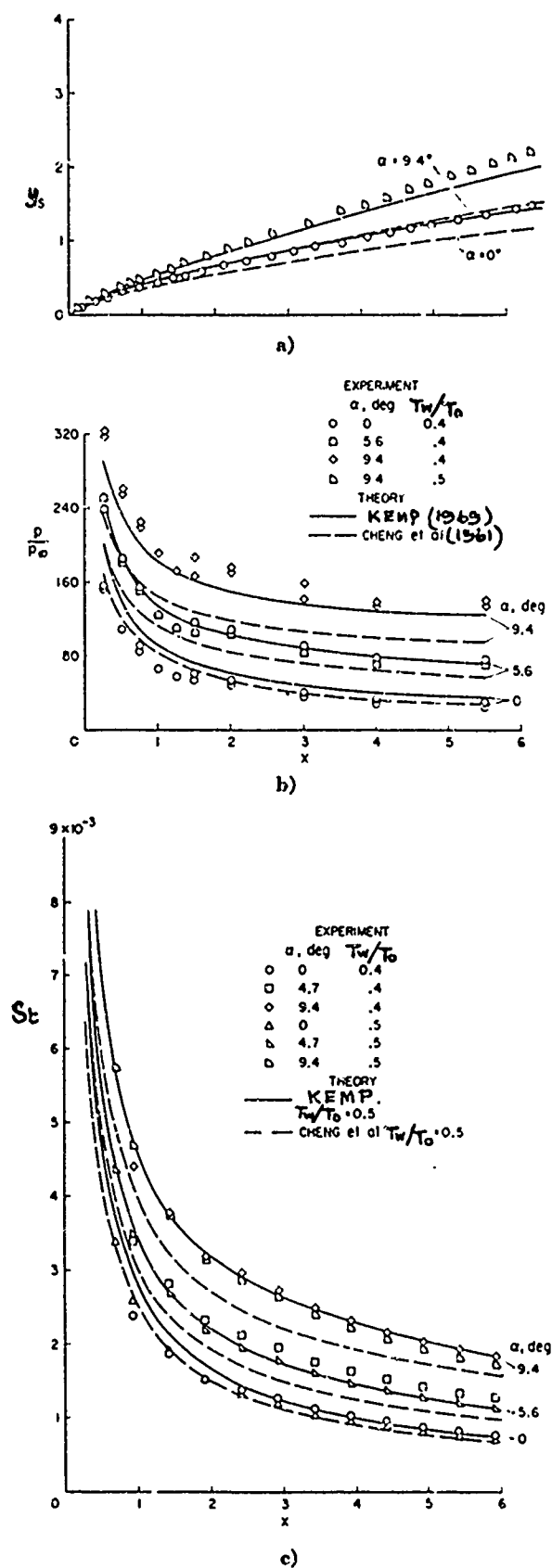


Fig.9 Data for a slightly blunted plate. (a) Shock-wave shape, (b) surface pressure, (c) surface heat-transfer rate.

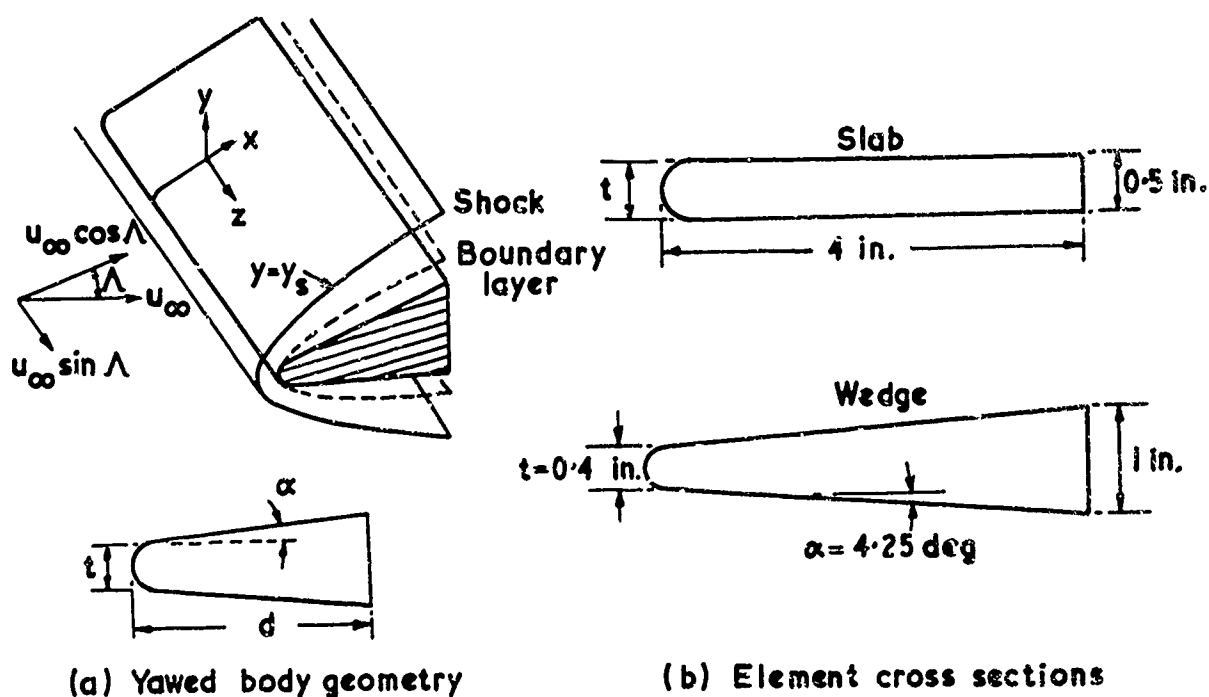
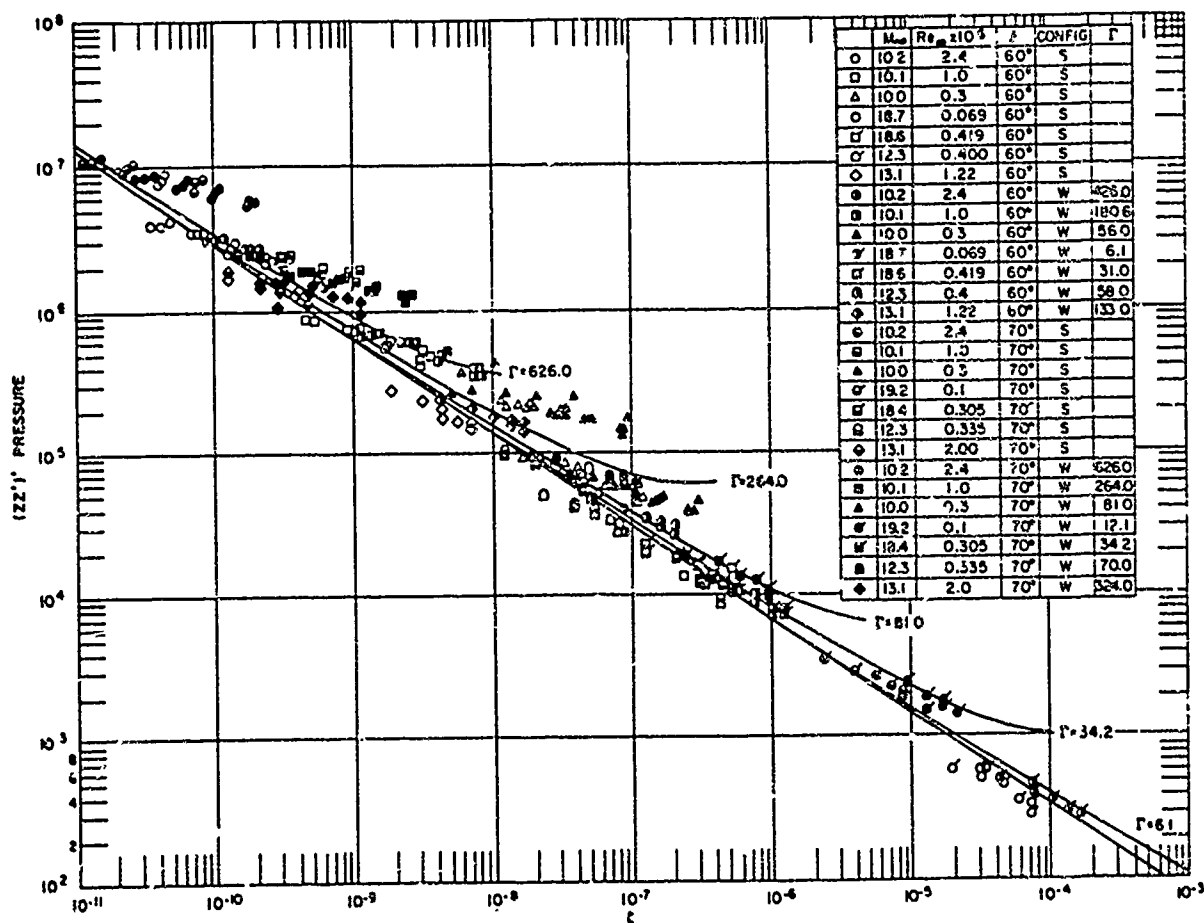


Fig.10 The swept back wing sections tested by Boger and Aiello (1970)

Fig.11 The pressure distribution over a swept wing - the data correlation of Boger and Aiello
(s = slab, w = wedge, see Fig.10b)

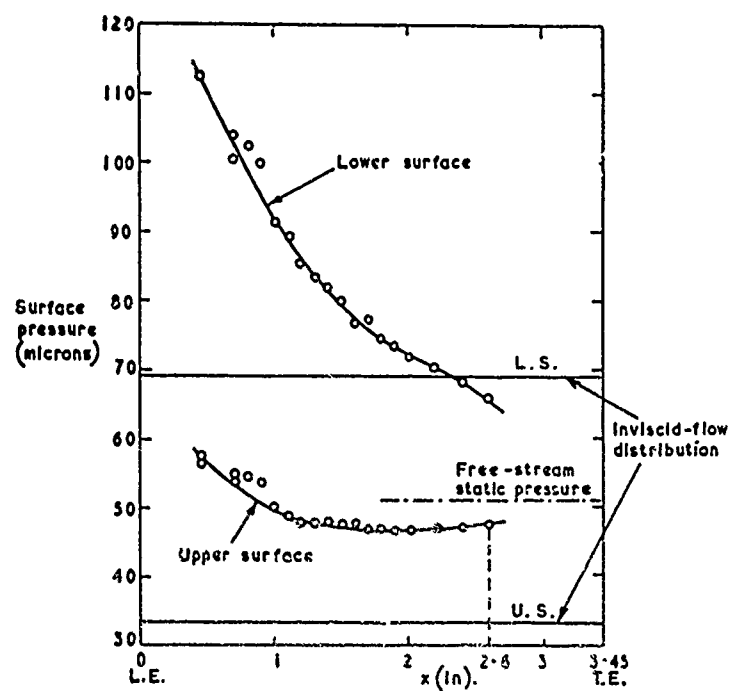
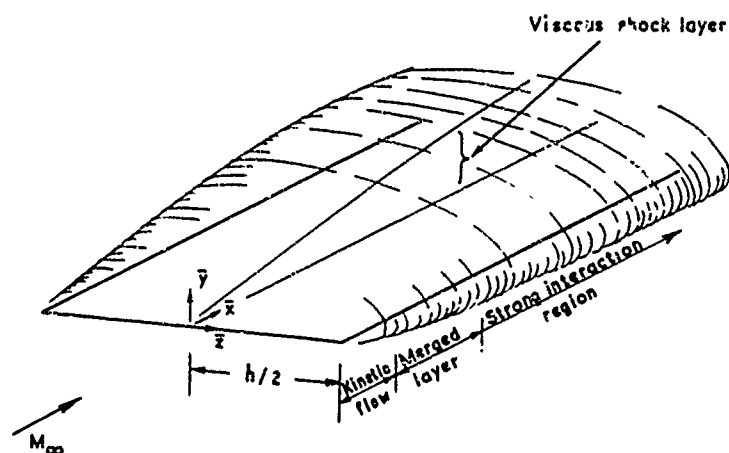
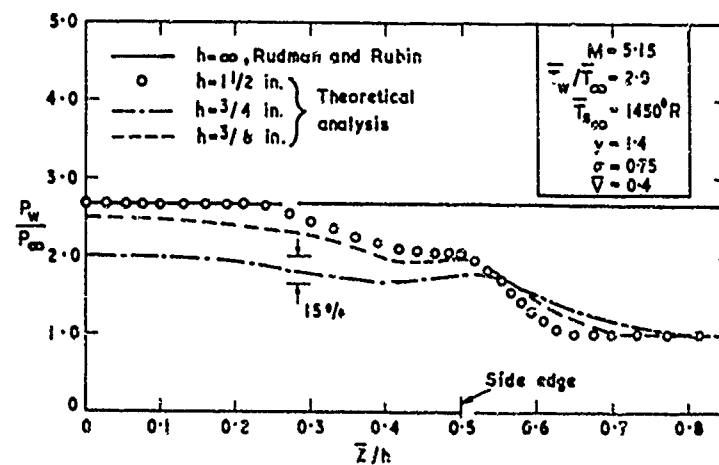


Fig.12 Surface pressure distribution on centre of flat plate at 7° incidence and $M_0 = 2.1$ ($Re \approx 180$ per inch)



(a) Flow system and physical coordinates



(b) Lateral surface pressure variation for different plate widths

Fig.13 the effect of finite span

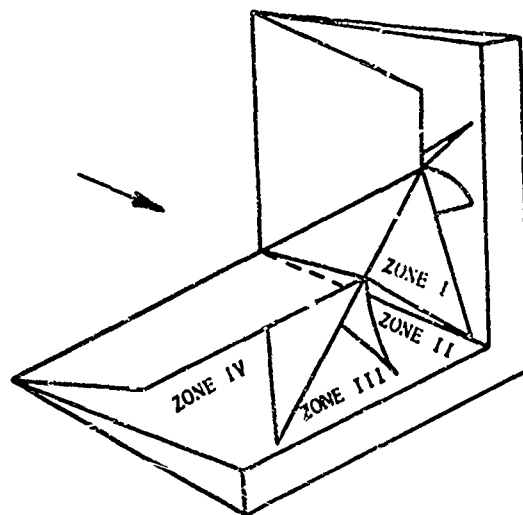


Fig.14 Flow field of Charwat and Redekopp at $M = 3.17$

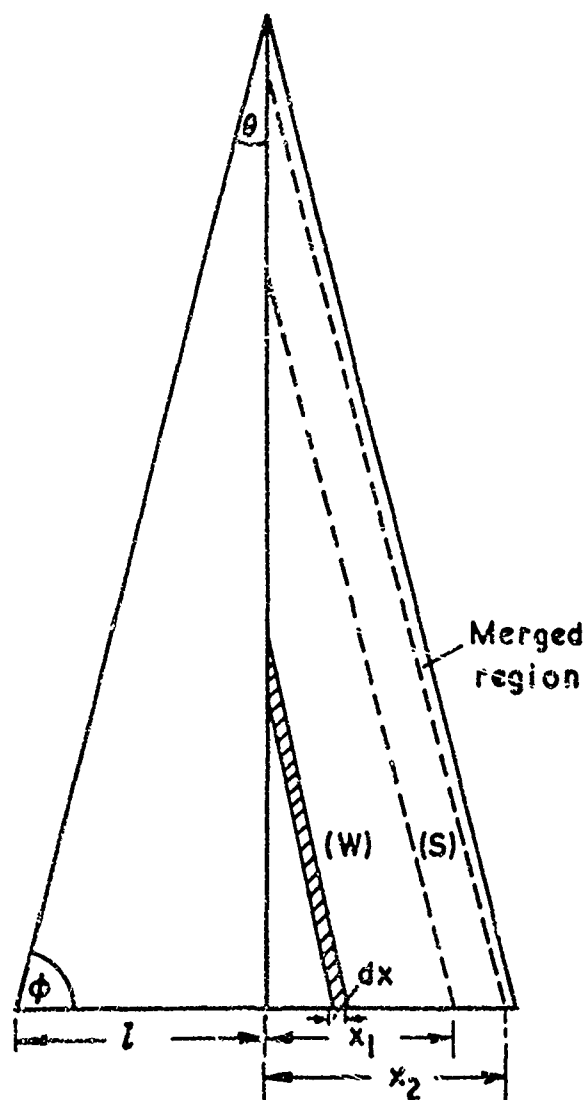
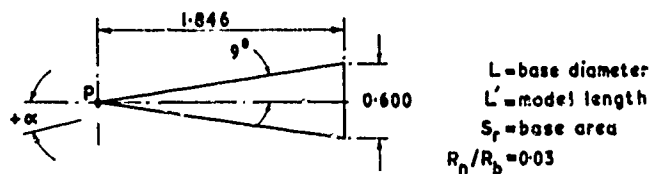
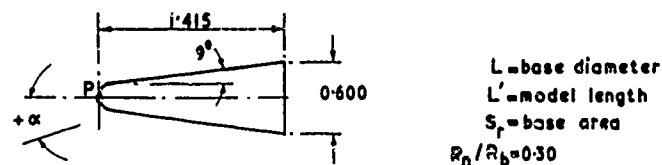


Fig.15 Indicating weak (W) interaction region and strong (S) interaction region

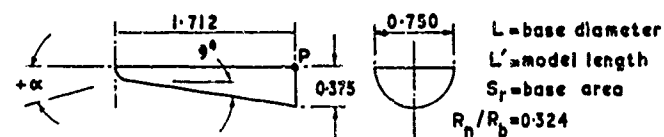
All dimensions in inches



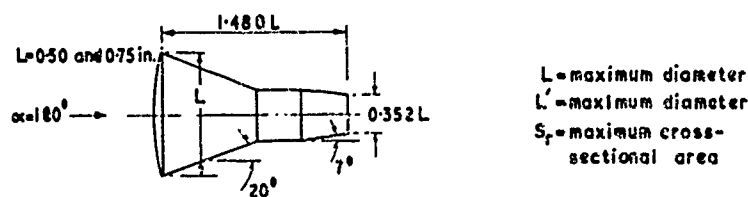
Model A, 9-deg right circular sharp-nosed cone



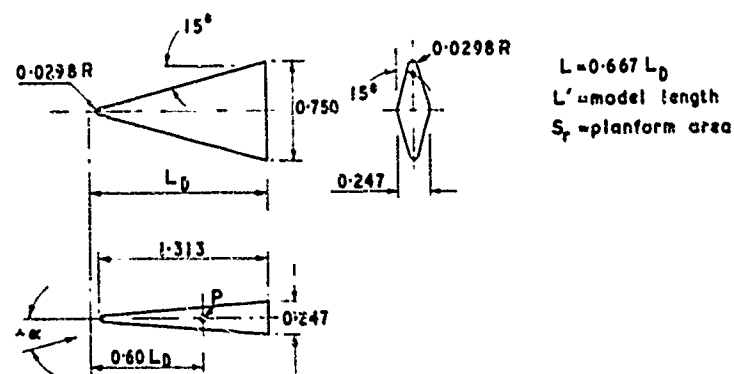
Model B, 9-deg right circular blunt-nosed cone



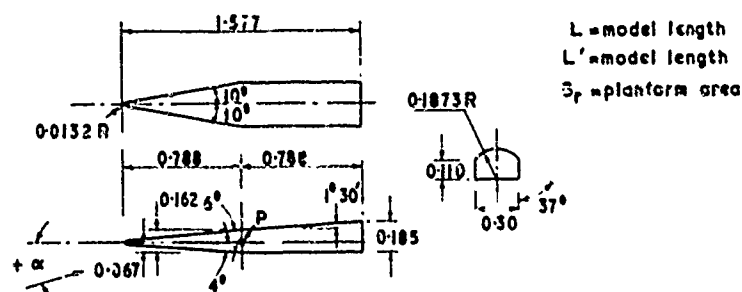
Model C, 9-deg flat-topped blunt-nosed half-cone



Model D, Gemini type model



Model E, 75-deg swept Delta wing



Model F, high lift body

Fig. 16 The shapes tested by Boylan and Potter

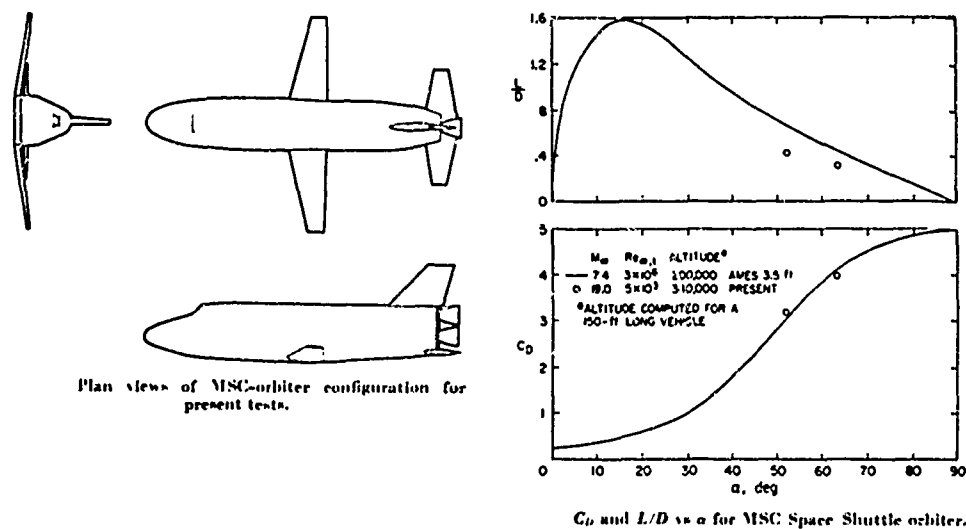


Fig.17 Viscous effects on the Faget Space Shuttle

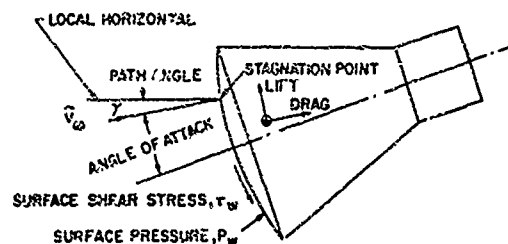
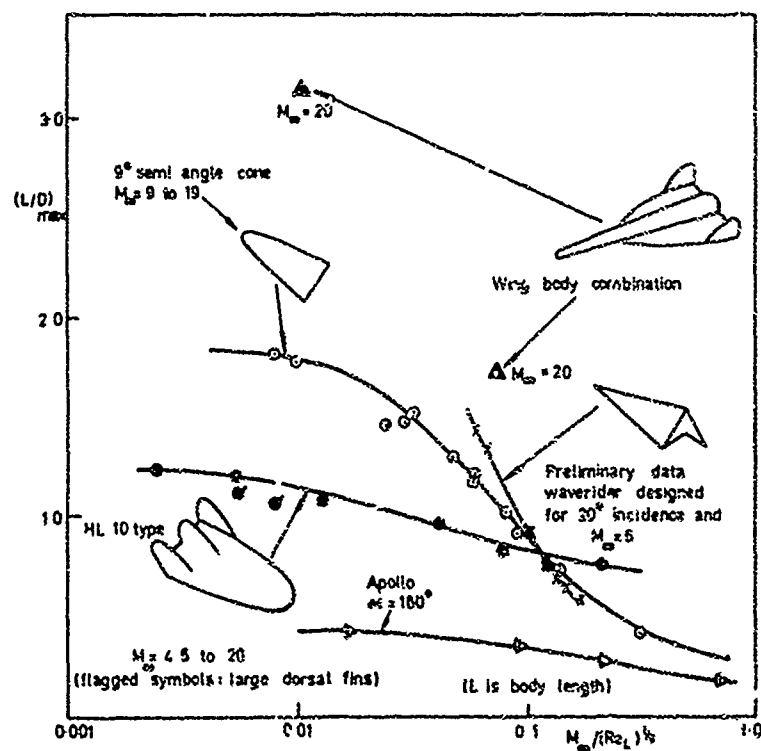


Fig.18 A manned, blunt lifting re-entry vehicle

Fig.19 Viscous effects on hypersonic $(L/D)_{max}$ for 5 classes of vehicle correlated with viscous rarefaction parameter